Solvothermale Synthese und Modifizierung von übergangsmetallhaltigen Antimonchalkogennetzwerken

sowie in-situ-EDXRD/EXAFS-Untersuchungen solvothermaler Reaktionen

Kumulative Dissertation

vorgelegt von

Wolff-Ragnar Kiebach

Institut für Anorganische Chemie der

Christian-Albrechts-Universität zu Kiel

Dezember 2005

Referent/in:.....

Koreferent/in:.....

Tag der Prüfung:.....

Zum Druck genehmigt: Kiel, ...

Der Dekan

Inhaltsverzeichnis

Abbildungsverzeichnis

1 Einleitung

1.1 Motivation, Zielsetzung und Übersicht

Die Darstellung von Materialen mit definierten Porengrößen hat sich in der Festkörperchemie zu einer der bedeutendsten Forschungsrichtungen entwickelt. So finden mikroporöse Materialien Anwendung in vielen chemischen Prozessen. Die Anwendung des Zeolithen ZSM-5 in der Benzinherstellung oder die von Zeolith-A als Ionentauscher seien hier am Rande erwähnt. Neben den bekannten oxidischen Materialien wie Zeolithen oder Aluminophosphaten hat sich in den letzten Jahren die Gruppe der Thioantimonate in der Klasse der mikroporösen Materialien etabliert.

Die Zielsetzung dieser Doktorarbeit bestand aus zwei Teilen: Der erste Teil beschäftigt sich mit der Modifizierung von übergangsmetall (ÜM)-freien oder „reinen“ Thioantimonaten. Hierbei sollen zum einen für die Anwendung nützliche Eigenschaften verbessert oder implementiert werden, zum anderen sollen Schwachstellen, die einer potentiellen Anwendung im Wege stehen, beseitigt werden. Der zweite Teil beschäftigt sich mit der Aufklärung von Bildungsmechanismen und den dazu gehörigen Kinetiken von Verbindungen, die unter solvothermalen Bedingungen gebildet werden. Während bei den oxidischen Materialien, besonders in der Gruppe der Zeolithe, eine Vielzahl an Untersuchungen durchgeführt wurde und relativ genaue Kenntnisse über den Bildungsmechanismus erhalten wurden, ist die Bildung von sulfidischen Materialien wie den Thioantimonaten bisher schlecht untersucht und kaum verstanden. Gerade aber dieses Verständnis ist wichtig um gezielt Parameter in der Synthese zu verändern, sei es um die Synthese zu optimieren oder Materialien mit bestimmten Eigenschaften gezielt zu designen.

1.1.1 Übergangsmetallfreie Thioantimonate

Da ÜM-freie Thioantimonate bereits seit Jahren erfolgreich in unserer Arbeitsgruppe dargestellt werden, soll an dieser Stelle nur eine knappe Beschreibung von Thioantimonaten und ihren Eigenschaften erfolgen.

Mit weit über 50 verschiedenen mikroporösen Verbindungen auf der Basis von Antimonchalkogeniden, die in den letzten Jahren dargestellt und charakterisiert wurden, haben sich besonders Thioantimonate zu einer Verbindungsklasse entwickelt, die bei der Diskussion um Alternativen und Weiterentwicklung von porösen Materialien einen bedeutenden Platz eingenommen hat. Mehrere Faktoren spielen eine Rolle, weshalb Thioantimonate mikroporöse Strukturen aufweisen. Ein wichtiger Punkt ist die große Anzahl an primären Baueinheiten, welche in den Thioantimonaten gefunden wird. Primäre Baueinheiten sind die Bausteine, aus denen die Netzwerkstrukturen aufgebaut sind, und während man bei den Silikaten und Alumosilikaten lediglich starre tetraedrische $[SiO_4]$- und $[AlO_4]$-Baueinheiten findet, kann die Vielfalt der primären Baueinheiten der Thioantimonate mit der allgemeinen Formel $[Sb(III)S_x]$ (x = 3-7) angegeben werden. Ein weiterer Vorteil ist die Flexibilität der SbS_x-Einheiten, besonders die der Bindungslängen und -Winkel aufgrund des stereochemisch aktiven freien Elektronenpaars (lone-pair). Als Folge der unterschiedlichen Baueinheiten und deren Flexibilität ergibt sich die große Vielfalt der Strukturmotive (Abb. 1.1) mit isolierten Anionen [1] bis hin zu dreidimensionalen Netzwerken [2], von $[SbS_3]$-Einheiten als Liganden [3] bis hin zu Neutralverbindungen [4]. Ein weiterer wichtiger Punkt ist der Unterschied der physikalischen Eigenschaften zwischen oxidischen Materialien wie Zeolithen und Thioantimonaten. Deutlich wird dies z.B. anhand der optischen Bandlücke. Bei Zeolithen liegt diese außerhalb des sichtbaren Spektrums, reine Thioantimonate hingegen besitzen eine Bandlücke im sichtbaren Bereich; die meisten ÜM-freien Thioantimonate weisen eine orange bis rote Farbe auf. Thioantimonate vereinen somit die positiven Eigenschaften oxidischer und sulfidischer Materialien in sich. Eine hohe potentielle Porosität und definierte, wenn auch meistens durch „Template“ besetzte, Hohlräume auf der einen sowie interessante physikalische Eigenschaften auf der anderen Seite lassen auf vielfältige Anwendungsmöglichkeiten hoffen. Als Synthesetechnik für diese Verbindungsklasse hat sich die solvothermale Synthese (vergleiche Kapitel 3.1) als geeignete

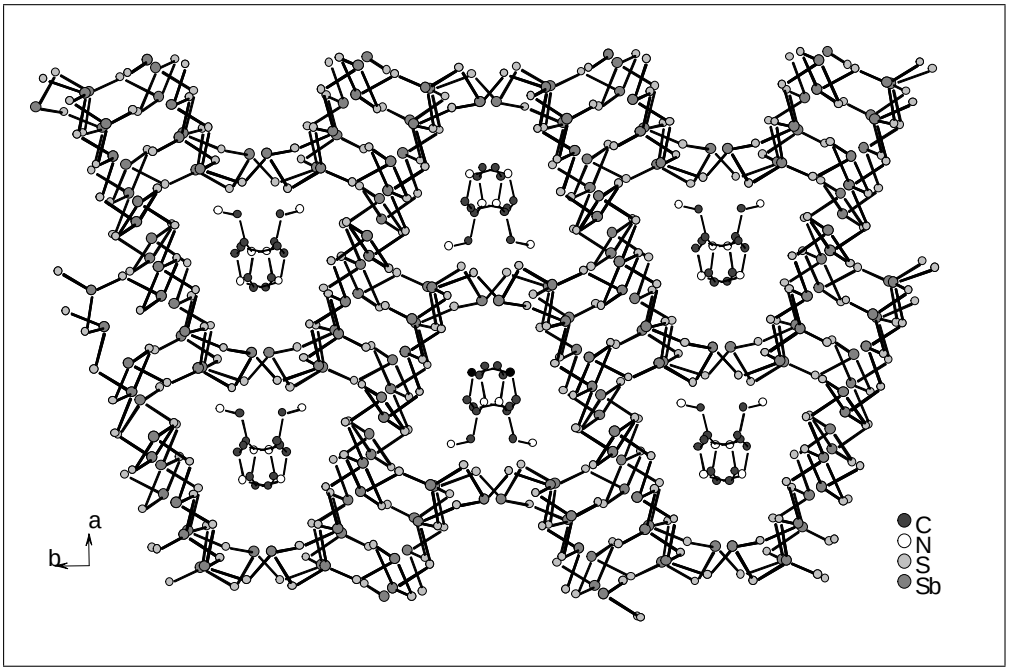

Abbildung 1.1: Kanalsystem in der Verbindung $[C_6H_{17}N_3][Sb_{10}S_{16}]$ mit Blick entlang der *c*-Achse.

Präparationsmethode etabliert. Eine ausführliche Beschreibung der primären und sekundären Baueinheiten, eine genaue Analyse zur Verteilung der Bindungslängen und -Winkel sowie eine Betrachtung zur Dimensionalität von Thioantimonaten finden sich in Übersichtsartikeln [5] sowie den Doktorarbeiten von Angela Puls [6], Ralph Stähler [7], Lars Engelke [8] und Michael Schaefer [9]. Im Rahmen dieser Doktorarbeit gelang die Synthese dreier bisher unbekannter ÜM-freier Thioantimonate. Eine ausführliche Beschreibung der Strukturen, Synthesen und Charakterisierungen der Verbindungen $[C_6H_{17}N_3][Sb_{10}S_{16}]$, $[C_7H_{13}N_2]_3[Sb_9S_{15}]$ und $[C_6H_9N_2][Sb_8S_{13}]\cdot 2.5H_2O$ sind den entsprechenden Publikationen auf Seite 33, 41 und 50 im Hauptteil zu entnehmen.

1.1.2 Modifizierung von Thioantimonaten durch Integration von Übergangsmetallen

Die im vorherigen Kapitel erwähnten strukturellen Eigenschaften der Thioantimonate lassen sich durch Integration von Übergangsmetallen erweitern. Neben den neu gebil-

deten Strukturmotiven ergeben sich interessante physikalische Eigenschaften, wobei magnetische und optische Eigenschaften im Vordergrund stehen. Beispiele für besondere physikalische Eigenschaften ÜM-haltiger Thioantimonate sind z.B. optisch durchstimmbare Bandlücken [10], thermisch induzierbare Phasenumwandlungen [11] oder Supraleitfähigkeit [12]. In den letzten Jahren wurde eine Vielzahl von Thioantimonaten, die zusätzlich zum organischen „Templat“ ÜM-Kationen enthalten, dargestellt. Die häufigsten ÜM sind Ni, Co, Mn, Zn und Cu. Thioantimonate mit ÜM lassen sich in zwei verschiedene Gruppen einteilen. Die erste enthält ÜM-Komplexe als „Template“, welche nicht mit dem Thioantimonatnetzwerk verbunden sind (Abb. 1.2, links). Die so entstehenden Hohlräume weisen ein wesentlich höheres Volumen auf als solche, in denen nur Amine als Platzhalter fungieren. Ein typisches Beispiel ist die Verbindung $[Ni(C_4H_{13}N_3)_2]_9[Sb_{22}S_{42}]$ [13], in der Porengrößen von bis 12 Å gefunden werden. In der zweiten Gruppe ist das ÜM koordinativ mit mindestens einem Schwefelatom des Sb-S-Netzwerkes verbunden. Die freien Koordinationsstellen können wahlweise mit weiteren Schwefelatomen und/oder dem organischem „Templat“ als Ligand besetzt sein (Abb. 1.2, rechts).

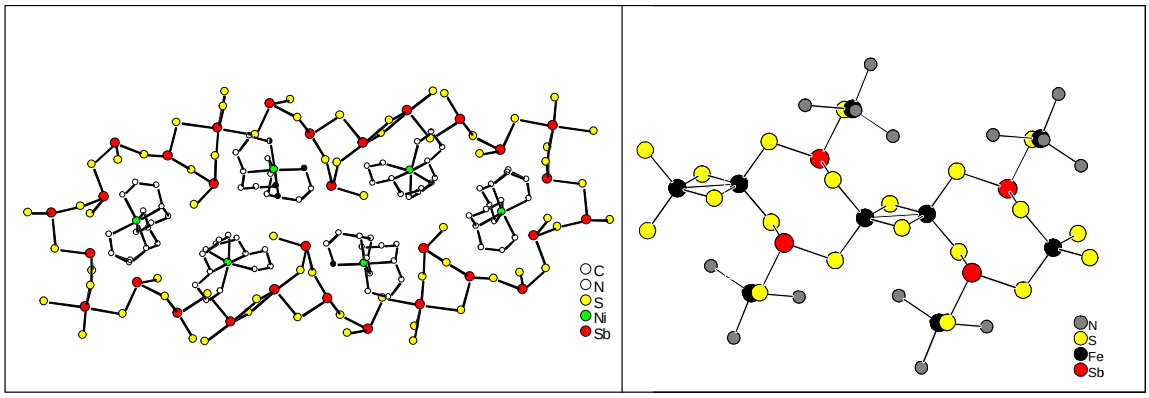

Abbildung 1.2: links: isolierte $[Ni(C_4H_{13}N_2)_2]^{2+}$-Komplexe; rechts: integrierte $[Fe_2S_4]^{2+}$-Gruppen

Während der Doktorarbeit gelang die Synthese vier neuer ÜM-haltiger Thioantimonate, wobei der Schwerpunkt der Synthesen auf Eisen als ÜM lag. Eisen ist besonders attraktiv, da es magnetisch interessant ist. Es tritt oft in der Oxidationsstufe +3 auf und ist damit ein gut geeignetes Ion zur Untersuchung des Guest-Charge-Host-

Matching geeignet. In diesem Konzept geht es um die Frage, wie sich Kationen mit hoher Ladungsdichte in die Thioantimonatnetzwerke mit negativer Ladung einfügen und ob hochgeladene Gastionen zu einem offeneren Netzwerk führen. Beispiele für die Integration von ÜM in die Netzwerkstruktur stellen die im Rahmen der Doktorarbeit dargestellten Verbindungen $[Fe(C_6H_{18}N_4)][FeSbS_4]$, $[Fe(C_6H_{13}N_3)_2][Fe_2Sb_4S_{10}]$ und $[Fe(C_6H_{18}N_4)][Sb_4S_7]$ dar. In der Verbindung $[Fe(C_6H_{13}N_3)_2][Fe_2Sb_4S_{10}]$ finden sich zusätzlich zu $[Fe_2S_4]^{2+}$-Gruppen im Sb-S-Netzwerk isolierte $[Fe(C_6H_{13}N_3)_2]^{2+}$-Komplexe. Somit besitzt diese Verbindung sowohl einen ÜM-Komplex als „Templat“ als auch ins Sb-S-Netzwerk integrierte ÜM. Ausführliche Strukturbeschreibungen und Charakterisierungen dieser Verbindungen sind den Veröffentlichungen auf Seite 79 und 89 zu entnehmen.

Die Verbindung $[Ni(C_4H_{13}N_3)_2]_3[(Sb_3S_6)_2]$ entstand bei einer Versuchsreihe, in welcher der Einfluss des Lösungsmittels auf die Produktbildung untersucht wurde. Thioantimonate mit $Ni(dien)_2^{2+}$-Komplexen als „Templaten“ wurden ausführlich in der Doktorarbeit von Ralph Stähler [8] untersucht und charakterisiert. Die Substitution von Wasser als Lösungsmittel durch Methanol führte zur Bildung der Verbindung $[Ni(C_4H_{13}N_3)_2]_3[(Sb_3S_6)_2]$, deren Struktur, Eigenschaften und Vergleich mit theoretischen Strukturmodellen auf Seite 98 vorgestellt werden.

1.1.3 Modifizierung von Thioantimonaten durch Variation des Chalkogenatoms

Eines der größten Probleme bei den Thioantimonaten stellt die Tatsache dar, dass es nicht möglich ist die Amine bzw. die organischen „Template“ durch Calcinierung thermisch aus der anorganischen Wirtsmatrix zu entfernen. Anders als bei Zeolithen, die nur SiO_4-Einheiten enthalten, sind bei Thioantimonaten in den seltensten Fällen die Sb-S-Netzwerke oder die organischen Komponenten ladungsneutral. Werden die Verbindungen erhitzt, werden zwar die organischen Komponenten emittiert, allerdings kollabiert das gesamte Netzwerk aufgrund der fehlenden Abstandshalter sowie der nicht mehr vorhandenen Ladungsneutralität. Die Hoffnung war, dass eine partielle Substitution von Schwefel durch Sauerstoff zu Verbindungen führen würde, die -OH Gruppen enthalten. In diesen Verbindungen wären Netzwerkstruktur und „Template“

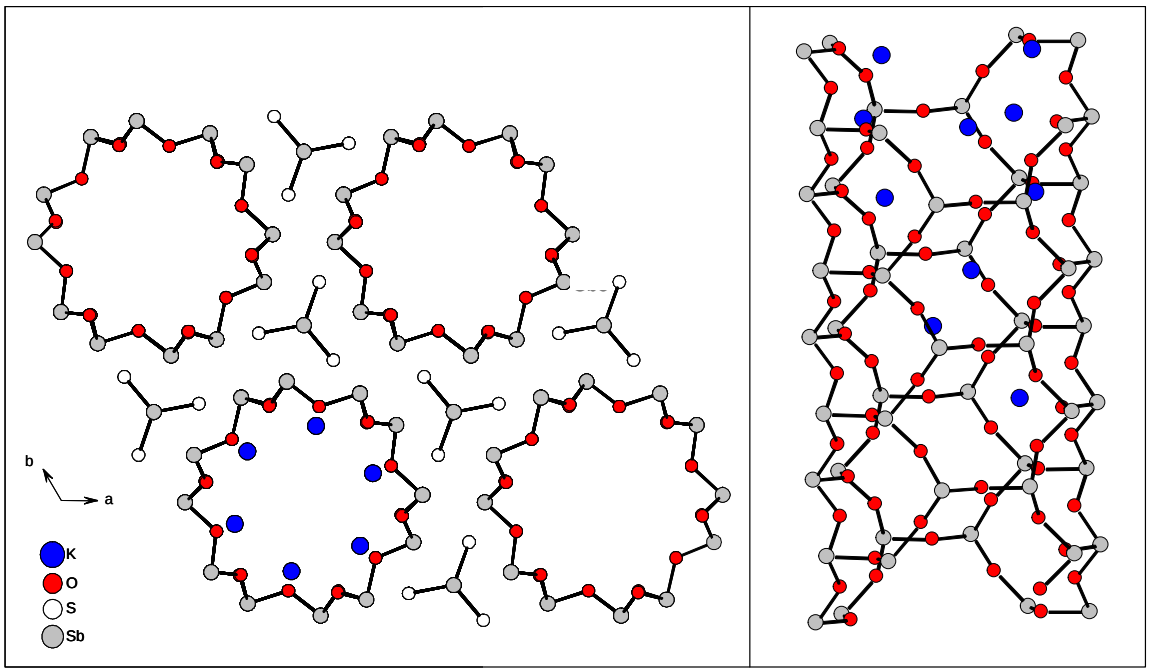

Abbildung 1.3: Kanalsystem in Cetineiten, links: Draufsicht, rechts: Seitenansicht

ladungsneutral. Trotzdem sollten die Verbindungen die gewünschten Eigenschaften sulfidischer Materialien aufweisen. Vorbild war die Gruppe der Cetineite, Mineralien, welche von Liebau und seinen Mitarbeitern synthetisch dargestellt werden konnten und die interessante Eigenschaft als Photohalbleiter aufweisen [14][15][16]. Allgemein können Cetineite mit der Summenformel $A_6[B_{12}O_{18}][CX_3]_2[D_x(H_2O,OH,O)]_{6-y}$ ($0 \leq x \leq 2$; $0 \leq y \leq 6$) (A = Li, Na, K, Rb, Cs, Tl, NH_4, Ca, Sr, Ba; B = C = As, Sb, Bi; X = S, Se; D = Na, Sb, C) beschrieben werden. Auffälligstes Strukturmerkmal der Cetineite sind 1-dimensionale elektroneutrale Kanäle aus $[SbO_3]$-Einheiten, in denen sich die jeweiligen Kationen (A) befinden. Ein Ladungsausgleich wird durch $[SbS_3]^{3-}$-Anionen erreicht (Abb. 1.3).

Die Synthese solcher oxysulfidischer Materialien erwies sich in der Praxis als wenig erfolgreich. Als mögliche Sauerstoffquellen wurden Sb_2O_3, $ÜM_xO_y$ und/oder Alkalihydroxide benutzt. In den meisten Fällen wurden als Produkte reine Thioantimonate erhalten, bei der Zugabe von Alkalihydroxiden die entsprechenden Cetineite. Nur die Kombination von Sb_2O_3 mit Tris-2-aminoethyl-amin (tren) als „Templat“ führte zu

einer neuen Verbindung der Zusammensetzung $[C_6H_{20}N_4][Sb_9S_{14}O]$, die sowohl Schwefel als auch Sauerstoff in der Netzwerkstruktur enthält. Interessanterweise wird in dieser nicht-centrosymetrischen Verbindung eine bislang unbekannte primäre Baueinheit $[SbS_2O]$ gefunden, die weder in oxysulfidischen Mineralien noch in synthetisch dargestellten Verbindungen beobachtet werden konnte. Eine weiterführende Beschreibung der Struktur und eine vollständige Charakterisierung sind der Veröffentlichung auf Seite 104 zu entnehmen. Eine Erklärung für das Entstehen reiner Antimon-Schwefel-Verbindungen könnte in der Dominanz von $[Sb_xS_y]^{-[2y-3x]}$-Einheiten als löslicher Spezies in alkalischer, sulfidischer Lösung liegen. Die durch Kristallisation entstehenden Produkte können nur Baugruppen enthalten, die auch in löslicher Form vorliegen. Für die Kristallisation ist zudem ein Überschreiten des Löslichkeitsproduktes erforderlich. $[SbX_y]$-Einheiten mit einer extrem hohen Löslichkeit - wie z.B. Antimonate(V)- sind daher nicht in den Kristallisationsprodukten enthalten. Eine ausführliche Beschreibung der in Lösung enthaltenen Sb-S-Spezies und mögliche Bildungsmechanismen werden im Kapitel 1.2 diskutiert.

Der Versuch, die Präsenz von $[SbS_xO_y]$-Einheiten in Lösung durch Variation des Oxid-Sulfid-Verhältnisses zugunsten der Sauerstoffkomponenten zu erzwingen, schlug fehl. Selbst ein minimaler Anteil an S von <10 % reicht aus, um rein sulfidische Produkte entstehen zu lassen. Ein völliger Verzicht auf eine Schwefelkomponente hat aber zur Folge, dass das Antimonedukt (Sb oder Sb_2O_3) nicht reagiert, folglich ist die Präsenz von Schwefel zur Produktbildung erforderlich.

Eine völlg neue Verbindungsgruppe erschließt sich allerdings, wenn bei Schwefelverzicht eine Vanadiumquelle (V_2O_5 oder NH_4VO_3) als zusätzliches Edukt eingesetzt wird. So konnten im Rahmen dieser Doktorarbeit drei neue Antimon-Vanadium-Oxid-Cluster mit organischen „Templaten“ dargestellt werden. Diese drei Verbindungen lassen sich als Antimonderivate der $[V_{18}O_{42}]$-Familie (Abb.1.4, rechts) [17] beschreiben. Als primäre Baueinheiten finden sich verzerrte tetragonale VO_5-Pyramiden und „henkelförmige“ Sb_2O_5-Polyeder. Eine Verknüpfung dieser Baueinheiten erfolgt über gemeinsame Ecken und Kanten. Die 24 verbrückenden μ_3-O-Atome bilden bei idealisierter Geometrie einen Rhombenkuboktaeder (Abb. 1.4, links). Ausgehend von einem $V_{18}O_{42}$-Gerüst gelangt man durch formalen Austausch von V=O- gegen Sb_2O_5-Gruppen zu den drei neuen Verbindungen $[trenH_3]_2[tren]_{0.33}[Sb_6V_{15}O_{42}]\cdot xH_2O$

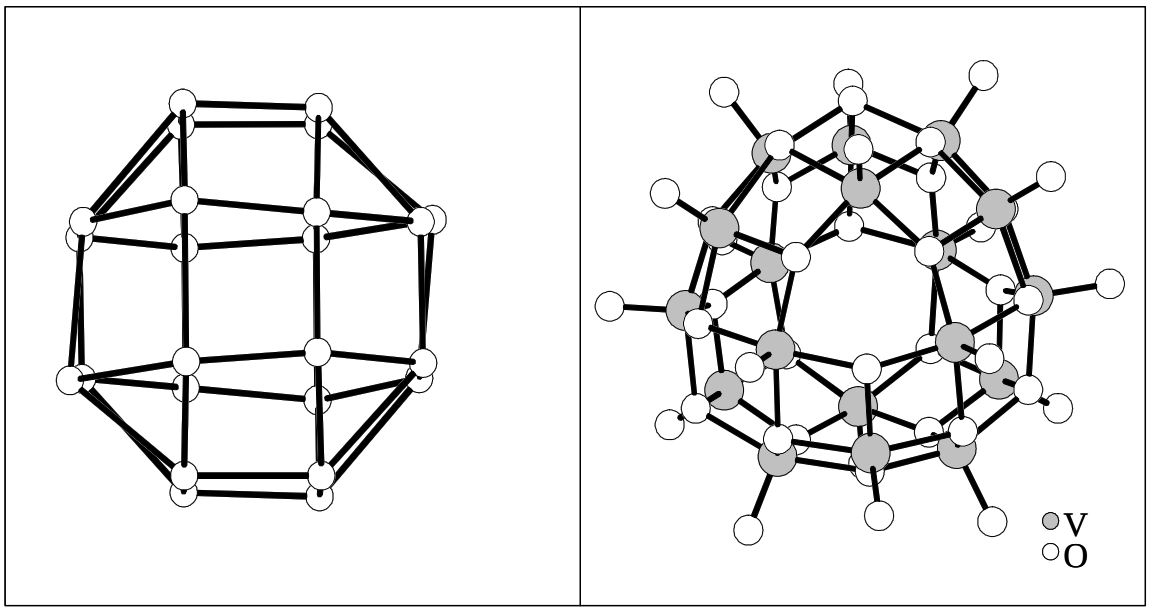

Abbildung 1.4: Rhombenkuboktaeder aus 24 Sauerstoffatomen, rechts: $[V_{18}O_{42}]$-Cluster der Verbindung $Na_6[V_{18}O_{42}H_9(VO_4)]\cdot 21\ H_2O$

(3<x<5), $[C_6H_{17}N_3]_4[Sb_4V_{16}O_{42}]\cdot 2H_2O$ und $[NH_4]_4[Sb_8V_{14}O_{42}]\cdot 2H_2O$. Allgemein lassen sich diese Verbindungen mit der Formel $[(AminH)_mSb_{2x}V_{18-x}O_{42}]\cdot nH_2O$ (x = 2 – 4) beschreiben. Eine ausführliche strukturelle Beschreibung der Verbindungen $[C_6H_{17}N_3]_4[Sb_4V_{16}O_{42}]\cdot 2H_2O$ und $[NH_4]_4[Sb_8V_{14}O_{42}]\cdot 2H_2O$ findet sich in der Veröffentlichung auf Seite 137, Struktur und Untersuchungen der Verbindung $[trenH_3]_2[tren]_{0.33}[Sb_6V_{15}O_{42}]\cdot xH_2O$ (3<x<5) sind der Publikation auf Seite 117 zu entnehmen.

Für potentielle Anwendungen sind diese neuen Verbindungen aus mehreren Gründen von Interesse. Zum einen werden Chalkogenverbindungen der elektronenarmen d-Gruppen Elemente V, Mo und W aufgrund ihrer bemerkenswerten strukturellen und elektronischen Eigenschaften seit längerem in der technischen Katalyse eingesetzt [18], zum anderen ist die Elementkombination Antimon-Vanadium-Sauerstoff ebenfalls für katalytische Anwendungen von Bedeutung, wie z.B. bei der selektiven Oxidation von o-Xylen [19].

Am bemerkenswertesten ist allerdings die strukturelle Ähnlichkeit der Verbindung $[trenH_3]_2[tren]_{0.33}[Sb_6V_{15}O_{42}]\cdot xH_2O$ (3<x<5) mit dem bekannten und intensiv unter-

suchten molekularen Magneten $K_6[As_6V_{15}O_{42}(H_2O)]\cdot 8H_2O$ [20][21].

1.1.4 Modifizierung von Thioantimonaten durch Verwendung chiraler Template

Seit Jahren ist die Synthese chiraler mikroporöser Materialien, besonders auf dem Gebiet oxidischer Materialien, Forschungsgebiet verschiedener Arbeitsgruppen. Die Erfolge sind bisher als gering zu bezeichnen. So lassen sich z.B. Zeolithe problemlos mit chiralen „Templaten“ synthetisieren, allerdings geben diese ihre chiralen Information nicht an die sie umgebende Netzwerkstruktur weiter. Wird also das organische „Templat“ aus der Wirtsstruktur entfernt, verliert das verbleibende mikroporöse Material seine chiralen Eigenschaften. Chirale Thioantimonate sind bis dato nicht bekannt, die Motivation hingegen solche darzustellen um so größer. Neben der potentiellen Anwendung chiraler Materialien in der Katalyse - Hauptmotivation zur Darstellung chiraler Zeolithe - ist die Anwendung in dem Bereich von Stoffen mit einem nicht linearem optischem Effekt (NLO) hervorzuheben. Oxidische Materialien sind oft farblos mit einer optischen Bandlücke von > 3.0 eV, Thioantimonate sind in der Regel farbig und decken einen weiten Bereich optischer Bandlücken ab. Chiralität oder Nicht-Centrosymmetrie ist die Voraussetzung für das Auftreten von NLO-Effekten, eine Bedingung, die bei der Anwesenheit von chiralen „Templaten“ erfüllt ist. Dass Thioantimonate, die in nicht-centrosymmetrischen Raumgruppen kristallisieren, viel versprechende Kandidaten sind, wurde mit der Verbindung $[Zn(tren)]_4[Sb_{12}S_{22}]$ eindrucksvoll bewiesen [9].

Bei den Thioantimonaten sind Verbindungen bekannt, in denen Übergangsmetallkomplexe in die Netzwerkstruktur integriert sind (vergleiche Kapitel 1.2). Bei weiteren synthetischen Arbeiten war die Überlegung, die koordinative ÜM-Schwefel-Bindung zwischen einem chiralen Komplex und dem Thioantimonatnetzwerk als Zugangspunkt zur Übertragung chiraler Information an das Netzwerk zu nutzen. Als geeignetes Reagenz wurde 1,2-Diaminopropanol gewählt, da es die nötige Basizität zum Auflösen der Edukte hat, und sowohl das racemische Gemisch als auch die chiralen Reagenzien sind günstig käuflich zu erwerben. Bisher waren keine Thioantimonate mit Aminoalkohlen als organischen „Templaten“ bekannt. Erfahrungsgemäß sind mehrere dutzend, oftmals sogar weit über hundert Versuche nötig um die Reaktionsbedingungen zu fin-

den, die zu kristallinen Produkten führen. Daher wurde zu Beginn der Arbeiten ein racemisches Gemisch eingesetzt, um die Kosten in Grenzen zu halten. Sind diese Reaktionsbedingungen optimiert, so können die reinen chiralen Reagenzien umgesetzt werden. Diese sind oft käuflich erwerblich oder lassen sich im Falle von Aminoalkohlen durch Reduktion der entsprechenden Aminosäuren einfach darstellen. Im Rahmen der Doktorarbeit gelang es, zwei Thioantimonate mit 1,2-Diaminopropanol als organischem „Templat“ zu synthetisieren. Eine genaue Beschreibung und Charakterisierung der formelgleichen Verbindungen $[C_3H_{10}NO]_2[Sb_4S_7]$ kann der Veröffentlichung auf Seite 157 entnommen werden. Die erfolgreiche Synthese dieser Verbindungen belegt, dass Aminoalkohole als Strukturdirektoren bei der solvothermalen Synthese von Thioantimonaten eingesetzt werden können, und damit ist ein erster Schritt auf dem Weg zu den gewünschten chiralen Materialien gemacht. Als nächster Schritt muss die Verknüpfung des Aminoalkohols mit dem Sb-S-Netzwerk über ein Übergangsmetall erfolgen.

1.2 Das Antimonatom in alkalischer, sulfidischer Lösung

Die Frage nach löslichen Antimonspezies beschäftigt seit langem besonders Geologen. So werden besonders bei hohen Temperaturen und hohen pH-Werten in geothermalen Systemen signifikante Mengen an Antimon gefunden, oft in Gesellschaft von Arsen. Die Kenntnis der vorliegenden gelösten Spezies ist von Bedeutung, um ablaufende hydrothermale Prozesse unter Beteiligung von Antimon zu verstehen, sowohl in der Synthese als auch in geochemischen Prozessen. Hinzu kommt, dass die Toxizität von Antimon zur Zeit neu diskutiert wird. Die Kenntnis, in welcher Form Antimon im Trinkwasser vorliegt, ist hierbei von besonderer Bedeutung.

In den letzten fünfzig Jahren erschien einen große Anzahl an Publikationen, in denen über mögliche lösliche Antimonspezies berichtet wurde. Die Zahl der vermuteten Spezies ist dabei allerdings genau so groß wie die Zahl der Publikationen, und eine ganze Bandbreite an verschiedenen Geometrien, Oxidationsstufen und Spezies mit unterschiedlichen Protonierungsgraden wurden postuliert. Im folgenden wird über die

verschieden Modelle und die dazu gehörigen Methoden ein Überblick erstellt. In stark chloridhaltigen oder schwefelfreien, alkalischen Lösungen liegen dreiwertige Chloro- bzw. Hydroxokomplexe des Antimons vor, während bei Anwesenheit von Schwefel fast ausschließlich $[Sb_xS_y]^{z-}$-Komplexe vorhanden sind. Die erste Veröffentlichung zur möglichen Zusammensetzung dieser Spezies erschien 1956 [22] und beschäftigte sich mit Reaktionsgleichgewichten bei der Bildung von Thiosalzen. Aus den Ergebnissen von Löslichkeitsexperimenten wurde eine $[SbS_2]^-$-Spezies formuliert. Mit derselben Methode kamen Dubey et al. im Jahre 1962 [23] und Arntson et al. 1966 [24] zu den Ergebnissen, dass $[Sb_2S_4]^{2-}$- bzw. $[Sb_4S_7]^{2-}$-Komplexe die dominierenden Spezies seien. Aufgrund der Resultate von Löslichkeitsmessungen und der Reinterpretation der Daten von Babko et al. wurde 1982 von Kolpakova et al. [25] postuliert, dass Antimon in sulfidischer Lösung als $[HSb_2S_4]^-$-Dimer vorliegt. Die ersten Ergebnisse aufgrund von potentiometrischen Untersuchungen veröffentlichten Shestiko et al. im Jahr 1971 [26]. Postuliert wurden neben der monomeren $[SbS_3]^{3-}$-Spezies die oligomeren $[Sb_2S_5]^{4-}$- und $[Sb_4S_7]^{2-}$-Einheiten. Die ersten in-situ-Untersuchungen wurden von Wood et al. im Jahr 1989 [27] mit Ramanspektroskopie durchgeführt. Als lösliche Spezies im sulfidischen Medium wurden entweder $[SbS_2]^-$- oder $[SbS_3]^{3-}$-, bei hohen Konzentrationen $[Sb_2S_4]^{2-}$-Einheiten postuliert. Eine exakte Bestimmung war allerdings auch hier nicht möglich, da die relativ ähnlichen Geometrien und Strukturmotive nicht unterscheidbare Moden liefern. Allerdings konnte aufgrund der Ergebnisse die Präsenz von Oligomeren bei niedrigen Konzentrationen ausgeschlossen werden.

Einen ausführlichen Vergleich von Modellen und Schwingungsfrequenzen aus abinitio Hartree-Fock-Rechnungen mit experimentellen Daten, unter anderem die von Wood et al., führten Tossell et al. 1994 [28] zu der Annahme, dass die monomeren Spezies $[SbS(SH)_2]^-$ oder $[SbS_2(SH)]^{2-}$ dominierend seien. Für koexestierende oligomere Spezies ist nach theoretischen Rechnungen $[Sb_2S_2(SH)_2]$ die stabilste Form.

Die ersten EXAFS-Messungen an sulfidischen, alkalischen Antimonlösungen veröffentlichten Mosselmanns et al. im Jahr 2000 [29]. Ergebnis dieser Untersuchungen war, dass bei pH-Werten unterhalb von 12 das $[Sb(V)S_4]^{3-}$-Anion die vorherrschende Spezies ist, bei höheren pH-Werten wurden dreiwertige Antimonsulfid-Monomere vermutet. Das Auftreten von Oligomeren, wie in vielen Veröffentlichungen postuliert, konnte nur in einem Fall bei hoher Antimonkonzentration nachgewiesen werden. Eine weitere

EXAFS-Untersuchung wurde von Sherman et al. im Jahre 2000 veröffentlicht [30]. Als lösliche Spezies wurden fünfwertige monomere Antimonschwefelkomplexe $[Sb(V)S_4]^{3-}$ gefunden. Interessanterweise traten bei höheren Temperaturen zwei Veränderungen auf. Zum einem wurde in der Koordinationssphäre des Antimonatoms eine Substitution von Schwefel durch Sauerstoff beobachtet, zum anderen war eine Dimerisierung der monomeren Spezies zu erkennen.

Zusammenfassend lässt sich sagen, dass bis heute keine eindeutige Bestimmung der löslichen Spezies gelungen ist und der Einsatz nur einer analytischen Methode nicht ausreicht. Die Unterschiede in den postulierten Modellen sind einerseits mit den verschiedenen Synthese- und Reaktionsbedingungen zu erklären. Die Temperatur, der pH-Wert, die Art der Edukte und die Konzentration der Edukte sind hierbei die am stärksten variierten Parameter. Andererseits lassen die experimentellen Daten in vielen Fällen mehrere Interpretationen zu. Zusätzlich könnten Parameter wie z.B. die intensive Röntgenstrahlung bei EXAFS-Messungen oder die Hg-Konzentrationen bei potentiometrischen Untersuchungen eine Rolle spielen. In der Mehrheit der Veröffentlichungen werden monomere Spezies wie $[SbS_3]^{3-}$ und $[Sb(V)S_4]^{3-}$ sowie das Dimer mit dem Grundgerüst $[Sb_2S_4]^{4-}$ favorisiert. Weniger Einigkeit herrscht bei dem vermuteten Protonierungsgrad und der Oxidationsstufe. Die Bandbreite der Vorschläge reicht hier von wasserstofffreien bis hin zu komplett protonierten, ladungsneutralen Komplexen, von einer dreifachen Wertigkeit des Antimons über gemischvalente Spezies bis hin zu fünffacher Wertigkeit.

Eine Übertragung der Ergebnisse auf die von uns verwendeten Syntheseparameter ist schwierig. Unterschiede bei der Art der Edukte und deren Konzentrationen sowie die durch die solvothermalen Bedingungen gegebenen hohen Temperaturen und Drücke lassen einen Vergleich mit anderen Arbeiten nur schwer zu. Das größte Problem beim Vergleich ergibt sich durch die Verwendung von Aminen statt klassischer Basen wie KOH oder NaOH. Der pH-Wert der Lösungen ist hoch und kann einen Wert von 14 übersteigen. Hinzu kommen die Redoxeigenschaften der Amine, welche die chemischen Reaktionen erheblich beeinflussen können. Bisher wurden noch keine EXAFS-Studien mit Aminen als Basen durchgeführt.

Die eigenen EXAFS-Experimente lassen den Schluss zu, dass $[SbS_3]^{3-}$- und

$[SbS_4]^{3-/5-}$-Spezies unter den gegebenen Reaktionsbedingungen dominieren. Das Auftreten von Oligomeren kann ausgeschlossen werden, da eine Sb-Sb-Wechselwirkung, wie z.B. analog in As-Trimeren [31] beobachtet, nicht beobachtet werden kann. Interessanterweise ändert sich lediglich die Konzentration der Spezies unter den gewählten Reaktionsbedingungen, Geometrie und Oxidationsstufe bleiben über den gesamten Reaktionszeitraum konstant. Eine ausführliche Erläuterung dieser Ergebnisse und Details zum Versuchsaufbau sowie zu den Versuchsbedingungen finden sich in der Veröffentlichung auf Seite 186.

2 Untersuchungsmethoden

In diesem Kapitel werden die eingesetzten Untersuchungsmethoden zur Charakterisierung der Produkte kurz vorgestellt. Methoden, die seit langem in der anorganischen Festkörperchemie etabliert sind, sind nur tabellarisch in Kapitel 3 aufgeführt. Hierzu gehören die Einkristallstrukturanalyse, Pulverdiffraktometrie, Raman-, UV/Vis- und Infrarotspektroskopie, Elektronenmikroskopie, Elementaranalyse sowie thermische Untersuchungsmethoden. Weiterführende Informationen zu diesen Methoden können der Literatur entnommen werden. Die in dem folgenden Kapitel vorgestellten Untersuchungsmethoden hingegen gehören nicht zum alltäglichen Handwerkszeug des anorganischen Festkörperchemikers und werden daher genauer erläutert.

2.1 Untersuchungsmethoden unter Verwendung von Synchrotronstrahlung

2.1.1 Synchrotronstrahlung

Synchrotronstrahlung entsteht bei der Ablenkung geladener Elementarteilchen in Beschleunigern oder Speicherringen. Ein Ablenkmagnet zwingt nahezu lichtschnelle Elektronenbündel auf eine Kurvenbahn. Hierbei verlieren die Teilchen einen Teil ihrer Energie, indem sie tangential zu ihrer Flugbahn einen intensiven Lichtstrahl aussenden - die Synchrotronstrahlung. Die so entstehende Strahlung hat eine Intensität, die rund eine Million mal stärker ist als die von in Arztpraxen verwendeten Röntgenröhren (Abb. 2.1). Das Wellenlängenspektrum erstreckt sich vom infraroten bis zur harten Röntgen- und Gammastrahlung. Da die Elektronen in kurzen Paketen durch den Speicherring kreisen, kommt es zu keinem kontinuierlichen Strahl, sondern zu kurzen Pulsen mit

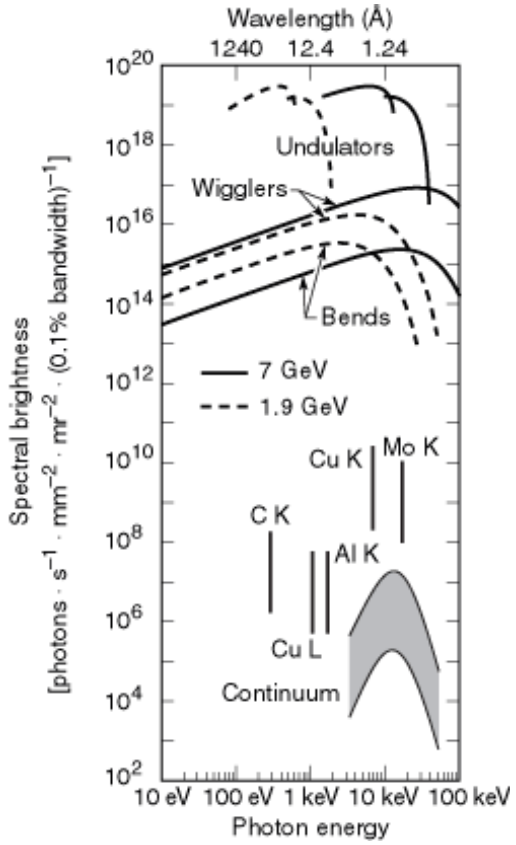

Abbildung 2.1: Intensitäten verschiedener Röntgenquellen [32]

einer Dauer von einer Zehnmilliardstel Sekunde. Die hohe Intensität und die intrinsische Kollimation der Synchrotronstrahlung erlauben die Aufnahme hochaufgelöster Pulverdiffraktogramme bei vergleichsweise moderaten Messzeiten. Durch spezielle Monochromatoren kann die jeweils gewünschte Wellenlänge aus dem Gesamtspektrum der elektromagnetischen Strahlung ausgewählt werden. Alle Experimente mit Synchrotronstrahlung dieser Arbeit wurden am Deutschen Elektronen-Synchrotron (DESY) in Hamburg im Hamburger Synchrotronstrahlungslabor (HASYLAB) durchgeführt. Die Synchrotronstrahlung wurde in dem Speicherring DORIS III (Elektronen oder Positronen) erzeugt. DORIS III zählt zu den Speicherringen der dritten Generation und ist eine der hellsten Röntgenquellen der Welt. DORIS III hat einen Umfang von 289 Metern, die Teilchen weisen eine Energie von 4,5 Milliarden Volt auf. Die Synchrotronstrahlung wird in den Kurven des Ringes, wo sich die Ablenkmagnete bzw. die

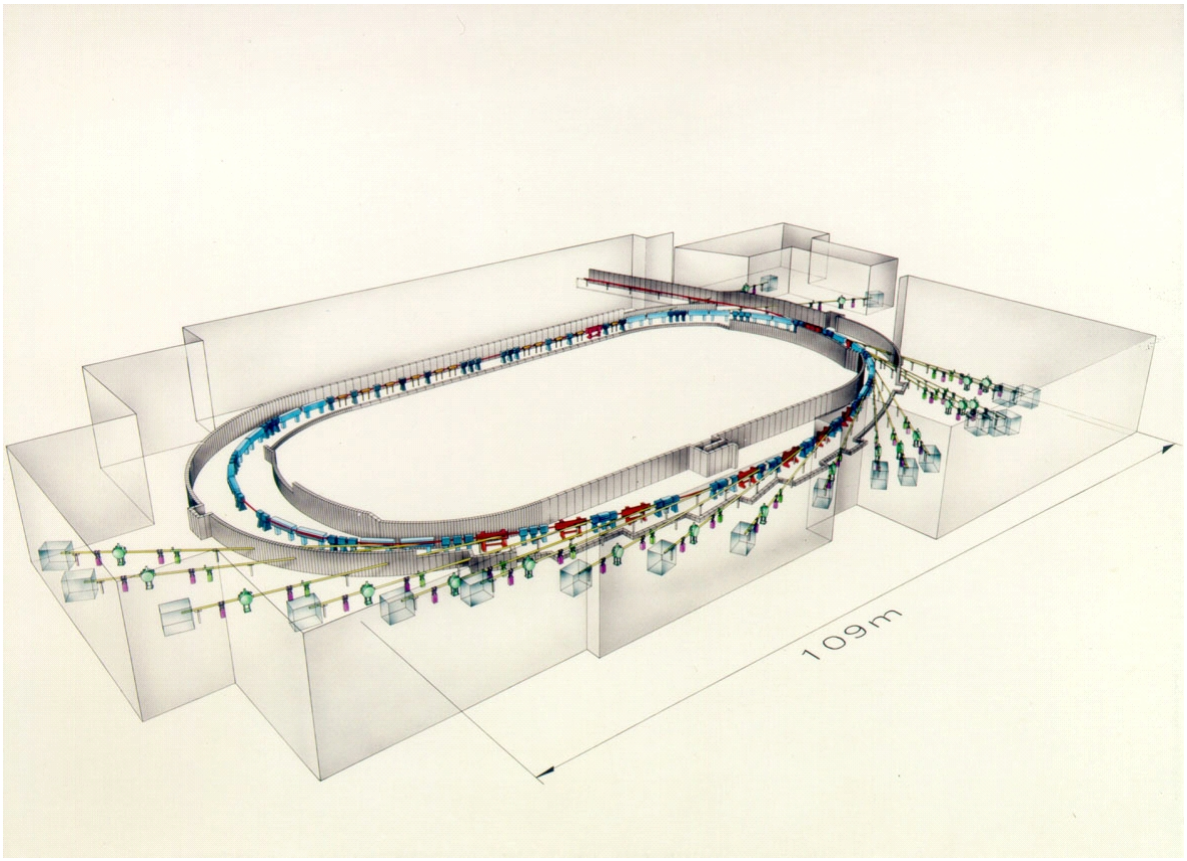

Abbildung 2.2: Experimentierhalle am HASYLAB

Wiggler und Undulatoren befinden erzeugt, und durch spezielle Strahlführung (Beamlines) gelangt das Licht zu den jeweiligen Messplätzen (Abb. 2.2) [32].

2.1.2 Energiedispersive Röntgendiffraktometrie (EDXRD)

Die Energiedispersivität bei vergleichsweise hohen Intensitäten kann zur Aufnahme von Röntgenbeugungsdiffraktogrammen mit einer sehr hohen Zeitauflösung genutzt werden. Im Vergleich zur winkeldispersiven Röntgendiffraktometrie verkürzt sich die Aufnahmezeit von mehreren Stunden auf wenige Minuten, bzw. in günstigen Fällen auf weniger als eine Minute. Aufgrund der hohen Intensität ist es möglich, das Reaktionsgefäß mit der Röntgenstrahlung zu durchdringen und das Auftreten von Feststoffen während der Reaktion direkt zu erfassen. Die relativ hohe Zeitauflösung

wird durch die energiedispersive Natur und hohe Intensität der Strahlung erreicht. EDXRD ist daher eine ideale Methode zur Untersuchung von Solvothermalsynthesen unter in-situ-Bedingungen. Solvothermale Synthesen sind heterogene Reaktionen in einem Multiparameterfeld mit einer großen Zahl an Parametern, welche sich gegenseitig in nicht gut verstandener Weise beeinflussen. Die Form und Konzentration der Edukte, die Temperatur, der pH-Wert, die Reaktionszeit und der Druck sind Beispiele für mögliche Reaktionsparameter. Die Reaktionen können als eine „Black-Box"-Chemie angesehen werden, da mit analytischen Methoden nur schwer der Reaktionsverlauf untersucht und der Einfluss einzelner Parameter erfasst werden kann. Bei einer Unterbrechung der Synthese mit anschließender Aufarbeitung der Reaktionslösung besteht die Gefahr, dass der tatsächliche Zustand des Reaktionsgemisches nicht erfasst wird, da intermediär gebildete Spezies nur unter realen Reaktionsbedingungen existieren und bei dem Abkühlungsprozess zerstört werden. Mit EDXRD wird der Reaktionsverlauf untersucht, mögliche Intermediate und/oder Zwischenstufen können erfasst, und der Einfluss einzelner Reaktionsparameter kann gezielt untersucht werden. Neben diesen Vorteilen sollen die Nachteile dieser Methode nicht verschwiegen werden. Aufgrund der zu erfüllenden Beugungsbedingungen können nur kristalline Phasen erfasst werden. Amorphe Phasen würden sich bei recht hohen Konzentrationen durch eine Modulation des Untergrundes zu erkennen geben. Die Analyse ist aber nicht trivial und der Aussagewert eingeschränkt. Die Reaktionen in Lösung können mit EDXRD nicht untersucht werden. Zusätzlich ist die spektrale Auflösung der Diffraktogramme schlecht und eine Strukturlösung bzw. -verfeinerung einer kristallinen Zwischenstufe erscheint ausgeschlossen. Allerdings reicht die Qualität zur Phasenidentifizierung und zu einer Quantifizierung des Reaktionsablaufes aus.

Alle EDXRD Messungen wurden an dem Messplatz F3 am HASYLAB durchgeführt. Ein schematischer Aufbau des Messplatzes mit Strahlführung ist in Kapitel 3.2.1 gezeigt.

2.1.3 Röntgenabsorptions-Spektroskopie (XAS)

Die Röntgenabsorptionsspektroskopie (XAFS = X-ray absorption fine structure) beruht auf der Absorption von Röntgenstrahlen durch kernnahe Elektronen und der

bei dem Prozess auftretenden Feinstruktur im Spektrum. Eine Probe wird mit einem Röntgenstrahl, dessen Energie durchstimmbar ist, bestrahlt und die Änderung des Absorptionskoeffizienten wird für ausgewählte Atome (Absorber) in Abhängigkeit von der Energie registriert (Abb. 2.3). Der Energiebereich ist hierbei entsprechend des zu

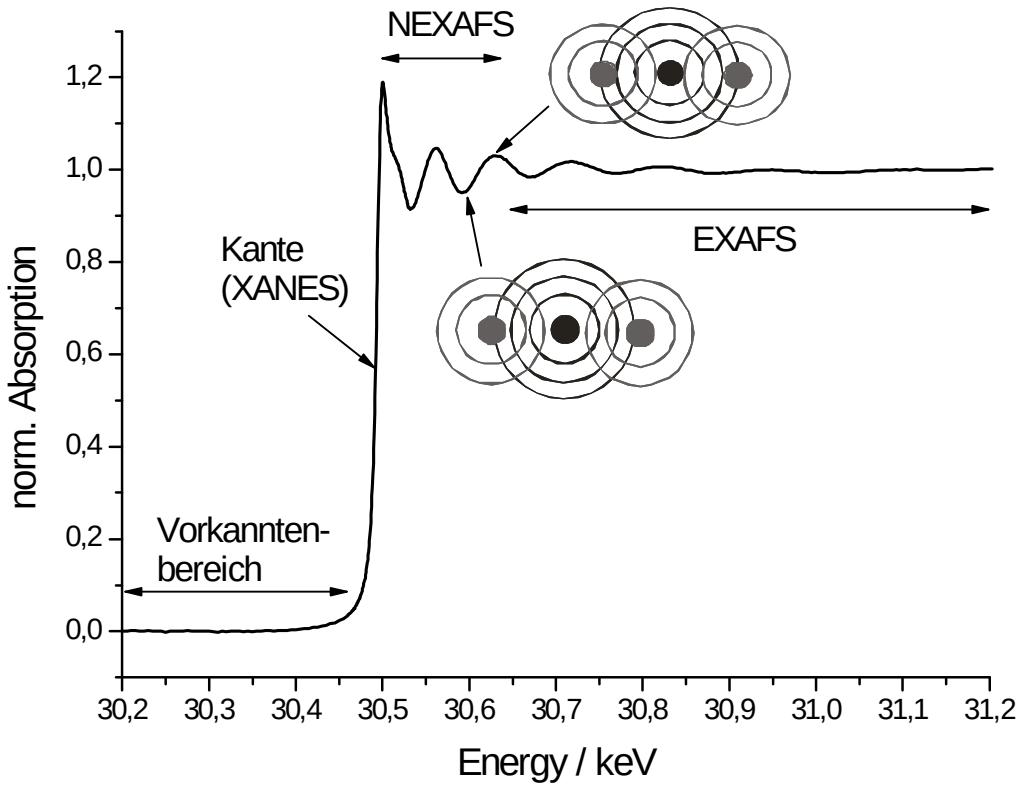

Abbildung 2.3: Spektrum einer XAS-Messung

untersuchenden Elementes gewählt. Ist die sogenannte Schwellenenergie erreicht, wird ein Elektron eines kernnahen Energieniveaus angeregt, was sich in einer drastischen Zunahme des Absorptionskoeffizienten bemerkbar macht. Bevor das Elektron in das Kontinuum angeregt wird, kann es gemäß den Dipol-Auswahlregeln zuerst in unbesetzte Energieniveaus (leere, bindende Orbitale) angeregt werden. Diese Anregung macht sich in den Spektren vor der eigentlichen Absorptionskante als sogenannter Vorkantenpeak bemerkbar. Nimmt die Energie weiter zu, wird das Elektron als Photoelektron von dem Atom losgelöst. Das austretende Photoelektron bzw. die dazugehörige Welle tritt in Wechselwirkung mit benachbarten Atomen, d.h. die auslaufende und die von

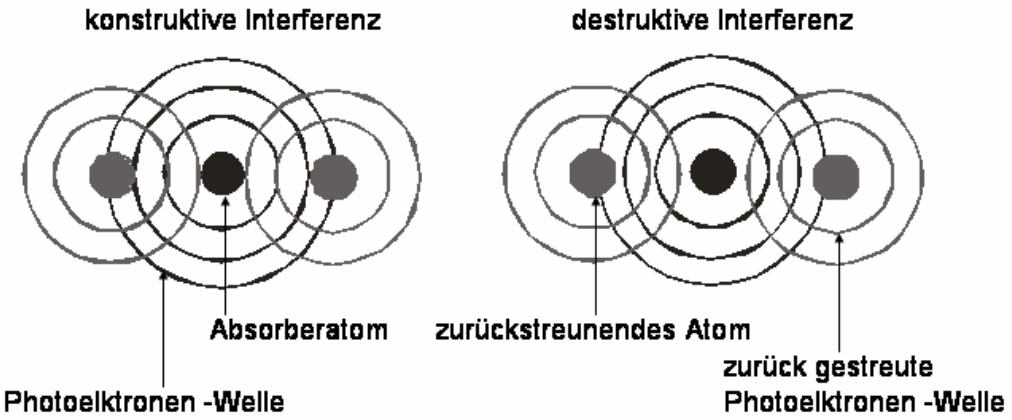

Abbildung 2.4: Konstruktive (links) und destruktive (rechts) Interferenz der Photoelektronenwellen

den Nachbaratomen rückgestreute Welle interferieren (Abb. 2.4). Je nach Gangunterschied zwischen den Wellen treten konstruktive und destruktive Interferenzen auf, die in den XAFS-Spektren als Maxima und Minima oberhalb der Absorptionskante auftreten (Abb. 2.3 und 2.5). Nahe der Absorptionskante findet so genannte Mehrfachstreuung statt. Der komplizierte Prozess der Mehrfachstreuung ist bis heute schlecht verstanden und eine theoretische Berechnung dieses Bereiches im XAS-Spektrum ist nur in Ansätzen möglich. Der Bereich bis ca. 50 eV oberhalb der Kante wird als XANES (X-ray absorption near edge structure) bezeichnet. Nimmt die Energie der Photoelektronen weiter zu, wird nur noch Einfachstreuung der Photoelektronenwellen beobachtet. Der Energiebereich > 50 eV bis einige Hundert eV oberhalb der Absorptionskante wird als EXAFS (extended X-ray absorption fine structure) bezeichnet. Der Grenzbereich zwischen XANES und EXAFS wird als NEXAFS (Near edge absorption fine structure) definiert.

Der Zusammenhang zwischen Modulationsfrequenz und Strukturparametern ist in der folgenden EXAFS-Gleichung enthalten.

$$\chi(k) = \frac{1}{k} \sum \frac{N_j}{R_j^2} \mid F_j(k) \mid \cdot \exp(-2 \cdot \sigma_j^2 \cdot k^2) \cdot \exp(\frac{-2R_j}{\lambda_j(k)}) \cdot \sin(2kR_j + \Phi_j(k))$$

Die EXAFS-Funktion $\chi(k)$ (k ist der Wellenvektor des Photoelektrons) berücksichtigt

N = die Zahl der rückstreuenden Atome

j = Index für die Schalen an Nachbaratomen um das absorbierende Atom

R = den Abstand zwischen dem Absorber- und dem Rückstreuatom

$\mid F(k) \mid$ = die Streukraft des rückstreuenden Atoms

σ = den Debye-Waller-Faktor, der statische und dynamische Fehlordnung bzw. thermische Schwingungen beschreibt

$\exp(\frac{-2R_j}{\lambda_j(k)})$ = die Dämpfung des Spektrums, welche durch die mittlere freie Weglänge λ der Elektronen verursacht wird

$\Phi(k)$ = die Phasenverschiebung des Photoelektrons im Potential des Absorber- und Rückstreuatoms.

Die χ(k)-Funktion beschreibt das Spektrum im reziproken Raum und über eine Fouriertransformation wird die Funktion im Realraum erhalten.

Um Informationen über die lokale Struktur um das Absorberatom zu erhalten muss das gemessene Spektrum Fourier-transformiert werden. Das erhaltene Spektrum weist ein oder mehrere Peaks auf, die den radialen Abständen zwischen absorbierendem Atom und seinen Nachbaratomen entsprechen.

Die geringe mittlere freie Weglänge $\lambda(k)$ der Photoelektronen sowie der Faktor R^{-2} in $\chi(k)$ machen die Methode zu einer lokalen Sonde.

Wenn mehr als eine Schale berücksichtigt werden soll, so muss eine Summation über die Nachbarn j erfolgen.

Die Lage der Absorptionskante hängt von der Ladungsabschirmung der Rumpfelektronen des Absorberatoms ab, welche sich mit der Oxidationsstufe ändert. Als Referenz gilt der elementare Zustand des untersuchten Absorbers. Zusätzlich muss berücksichtigt werden, dass chemische Bindungen einen unterschiedlichen Kovalenzgrad haben und damit einhergehend die Abschirmung der Rumpfniveaus in unterschiedlichen Verbindungen verschieden ist.

Die XAFS-Spektroskopie hat gegenüber anderen analytischen Methoden wie z.B. XPS/UPS oder Augerspektroskopie einige wesentliche Vorteile. Der Aggregatzustand der zu untersuchenden Probe spielt keine Rolle, d.h. es können Flüssigkeiten, Gase,

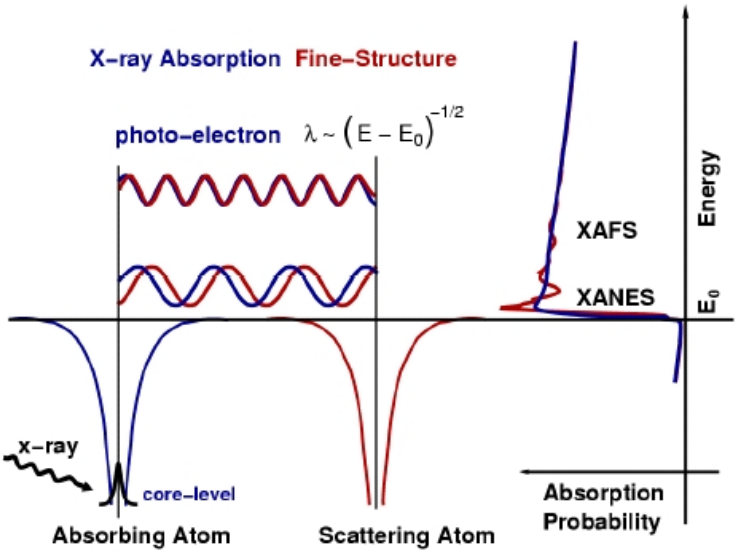

Abbildung 2.5: Modulation im XAS-Spektrum durch Interferenzen der zurückgestreuten Photoelektronenwellen

kristalline oder amorphe Festkörper untersucht werden. Neben dem chemischen Zustand des Absorberatoms werden die Koordinationszahl, die Bindungslängen zwischen Absorber und Rückstreuatomen sowie die Art der Rückstreuatome als Information in einem Spektrum erhalten.

Der Nachteil dieser Methode ist, dass sie, obwohl elementspezifisch, nur einen Mittelwert über die Absorptionen aller Atome des gleichen Elements gibt. Daher ist es schwierig, die Struktur unterschiedlicher Molekülgruppen des gleichen Atomtyps in einem System aufzuklären, besonders wenn kein Strukturmodell vorhanden ist.

2.1.4 Strukturverfeinerung aus Pulverdaten: Die Rietveld-Methode

In einem Pulverdiffraktogramm sind die für eine erfolgreiche Strukturaufklärung und –verfeinerung notwendigen Intensitätsdaten auf eine Dimension reduziert, d.h. die Intensitäten werden in Abhängigkeit vom Streuwinkel Θ erhalten und nicht wie bei einer Einkristallstrukturanalyse in Abhängigkeit von der Orientierung im dreidimensionalen

Raum. Diese Reduktion an Information führt zu Problemen bei der Strukturlösung und –verfeinerung, da im Vergleich zu einem Einkristalldatensatz viel zu wenige unabhängige Beobachtungen zur Verfügung stehen.

Dieser Mangel an Information kann partiell dadurch behoben werden, in dem das gesamte Pulverdiffraktogramm für eine Strukturverfeinerung genutzt wird, d.h. als Informationen werden die Intensitäten an jedem Messpunkt ausgenutzt. Dieser Ansatz wurde von Rietveld zuerst für Neutronenbeugungsdaten eingeführt und wurde später auf Röntgenbeugungdiagramme ausgeweitet. Voraussetzung für die Strukturverfeinerung mit Röntgenpulverdaten ist die Kenntnis eines guten Strukturmodells als Startwert. Als Strukturmodell können Atomkoordinaten einer isotypen Verbindung, aus einer ab-initio-Strukturlösung oder Atomkoordinaten aus einem Abstandsminimierungs-Verfahren dienen. Im Gegensatz zur Verfeinerung von Einkristallstrukturdaten müssen bei der Rietveldverfeinerung die Reflexprofile mit geeigneten Funktionen modelliert werden. Zusätzlich muss der Untergrund berücksichtigt werden, was mit einer Spline-Funktion, handverlesenen Stützpunkten oder Fourier-Reihen erfolgen kann. Bei der Verfeinerung nach der Rietveldmethode muss zwischen lokalen und globalen Parametern unterschieden werden. Als Ergebnis einer Rietveld-Verfeinerung erhält man eine quantitative Phasenanalyse, die Gitterparameter, Atomkoordinaten und Besetzungfaktoren sowie die Temperaturschwingungen. Zusätzlich können Aussagen über Kristallitgröße, Texturen und Mikrospannungen getroffen werden. Eine ausführliche Beschreibung der Methode, der zur Verfügung stehenden Parameter, die möglichen Linienformen und Asymmetrieparameter sowie die Interpretation der verschieden R-Werte zur Einschätzung der Güte, kann der Literatur entnommen werden [33].

3 Experimenteller Teil

3.1 Die solvothermale Synthese

Für die Synthese von porösen Festkörpern ist die solvothermale Synthese die Präparationsmethode der Wahl. Der überwiegende Teil neuer Verbindungen mit offenen Strukturen wurde mit dieser „state of the art"–Methode dargestellt. Auch für die Synthese von Thioantimonaten sind die von Rabenau [34] ausführlich beschrieben Eigenschaften und Vorteile der solvothermalen Synthese besonders geeignet, wie die 15 neuen Verbindungen, die in dieser Doktorarbeit vorgestellt und diskutiert werden, eindrücklich nachweisen.

Für die Synthesen wurden aus Teflon gefertigte Becher mit einem inneren Volumen von ca. 30 cm^3 als Reaktionsgefäß benutzt. Das inerte Verhalten von Teflon gegenüber Basen und Säuren und die Stabilität in dem erforderlichen Temperatur-Druck-Bereich entsprechen den Anforderungen der Synthese. Die Teflonbecher wurden als „schwimmender Einsatz" in einen Edelstahlautoklaven eingesetzt (Abb. 3.1).

Die Reaktionsgemische können unter diesen statischen Bedingungen in einem Ofen bis auf 220 °C erhitzt werden. Dynamische Reaktionsbedingungen werden erreicht, indem zu dem Eduktgemisch eine magnetische Rührpille gegeben wird, um eine permanente Durchmischung des Reaktionsgemisches zu gewährleisten. Vorteile dieser Reaktionsführung sind, dass höhere Ausbeuten erzielt werden und die Reaktionszeit enorm verkürzt wird. Nachteilig ist, dass das Produkt in Pulverform erhalten wird und nicht wie unter statischen Bedingungen in Form von Einkristallen. Daher eignen sich dynamische Reaktionsbedingungen besonders gut zur Nachpräparation bereits bekannter Verbindungen in großen Mengen. Eine detaillierte Beschreibung der von Michael Schaefer entwickelten Apparatur findet sich in seiner Diplomarbeit [35].

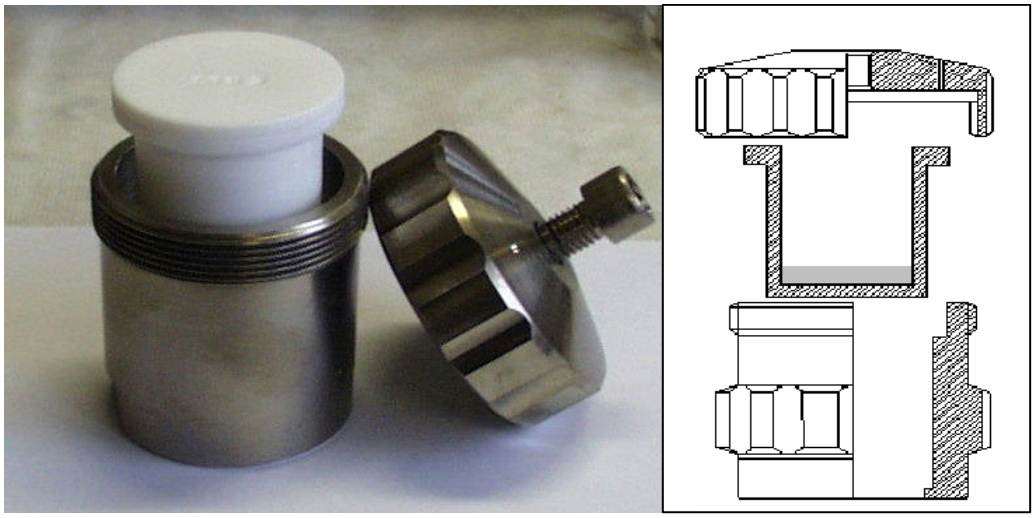

Abbildung 3.1: Edelstahlautoklav mit Tefloneinsatz, rechts schematisch

Im Allgemeinen lassen sich die Synthesebedingungen für Thioantimonate wie folgt beschreiben: Eine Antimonquelle (in den meisten Fällen Sb oder Sb_2S_3) und eine Schwefelquelle (überwiegend elementarer S, selten H_2S) werden in einer wässrigen Aminlösung für einen bestimmten Zeitraum (üblicherweise mehrere Tage) bei Temperaturen zwischen 90 °C und 220 °C in einem Autoklaven erhitzt. Als Reaktionsparameter sind die Temperatur, die Eduktmengen und Eduktverhältnisse, die Reaktionsdauer und die Aminkonzentration sowie die Füllhöhe variierbar.

3.1.1 In-situ-Apparatur

Für die Messungen am Hasylab in Hamburg war die Konstruktion einer speziellen Apparatur erforderlich. Zum einem müssen dort geltende Sicherheitsmaßgaben erfüllt werden, zum anderen sind Modifikationen nötig, um den Synchrotronstrahl in geeigneter Weise durch die Messzelle zu führen.

Die in Abbildung 3.2 gezeigte Apparatur besteht im wesentlichen aus zwei Teilen, einem Autoklaven und einer Ölheizung. Als Material für den Autoklaven ist Aluminium geeignet, welches sowohl die notwendige Wärmeleitfähigkeit besitzt als auch eine geringe Absorption von Primärstrahl und reflektiertem Strahl, so dass eine ausreichende

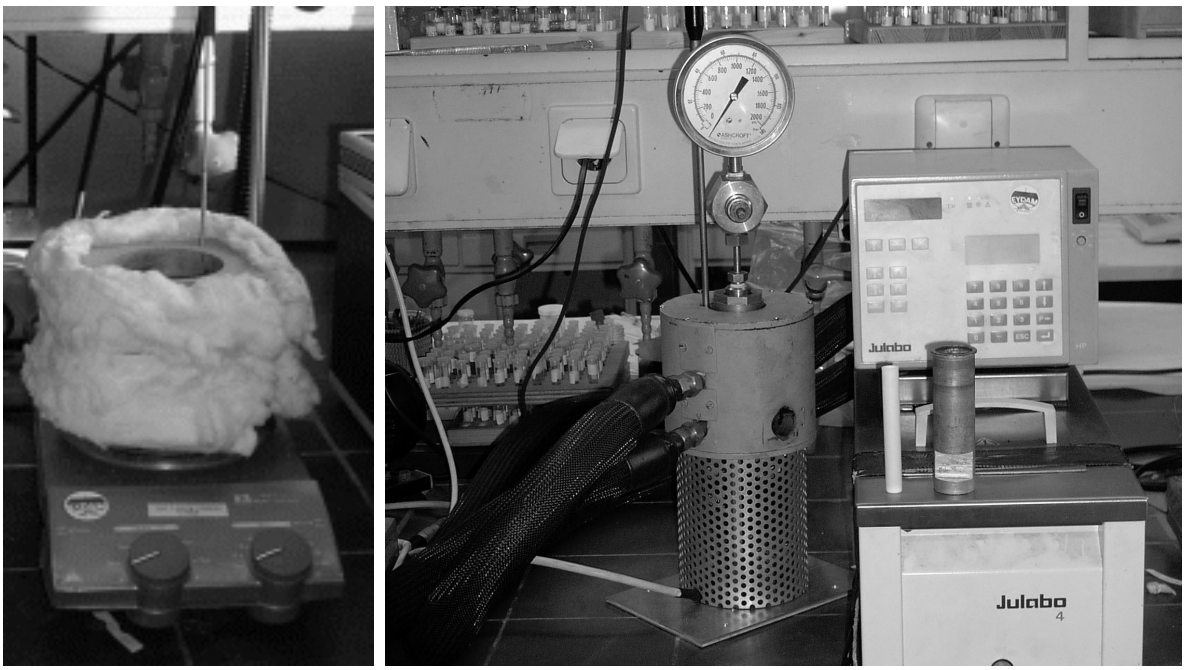

Abbildung 3.2: links: Apparatur für Synthese unter dynamischen Bedingungen, rechts: Apparatur für in-situ-Messungen am HASYLAB

Intensität in den detektierten Spektren gewährleistet ist. Zur Druckabsicherung ist der Autoklav mit einem Druckmesser versehen. Die verwendeten Teflonliner sind mit einem Volumen von ca. 7 ml und einer Höhe von 10 cm deutlich kleiner als die im Labor verwendeten Reaktionsgefäße. Eine Anpassung der Reaktionsparameter des jeweilig untersuchten Systems war daher erforderlich.

Für die Untersuchungen, welche in den Publikationen auf Seite 186, 238 und 245 präsentiert werden, wurden Kulturröhrchen aus Glas verwendet. Neben der einfacheren Handhabung sind die geringen Anschaffungskosten von Vorteil. Die Röhrchen werden nur einmal verwendet, so dass eine höhere Reproduzierbarkeit gewährleistet ist. Eventuelle Einflüsse durch Kristallisationskeime oder Veränderung der Oberfläche durch Reinigungsprozesse können ausgeschlossen werden.

Beheizt werden die Aluminiumautoklaven mit einer externen Ölheizung, das erreichbare Temperaturmaximum liegt bei 200 °C. Der vorgestellte Aufbau kann sowohl am Messplatz F3 (Kapitel 3.2.1) als auch an Messplatz X1 (Kapitel 3.2.2) genutzt werden.

3.2 Messplätze am HASYLAB

3.2.1 Aufbau des Messplatzes F3

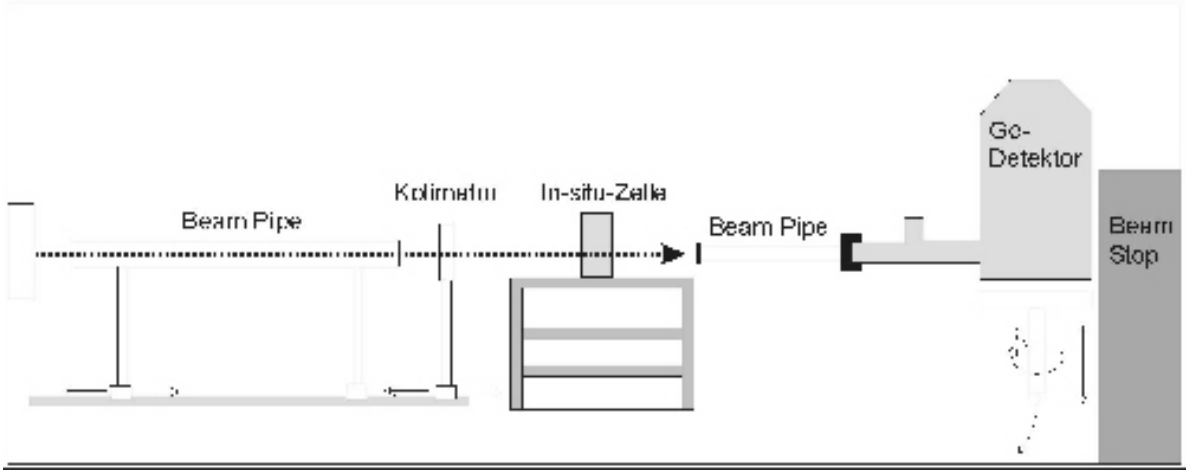

Abbildung 3.3: Schematischer Aufbau des Messplatzes F3

Wie in der schematischen Abbildung 3.3 zu erkennen ist, wird die aus dem Strahlrohr kommende weiße Synchrotronstrahlung mittels eines Kollimators auf die gewünschte Strahlbreite und Strahlhöhe und damit auf die gewünschte Intensität eingestellt. Nach Durchstrahlung der in-situ-Apparatur, welche auf einem XYZ-Tisch arretiert ist, wird die reflektierte Strahlung mit einem Ge-Detektor energie-dispersiv aufgezeichnet. Eine genaue Beschreibung der Zusammenhänge zwischen Detektorwinkel und d-Werten der untersuchten Probe sowie Kriterien zur Auswahl des Winkels finden sich in den Doktorarbeiten [8][9].

3.2.2 Aufbau des Messplatzes X1

Bei dieser Versuchsanordnung (Abb. 3.4) [32] tritt der Synchrotronstrahl aus dem Strahlrohr durch einen verstellbaren Eintrittsspalt zuerst in die Monochromatorkammer ein. Durch einen auf einem Goniometer befestigten Si-Doppelkristall wird die gewünschte Wellenlänge aus der weißen Synchrotronstrahlung herausgefiltert. Die Strah-

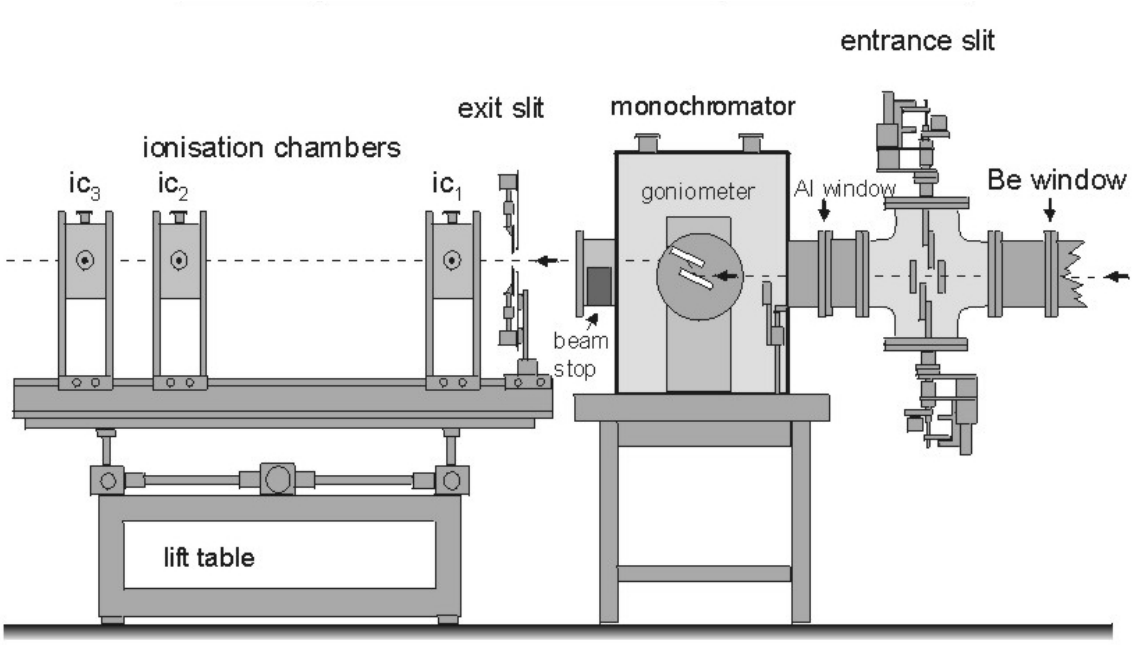

Abbildung 3.4: Schematischer Aufbau des Messplatzes X1

lung, die durch höhere Beugungsordnungen erzeugt wird, wird durch ein leichtes Versetzen der beiden Si-Kristalle eliminiert. Ein zweites Spaltsystem beim Austritt aus der Monochromatorkammer stellt die für den Versuch gewünschte Strahlbreite und damit die Intensität ein, zudem wird der Anteil des Streulichtes vermindert. Die Intensitäten Ic_1, Ic_2 und Ic_3 wurden in Gas-Ionisationskammern bestimmt. Dieser Versuchsaufbau ermöglicht es, gleichzeitig die Intensität von Probe und Referenz zu messen. Die in der Veröffentlichung auf Seite 186 diskutierten Spektren wurden an der Sb-K-Kante bei 30.49 keV in Transmissionsgeometrie aufgenommen.

3.3 Verwendete Geräte

Methode	Gerät	Bemerkungen
Einkistallstruktur-analyse	STOE AED II	Mo – K_α(0.71073 Å), Graphit-Monochromator
	Philips PW1100	Mo – K_α(0.71073 Å), Graphit-Monochromator
	STOE IPDS	Mo – K_α(0.71073 Å)
Pulverdiffraktometrie	STOE Stadi – P	Transmissionsgeometrie, Cu – $K_{\alpha 1}$ (1.54056 A);
	Siemens D5000	Reflexionsgeometrie Cu – $K_{\alpha 1}$ (1.54056 Å); Detektor: Szintillationszähler, Punktdetektor
DTA/TG – Untersuchungen	Netzsch STA – 409CD	Pt – Rh – Thermoelement, Gasstrom 75 ml/min; mit QMA 400 Massenspektrometer (Fa. Balzer)
MIR	ATI Matheson Genesis	in KBr – Matrix, 400 – 4000 cm^{-1}; Auflösung: 1 cm^{-1}
FIR	Bruker IFS 66	in Polyethylen – Matrix, 80 – 500 cm^{-1}, Auflösung: 1 cm^{-1}
FT – Raman	Bruker IFS 66	Nd/YAG – Laser, (1064 nm), 100 – 3500 cm $^{-1}$, Auflösung: 2 cm^{-1}
ESEM/EDX	Philips ESEM XL 30	Rasterelektronenmikroskop mit EDX – Aufsatz (Fa. EDAX)
Elementaranalyse	Eurovektor EuroEA Elemental Analyzer	C – , H – , N – , S – Analyse, He – Trägergas; Verbrennung in O_2 bei 1010 °C; Detektion über Wärmeleitzelle

3.4 Verwendete Chemikalien

Substanz	Formel	Reinheitsgrad	Hersteller
Antimon	Sb	99.99 %	Alfa Aesa
Antimon(III)oxid	Sb_2O_3	99.9 %	Merck
Schwefel	S	99.99 %	Alfa Aesa
Eisen(III)chlorid	$FeCl_3$	98 %	Fluka
Eisen(II)sulfat-heptahydrat	$FeSO_4 \cdot 7H_2O$	99 %	Fluka
Nickel(II)acetat-tetrahydrat	$Ni(OCOCH_3) \cdot 4H_2O$	99 %	Fluka
Vanadium(V)oxid	V_2O_5	99 %	Fluka
Ammoniumvanadat	NH_4VO_3	99 %	Fluka
Tris-(2-aminoethyl)-amin	$C_6H_{18}N_4$	95 %	Fluka
Diethylentriamin	$C_4H_{13}N_3$	98 %	Fluka
(±)-trans-1,2-Diamino-cyclohexan	$C_6H_{14}N_2$	98 %	Fluka
3-(Aminomethyl)-pyridin	$C_6H_8N_2$	98 %	Merck
N,N,N',N'-Tetrakis-(2-Hydroxyethyl)-ethylendiamin	$C_{10}H_{24}N_2O_4$	97 %	Fluka
2-(Aminoethyl)-piperazin	$C_6H_{15}N_3$	98 %	Merck
(±)-1-Amino-2-propanol	C_3H_9NO	93 %	Fluka

3.5 Verwendete Programme

- $SHELXS-97/94/93$ [36] : Programme zur Strukturlösung von Einkristalldaten
- $SHELXL-97$ [37] : Programm zur Strukturverfeinerung von Einkristalldaten
- $PLATON$ [38] : Programmpaket zur Überprüfung von Kristallstrukturdaten
- $SQUEEZE$ [38] : Unterprogramm von PLATON zur Bestimmung des freien Raumes sowie der vorhandenen Restelektronen

- $X - Red$ [39] und $X - Shape$ [40]: Programme zur Durchführung der numerischen Absorptionskorrektur
- $WinXPOW$ [41] : Programmpaket zur Datensammlung von Pulverdiffraktogrammen, ihrer graphischen Auswertung sowie zur Berechnung von theoretischen Pulverdiffraktogrammen
- Netzsch – Programmpaket Netzsch TA4 [42] : Datensammlung und Auswertung von DTA – TG – MS – Daten
- *Diamond* (Version 2.1c) [43] : Erstellung der Strukturbilder für die einzelnen Verbindungen
- $WinXAS$ [44] : Programm zur Auswertung von EXAFS-Spektren
- $FEFF$ [45][46] : Progamm zur Erstellung theoretischer XAS-Spektren
- $FULLPROF$ [47] : Progamm zur Rietveldverfeinerung
- $EDXPOW$ [48] : Programm zur Bestimmung von Reflexintensitäten aus in-situ-Spektren

4 Kumulativer Haupteil

4.1 Ergebnisse und Publikationen zu übergangsmetallfreien Thioantimonaten

4.1.1 Die Verbindung $[C_6H_{17}N_3][Sb_{10}S_{16}]$

Zusammenfassung der Veröffentlichung „*Solvothermal Synthesis of* $[C_6H_{17}N_3]Sb_{10}S_{16}$*: a New Thioantimonate with an in-situ formed Organic Amine Cation*“.

In der folgenden Veröffentlichung werden die solvothermale Synthese und die Struktur der Verbindung $[C_6H_{17}N_3][Sb_{10}S_{16}]$ ($C_6H_{17}N_3$ = 2-Piperazin-N-ethylamin-Kation) vorgestellt. Die Darstellung erfolgte mit einem Gemisch aus Sb, $FeCl_3$ und S (1:1:3 mmol) in 4 ml einer 50 % tren Lösung, das 7 Tage bei 200 °C in einem in Kapitel 3.1 beschriebenen Autoklaven erhitzt wurde. Die Verbindung $[C_6H_{17}N_3][Sb_{10}S_{16}]$ fiel als Nebenprodukt in Form roter Kristalle an. Zwei Beobachtungen sind bei dieser Synthese bemerkenswert. 1. Das 2-Piperazin-N-ethylamin-Kation wird unter in-situ-Bedingungen aus einem tren-Molekül gebildet. 2. Die Ergebnisse umfangreicher Synthesen belegen, dass die Zugabe von $FeCl_3$ essentiell für die Bildung der Verbindung ist. Ohne $FeCl_3$ wird ein unbekanntes pulverförmiges Produkt gebildet.

Die Verbindung $[C_6H_{17}N_3][Sb_{10}S_{16}]$ kristallisiert in der monoklinen Raumgruppe $P2_1/c$ mit vier Formeleinheiten pro Elementarzelle. Die Struktur besteht aus einem isolierten doppelt protonierten 2-Piperazin-N-ethylamin-Kation und einem 2-dimensionalen $[Sb_{10}S_{16}]^{2-}$-Anion. Als primäre Baueinheiten werden neun SbS_3-Pyramiden und eine SbS_4-Einheit gefunden. Die Verknüpfung über gemeinsame Ecken und Kanten führt zur Bildung von Sb_3S_3- und Sb_4S_4-Heteroringen als sekundäre Baueinheiten. Die weitere Verknüpfung dieser Baugruppen ergibt stark modulierte, zwei

Atome dicke Schichten. Die Modulationsperiode entlang der [010]-Richtung beträgt etwa 14 Å. In diesen Schichten werden große $Sb_{31}S_{31}$-Ringe mit doppelt ellipsoidaler Form beobachtet. Diese Poren weisen Dimensionen von 8.9·9.3 Å auf. Die Schichten sind so übereinander gestapelt, dass Kanäle parallel zu [001] gebildet werden. Werden Sb-S-Abstände größer als 3 Å als schwache Bindungen betrachtet, ergibt sich ein dreidimensionales Thioantimonat-Netzwerk. Dabei sind die langen Sb-S-Abstände in den Schichten signifikant kürzer als die Sb-S-Abstände zwischen den Schichten. Die Kationen befinden sich an den Wendepunkten benachbarter Schichten und wirken als eine Art Abstandshalter.

Solvothermal Synthesis of $[C_6H_{17}N_3]Sb_{10}S_{16}$: A New Thioantimonate(III) with an *in-situ* Formed Organic Amine Cation

Ragnar Kiebach, Christian Näther, and Wolfgang Bensch

Institut für Anorganische Chemie, Christian-Albrechts-Universität Kiel, Olshausenstraße 40, D-24098 Kiel, Germany

Reprint requests to Prof. Dr. Wolfgang Bensch. Fax: +49-(0)431-880-1520.
E-mail: wbensch@ac.uni-kiel.de

Z. Naturforsch. **59b,** 1314 – 1319 (2004); received August 9, 2004

Dedicated to Prof. Dr. H. Schmidbaur on the occasion of his 70th birthday

The new thioantimonate(III) $[C_6H_{17}N_3][Sb_{10}S_{16}]$ ($C_6H_{17}N_3$ = 2-piperazine-N-ethylamine cation) was obtained under solvothermal conditions showing a unique anionic framework. The compound crystallizes in the monoclinic space group $P2_1/c$ with four formula units in the unit cell. The lattice parameters are $a = 11.530(2)$, $b = 25.042(5)$, $c = 13.709(3)$ Å, $\beta = 111.25(3)^\circ$, $V = 3689(2)$ Å^3. The thioantimonate(III) anion is formed by interconnection of nine trigonal pyramidal SbS_3 units and one SbS_4 moiety. These primary building units share common corners and edges yielding Sb_3S_3 and Sb_2S_2 hetero-rings. Further condensation leads to strong undulated two atoms thick layers extending in the [010] direction, with a modulation period of about 14 Å. Very large $Sb_{31}S_{31}$ rings within the layers show a 'double-ellipsoidal' shape with approximate dimensions of $8.9 \cdot 9.3$ Å. The cations are located at the inflexion points of the layers and act as pillars between successive layers. The layers are stacked onto each other in a way that channels parallel to [001] are formed accommodating the organic cations. A remarkable observation is that the 2-piperazine-N-ethylamine cation is formed by cyclization of tren molecules (tren = tris(2-aminoethyl)amine) under *in-situ* conditions.

Key words: Thioantimonate(III), Solvothermal Synthesis, Crystal Structure

Introduction

The structures of thioantimonate(III) compounds show some highly interesting and unique features. The most dense antimony sulfide Sb_2S_3 has a Sb : S ratio of 1 : 1.5 and the negatively charged thioantimonates(III) must have a ratio larger than 1 : 1.5. Examples are compounds with a ratio of 1 : 1.6 ($[Sb_5S_8]^-$ [1], $[Sb_{10}S_{16}]^{2-}$ [2], 1 : 1.67 ($[Sb_3S_5]^-$ [3 – 7], $[Sb_6S_{10}]^{2-}$ [8, 9], $[Sb_{12}S_{20}]^{4-}$ [10]), 1 : 1.75 ($[Sb_4S_7]^{2-}$ [11 – 21], $[Sb_{12}S_{21}]^{6-}$ [22]), 1 : 1.8 ($[Sb_5S_9]^{3-}$ [23], $[Sb_{10}S_{18}]^{6-}$ [24]), or 1:2 ($[SbS_2]^-$ [25, 26], $[Sb_2S_4]^{2-}$ [27], $[Sb_3S_6]^{3-}$ [28], $[Sb_4S_8]^{2-}$ [29], $[Sb_4S_8]^{4-}$ [30]). One remarkable feature of these compounds is that for a given Sb : S ratio different thioantimonate(III) anions are observed which then exhibit different connectivities of the primary SbS_3 and SbS_4 building units and show different dimensionalities of the anions. For the overwhelming number of thioantimonates(III) the dimensionality is mainly determined by the size of the counter cation, *i.e.* the cation exerts a structure directing effect. The most impressive example for the 'template' effect of the cations is the series of compounds containing the $[Sb_4S_7]^{2-}$ anion [11 – 21]. A three-dimensional interconnected $[Sb_4S_7]^{2-}$ anion [11] is observed in $K_2Sb_4S_7$, and with increasing size of the cation the dimensionality is reduced to two-dimensional layers [13, 15 – 18] and finally to one-dimensional chains [12, 14, 19]. Until now, several compounds with a Sb : S ratio of 1 : 1.67 were reported including the $[Sb_3S_5]^-$ [3 – 7], the $[Sb_6S_{10}]^{2-}$ [8, 9], and the $[Sb_{12}S_{20}]^{4-}$ anions [10]. One-dimensional chains are observed in $[C_6H_{15}N_2][Sb_3S_5]$ [7], $[[N(C_3H_7)_4][Sb_3S_5]$ [5], $[Ph_4P]_2[Sb_6S_{10}]$ [8] and in $[(MA)_{1.03}K_{2.97}][Sb_{12}S_{20}] \cdot 1.34\ H_2O$ [10]. Two-dimensional layered anions are found in $RbSb_3S_5 \cdot H_2O$ [4] and in $[M(C_4H_{13}N_3)_2][Sb_6S_{10}] \cdot 0.5\ H_2O$ (M = Fe, Ni) [9]. Finally, a complex three-dimensional network is formed in $TlSb_3S_5$ [6]. The description of the structures presented above base on a cut-off for the Sb-S distances of about 3 Å. But

Table 1. Technical details of data acquisition and selected refinement results for $[C_6H_{17}N_3]Sb_{10}S_{16}$.

Formula	$[C_6H_{17}N_3]Sb_{10}S_{16}$
MW [g/mol]	1861.69
Space group	$P2_1/c$
a [Å]	11.530(2)
b [Å]	25.042(5)
c [Å]	13.709(3)
β [°]	111.25(3)
Volume [Å^3]	3689.1(2)
Z	4
Temperature [K]	293
μ [mm^{-1}]	8.12
$F(000)$	3360
$d_{calcd.}$ [g·cm^{-3}]	3.352
2θ Range [°]	3 – 54
hkl Range	0/14; −32/13; −17/16
Refl. collected	13442
Reflections unique	8071
Data ($Fo > 4\sigma(Fo)$)	7082
$R_{int.}$	0.0305
$\delta\rho$ [e/Å^3]	−1.43/2.35
Parameters	334
$R1[F_o > 4\sigma(F_o)]$[a]	0.0310
wR2 for all data	0.0814
Goodness of fit	1.102

[a] $R1 = \Sigma||F_o| - |F_c||/\Sigma|F_o|$.

the assignment of the dimensionality is arbitrary in thioantimonates(III) because Sb-S distances scatter in the large range between 2.2 and 4 Å. Therefore, the description of the structures of thioantimonates(III) and the final assignment of the dimensionality is not straight forward.

Very recently we reported the solvothermal syntheses and structures of two new thioantimonates(III) with the compositions $[C_6H_{17}N_3{}^{2+}][Sb_6S_{10}]$ and $[C_7H_{13}N_2{}^+]_3[Sb_9S_{15}]$ ($C_6H_{17}N_3{}^{2+}$: 1-(2-aminoethyl)-piperazinium dication; $C_7H_{13}N_2{}^+$: 1,5-diazabicyclo[4.3.0.]non-5-en) [31]. Interestingly, in both syntheses a Sb : S ratio of 1 : 3 was used (on a mmol scale) and using tren (tris(-aminoethyl)amin) as the organic solvent and applying a Sb : S ratio of 1 : 3 another compound with a $[Sb_6S_{10}]^{2-}$ anion could be isolated. Here we report the synthesis and crystal structure of the thioantimonate(III) $[C_6H_{17}N_3][Sb_{10}S_{16}]$ exhibiting a new anionic framework.

Experimental Section

Synthesis

The solvothermal synthesis was performed using Sb, $FeCl_3$, and S (Merck, 1 : 1 : 3 mmol) as starting agents, which were mixed with 4 ml of 50% aqueous tren (Fluka) solution in a teflon lined steel autoclave with an inner volume of 30 ml. The autoclave was heated for 7 days at 200 °C yielding red single crystals of $[C_6H_{17}N_3]Sb_{10}S_{16}$ as the minor product. All attempts to synthesize the compound in higher yields and as a phase pure material were not successful. In the powder pattern of the product only elemental Sb could be identified as additional crystalline phase. The background of the pattern is modulated indicative for the presence of an amorphous material. It must be noted that syntheses without $FeCl_3$ leads to the formation of a hitherto not identified product without crystals of the title compound.

Table 2. Atomic coordinates [$\times 10^4$] and equivalent isotropic displacement parameters [Å$^2 \cdot 10^3$] for $[C_6H_{17}N_3]Sb_{10}S_{16}$.

Atom	x	y	z	U_{eq}
Sb(1)	8311(1)	10366(1)	4808(1)	20 (1)
Sb(2)	8002(1)	8853(1)	4272(1)	28(1)
Sb(3)	9844(1)	9125(1)	7204(1)	24(1)
Sb(4)	13144(1)	9692(1)	8107(1)	22(1)
Sb(5)	16434(1)	10123(1)	9230(1)	22(1)
Sb(6)	15408(1)	10161(1)	6421(1)	25(1)
Sb(7)	18722(1)	10637(1)	7423(1)	24(1)
Sb(8)	20349(1)	10795(1)	10316(1)	21(1)
Sb(9)	21942(1)	11238(1)	8458(1)	24(1)
Sb(10)	21241(1)	12687(1)	8721(1)	29(1)
S(1)	6428(1)	10717(1)	3353(1)	24(1)
S(2)	9043(1)	9904(1)	3595(1)	22(1)
S(3)	7291(2)	9525(1)	5227(1)	27(1)
S(4)	10079(1)	8708(1)	5631(1)	24(1)
S(5)	11969(2)	8883(1)	8343(1)	27(1)
S(6)	15207(1)	9324(1)	9402(1)	26(1)
S(7)	17085(1)	9692(1)	7877(1)	24(1)
S(8)	14723(1)	10609(1)	7709(1)	25(1)
S(9)	16677(2)	10944(1)	6189(1)	32(1)
S(10)	18325(1)	11014(1)	8934(1)	25(1)
S(11)	19859(2)	11428(1)	7137(1)	30(1)
S(12)	21539(2)	11566(1)	9979(1)	27(1)
S(13)	21048(1)	10212(1)	9255(1)	23(1)
S(14)	22665(2)	12141(1)	8188(2)	35(1)
S(15)	22991(2)	13126(1)	10059(2)	76(1)
S(16)	20982(2)	13294(1)	7257(2)	47(1)
N(1)	6143(8)	12338(4)	3136(8)	75(3)
N(2)	7629(10)	12917(4)	4924(7)	74(3)
N(3)	4038(9)	11614(4)	2330(10)	105(5)
C(1)	5893(9)	12895(4)	3261(8)	54(2)
C(2)	6245(10)	13030(5)	4388(8)	71(3)
C(3)	7945(14)	12363(5)	4799(14)	133(8)
C(4)	7478(11)	12243(5)	3602(12)	113(6)
C(5)	5678(11)	12171(6)	2054(11)	101(5)
C(6)	4276(10)	12038(5)	1715(10)	86(4)

U_{eq} is calculated as one third of the trace of the orthogonalised U_{ij} tensor.

Single crystal X-ray diffractometry

Intensity data were collected on a AED2 four circle diffractometer at room temperature using graphite monochromated Mo-K_α radiation ($\lambda = 0.7107$ Å). The intensities were corrected for Lorentz, polarization ef-

Table 3. Selected interatomic distances [Å] and angles [°] for $[C_6H_{17}N_3]Sb_{10}S_{16}$.

Sb(1)-S(2)	2.416(2)	Sb(1)-S(1)	2.516(2)
Sb(1)-S(3)	2.575(2)	Sb(2)-S(3)	2.450(2)
Sb(2)-S(4)	2.470(2)	Sb(2)-S(15a)	2.494(2)
Sb(3)-S(5)	2.456(2)	Sb(3)-S(4)	2.497(2)
Sb(3)-S(16a)	2.509(2)	Sb(4)-S(1b)	2.453(2)
Sb(4)-S(5)	2.523(2)	Sb(4)-S(6)	2.569(2)
Sb(4)-S(2b)	2.926(2)	Sb(5)-S(7)	2.485(2)
Sb(5)-S(6)	2.510(2)	Sb(5)-S(8)	2.595(2)
Sb(6)-S(8)	2.452(2)	Sb(6)-S(7)	2.511(2)
Sb(6)-S(9)	2.533(2)	Sb(7)-S(10)	2.465(2)
Sb(7)-S(9)	2.475(2)	Sb(7)-S(11)	2.484(2)
Sb(8)-S(13)	2.396(2)	Sb(8)-S(10)	2.477(2)
Sb(8)-S(12)	2.506(2)	Sb(9)-S(12)	2.438(2)
Sb(9)-S(11)	2.474(2)	Sb(9)-S(14)	2.485(2)
Sb(10)-S(15)	2.442(3)	Sb(10)-S(14)	2.445(2)
Sb(10)-S(16)	2.448(2)		
S(1)-Sb(1)-S(3)	97.45(5)	S(2)-Sb(1)-S(1)	92.17(5)
S(2)-Sb(1)-S(3)	93.63(5)	S(3)-Sb(2)-S(4)	96.80(5)
S(3)-Sb(2)-S(15a)	91.01(2)	S(4)-Sb(2)-S(15a)	93.67(7)
S(4)-Sb(3)-S(16a)	94.54(6)	S(5)-Sb(3)-S(4)	92.89(6)
S(5)-Sb(3)-S(16a)	90.35(7)	S(1b)-Sb(4)-S(5)	92.60(6)
S(1b)-Sb(4)-S(2b)	82.18(5)	S(1b)-Sb(4)-S(6)	90.23(5)
S(5)-Sb(4)-S(6)	91.69(5)	S(5)-Sb(4)-S(2b)	91.86(5)
S(6)-Sb(4)-S(2b)	171.76(5)	S(6)-Sb(5)-S(8)	99.12(5)
S(7)-Sb(5)-S(6)	93.26(6)	S(7)-Sb(5)-S(8)	87.23(5)
S(7)-Sb(6)-S(9)	98.53(6)	S(8)-Sb(6)-S(7)	89.87(5)
S(8)-Sb(6)-S(9)	95.08(6)	S(9)-Sb(7)-S(11)	94.06(6)
S(10)-Sb(7)-S(9)	91.93(6)	S(10)-Sb(7)-S(11)	95.54(6)
S(10)-Sb(8)-S(12)	96.62(6)	S(13)-Sb(8)-S(10)	95.83(5)
S(13)-Sb(8)-S(12)	91.76(5)	S(11)-Sb(9)-S(14)	90.26(6)
S(12)-Sb(9)-S(11)	97.24(6)	S(12)-Sb(9)-S(14)	89.94(6)
S(14)-Sb(10)-S(16)	89.85(6)	S(15)-Sb(10)-S(14)	90.86(8)
S(15)-Sb(10)-S(16)	99.13(2)		

fects. The structure was solved with direct methods using SHELXS-97 [32] and refinement was done against F^2 using SHELXL-97 [33]. All non-hydrogen atoms were refined using anisotropic displacement parameters. The hydrogen atoms were positioned with idealized geometry and refined using the riding model with free varying isotropic displacement parameters. The technical details of data acquisition and some selected refinement results are summarized in Table 1. The atomic coordinates and equivalent isotropic displacement parameters are presented in Table 2.

Crystallographic data (excluding structure factors) have been deposited with the Cambridge Crystallographic Data Centre as supplementary publication no. CCDC 250600. Copies of the data can be obtained, free of charge, on application to CCDC, 12 Union Road, Cambridge CB2 1 EZ, UK. (Fax: +44-(0)1223-336033 or E-mail: deposit@ccdc.cam.ac.uk).

Results and Discussion

The new compound $[C_6H_{17}N_3][Sb_{10}S_{16}]$ crystallizes in the monoclinic space group $P2_1/c$ with four

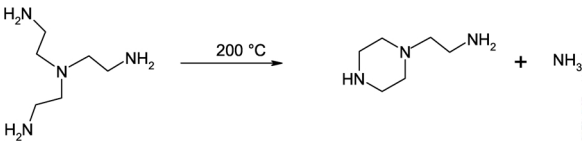

Scheme 1.

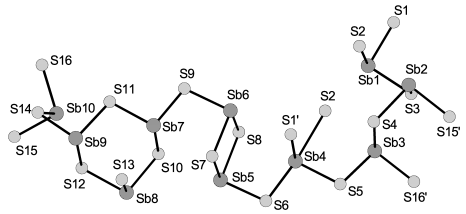

Fig. 1. Interconnection of the trigonal SbS_3 pyramids and the SbS_4 units in $[C_6H_{17}N_3][Sb_{10}S_{16}]$ together with labeling. Note that the primed atoms are generated by symmetry operations.

formula units per unit cell with 10 independent Sb and 16 unique S atoms.

The structure consists of isolated double-protonated 2-piperazine-N-ethylamine cations and a two dimensional $[Sb_{10}S_{16}]^{2-}$ anionic network. The 2-piperazine-N-ethylamine cation is formed under *in-situ* conditions by cyclization of tren molecules as proposed in the reaction Scheme 1.

The interatomic distances and angles are in the typical range (Table 3). We note that Parise *et al*. reported the synthesis of $[C_4H_8N_2][Sb_4S_7]$ with a piperazinium cation formed under *in-situ* conditions applying TETN (triethylenetetramine) as solvent [5].

Nine trigonal pyramidal SbS_3 units and one SbS_4 moiety are the primary building units (PBU) of the $[Sb_{10}S_{16}]^{2-}$ anion (Fig. 1).

The Sb-S bond lengths range from 2.3965(2) to 2.9261(2) Å and the S-Sb-S angles are between 82.18(5) and 171.76(5)° (Table 3). These values are in the range reported for many thioantimonates(III). The PBUs share common corners and edges yielding Sb_3S_3 and Sb_2S_2 hetero-rings as secondary building units (SBU) (Fig. 1). Further condensation leads to strong undulated two atoms thick layers extending in the [010] direction (Fig. 2). The modulation period of the layers is about 14 Å.

Very large $Sb_{31}S_{31}$ rings (Fig. 3) are observed within the layers which show a 'double-ellipsoidal' shape. The two ellipsoidal parts of the ring are separated by a bottleneck. The pores have approximate dimensions of $8.9 \cdot 9.3$ Å. The interlayer distance is be-

$D-H$	$d(H\cdots A)$	$\langle DHA$	$d(D\ldots A)$	A
N2-H2A	2.418	150.56	3.232 S10	$[x-1,-y+5/2,z-1/2]$
N2-H2B	2.621	133.09	3.302 S5	$[-x+2,y+1/2,-z+3/2]$
N3-H3A	2.684	151.97	3.495 S16	$[x-2,-y+5/2,z-1/2]$
N3-H3A	2.871	125.15	3.461 S12	$[x-2,y,z-1]$
N3-H3C	2.715	138.96	3.436 S1	
N3-H3C	2.933	140.35	3.663 S6	$[-x+2,-y+2,-z+1]$

Table 4. Geometry parameters [Å, °] for S···H bonding in $[C_6H_{17}N_3]Sb_{10}S_{16}$.

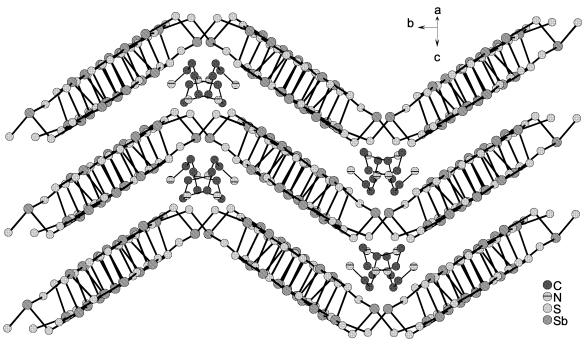

Fig. 2. The crystal structure of $[C_6H_{17}N_3][Sb_{10}S_{16}]$ viewed along [201].

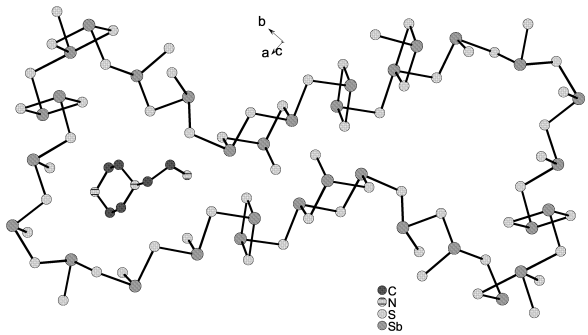

Fig. 3. The layer in $[C_6H_{17}N_3][Sb_{10}S_{16}]$ with the large double ellipsoidal $Sb_{31}S_{31}$ rings.

tween 3.6 and 4 Å. The cations are located at the inflexion points of the layers (Fig. 2) and act as pillars between successive layers. Relatively short S···H separations are observed which indicate H bonding interactions between the cation and the thioantimonate(III) anion (Table 4).

The layers are stacked onto each other in a way that channels parallel to [001] are formed accommodating the organic cations (Fig. 4). We note that smaller channels (diameter: $6.5 \cdot 5.7$ Å) run along the *a* axis.

When long Sb-S bonds above 3.0 Å are considered (Table 5), the structure may be viewed as a 3-dimensional network. Taking these Sb-S distances into account the Sb(1,2,4,5,6,7,8) atoms are sixfold coordinated forming strong distorted octahedra, Sb(3,10) form SbS_5 units and Sb(9) is surrounded by 4 S atoms.

Table 5. The long Sb-S bonds [Å] in $[C_6H_{17}N_3]Sb_{10}S_{16}$.

Sb(1)-S(4)	3.163(2)	Sb(1)-S(6)	3.117(6)
Sb(1)-S(9)	3.437(3)	Sb(2)-S(2)	3.168(1)
Sb(2)-S(8)	3.589(7)	Sb(3)-S(2)	3.128(2)
Sb(3)-S(3)	3.352(7)	Sb(4)-S(8)	3.098(9)
Sb(4)-S(13)	3.573(3)	Sb(5)-(6)	3.405(3)
Sb(5)-S(10)	3.245(8)	Sb(5)-S(13)	3.013(6)
Sb(6)-S(1)	3.145(6)	Sb(6)-S(3)	3.211(6)
Sb(6)-S(3)	3.537(6)	Sb(7)-S(2)	3.609(3)
Sb(7)-S(7)	3.224(1)	Sb(7)-S(13)	3.122(6)
Sb(8)-S(7)	3.326(6)	Sb(8)-S(13)	3.160(9)
Sb(8)-S(16)	3.379(2)	Sb(9)-S(13)	3.109(1)
Sb(10)-S(4)	3.257(2)	Sb(10)-S(12)	3.248(5)

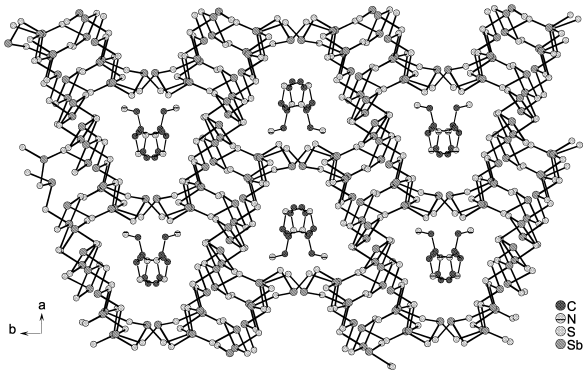

Fig. 4. The channels in $[C_6H_{17}N_3][Sb_{10}S_{16}]$ running along [001].

We note that the Sb-S bond lengths within the layers are significantly shorter than those between the layers.

The arrangement of the thioantimonate anion together with the formation of the large rings reflect the structure directing effect of the *in-situ* formed cations.

Several thioantimonates(III) with a Sb:S ratio of 1 : 1.67 were reported in the past, but all show a different connection mode compared to that in the title compound. In $[C_6H_{15}N_2][Sb_3S_5]$ one SbS_3 and two SbS_4 groups are joined to form the layered anion which comprises Sb_2S_2, Sb_4S_4 and Sb_5S_5 rings as secondary building units [7]. One-dimensional chain anions are observed in $[N(C_3H_7)_4][Sb_3S_5]$ [5] and in $[Ph_4P]_2[Sb_6S_{10}]$ [8]. In the two compounds only trigonal SbS_3 pyramids appear which are joined into Sb_5S_5 rings that are condensed yielding the chain anions.

In $RbSb_3S_5{\cdot}H_2O$ the SbS_3 groups are joined to form small Sb_2S_2 and large $Sb_{12}S_{12}$ heterorings which are connected into a two atoms thick layered anion [4]. In $TlSb_3S_5$ also only trigonal SbS_3 pyramids are observed and the thioantimonate(III) anion is a complex three-dimensional network composed of Sb_2S_2, Sb_5S_5, and Sb_8S_8 heterorings [6]. In the two thioantimonates(III) $[M(C_4H_{13}N_3)_2][Sb_6S_{10}]{\cdot}0.5H_2O$ (M = Fe, Ni) [9] five SbS_3 pyramids and one SbS_4 unit are the PBUs. The topology of the network is complex and a short description base on chains built up by the interconnection of -Sb_4S_4-SbS_3-SbS_4-Sb_4S_4-units. These chains are joined into the final layered anion *via* common corners and edges. Besides small heterorings (Sb_2S_2, Sb_4S_4, Sb_5S_5) a ring containing 32 atoms ($Sb_{16}S_{16}$) represents the largest SBU in these compounds [9]. A two atoms thick one-dimensional $[Sb_{12}S_{20}]^{4-}$ chain anion is observed in $[(NH_3CH_3)_{1.03}K_{2.97}][Sb_{12}S_{20}]{\cdot}1.34H_2O$ [10] which is composed of 10 SbS_3 pyramids and two SbS_4 moieties. A central Sb_4S_4 ring is bound to 6 Sb_3S_3 units forming the next hierarchical building block. These blocks are joined *via* S atoms and larger Sb_8S_8 heterorings are formed [10]. In the two thioantimonates(III) $[C_6N_3H_{17}{}^{2+}][Sb_6S_{10}]$ and $[C_7N_2H_{13}{}^{+}]_3[Sb_9S_{15}]$ primary building units are trigonal SbS_3 pyramids and SbS_4 moieties [31]. In the former compound five SbS_3 groups and one SbS_4 unit form Sb_3S_3 rings and Sb_3S_4 semi-cubes as the SBUs, which are joined *via* common S atoms to form the one-dimensional $^1_\infty[Sb_6S_{10}]^{2-}$ anion [31]. In $[C_7N_2H_{13}{}^{+}]_3[Sb_9S_{15}]$ the six SbS_3 pyramids and the three SbS_4 units each form individual chains by vertex linking. Interestingly, one chain is exclusively formed by SbS_4 units whereas the other two chains are composed of SbS_3 pyramids. The chains are joined *via* common corners yielding the one-dimensional $^1_\infty[Sb_9S_{15}]^{3-}$ multiple chain anion. Within these chains Sb_4S_4 rings as SBUs are observed [31].

Analyzing the structures of all compounds with the Sb : S ratio of 1 : 1.67 there are no obvious relationships between the number and kind of PBUs and SBUs in the different compounds, the final topology and the dimensionality of the anionic networks. Even when Sb-S distances up to about 3.9 Å are treated as weak Sb-S interactions the situation is still complex. Obviously, in several of the above mentioned compounds the organic cations are large and a higher dimensionality of the anionic framework cannot be achieved. This may be the case for the one-dimensional chains in $[[N(C_3H_7)_4][Sb_3S_5]$ [5] and $[Ph_4P]_2[Sb_6S_{10}]$ [8], where the largest extensions of the cations are about 7 Å and 9.5 Å. On the other hand, a layered thioantimonate(III) is oberved in $[M(C_4H_{13}N_3)_2][Sb_6S_{10}]{\cdot}0.5H_2O$ [9] with cations having dimensions of about 7.7 Å. As a general tendency, the dimensionality of the anionic framework is reduced with increasing size of the cation. But other factors like for instance the charge distribution on the cations or S···H interactions seem to be also important for the formation of the actual thioantimonate(III) anion.

[1] P. Berlepsch, R. Miletich, T. Armbruster, Z. Kristallogr. **214**, 57 (1999).
[2] X. Wang, Eur. J. Solid State Inorg. Chem. **32**, 303 (1995).
[3] J. B. Parise, Science **251**, 293 (1991).
[4] K. Volk, H. Schäfer, Z. Naturforsch. **24b**, 172 (1979).
[5] J. B. Parise, Y. Ko, Chem. Mater. **4**, 1446 (1992).
[6] M. Gostojic, W. Nowacki, P. Engel, Z. Kristallogr. **159**, 217 (1982).
[7] L. Engelke, C. Näther, W. Bensch, Eur. J. Inorg. Chem. 2936 (2002).
[8] J. Rijnberk, C. Näther, W. Bensch, Monatsh. Chem. **131**, 721 (2000).
[9] R. Stähler, C. Näther, W. Bensch, Eur. J. Chem. 1835 (2001).
[10] X. Wang, A. J. Jacobson, F. Liebau, J. Solid State Chem. **140**, 387 (1998).
[11] H. A. Graf, H. Schäfer, Z. Naturforsch. **27b**, 735 (1972).
[12] G. Dittmar, H. Schäfer, Z. Anorg. Allg. Chem. **437**, 183 (1977).
[13] G. Dittmar, H. Schäfer, Z. Anorg. Allg. Chem. **441**, 93 (1978).
[14] G. Dittmar, H. Schäfer, Z. Anorg. Allg. Chem. **441**, 98 (1978).
[15] B. Eisenmann, H. Schäfer, Z. Naturforsch. **34b**, 383 (1979).
[16] G. Cordier, H. Schäfer, C. Schwidetzky, Z. Naturforsch. **39b**, 131 (1984).
[17] W. Bensch, M. Schur, Z. Naturforsch. **52b**, 405 (1997).
[18] W. S. Sheldrick, H.-J. Häusler, Z. Anorg. Allg. Chem. **557**, 105 (1988).
[19] M. Schur, W. Bensch, Eur. J. Solid State Inorg. Chem. **34**, 457 (1997).

[20] M. Schaefer, D. Kurowski, A. Pfitzner, C. Näther, W. Bensch, Acta. Crystallogr. **E60**, m183 (2004).
[21] M. Schaefer, R. Kiebach, R. Stähler, C. Näther, W. Bensch, Z. Anorg. Allg. Chem., in press (2004).
[22] R. Stähler, C. Näther, W. Bensch, J. Solid State Chem. **174**, 264 (2003).
[23] W. S. Sheldrick, H.-J. Häusler, Z. Anorg. Allg. Chem. **561**, 149 (1988).
[24] J. B. Parise, J. Chem. Soc., Chem. Commun. 1553 (1990).
[25] K. Volk, P. Bickert, R. Kolmer, H. Schäfer, Z. Naturforsch. **34b**, 380 (1979).
[26] H. A. Graf, H. Schäfer, Z. Anorg. Allg. Chem. **414**, 211 (1975).
[27] G. Cordier, C. Schwidetzky, H. Schäfer, J. Solid State Chem. **54**, 84 (1984).
[28] R. Kiebach, F. Studt, C. Näther, W. Bensch, Eur. J. Inorg. Chem. 2553 (2004).
[29] T. J. McCarthy, M. G. Kanatzidis, Inorg. Chem. **33**, 1205 (1994).
[30] W. Bensch, C. Näther, R. Stähler, Chem. Commun. 477 (2001).
[31] V. Spetzler, R. Kiebach, C. Näther, W. Bensch, Z. Anorg. Allg. Chem. **630**, 2398 (2004).
[32] G. M. Sheldrick, SHELXS-97, Program for Crystal Structure Determination, University of Göttingen, Germany (1997).
[33] G. M. Sheldrick, SHELXL-97, Program for the Refinement of Crystal Structures, University of Göttingen, Germany (1997).

4.1.2 Die Verbindung $[C_7H_{13}N_2]_3[Sb_9S_{15}]$

Zusammenfassung der Veröffentlichung „*Two Novel Thioantimonates(III) with the same Stoichiometric Sb:S Ratio but Different Crystal Structures: Solvothermal Synthesis, Crystal Structures, Thermal Stability and Spectroscopy of* $(C_6N_3H_{17})Sb_6S_{10}$ *and of* $(C_7N_2H_{13})_3Sb_9S_{15}$“.

Die Synthese von $[C_7N_2H_{13}]_3[Sb_9S_{15}]$ ($C_7N_2H_{13}$ = 1,5- Diazobicyclo[4.3.0]non-5-en = DBN) erfolgte mit 1 mmol Sb und 3 mmol S in 4 ml 50 %iger DBN-Lösung. Das Reaktionsgemisch wurde 7 Tage bei 160 °C in einem Autoklaven erhitzt. Das Produkt fällt in Form roter Nadeln mit einer Ausbeute von 95 % an. $[C_7N_2H_{13}]_3[Sb_9S_{15}]$ kristallisiert in der monoklinen Raumgruppe $P2_1/c$ mit vier Formeleinheiten pro Elementarzelle. Die Struktur besteht aus isolierten $[C_7N_2H_{13}]^+$-Kationen und einem kettenförmigen 1-dimensionalen $[Sb_9S_{15}]^{3-}-$Anion. Sechs SbS_3- und drei SbS_4- Einheiten bilden die primären Baueinheiten. Das Anion wird aus drei Kettensträngen bebildet, wobei die mittlere Kette aus eckenverknüpften SbS_4-Einheiten, die beiden äußeren Kettenstränge aus SbS_3-Einheiten aufgebaut sind. Die Verknüpfung der individuellen Kettenstränge über gemeinsame Ecken führt zur Bildung des $[Sb_9S_{15}]^{3-}-$Anions (Abb. 4.1, rechts). Durch den Verknüpfungsmodus werden Sb_4S_4-Ringe gebildet, welche längs [001] aneinander kondensiert sind. Die Ketten sind entlang [100] gestapelt, und der kürzeste Interkettenabstand beträgt ca. 7 Å. In der [010]-Richtung liegen die Ketten mit einem Abstand von etwa 3.4 Å nebeneinander. Werden längere Sb-S-Abstände berücksichtigt, kommt es zur Ausbildung von Schichten in der (100)-Ebene. Die Kationen befinden sich zwischen diesen Schichten in einer Art „Sandwichstruktur“.

Die Verbindung $[C_7N_2H_{13}]_3[Sb_9S_{15}]$ zersetzt sich ab einer Temperatur von 245 °C in zwei Stufen mit einem Gesamtmassenverlust von 20.1 %. Der thermische Abbau wird von endothermen Ereignissen in der DTA-Kurve begleitet. In dem grauen Abbauprodukt konnten Sb_2S_3 und elementares Sb in dem Pulverdiffraktogramm identifiziert werden. Die optische Bandlücke wurde mit UV/Vis-Spektren zu 2 eV bestimmt, womit $[C_7N_2H_{13}]_3[Sb_9S_{15}]$ als optischer Halbleiter eingestuft werden kann.

Die zweite Verbindung $[C_6N_3H_{17}][Sb_6S_{10}]$ wurde von V. Spetzler dargestellt und charakterisiert. Interessant ist, dass das Sb:S-Verhältnis in beiden 1:1.66 beträgt, die Thioantimonatanionen jedoch unterschiedliche sekundäre Baueinheiten aufweisen. Die

SbS_3- und SbS_4-Einheiten sind in beiden Verbindungen in unterschiedlicher Weise verknüpft (Abb 4.1, links) und bilden so verschiedene sekundäre Baueinheiten. Auch wenn die thermischen und physikalischen Eigenschaften, wie z.B. die optische Bandlücke, vergleichbar sind, stellen die beiden Verbindungen ein Beispiel für die Strukturvielfalt der Thioantimonate dar, die sich aus der Flexibilität der primären Baueinheiten ergibt. Die Ramanspektren von Thioantimonaten sind bis heute schlecht verstanden und können noch nicht umfassend interpretiert werden. Auch bei den Verbindungen $[C_7N_2H_{13}]_3[Sb_9S_{15}]$ und $[C_6N_3H_{17}][Sb_6S_{10}]$ war eine eindeutige Zuordnung der Banden nicht möglich, obwohl die primären Baueinheiten identisch sind.

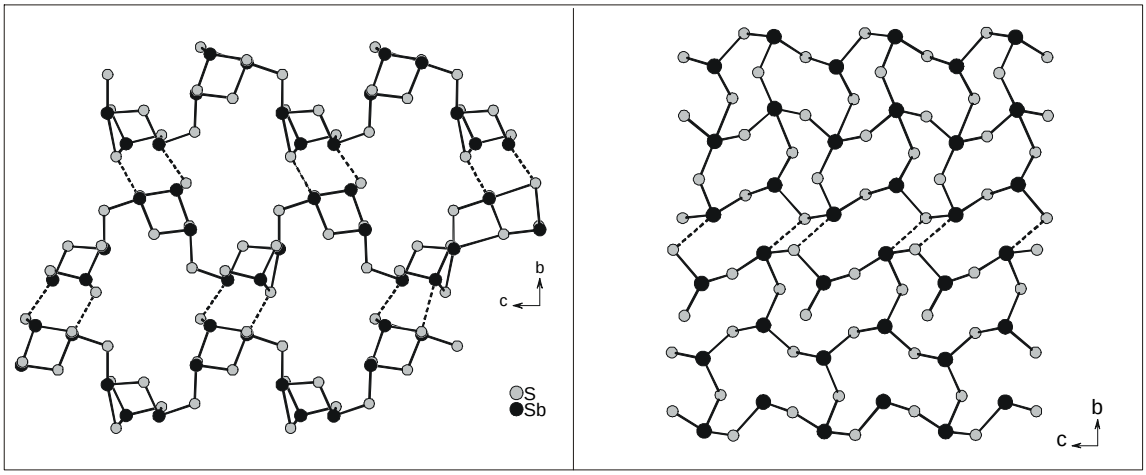

Abbildung 4.1: Unterschiedliche Verknüpfungsmuster der Anionen: $[Sb_6S_{10}]^{2-}$- (links) und $[Sb_9S_{15}]^{3-}$-Anion (rechts)

Two Novel Thioantimonates(III) with the Same Stoichiometric Sb:S Ratio but Different Crystal Structures: Solvothermal Synthesis, Crystal Structures, Thermal Stability and Spectroscopy of $(C_6N_3H_{17})Sb_6S_{10}$ and $(C_7N_2H_{13})_3Sb_9S_{15}$

Volker Spetzler, Ragnar Kiebach, Christian Näther, and Wolfgang Bensch*

Kiel, Institut für Anorganische Chemie der Christian-Albrechts Universität

Received Mai 28th, 2004.

Dedicated to Professor Martin Jansen on the Occasion of his 60th Birthday

Abstract. The two novel thioantimonates(III) $(C_6N_3H_{17}^{2+})Sb_6S_{10}$ (**I**) and $(C_7N_2H_{13}^{+})_3Sb_9S_{15}$ (**II**) were synthesized under solvothermal conditions reacting Sb and S with the amines 1-(2-aminoethyl)-piperazine ($C_6N_3H_{15}$) and 1,5-diazabicyclo[4.3.0.]non-5-en (DBN, $C_7N_2H_{12}$), respectively. The compounds crystallize as red needles in the monoclinic non-centrosymmetric space group $P2_1$ (**I**) and in the monoclinic space group $P2_1/c$ (**II**) with lattice parameters a = 6.120(4) Å, b = 17.759(1) Å, c = 11.478(7) Å, β = 90.70(7)° for **I** and a = 10.2643(6) Å, b = 23.648(2) Å, c = 20.4655(11) Å, β = 104.430(7)° for **II**.

In both compounds the primary building units (PBUs) are trigonal SbS_3 pyramids and SbS_4 moieties. The interconnection of these PBUs leads to the formation of six-membered rings Sb_3S_3 and Sb_3S_4 semi-cubes in **I** which are joined via common S atoms to form the one-dimensional $^1_\infty[Sb_6S_{10}]^{2-}$ anion being directed along [001]. Neighbored chains are arranged in a way that pockets are formed which host the organic cations. The ammonium groups of the organic molecules are oriented towards the anion ensuring optimal S···H bonding interactions. Taking into account the longer Sb−S bonds above 3 Å a three-dimensional network is formed with large cages containing the organic cations. In compound **II** the SbS_3 pyramids and the SbS_4 units each form individual chains by vertex linking. The central chain is exclusively formed by SbS_4 units whereas the other two chains are composed of SbS_3 pyramids. The interconnection of the chains via common corners yields the one-dimensional $^1_\infty[Sb_9S_{15}]^{3-}$ multiple chain anion. Due to the connection mode Sb_4S_4 rings are formed which are condensed along [001]. The chains are stacked along [100] with an inter-chain separation of about 7 Å. In the [010] direction the anions are lined-up with the shortest distance between neighbored anions of about 3.4 Å. With the long Sb−S distances layers within the (100) plane are formed. At elevated temperatures both compounds decompose via an internal redox reaction into Sb_2S_3 (Stibnite) and Sb. The optical band gaps of about 2 eV indicate that both compounds are semiconductors.

Keywords: Thioantimonates; Solvothermal synthesis; Crystal structure; Spectroscopy; Thermal investigation; Hybrid compounds

Zwei neue Thioantimonate(III) mit identischem stöchiometrischem Sb:S-Verhältnis aber unterschiedlichen Kristallstrukturen: Solvothermale Synthese, Kristallstrukturen, thermische Stabilität und optische Spektren von $(C_6N_3H_{17})Sb_6S_{10}$ und $(C_7N_2H_{13})_3Sb_9S_{15}$

Inhaltsübersicht. Die zwei neuen Thioantimonate(III) $(C_6N_3H_{17}^{2+})Sb_6S_{10}$ (**I**) und $(C_7N_2H_{13}^{+})_3Sb_9S_{15}$ (**II**) wurden unter solvothermalen Bedingungen bei der Reaktion von Antimon und Schwefel mit den Aminen 1-(2-aminoethyl)-Piperazin ($C_6N_3H_{15}$) (**I**) und 1,5-diazabicyclo[4.3.0.]non-5-en (DBN, $C_7N_2H_{12}$) (**II**) erhalten. Die Verbindungen kristallisieren in Form roter Nadeln in der monoklinen nicht-zentrosymmetrischen Raumgruppe $P2_1$ (**I**) und in der monoklinen Raumgruppe $P2_1/c$ (**II**) mit den Gitterparametern a = 6.120(4) Å, b = 17.759(1) Å, c = 11.478(7) Å, β = 90.70(7)° für **I** und a = 10.2643(6) Å, b = 23.648(2) Å, c = 20.4655(11) Å, β = 104.430(7)° für **II**.

In beiden Verbindungen bilden trigonale SbS_3-Pyramiden und SbS_4-Einheiten die primären Baugruppen. In Verbindung **I** werden diese zu sechsgliedrigen Sb_3S_3-Ringen und Sb_3S_4-Halbwürfeln verknüpft, welche über gemeinsame S-Atome zu dem eindimensionalen $^1_\infty[Sb_6S_{10}]^{2-}$ -Kettenanion verbunden sind. Die Ketten verlaufen parallel zu [001] und benachbarte Ketten sind so angeordnet, dass Taschen gebildet werden, in welchen sich die organischen Kationen befinden. Die Ammoniumgruppen des Kations sind in Bezug auf das Anion so angeordnet, dass S···H-Bindungen gebildet werden können. Werden bei der Strukturbeschreibung Sb−S-Kontakte länger als 3 Å berücksichtigt, dann kann ein dreidimensionales Netzwerk mit großen Käfigen identifiziert werden, in denen sich die organischen Kationen befinden. In Verbindung **II** bilden die SbS_3-Pyramiden und die SbS_4-Gruppen individuelle Ketten durch Eckenverknüpfung. Die zentrale Kette wird ausschließlich von SbS_4-Einheiten gebildet, während zwei weitere Ketten nur SbS_3-Pyramiden enthalten. Die individuellen Ketten sind über gemeinsame Ecken zu dem eindimensionalen $^1_\infty[Sb_9S_{15}]^{3-}$-Anion verknüpft. Durch den Verknüpfungsmodus werden Sb_4S_4-Ringe gebildet, welche längs [001] aneinander kondensiert sind. Die Ketten sind entlang [100] gestapelt und der kürzeste Interkettenabstand beträgt etwa 7 Å. In der [010]-Richtung liegen die Ketten mit einem Abstand von etwa 3.4 Å nebeneinander. Unter Berücksichtigung der längeren Sb−S-Abstände werden Schichten in der (100)-Ebene ausgebildet. Bei erhöhten Temperaturen zersetzen sich die Verbindungen über eine interne Redoxreaktion zu Sb und Sb_2S_3. Die optischen Bandlücken von ca. 2 eV weisen darauf hin, dass es sich bei den Verbindungen um Halbleiter handelt.

  DOI: 10.1002/zaac.200400194

1 Introduction

A detailed analysis of the structures of thioantimonate(III) compounds reveals some remarkable and unique features. Starting with the most dense antimony sulfide Sb_2S_3 all negatively charged Sb−S compounds must have a Sb : S ratio which is larger than 1: 1.5. In addition, for an identical Sb:S ratio different chemical compositions are observed, and examples are thioantimonates(III) with Sb : S ratios of 1 : 1.75 ($[Sb_4S_7]^{2-}$ [1−9], $[Sb_{12}S_{21}]^{6-}$ [10]), 1:2 ($[SbS_2]^-$ [11, 12], $[Sb_2S_4]^{2-}$ [13], $[Sb_3S_6]^{3-}$ [14], $[Sb_4S_8]^{2-}$ [15], $[Sb_4S_8]^{4-}$ [16]), 1 : 1.67 ($[Sb_3S_5]^-$ [17−21], $[Sb_6S_{10}]^{2-}$ [22, 23], $[Sb_{12}S_{20}]^{4-}$ [24]), or 1 : 1.8 ($[Sb_5S_9]^{3-}$ [25], $[Sb_{10}S_{18}]^{6-}$ [26]). Furthermore, for a given composition different connectivities of the primary SbS_3 and SbS_4 building units and different dimensionalities of the thioantimonate(III) anions are observed. The dimensionality of a given thioantimonate(III) anion is mainly determined by the size of the counter cation. Hence, the cation supplied during the syntheses has a structure directing effect. This can be demonstrated on the series of compounds containing the $[Sb_4S_7]^{2-}$ anion [1−9]. Only $K_2Sb_4S_7$ shows a three-dimensional interconnected $[Sb_4S_7]^{2-}$ anion [1] and with increasing size of the cation the dimensionality is reduced to two-dimensional layers [3, 5, 6, 7, 8] and finally to one-dimensional chains [2, 4, 9]. Another example are compounds with a Sb:S ratio of 1:1.67. Five different thioantimonates(III) were reported with the $[Sb_3S_5]^-$ anion [17−21], two with the $[Sb_6S_{10}]^{2-}$ anion [22, 23] and one with the $[Sb_{12}S_{20}]^{4-}$ anion [24]. In the compound $[C_6H_{15}N_2][Sb_3S_5]$ the anions form layers with Sb_2S_2, Sb_4S_4 and Sb_5S_5 rings as the secondary building units [21]. A very different type of an one-dimensional chain is observed in $[[N(C_3H_7)_4][Sb_3S_5]$ [19] and in $[Ph_4P]_2[Sb_6S_{10}]$ [22]. In both compounds the SbS_3 pyramids joined to form Sb_5S_5 rings which are condensed yielding the chain anions. In $RbSb_3S_5 \cdot H_2O$ small Sb_2S_2 and large $Sb_{12}S_{12}$ heterorings are joined to form a two atoms thick layered anion [18]. Finally, a complex three-dimensional network is formed in $TlSb_3S_5$ [20]. The topology of the anion in $[M(C_4H_{13}N_3)_2]Sb_6S_{10} \cdot 0.5\ H_2O$ (M = Fe, Ni) [23] is complex and may be shortly described as chains built up by the interconnection of -Sb_4S_4-SbS_3-SbS_4-Sb_4S_4- units. These chains are then further joined into the final layered anion via common corners and edges. The largest ring contains 32 atoms ($Sb_{16}S_{16}$) [23]. The one-dimensional $[Sb_{12}S_{20}]^{4-}$ chain anion in $((MA)_{1.03}K_{2.97})[Sb_{12}S_{20}] \cdot 1.34\ H_2O$ is two atoms thick. A central Sb_4S_4 ring is bound to 6 Sb_3S_3 units forming the next hierarchical building block. These blocks are joined via S atoms and larger Sb_8S_8 heterorings are formed [24]. The description of the structures presented above base on a cut-off for the Sb−S distances of about 3 Å. But the assignment of the dimensionality is arbitrary in thioantimonates(III) because Sb−S distances scatter in the large range between 2.2 and 3.9 Å. Therefore, the description of the structures of thioantimonates(III) and the final assignment of the dimensionality is not straight forward.

During our continuing efforts to synthesize new thioantimonates(III) we prepared the two new compounds $(C_6N_3H_{17}{}^{2+})Sb_6S_{10}$ and $(C_7N_2H_{13}{}^+)_3Sb_9S_{15}$. In the present contribution we report on the syntheses, crystal structures, thermal stability and optical properties of these new thioantimonates(III).

2 Experimental details

Syntheses

The compounds $(C_6N_3H_{17}{}^{2+})Sb_6S_{10}$ (**I**) and $(C_7N_2H_{13}{}^+)_3Sb_9S_{15}$ (**II**) were prepared under solvothermal conditions in a Teflon-lined steel autoclave. A mixture of Sb (1 mmol), S (3 mmol) and 5 ml 1-(2-aminoethyl)-piperazine respectively 2 ml DBN (1,5-diazabicyclo [4.3.0.]non-5-en) diluted with 2 ml water were heated at 170 °C (**I**) or 160 °C (**II**) for 7 days followed by cooling to room temperature. The products were collected by filtration and washed with deionised water and acetone. The yields of the products were about 95 % based on Sb. The compounds consist of red needle-like crystals (see Fig. 1). Elemental analysis **I**: found: C 6.0, H 1.4, N 3.5 %; calc.: C 5.5, H 1.2, N 3.4 %; **II**: found: C 13.3, H 2.1, N 4.7; calc.: C 12.9, H 2.1, N 4.6 %; We also prepared compound **I** under the same experimental conditions with a mixture of Cu (2 mmol), Sb (2 mmol), S (5 mmol) and 5 ml 1-(2 aminoethyl)-piperazine yielding only 30 % based on Sb. In the X-ray powder pattern of this product $CuSbS_2$ could be identified as the second product.

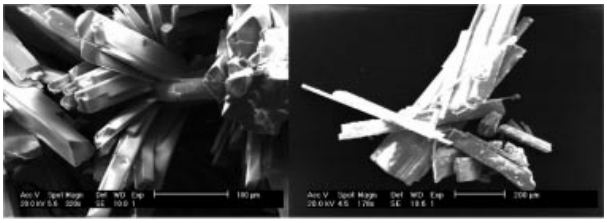

Fig. 1 SEM micrographs of the needle-like crystals of $(C_6N_3H_{17}{}^{2+})Sb_6S_{10}$ (**I**) (left) and $(C_7N_2H_{13}{}^+)_3Sb_9S_{15}$ (**II**) (right).

X-Ray scattering studies

The X-ray intensity data of single crystals of **I** and **II** were collected at 293 K using a STOE AED 4 diffractometer with graphite monochromated MoK_α radiation (λ = 0.71073 Å). The raw intensities were treated in the usual way applying a Lorentz, polarization as well as an absorption correction. The structures were solved using SHELXS-97 [27]. Crystal structure refinements were done against F^2 with SHELXL-97 [28]. All non-hydrogen atoms in compound **II** except those which are disordered were refined with anisotropic displacement parameters. The hydrogen atoms in compound **I** were positioned with idealized geometry and refined with fixed isotropic

* Prof. Dr. W. Bensch
Institut für Anorganische Chemie der Universität Kiel
Olshausenstr. 40
D-24098 Kiel
Fax: +49 (0)431/880-1520
e-mail: wbensch@ac.uni-kiel.de

Table 1 Details of the data collections and selected refinement results for $(C_6N_3H_{17}^{2+})Sb_6S_{10}$ (**I**) and $(C_7N_2H_{13}^{+})_3Sb_9S_{15}$ (**II**).

	I	II
a / Å	6.120(4)	10.2634(6)
b / Å	17.759(1)	23.648(2)
c / Å	11.478(7)	20.4655(11)
β / °	90.70(7)	102.430(7)
V /Å^3	1247.4(1)	4858.2(5)
Z	2	4
μ / mm^{-1}	7.25	5.48
MW / g·mol^{-1}	1128.33	1872.08
Space group	$P2_1$	$P2_1/c$
$\rho_{(calc)}$ / g·cm^{-3}	3.148	2.560
2θ range / °	4−56	4−53
Data collected	12066	42188
R_{int}	0.0370	0.0310
unique data	5770	10341
Data $F_0 > 4\sigma(F_0)$	5465	7063
parameters	228	461
R1 for $F_0 > 4\sigma(F_0)$	0.0322	0.0341
wR2 all reflections	0.0810	0.0880
wR2 for $F_0 > 4\sigma(F_0)$	0.0789	0.0784
δF/(e/Å^3)	1.25/−1.31	0.85/−1.28

displacement parameters using a riding model. The absolute structure of compound **I** was determined and is in agreement with the selected setting (Flack-x parameter: 0.03(3)). In addition, refinement of the inverse structure leads to significant poorer reliability factors. Because compound **I** was additionally merohedrally twinned a twin refinement was performed using the twin option in SHELXL-97 leading to significant better reliability factors (BASF parameter: 0.02626)). In compound **II** several atoms of the organic cations are disordered and were refined using a split model and isotropic displacement parameters. Details of the data collections and refinement results are summarized in Table 1. Bond lengths and angles for the two compounds are listed in Table 2 and 5.
Crystallographic data (excluding structure factors) for the structures reported in this paper have been deposited with the Cambridge Crystallographic Data Centre as supplementary publication no. CCDC 240308 for **I** and CCDC 240309 for **II**. Copies of the data can be obtained, free of charge, on application to CCDC, 12 Union Road, Cambridge CB2 1EZ, UK. (fax: +44-(0)1223-336033 or email: deposit@ccdc.cam.ac.uk).

Spectroscopy

The Raman spectra were measured from 100 to 500 cm^{-1} with a Bruker IFS 66 Fourier transform Raman spectrometer (wavelength: 514.5 nm, T = 20 K).

Thermoanalytical investigations

Thermogravimetry analyses were performed using a Netzsch STA 429 DTA-TG device. The samples were heated in Al_2O_3 crucibles at a rate of 4 K·min^{-1} to 400 °C under a flow of argon of 100 ml min^{-1}.

3 Results and Discussion

The new compound $(C_6N_3H_{17}^{2+})Sb_6S_{10}$ (**I**) crystallizes as red needles (Fig.1 left) in the monoclinic non-centrosymmetric space group $P2_1$ with two formula units. In the following the description of the structure base on a cut-off for the Sb−S distances of about 3.0 Å. Five of the six unique Sb atoms have bonds to 3 S atoms forming the well established trigonal SbS_3 pyramids and one Sb atom is bound to 4 S atoms yielding a SbS_4 unit (Fig. 2). These units may be called the primary building units (PBUs). Two different secondary building units (SBUs) are generated by the interconnection of the PBUs. A six-membered Sb_3S_3 ring is formed by three SbS_3 pyramids (Sb(1,2,6)), and a Sb_3S_4 semi-cube is constructed by two SbS_3 groups and the SbS_4 unit (Sb(3,4,5)) (Fig. 2). In the semi-cube the Sb(3)S_4 and Sb(4)S_3 units are joined by a common edge whereas all other PBUs share common corners. The Sb_3S_3 rings and the Sb_3S_4 semi-cubes are joined by common S atoms to form the one-dimensional $^1_\infty[Sb_6S_{10}]^{2-}$ chain anion which is directed along [001] (Fig. 3). The Sb−S bond lengths vary between 2.379(3) Å and 2.985(2) Å and S−Sb−S angles range from 84.92 (6)° to 110.11 (7)° (Table 2). We note that the long Sb(3)−S(7) distance is in *trans* position to the shorter Sb(3)−S(4) bond of 2.522(2) Å. All structural parameters are typical for the well known trigonal pyramidal SbS_3 unit and the SbS_4 moiety. All Sb atoms except the atom Sb(1) enhance their coordination spheres with S atoms at distances up to 3.8 Å (Table 3). The resulting polyhedra may be described as distorted SbS_6 octahedra (Sb(2,3,5,6)) and as a distorted SbS_5 rectangular pyramid (Sb(4)).

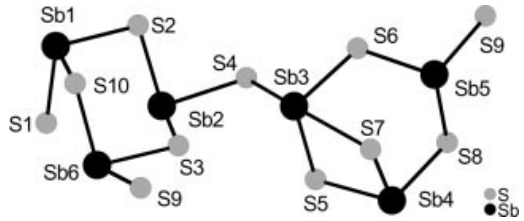

Fig. 2 Interconnection of the primary building units in $(C_6N_3H_{17}^{2+})Sb_6S_{10}$ (**I**) together with labelling.

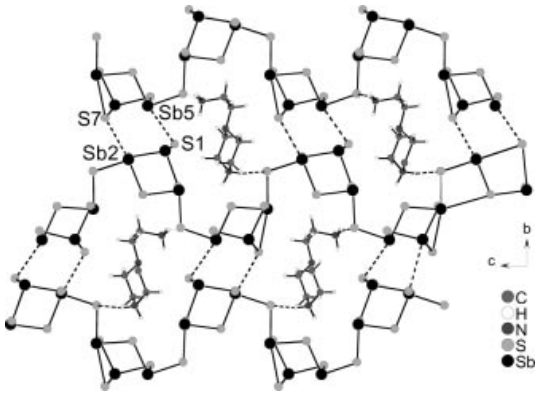

Fig. 3 Interconnection of the $^1_\infty[Sb_6S_{10}]^{2-}$ chains which are directed along [001] via the long Sb−S bonds (dotted lines) forming a three-dimensional network with large cages accommodating the organic cations in $(C_6N_3H_{17}^{2+})Sb_6S_{10}$ (**I**) (The S···H bonds are indicated as dotted lines).

Table 2 Selected interatomic distances/Å and angles/° in the compound $(C_6N_3H_{17}^{2+})Sb_6S_{10}$ (**I**). Estimated standard deviations are given in parentheses.

Sb(1)−S(1)	2.379(3)	Sb(4)−S(7)	2.393(2)
Sb(1)−S(2)	2.450(2)	Sb(4)−S(8)	2.470(2)
Sb(1)−S(10)[a]	2.512(2)	Sb(4)−S(5)	2.487(2)
Sb(2)−S(4)	2.457(2)	Sb(5)−S(8)	2.453(2)
Sb(2)−S(2)	2.476(2)	Sb(5)−S(6)	2.499(2)
Sb(2)−S(3)	2.510(2)	Sb(5)−S(9)	2.521(2)
Sb(3)−S(5)	2.452(2)	Sb(6)−S(10)	2.469(2)
Sb(3)−S(6)	2.488(2)	Sb(6)−S(9)	2.512(2)
Sb(3)−S(4)	2.522(2)	Sb(6)−S(3)[b]	2.448(2)
Sb(3)−S(7)	2.985(2)		
S(1)−Sb(1)−S(2)	99.62(8)	S(8)−Sb(5)−S(9)	93.80(7)
S(1)−Sb(1)−S(10)[a]	93.54(8)	S(6)−Sb(5)−S(9)	92.34(6)
S(2)−Sb(1)−S(10)	100.22(8)	S(3)−Sb(6)−S(10)	98.18(8)
S(4)−Sb(2)−S(2)	90.72(8)	S(3)−Sb(6)−S(9)[b]	85.60(7)
S(4)−Sb(2)−S(3)	93.76(7)	S(10)−Sb(6)−S(9)	93.93(7)
S(2)−Sb(2)−S(3)	96.26(8)	Sb(1)−S(2)−Sb(2)	98.65(8)
S(4)−Sb(3)−S(7)	163.55(7)	Sb(6)−S(3)−Sb(2)	104.24(8)
S(5)−Sb(3)−S(6)	100.93(7)	Sb(2)−S(4)−Sb(3)	107.83(7)
S(5)−Sb(3)−S(4)	87.81(7)	Sb(3)−S(5)−Sb(4)	98.02(7)
S(6)−Sb(3)−S(4)	84.92(6)	Sb(3)−S(6)−Sb(5)	104.86(7)
S(7)−Sb(4)−S(8)	97.36(7)	Sb(3)−S(7)−Sb(4)	87.07(6)
S(7)−Sb(3)−S(6)	87.27(6)	Sb(5)−S(8)−Sb(4)	96.22(7)
S(7)−Sb(3)−S(5)	79.48(7)	Sb(6)−S(9)−Sb(5)	110.11(7)
S(7)−Sb(3)−S(6)	100.93(7)	Sb(6)−S(10)−Sb(1)	96.98(8)
S(7)−Sb(4)−S(5)	91.63(7)		
S(8)−Sb(4)−S(5)	98.13(8)		
S(8)−Sb(5)−S(6)	92.94(8)		

Symmetry codes: [a] x, y, −1+z, [b] x, y, 1+z;

Table 3 Long Sb−S distances/Å in $(C_6N_3H_{17}^{2+})Sb_6S_{10}$ (**I**). Estimated standard deviations are given in parentheses.

Sb(2)−S(1)	3.262(3)	Sb(2)−S(2)[c]	3.654(3)
Sb(2)−S(7)[d]	3.167(2)	Sb(3)−S(3)[d]	3.396(3)
Sb(3)−S(5)[e]	3.694(3)	Sb(4)−S(2)[c]	3.524(3)
Sb(4)−S(6)[d]	3.557(3)	Sb(5)−S(7)	3.046(3)
Sb(6)−S(10)	3.670(3)		

Symmetry codes: [c] 1+x, y, z; [d] −x, 0.5+y, 1−z; [e] −1+x, y, z;

Table 4 Intermolecular N−H···S contacts and angles/Å, ° for $(C_6N_3H_{17}^{2+})Sb_6S_{10}$ (**I**).

D−H	d(H···A)	<DHA	A
N2−H2C	2.483	152.92	S4
N2−H2C	2.752	120.72	S5
N3−H3C	2.454	157.11	S9[f]
N3−H3D	2.891	141.46	S1[g]
N3−H3E	2.545	156.47	S9[h]
N3−H3E	2.954	119.42	S10[i]

Symmetry codes: [f] 1−x, 0.5+y, 2−z; [g] 1+x, y, 1+z, [h] −x, y+0.5, −z+2; [i] −x, y+0.5, −z+2;

Along [010] neighbored chains are arranged in a way that pockets are formed which host the organic cations (Fig. 3). The cations are oriented towards the thioantimonate(III) anion in a way that optimal S···H bonding interactions are achieved. The H···S distances range from 2.454 Å to 2.954 Å with corresponding N−H···S angles between 119.42° and 157.11° (Table 4).

The shortest inter-chain Sb−S distances are 3.167(2) Å along [010] and 3.558(2) Å along [100]. Taking these Sb−S contacts into account a three-dimensional network is formed with large cages accommodating the organic cations (Fig. 3). The cages are interconnected along [100] forming ellipsoidal tunnels with dimensions of about 7.1 · 7.6 Å (measured from coordinate to coordinate). The opening of the cages consist of a puckered Sb_6S_6 heteroring.

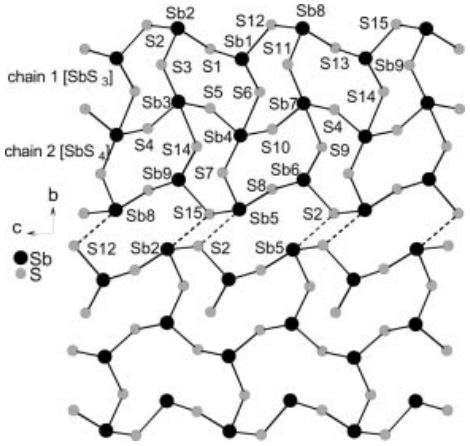

Fig. 4 The interconnection of the primary SbS_3 and Sb_4 units in $(C_7N_2H_{13}^{+})_3Sb_9S_{15}$ (**II**) forming the $^1_\infty[Sb_9S_{15}]^{3-}$ chains which are joined into layers via the long Sb−S bonds (dotted lines) together with atom labelling. The individual chains composed of SbS_3 pyramids and SbS_4 groups are denoted as chain 1 and 2.

The second new compound $(C_7N_2H_{13}^{+})_3Sb_9S_{15}$ (**II**) crystallizes also as red needles (Fig.1 right) in the monoclinic space group $P2_1/c$ with four formula units in the unit cell. All atoms are on general positions. Six Sb atoms (Sb(1, 2, 5, 6, 8, 9)) have bonds to three S atoms yielding the trigonal SbS_3 pyramids whereas the remaining Sb atoms form SbS_4 moieties (Fig. 4). In the $[Sb_9S_{15}]^{3-}$ anion individual chains may be identified that are formed by the interconnection of the PBUs. One chain is composed of the six alternating SbS_3 pyramids by vertex linkage (in Fig. 4 denoted as chain 1) and the second one is formed by corner sharing of the SbS_4 units (in Fig. 4 denoted as chain 2). Another chain is generated from the former chain by the n-glide plane. The two chains composed by the SbS_3 pyramids form the exterior of the $[Sb_9S_{15}]^{3-}$ ion and in the central part of the anion is located the chain which is constructed by the SbS_4 units (Sb(3,4,7)). The central chain is joined to the two other chains via common corners thus yielding the final $^1_\infty[Sb_9S_{15}]^{3-}$ anion. The connection mode leads to the formation of Sb_4S_4 rings which are condensed along [001] (Fig. 4). The width of the thioantimonate(III) anion is determined by two Sb_4S_4 rings. The chains are stacked along [100] with an inter-chain separation of about 7 Å. In the [010] direction the anions are lined-up with the shortest distance between neighbored anions of about 3.4 Å (Fig. 5). The Sb−S bond lengths scatter over a large range from 2.372(2) to 2.943(2) Å (Table 5). The long Sb−S distances are always found in the SbS_4 units and they are always located in *trans* position to a shorter Sb−S bond. The

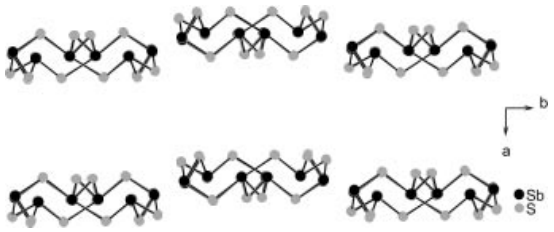

Fig. 5 Arrangement of the $[Sb_9S_{15}]^{3-}$ anion in $(C_7N_2H_{13}^+)_3Sb_9S_{15}$ (**II**) showing the large inter-chain separation along [100].

Table 5 Selected interatomic distances/Å and angles/° in the compound $(C_7N_2H_{13}^+)_3Sb_9S_{15}$ (**II**). Estimated standard deviations are given in parentheses.

Sb(1)−S(1)	2.496(2)	Sb(1)−S(6)	2.381(2)
Sb(1)−S(12)	2.530(2)	Sb(2)−S(1)	2.470(2)
Sb(2)−S(2)	2.451(2)	Sb(2)−S(3)	2.423(2)
Sb(3)−S(3)	2.584(2)	Sb(3)−S(4)	2.456(2)
Sb(3)−S(5)	2.522(2)	Sb(4)−S(5)	2.458(2)
Sb(4)−S(6)	2.885(2)	Sb(4)−S(7)	2.641(2)
Sb(4)−S(10)	2.525(2)	Sb(5)−S(7)	2.419(2)
Sb(5)−S(8)	2.474(3)	Sb(5)−S(15)	2.445(2)
Sb(6)−S(2)	2.542(2)	Sb(6)−S(8)	2.494(2)
Sb(6)−S(9)	2.379(2)	Sb(7)−S(4)[a]	2.511(2)
Sb(7)−S(9)	2.855(2)	Sb(7)−S(10)	2.460(2)
Sb(7)−S(11)	2.655(2)	Sb(8)−S(11)	2.412(2)
Sb(8)−S(12)	2.451(2)	Sb(8)−S(13)	2.480(2)
Sb(9)−S(13)	2.497(2)	Sb(9)−S(14)	2.372(2)
Sb(9)−S(15)	2.544(2)	Sb(3)−S(14)	2.943(2)
S(6)−Sb(1)−S(1)	92.80(5)	S(6)−Sb(1)−S(12)	97.33(5)
S(1)−Sb(1)−S(12)	92.59(5)	S(3)−Sb(2)−S(2)	99.95(5)
S(3)−Sb(2)−S(1)	98.52(5)	S(2)−Sb(2)−S(1)	95.59(5)
S(3)−Sb(3)−S(14)[b]	174.75(5)	S(4)−Sb(3)−S(14)[b]	88.07(4)
S(4)−Sb(3)−S(5)	92.41(4)	S(4)−Sb(3)−S(3)	88.62(5)
S(5)−Sb(3)−S(3)	86.80(4)	S(5)−Sb(4)−S(10)	92.45(4)
S(5)−Sb(3)−S(14)[b]	90.08(4)	S(5)−Sb(4)−S(7)	88.07(4)
S(10)−Sb(4)−S(7)	87.15(4)	S(5)−Sb(4)−S(6)	87.80(4)
S(10)−Sb(4)−S(6)	89.80(4)	S(7)−Sb(4)−S(6)	174.76(4)
S(7)−Sb(5)−S(15)[a]	101.52(4)	S(7)−Sb(5)−S(8)	99.40(4)
S(15)−Sb(5)−S(8)	94.88(4)	S(9)−Sb(6)−S(8)	92.76(4)
S(9)−Sb(6)−S(2)[a]	95.16(5)	S(8)−Sb(6)−S(2)[a]	94.50(4)
S(10)−Sb(7)−S(4)[b]	91.49(4)	S(10)−Sb(7)−S(11)	89.10(5)
S(4)[a]−Sb(7)−S(11)	85.57(4)	S(10)−Sb(7)−S(9)	88.07(4)
S(4)[a]−Sb(7)−S(9)	90.08(4)	S(11)−Sb(7)−S(9)	174.75(4)
S(11)−Sb(8)−S(12)	100.91(5)	S(11)−Sb(8)−S(13)	99.88(4)
S(12)−Sb(8)−S(13)	96.29(5)	S(14)−Sb(9)−S(13)	93.07(5)
S(14)−Sb(9)−S(15)	98.20(4)	S(13)−Sb(9)−S(15)	94.07(4)
Sb(2)−S(1)−Sb(1)	100.62(5)	Sb(2)−S(2)−Sb(6)[b]	98.40(5)
Sb(2)−S(3)−Sb(3)	103.71(5)	Sb(3)−S(4)−Sb(7)[b]	100.68(5)
Sb(4)−S(5)−Sb(3)	101.52(4)	Sb(1)−S(6)−Sb(4)	101.94(4)
Sb(5)−S(7)−Sb(4)	103.30(4)	Sb(5)−S(8)−Sb(6)	100.01(5)
Sb(6)−S(9)−Sb(7)	103.23(4)	Sb(7)−S(10)−Sb(4)	101.60(5)
Sb(8)−S(11)−Sb(7)	105.09(5)	Sb(8)−S(12)−Sb(1)	98.71(5)
Sb(8)−S(13)−Sb(9)	97.75(5)	Sb(9)−S(14)[b]−Sb(3)	103.23(4)
Sb(9)−S(15)−Sb(5)[a]	99.27(4)		

Symmetry codes: [a] x, 0.5−y, −0.5+z; [b] x, 0.5−y, 0.5+z,

S−Sb−S angles between 86.80(4)° and 174.76(4)° are also distributed over a large range (Table 5). We note that both Sb−S bond lengths and the S−Sb−S angles are in the range observed in many other thioantimonates(III).

The Sb atoms enhance their coordination by S atoms located at longer distances (Table 6). The atoms Sb(2,5,8) have coordination numbers CN 4, Sb(1,6,9) CN = 5 and all Sb atoms of the SbS_4 units have CN = 6 forming distorted octahedra. Hence, the central part of the anion may be viewed as a chain of edge sharing SbS_6 octahedra. Whereas most of the long Sb−S contacts are within the thioantimonate(III) anion the atoms Sb(1,2,5,9) have such bonds to S atoms of neighbored chains. Considering the longer Sb−S distances as weak interactions the chains are interconnected into layers extending within the (100) plane (Fig. 5). The layers are separated by the organic amine cations and a sandwich-like arrangement of anions and cations is observed.

Table 6 Long Sb−S distances/Å in $(C_7N_2H_{13}^+)_3Sb_9S_{15}$ (**II**). Estimated standard deviations are given in parentheses.

Sb(1)−S(5)	3.301(9)	Sb(1)−S(11)	3.346(6)
Sb(2)−S(15)	3.42(2)[c]	Sb(3)−S(1)	3.476(5)
Sb(3)−S(9)	3.153(8)[d]	Sb(4)−S(8)	3.493(5)
Sb(4)−S(14)	3.196(8)[d]	Sb(5)−S(2)	3.42(2)[f]
Sb(6)−S(3)	3.259(9)[e]	Sb(6)−S(10)	3.381(5)
Sb(7)−S(11)	3.611(5)	Sb(7)−S(6)	3.189(8)
Sb(8)−S(12)	3.50(2)	Sb(9)−S(4)	3.436(2)[e]
Sb(9)−S(7)	3.307(9)		

Symmetry codes: [c] 1−x, 1−y,1−z; [d] x, 0.5−y, 0.5+z; [e] x, 0.5−y,0.5+z; [f] 1−x, −0.5+y, 1.5−z

Optical spectroscopy

Charge compensation in the two compounds requires that the amine molecules are protonated. In **I** the H atoms could be located in the difference Fourier map. In the IR spectra the absorptions located at 1500, 2000, 2500 and 3500 cm^{-1} are typical for R- NH_3 groups in **I** while **II** shows intensive bands of absorption at 1500, 1650, 2400 and 3200 cm^{-1}. In the Raman spectra (Fig. 6) a large number of intense bands are seen. The most intense resonances are located at 281.1 cm^{-1}, 292.9 cm^{-1}, 304.5 cm^{-1}, 318.5 cm^{-1}, 336.2 cm^{-1}, 348.9 cm^{-1} (**I**) and 263.3 cm^{-1}, 289.3 cm^{-1}, 315.3 cm^{-1}, 340.3 cm^{-1} and 361.1 cm^{-1} (**II**). The bands between 362 cm^{-1} and 339 cm^{-1} are typical for SbS_3 units [29, 30]. We note that for the copper(I)-thioantimonates(III) the bands are observed at lower wave numbers, i.e. at 337 cm^{-1} [31]. The strong absorptions at 281.3 cm^{-1} and

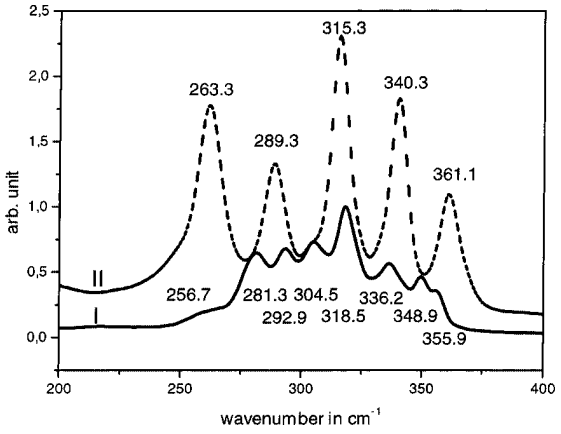

Fig. 6 Raman spectra of $(C_6N_3H_{17}^{2+})Sb_6S_{10}$ (**I**) (solid line) and of $(C_7N_2H_{13}^+)_3Sb_9S_{15}$ (**II**) (dotted line).

318.5 cm^{-1} (**I**) respectively 289.3 cm^{-1} and 315.3 cm^{-1} (**II**) may be due to the SbS_x units with x > 3 [29]. Pfitzner et al. reported that a decrease of the bonding interactions between Sb and S atoms leads to a strong shift to lower wave numbers and the bands at 321 cm^{-1} and about 290 cm^{-1} are explained with SbS_5 units [29, 30]. In $MnSb_2S_4$ the resonances are at even lower wave numbers of 300 and 283 cm^{-1} which is due to the high coordination number of the Sb atoms [30].

UV-Vis diffuse reflectance measurements allowed the determination of the optical band gaps of the two compounds. For both thioantimonates E_g is about 2 eV demonstrating the semiconducting nature.

Thermal Investigations

The DTA-TG-DTG curves for compounds **I** and **II** are shown in Fig. 7. Compound (**I**) decomposes in one step (T_{onset} = 238 °C) which is accompanied by an endothermic signal and a mass loss of 12.5 %. The expected value for the emission of the organic ligand is 13.4 %. The removal of the DBN molecule in (**II**) proceeds in two steps with two endothermic events at T_p = 266 °C and T_p = 301 °C. The decomposition of this compound starts at a temperature T_{onset} = 245 °C and the total mass loss amounts to 20.1 % which is in good agreement with the emission of the organic part of the compound (calculated: 19.2 %). The elemental analysis of the gray residues indicates only 0.13 % C for **I** and 0.238 % N, 0.035 % H and 0.795 % C for **II**. In the X-ray powder pattern of the residues Stibnit Sb_2S_3 and Sb could be identified. The occurrence of elemental Sb suggests that a redox reaction takes place during the thermal reaction and due to the Sb:S ratio of the starting material it must be assumed that also sulfur is emitted.

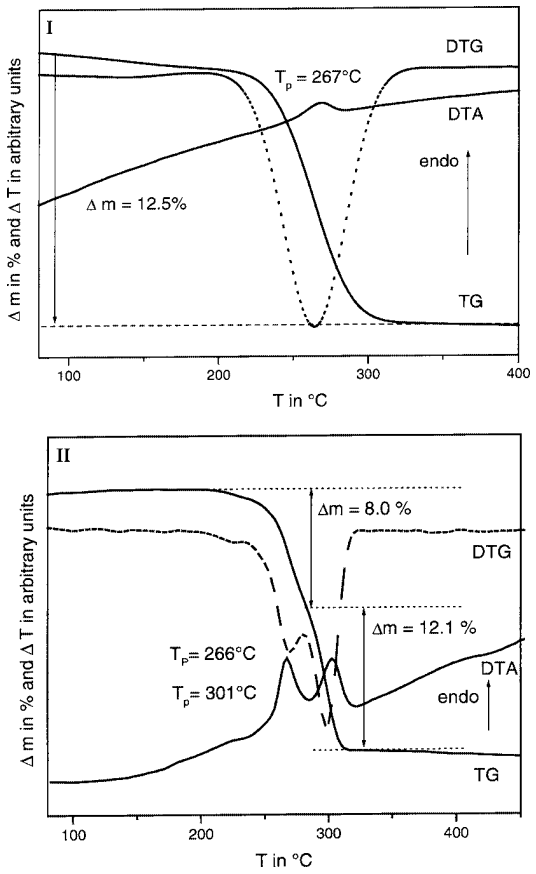

Fig. 7 DTA-TG-DTG curves for $(C_6N_3H_{17}^{2+})Sb_6S_{10}$ (**I**) (top) and $(C_7N_2H_{13}^{+})_3Sb_9S_{15}$ (**II**) (bottom).

Summary

We noted in the introduction that several structures of thioantimonates(III) were reported in the past which have an identical Sb : S ratio but a different network topology. The two new compounds belong to the group of thioantimonates(III) with a Sb:S ratio of 1:1.67. The network topology of the anion in $(C_6N_3H_{17}^{2+})Sb_6S_{10}$ (**I**) is different to all other compounds containing the $[Sb_6S_{10}]^{2-}$ anion. With the second new compound $(C_7N_2H_{13}^{+})_3Sb_9S_{15}$ (**II**) the series of thioantimonates(III) with the Sb:S ratio of 1:1.67 covers now four different anions, i.e. $[Sb_3S_5]^-$, $[Sb_6S_{10}]^{2-}$, $[Sb_9S_{15}]^{3-}$, and $[Sb_{12}S_{20}]^{4-}$. Using other amines in the syntheses it should be possible to synthesize other thioantimonates(III) with the Sb:S ratio of 1:1.67. For a better understanding of the relation between the network topology, the dimensionality and the size, charge and shape of the structure directing organic molecule more compounds must be prepared.

Acknowledgements. The financial support by the State of Schleswig-Holstein and the Deutsche Forschungsgemeinschaft (DFG) is gratefully acknowledged.

References

[1] H. A. Graf, H. Schäfer, *Z. Naturforsch.* **1972**, *27b*, 735.
[2] G. Dittmar, H. Schäfer, *Z. Anorg. Allg. Chem.* **1977**, *437*, 183.
[3] G. Dittmar, H. Schäfer, *Z. Anorg. Allg. Chem.* **1978**, *441*, 93.
[4] G. Dittmar, H. Schäfer, *Z. Anorg. Allg. Chem.* **1978**, *441*, 98.
[5] B. Eisenmann, H. Schäfer, *Z. Naturforsch.* **1979**, *34b*, 383.
[6] G. Cordier, H. Schäfer, C. Schwidetzky, *Z. Naturforsch.* **1984**, *39b*, 131.
[7] W. Bensch, M. Schur, *Z. Naturforsch.*, **1997** *52b*, 405.
[8] W. S. Sheldrick, H.-J. Häusler, *Z. Anorg. Allg. Chem.* **1988**, *557*, 105.
[9] M. Schur, W. Bensch, *Eur. J. Solid State Inorg. Chem.* **1997**, *34*, 457.
[10] R. Stähler, C. Näther, W. Bensch, *J. Solid State Chem*. **2003**, *174*, 264.
[11] K. Volk, P. Bickert, R. Kolmer, H. Schäfer, *Z. Naturforsch*. **1979**, *34b* 380.
[12] H. A. Graf, H. Schäfer, *Z. Anorg. Allg. Chem*. **1975**, *414*, 211.
[13] G. Cordier, C. Schwidetzky, H. Schäfer, *J. Solid State Chem*. **1984**, *54*, 84.
[14] R. Kiebach, F. Studt, C. Näther, W. Bensch, *Eur. J. Inorg. Chem*. **2004**, 2553.
[15] T. J. McCarthy,M. G. Kanatzidis, *Inorg. Chem*. **1994**, *33*,1205.
[16] W. Bensch, C. Näther, R. Stähler, *Chem. Commun.* **2001**, 477.

[17] J. B. Parise, *Science* **1991**, *251*, 293.
[18] K. Volk, H. Schäfer, *Z. Naturforsch*. **1979**, *34b***,** 172.
[19] J. B. Parise, Y.Ko, *Chem. Mater*. **1992**, *4*, 1446.
[20] M. Gostojic, W. Nowacki, P. Engel, *Z. Kristallogr*. **1982,** *159*, 217.
[21] L. Engelke, C. Näther, W. Bensch, *Eur. J. Inorg. Chem.* **2002**, 2936.
[22] J. Rijnberk, C. Näther, W. Bensch, *Monatsh. Chem.* **2000**, *131,* 721.
[23] R. Stähler, C. Näther, W. Bensch, *Eur. J. Chem.* **2001**, 1835.
[24] X. Wang, A. J. Jacobson, F. Liebau, *J. Solid State Chem*. **1998**, *140*, 387.
[25] W. S. Sheldrick, H.-J. Häusler, *Z. Anorg. Allgem. Chem*. **1988**, *561***,** 149.
[26] J. B. Parise, *J. Chem. Soc., Chem. Commun*. **1990**, 1553.
[27] G. M. Sheldrick, SHELXS-97, Program for Crystal Structure Determination, University of Göttingen, Germany (**1997**)
[28] G. M. Sheldrick, SHELXL-97, Program for the Refinement of Crystal Structures, University of Göttingen, Germany (**1997**)
[29] A. Pfitzner, *Chem. Eur. J.* **1997**, *3*, 2032.
[30] A. Pfitzner, D. Kurowski, *Z. Kristallogr*. **2000**, *215***,**373.
[31] V. Spetzler, H. Rijnberk, C. Näther, W. Bensch, *Z. Anorg. Allg. Chem.* **2004**, *630* 142.

4.1.3 Die Verbindung $[C_6H_9N_2][Sb_8S_{13}]\cdot 2.5H_2O$

Zusammenfassung der Veröffentlichung „*The structure directing effect of organic cations onto the crystal structures of layered thioantimonates(III): Solvothermal synthesis and crystal structures of five new compounds containing the* $[Sb_8S_{13}]^{2-}$*-anion*“.

Von den fünf Verbindungen, die in dieser Veröffentlichung beschrieben werden, soll hier nur die Verbindung $[C_6H_9N_2][Sb_8S_{13}]\cdot 2.5H_2O$ ($C_6H_7N_2$ = 3-(Aminomethyl)-pyridin) diskutiert werden. Eine ausführliche Diskussion der anderen Verbindungen findet sich in der Doktorarbeit von Angela Puls [6]. Die neue Verbindung wurde unter hydrothermalen Bedingungen bei der Reaktion von Sb_2O_3 (6.6 mmol) und S (10 mmol) in 4 ml 50 %igem 3-(Aminoethyl)-pyrimidin bei 150 °C nach 7 Tagen in Form roter Nadeln in guten Ausbeuten (Ausbeute ca. 60 % bezogen auf Sb) erhalten. Die Verbindung ist in Wasser und an Luft stabil. $[C_6H_9N_2][Sb_8S_{13}]\cdot 2.5H_2O$ kristallisiert in der monoklinen Raumgruppe $P2_1/m$ mit vier Formeleinheiten pro Elementarzelle. Alle 8 Antimonatome sind von 3 Schwefelatomen umgeben. Jeweils vier dieser SbS_3-Einheiten bilden über Eckenverknüpfung Fragmente, welche Sb_3S_3-Ringe enthalten. Die Verknüpfung dieser Fragmente führt zur Bildung von Ketten, die entlang [010] verlaufen. Zentrales Strukturmotiv dieser Ketten ist ein 24-gliedriger Ring, an den zwei Sb_4S_4- und zwei Sb_3S_3-Ringe kondensiert sind (Abb. 4.2). Unter Berücksichtigung von Sb-S-Bindungen um 2.9 Å findet eine Verknüpfung der Ketten zu zwei Atomen dicken Schichten statt. Die Stapelung der Schichten entlang [100] führt zur Ausbildung von Tunneln, in denen sich protoniertes Amin und das Kristallwasser befinden. Der kürzeste Sb-S-Abstand zwischen den Schichten beträgt 3.5 Å. Berücksichtigt man diese langen Bindungen bei der Strukturbeschreibung gelangt man zu einer 3-dimensionalen Netzwerktopologie. Die Netzwerktopologien der Verbindung $[C_6H_9N_2][Sb_8S_{13}]\cdot 2.5H_2O$ und der isostrukturellen Verbindung $[C_6H_{15}N_3][Sb_8S_{13}]\cdot 1.5H_2O$, die ebenfalls in der Veröffentlichung diskutiert wird, sind sehr ähnlich zu der von $Rb_2[Sb_8S_{13}]\cdot H_2O$ und eine genaue Analyse der interatomaren Abstände sowie der S-Sb-S-Winkel zeigt nur geringe Unterschiede der drei Verbindungen.

Bemerkenswert ist, dass bei allen 11 bekannten Verbindungen mit einem $[Sb_8S_{13}]^{2-}$-Anion die Sb-S-Abstandsverteilung das gleiche Muster aufweist. Während man bei Thioantimonaten im allgemeinen eine lückenlose Abstandsverteilung zwischen 2.3 Å

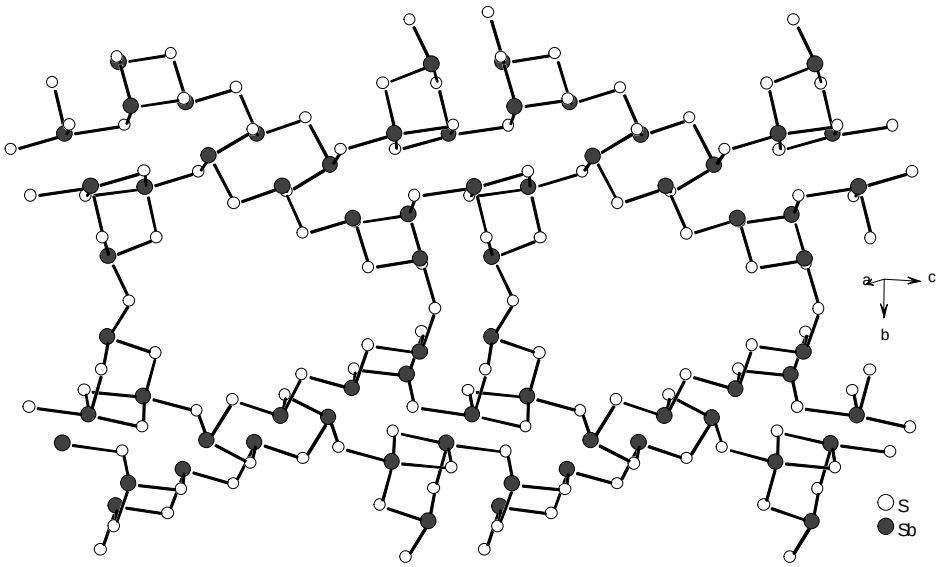

Abbildung 4.2: Ketten mit 24-gliedrigen Ringen in der Struktur der Verbindung $[C_6H_9N_2][Sb_8S_{13}]\cdot 2.5H_2O$

bis 3.8 Å findet, ist die Verteilung der Abstände bei den $[Sb_8S_{13}]^{2-}$-Anionen diskreter verteilt. Alle Verbindungen weisen eine Lücke zwischen 2.52 Å -2.9 Å in der Abstandsverteilung auf. An diese Lücke schließt sich ein Bereich bis 3.25 Å an, in dem relativ viele Sb-S-Bindungen gefunden werden.

Bei der Untersuchung der thermischen Stabilität der Verbindung wurde ein zweistufiger Massenabbau ($\Delta m_{(gesamt)} = 9.5$ %) mit endothermen Ereignissen in der DTA-Kurve detektiert. Die Emission von Wasser beginnt bereits bei 80 °C, das Amin wird ab einer Temperatur von 257 °C emittiert. Im grauen DTA-Abbauprodukt konnte im Pulverdiffraktogramm Sb_2S_3 nachgewiesen werden. Die Bestimmung der Bandlücke nach der Methode von Kubelka-Munk ergab einen Wert von 2.0 eV und $[C_6H_9N_2][Sb_8S_{13}]\cdot 2.5H_2O$ stellt somit einen optischen Halbleiter dar.

The structure directing effect of organic cations onto the crystal structures of layered thioantimonates(III): Solvothermal synthesis and crystal structures of five new compounds containing the $[Sb_8S_{13}]^{2-}$ anion

Angela Puls, Christian Näther, Ragnar Kiebach, Wolfgang Bensch*

Institut für Anorganische Chemie, Universität Kiel, Olshausenstr.40, D-24098 Kiel, Germany

* Correspondence and reprints. *Fax:* +49-431-8801520

E-mail address: wbensch@ac.uni-kiel.de

Abstract

The five new thioantimonates(III) (*i*prH)$_2$[Sb_8S_{13}] (**I**), (1,2-dapH)$_2$[Sb_8S_{13}] (**II**), (1,3-dapH$_2$)[Sb_8S_{13}] (**III**), (dienH$_2$)[Sb_8S_{13}]·1.5 H_2O (**IV**), and ($C_6H_9N_2$)[Sb_8S_{13}]·2.5H_2O (**V**) were synthesised under solvothermal conditions (ipr = iso-propylamine; 1,2-dap = 1,2-diaminopropane; 1,3-dap = 1,2-diaminopropane; dien = diethylentriamine; $C_6H_9N_2$ = 3-(aminoethyl)-pyridine). The structures of compounds **I** and **II** are topological very similar and a central motif is a 20 membered $Sb_{10}S_{10}$ ring (20 MR). On both sides of this ring Sb_5S_5 rings are condensed. These rings are connected via Sb_4S_4 rings leading to the sequence $Sb_{10}S_{10}$-Sb_5S_5-Sb_4S_4-Sb_5S_5-$Sb_{10}Sb_{10}$ in the [010] direction. Further interconnection into the two-dimensional $[Sb_8S_{13}]^{2-}$ anion produces a large central ring which is composed of 18 Sb and 18 S atoms, i.e. a 36 membered ring. Dimensions of this nearly rectangular ring are 11·11 Å in both compounds. The two atoms thick layers are linear and stacked along the a axis generating large channels running along [010]. The layered anion of compound **III** is constructed by interconnection of the SbS_3 and SbS_4 units yielding different types of large rings, i.e. $Sb_{19}S_{19}$ (38 MR), $Sb_{14}S_{14}$ (28 MR), $Sb_{13}S_{13}$ (26 MR), Sb_8S_8 (16 MR). The linear layers are two atoms thick and are stacked perpendicular to [001] to form channels running along the same direction. The last two compounds **IV** and **V** show a similar network topology. The layered anion is constructed by SbS_3 trigonal pyramids and SbS_4 units. The layer contains

24 membered $Sb_{12}S_{12}$ rings as the main structural motif. The corrugated layers extending in the (100) plane are two atoms thick and are stacked in a manner that large tunnels run along [100]. The total potential solvent areas are large and range from 20.7% for **III** to 35% for **II**. The dimensionality of the structures of the thioantimonate(III) ions depends on the cut-off for Sb-S bonding interactions chosen. This phenomenosn is discussed in detail in the paper.

Keywords: Solvothermal Synthesis, Thioantimonates, Aminoalcohol, organic-inorganic hybrid material

Introduction

An interesting structural feature of thioantimonates(III) is that for a given Sb:S ratio different crystal structures and dimensionalities of the anionic networks are observed. An example is the Sb : S ratio 1 : 1.67 for which four different anions were reported, i. e. $[Sb_3S_5]^-$, $[Sb_6S_{10}]^{2-}$, $[Sb_9S_{15}]^{3-}$, and $[Sb_{12}S_{20}]^{4-}$. Until now, five different compounds were reported with the $[Sb_3S_5]^-$ anion [1-5], three with $[Sb_6S_{10}]^{2-}$ [6-8], and one with the $[Sb_{12}S_{20}]^{4-}$ anion [9]. A three-dimensional network with a two-dimensional intersecting system of channels composed of four crystallographically unique SbS_4 groups was reported for $[Me_4N][Sb_3S_5]$ [1]. All Sb atoms have three short Sb-S bonds and one longer of about 3.0 Å. In $[C_6H_{15}N_2][Sb_3S_5]$ the anions form layers with Sb_2S_2, Sb_4S_4 and Sb_5S_5 rings as the secondary building units [5]. One-dimensional chains are observed in $[N(C_3H_7)_4][Sb_3S_5]$ [3] and in $[Ph_4P]_2[Sb_6S_{10}]$ [6]. In both compounds SbS_3 pyramids form Sb_5S_5 rings which are condensed into the chain anions. The structure of $RbSb_3S_5 \cdot H_2O$ contains Sb_2S_2 and large $Sb_{12}S_{12}$ heterorings which are condensed to form a two atoms thick layered anion [2]. Finally, the structure of $TlSb_3S_5$ is complex and a three-dimensional network [4]. The anion in $[M(C_4H_{13}N_3)_2][Sb_6S_{10}]\cdot 0.5H_2O$ (M = Fe, Ni) [7] is also complex. Chains built up by the interconnection of -Sb_4S_4-SbS_3-SbS_4-Sb_4S_4- units are found which are then further joined into the final layered anion via common corners and edges. The largest ring contains 32 atoms ($Sb_{16}S_{16}$) [7]. In $[C_6N_3H_{17}][Sb_6S_{10}]$ trigonal SbS_3 pyramids and SbS_4 moieties are interconnected to form six-membered rings Sb_3S_3 and Sb_3S_4 semi-cubes which are joined via common S atoms to form the one-dimensional $[Sb_6S_{10}]^{2-}$ anion [8]. In $[C_7N_2H_{13}]_3[Sb_9S_{15}]$ SbS_3 pyramids and SbS_4 units each form individual chains by vertex linking with the central chain being exclusively formed by SbS_4 units whereas the other two chains are composed of SbS_3 pyramids. The chains are

joined via common corners yielding the one-dimensional $[Sb_9S_{15}]^{3-}$ anion. The one-dimensional $[Sb_{12}S_{20}]^{4-}$ anion in $[(MA)_{1.03}K_{2.97}][Sb_{12}S_{20}]\cdot 1.34H_2O$ is two atoms thick. The main structural motifs are a central Sb_4S_4 ring which is bound to 6 Sb_3S_3 units forming the next hierarchical building block. The blocks are joined via S atoms and larger Sb_8S_8 heterorings are formed [9].

A crucial point describing the crystal structures of these compounds is the cut-off for Sb-S distances, and several approaches are used in the literature. Several authors consider only Sb-S bonds up to about 2.6 Å because the majority of Sb-S distances are observed between about 2.3 and 2.6 Å (Fig. 1).

But our analysis shown in Fig. 1 demonstrates that there is no gap between about 2.3 and 3.8 Å, i. e. up to the sum of the van der Waals radii of Sb and S the two atoms seem to have a contact with a bonding nature being not clear. Other authors calculate the bond valence sums (BVS) applying the method of Brown and Altermatt to get an 'impression' whether a specific Sb-S distance should be treated as a bond, or not. But as was impressively demonstrated by Wang and Liebau the classical BVS approach is a very crude estimation, and the stereochemical activity of the Sb(III) lone electronic pair must be taken into account for an adequately evaluation whether a distinct Sb-S distance can be considered as a significant bonding interaction [10,11]. A different approach is used by Mackoviky, Moelo and others to classify sulfosalts which will be not considered in the present contribution.

Unfortunately, most of the thioantimonates(III) crystallise with low symmetries, the structures are open and the unit cells contain a large number of atoms. These observations prevent, at the moment, the application of well developed, powerful and highly advanced methods of band structure calculations which would shed new light onto the Sb-S bonding situation.

The somewhat unsatisfying situation should be highlighted for the six known compounds with the Sb : S ratio of 1 : 1.625, i.e. for compounds with the $[Sb_8S_{13}]^{2-}$ anion. With these examples the influence onto the dimensionality of the structure and the identification of primary building units (PBUs) using different values for the Sb-S cut-off is demonstrated. The values for the cut-off are chosen according to the following observations made for the previously reported and the five new compounds:

i) In all 11 structures there is a small gap for Sb-S distances between about 2.52 and 2.9 Å with distinct values for each compound (see Table 1).

ii) A relatively narrow group of Sb-S separations occurs between about 2.9 and 3.25 Å.

Observation i) results simply from the fact that a distinct value is required so that the Sb atoms are bound to at least 3 S atoms. In the three-dimensional compound $Cs_2[Sb_8S_{13}]$ [12]

most Sb-S bond lengths scatter in a very narrow range from 2.39 to 2.55 Å. But with this range one Sb atom has only bonds to two S atoms but the structure is still 3 D. For a completion of the environment of this Sb atom the Sb-S distances must be extended at least to about 2.725 Å. This Sb atom has then two short Sb-S bonds and one long bond (2.725 Å), and as often observed another long Sb-S bond is in *trans* position (Sb-S: 2.781 Å). The situation is similar for [MA][Sb_8S_{13}] (narrow range: 2.38 – 2.57 Å, 3 D) with one Sb having only two S neighbours but the thioantimonate network is also still 3 D [13]. Extending the Sb-S bond lengths this Sb atom has two short and two long Sb-S bonds (long: 2.656 and 2.855 Å). In [$(CH_3NH_3)_{0.5}(NH_4)_{1.5}$][$Sb_8S_{13}$]·2.8 H_2O all Sb atoms form SbS_3 pyramids with Sb-S bonds ranging from 2.38 to 2.65 Å, and interestingly the structure of the anion is 3 D despite the relatively short Sb-S bond lengths [14]. The next block of Sb-S distances is in the range from 2.85 to 3.11 Å enhancing the environment of four Sb atoms to 4 and of one Sb atom to 5. Above 3.11 Å is a clear gap and several longer Sb-S separations are between 3.23 and 3.32 Å. In $Rb_2[Sb_8S_{13}]$·3.28 H_2O [14] three Sb atoms require an extension of the selected Sb-S distance to form SbS_4 units with the bonding pattern "two-short-two-long" Sb-S bonds. With these longer bonds the anion is 2 D, without these bonds the structure is composed of two fragments Sb_6S_9 and $Sb_{10}S_{17}$, i.e. it is 0 D. On the other hand, extending the Sb-S interactions up to 3.25 Å the anion remains 2 D. For $[en]_2[Sb_8S_{13}]$ [15] Sb-S bonds are found between 2.38 and 2.52 Å, and all Sb atoms are bound to 3 S atoms. The next shortest Sb-S separation is 3.113 Å, i.e. there is a very large gap between the short and long bonds. Below the long distance the compound contains a one-dimensional anionic chain, and with separations up to about 3.25 Å a 3 D network results. In the last compound, $[Pyrrol]_2[Sb_8S_{13}]$·0.15H_2O [16], SbS_3 pyramids are present for Sb-S bond lengths between 2.39 and 2.64 Å, and the anion is layered. Including the Sb-S separations mentioned under ii) the material becomes a 3 D network.

In the contribution the solvothermal syntheses, crystal structures and thermal stability of five new thioantimonates(III) ($i$prH)$_2$[Sb_8S_{13}] (**I**), (1,2-dapH)$_2$[Sb_8S_{13}] (**II**), (1,3-dapH_2)[Sb_8S_{13}] (**III**), (dienH_2)[Sb_8S_{13}]·1.5 H_2O (**IV**), and ($C_6H_9N_2$)[Sb_8S_{13}] ·2.5H_2O (**V**) are presented.

Results and Discussion

Crystal structures

The two new compounds ($i$prH)$_2$[Sb_8S_{13}] (**I**) and (1,2-dapH)$_2$[Sb_8S_{13}] (**II**) are topological identical. Both crystallise in P-1 with the 8 Sb atoms and the 13 S atoms being located on

general positions. The unit cell parameters, unit cell volume as well as the calculated densities of the two compounds are different (Table 3). The Sb-S bonds of category i) are between 2.410 and 2.644 Å (**I**) (2.409 to 2.641 Å for **II**) (Table 2) and all Sb atoms form SbS_3 pyramids (Fig. 2). Five SbS_3 units share common corners to form a Sb_5S_5 ring (10 MR). The remaining three SbS_3 groups are joined via corners into a Sb_3S_7 unit which is bound to the ring via S(7) (Fig. 2). A central motif of the anion is a 20 membered $Sb_{10}S_{10}$ ring (20 MR) produced by the centre of inversion involving Sb(3-7) and the symmetry related atoms (Fig. 3). On both sides of this ring the Sb_5S_5 rings are condensed. The latter are also condensed to each other yielding a Sb_4S_4 ring. Hence, the sequence of rings along [010] is ...$Sb_{10}S_{10}$-Sb_5S_5-Sb_4S_4-Sb_5S_5-$Sb_{10}Sb_{10}$... (Fig. 3). The $Sb_{10}S_{10}$ rings are joined parallel to [001] by two Sb(8)S_3 groups which share a common edge giving the final two-dimensional $[Sb_8S_{13}]^{2-}$ anion (Fig. 3). The connection mode generates a large central ring which is composed of 18 Sb and 18 S atoms, i.e. a 36 membered ring. Dimensions of this nearly rectangular ring are 11·11 Å in both compounds. The two atoms thick layers are linear (interlayer distances: 3.42 Å for **I** and 3.45 Å for **II**) and stacked along the a axis so that large channels are generated running along [010] (Fig. 3).

As noted above the Sb-S bonds are grouped in a narrow range and the next block of Sb-S distances is found between about 2.946 and 3.175 Å (I) (2.916 – 3.211 Å in **II**) (Table 2), i.e. distances of category ii). Extending the range for Sb-S bonds to 3.175 Å (3.211 Å in **II**) 4 SbS_4 and 4 SbS_5 units are formed and the smaller rings are all cut into either Sb_2S_2 or Sb_3S_3 rings. The formerly $Sb_{18}S_{18}$ ring is reduced to a 28 membered ring, i.e. it is a $Sb_{14}S_{14}$ ring. Note that the thioantimonate(III) anions in **I** and **II** are still 2 D and a 3 D anionic structure is obtained when Sb-S distances larger than 3.26 Å (**I**) (3.275 Å for **II**) are considered. The total potential solvent areas for these two compounds amounts to 30% for **I** and 35% for **II**, i.e. in the latter compound the structure directing molecule requires more space.

The structure directing effect of the cations is demonstrated for **I**. The N atoms point towards the corners of the large nearly rectangular ring and are located above/below the layers (Fig. 5). Relatively short N···S separations indicate weak hydrogen bonding interactions. We note that a similar arrangement of the 1,2-dapH molecules is observed in **II**, and again short N···S separtions suggest weak hydrogen bonding interactions. We note that the network topology of **I** and **II** is similar to that reported for $[Pyrrol]_2[Sb_8S_{13}]\cdot 0.15H_2O$ [16]. As expected the main differences are the lattice parameters and unit cell volumes as well as slightly differing Sb-S distances and S-Sb-S angles. The inter-layer separation of 3.366 Å is longer than in **I** and **II** due to the larger size of the structure directing cation and the small amount of water which are

located between the layers. The potential solvent area of 35% is identical with that of compound **II**.

The new compound (1,3-dapH_2)[Sb_8S_{13}] (**III**) crystallizes in the tetragonal space group $I4_1md$ with 10 unique Sb and 16 S atoms and with 4 Sb and 6 S atoms located on special positions. With the Sb-S bond criterion i) Sb(3) has only two bonds to S atoms and all other Sb are in a SbS_3 trigonal pyramidal environment. The Sb-S distances must be extended to 2.88 Å, and Sb(3) has then bonds to 4 S atoms with the above mentioned bond alternation "two long – two short" bonds (Fig. 6, Table 2). The PBUs are joined into two Sb_3S_3 rings which have bonds to two Sb_2S_5 (Sb(1,2) and Sb(9,10)) groups and one SbS_3 (Sb(8)) pyramid (Fig. 6). The layered anion is then constructed in the following way. Along [001] the unique part of the structure is joined via a symmetry related $Sb(2)S_3$ group sharing two S atoms with the $Sb(1)Sb(2)S_5$ moiety to form another Sb_3S_3 ring (Fig. 7). In the opposite direction of [100] the $Sb(8)S_3$ unit connects two neighboured symmetry related unique structural motifs. Finally, along [010] the unique part of the thioantimonate anion is interconnected by a symmetry related $Sb(9)S_3$ pyramid which shares two S atoms with the $Sb(9)Sb(10)S_5$ unit. Again this binding mode produces another Sb_3S_3 ring. The resulting layered $[Sb_8S_{13}]^{2-}$ anion contains different types of larger rings: $Sb_{19}S_{19}$ (38 MR, ∅: 9.9 · 7.8 Å), $Sb_{13}S_{13}$ (26 MR, ∅: 10.2 · 3.5 Å), Sb_8S_8 (16 MR, ∅: 13.2 · 4.2 Å), $Sb_{14}S_{14}$ (28 MR, ∅: 6.8 · 7 Å). Hence, another description of the structure may base on the condensation of these large rings alternating along the [100] and [010] directions. The total potential solvent area was calculated as 20.7%.

The linear layers are two atoms thick and are stacked perpendicular to [001] (Fig. 8) to form channels running along the same direction. The disordered organic molecules (see Experimental section) are most probably located betwen the layers.

Analysing the Sb-S distances in this compound there is no gap around 3.25 Å but rather at about 3.1 Å. Including the Sb-S interactions up to 3.1 Å the atoms Sb(1,4,6,8,10) have still only bonds to three S atoms whereas the remaining Sb atoms are surrounded by 4 S atoms, again showing the above mentioned bonding pattern. The effect of the extension of Sb-S interactions is that the sizes of the 38 MR and of the 26 MR are reduced to 24 MR and 12 MR respectively. The other two heterorings are not affected. A 3 D network results when Sb-S interactions up to about 3.45 Å are considered.

The last two compounds (dienH_2)[Sb_8S_{13}]·1.5H_2O (**IV**) and ($C_6H_9N_2$)[Sb_8S_{13}]·2.5H_2O (**V**) both crystallise in $P2_1/m$ with 8 Sb and 14 S atoms of which 2 S atoms are on special positions and all other atoms are located on general positions. The network topology of these two compounds is very similar, and only small differences are observed for interatomic

distances and angles (Table 2). In the compounds Sb-S bonds scatter from 2.419 to 2.690 Å (**IV**) and from 2.419 to 2.694 Å (**V**), and all Sb atoms form SbS_3 pyramids (Fig. 9).

Two crystallographically independent but similar fragments are formed by interconnection of 4 SbS_3 pyramids, i.e. two Sb_3S_3 rings each having a bond to a SbS_3 group are the unique features of the structures. The fragments are joined into chains which are directed along [010] (Fig. 10). The chains contain rings of different sizes. A central 24 membered ring **(**$Sb_{12}S_{12}$, sizeabout 8.7 · 14.6 Å in **IV** and **V**) is surrounded by two Sb_4S_4 (8 MR) and 4 Sb_3S_3 (6 MR) rings (Fig. 10). Adjacent 24 MR are joined by the 8 MR along [010] and the tioantimonate(III) anion is one-dimensional.

Expansion of Sb-S distances to about 2.9 Å changes the environement of Sb(2,3) which are now surrounded by 4 S atoms and $Sb(3)S_4$ interconnects the 1 D anion into a two-dimensional layered one (Fig.'s 9 and 11). With the longer Sb-S bonds a new $Sb_{12}S_{12}$ ring (24 MRa) is formed and only one type of the 6 MR is affected yielding a 4 MR whereas all other heterorings survive.

Criterion ii) is fullfilled in the two compounds and a gap occurs at about 3.22 Å. Extension of the Sb-S interactions to this value enhances the coordination number of Sb(1,2,3,6) to four and of Sb(4,5,7,8) to five, but the layered nature is maintained. Furthermore, the 24 MR is still intact but the 24 MRa is reduced in size to a 12 MR.

The corrugated layers extending in the (100) plane are two atoms thick (Fig. 12) and are stacked in a manner that large tunnels run along [100].

The location of the water molecules and the organic cation in the structure clearly reflect the structure directing effect (see Fig. 11). The organic ions are above/below the large ringes whereas some water molecules are in the plane of the ring. Between N/O and S atoms the interatomic separations suggest weak hydrogen bonding inetractions. The shortest interlayer Sb-S separation is 3.452 Å in **V** (3.447 Å in **IV**) and treating this distance as a weak interacion the strcuture is three-dimensional. The total potential solvent areas for the two compounds are 26.5% for **IV** and 26.3% for **V**. We note that the structure of the thioantimonate(III) anions in the two compounds are topologically similar with that of $Rb_2[Sb_8S_{13}]\cdot 2\ H_2O$ [14]. Small differences are observed for the individual Sb-S bond lengths as well as for S-Sb-S angles. In the Rb compound the hydrated Rb^+ ions are also located at the inflection points of the layers with the shortest interlayer separation of 3.562 Å. The potential solvent area of 26.7% is identical with the values calculated for **IV** and **V**.

Thermal stability

The two compounds (**I**) and (**II**) decompose in one step at T_{onset} = 221 and 241 °C, respectively. The thermal decompositions are accompanied by endothermic events and the mass loss amounts to 10 % for (**I**) (theoretical: 10.02 %) and to 12.0 % for (**II**) (theoretical: 11.8 %). Compound (**III**) is also decomposed in one step at T_{onset} = 220 °C, and again a strong endothermic peaks is seen in the DTA curve. The experimental mass loss of 8.4 % is in good agreement with the expected value of 7.7 %. Compound (**IV**) looses weight starting below 100 °C and a strong mass loss occurs above about 220 °C (T_{onset} = 245 °C). The total weight loss of 10.4 % agrees well with the emission of 1.5 H_2O, the dien ligands and one molecule H_2S (theoretical: 10.08 %). The removal of H_2O, dien and H_2S was proved with mass spectroscopy. Finally, compound (**V**) starts to decompose at about 80 °C and it can be assumed that first the water molecules are released. At T_{onset} = 257 °C a steep mass loss occurs and the total weight change of 9.5 % is also in nice agreement with the expected value of 9.57 %.

Optical bandgaps

The optical band gaps of the samples were determined applying the Kubelka-Munk method. The values are 1.76 eV (**I**), 1.98 eV (**II**), 1.83 eV (**III**), 2.14 eV (**IV**), and 2.0 eV (**V**). All values are in agreement with the colours of the compounds and indicate that the samples are narrow band gap semiconductors.

Summary

The successful synthesis of five new compounds with the $[Sb_8S_{13}]^{2-}$ anion demonstrates the large potential of the solvothermal approach. The different compounds were obtained under different synthesis conditions with reaction temperatures between 150 and 200 °C suggesting that the $[Sb_8S_{13}]^{2-}$ anion is a very stable species. A fascinating observation in the field of thioantimonate(III) chemistry is the enormous flexibility and variability of the primary building units to form different structures for an identical Sb:S ratio. These structures are characterised by a large range for Sb-S interatomic separations and very different secondary building units like Sb_xS_x heterorings of different size. In addition, the structure directing effect of the organic ions is nicely seen analysing their arrangements with respect to the thioantimonate(III) anion. We are currently investigating whether other polyamines are suitable structure directors for the preparation of thioantimonate(III) compounds with the $[Sb_8S_{13}]^{2-}$ anion.

Experimental section

Syntheses

The title compounds were prepared in stainless steel autoclaves with Teflon liners of 30 ml volume mixing the elements and the amine solutions. For (*i*prH)$_2$[Sb$_8$S$_{13}$] (**I**) Sb and S were mixed in a molar ratio of 1: 3 (mmol scale) adding 3 ml 60% aqueous solution of isopropylamine (*i*pr). The mixture was heated at 170°C for 7 days. Compound (**1**) was obtained as long gray violet needles with a yield of 75 % based on Sb. For (1,2-dapH)$_2$[Sb$_8$S$_{13}$] (**II**) also a molar ratio of 1: 3 mmol (Sb: S) was used with 3 ml of 50% aqueous 1,2-diaminopropane (1,2-dap). The slurry was heated at 170 °C for 7 days giving long gray-red needles with a yield of 75% based on Sb. For (1,3dapH$_2$)[Sb$_8$S$_{13}$] (**III**) the same molar ratio Sb : S was applied as before. After adding 3 mL 50% aqueous 1,3–diaminopropane (1,3-dap) the mixture was heated 6 days at 190 °C. Red needles with a yield of 70% based on Sb were obtained. (dienH$_2$)[Sb$_8$S$_{13}$]·1.5H$_2$O (**IV**) was synthesised with a special designed diffusion cell. 1 mmol Sb and 3 mmol S are horizontally separated by a porous glass membrane (pore size 4) and after adding 3 ml 50% aqueous diethylenetriamine (dien) the mixtures was heated using a temperature program: in 4 °C/h to 200 °C, hold for 96 h, cool with 2 °C/h to 25 °C. Compound (**IV**) was obtained as very long bright red needles with a yield of over 95% based on antimony. The products of the syntheses were washed with water, ethanol, acetone and dried on air. For (C$_6$H$_9$N$_2$)[Sb$_8$S$_{13}$]·2.5H$_2$O (**V**) 6.6 mmol Sb$_2$O$_3$ and 10 mmol S were mixed with 4 ml 50 % aqueous solution of 3-aminomethylpiperazin as solvent. The reaction mixture was kept for 7 days at 150 °C and cooled to room temperature within 3 h. The product was washed with water, ethanol and acetone. The compound was obtained as red needles with a yield of 70 % based on Sb. In the powder diffraction pattern of the product Sb$_2$O$_3$ could be identified as minor phase.

Chemical analysis

Data of the C, H, N, S analyses are summarised in Table 1.

	I		**II**		**III**		**IV**		**V**	
	exp.	theo.	exp.	theo.	exp.	theo.	exp.	theo.	exp.	theo.
C [wt%]	4.88	4.69	4.706	4.765	2.691	2.457	3.330	3.217	4.799	4.674
H [wt%]	1.257	1.334	1.501	1.466	0.98	0.825	1.114	1.012	0.896	0.915
N [wt%]	2.161	1.854	1.863	1.852	2.071	1.910	2.517	2.814	2.004	1.817
S [wt%]	27.58	27.55	27.55	27.52	28.41	28.39	27.63	27.87	27.00	27.11

X-ray single crystal work

Data sets for all five compounds were collected on an Imaging Plate Diffraction System (IPDS-1, STOE, λ = 0.7107 Å). The raw data were treated in the usual way applying a Lorentz and polarisation correction. The structures were solved with SHELXS-97 [17] and refined against F^2 with SHELXL-97 [18]. The total potential volume areas of the compounds were calculated with the Platon program suite [19]. All non-hydrogen atoms except disordered C and N atoms were refined anisotropically. The hydrogen atoms if considered were positioned with idealised geometry and were refined isotropic using a riding model. The crystal investigated for compound **I** was non-merohedrically twinned. Both individuals were indexed and integrated separately. Overlapping reflections have to be omitted. In compounds **III** and **IV** the organic cations are fully disordered and no reasonable structure model was found. The water molecules in **III** are also fully disordered. Therefore the data were corrected for disordered solvents using the Squeeze option in Platon [19]. In compounds **I**, **II** and **V** some atoms of the organic cations are disordered and were refined using a split model. Due to the disorder the hydrogen atoms were not included in the refinement and the carbon atoms were refined only isotropic for **II**.

The absolute structure for **III** was determined and is in agreement with the selected setting (Flack-x-parameter: 0.07(5)).

Selected interatomic distances and S-Sb-S angles are summarised in Table 2, details of data collection and selected refinement results are compiled in Table 3.

Crystallographic data (excluding structure factors) have been deposited with the Cambridge Crystallographic Data Centre as supplementary publication no. CCDC xxxxx **(I)** CCDC xxxxx **(II)**, CCDC xxxxx **(III)**, CCDC xxxxx **(IV)** and CCDC xxxxx **(V)**. Copies of the data can be obtained, free of charge, on application to CCDC, 12 Union Road, Cambridge CB2 1 EZ, UK. (fax: +44-(0)1223-336033 or email: deposit@ccdc.cam.ac.uk).

Thermoanalytical measurements

Thermal investigations were performed on a Netzsch STA-409CD DTA-TG measurement device. All measurements were corrected for buoyancy and current effects and were performed using a heating rate of 4 K/min in Al_2O_3 crucibles under a dynamic nitrogen atmosphere (flow rate: 75 mL/min, purity: 99.999%).

Solid-State UV/Vis/NIR Spectroscopy

UV/Vis spectroscopic investigations were conducted at room temperature using a UV-VIS-NIR two-channel spectrometer Cary 5 from Varian Techtron Pty., Darmstadt. The optical properties of the compounds were investigated by studying the UV/Vis reflectance spectrum of the powdered sample. The absorption data were calculated using the Kubelka-Munk relation for diffuse reflectance data. BaSO4 powder was used as reference material.

References

[1] Parise J. B., Science 251 (1991) 293.

[2] Volk K., Schäfer H., Z. Naturforsch. 34b (1979) 172.

[3] Parise J. B., Ko Y., Chem. Mater. 4 (1992) 1446.

[4] Gostojic M., W. Nowacki W., Engel P., Z. Kristallogr. 159 (1982) 217.

[5] Engelke L., Näther C., Bensch W., Eur. J. Inorg. Chem. (2002) 2936.

[6] Rijnberk H., Näther C., Bensch W., Monatsh. Chem.131 (2000) 721.

[7] Stähler R., Näther C., Bensch W., Eur. J. Chem. (2001) 1835.

[9] Wang X., Jacobson A. J., Liebau F., J. Solid State Chem. 140 (1998) 387.

[8] Spetzler V., Kiebach R., Näther C., Bensch W., Z. Anorg. Allg. Chem. 630 (2004) 2398.

[10] Wang X., Liebau F., Acta Cryst. B52 (1996) 7.

[11] Wang X., Liebau F., Z. Krist. 211 (1996) 437.

[12] Volk K., Schäfer H., Z. Naturforsch. 34b (1979) 1637.

[13] Wang X., Liebau F., J. Solid State Chem. 111 (1994) 385.

[14] Wang X., Liu L., Jacobson A. J., J. Solid State Chem. 155 (2000) 409.

[15] Tan K., Ko Y., Parise J. B., Acta Crystallogr. C50 (1994) 1439.

[16] Ko Y., Tan K., Parise J. B., Darovsky A., Chem. Mater. 8 (1996) 493.

[17] Sheldrick G. M., SHELXS-97, Program for Crystal Structure Solution, University of Göttingen, Germany (1997).

[18] Sheldrick G. M., SHELXL-97, Program for the Refinement of Crystal Structures, University of Göttingen, Germany, 1997.

[19] Spek A. L., PLATON, A Multipurpose Crystallographic Tool, Utrecht University, Utrecht, The Netherlands, 2000.

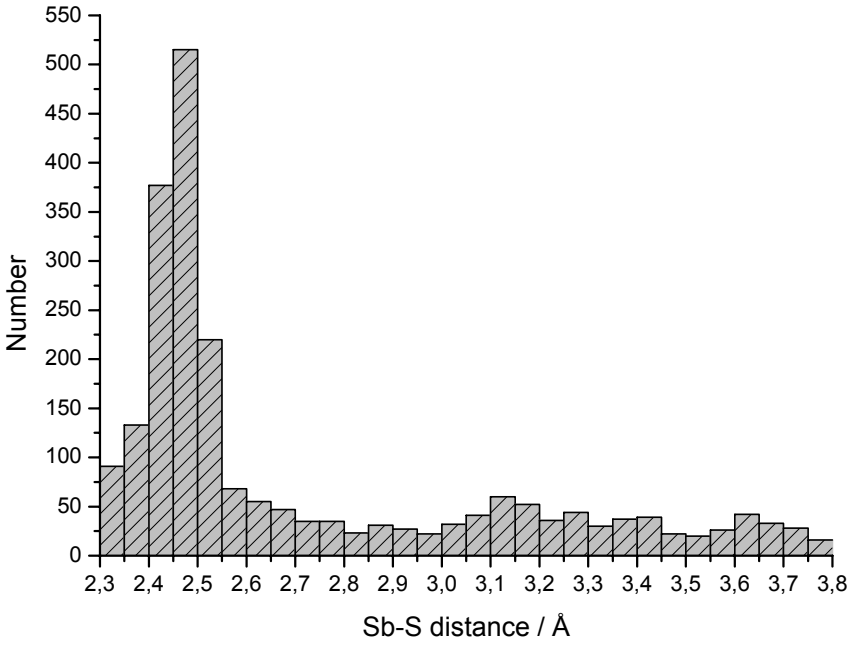

Fig. 1: Histogram of Sb-S distance distribution in thioantimonates(III).

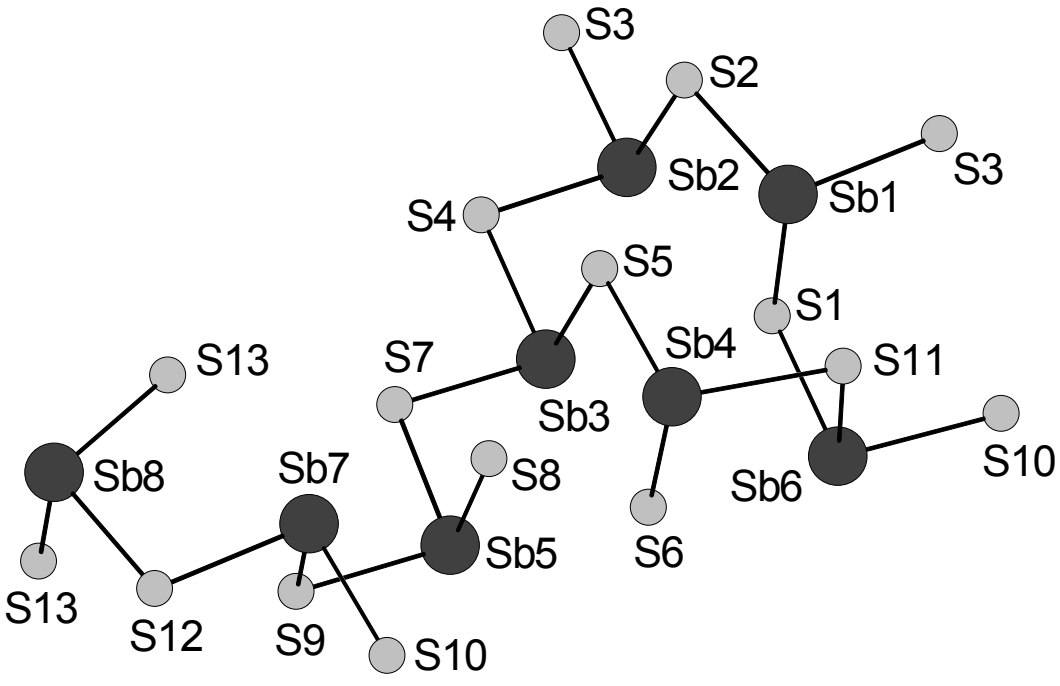

Fig. 2: Interconnection of the SbS_3 pyramids in the structure of compound **I**. Note that the structures of **I** and **II** are topological very similar.

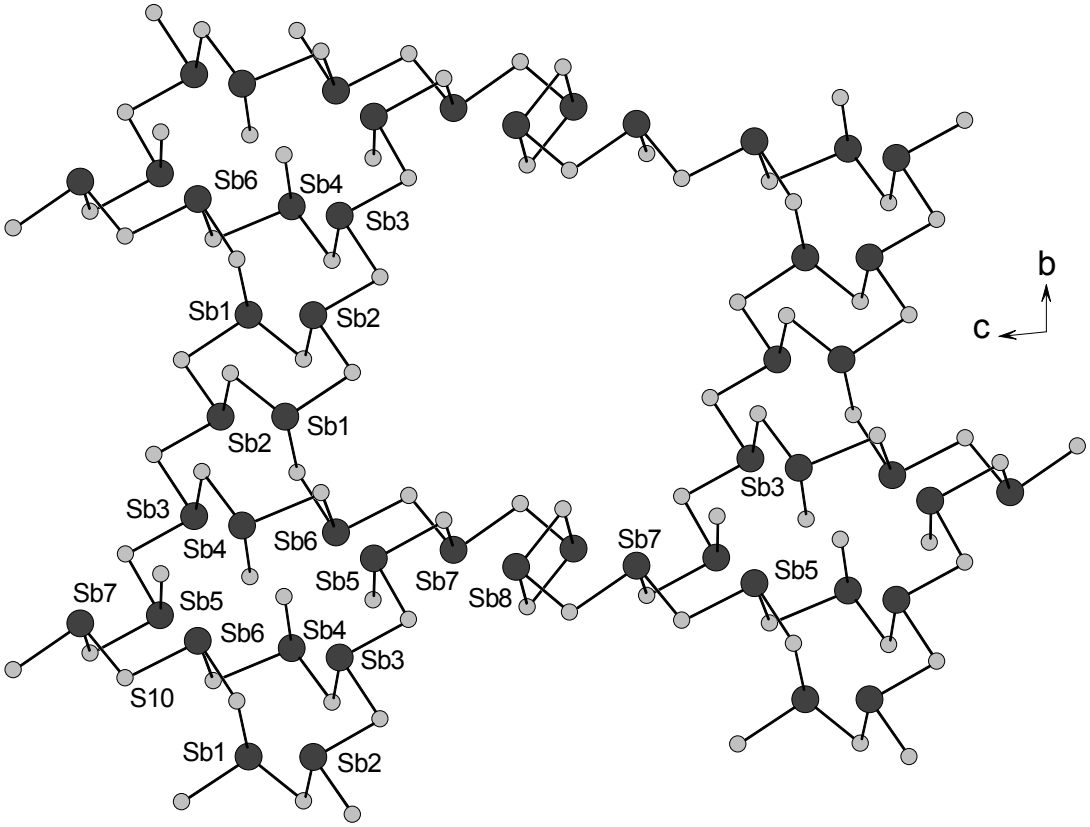

Fig. 3: The layered anion in the structure of **I** with the different heterorings mentioned in the text. The organic cations are not shown for clarity.

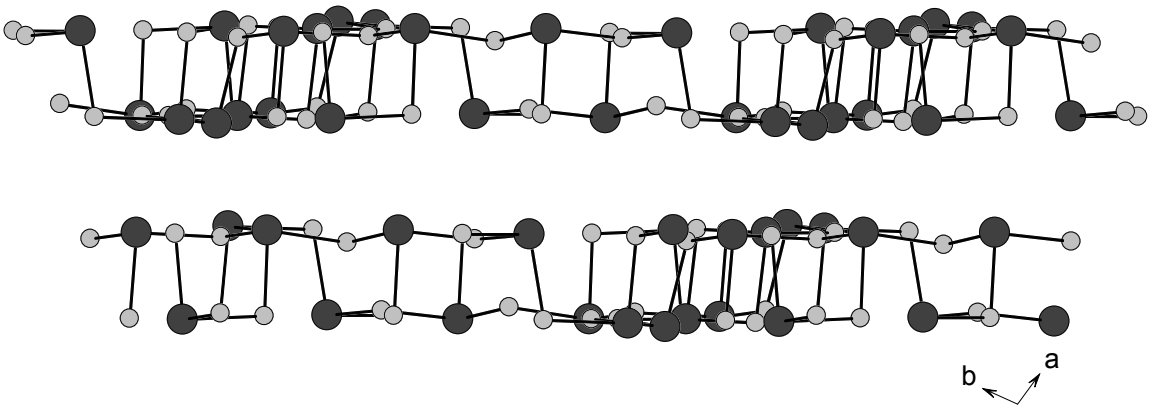

Fig. 4: Stacking of the two atoms thick layers in the structure of compound **I**. The organic cation is not shown for clarity.

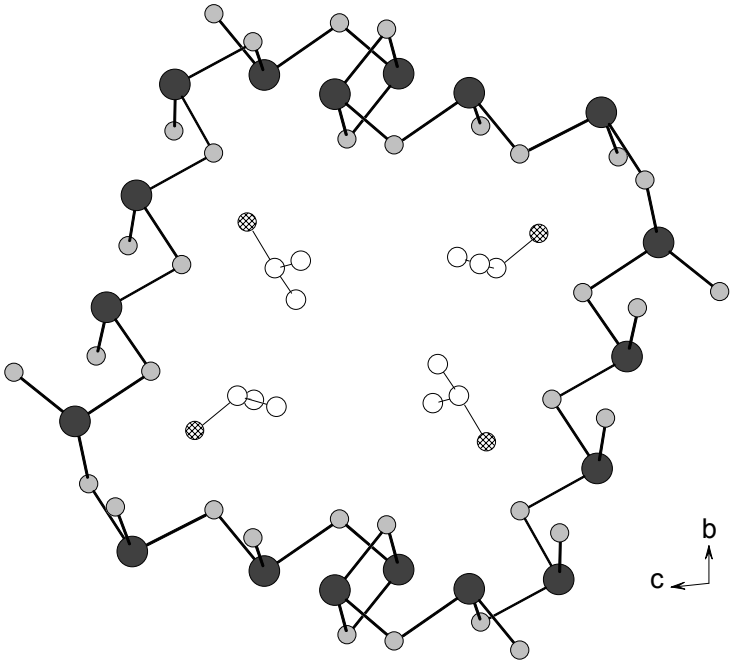

Fig. 5: The arrangement of the iPrH molecules with respect to the large ring in **I**. Open spheres: C; hatched speres: N.

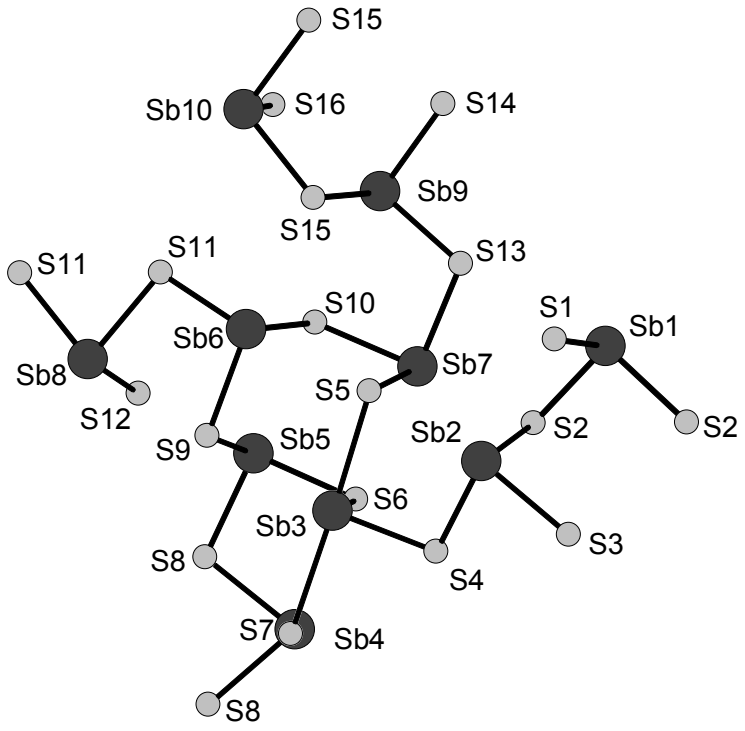

Fig. 6: The interconnection of the primary building units in the structure of compound **III**.

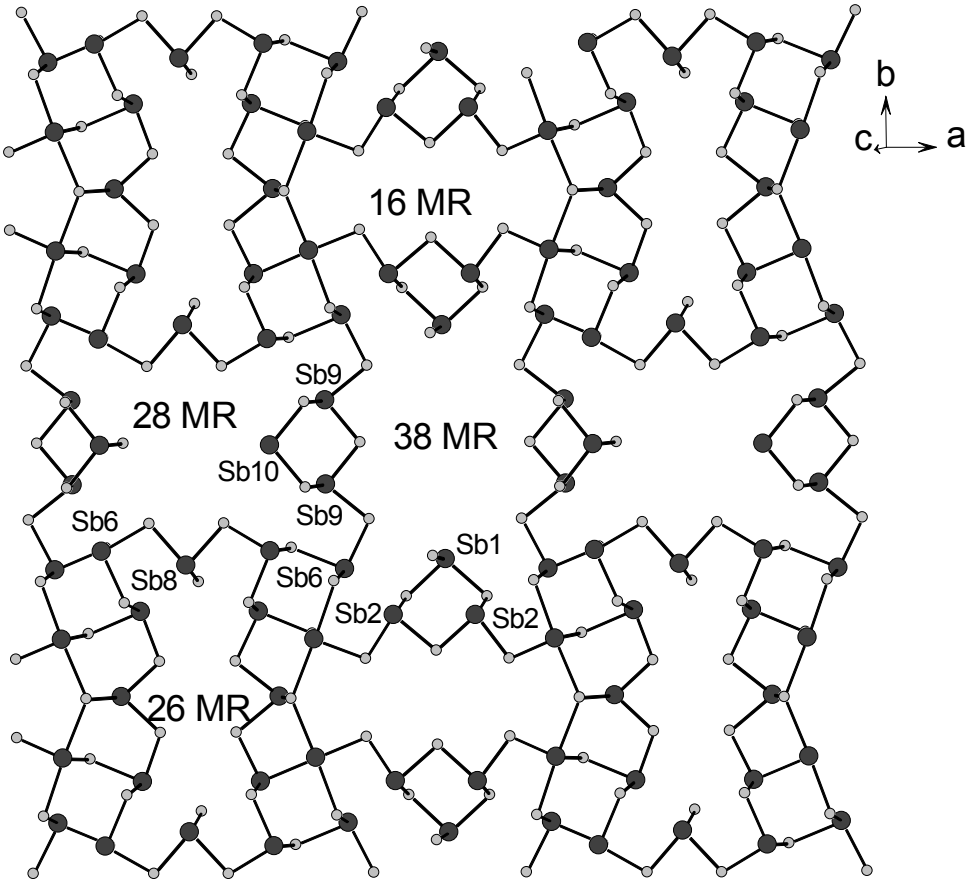

Fig. 7: The layered anion in the structure of compound **III** with the large rings labeled. Some Sb atoms are also labelled for a better understanding of the description given in the text.

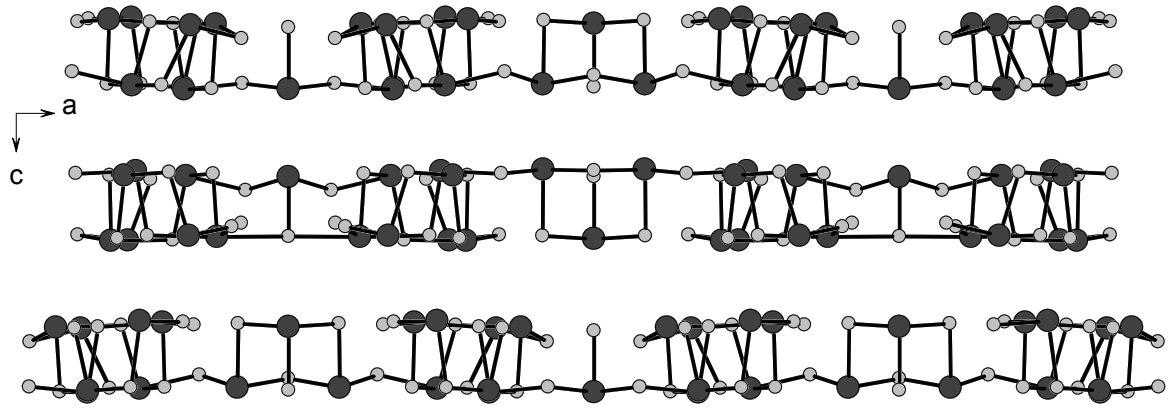

Fig. 8: Stacking of the two atoms thick layers in the structure of compound **III**.

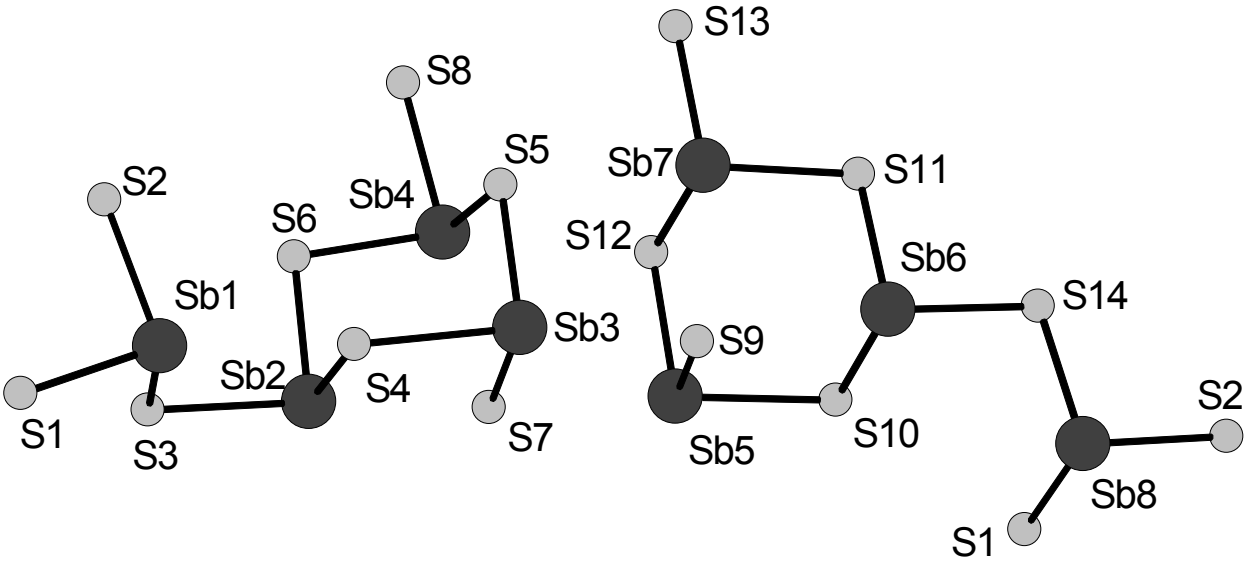

Fig. 9: Interconnection of the basic builing units in the structure of compound **V**. Note that the structure of compound **IV** is topological very similar with that of **V**.

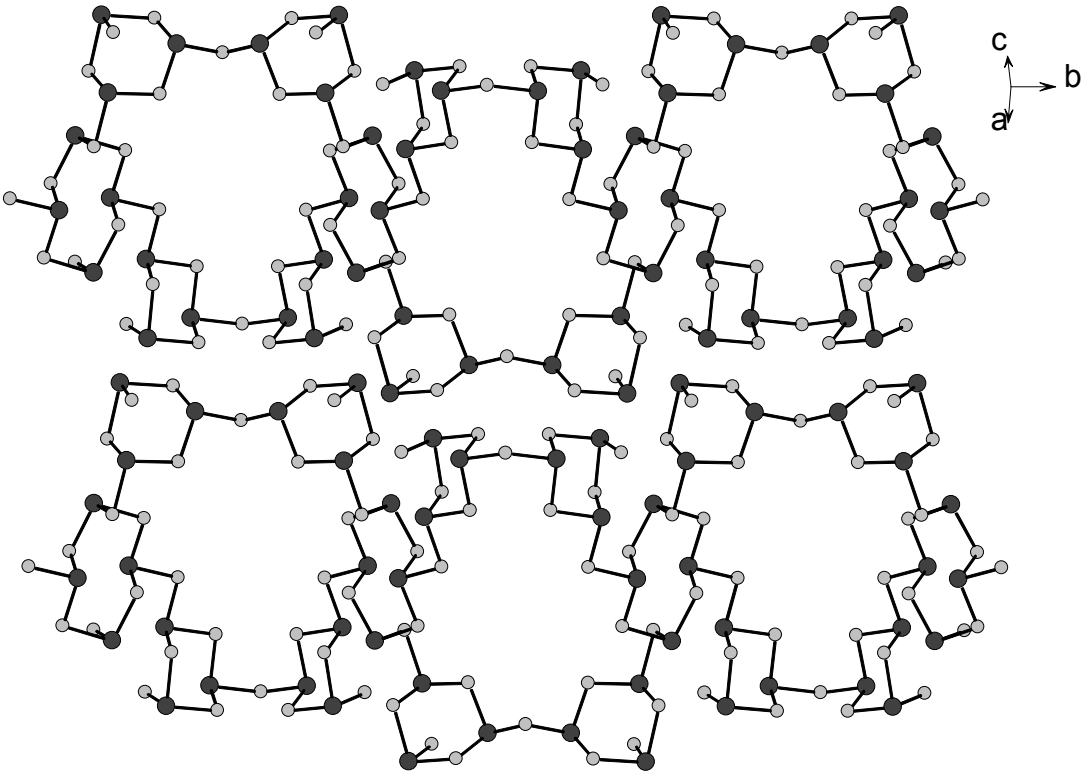

Fig. 10: The chains with the different heterorings in the structure of compound **V**.

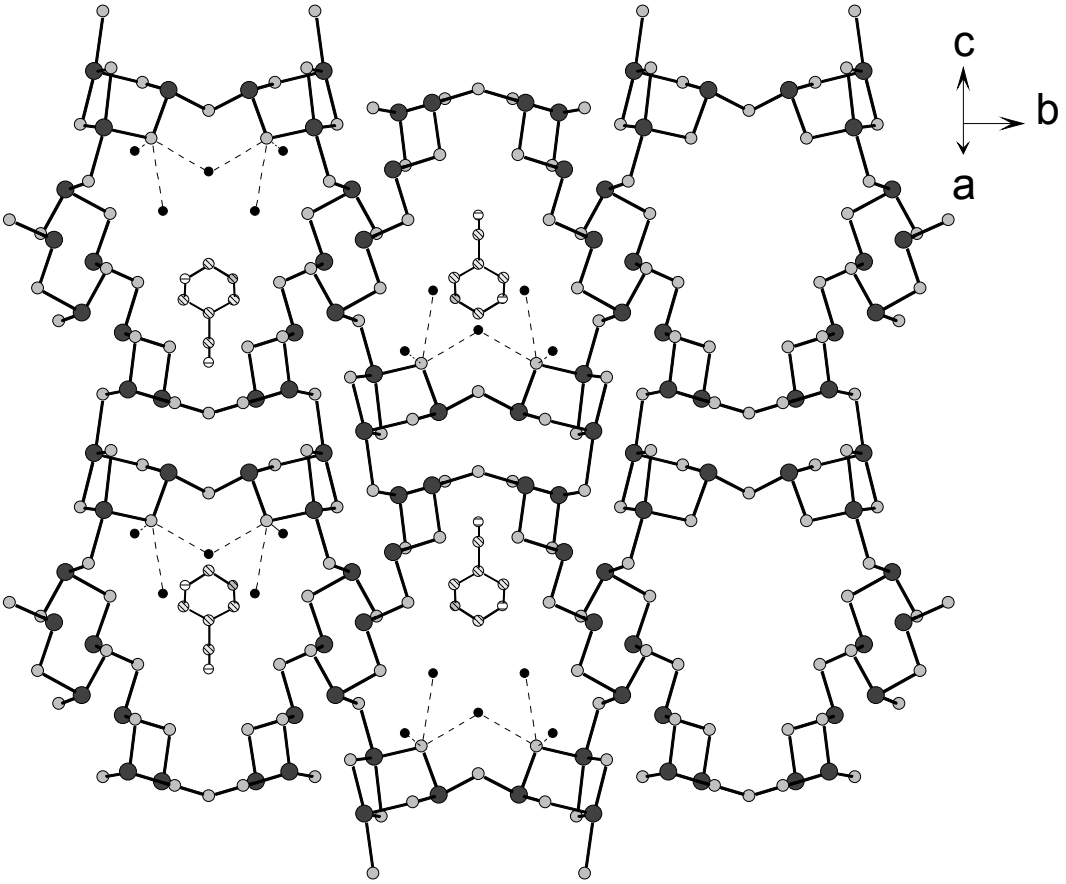

Fig. 11: Structure of the layered anion in compound **V** with view onto the (101) plane. Note that only one orientation of the disordered organic cation is displayed. Possible O-H···S bonds are indicated as broken lines.

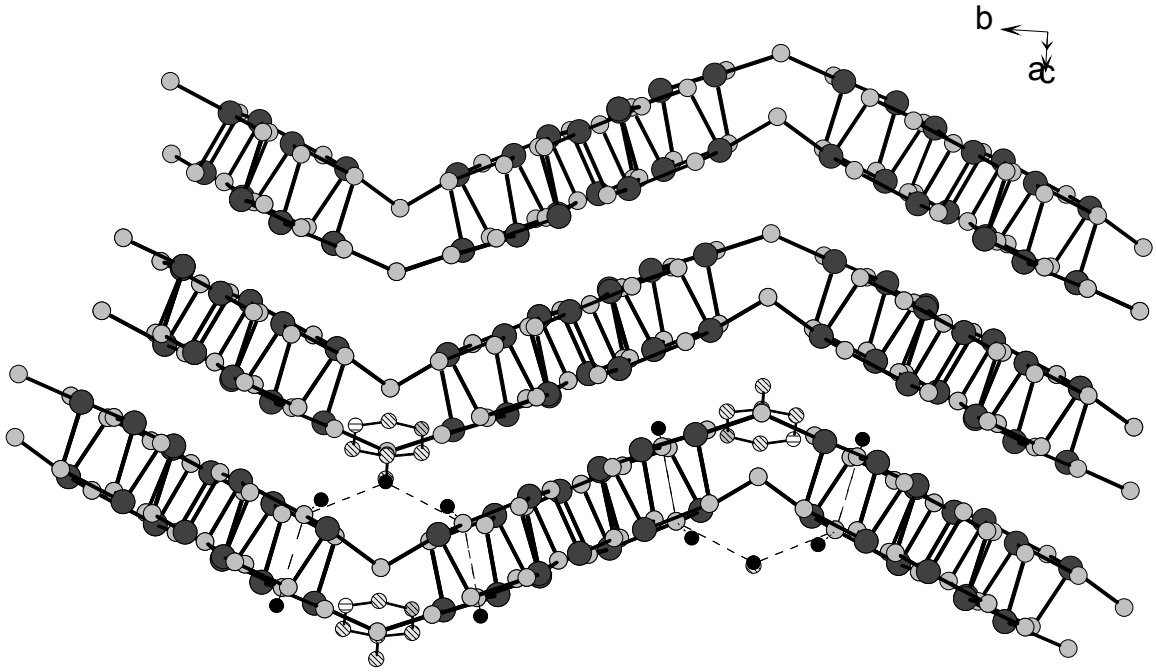

Fig. 12: The two atoms thick undulated layers of compound **V** with view along [10-1]. The inflection points of the layers coincide with the large 24 membered rings (see text). Note: only a few organic ions and O atoms of H_2O are shown.

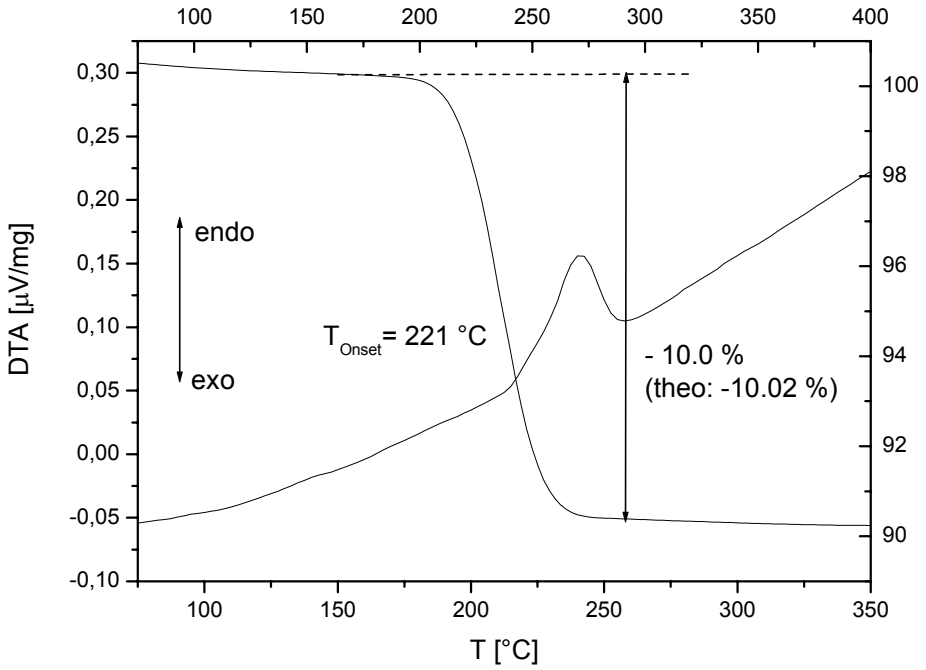
DTA [µV/mg]
T [°C]
endo
exo
T Onset = 221 °C
- 10.0 %
(theo: -10.02 %)

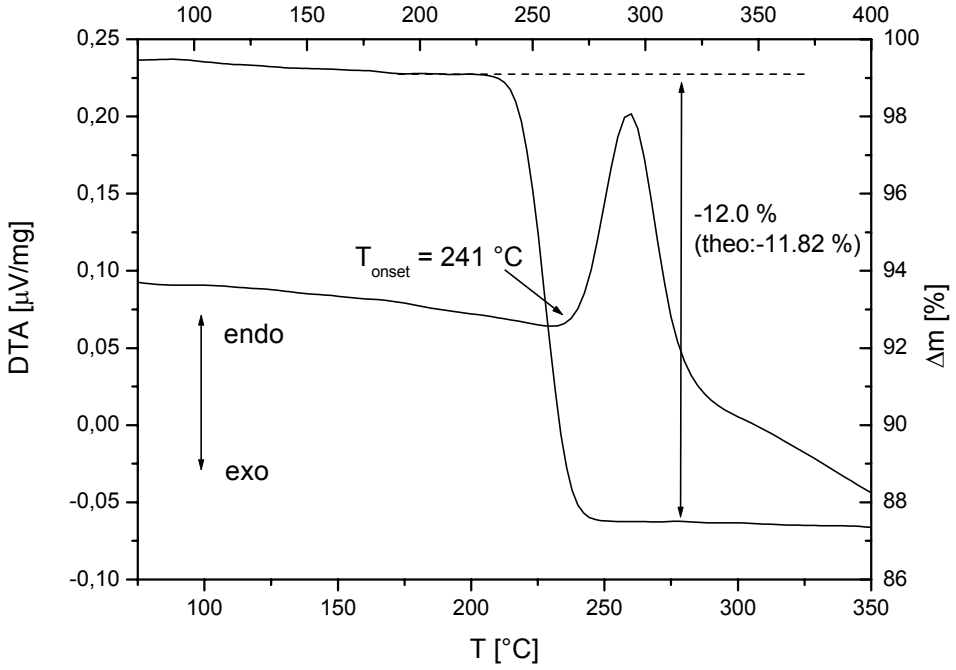
DTA [µV/mg]
Δm [%]
T [°C]
endo
exo
T onset = 241 °C
-12.0 %
(theo:-11.82 %)

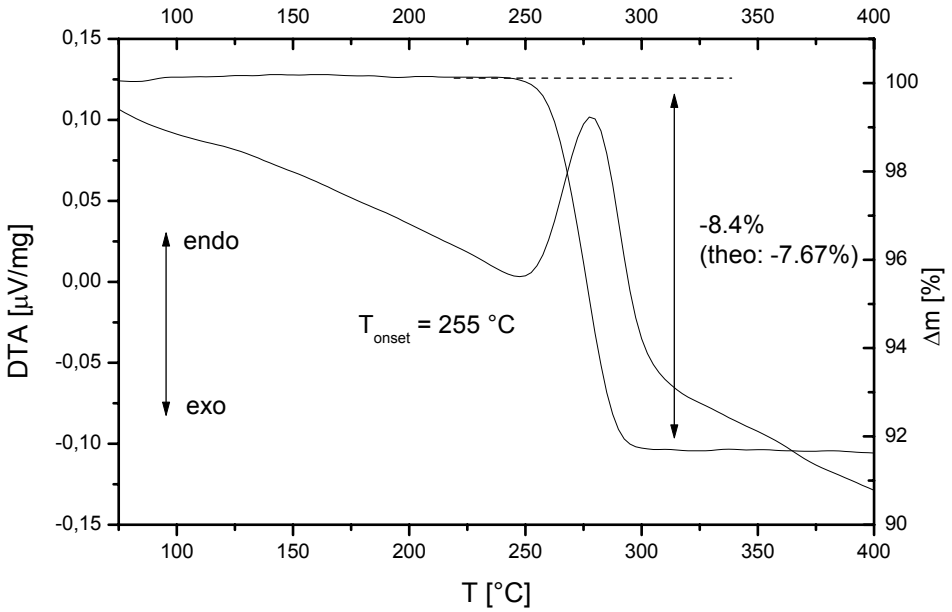
DTA [µV/mg]
Δm [%]
T [°C]
endo
exo
T$_{onset}$ = 255 °C
-8.4%
(theo: -7.67%)

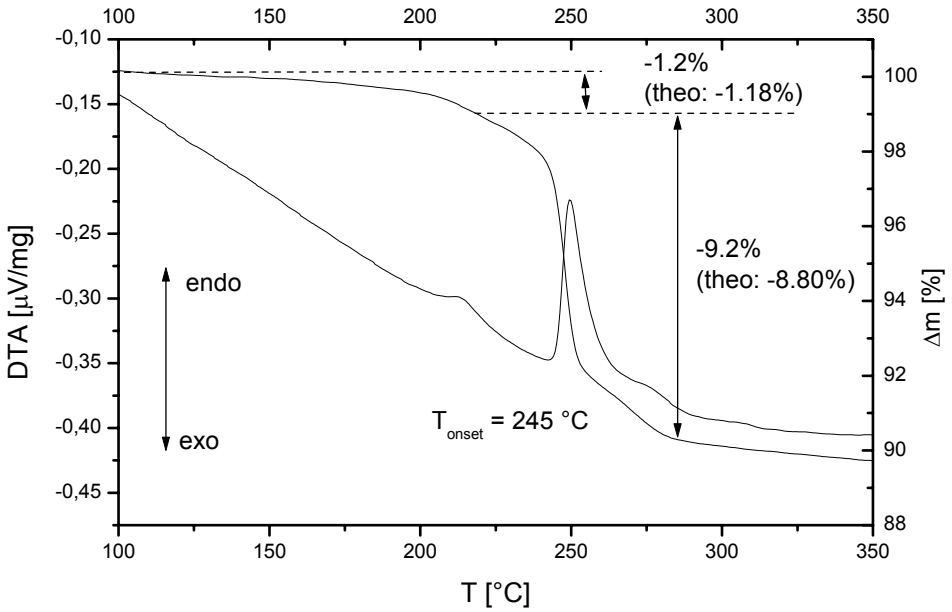
DTA [µV/mg]
Δm [%]
T [°C]
endo
exo
T$_{onset}$ = 245 °C
-1.2%
(theo: -1.18%)
-9.2%
(theo: -8.80%)

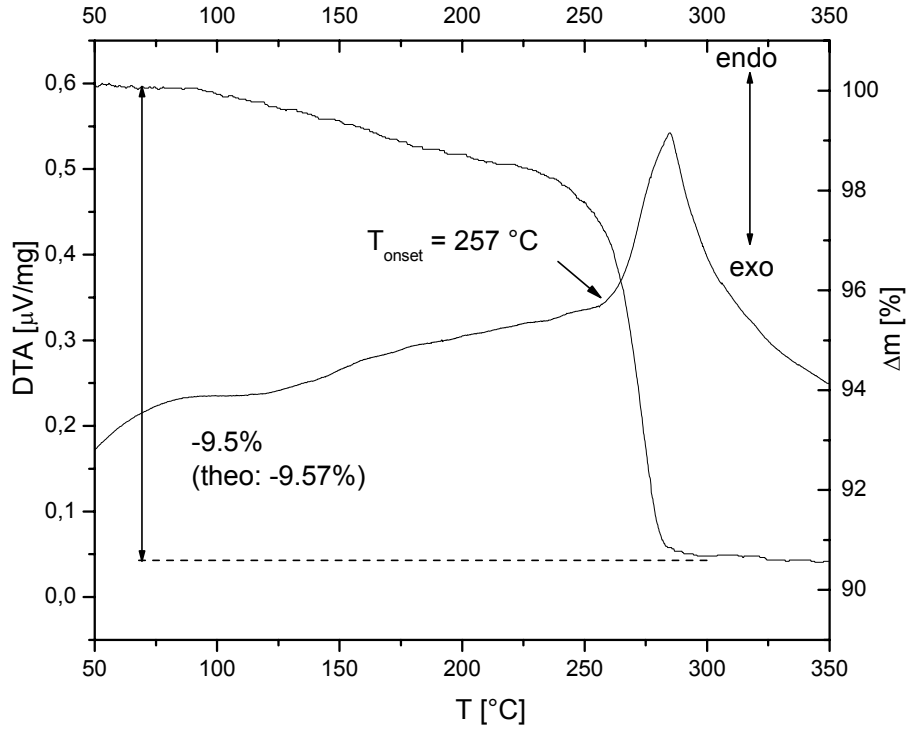

Fig. 13: DTA-TG curves for ($i$prH)$_2$[Sb_8S_{13}] (**I**), (1,2-dapH)$_2$[Sb_8S_{13}] (**II**), (1,3-dapH$_2$)[Sb_8S_{13}] (**III**), (dienH$_2$)[Sb_8S_{13}]·1.5 H_2O (**IV**), and ($C_6H_9N_2$)[Sb_8S_{13}]·2.5H_2O (**V**) (from top to bottom).

Table 2. Bond lengths (Å) and angles (°) for ($i$prH)$_2Sb_8S_{13}$ (**I**), (1,2dapH)$_2Sb_8S_{13}$ (**II**), (1,3dapH$_2$)Sb_8S_{13} (**III**), (dienH$_2$)Sb_8S_{13}·1.5H_2O (**IV**), and ($C_6H_9N_2$)Sb_8S_{13}·2.5H_2O (**V**). Estimated standard deviations are given in parentheses.

($i$prH)$_2Sb_8S_{13}$ (**I**)

Sb(1)-S(1)	2.424(3)	Sb(1)-S(2)	2.498(3)
Sb(1)-S(3a)	2.591(3)	Sb(2)-S(3)	2.431(3)
Sb(2)-S(2)	2.469(3)	Sb(2)-S(4)	2.512(3)
Sb(3)-S(5)	2.462(3)	Sb(3)-S(7)	2.485(3)
Sb(3)-S(4)	2.535(3)	Sb(4)-S(6)	2.410(2)
Sb(4)-S(5)	2.586(3)	Sb(4)-S(11b)	2.644(3)
Sb(5)-S(8)	2.430(3)	Sb(5)-S(9)	2.516(3)
Sb(5)-S(7)	2.570(3)	Sb(6)-S(11)	2.441(3)
Sb(6)-S(10)	2.512(3)	Sb(6)-S(1b)	2.629(3)
Sb(7)-S(10)	2.465(3)	Sb(7)-S(9)	2.466(3)
Sb(7)-S(12)	2.517(3)	Sb(8)-S(13)	2.446(3)
Sb(8)-S(12)	2.501(3)	Sb(8)-S(13c)	2.536(3)
Sb(1)-S(5)	3.136(3)	Sb(1)-S(11b)	3.157(3)
Sb(1)-S(2g)	3.546(3)	Sb(2)-S(2f)	3.165(3)
Sb(2)-S(1)	3.324(3)	Sb(2)-S(5e)	3.426(3)
Sb(3)-S(6)	3.081(3)	Sb(3)-S(1)	3.442(3)
Sb(3)-S(8e)	3.514(3)	Sb(4)-S(8)	2.946(3)
Sb(4)-S(6b)	2.999(3)	Sb(5)-S(6)	3.001(3)

Sb(5)-S(11)	3.140(3)	Sb(5)-S(10e)	3.638(3)
Sb(6)-S(6b)	3.045(3)	Sb(6)-S(8)	2.950(3)
Sb(7)-S(8)	3.018(3)	Sb(7)-S(13)	3.383(3)
Sb(7)-S(7d)	3.695(3)	Sb(8)-S(9c)	3.175(3)
Sb(8)-S(12h)	3.260(3)	Sb(8)-S(7c)	3.691(3)
S(1)-Sb(1)-S(2)	97.07(9)	S(1)-Sb(1)-S(3a)	92.64(10)
S(2)-Sb(1)-S(3a)	95.62(9)	S(3)-Sb(2)-S(2)	94.13(10)
S(3)-Sb(2)-S(4)	95.82(10)	S(2)-Sb(2)-S(4)	93.26(10)
S(5)-Sb(3)-S(7)	96.77(10)	S(5)-Sb(3)-S(4)	90.86(9)
S(7)-Sb(3)-S(4)	93.45(9)	S(6)-Sb(4)-S(5)	90.50(8)
S(6)-Sb(4)-S(11b)	91.16(8)	S(5)-Sb(4)-S(11b)	94.78(8)
S(8)-Sb(5)-S(9)	91.72(9)	S(8)-Sb(5)-S(7)	95.21(9)
S(9)-Sb(5)-S(7)	97.41(9)	S(11)-Sb(6)-S(10)	91.58(10)
S(11)-Sb(6)-S(1a)	91.84(8)	S(10)-Sb(6)-S(1b)	91.69(9)
S(10)-Sb(7)-S(9)	97.41(10)	S(10)-Sb(7)-S(12)	90.13(10)
S(9)-Sb(7)-S(12)	91.62(9)	S(13)-Sb(8)-S(12)	102.23(10)
S(13)-Sb(8)-S(13c)	87.62(9)	S(12)-Sb(8)-S(13c)	95.88(10)

a: -x, -y+2, -z ; b : -x+1, -y+1, -z ; c :-x+1, -y+1, -z+1 ; d : x+1, y, z ; e : x-1, y, z ; f : -x, 2-y, -z ; g : -x+1, -y+2, z ; h : -x+2, -y+1, -z +1

$(1,2dapH)_2Sb_8S_{13}$ (**II**)

Sb(1)-S(1)	2.422(2)	Sb(1)-S(2)	2.495(2)
Sb(1)-S(3a)	2.610(2)	Sb(2)-S(3)	2.422(2)
Sb(2)-S(2)	2.460(2)	Sb(2)-S(4)	2.520(2)
Sb(3)-S(5)	2.461(2)	Sb(3)-S(7)	2.493(2)
Sb(3)-S(4)	2.522(2)	Sb(4)-S(6)	2.409(2)
Sb(4)-S(5)	2.595(2)	Sb(4)-S(11b)	2.624(2)
Sb(5)-S(8)	2.421(2)	Sb(5)-S(9)	2.520(2)
Sb(5)-S(7)	2.549(2)	Sb(6)-S(11)	2.438(2)
Sb(6)-S(10)	2.526(2)	Sb(6)-S(1b)	2.641(2)
Sb(7)-S(10)	2.448(2)	Sb(7)-S(9)	2.451(2)
Sb(7)-S(12)	2.510(2)	Sb(8)-S(13)	2.425(2)
Sb(8)-S(12)	2.489(2)	Sb(8)-S(13c)	2.526(2)
Sb(1)-S(5)	3.053(2)	Sb(1)-S(11c)	3.129(2)
Sb(1)-S(2g)	3.600(2)	Sb(2)-S(2f)	3.139(2)
Sb(2)-S(1)	3.307(2)	Sb(2)-S(5e)	3.451(2)
Sb(3)-S(6)	3.093(2)	Sb(3)-S(1)	3.399(2)
Sb(3)-S(8e)	3.520(2)	Sb(4)-S(8)	3.027(2)
Sb(4)-S(6b)	2.951(2)	Sb(5)-S(6)	3.038(2)
Sb(5)-S(11)	3.165(2)	Sb(5)-S(10e)	3.689(2)
Sb(6)-S(6b)	3.057(2)	Sb(6)-S(8)	2.916(2)
Sb(7)-S(8)	3.106(2)	Sb(7)-S(13)	3.547(2)
Sb(8)-S(9c)	3.211(2)	Sb(8)-S(12h)	3.275(2)
S(1)-Sb(1)-S(2)	96.97(7)		
S(1)-Sb(1)-S(3a)	91.64(7)	S(2)-Sb(1)-S(3a)	95.54(7)
S(3)-Sb(2)-S(2)	92.65(7)	S(3)-Sb(2)-S(4)	96.06(7)
S(2)-Sb(2)-S(4)	93.22(7)	S(5)-Sb(3)-S(7)	96.54(7)
S(5)-Sb(3)-S(4)	91.51(7)	S(7)-Sb(3)-S(4)	93.74(7)
S(6)-Sb(4)-S(5)	90.06(6)	S(6)-Sb(4)-S(11b)	91.49(6)
S(5)-Sb(4)-S(11b)	94.47(6)	S(8)-Sb(5)-S(9)	92.02(6)
S(8)-Sb(5)-S(7)	95.73(7)	S(9)-Sb(5)-S(7)	98.07(7)
S(11)-Sb(6)-S(10)	90.53(7)	S(11)-Sb(6)-S(1b)	91.51(6)
S(10)-Sb(6)-S(1b)	91.04(7)	S(9)-Sb(6)-S(1b)	176.47(6)
S(10)-Sb(7)-S(9)	99.59(8)	S(10)-Sb(7)-S(12)	85.59(7)
S(9)-Sb(7)-S(12)	92.82(8)	S(13)-Sb(8)-S(12)	99.92(8)
S(13)-Sb(8)-S(13c)	87.67(7)	S(12)-Sb(8)-S(13c)	97.98(8)

a: -x, -y+2, -z; b: -x+1, -y+1, -z; c:-x+1, -y+1, 1-z; d: x+1, y, z;
e: x-1, y, z; f: -x, 2-y, -z; g: -x+1, -y+2z; h: -x+2; -y+1, -z+1

$(1,3dapH_2)Sb_8S_{13}$ (**III**)

Sb(1)-S(1)	2.359(8)	Sb(1)-S(2)	2.491(4)
Sb(2)-S(4)	2.451(4)	Sb(2)-S(2)	2.479(4)
Sb(2)-S(3)	2.488(4)	Sb(3)-S(4)	2.444(4)
Sb(3)-S(6)	2.448(4)	Sb(3)-S(5)	2.739(3)
Sb(3)-S(7)	2.861(2)	Sb(4)-S(7)	2.453(6)
Sb(4)-S(8)	2.504(4)	Sb(5)-S(9)	2.441(4)
Sb(5)-S(8)	2.455(4)	Sb(5)-S(6)	2.620(4)
Sb(6)-S(10)	2.456(4)	Sb(6)-S(11)	2.487(3)
Sb(6)-S(9)	2.510(3)	Sb(7)-S(5)	2.431(4)
Sb(7)-S(13)	2.507(4)	Sb(7)-S(10)	2.584(4)
Sb(8)-S(12)	2.422(6)	Sb(8)-S(11)	2.525(4)
Sb(9)-S(14)	2.467(3)	Sb(9)-S(15)	2.481(4)
Sb(9)-S(13)	2.525(4)	Sb(10)-S(16)	2.371(7)
Sb(10)-S(15)	2.469(4)	Sb(1) - S(7e)	3.627(6)
Sb(2) - S(5)	3.092(3)	Sb(2) - S(1)	3.247(6)
Sb(2) - S(13f)	3.653(4)	Sb(2) - S(14f)	3.718(5)
Sb(3) - S(2f)	3.568(4)	Sb(4) - S(6)	3.170 4)
Sb(5) - S(12)	3.004(3)	Sb(5) - S(10)	3.232(4)
Sb(6) - S(5)	3.162(3)	Sb(6) - S(15)	3.251(4)
Sb(6) - S(6f)	3.324(4)	Sb(7) - S(2)	3.053(4)
Sb(7) - S(6)	3.233(4)	Sb(7) - S(5e)	3.444(4)
Sb(8) - S(9)	3.296(3)	Sb(9) - S(16)	3.074(5)
Sb(9) - S(10)	3.202(4)	Sb(9) - S(1e)	3.690(6)
Sb(10) - S(12f)	3.607(6)	S(1)-Sb(1)-S(2)	96.95(16)
S(2a)-Sb(1)-S(2)	96.53(19)	S(4)-Sb(2)-S(2)	93.33(15)
S(4)-Sb(2)-S(3)	84.45(13)	S(2)-Sb(2)-S(3)	93.14(18)
S(4)-Sb(3)-S(6)	93.90(14)	S(4)-Sb(3)-S(5)	91.88(12)
S(6)-Sb(3)-S(5)	91.05(12)	S(4)-Sb(3)-S(7)	90.43(14)
S(6)-Sb(3)-S(7)	86.76(15)	S(5)-Sb(3)-S(7)	176.92(14)
S(7)-Sb(4)-S(8)	98.85(16)	S(8)-Sb(4)-S(8b)	78.46(17)
S(9)-Sb(5)-S(8)	89.75(15)	S(9)-Sb(5)-S(6)	92.87(12)
S(8)-Sb(5)-S(6)	91.57(12)	S(10)-Sb(6)-S(11)	92.35(14)
S(10)-Sb(6)-S(9)	94.23(12)	S(11)-Sb(6)-S(9)	95.50(12)
S(5)-Sb(7)-S(13)	96.00(13)	S(5)-Sb(7)-S(10)	92.00(12)
S(13)-Sb(7)-S(10)	95.11(12)	S(12)-Sb(8)-S(11)	100.17(17)
S(11)-Sb(8)-S(11c)	85.00(15)	S(14)-Sb(9)-S(15)	94.51(17)
S(14)-Sb(9)-S(13)	87.66(12)	S(15)-Sb(9)-S(13)	92.64(14)
S(16)-Sb(10)-S(15)	95.08(15)	S(15)-Sb(10)-S(15d)	100.97(19)

a: x, -y , z ; b: -x, y, z; c: x, -y+1, z; d: -x+1, y, z ; e: 0,5-y, x, -0,25+z; f: y, 0,5-x, 0,25+z; g: x, 1-y, z

$(dienH_2)Sb_8S_{13}\cdot 1.5H_2O$ (**IV**) and $(C_6H_9N_2)Sb_8S_{13}\cdot 2.5H_2O$ (**V**)

	IV	**V**		**IV**	**V**
Sb(1)-S(3)	2.421(2)	2.429(2)	Sb(1)-S(1)	2.469(2)	2.484(2)
Sb(1)-S(2)	2.594(2)	2.612(2)	Sb(2)-S(4)	2.427(2)	2.433(2)
Sb(2)-S(6)	2.534(2)	2.524(2)	Sb(2)-S(3)	2.680(2)	2.668(2)
Sb(2)-S(7)	2.854(2)	2.878(2)	Sb(3)-S(7)	2.419(2)	2.419(2)
Sb(3)-S(5)	2.549(2)	2.545(2)	Sb(3)-S(4)	2.690(2)	2.694(2)
Sb(3)-S(9)	2.887(2)	2.884(2)	Sb(4)-S(5)	2.463(2)	2.463(2)
Sb(4)-S(6)	2.495(2)	2.494(2)	Sb(4)-S(8)	2.504(2)	2.497(2)
Sb(5)-S(9)	2.422(2)	2.424(2)	Sb(5)-S(12)	2.514(2)	2.510(2)
Sb(5)-S(10)	2.542(2)	2.558(2)	Sb(6)-S(11)	2.464(2)	2.468(2)
Sb(6)-S(10)	2.466(2)	2.472(2)	Sb(6)-S(14)	2.504(2)	2.508(2)
Sb(7)-S(12)	2.435(2)	2.441(2)	Sb(7)-S(13)	2.489(2)	2.489(2)
Sb(7)-S(11)	2.496(2)	2.507(2)	Sb(8)-S(2a)	2.435(2)	2.441(2)
Sb(8)-S(1b)	2.471(2)	2.472(2)	Sb(8)-S(14)	2.476(2)	2.483(2)
Sb(1)-S(4)	3.207(2)	3.185(2)	Sb(1)-S(2e)	3.621(2)	3.592(2)
Sb(1)-S(10)	3.092(2)	3.061(2)	Sb(2)-S(9b)	3.181(2)	3.190(2)
Sb(2)-S(5g)	3.540(2)	3.548(2)	Sb(3)-S(7b)	3.215(2)	3.221(2)
Sb(4)-S(12)	3.347(2)	3.360(2)	Sb(4)-S(7)	3.148(2)	3.138(2)
Sb(4)-S(13g)	3.447(2)	3.452(2)	Sb(5)-S(7)	3.102(2)	3.084(2)
Sb(5)-S(11g)	3.701(2)	3.699(2)	Sb(5)-S(4b)	3.220(2)	3.219(2)
Sb(6)-S(9)	3.179(2)	3.163(2)	Sb(6)-S(3b)	3.469(2)	3.477(2)
Sb(7)-S(5)	3.366(2)	3.344(2)	Sb(7)-S(9)	3.118(2)	3.106(2)
Sb(7)-S(7h)	3.678(2)	3.682(2)	Sb(8)-S(3b)	3.400(2)	3.357(2)
Sb(8)-S(1a)	3.187(2)	3.195(2)			
S(3)-Sb(1)-S(1)	98.76(5)	98.25(6)	S(3)-Sb(1)-S(2)	93.28(6)	92.13(6)
S(1)-Sb(1)-S(2)	94.82(5)	95.54(5)	S(4)-Sb(2)-S(6)	92.31(5)	92.96(6)
S(4)-Sb(2)-S(3)	90.82(5)	90.85(5)	S(6)-Sb(2)-S(3)	94.94(5)	95.06(5)
S(4)-Sb(2)-S(7)	83.67(5)	83.18(5)	S(6)-Sb(2)-S(7)	92.21(5)	92.47(5)
S(3)-Sb(2)-S(7)	171.15(5)	170.62(5)	S(7)-Sb(3)-S(5)	93.30(5)	93.24(5)
S(7)-Sb(3)-S(4)	87.46(5)	87.49(5)	S(5)-Sb(3)-S(4)	94.70(5)	94.52(5)
S(7)-Sb(3)-S(9)	87.14(5)	87.16(5)	S(5)-Sb(3)-S(9)	93.59(5)	94.00(5)
S(4)-Sb(3)-S(9)	170.35(5)	170.18(5)	S(5)-Sb(4)-S(6)	95.72(5)	96.49(6)
S(5)-Sb(4)-S(8)	90.71(6)	90.69(7)	S(6)-Sb(4)-S(8)	90.49(7)	89.08(7)
S(9)-Sb(5)-S(12)	93.96(5)	94.09(6)	S(9)-Sb(5)-S(10)	92.72(5)	92.22(6)
S(12)-Sb(5)-S(10)	95.97(5)	95.25(5)	S(11)-Sb(6)-S(10)	95.52(5)	95.06(6)
S(11)-Sb(6)-S(14)	89.52(5)	89.87(6)	S(10)-Sb(6)-S(14)	93.72(6)	93.89(6)
S(12)-Sb(7)-S(13)	95.81(6)	95.45(7)	S(12)-Sb(7)-S(11)	96.71(6)	96.44(6)
S(13)-Sb(7)-S(11)	95.69(7)	96.14(7)	S(2a)-Sb(8)-S(1b)	95.22(6)	94.83(6)
S(2a)-Sb(8)S(14)	93.68(6)	94.02(6)	S(1b)-Sb(8)-S(14)	94.03(6)	94.36(6)

a: x-1,y,z+1; b: -x+1,-y+1,-z+1; c: x+1,y,z-1; d: x,-y+3/2,z; e: 1-x, 1-y, -z; f: -x, 1-y, 1-z; g: 1+x, y, z; h: -1+x, y, z;

Table 3: Details of data collection and selected refinement results for (*i*prH)$_2$Sb$_8$S$_{13}$ (**I**), (1,2dapH)$_2$Sb$_8$S$_{13}$ (**II**), (1,3dapH$_2$)Sb$_8$S$_{13}$ (**III**), (dienH$_2$)Sb$_8$S$_{13}$·1.5H$_2$O (**IV**), and (C$_6$H$_9$N$_2$)Sb$_8$S$_{13}$·2.5H$_2$O (**V**). Estimated standard deviations are given in parentheses.

	I	**II**	**III**	**IV**	**V**
Compound	(*i*prH)$_2$Sb$_8$S$_{13}$	(1,2dapH)$_2$Sb$_8$S$_{13}$	(1,3dapH$_2$)Sb$_8$S$_{13}$	(dienH$_2$)Sb$_8$S$_{13}$·1.5H$_2$O	(C$_6$H$_9$N$_2$)Sb$_8$S$_{13}$ · 2.5H$_2$O
Crystal system	triclinic	triclinic	tetragonal	monoclinic	monoclinic
a / Å	7.0122(8)	6.9922(5)	22.590(1)	7.1903(4)	7.2080(5)
b / Å	13.794(2)	13.705(1)	22.590(1)	25.900(2)	25.7407(15)
c / Å	17.216(3)	18.105(2)	22.461(1)	15.979(1)	15.9366(12)
α / °	94.45(2)	100.15(1)	90	90	90
β / °	96.49(2)	96.22(1)	90	97.39 (1)	96.960(8)
γ / °	101.21(2)	101.09(1)	90	90	90
V / Å^3	1614.4(4)	1657.5(2)	11461.4(10)	2951.0(3)	2935.1(3)
Space group	P-1	P-1	I4$_1$md	P2$_1$/m	P2$_1$/m
Z	2	2	16	4	4
Calc. density / g cm^{-3}	3.108	3.088	3.400	3.599	3.396
Crystal color	grey violet	grey red	dark red	light red	red
μ / mm^{-1}	7.43	7.24	8.37	8.15	8.18
Scan range	5° ≤ 2θ ≤ 56°	4° ≤ 2θ ≤ 56°	4° ≤ 2θ ≤ 56°	4° ≤ 2θ ≤ 54°	5° ≤ 2θ ≤ 56°
Index range	-8 ≤ h ≤ 8	-9 ≤ h ≤ 8	-29 ≤ h ≤ 29	-8 ≤ h ≤ 8	-8 ≤ h ≤ 8
	-18 ≤ k ≤ 18	-18 ≤ k ≤ 18	-29 ≤ k ≤ 29	-32 ≤ k ≤ 32	-32 ≤ k ≤ 32
	-22 ≤ l ≤ 22	-23 ≤ l ≤ 23	-29 ≤ l ≤ 29	-20 ≤ l ≤ 20	-20 ≤ l ≤ 20
Reflections collected	11693	16192	54892	25958	23199
Independent reflections	4337	7406	7191	6293	6145
R_{int}	0.0498	0.0424	0.0423	0.0367	0.0401
Temperature / K	293	293	293	293	293
Min./max. transmission	-	0.3227/0.4430	0.2592/0.3962	0.2926/0.3351	0.2879/0.3391
refl. with $F_o>4\sigma(F_o)$	3563	5935	6969	5380	4967
Number of parameters	261	239	206	194	254
weight	0.0571[a)]	0.1011[b)]	0.0324[c)]	0.0628[d)]	0.0478[e)]
R_1 for $F_o>4\sigma(F_o)$	0.0396	0.0495	0.0518	0.0343	0.0299
wR_2 for all reflections	0.1083	0. 1366	0.1255	0.0880	0.0750
GOOF	1.080	0.976	1.174	1.021	0.997
Δρ [e/ Å^3]	-0.96/1.14	-1.98/2.42	-1.83/2.05	-1.39/1.50	-1.12/1.62

a) $w = 1/[\sigma^2(F_o^2) + (0.0571 \cdot P)^2 + 10.7008 \cdot P]$; $P = (\text{Max}(F_o^2) + 2 \cdot F_c^2) / 3$

b) $w = 1/[\sigma^2(F_o^2) + (0.1011 \cdot P)^2 + 0.0 \cdot P]$; $P = (\text{Max}(F_o^2) + 2 \cdot F_c^2) / 3$

c) $w = 1/[\sigma^2(F_o^2) + (0.0324 \cdot P)^2 + 720.3773 \cdot P]$; $P = (\text{Max}(F_o^2, 0) + 2 \cdot F_c^2) / 3$

d) $w = 1/[\sigma^2(F_o^2) + (0.0628 \cdot P)^2 + 0.0 \cdot P]$; $P = (\text{Max}(F_o^2, 0) + 2 \cdot F_c^2) / 3$

e) $w = 1/[\sigma^2(F_o^2) + (0.0478 \cdot P)^2 + 0.0 \cdot P]$; $P = (\text{Max}(F_o^2, 0) + 2 \cdot F_c^2) / 3$

4.2 Ergebnisse und Publikationen zu übergangsmetallhaltigen Thioantimonaten

4.2.1 Die Verbindungen $[Fe(C_6H_{18}N_4)][FeSbS_4]$ und $[Fe(C_6H_{13}N_3)_2][Fe_2Sb_4S_{10}]$

Zusammenfassung der Veröffentlichung „*Solvothermal Synthesis and Characterization of the New Iron Thioantimonates(III) [Fe(C$_6$H$_{18}$N$_4$)]FeSbS$_4$ and [Fe(C$_4$H$_{13}$N$_3$)$_2$]Fe$_2$Sb$_4$S$_{10}$ Containing Fe^{II} and Fe^{III} and Protein-Analogous [2Fe^{III}-2S]$^{2+}$ Clusters*“.

Die Verbindungen $[Fe(C_6H_{18}N_4)][FeSbS_4]$ (**1**) und $[Fe(C_4H_{13}N_3)_2][Fe_2Sb_4S_{10}]$ (**2**) wurden unter solvothermalen Bedingungen dargestellt. In beiden liegen Fe(II) und Fe(III) nebeneinander vor, und in den Strukturen wird eine proteinanaloge [2Fe(III)-2S]$^{2+}$-Einheit beobachtet.

Zur Synthese von (**1**) wurden 1 mmol $FeCl_3$, 1 mmol Sb und 3 mmol S in 8 ml einer 50 %igen tren-Lösung 5 Tage lang in einem Autoklaven bei 170 °C erhitzt. Das Produkt bestand aus schwarzen, rhombenförmigen Kristallen mit einer Ausbeute von 40 % bezogen auf Sb. Die Synthese von (**2**) erfolgte analog zu (**1**), jedoch mit 8 ml einer 50 %igen dien-Lösung. Die schwarzen Kristalle waren ebenfalls rhombenförmig, die Ausbeute betrug 65 % bezogen auf Sb.

(**1**) kristallisiert in der triklinen Raumgruppe $P\bar{1}$ mit zwei Formeleinheiten pro Elementarzelle. Die kettenförmige Struktur wird aus zwei verschiedenen Fragmenten aufgebaut. Das erste Fragment ist eine [Fe(tren)SbS_3]-Einheit, welche aus dem [Fe(tren)]-Komplex und einer SbS_3-Einheit gebildet wird. Dieses Fragment ist alternierend über gemeinsame Ecken mit $[Fe_2S_6]$-Einheiten zur [Fe(tren)][$FeSbS_4$]-Kette verknüpft (Abb. 4.3, rechts). Diese Verknüpfung führt zur Bildung eines 8-gliedrigen $Fe_2Sb_2S_4$-Ringes in Wannenkonformation. Unter Berücksichtigung langer Sb-S-Bindungen entstehen Schichten in der (010)-Ebene. Die dreidimensionale Anordnung wird durch Wasserstoffbrückenbindungen erreicht.

Die Verbindung (**2**) kristallisiert ebenfalls in der triklinen Raumgruppe $P\bar{1}$ mit einer Formeleinheit pro Elementarzelle. Die Struktur besteht aus isolierten [Fe(dien)]$^{2+}$-

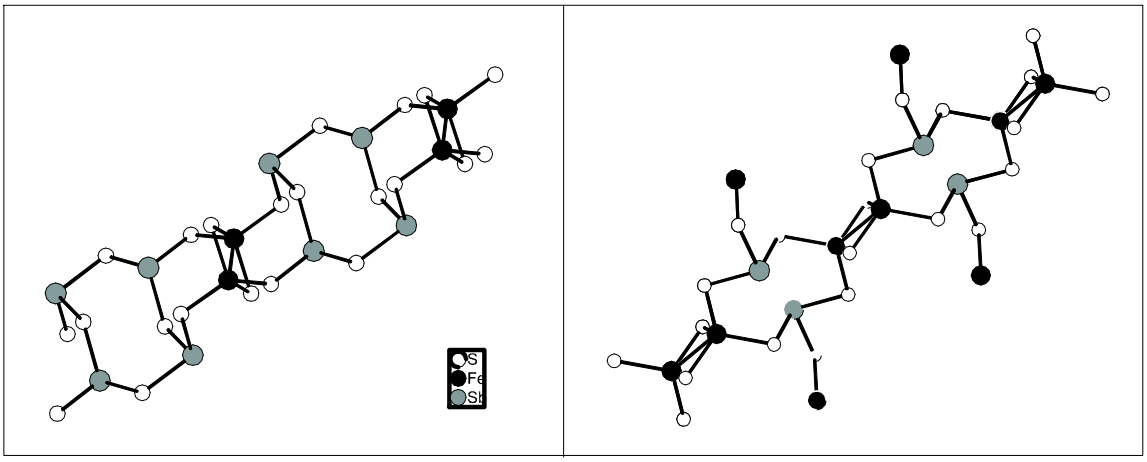

Abbildung 4.3: Kettenstruktur der Anionen: $[Fe_2Sb_4S_{10}]^{2-}$ (links) und $[FeSbS_4]^{2-}$ (rechts)

Kationen and einem kettenförmigen $[Fe_2Sb_4S_{10}]^{2-}$-Anion (Abb. 4.3, links). Als primäre Baueinheiten können $[Fe_2S_6]$- und SbS_3-Einheiten in dem Anion identifiziert werden. Das Kettenanion kann als Kondensationsprodukt wannenförmiger Sb_4S_4-Ringe, sekundären Baueinheiten aus vier eckenverknüpften SbS_3-Pyramiden, und $[Fe_2S_6]$-Einheiten angesehen werden. Die Verknüpfung führt zur Bildung siebengliedriger $Fe_2Sb_2S_3$-Ringe. Unter Berücksichtigung langer Sb-S-Bindungen kommt es zur Ausbildung von Schichten in der (001)-Ebene. Diese Schichten sind alternierend mit den Kationen senkrecht zur [001]-Richtung „sandwichartig“ angeordnet. Die dreidimensionale Struktur wird unter Berücksichtigung von S-H-Wasserstoffbrücken erreicht.

Beide Verbindungen zersetzen sich thermisch in einer Stufe, die von einem endothermen Signal in der DTA-Kurve begleitet ist. Der thermische Abbau von (**1**) beginnt bei einer Temperatur von 278 °C und es wird ein Gesamtmassenverlust von 31.3 % beobachtet. Der Gesamtmassenverlust für die Verbindung (**2**) beträgt 19.4 % und beginnt bei einer Temperatur von 285 °C. Im Pulverdiffraktogramm der thermischen Abbauprodukte können in beiden Fällen Sb_2S_3, $Fe_{1-x}S$ und $FeSb_2S_4$ identifiziert werden.

Beide Verbindungen weisen paramagnetisches Verhalten auf. Für (**1**) wird bei tiefen Temperaturen zusätzlich eine Abweichung vom linearen Verhalten gefunden, was auf eine Nullfeldaufspaltung zurückzuführen ist (Abb. 4.4, links). Der gemischtvalente Charakter von (**1**) wurde mit Mössbauerspektroskopie bewiesen. Für Fe(II) und

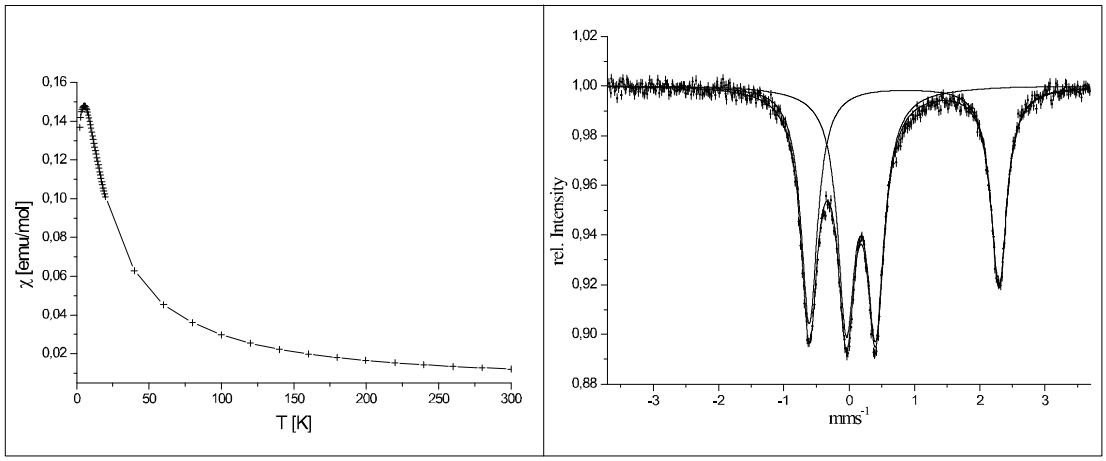

Abbildung 4.4: Magnetmessung (links) und Mössbauerspektrum (rechts) der Verbindung $[Fe(C_6H_{18}N_4)][FeSbS_4]$

Fe(III) werden die typischen chemischen Verschiebungen und Quadropolaufspaltungen beobachtet (Abb. 4.4, rechts).

Nicht nur die beobachtete Geometrie der [2Fe-2S]-Cluster ist vergleichbar mit den in Proteinen vorkommenden analogen Eisen-Schwefel-Clustern, auch die magnetischen Eigenschaften sind identisch. In natürlichen Redoxsystemen wird für Fe oft eine gemischte Valenz beobachtet. Im Unterschied zu den Verbindungen (**1**) und (**2**) werden in Proteinen allerdings Eisenkationen mit unterschiedlichen Oxidationsstufen innerhalb eines Eisen-Schwefel-Clusters gefunden.

Solvothermal Synthesis and Characterization of the New Iron Thioantimonates(III) $[Fe(C_6H_{18}N_4)]FeSbS_4$ and $[Fe(C_4H_{13}N_3)_2]Fe_2Sb_4S_{10}$ Containing Fe^{II} and Fe^{III} and Protein-Analogous $[2Fe^{III}\text{-}2S]^{2+}$ Clusters

Ragnar Kiebach[a], Wolfgang Bensch[a,*], Rolf-Dieter Hoffmann[b], and Rainer Pöttgen[b]

[a] Kiel, Institut für Anorganische Chemie der Christian-Albrechts-Universität

[b] Münster, Institut für Anorganische und Analytische Chemie der Westfälischen Wilhelms-Universität

Received November 4th, 2002.

Dedicated to Professor Hartmut Bärnighausen in the Occasion of his 70th Birthday

Abstract. The two new compounds $[Fe(tren)]FeSbS_4$ (**1**) (tren = tris(2-aminoethyl)amine) and $[Fe(dien)_2]Fe_2Sb_4S_{10}$ (**2**) (dien = diethylendiamine) were prepared under solvothermal conditions and represent the first thioantimonates(III) with iron cations integrated into the anionic network. In both compounds Fe^{3+} is part of a $[2Fe^{III}\text{-}2S]$ cluster which is often found in ferredoxines. In addition, Fe^{2+} ions are present which are surrounded by the organic ligands. In (**1**) the Fe^{2+} ion is also part of the thioantimonate(III) network whereas in (**2**) the Fe^{2+} ion is isolated. In both compounds the primary SbS_3 units are interconnected into one-dimensional chains. The mixed-valent character of $[Fe(tren)]FeSbS_4$ was unambiguously determined with Mössbauer spectroscopy. Both compounds exhibit paramagnetic behaviour and for (**1**) a deviation from linearity is observed due to a strong zero-field splitting. Both compounds decompose in one single step.

Keywords: Iron; Thioantimonates; Solvothermal synthesis; Crystal structure; Magnetic properties; Mössbauer spectroscopy

Solvothermale Synthese und Charakterisierung der neuen Eisen-Thioantimonate(III) $Fe(C_6H_{18}N_4)]FeSbS_4$ und $[Fe(C_4H_{13}N_3)_2]Fe_2Sb_4S_{10}$ mit Fe^{II}- und Fe^{III}-Kationen und Protein-analogen $[2Fe^{III}\text{-}2S]^{2+}$-Clustern

Inhaltsübersicht. $[Fe(tren)]FeSbS_4$ (**1**) (tren = tris(2-aminoethyl)-amin) und $[Fe(dien)_2]Fe_2Sb_4S_{10}$ (**2**) (dien = diethylendiamin) sind die ersten Verbindungen mit einem Thioantimonatnetzwerk, in welches Eisen integriert ist. In beiden Verbindungen ist Fe^{III} in Form von $[2Fe^{III}\text{-}2S]$-Clustern zu finden, ein Clustertyp wie man ihn häufig in Ferredoxinen findet. Zusätzlich enthalten beide Verbindungen Fe^{2+}-Kationen, welche von organischen Liganden umgeben sind. In (**1**) ist dieses Ion ebenfalls in das Thioantimonatnetzwerk integriert, in (**2**) liegt es isoliert vor. Die primären $[SbS_3]$-Einheiten sind in beiden Verbindungen zu Ketten verbunden. Der gemischvalente Charakter von (**1**) wird im Mössbauerspektrum deutlich. Beide Verbindungen weisen paramagnetisches Verhalten auf. Für (**1**) wird bei tiefen Temperaturen eine deutliche Abweichung vom linearen Verhalten beobachtet, was auf eine Nullfeld-Aufspaltung zurückzuführen ist. Die thermische Zersetzung verläuft bei beiden Verbindungen in einem einzigen Schritt.

Introduction

Many binary or multinary chalcogenides show interesting electrical, optical, and magnetic properties. Often such chalcogenides are prepared at elevated temperatures using the elements as starting materials. In the overwhelming number of cases the most thermodynamic stable products are formed and the structures are relatively dense. For the syntheses of new chalcogenides which are kinetically stabilized and exhibit a less dense packing of the constituents, hydrothermal techniques are promising as it was demonstrated for thioantimonates [1], thiostannates [2], and thiogermanates [3]. A large number of thioantimonates(III) were synthesized in the past [4–7], but only a few contain transition metal cations (TM) within the thioantimonate(III) framework. Selected examples are the compounds $Mn_2Sb_2S_5(L)$ (L = amine) [8–9], $[Co(C_6H_{18}N_4)_2]Sb_4S_8$, $[Co(C_6H_{18}N_4)_2]Sb_2S_5$ [10], $[Ni(C_6H_{18}N_4)]Sb_2S_4$ [4] and $[C_4H_{12}N_2]_{0.5}CuSb_6S_{10}$ [11]. During the last few years we explored solvothermal syntheses using transition metal complexes (TMC) as structure directing molecules with the aim to prepare new thioantimonates(III) which show different structures compared to the hitherto known compounds. In

* Prof. Dr. Wolfgang Bensch
Institut für Anorganische Chemie
Universität Kiel, Olshausenstrasse 40
D-24098 Kiel, Germany
Fax: +49 (0)431/880 -1520
E-Mail: wbensch@ac.uni-kiel.de

Prof. Dr. Rainer Pöttgen
Institut für Anorganische und Analytische Chemie, Universität Münster
Wilhelm-Klemm-Straße 8, D-48149 Münster, Germany
Fax: +49 (0)251/8336002
E-Mail: pottgen@uni-muenster.de

  0044–2313/03/629/532–538 $ 20.00+.50/0 Z. Anorg. Allg. Chem. **2003**, *629*, 532–538

several cases the TMC acted not as a "template" molecule [4] but was integrated into the anionic framework. In continuing work we synthesized the two new compounds $[Fe(C_6H_{18}N_4)]FeSbS_4$ and $[Fe(C_4H_{13}N_3)_2]Fe_2Sb_4S_{10}$. Here we report on the synthesis, crystal structures, thermal stability and magnetic properties of these iron containing thioantimonates(III).

Results and Discussion

*Crystal Structure of [Fe(tren)]FeSbS$_4$ (**1**)*

In the new compound [Fe(tren)]$FeSbS_4$ (**1**) (tren = tris(2-aminoethyl)amine) the $Fe(1)^{2+}$ ion is coordinated by four N atoms of one tren ligand and by one S atom (S(1)) in a distorted trigonal bipyramidal coordination (Fig. 1, left). The Fe−N distances range from 2.135(4) to 2.302(4) Å and as expected [12] the longer Fe(1)−N(4) bond (2.302(4) Å) is *trans* to the Fe(1)−S(1) bond (2.404(1) Å) (Table 1). The N−Fe−N angles vary between 77.6(2) and 103.1(2)° and are typical for the Fe^{2+} cation coordinated by tren [13−14]. The Sb(1) atom is surrounded by three S atoms (S(1), S(2) and S(3)) to form a trigonal pyramidal $[SbS_3]^{3-}$ unit. The S(1) atom is bound to Fe(1)

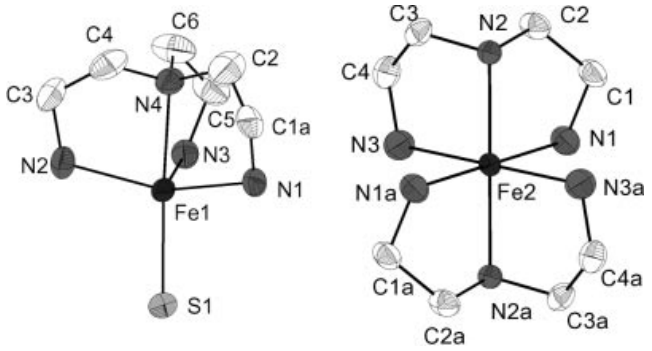

Fig. 1 (left) View of the [Fe(tren)]S unit with labelling. Note: the position of C1 is split into two positions. C1a represents the site with higher occupancy. (right) The s-fac $[Fe(dien)_2]^{2+}$ cation with labelling. Atoms with "a" are generated by symmetry operations. The displacement ellipsoids are drawn at the 50 %-probability level. Hydrogen atoms are omitted for clarity.

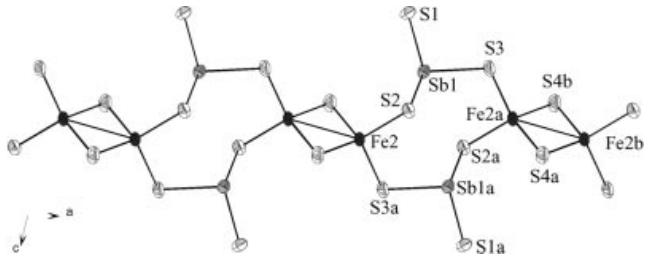

Fig. 2 The $^1_\infty$[Fe(tren)]$FeSbS_4$ chain with the $[Fe_2S_6]$ units and the eight-membered $Fe_2Sb_2S_4$ rings. The $Fe(tren)^{2+}$ cations are omitted for clarity. The displacement ellipsoids are drawn at the 50 %-probability level.

Table 1 Selected distances /Å and angles /° for $[Fe(C_6H_{18}N_4)]FeSbS_4$. Estimated standard deviations are given in parentheses.

Sb(1)−S(1)	2.409(1)	Sb(1)−S(2)	2.431(9)
Sb(1)−S(3)	2.432(1)	Fe(1)−S(1)	2.404(1)
Fe(1)−N(1)	2.149(3)	Fe(1)−N(2)	2.149(3)
Fe(1)−N(3)	2.135(4)	Fe(1)−N(4)	2.302(4)
Fe(2)−Fe(2)[a)]	2.720(1)	Fe(2)−S(2)	2.299(1)
Fe(2)−S(3)[b)]	2.292(1)	Fe(2)−S(4)[a)]	2.209(1)
Fe(2)−S(4)	2.216(1)		
S(1)−Sb(1)−S(2)	98.40(4)	S(1)−Sb(1)−S(3)	96.45(4)
S(2)−Sb(1)−S(3)	95.57(4)	N(1)−Fe(1)−S(1)	96.8(2)
N(1)−Fe(1)−N(2)	142.5(2)	N(1)−Fe(1)−N(4)	78.2(2)
N(2)−Fe(1)−S(1)	105.4 (2)	N(2)−Fe(1)−N(4)	77.6(2)
N(3)−Fe(1)−S(1)	105.6(1)	N(3)−Fe(1)−N(1)	103.1(2)
N(3)−Fe(1)−N(2)	99.4(2)	N(3)−Fe(1)−N(4)	78.2(2)
N(4)−Fe(1)−S(1)	174.4(1)	S(2)−Fe(2)−Fe(2)[a)]	127.15(4)
S(3)[b)]−Fe(2)−Fe(2)[a)]	126.44(4)	S(3)[b)]−Fe(2)−S(2)	106.41(4)
S(4)[a)]−Fe(2)−S(2)	111.29(5)	S(4)−Fe(2)−S(2)	112.26(4)
S(4)[a)]−Fe(2)−S(3)[b)]	111.65(4)	S(4)−Fe(2)−S(3)[b)]	111.15(5)
S(4)[a)]−Fe(2)−S(4)	104.20(4)	S(4)[a)]−Fe(2)−Fe(2)[a)]	52.24(3)
S(4)−Fe(2)−Fe(2)[a)]	51.96(3)	Fe(1)−S(1)−Sb(1)	99.29(4)
Fe(2)−S(2)−Sb(1)	96.34(4)	Fe(2)[a)]−S(3)−Sb(1)	103.38(4)
Fe(2)[a)]−S(4)−Fe(2)	75.80(4)		

Symmetry code: [a)] −x, 1−y, 1−z; [b)] 1−x, 1−y, 1−z;

Table 2 Additional long Sb−S bonds /Å for $[Fe(C_6H_{18}N_4)]FeSbS_4$. Estimated standard deviations are given in parentheses.

Sb1−S2[a)]	3.508(2)
Sb1−S4	3.650(4)

Symmetry code: [a)] 1−x, 1−y, 1−z;

Table 3 Selected H···S distances /Å and angles /° for $[Fe(C_6H_{18}N_4)]FeSbS_4$.

D−H	A	D−H	H···A	D−H···A	D···A
N(2)−H(1N2)	S(1)[c)]	0.900	2.676	148.07	3.472
N(3)−H(3A)	S(3)[a)]	0.900	2.404	176.48	3.302
N(3)−H(3B)	S(1)[b)]	0.900	2.497	168.04	3.382
N(1)−H(1A_a)	S(3)	0.900	2.484	169.39	3.373
N(1)−H(1B_a)	S(1)[a)]	0.900	2.977	133.55	3.656
N(2)−H(2C)	S(1)[b)]	0.900	2.752	148.32	3.550
N(2)−H(2D)	S(2)	0.900	2.769	120.61	3.319

Symmetry code: [a)] 1−x, 1−y, −z; [b)] −x, 1−y, −; [c)] 2−x, 1+y, 1−z;

and considering the SbS_3 pyramid a [Fe(tren)SbS_3] unit is formed. The Fe(2) atom is in a tetrahedral environment of four S atoms. Two tetrahedra are joined by a common edge by the $\bar{1}$-symmetry operation to build a $[Fe_2S_6]$ unit (Fig. 2). This unit is reminiscent of the well known $[2Fe\text{-}2S]^{+/2+}$ cluster found in ferredoxines [15−19] or in ternary iron sulfides [20−24]. The Sb−S distances range from 2.409(1) to 2.432(1) Å and the S−Sb−S angles vary from 95.57(4) to 98.40(4)°, both being in good agreement with data found in the literature [1, 4−11, 25−31]. The coordination sphere of Sb(1) is completed by two intramolecular secondary bonds to S4 (3.650(2)) and S(2a) (3.508(2)) (Tab. 2) forming a SbS_5 ψ-octahedron. The Fe−S bonds in the $[Fe_2S_6]$ unit are between 2.209(1) and 2.299(1) Å and the S−Fe−S angles range from 104.2(4) (S(4)−Fe(2)−S(4a)) to 112.26(4)° (S(4)−Fe(2)−S(2)) which indicate a moderate distortion of

the FeS_4 tetrahedron (Table 1). The Fe−Fe distance of 2.720(1) Å, the Fe−S bond lengths and the angles are nearly identical with the values reported in the literature for the $[2Fe-2S]^{+/2+}$ cluster [15−19, 32]. They agree also with those found in ternary iron sulfides [20−24]. The $[Fe_2S_6]$ bitetrahedron is joined via S(2) and S(3) with two $[Fe(tren)SbS_3]$ units to form the $^1_\infty\{[Fe(tren)]FeSbS_4\}$ chain which runs parallel to the *a* axis (Fig. 2). The interconnection of alternating $[Fe_2S_6]$ units and $[Fe(tren)SbS_3]$ moieties yields eight-membered $Fe_2Sb_2S_4$ rings in a chair-like conformation (see Fig. 2). At the outerior of the backbone of the chain the organic ligands are located. The chains form pseudo-layers within the (010) plane with the shortest distances between neighboured chains of about 3.3 Å (Fig. 3). Seven short intermolecular H···S contacts with distances in the range from 2.404 to 2.977 Å and angles N−H···S between 120.61 and 176.48° are observed (Fig. 3), which may indicate weak hydrogen bonding (see Table 3).

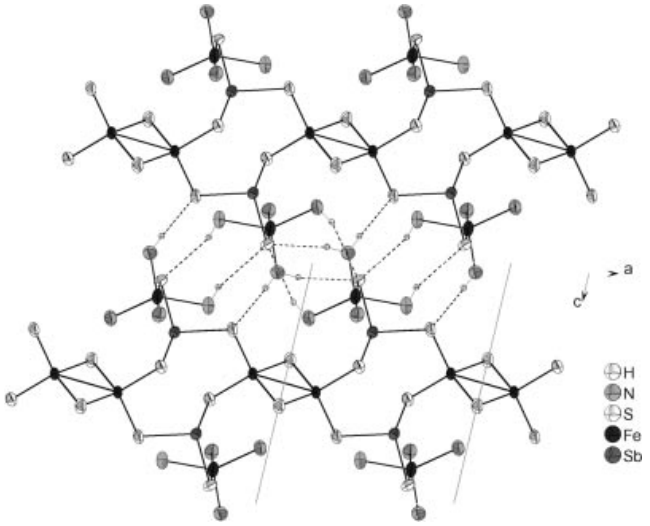

Fig. 3 Pseudo-layers of $^1_\infty[[Fe(tren)]FeSbS_4]$ chains within the (010) plane. Possible S···H bonds are indicated as dotted lines. One unit cell is outlined. The displacement ellipsoids are drawn at the 50 %-probability level and the H atoms are drawn with arbitrary radius.

*Crystal Structures of [Fe(dien)$_2$]Fe$_2$Sb$_4$S$_{10}$ (**2**)*

The structure of $[Fe(dien)_2]Fe_2Sb_4S_{10}$ (**2**) consists of an isolated $[Fe(dien)_2]^{2+}$ cation and an one-dimensional $^1_\infty[Fe_2Sb_4S_{10}]^{2-}$ anionic chain. In the $[Fe(2)(dien)_2]^{2+}$ cation the iron ion exhibits a distorted octahedral environment of six N atoms of two dien ligands (Fig. 1, right). For this complex a s-facial conformation is found. The Fe(2)−N distances are between 2.234(3) and 2.283(4) Å, the N−Fe−N angles vary from 75.7(1) to 104.3(1)° (Table 4). Due to symmetry reasons all *trans* angles have a value of 180°. The Fe−N bond lengths and the angles are comparable with those reported in literature [13−14, 28, 33] and found in (**1**). We note that a $[Fe(dien)_2]^{2+}$ cation was reported in the literature only once [28]. The $^1_\infty[Fe_2Sb_4S_{10}]^{2-}$ anionic chain is formed by the interconnection of two $[SbS_3]^{3-}$ trigonal pyramids (Sb(1), Sb(2)) and one $[FeS_4]$ tetrahedron (Fe(1)). Like in compound (**1**) two $[FeS_4]$ units are linked through the $\bar{1}$-symmetry operation to form a $[Fe_2S_6]$ bitetrahedron by sharing a common edge (Fig. 4). The two $[SbS_3]$ pyramids are vertex-linked via S(3) into a $[Sb_2S_5]$ unit which is joined via S(2) and S(4) to the $[Fe_2S_6]$ unit thus yielding a $[Fe_2Sb_2S_6]$ moiety that contains a seven membered ring ($Fe_2Sb_2S_3$) (Fig. 4). Another heteroring with composition Sb_4S_4 being in chair conformation is found which is generated by the $\bar{1}$-symmetry operation applied to the $[Sb_2S_5]$ unit (Fig. 4). We note that such heterorings are often found in thioantimonates (III) [4, 7, 10−11, 28−30]. The anionic chain $^1_\infty[Fe_2Sb_4S_{10}]^{2-}$ is directed along [1-10] and may be viewed as a condensation product of $[Sb_4S_4]$ and $[Fe_2S_6]$ building blocks (Fig. 4). The Sb-S bonds in the range from 2.430(1) to 2.500(1) Å and the angles S−Sb−S between 87.43(3) and 102.30(3)° (Table 4) are in the range observed in many other thioantimonates(III) [1, 4−11, 25−31]. In the $[Fe_2S_6]$ unit the Fe−S distances are between 2.216(1) and 2.298(1) Å, and for the angles S−Fe−S values from 107.86(4) to 115.62(4)° are observed (Table 4). A comparison with the $[Fe_2S_6]$ unit in (**1**) shows that the tetra-

Table 4 Selected distances /Å and angles / ° for $[Fe(C_4H_{13}N_3)_2]$-$Fe_2Sb_4S_{10}$. Estimated standard deviations are given in parentheses.

Sb(1)−S(1)	2.447(1)	Sb(1)−S(2)	2.455(1)
Sb(1)−S(3)	2.500(1)	Sb(2)−S(1)[b)]	2.489(1)
Sb(2)−S(3)	2.457(1)	Sb(2)−S(4)	2.430(1)
Fe(1)−Fe(1)[a)]	2.734(1)	Fe(1)−S(2)	2.298(1)
Fe(1)−S(4)	2.276(1)	Fe(1)−S(5)	2.223(1)
Fe(1)−S(5)[a)]	2.216(1)	Fe(2)−N(1)	2.283(4)
Fe(2)−N(2)	2.234(3)	Fe(2)−N(3)	2.239(4)
S(1)−Sb(1)−S(2)	87.43(3)	S(1)−Sb(1)−S(3)	94.64(3)
S(2)−Sb(1)−S(3)	95.72(4)	S(3)−Sb(2)−S(1)[b)]	96.60(3)
S(4)−Sb(2)−S(1)[b)]	92.39(3)	S(4)−Sb(2)−S(3)	102.30(3)
S(2)[a)]−Fe(1)−Fe(1)[a)]	123.93(4)	S(4)−Fe(1)−Fe(1)[a)]	120.43(4)
S(4)−Fe(1)−S(2)[a)]	115.62(4)	S(5)−Fe(1)−Fe(1)[a)]	51.87(3)
S(5)−Fe(1)−S(2)[a)]	109.31(4)	S(5)−Fe(1)−S(4)	107.86(4)
S(5)[a)]−Fe(1)−Fe(1)[a)]	52.11(3)	S(5)[a)]−Fe(1)−S(2)[a)]	110.90(4)
S(5)[a)]−Fe(1)−S(4)	108.49(4)	S(5)[a)]−Fe(1)−S(5)	103.97(3)
Sb(1)−S(1)−Sb(2)[b)]	103.16(3)	Fe(1)[a)]−S(2)−Sb(1)	93.47(4)
Sb(2)−S(3)−Sb(1)	103.37(3)	Fe(1)−S(4)−Sb(2)	96.48(4)
Fe(1)[a)]−S(5)−Fe(1)	76.03(3)	N(2)−Fe(2)−N(1)	75.7(1)
N(2)−Fe(2)−N(1)[c)]	104.3(1)	N(2)−Fe(2)−N(3)	78.0(1)
N(2)[c)]−Fe(2)−N(3)	102.0(1)	N(3)−Fe(2)−N(1)	94.4(1)
N(3)[c)]−Fe(2)−N(1)	85.6(1)		

Symmetry code: [a)] 2−x, 1−y, 2−z ;[b)] 1−x, 2−y, 2−z; [c)] 2−y, 1−z;

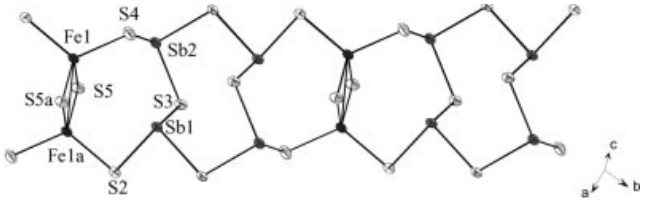

Fig. 4 The anionic chain $^1_\infty[Fe_2Sb_4S_{10}]^{2-}$ containing $[Sb_4S_4]$ and $[Fe_2S_6]$ units. Atoms labelled are generated by symmetry. The displacement ellipsoids are drawn at the 50 %-probability level.

Table 5 Additional long Sb−S bonds/Å for $[Fe(C_4H_{13}N_3)_2]Fe_2Sb_4S_{10}$.

Sb1−S1[a)]	3.331(1)
Sb1−S3[b)]	3.333(1)
Sb1−S4	3.571(1)
Sb1−S5[a)]	3.677(2)
Sb2−S2[c)]	3.757(1)
Sb2−S5[d)]	3.410(2)
Sb2−S5	3.288(2)

Symmetry code: [a)] 2−x, 2−y, 2−z; [b)] 1−x, 2−y, 2−z; [c)] −1+x, y, z; [d)] 1−x, 1−y, 2−z;

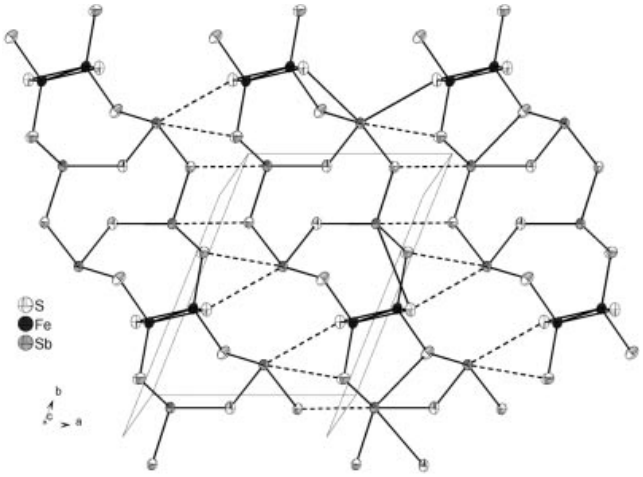

Fig. 5 Layers within the (001) plane formed by the long Sb−S bonds (dotted lines) between neighboured $^1_\infty[Fe_2Sb_4S_{10}]^{2-}$ chains. The displacement ellipsoids are drawn at the 50 %-probability level.

hedral coordination in (**2**) is slightly more distorted. The Fe−Fe distance of 2.734(1) Å is identical with that of (**1**) and reported ones in the literature [23−24]. All geometrical parameters are comparable with those found in proteins [15−19, 32] or in ternary iron sulfides ($A_3Fe_2S_4$ (A = K, Rb, Cs) [20−24]). All Sb atoms have additional S neighbours at longer distances between 3.288(2) and 3.757(1) Å (Tab. 5). The coordination sphere of Sb(1) is completed by four additional S atoms yielding a sevenfold environment. Taking the three long Sb−S separations into account Sb(2) resides in a distorted octahedral environment. Three of the long Sb−S contacts (Sb(1)−S(1a), Sb(2)−S(2), Sb(2)−S(5a)) connect the chains into layers within the (001) plane (Fig. 5). The anionic layers and the isolated $[Fe(dien)_2]^{2+}$ cations are stacked in a sandwich-like manner perpendicular to [001]. The interlayer separation amounts to 8 Å. Between the H atoms bound to the N atoms and the S atoms of the thioantimonate(III) anion ten N−H···S contacts are found which are short enough to be considered as hydrogen bonds. The H···S distances vary between 2.640 and 3.015 Å with corresponding angles N−H···S ranging from 113.21 to 172.38° (Table 6). It is well known that H···S bonds are weak but the large numbers observed here may also contribute to the stability of the compound.

Table 6 Selected H···S distances /Å and angles /° for $[Fe(C_4H_{13}N_3)_2]Fe_2Sb_4S_{10}$.

D−H	A	D−H	H···A	D−H···A	D···A
N(3)−H(3B)	S(1)[a)]	0.900	2.845	147.33	3.635
N(1)−H(1B)	S(2)[b)]	0.900	2.876	172.38	3.770
N(1)−H(1A)	S(3)[a)]	0.900	2.732	113.21	3.195
N(2)−H(2)	S(3)	0.900	2.640	135.38	3.349
N(2)−H(2)	S(5)	0.910	3.015	124.51	3.610

Symmetry code: [a)] 1−x, 2−y, 1−z; [b)] 2−x, 2−y, 1−z;

Thermal Investigations

The thermal stability was investigated using simultaneous difference thermal analysis and thermogravimetry experiments. Heating single crystals of (**1**) under argon a mass loss of 31.3 % is observed at T_{onset} = 278 °C which is accompanied by one endothermic event at T_{Peak} = 311.2 °C (Fig. 6). For the removal of the tren ligands a mass change $-\Delta m_{theo(tren)} = -28.75$ % is expected. For (**2**) the decomposition proceeds also in one step with a mass loss of 19.4 % at T_{onset} = 285 °C (T_{Peak} = 302.5 °C). For the emission of the dien ligands the mass loss would be $-\Delta m_{theo(dien)}$ = 17.46 %. The discrepancies between experimental and theoretical mass changes are caused by the emission of H_2S which was observed in mass spectra. In the X-ray powder pattern of both decomposition products Sb, Sb_2S_3 (*stibnite*) and $Fe_{1-x}S$ (syn. *pyrrothite*) are found. In addition, weak reflections of $FeSb_2S_4$ (syn. *berthierite*) are observed in the product of (**1**). The formation of elemental Sb is an indication for complex decomposition reactions involving redox reactions between the different species. Chemical analysis of the residues yields for (**1**) C = 0.97 % and N = 0.36 %; and for (**2**) C =5.1 %and N = 2.1 %. In the IR spectra no vibrations of the organic ligand could be observed.

Magnetic Properties and Mössbauer Spectroscopy

Formal valence considerations suggest that all Sb atoms are trivalent and that charge neutrality requires the occurrence of Fe^{II} and Fe^{III}. Both compounds show paramagnetic behaviour in the temperature range between 6 and 300 K for (**1**) and from 4 to 300 K for (**2**) (Fig. 7). The susceptibility of (**1**) passes a maximum at about 5.6 K. The shape of the curve indicates that the deviation from paramagnetic behaviour is rather due to a zero-field splitting effect than due to antiferromagnetic exchange interactions. It can be assumed that the Fe^{3+} ions in the $[Fe_2S_6]$ units are in an antiferromagnetic ground state [35] and hence they are magnetically silent. The susceptibility curves were fitted with a Curie-Weiss law yielding μ_{exp} = 5.37 μ_B for (**1**) and 5.41 μ_B for (**2**) which are typical for Fe^{2+} ions in the $3d^6$ high-spin configuration (5.1−5.7 μ_b). The value for the Weiss constant θ for (**1**) of −16.0(4) K suggests weak antiferromagnetic interactions. For (**2**) θ amounts to −2.74(6) K.

Clear evidences for the presence of Fe^{II} and Fe^{III} in compound (**1**) are seen in the Mössbauer spectrum (Fig. 8). For

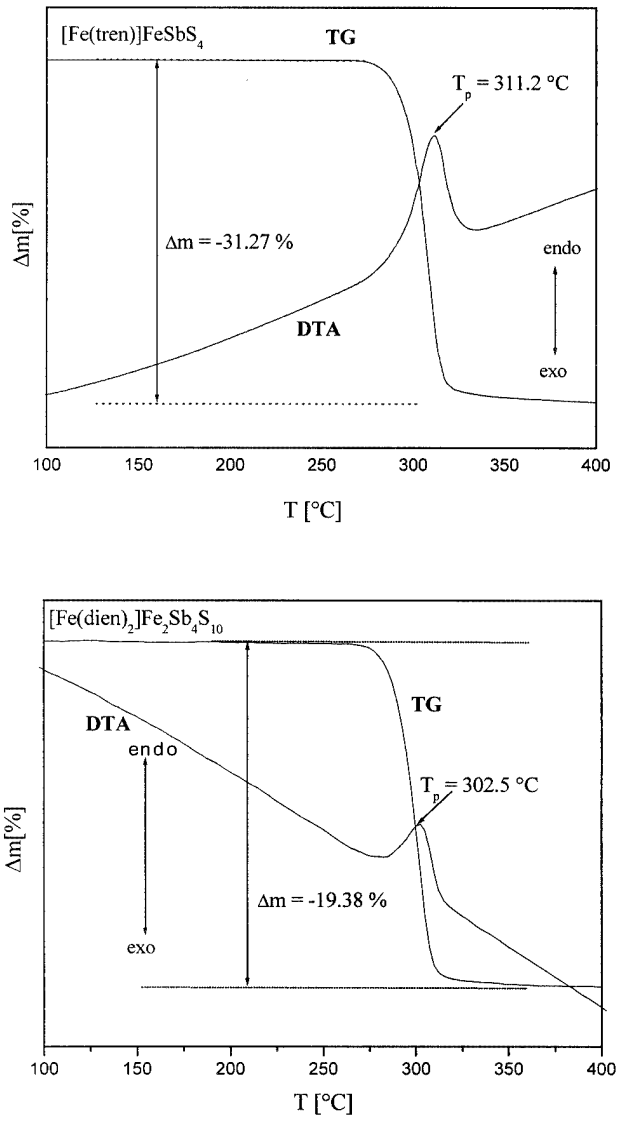

Fig. 6 DTA-TG curves for $Fe(C_6H_{18}N_4)]FeSbS_4$ (*top*) and $[Fe(C_4H_{13}N_3)_2]Fe_2Sb_4S_{10}$ (*bottom*). T_p is the peak temperature and Δm the mass change.

each Fe species a doublet with nearly the same intensity is observed. The doublet with an isomer shift of $\delta = 0.29(1)$ and a quadrupole splitting of 0.44(1) $mm \cdot s^{-1}$ can be assigned to the Fe^{3+} ions in the $[Fe_2S_6]$ unit. The hyperfine field data are typical for Fe^{3+} ions with S = 5/2 and they agree well with the data reported for Fe^{3+} in the protein clusters [36]. The second doublet with an isomer shift of $\delta = 0.95(1)$ and a quadrupole splitting of 2.90(4) mms^{-1} shows the typical data for Fe^{2+} in the high-spin d^6 configuration.

Experimental

Synthesis of [Fe(C6H18N4)]FeSbS4 (1)

Black crystals of $[Fe(C_6H_{18}N_4)]FeSbS_4$ were synthesized applying Sb (0.1217 g; 1 mmol), S (0.0962 g; 3 mmol) and $FeCl_3$ (0.1622 g; 1 mmol) in a solution of 8 ml 50 % tris(2-aminoethyl)amine (= tren) solved in water. The mixture was heated to 170 °C for 5 days in a teflon-lined steel autoclave (volume ≈20 ml) and was

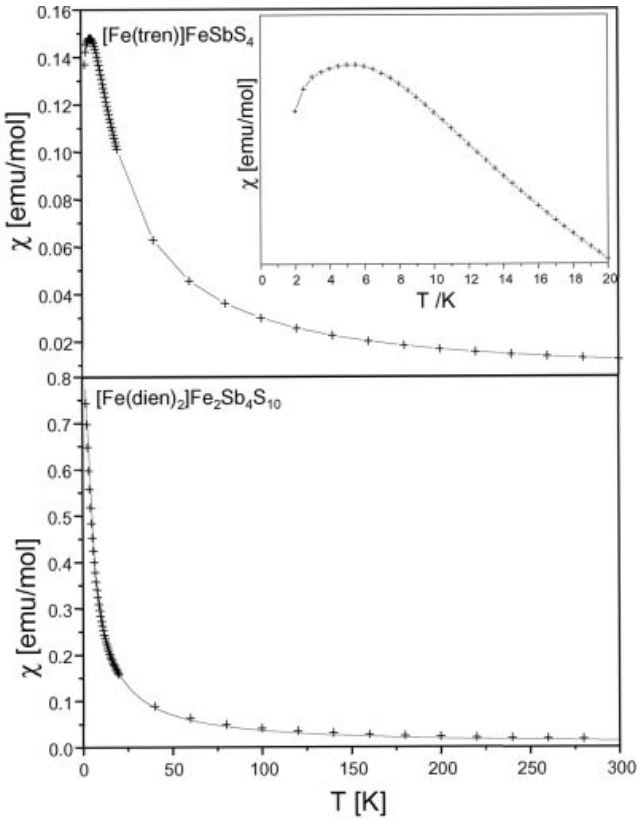

Fig. 7 The magnetic susceptibiliy curves for $[Fe(C_6H_{18}N_4)]FeSbS_4$ together with an enlarged view of the low temperature region (*top*) and $[Fe(C_4H_{13}N_3)_2]Fe_2Sb_4S_{10}$ (*bottom*). Note: the lines joining the experimental data are only guides to the eyes.

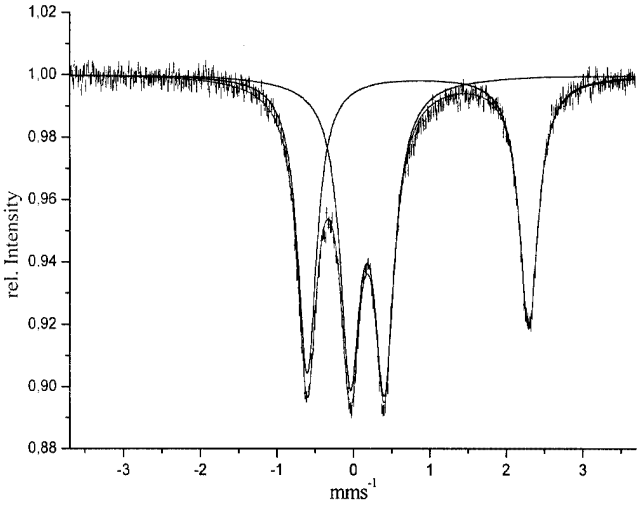

Fig. 8 Mössbauer spectrum of $Fe(C_6H_{18}N_4)]FeSbS_4$. The continuous line is the fitted spectrum.

subsequently cooled to room temperature within 3 h. The crystalline black product was filtered off, washed with water and acetone, cleaned in an ultrasonic bath and stored under vacuum. The compound is stable in air, in water and in acetone. The yield based on Fe is about 40 %.

*Synthesis of $[Fe(C_4H_{13}N_3)_2]Fe_2Sb_4S_{10}$ (**2**)*

Black crystals of $[Fe(C_4H_{13}N_3)_2]Fe_2Sb_4S_{10}$ were synthesized from Sb (0.1217 g; 1 mmol), S (0.0962 g; 3 mmol) and $FeCl_3$ (0.1622 g 1 mmol) in a solution of 8 ml 50 % diethylendiamine solved in water. The mixture was heated to 170 °C for 5 days in a teflon-lined steel autoclave (volume ≈20 ml) and was subsequently cooled to room temperature within 3 h. The crystalline black product was filtered off, washed with water and acetone, cleaned in an ultrasonic bath and stored under vacuum. The compound is stable in air, in water and in acetone. The yield based on Fe is about 65 %.

Structure Determination

X-ray intensities were collected on a STOE Imaging Plate Diffraction System (IPDS) using monochromatized Mo-K_α radiation (λ = 0.71073 Å). The intensities were corrected for Lorentz, polarization and absorption effects. Structure solution was performed using SHELXS-97 [37]. Refinement was done against F^2 using SHELXL-97 [38]. The Sb, Fe, S, C, and N atoms were refined with anisotropic displacement parameters. The hydrogen atoms were positioned with idealized arrangement and refined with fixed isotropic displacement parameters using a riding model. The atom C1 in compound **1** is disordered and the occupation factors were refined to 60:40 for C1a and C1b. Technical details of data acquisition and refinement results are summarized in Table 7. Atomic coordinates and equivalent isotropic displacement parameters are given in Tables 8 and 9.

Crystallographic data (excluding structure factors) for the structure reported in this paper have been deposited with the Cambridge Crystallographic Data Centre as supplementary publication no. CCDC 199577 (**1**) and CCDC 199576 (**2**). Copies of the data can be obtained free of charge on application to CCDC, 12 Union Road, Cambridge CB2 1EZ, UK (fax: +44-(0)1223-336-033 or e-mail: deposit@ccdc.cam.ac.uk).

Table 7 Technical details of data acquisition and selected refinement results for $[Fe(C_6H_{18}N_4)]FeSbS_4$ and $[Fe(C_4H_{13}N_3)_2]Fe_2Sb_4S_{10}$. Estimated standard deviations are given in parentheses.

formula	$[Fe(C_6H_{18}N_4)]FeSbS_4$	$[Fe(C_4H_{13}N_3)_2]Fe_2Sb_4S_{10}$
colour, -habit	black, rhombic	black, rhombic
molecular weight	507.93 g/mol	1181.5 g/mol
crystal system	triclinic	triclinic
space group	$P\bar{1}$	$P\bar{1}$
calculated density	2.151 g/cm^3	2.719 g/cm^3
a / Å	8.3370(8)	7.7104(2)
b / Å	9.6277(9)	9.8631(4)
c / Å	10.714(1)	10.5241(3)
α / °	107.35(1)	76.182(2)
β / °	99.15(1)	83.644(2)
γ / °	100.944(3)	68.229(2)
V / A^3	784.3(1)	721.53(3)
Z	2	1
temperature / K	293	293
scan range	$5° \le 2\theta \le 55.9°$	$3° \le 2\theta \le 60°$
	$-10 \le h \le 10$	$0 \le h \le 10$
	$-12 \le k \le 12$	$-12 \le h \le 13$
	$-14 \le l \le 14$	$-14 \le h \le 14$
measured reflections	7533	4508
independent reflections	3464	4213
reflections with Fo > 4σ(Fo)	3017	3734
μ / mm^{-1}	4.05	5.89
$R_{int.}$	0.0501	0.0760
absorption correction	numerical	numerical
min./max. trans.	0.4881, 0.6155	0.2728, 0.5506
weight[a)]	y = 0.0631, z = 0	y = 0.0381, z = 0.9856
R1 for F_o>4σ(F_o)	0.0364	0.0255
R1 for all reflections	0.0421	0.0324
wR2 for F_o>4σ(F_o)	0.0907	0.0676
wR2 all reflections	0.0938	0.0699
Δρ[e/Å^3]	−1.54/1.39	−1.39/2.00
Goodness of fit	1.040	1.093

[a)] $w = 1/[\sigma^2(F_o^2) + (y \cdot P)^2 + z \cdot P]$; $P = (\mathrm{Max}(F_o^2,0) + 2 \cdot F_c^2) / 3$

Table 8 Atomic coordinates (· 10^4) and isotropic displacement parameters / Å^2 · 10^3 for $[Fe(C_6H_{18}N_4)]FeSbS_4$. Estimated standard deviations are given in parentheses.

	x	y	z	U_{eq}
Sb(1)	3852(1)	3953(1)	2894(1)	23(1)
Fe(1)	2567(1)	6660(1)	1410(1)	31(1)
Fe(2)	1704(1)	5362(1)	5381(1)	25(1)
S(1)	2532(1)	4036(1)	756(1)	28(1)
S(2)	3580(1)	6349(1)	4320(1)	28(1)
S(3)	6727(1)	4891(2)	2778(1)	37(1)
S(4)	−4(1)	3177(1)	4047(1)	34(1)
N(1)	5239(4)	7511(4)	1792(4)	38(1)
N(2)	453(4)	6857(4)	2306(4)	38(1)
N(3)	1666(5)	7040(4)	−409(3)	36(1)
N(4)	2859(5)	9218(4)	2159(4)	38(1)
C(1A)	5674(1)	9066(11)	2880(9)	40(2)
C(1B)	5820(2)	9053(19)	2220(20)	64(5)
C(2)	4649(7)	9969(6)	2609(8)	75(2)
C(3)	329(7)	8398(6)	2918(6)	55(1)
C(4)	1974(7)	9492(6)	3263(5)	52(1)
C(5)	2179(8)	8630(6)	−291(5)	54(1)
C(6)	2016(9)	9612(6)	1047(6)	63(2)

The equivalent isotropic displacement parameter U_{eq} is defined as one third of the trace of the orthogonalised U_{ij} tensor

Table 9 Atomic coordinates (· 10^4) and isotropic displacement parameters U_{eq} / Å^2 · 10^3 for $[Fe(C_4H_{13}N_3)_2]Fe_2Sb_4S_{10}$. Estimated standard deviations are given in parentheses.

	x	y	z	U_{eq}
Sb(1)	8254(1)	8848(1)	9757(1)	18(1)
Sb(2)	4498(1)	7009(1)	10135(1)	19(1)
Fe(1)	9008(1)	4522(1)	11055(1)	19(1)
Fe(2)	5000	10000	5000	26(1)
S(1)	8104(1)	11374(1)	8665(1)	21(1)
S(2)	10438(1)	7950(1)	8000(1)	25(1)
S(3)	5392(1)	9028(1)	8717(1)	20(1)
S(4)	6589(1)	6200(1)	11954(1)	25(1)
S(5)	8452(1)	4931(1)	8942(1)	23(1)
N(1)	7454(5)	9152(5)	3611(3)	38(1)
N(2)	6526(4)	7640(3)	6004(3)	24(1)
N(3)	3345(6)	8791(5)	4449(4)	46(1)
C(1)	8962(5)	7962(5)	4393(4)	39(1)
C(1)	8962(5)	7962(5)	4393(4)	39(1)
C(2)	8178(5)	6868(5)	5254(4)	34(1)
C(3)	5141(6)	6893(5)	6281(4)	32(1)
C(4)	4061(6)	7184(5)	5068(4)	36(1)

The equivalent isotropic displacement parameter Ueq is defined as one third of the trace of the orthogonalised Uij tensor

X-ray Powder Diffractometry

The X-ray powder patterns were recorded on a STOE Stadi-P diffractometer (Co-$K_{\alpha 1}$ radiation, λ = 1.78897 Å) in transmission geometry.

Thermoanalytical Measurements

Thermoanalytical measurements were performed using a DTA/TG device STA 409 from Netzsch under argon atmosphere (flow rate 75 ml·min^{-1}) with Al_2O_3 crucibles and heating rates of 4 K min^{-1}.

Magnetic Measurements

Magnetic susceptibilities were measured on a MPMS SQUID device (Quantum Design) in the temperature range from 4 to 300 K with an external field of 10 kOe. 6.965 mg of (**1**) and 6.914 mg of (**2**) were used.

Mössbauer Spectroscopy

Mössbauer spectra were obtained in transmission geometry using a 25-mCi ^{57m}Co source in a Rh matrix. The samples were investigated using polyacryl containers of 2 cm^2 area; 50 mg of the samples was used. The spectra were recorded at 78 K. The source was kept at room temperature. The hyperfine field parameters were obtained by fitting the raw data with Lorentz-shaped lines using the program "Environment for Fitting" (EFFI) by Dr. H. Spiering (Johannes Gutenberg Universität, Mainz). The hyperfine field data are referenced against α-Fe.

Acknowledgement. Financial support by the Deutsche Forschungsgemeinschaft, the Fonds der Chemischen Industrie, and the State of Schleswig-Holstein is gratefully acknowledged. Many thanks are due to Ralph Warratz for the Mössbauer spectroscopy measurements.

References

[1] a) W. S. Sheldrick, H.-J. Häusler, *Z. Anorg. Allg. Chem.* **1988**, *561*, 149; b) X. Wang, *Eur. J. Solid State Inorg. Chem.* **1995**, *32*, 303; c) W. Bensch, M. Schur, *Eur. J. Solid State Inorg. Chem.* **1997**, *34*, 457; d) R. Stähler, W. Bensch, *J. Chem. Soc. Dalton Trans.* **2001**, 2001, 2518.
[2] a) W. S. Sheldrick, *Z. Anorg. Allg. Chem.* **1988**, *562*, 23; b) T. Jiang, G. A. Ozin, R. L. Bedard, *Adv. Mater.* **1995**, *7*, 166; c) Y. Ko, K. Tan, D. M. Nellis, S. Koch, J. B. Parise, *J. Solid State Chem*. **1995**, *114*, 506.
[3] a) B. Krebs, S. Pohl, *Z. Naturforsch*. **1971**, *26 b*, 853; b) M. Fröba, N. Oberender, *J. Chem. Soc., Chem. Commun.* **1997**, 1997, 1729; c) D. M. Nellis, Y. Ko, K. Tan, S. Koch, J. B. Parise, *J. Chem. Soc., Chem. Commun.* **1995**, 1995, 541.
[4] R. Stähler, W. Bensch, *Eur. J. Inorg. Chem.* **2001**, 2001, 3073.
[5] G. Dittmar, H. Schäfer, *Z. Anorg. Allg. Chem.* **1977**, *437*,183.
[6] W. S. Sheldrick, H.-J. Häusler, *Z. Anorg. Allg. Chem.* **1988**, *557*, 105.
[7] A. V. Powell, S. Boissiere, A. M. Chippindale, *Chem. Mater.* **2000**, *12*, 182.
[8] W. Bensch, M. Schur, *Eur. J. Solid State Inorg. Chem.* **1996**, *33*, 1149.
[9] M. Schur, C. Näther, W. Bensch, *Z. Naturforsch.* **2001**, *56 b*, 79.
[10] R. Stähler, W. Bensch, *J. Chem. Soc., Dalton. Trans.* **2001**, 2001, 2518.
[11] A. V. Powell, R. Paniagua, P. Vaquerio, A. M. Chippindale, *Chem. Mater.* **2002**, *12*, 1220.
[12] R. Demuth, F. Kober, *Grundlagen der Komplexchemie*, 1992, p.145.
[13] C. S. Hong, J. Kim, N. H. Hur, Y. Do, *Inorg. Chem.* **1996**, *35*, 5110.
[14] T. C. W. Mak, *J. Chem. Soc., Chem. Commun.* **1997**, 1997, 2407.
[15] T. Tsukihara, K. Fukuyama, Y. Katsube, *J. Biol. Chem.* **1981**, *90*, 1763.
[16] C. E. Johnson, E. Elstner, G. F. Gibson, G. Benfield, M. W. C. Evans, *Nature* **1968**, *220*, 1291.
[17] J. A. Fee, K. L. Findling, T. Yoshida, R. Hille, *J. Biol. Chem.* **1984**, *259*, 124.
[18] K. Fukuyama, T. Hase, S. Matsumuto, T. Tsukihara, *Nature* **1986** , *286*, 522.
[19] W. R. Dunham, A. J. Bearden, I. Salmeen, G. Palmer, *Biochim. Acta* **1971**, *253*, 134.
[20] W. Bronger, U. Ruschewitz, *J. Alloys Compds.* **1993**, *197*, 83.
[21] W. Bronger, H. Balk-Hardtdegen, U. Ruschewitz, *Z. Anorg. Allg. Chem.* **1992**, *616*, 14.
[22] W. Bronger, P. Müller, *J. Less-Common Met.* **1984**, *100*, 241.
[23] W. Bronger, *Z. Anorg. Allg. Chem.* **1968**, *359*, 224.
[24] W. Bronger, U. Ruschewitz, P. Müller, *J. Alloys Compds.* **1995**, *218*, 22.
[25] R. Stähler, C. Näther, W. Bensch, *Acta Crystallogr.* **2001**, *C 57*, 26.
[26] M. Schur, W. Bensch, *Acta Crystallogr.* **2000**, *C 56*, 1107.
[27] M. Schur, H. Rijnberk, C. Näther, W. Bensch, *Polyhedron* **1998**, *18*, 101.
[28] R. Stähler, C. Näther, W. Bensch, *Eur. J. Inorg. Chem.* **2001**, 2001, 1835.
[29] W. Bensch, C. Näther, R. Stähler, *J. Chem. Soc., Chem. Commun.* **2001**, 2001, 477.
[30] A. V. Powell, S. Boissiere, A. M. Chippindale, *Chem. Mater.* **2000**, *12*, 182**.**
[31] J. B. Parise, Y. Ko, *Chem. Mater.* **1992**, *4*, 1446.
[32] S. Ciurli, R. H. Holm, *Inorg. Chem.* **1991**, *30*, 743.
[33] A. Zalkin, D. H. Tempelton, T. Ueki, *Inorg. Chem.* **1973**, *12*, 1641.
[34] A. H. Robbins, C. D. Scout, *Proteins* **1989**, *5*, 289.
[35] K. W. H. Stevens in: R. D. Willet, D. Gatteschi, O. Kahn, *Magnetostructral correlations in exchange-coupled systems*, Reidel-Verlag Dordrecht **1985**, p. 105.
[36] a) P. J. Geary, D. P. E. Dickson, *J. Biochem. 1981*, *185*, 199; b) I. Bertini, S. Ciurli, C. Luchinat in: *Structure and Bonding*, Vol. *83*, Springer-Verlag, Berlin, Heidelberg, New York **1995**, p. 1.
[37] G. M. Sheldrick, *SHELXS-97*, Program for the solution of crystal structures, Universität Göttingen, **1997**.
[38] G. M. Sheldrick, *SHELXL-97*, Program for the refinement of crystal structures, Universität Göttingen, **1997**.

4.2.2 Die Verbindung [Fe($C_6H_{18}N_4$)][Sb_4S_7]

Zusammenfassung der Veröffentlichung „*Four New Thioantimonates(III) with the General Formula [TM(tren)]Sb_4S_7 (TM = Mn, Fe, Co, Zn) with the Transition Metal as Part of a Thioantimonate(III) Network Synthesized under Solvothermal Conditions and Tuning of the Optical Band Gap by the Transition Metal Cation*“.

Von den vier vorgestellten isostrukturellen Verbindungen werden im folgenden nur die Synthese, Struktur und Charakterisierung von ([Fe(tren)][Sb_4S_7]) diskutiert. Eine Beschreibung der anderen Verbindung findet sich in den Doktorarbeiten von Ralph Stähler [7] und Michael Schaefer [9].

Zur Darstellung von [Fe(tren)][Sb_4S_7] wurden $FeCl_3$ (1 mmol), Sb (1 mmol) und S (3 mmol) in einem Gemisch aus 2 ml Wasser und 2 ml tren für 7 Tage bei 170 °C unter solvothermalen Bedingungen erhitzt. Das Reaktionsprodukt fiel in Form von roten Kristallen mit einer Ausbeute von 70 % basierend auf Sb an. Als Beiprodukt konnte [Fe(tren)][$FeSbS_4$] identifiziert werden.

[Fe(tren)][Sb_4S_7] kristallisiert in der monoklinen Raumgruppe $P2_1/n$ mit vier Formeleinheiten in der Elementarzelle. Das $[Sb_4S_7]^{2-}$-Anion ist aus drei trigonalen SbS_3- und einer SbS_4-Einheit aufgebaut. Diese primären Baueinheiten sind über Ecken und Kanten unter Bildung von Sb_3S_4-Halbwürfeln verknüpft. SbS_3-Pyramiden und Sb_3S_4-Halbwürfel sind alternierend verbunden und bilden so das kettenförmige $[Sb_4S_7]^{2-}$-Anion, welches parallel zu [100] verläuft (Abb. 4.5, links). Lange Sb-S-Bindungen zwischen den Ketten führen zur Bildung von Schichten. Zwischen diesen Schichten befinden sich die $[Fe(tren)]^{2+}$-Kationen. Das Fe-Atom ist in einer trigonal-bipyramidalen Umgebung aus vier Stickstoffatomen und einem Schwefelatom des Sb-S-Netzwerkes.

Die thermische Zersetzung von [Fe(tren)][Sb_4S_7] beginnt bei T = 295 °C und erfolgt in einer Stufe, welche von einem endothermen Ereignis in der DTA-Kurve begleitet ist. Der beobachtete Gesamtmassenverlust stimmt gut mit dem theoretischen Verlust des tren-Liganden überein. Als Abbauprodukte konnten im Pulverdiffraktogramm FeS, Sb_2S_3 und $FeSb_2S_4$ identifiziert werden.

Im Ramanspektrum von [Fe(tren)][Sb_4S_7] war eine Zuordnung der Moden zu den einzelnen SbS_x-Gruppen möglich. Die Bindungslängen zwischen ÜM und dem Stick-

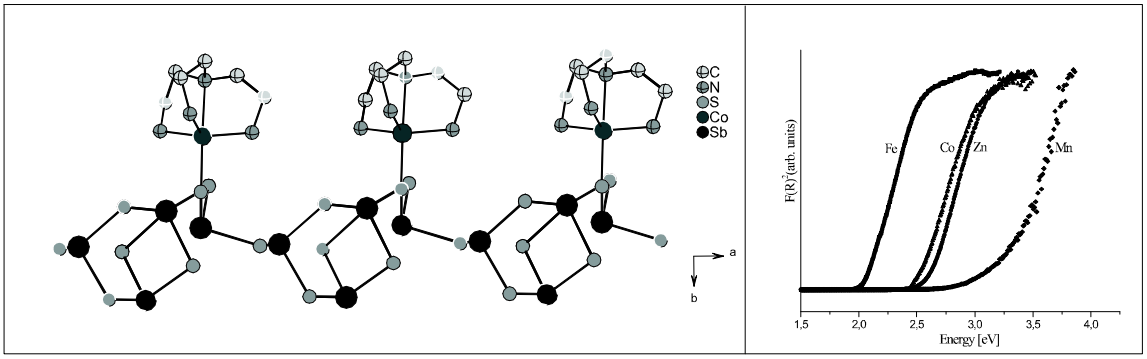

Abbildung 4.5: Kettenstruktur von [Üm(tren)][Sb_4S_7] (links), Abhängigkeit der optischen Bandlücke vom Übergangsmetall (rechts)

stoffatom des tren-liganden variieren mit dem entsprechenden ÜM, die Sb-S-Abstände sind in allen Verbindungen nahezu konstant. Folglich unterscheiden sich die Ramanspektren der vier Verbindungen nur in den Banden, die ÜM-N-Schwingungen zugeordnet werden.

Die optische Bandlücke, welche stark von dem verwendeten Übergangsmetall abhängt, konnte für [Fe(tren)][Sb_4S_7] mit UV/Vis-Spektren zu 2.04 eV bestimmt werden, d.h. das Material gehört zur Gruppe der optischen Halbleiter. Hervorzuheben ist, dass die optische Bandlücke der isostrukturellen Verbindungen stark von dem ÜM abhängt und von 3.11 eV für Mn bis 2.04 eV für Fe reicht. Das bedeutet, dass bei einer gezielten Substitution vom Mn durch z.B. Co oder Fe in Abhängigkeit von Mn/Co- bzw. Mn/Fe-Verhältnis die optische Bandlücke nahezu stufenlos über einen Bereich von ca. 1 eV eingestellt werden kann (Abb. 4.5, rechts).

Four New Thioantimonates(III) with the General Formula [*TM*(tren)]Sb_4S_7 (*TM* = Mn, Fe, Co, Zn) with the Transition Metal as Part of a Thioantimonate(III) Network Synthesized under Solvothermal Conditions and Tuning of the Optical Band Gap by the Transition Metal Cation

Michael Schaefer, Ralph Stähler, Wolff-Ragnar Kiebach, Christian Näther, and Wolfgang Bensch*

Kiel, Institut für Anorganische Chemie der Christian-Albrechts Universität

Received April 26th, 2004.

Dedicated to Professor Michael Veith on the Occasion of his 60th Birthday

Abstract. Four new thioantimonate(III) compounds with the general formula [*TM*(tren)]Sb_4S_7, *TM* = Mn **1**, Fe **2**, Co **3** and Zn **4**, were synthesized under solvothermal conditions by reacting elemental *TM*, Sb and S in an aqueous solution of *tren* (*tren* = tris(2-aminoethyl)amine). All compounds crystallize in the monoclinic space group $P2_1/n$ with four formula units in the unit cell. Single crystal X-ray analyses of **1** [a = 8.008(2), b = 10.626(2), c = 25.991(5) Å, β = 90.71(3)°, V = 2211.4(8) Å^3], **2** [a = 8.0030(2), b = 10.5619(2), c = 25.955(5) Å, β = 90.809(3)°, V = 2193.69(8) Å^3], **3** [a = 7.962(2), b = 10.541(2), c = 25.897(5) Å, β = 90.90(3)°, V = 2173.0(8) Å^3] and **4** [a = 7.978(2), b = 10.625(2), c = 25.901(5) Å, β = 90.75(3)°, V = 2195.2(8) Å^3] reveal that the compounds are isostructural. The $[Sb_4S_7]^{2-}$ anions are composed of three SbS_3 trigonal pyramids and one SbS_4 unit as primary building units (PBU). The PBUs share common edges and corners to form semicubes (Sb_3S_4) which may be regarded as secondary building units (SBU). The SBUs and SbS_3 pyramids are joined in an alternating fashion yielding the $^1_\infty[Sb_4S_7^{2-}]$ anionic chain which is directed along [100]. Weaker Sb-S bonding interactions between neighbored chains lead to the formation of layers within the (001) plane which contain pockets that are occupied by the cations. The TM^{2+} ions are in a trigonal bipyramidal environment of four N atoms of the *tren* ligand and one S atom of the thioantimonate(III) anion. The optical band gaps depend on the TM^{2+} ion and amount to 3.11 eV for **1,** 2.04 eV for **2**, 2.45 eV for **3**, and 2.60 eV for **4**.

Keywords: Thioantimonate; Solvothermal synthesis; Thermal stability; Raman spectroscopy; UV/Vis spectroscopy

Vier neue Thioantimonate(III) der allgemeinen Formel [*TM*(tren)]Sb_4S_7 (*TM* = Mn, Fe, Co, Zn) mit dem Übergangsmetall als Teil des Thioantimonatnetzwerks dargestellt unter solvothermalen Bedingungen und mit durch das Übergangsmetallkation einstellbarer optischer Bandlücke

Inhaltsübersicht. Die vier neuen Thioantimonate(III) der allgemeinen Zusammensetzung [*TM*(tren)]Sb_4S_7, *TM* = Mn **1**, Fe **2**, Co **3** und Zn **4**, wurden unter solvothermalen Bedingungen durch die Reaktion von elementarem *TM*, Sb und S in einer wässrigen *tren*-Lösung (*tren* = Tris(2-Aminoethyl)amin) synthetisiert. Alle Verbindungen kristallisieren in der monoklinen Raumgruppe $P2_1/n$ mit vier Formeleinheiten in der Elementarzelle. Die Einkristallstrukturanalysen von **1** [a = 8.008(2), b = 10.626(2), c = 25.991(5) Å, β = 90.71(3)°, V = 2211.4(8) Å^3], **2** [a = 8.0030(2), b = 10.5619(2), c = 25.955(5) Å, β = 90.809(3)°, V = 2193.69(8) Å^3], **3** [a = 7.962(2), b = 10.541(2), c = 25.897(5) Å, β = 90.90(3)°, V = 2173.0(8) Å^3] und **4** [a = 7.978(2), b = 10.625(2), c = 25.901(5) Å, β = 90.75(3)°, V = 2195.2(8) Å^3] ergaben, dass diese isostrukturell sind. Die $[Sb_4S_7]^{2-}$-Anionen werden aus drei trigonalen SbS_3-Pyramiden und einer SbS_4-Einheit aufgebaut, welche die primären Baueinheiten (PBU) darstellen. Diese PBU's sind über Ecken und Kanten unter Bildung von Halbwürfeln (Sb_3S_4) verknüpft, wobei die Sb_3S_4-Gruppen als sekundäre Baueinheiten bezeichnet werden können. Die SBU's und die SbS_3-Pyramiden sind in alternierender Weise zu einer anionischen $^1_\infty[Sb_4S_7^{2-}]$-Kette verbunden, welche entlang [100] verläuft. Schwache Sb-S-Bindungen zwischen benachbarten Ketten führen zur Ausbildung von Schichten in der (001)-Ebene. Diese Schichten enthalten Taschen, welche von den Kationen besetzt sind. Die TM^{2+}-Ionen befinden sich in einer trigonal-bipyramidalen Umgebung aus vier N-Atomen des *tren*-Liganden und einem S-Atom des Thioantimonat(III)-Anions. Die optischen Bandlücken hängen von dem TM^{2+}-Ion ab und betragen 3.11 eV für **1,** 2.04 eV für **2**, 2.45 eV für **3** und 2.60 eV für **4**.

  DOI: 10.1002/zaac.200400124

Introduction

During the last decade the number of new thiometallate compounds synthesized under solvothermal conditions increased dramatically. Despite the successful application of the solvothermal route in the area of such non-oxidic compounds a directed preparation or a rational design is not possible, and many experiments are necessary to find the best conditions leading to the crystallization of a new compound. One way to acquire a deeper knowledge about the reactions is to conduct in-situ X-ray scattering and X-ray absorption experiments. We demonstrated that the in-situ technique is a powerful method for the investigation of the crystallization of thioantimonates(III) [1, 2]. These experiments deliver information about the crystallization kinetics and allow the detection of crystalline precursors and/or intermediates. But the important and product determining reactions in the heterogeneous systems cannot be probed with X-ray scattering techniques and more sophisticated techniques are necessary to identify the product determining species that are present in solution. A different and more empirical approach is the analysis of the structures, compositions and reaction conditions of known thioantimonate-(III) compounds [3−30].

Such an analysis yields information about the Sb:S ratio, the number and nature of primary and secondary Sb_xS_y building units, the binding modes of the S atoms and the dimensionality of the compounds. The result of such an analysis is then compared with the synthesis conditions hoping that there are some general trends and/or rules which can be extracted. But the number of thioantimonate-(III) compounds is still too low to formulate a general advice for a more directed synthesis. A larger group of compounds with the general formula ASb_4S_7 (A = alkali metal, transition metal complex or protonated amine) were obtained relatively often compared to other thioantimonate-s(III) [3−7, 11, 17−21]. The analysis of the structures reveals a general correlation between the dimensionality of the anion and the size of the cation. Only $K_2Sb_4S_7$ shows a three-dimensional $[Sb_4S_7]^{2-}$ anion [3] and with increasing size of the cation the dimensionality is reduced to two-dimensional layers [5, 7, 8, 11, 17, 18, 20] and finally to one-dimensional chains [4, 6, 14, 19, 21]. A serious problem with the assignment of the dimensionality is the fact that Sb-S distances show no clear cut-off in the large range between 2.2 and 3.9 Å. Therefore, the description of the structures of thioantimonates(III) and the final assignment of the dimensionality is a little bit arbitrary.

A different analysis of the structures uses the connectivity of the S atoms. In many thioantimonates(III) the S atoms simply connect two Sb atoms and such a mode may be denoted as $S^{[2]}$ (Note that for this analysis a cut-off of about 3 Å is used for the Sb-S distances). For instance, in $K_2Sb_4S_7$ [3], $Cs_2Sb_4S_7$ [6], $[Ni(dien)_2]Sb_4S_7{\cdot}H_2O$ [8], $(EA)_2Sb_4S_7$ [20], and $[Mn(dien)_2]Sb_4S_7$ [30] all S atoms act in a $S^{[2]}$ mode. In $K_2Sb_4S_7{\cdot}H_2O$ [7] and $Rb_2Sb_4S_7{\cdot}H_2O$ [5] besides the $S^{[2]}$ mode also $S^{[3]}$ atoms are observed. Interestingly, in $Rb_2Sb_4S_7$ [18] there is one $S^{[4]}$ atom and all others act as $S^{[2]}$. Finally, the structures of $Mn(en)_3Sb_4S_7$ [17], $Ni(en)_3Sb_4S_7$ [21], $(pipH_2)Sb_4S_7$ [19], $(NH_4)_2Sb_4S_7$ [4] and $SrSb_4S_7{\cdot}6H_2O$ [11] contain $S^{[2]}$ and $S^{[1]}$ atoms. The $S^{[1]}$ atoms are able to form a bond to a transition metal cation enhancing the structural chemistry. In several contributions we demonstrated that choosing tren (tren = tris(2-aminoethyl)amine; $C_6H_{18}N_4$) as the amine many transition metals are coordinated by the four N atoms of tren leaving one or two sites free for a bond to S atoms of the thioantimonate-(III) anion [22−25].

Here we report the solvothermal synthesis, crystal structures as well as the spectroscopic and the thermal properties of the four novel one-dimensional thioantimonate(III) compounds [*TM*(tren)]Sb_4S_7 with *TM* = Mn, Fe, Co and Zn.

Results and Discussion

The conditions of the syntheses of the title compounds require some comments, especially with respect to the different Sb : S ratios applied. Using the elements as starting materials they must be first transformed from the solid state to a soluble species. It is believed that the polysulfide species (S_x^{2-}) and/or thiosulfates which are immediately formed during the reaction of S within the very basic solutions dissolve and oxidize the metals. The dissolved species are not known and therefore it can only be speculated about the reactions. In the present examples the syntheses with *TM* = Mn, Co, and Zn were performed with different Sb : S ratios. It may be assumed that the key step, i.e. the dissolution of *TM*, requires different concentrations of S_x^{2-} and/or thiosulfates for the distinct metals. Furthermore, the heterogeneous reactions occurring under solvothermal syntheses are complex and only very little is known about the reaction mechanisms. Hence, no rational explanation is at hand why different Sb : S ratios are necessary for the formation of the title compounds.

The new compounds $^1_\infty$[*TM*(tren)]Sb_4S_7 (*TM* = Mn **1**, Fe **2**, Co **3**, Zn **4**) are isostructural crystallizing in the monoclinic space group $P2_1/n$ with four formula units in the unit cell (Table 1). In all compounds the unique atoms (one *TM*, four Sb, seven S, and all atoms of the tren ligand) are located in general positions. In the compounds the *TM* atom is in a distorted trigonal bipyramidal environment (TMN_4S_1) of four N atoms of the tren ligand and the S(1) atom of the thioantimonate(III) anion (see Fig. 1). The *TM*-N distances in **1** vary between 2.200(3) and 2.376(2) Å, in **2** from 2.129(4) to 2.308(4) Å, in **3** from 2.071(4) to 2.273(4) Å and in **4** they are between 2.074(4) and 2.348(4) Å (Table 2). These bond lengths are in the range

* Prof. Dr. W. Bensch
Institut für Anorganische Chemie der Universität Kiel
Olshausenstr. 40
D-24098 Kiel
Fax: +49 (0)431/880 −1520
e-Mail: wbensch@ac.uni-kiel.de

Table 1 Technical details of data acquisition and selected refinement results for [*TM*(tren)]Sb_4S_7, *TM* = Mn, Fe, Co, Zn

formula	[Mn(tren)]Sb_4S_7 (**1**)	[Fe(tren)]Sb_4S_7 (**2**)	[Co(tren)]Sb_4S_7 (**3**)	[Zn(tren)]Sb_4S_7 (**4**)
molecular weight	912.60	913.51	916.59	923.03
crystal system	monoclinic	monoclinic	monoclinic	monoclinic
space group	$P2_1/n$	$P2_1/n$	$P2_1/n$	$P2_1/n$
calculated density	2.741	2.766	2.802	2.793
a / Å	8.008(2)	8.0030(2)	7.962(2)	7.978(2)
b / Å	10.626(2)	10.5619(2)	10.541(2)	10.625(2)
c / Å	25.991(5)	25.955(5)	25.897(5)	25.901(5)
β / °	90.71(3)	90.809(3)	90.90(3)	90.75(3)
V / A^3	2211.4(8)	2193.69(8)	2173.0(8)	2195.4(8)
Z	4	4	4	4
temperature / K	293	293	293	293
scan range	3?2θ?60	5?2θ?56	4?2θ?56	3?2θ?60
	0≤h≤11	−10≤h≤10	−10≤h≤10	0≤h≤11
	−14≤k≤4	−13≤k≤13	−13≤k≤13	−14≤k≤1
	−36≤l≤36	−34≤l≤34	−34≤l≤34	−36≤l≤36
measured reflections	9517	21611	18105	7388
independent reflections	6436	5329	5259	6404
reflections with $F_o > 4\sigma(F_o)$	5464	4804	4821	4792
μ / mm^{-1}	6.04	6.17	6.33	6.6
$R_{int.}$	0.0141	0.0460	0.0326	0.0258
min./max. trans.	0.3774/0.4551	0.3463/0.4596	0.3379/0.4591	0.3074/0.4475
extinction coefficient [a]	none	0.0032(2)	0.0060(2)	none
weight[b]	y=0.0267, z=0.35	y=0.0672, z=3.2864	y=0.0556, z=4.4078	y=0.0296, z=2.8771
R1 for all $F_o > 4\sigma(F_o)$	0.0201	0.0364	0.0310	0.0277
R1 for all reflections	0.0302	0.0404	0.0341	0.0569
wR2 for all $F_o > 4\sigma(F_o)$	0.0482	0.0930	0.0823	0.0639
wR2 for all reflections	0.0503	0.0960	0.0845	0.0696
Δρ /e/$Å^3$	−0.96/0.63	−1.54/1.39	−1.01/1.18	−0.92/0.76
GOF	1.062	1.031	1.041	1.051

[a] $F^* = F_c\,(k[1 + 0.001 \cdot x \cdot F_C^2 \cdot \lambda^3 / \sin(2\theta)]^{-0.25})$.
[b] $w = 1/[\sigma^2(F_o^2) + (y \cdot P)^2 + z \cdot P]$; $P = (\mathrm{Max}\,(F_o^2,0) + 2 \cdot F_c^2) / 3$.

reported in the literature [8, 14−17, 21−24, 28]. The N-*TM*-N angles are indicative for a distorted coordination ((**1**): 76.08(9)−113.2(1)°; (**2**): 78.0(2)−128.5(2)°; (**3**): 78.6(2)−125.5(2)°; (**4**): 78.4(2)− 123.1(2)°). The *TM*-S(1) distances are between 2.355(1) Å (Co compound) and 2.4559(9) Å (Mn compound) (Table 2). As expected the long *TM*-N(1) bonds are in *trans* position to the *TM*-S(1) bonds. The S(1)-*TM*-N(1) angles slightly deviate from the ideal value of 180° and spread from 168.94(6)° (Mn compound) to 174.6(1)° (Zn compound) (Table 2). The variation of the bond lengths is in accordance with the evolution of the ionic radii going from Mn^{2+} to Zn^{2+} [31].

The Sb(1), Sb(3) and Sb(4) atoms have short bonds to three S atoms forming the common SbS_3 trigonal pyramids (Fig. 1). The Sb(2) atom is coordinated by four S atoms yielding a SbS_4 unit. The Sb(1)S_3 pyramid shares a common corner with the Sb(2)S_4 unit. The Sb(2)S_4 moiety is linked to the Sb(3)S_3 pyramid via a corner and has a common edge with the Sb(4)S_3 unit forming the Sb_4S_7 assembly. The binding mode leads to the formation of a Sb_2S_2 heterocyle and to a Sb_3S_4 semicube as secondary building units within the $^1_\infty[Sb_4S_7^{2-}]$ anion. Such semicubes are common and were also found in other thioantimonates(III) [3-5, 7, 11, 17, 20, 25, 27]. Along [100] semicubes and Sb(1)S_3 pyramids alternate and are linked by the S(2) and S(3) atoms into the one-dimensional anion (Fig. 2). In every chain the [*TM*(tren)]$^{2+}$ cations are oriented in the same direction. The [*TM*(tren)]$^{2+}$ cations have strong bonding interactions to the S(1) atoms with a high covalent character. It can be assumed that this strong interaction together with the shape and size of the [*TM*(tren)]$^{2+}$ complex have a significant structure directing effect onto the structure of the thioantimonate(III) anion. Such a structure directing influence was also observed in the compounds [Co(tren)]Sb_2S_4 and [Ni(tren)]Sb_2S_4 [24]. In the former compound Co^{2+} has a bond to a S atoms of the thioantimonate(III) anion and due to the special arrangement of the [Co(tren)]$^{2+}$ ions layers with large pores are formed. In the latter compound the Ni^{2+} ion has two bonds to the thioantimonate(III) anion yielding a one-dimensional chain [24]. Another example is the mixed-valent compound [Fe(II)(tren)]Fe(III)SbS_4 [22]. The [Fe(tren)]$^{2+}$ cation is located at the periphery of the chain anion and the Fe^{3+} ion is directly incorporated into the thioantimonate(III) anion.

We note that all S atoms act in the $S^{[2]}$ mode. In the SbS_3 pyramids the Sb-S distances vary between 2.371(1) and 2.4820(8) Å (Table 2). In the SbS_4 units the bond lengths range from 2.451(1) up to 2.7974(9) Å (Table 2). Such SbS_4 units are not uncommon and they were observed in [Fe($C_4H_{13}N_3$)$_2$]$Sb_6S_{10} \cdot 0.5\ H_2O$ [28], [Co(tren)]Sb_4S_8 [23], [Co(tren)]Sb_2S_4 [24] and $Cs_5Sb_8S_{18}(HCO_3)$ [29]. All Sb-S distances and S-Sb-S angles are in the range reported in the literature. The Sb atoms complete their coordination spheres by so called secondary bonds to S atoms (cut-off: 3.8 Å) (see Fig. 3). The Sb(1) and Sb(4) atoms each have two S atoms and the Sb(3) atom three S atoms as second nearest neighbors. Taking these contacts into account the environment of Sb(1) and Sb(4) may be viewed as a ψ-octa-

Table 2 Selected atom distances /Å and angles /° for [*TM*(tren)]Sb_4S_7, *TM* = Mn **1**, Fe **2**, Co **3**, Zn **4**. Estimated standard deviations are given in parentheses.

	1	2	3	4
Sb(1)-S(1)	2.3987(7)	2.4031(2)	2.402(1)	2.408(1)
Sb(1)-S(2)	2.4262(7)	2.422(2)	2.415(1)	2.418(1)
Sb(1)-S(3)	2.4566(8)	2.454(2)	2.451(1)	2.455(1)
Sb(2)-S(2)	2.6393(9)	2.633(2)	2.633(1)	2.634(1)
Sb(2)-S(4)	2.457(1)	2.457(2)	2.451(1)	2.458(2)
Sb(2)-S(5)	2.4609(8)	2.4618(2)	2.455(1)	2.460(1)
Sb(2)-S(6)	2.7974(9)	2.793(2)	2.781(1)	2.785(1)
Sb(3)-S(3)[a]	2.4705(9)	2.476(2)	2.471(1)	2.476(1)
Sb(3)-S(4)	2.4820(8)	2.481(2)	2.476(1)	2.479(1)
Sb(3)-S(7)	2.4357(8)	2.433(2)	2.428(1)	2.435(1)
Sb(4)-S(5)	2.4808(8)	2.478(2)	2.474(1)	2.480(1)
Sb(4)-S(6)	2.3743(9)	2.377(2)	2.371(1)	2.377(1)
Sb(4)-S(7)	2.467(1)	2.469(2)	2.462(1)	2.469(1)
TM-S(1)	2.4559(9)	2.387(2)	2.355(1)	2.387(1)
TM-N(1)	2.376(2)	2.308(4)	2.273(4)	2.348(4)
TM-N(2)	2.217(2)	2.137(4)	2.085(4)	2.082(4)
TM-N(3)	2.204(3)	2.132(4)	2.071(4)	2.074(4)
TM-N(4)	2.200(3)	2.129(4)	2.083(4)	2.078(4)
long Sb-S bonds				
Sb(1)-S(4)	3.624(1)	3.618(2)	3.599(2)	3.605(2)
Sb(1)-S(5)	3.3816(9)	3.385(2)	3.389(1)	3.399(1)
Sb(3)-S(2)[a]	3.6958(9)	3.691(1)	3.654(1)	3.664(1)
Sb(3)-S(5)[a]	3.638(1)	3.644(2)	3.624(1)	3.632(1)
Sb(3)-S(6)	3.121(1)	3.108(2)	3.113(2)	3.125(2)
Sb(4)-S(2)[c]	3.437(1)	3.404(2)	3.374(1)	3.373(2)
Sb(4)-S(4)[b]	3.723(1)	3.719(2)	3.696(2)	3.671(2)
N(1)-*TM*-S(1)	168.94(6)	173.4(2)	173.7(1)	174.6(1)
TM-S(1)-Sb(1)	101.66(3)	105.40(5)	106.22(4)	106.92(5)
Sb(1)-S(2)-Sb(2)	98.24(3)	98.34(4)	98.48(4)	98.63(4)
Sb(1)-S(3)-Sb(3)[d]	104.00(4)	103.67(5)	103.48(5)	103.73(5)
Sb(2)-S(4)-Sb(3)	105.77(3)	105.64(5)	105.50(4)	105.55(5)
Sb(2)-S(5)-Sb(4)	94.91(3)	94.92(4)	94.67(4)	94.67(4)
Sb(4)-S(6)-Sb(2)	89.10(3)	89.12(4)	89.05(4)	89.10(4)
Sb(3)-S(7)-Sb(4)	98.97(3)	98.77(4)	98.70(4)	98.68(4)
S(1)-Sb(1)-S(2)	99.95(3)	99.44(4)	100.32(4)	100.93(4)
S(2)-Sb(2)-S(5)	85.46(3)	85.58(4)	85.37(4)	85.48(4)
S(2)-Sb(2)-S(6)	164.74(2)	164.90(4)	165.27(3)	165.40(4)

[a] −1+x, y, z; [b] 0.5−x, 0.5+y, 1.5−z; [c] 1.5−x, 0.5+y, 1.5−z; [d] 1+x, y, z

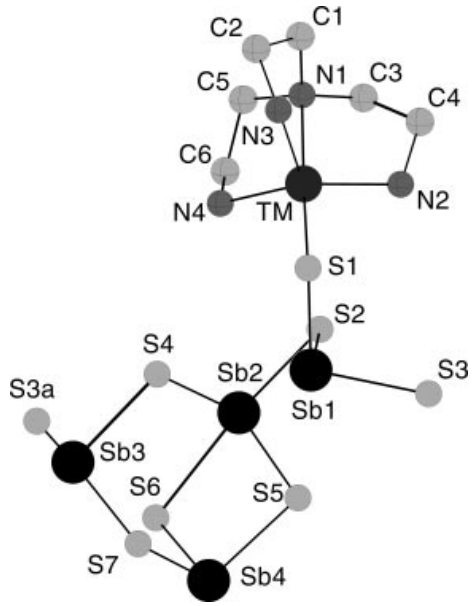

Fig. 1 View of the [*TM*(tren)]Sb_4S_7 unit with labeling. Hydrogen atoms are omitted for clarity. Symmetry code: a = −1+x, y, z.

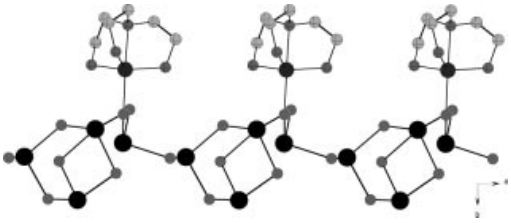

Fig. 2 The crystal structure of [*TM*(tren)]Sb_4S_7 viewed along the crystallographic *c*-axis neglecting the long Sb-S contacts. Hydrogen atoms are omitted for clarity.

hedron and that of Sb(3) as a distorted SbS_6 octahedron. The additional long Sb-S bonds range from 3.108(2) to 3.723(1) Å (Table 2). We note that Sb(1) and Sb(3) have long distances to S atoms within the same chain whereas Sb(4) located at one corner of the semicube has contacts to S(2) and S(4) of a neighbored chain. Considering the two Sb(4)···S distances as weak bonds the chains are connected into layers within the (001) plane. The neighbored layers are stacked perpendicular to [001] forming pockets which are occupied by the [*TM*(tren)]$^{2+}$ cations (Fig. 4). The Sb(4)···S(2) and Sb(4)···S(4) separations become shorter going from the Mn to the Zn compound (Table 2). This is the result of several alterations of interatomic bond lengths and the change of the spatial extension of the ligands around the TM^{2+} ions. The *TM*-S(1) bond decreases from Mn to Co and increases again. The largest dimension of the ligand measured from coordinate-to-coordinate decreases from 4.534 Å (Mn), 4.473 Å (Fe), 4.376 Å (Co) to 4.341 Å (Zn). Finally, the Sb(1)-S(1) bond lengths slightly increase from the Mn to the Zn compound (Table 2). The shortest interlayer distance (S(1)-S(1)) is first reduced from 5.002 Å (Mn) to 4.913 Å (Co) and slightly expands again for Zn (4.940 Å). In all compounds four short intermolecular H···S separations indicate weak hydrogen bonding between adjacent chains.

The structure of the title compounds can be compared with that of $Mn(en)_3Sb_4S_7$ [17], $Ni(en)_3Sb_4S_7$ [21], and $(pipH_2)Sb_4S_7$ [19]. Considering Sb-S distances above 3 Å SbS_3 pyramids and semicubes alternate within the $[Sb_4S_7]^{2-}$ chain anion. The chains are interconnected into layers via long Sb-S bonds of about 3.3 Å. The S atom showing the $S^{[1]}$ bonding mode points alternately up and down towards the neighbored layers (Fig. 5). The cations are located between the layers and the inter-layer separation is determined by the size of the charge balancing cation. Formally, the title compounds are generated by bond formation between this $S^{[1]}$ atom and the [*TM*(tren)]$^{2+}$ complexes. The S(6) atom has two additional long contacts (intra-chain to Sb(2), inter-chain to Sb(1)a, not shown in Fig. 5), and taking these long bonds into account a $S^{[3]}$ mode is found. A remarkable difference between the title compounds and that shown in Figure 5 is the angle Sb(2)-Sb(4)-S(6) of 63° and the com-

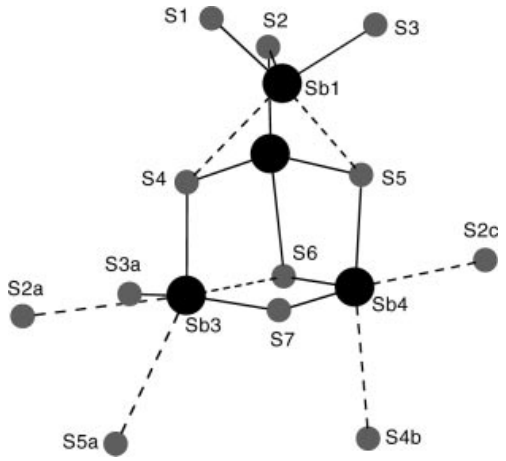

Fig. 3 The environments of the Sb atoms with their long secondary bonds (dotted lines). Symmetry codes: a = −1+x, y, z; b = 0.5−x, 0.5+y, 1.5−z; c = 1.5−x, 0.5+y, 1.5−z.

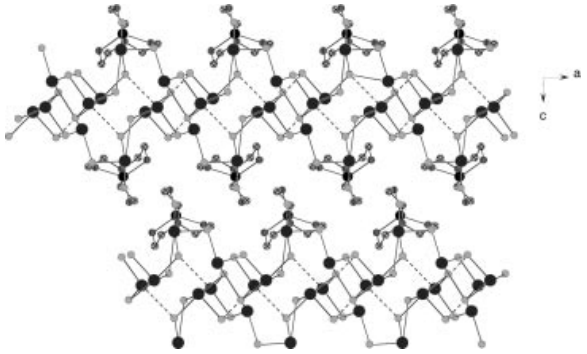

Fig. 4 Interconnection of the chains into the layers via the longer Sb-S bonds (dotted lines). Hydrogen atoms are omitted for clarity.

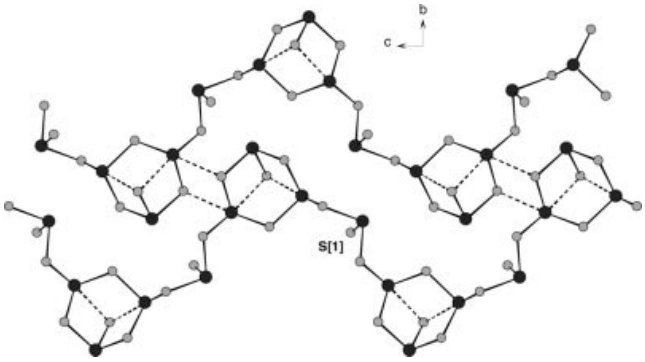

Fig. 5 The $[Sb_4S_7]^{2-}$ chains in $Mn(en)_3Sb_4S_7$ [17], $Ni(en)_3Sb_4S_7$ [21], and $(pipH_2)Sb_4S_7$ [19]. The dotted lines indicate Sb-S distances above 3 Å. The S atom with the $S^{[1]}$ binding mode is labeled. The cations are not displayed.

parable angle Sb(2)-Sb(1)-S(1) for 1 - 4 with a value of 130°. The different orientation, the S(1)-TM^{2+} covalent bonds as well as the space requirements of the $[TM(\text{tren})]^{2+}$ complexes may be responsible that the S(1) atom has no long bonds to other Sb atoms in the title compounds.

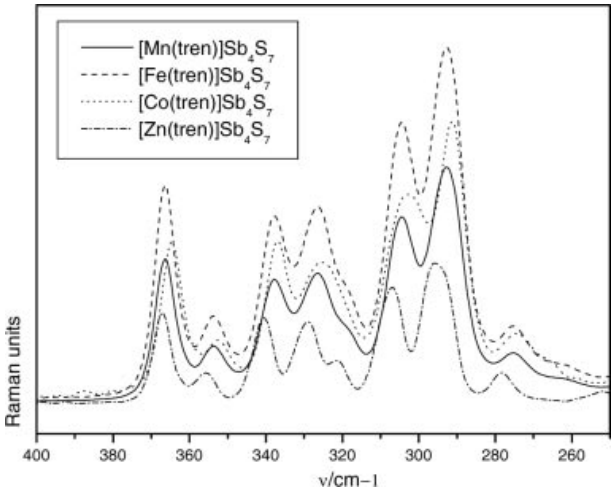

Fig. 6 Raman spectra of the $[TM(\text{tren})]Sb_4S_7$ compounds (TM = Mn, Fe, Co, Zn) in the region between 400 and 250 cm^{-1}.

The Raman spectra of all compounds are shown in Figure 6. Intensive bands are located between 380 and 280 cm^{-1}. The assignment is not straightforward, but according to the literature the resonance located at higher frequencies could be assigned to the $Sb(1,3,4)S_3$ units [32]. The modes at lower frequencies are due to the $Sb(2)S_4$ unit. The slight differences observed in the spectra are in accordance with the alterations of the environments around the Sb atoms.

The thermal stability of all compounds was investigated with DTA-TG measurements. For all compounds a one step decomposition is observed which is in all cases accompanied by a strong endothermic event (Mn: T_{onset} = 300 °C; Fe: T_{onset} = 295 °C; Co: T_{onset} = 298 °C; Zn: T_{onset} = 284 °C).

For all compounds the experimental weight loss is comparable to that expected for the emission of the organic component. Small differences are due to a slight contamination of the decomposition products with C, N, and H. In the grey residues obtained after the heat treatment the following compounds were identified with X-ray powder diffractometry: **1**: Sb_2S_3 and MnS; **2**: Sb_2S_3, FeS and $FeSb_2S_4$; **3**: Sb_2S_3, CoSbS and CoS; **4**: Sb_2S_3 and ZnS.

For the estimation of the optical band gaps UV/Vis diffuse reflectance spectra in the range of 200 to 2000 nm were recorded (Fig. 7). The results for the compounds (**1**: 3.11 eV (398 nm), **2**: 2.04 eV, (607 nm), **3**: 2.45 eV, (506 nm), **4**: 2.60 eV, (476 nm)) are in good agreement with the color of the crystals. The explanation of the variation of the optical band gap for the different compounds is not easy because the transition cannot be simply a transition from the S 3p based top of the valence band into the conduction band composed mainly by empty metal centred d-states. Therefore, it must be assumed that the bonding interactions between the TM^{2+} cations and the thioantimonate(III) anion sensitively influence the energy of the electronic levels which are responsible for the transition. Nevertheless, the results

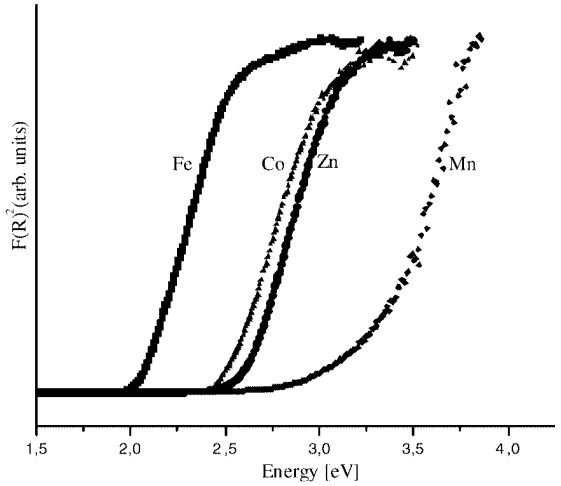

Fig. 7 UV/Vis spectra of the [*TM*(tren)]Sb_4S_7 compounds (*TM* = Mn, Fe, Co, Zn).

show that the optical properties of such thioantimonates-(III) can be tuned by the choice of the transition metal. Mixtures of TM^{2+} ions should allow the adjustment of a specific value for the optical band gap.

Experimental

Synthesis

Yellow orange polyhedra of [Mn(*tren*)]Sb_4S_7 (**1**) were prepared by reacting a mixture of Mn (0.055 g, 1 mmol), Sb (0.121 g, 1 mmol) and S (0.080 g, 2.5 mmol) in 3 mL of an aqueous solution of 20 % *tren* (Merck Chemical). The synthesis was performed in a Teflon-lined steel autoclave (inner volume: 30 mL) which was heated to 140 °C, held at this temperature for 7 days and then cooled to room temperature within 3 h (yield: 36 % based on Mn). The EDX analysis of the by-product yields Mn, S, and Sb. In the powder pattern (XRD) MnS and Sb were identified. C, H, N, S analysis of the pure product: calcd.: C: 7.90, H: 1.99, N: 6.14, S: 24.59 %; found: C: 7.77, H: 1.78, N: 6.17, S: 25.06 %.

[Fe(*tren*)]Sb_4S_7 (**2**) was synthesized applying $FeCl_3$ (0.162 g, 1 mmol), elemental Sb (0.121 g, 1 mmol) and elemental S (0.096 g, 3 mmol) in an aqueous solution of 8 mL 50 % *tren*/H_2O. The Teflon-lined steel autoclave (inner volume: 30 mL) was heated for 3 days up to 170 °C then cooled to room temperature within 3 h. The red-brown polyhedral crystals were filtered off, washed with a mixture of H_2O/Ethanol/Acetone (1:1:1) in an ultrasonic bath (yield: 70 % based on Fe). According to the X-ray powder pattern the by-product consists of [Fe(*tren*)]$FeSbS_4$ [22]. C, H, N, S analysis of the pure product: calcd.: C: 7.89, H: 1.99, N: 6.13, S: 24.57 %; found: C: 6.85, H: 1.675, N: 5.359, S: 22.207 %.

[Co(*tren*)]Sb_4S_7 (**3**) was prepared by reacting elemental Co (0.058 g, 1 mmol), Sb (0.121 g, 1 mmol) and S (0.096 g, 3 mmol) in 3 mL 20 % *tren*/H_2O solution. The mixture was heated for 6 days at 180 °C in a Teflon-lined steel autoclave (inner volume: 30 mL) then cooled to room temperature within 3 h. The product was filtered off, washed with water and acetone and cleaned in an ultrasonic bath. The product consists of green polyhedra (yield: 40 % based on Co). Binary CoS and elemental Sb were identified in the XRD as the by-product, and no reflections of other compound were seen. But the existence of amorphous by-products cannot be excluded. C, H, N, S analysis of the pure product: calcd.: C: 7.86, H: 1.98, N: 6.11, S: 24.49 %; found: C: 7.57, H: 1.85, N: 5.97, S: 26.11 %.

[Zn(*tren*)]Sb_4S_7 (**4**) was prepared by reacting elemental Zn, Sb and S in a *tren*/H_2O solution under solvothermal conditions in a Teflon-lined steel autoclave (inner volume: 30 mL). In a typical synthesis 1 mmol Zn (0.0654 g), 2 mmol Sb (0.243 g) and 4 mmol S (0.128 g) were added to 5 mL of a 50 % *tren*/H_2O solution. The mixture was heated to 140 °C for 7 days then cooled to room temperature within 3 h. The reaction mixture was filtered off, washed with water and acetone. The product consists of yellow polyhedra (yield: 44 % based on Zn). The powder pattern of the by-product shows reflections of ZnS and Sb. C, H, N, S analysis of the pure product: calcd.: C: 7.81, H: 1.97, N: 6.07, S: 24.32 %; found: C: 7.89, H: 2.04, N: 6.15, S: 24.34 %.

Structure determination

Single crystal X-ray investigations were performed using the CAD-4 four circle diffractometer for compound **1,** Imaging Plate Diffraction System (Stoe & Cie) for **2**, **3** and a STOE AED-II 4-circle diffractometer for **4** using graphite monochromated Mo-K_α radiation (λ = 0.71073 Å). The intensities were corrected for Lorentz, polarization and absorption effects. The structures were solved using SHELXS-97 [33] and structure refinements were done against F^2 with SHELXL-97 [34]. All non-hydrogen atoms were refined with anisotropic displacement parameters. The hydrogen atoms were positioned with idealized geometry and refined with fixed isotropic displacement parameters using a riding model. The hydrogen atoms were positioned at 0.90 Å (primary amino groups). Technical details of the data acquisition as well as some selected refinement results are summarized in Table 1.

Crystallographic data (excluding structure factors) for the structure reported in this paper have been deposited with the Cambridge Crystallographic Data Centre as supplementary publication no. CCDC 235170 **1**, no. CCDC 235169 **2**, no. CCDC 235171 **3**, no. CCDC 235168 **4**. Copies of the data can be obtained free of charge on application to CCDC, 12 Union Road, Cambridge CB2 1 EZ, UK [Fax: +44-(0)1223-336033 or email: deposit@ccdc.cam.ac.uk].

X-ray powder diffractometry

The X-ray powder patterns were recorded on a STOE Stadi-P diffractometer (Cu-$K_{\alpha1}$ radiation, λ = 1.5406 Å) in transmission geometry.

Thermal investigations

The thermal measurements were performed on a Netzsch STA 429 DTA-TG measurement device. The samples were heated up to 400 °C in Al_2O_3 crucibles with a rate of 3 K min^{-1} and purged in an argon stream of approximately 50 mL min^{-1}. DTA-TG-MS measurements were conducted simultaneously using the STA-409CD device (Netzsch) with Skimmer coupling, which is equipped with a quadrupole mass spectrometer QMA 400 (max. 512 amu) from Balzers. The MS measurements were performed in the analogue and trend scan mode. All measurements were corrected for buoyancy and current effects and were done with heating rates of 4 K min^{-1} in Al_2O_3 crucibles under a dynamic nitrogen atmosphere (flow-rate: 75 mL min^{-1}, purity: 5.0).

EDX experiments

Scanning electron microscopy investigations and energy dispersive analysis of X-rays (EDX) were conducted with a Philips Environmental Scanning Electron Microscope ESEM XL30.

Raman Spectroscopy

Raman spectra were recorded in the region 100 to 3500 cm^{-1} with a Bruker IFS 66 Fourier transform Raman spectrometer (wavelength: 541.5 nm).

Solid-State UV/Vis/NIR Spectroscopy

UV/Vis spectroscopic investigations were conducted at room temperature using a UV-VIS-NIR two-channel spectrometer Cary 5 from Varian Techtron Pty., Darmstadt. The optical properties of the compounds were investigated by studying the UV/Vis reflectance spectrum of the powdered sample. The absorption data were calculated using the Kubelka-Munk relation for diffuse reflectance data. $BaSO_4$ powder was used as reference material.

Acknowledgements. Financial support by the Deutsche Forschungsgemeinschaft and the State Schleswig-Holstein is gratefully acknowledged. We thank *I. Jess* for the acquisition of the single crystal data. Our thanks are due to *U. Cornelissen* for carrying out the spectroscopic measurements.

References

[1] L. Engelke, M. Schaefer, M. Schur, W. Bensch, *Chem. Mater.* **2001**, *13*, 1383.
[2] L. Engelke, M. Schaefer, F. Porsch, W. Bensch, *Eur. J. Inorg. Chem.* **2003**, 506.
[3] H. A. Graf, H. Schäfer, *Z. Naturforsch.* **1972**, *27b*, 735.
[4] G. Dittmar, H. Schäfer, *Z. Anorg. Allg. Chem.* **1977**, *437*, 183.
[5] G. Dittmar, H. Schäfer, *Z. Anorg. Allg. Chem.* **1978**, *441*, 93.
[6] G. Dittmar, H. Schäfer, *Z. Anorg. Allg. Chem.* **1978**, *441*, 98.
[7] B. Eisenmann, H. Schäfer, *Z. Naturforsch.* **1979**, *34b*, 383.
[8] R. Stähler, C. Näther, W. Bensch *J. Solid State Chem.* **2003**, *174*, 264.
[9] K. Volk, P. Bickert, R. Kolmer, H. Schäfer, *Z. Naturforsch.* **1979**, *34b*, 380.
[10] G. Cordier, H. Schäfer, *Rev. Chim. Miner.* **1981**, *18*, 218.
[11] G. Cordier, H. Schäfer, C. Schwidetzky, *Z. Naturforsch.* **1984**, *39b*, 131.
[12] A. Pfitzner, D. Kurowski, *Z. Kristallogr.* **2000**, *215*, 373.
[13] A. V. Powell, S. Boissiere, A. M. Chippindale, *J. Chem. Soc., Dalton Trans.* **2000**, *22*, 4192.
[14] W. Bensch, M. Schur, *Eur. J. Solid State Inorg. Chem.* **1996**, *33*, 1149.
[15] M. Schur, C. Näther, W. Bensch, *Z. Naturforsch.* **2001**, *56b*, 79.
[16] R. Stähler, B.-D. Mosel, H. Eckert, W. Bensch, *Angew. Chem.* **2002**, *114*, 4671; *Angew. Chem. Int. Ed.* **2002**, *41*, 4487.
[17] W. Bensch, M. Schur, *Z. Naturforsch.* **1997**, *52b*, 405.
[18] W. S. Sheldrick, H.-J. Häusler, *Z. Anorg. Allg. Chem.* **1988**, *557*, 105.
[19] J. B. Parise, Y. Ko, *Chem. Mater.* **1992**, *4*, 1446.
[20] M. Schur, W. Bensch, *Eur. J. Solid State Inorg. Chem.* **1997**, *34*, 457.
[21] H.-O. Stephan, M. G. Kanatzidis, *Inorg. Chem.* **1997**, *36*, 6050.
[22] R. Kiebach, C. Näther, W. Bensch, *Z. Anorg. Allg. Chem.* **2002**, *628*, 2176.
[23] R. Stähler, W. Bensch, *J. Chem. Soc., Dalton Trans.* **2001**, 2518.
[24] R. Stähler, W. Bensch, *Eur. J. Inorg. Chem.* **2001**, 3073.
[25] M. Schaefer, C. Näther, W. Bensch, *Solid State Sci.*, **2003**, *5*, 1135.
[26] K. Volk, H. Schäfer, *Z. Naturforsch.* **1979**, *34b*, 1637.
[27] A. Powell, S. Bossière, A. Chippindale, *Chem. Mater.* **2000**, *12*, 182.
[28] R. Stähler, C. Näther, W. Bensch, *Eur. J. Inorg. Chem.* **2001**, 1835.
[29] G. L. Schimek, J. W. Kolis, *Inorg. Chem.* **1997**, *36*, 1689.
[30] M. Schaefer, D. Kurowski, A. Pfitzner, C. Näther, W. Bensch, *Acta. Crystallogr.* **2004**, *E60*, m183.
[31] R. D. Shannon, *Acta Crystallogr.* **1976**, *A32*, 751.
[32] A. Pfitzner, *Chem. Eur. J.* **1997**, *3*, 2032.
[33] G. M. Sheldrick, SHELXS-97, Program for Crystal Structure Determination, University of Göttingen, Germany, 1997.
[34] G. M. Sheldrick, SHELXL-97, Program for the Refinement of Crystal Structures, University of Göttingen, Germany, 1997.

4.2.3 Die Verbindung $[Ni(C_4H_{13}N_3)_2]_3[(Sb_3S_6)_2]$

Zusammenfassung der Veröffentlichung *„[Ni(C$_4$H$_{13}$N$_3$)]$_3$(Sb$_3$S$_6$)$_2$: The First Structure Containing Isolated Heterocyclic [Sb$_3$S$_6$]$^{3-}$ Anions“*.

Die Darstellung der Verbindung $[Ni(C_4H_{13}N_3)]_3[Sb_3S_6]_2$ erfolgte unter solvothermalen Bedingungen. 1 mmol Sb, 3 mmol S und 1 mmol $Ni(CH_3COO)_2{\cdot}4H_2O$ wurden 4 Tage in einer Lösung aus 1 ml dien und 1 ml Methanol bei einer Temperatur von 140 °C gehalten. Die Ausbeute betrug ca. 30 % in Form braun-gelber Kristalle (basierend au Sb).

$[Ni(C_4H_{13}N_3)]_3[Sb_3S_6]_2$ kristallisiert in der triklinen Raumgruppe $P\bar{1}$ mit zwei Formeleinheiten pro Elementarzelle. In der Struktur werden zwei kristallographisch unabhängige $[Ni(dien)_2]^{2+}$-Kationen (eines in *u-fac-*, das andere in *s-fac*-Konformation) und einem isolierten $[Sb_3S_6]^{3-}$-Ring (Abb. 4.6, links) gefunden. Das $[Sb_3S_6]^{3-}$-Anion wird aus drei eckenverknüpften SbS_3-Pyramiden gebildet, wobei jedes Antimonatom von zwei verbrückenden und einem terminalen Schwefelatom umgeben ist. Die Sb-S-Abstände zu den terminalen S-Atomen sind signifikant kürzer als zu den verbrückenden S-Atomen. Anionen und Kationen bilden individuelle Stapel entlang der a-Achse. Vier Kationen- und zwei Anionen-Stapel formen einen Kanal entlang der *a*-Achse, in dem sich ungeordnete Lösungsmittelmoleküle befinden (Abb. 4.6, rechts). Eine vergleichbare Anordnung der Kationen und Anionen wurde in den beiden Verbindungen $[Ni(dien)_2]_3[SbS_4]_2$ [49] und $[Ni(dien)_2]_2[Sb_4S_8]$ [50] beobachtet. Die 3-dimensionale Anordnung von Kationen und Anionen wird über S-H-Wasserstoffbrückenbindungen erreicht. Die Geometrie des $[Sb_3S_6]^{3-}$-Ringes kann als „wannenförmig“ bezeichnet werden. Theoretische Berechnungen mit GAUSSIAN98 zeigten, dass die Wannenform mit 2 kcal/mol gegenüber der Sesselform energetisch begünstigt ist.

DTA-TG-MS-Experimente zeigten einen thermischen Abbau in vier Stufen. Der ermittelte Gesamtmassenverlust von 37.3 % ist um 5.9 % größer als der theoretische Wert für die Emission der dien-Liganden. Diese Differenz wird durch die Emission von Lösungsmittelmolekülen verursacht, welche in den Kanälen enthalten sind. Zusätzlich wird Schwefelwasserstoff emittiert, der bei der Zersetzung gebildet wird. Alle Stufen sind in der DTA-Kurve von endothermen Ereignissen begleitet. In dem grauen Abbauprodukt konnten NiSbS und Sb_2S_3 als kristalline Produkte identifiziert werden.

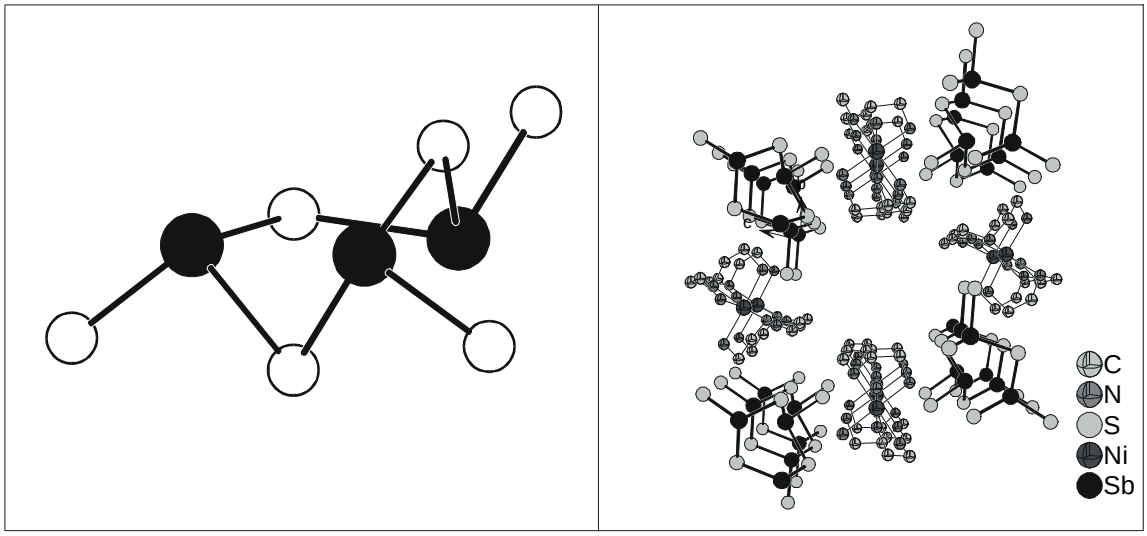

Abbildung 4.6: $[Sb_3S_6]^{3-}$-Anion (links), Packungsbild mit Blick entlang der *a*-Achse (rechts)

Bemerkenswert an der Verbindung ist, dass das $[Sb_3S_6]^{3-}$-Anion erstmals isoliert werden konnte, und es stellt somit das kleinste isolierte heterocyclische Sb-S-Anion dar. Das häufige Auftreten als sekundäre Baueinheit in anderen Strukturen und die mit der Verbindung $[Ni(C_4H_{13}N_3)]_3[Sb_3S_6]_2$ gelungene Isolation sind kein Beweis für die Existenz der $[Sb_3S_6]^{3-}$-Einheit unter solvothermalen Bedingungen in Lösung, können aber als ein Indiz hiefür gewertet werden.

$[Ni(C_4H_{13}N_3)_2]_3(Sb_3S_6)_2$: The First Structure Containing Isolated Heterocyclic $[Sb_3S_6]^{3-}$ Anions

Ragnar Kiebach,[a] Felix Studt,[a] Christian Näther,[a] and Wolfgang Bensch*[a]

Keywords: Thioantimonates / Heterocycles / Hydrothermal synthesis / Antimony / Sulfur

The novel thioantimonate(III) compound $[Ni(dien)_2]_3(Sb_3S_6)_2$, which was synthesised under solvothermal conditions, contains isolated $[Sb_3S_6]^{3-}$ anions. In the X-ray crystal structure, isolated cyclic $[Sb_3S_6]^{3-}$ anions occupy a boat-like conformation and two different isomeric $[Ni(dien)_2]^{2+}$ cations are arranged in separate stacks.

Introduction

In the structures of thioantimonates(III), the primary building units (PBU's) SbS_3, SbS_4 and the less common SbS_5 [1] or SbS_6 [1,2] PBU's are interconnected to form secondary building units (SBU's) such as the heterorings Sb_xS_x, with x ranging from 2 to 32. Rings with small values of x are very common in thioantimonate(III) structures whereas the larger rings are quite rare.[3,4] Very little is known about the processes occurring in the heterogeneous reaction mixtures, which result in the crystallisation of distinct thioantimonates(III). A few years ago, we isolated and characterised several antimony polysulfides such as $[Ph_4P]_2[Sb_2S_{15}]$,[5] $[Ph_4P]_3Sb_3S_{25}$ [6] and $[Ph_4P]_2[Sb_2S_{17}]$[7] which may play important roles as precursors in the syntheses. More recently, we synthesised and characterised $[Ni(dien)_2]_2Sb_4S_8$ [8] as well as $[Mn(C_3H_{10}N_2)_3]_2(Sb_4S_8)\cdot 2H_2O$[9] with the cyclic Sb_4S_4 heteroring as the main structural motif. The successful isolation of these compounds suggests that even these small heterocycles exist in solution. Using an upper limit of 3 Å for Sb−S bonds, the Sb_2S_2 ring can be found in $Ca_2Sb_2S_5$.[10] However, the Sb atoms of this ring have two additional S atoms at a distance less than 3.2 Å, in contrast to the Sb atoms of the Sb_4S_4 ring where no Sb···S contacts were observed below 4 Å. The small Sb_xS_x heteroring with $x = 3$ is commonly observed in extended thioantimonate(III) structures and two different conformations have been identified. In such structures, the Sb_3S_3 rings mostly occupy a chair-like conformation.[4,11−13] A special case of this chair-like conformation is an arrangement in which one endo-cyclic terminal sulfur atom is rotated by nearly 180° thus forming long bonds to the two other antimony atoms.[14,15] This arrangement has been classified as an Sb_3S_4 "semicube". We note that some authors also denote an Sb_3S_6 unit as a "semicube".[12] The boat-like conformation has also been identified in several thioantimonates.[16−18] During our continuing efforts in this area, we obtained the new compound $[Ni(dien)_2]_3(Sb_3S_6)_2$ which contains an isolated Sb_3S_3 heteroring as the main structural feature. This is the first compound containing this isolated Sb_3S_3 ring and it is only the third thioantimonate(III) compound reported with a small isolated thioantimonate(III) heteroring.

[a] Institut für Anorganische Chemie CAU Kiel
Olshausenstr. 40, 24098 Kiel, Germany
Fax: (internat.) +49-(0)431-880-1520
E-mail: wbensch@ac.uni-kiel.de

Results and Discussion

Crystal Structure

$[Ni(dien)_2]_3(Sb_3S_6)_2$ (dien = diethylenetriamine) crystallises in the triclinic space group $P\bar{1}$ with two formula units in the unit cell. In the crystal structure, there are two crystallographically independent $[Ni(dien)_2]^{2+}$ cations and one isolated heterocyclic $[Sb_3S_6]^{3-}$ anion (Figures 1−3). The $[Sb_3S_6]^{3-}$ anion and one of the two crystallographically independent $[Ni(dien)_2]^{2+}$ cations are located in general position whereas the second cation is located on a centre of inversion.

The Sb_3S_3 ring is formed by three vertex-linked SbS_3 trigonal pyramids (Figure 1). Each Sb atom of the Sb_3S_3 heteroring has a bond to a terminal S atom thus forming the final anion. The Sb−S distances in the Sb_3S_3 ring are similar to those reported for extended thioanti-

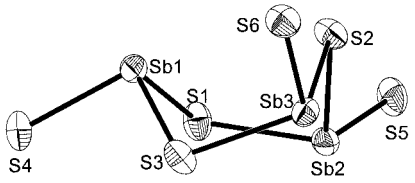

Figure 1. The $[Sb_3S_6]^{3-}$ anion in $[Ni(dien)_2]_3(Sb_3S_6)_2$ with labelling and displacement ellipsoids drawn at the 50% probability level

monates(III).[19−22] The Sb(1) and Sb(2) atoms each have one long intramolecular contact to an S atom [Sb(1)−S(2) 3.606 Å, Sb(2)−S(3) 3.891 Å]. No intermolecular Sb−S contacts shorter than 4.8 Å are present Table 1).

Table 1. Selected bond lengths (Å) and angles (°) for the $[Sb_3S_6]^{3-}$ anion in $[Ni(dien)_2]_3(Sb_3S_6)_2$

Sb(1)−S(4)	2.3310(9)	Sb(1)−S(3)	2.4756(10)
Sb(1)−S(1)	2.4838(9)	Sb(2)−S(5)	2.3333(9)
Sb(2)−S(2)	2.4617(9)	Sb(2)−S(1)	2.4623(9)
Sb(3)−S(6)	2.3216(9)	Sb(3)−S(3)	2.4702(9)
Sb(3)−S(2)	2.4774(9)		
S(4)−Sb(1)−S(3)	93.47(3)	S(4)−Sb(1)−S(1)	98.40(3)
S(3)−Sb(1)−S(1)	99.56(3)	S(5)−Sb(2)−S(2)	102.22(3)
S(5)−Sb(2)−S(1)	99.00(3)	S(2)−Sb(2)−S(1)	98.00(3)
S(6)−Sb(3)−S(3)	104.70(3)	S(6)−Sb(3)−S(2)	101.46(3)
S(3)−Sb(3)−S(2)	97.68(3)	Sb(2)−S(1)−Sb(1)	102.03(3)
Sb(2)−S(2)−Sb(3)	93.44(3)	Sb(3)−S(3)−Sb(1)	106.65(3)

The Ni^{2+} cations are in a distorted octahedral environment formed by six N atoms of two dien ligands with one unique $[Ni(dien)_2]^{2+}$ cation in the *u-fac* conformation [Ni(1)] and the other in the *s-fac* conformation (Figure 2). The Ni−N distances range between 2.100(3) and 2.145(3) Å, with N−Ni−N angles varying from 81.04(2) to 180.00(2)°. Angles and distances are similar to the corresponding literature values for $[Ni(dien)_2]^{2+}$ complexes (Table 2).[8,19,20]

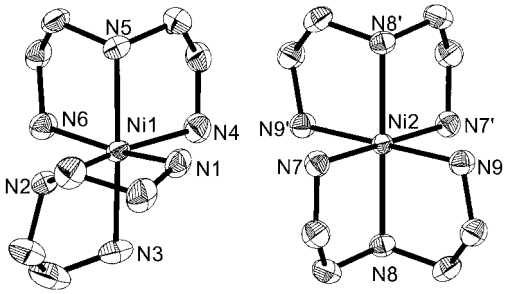

Figure 2. Coordination of the Ni cations in $[Ni(dien)_2]_3(Sb_3S_6)_2$ with labelling and displacement ellipsoids drawn at the 50% probability level (hydrogen atoms are omitted for clarity)

Cations and anions are packed in such a way that both form individual stacks parallel to the *a* axis (Figure 3). Four cations and two anions are arranged around a channel which is directed along the *a* axis. Disordered solvent molecules are located in this channel (see Exp. Sect.). A similar arrangement of cations and anions is also found in $[Ni(dien)_2]_3[SbS_4]_2$[20] and $[Ni(dien)_2]_2Sb_4S_8$.[8]

The three-dimensional arrangement of cations and anions is caused by N−H···S contacts. Every $[Sb_3S_6]^{3-}$ anion has fifteen such contacts with H···S distances between 2.440 and 2.903 Å and N−H···S angles ranging from 138.2 to 166.7°. The terminal S atoms have significantly more S···H contacts than the μ-S atoms (ratio: 2:1). The N−H atoms of the $[Ni(1)(dien)_2]^{2+}$ cation are involved in 10 and those of the second $[Ni(2)(dien)_2]^{2+}$ cation, in 5 H···S contacts.

Table 2. Selected bond lengths (Å) and angles (°) for the $[Ni(dien)_2]^{2+}$ cations in $[Ni(dien)_2]_3(Sb_3S_6)_2$

Ni(1)−N(4)	2.114(3)	Ni(1)−N(3)	2.114(3)
Ni(1)−N(1)	2.117(3)	Ni(1)−N(2)	2.127(3)
Ni(1)−N(5)	2.134(3)	Ni(1)−N(6)	2.145(3)
N(1)−C(1)	1.467(6)	C(1)−C(2)	1.522(6)
N(4)−Ni(1)−N(3)	94.70(14)	N(4)−Ni(1)−N(1)	93.88(13)
N(3)−Ni(1)−N(1)	95.88(13)	N(4)−Ni(1)−N(2)	173.65(12)
N(3)−Ni(1)−N(2)	81.48(13)	N(1)−Ni(1)−N(2)	81.52(12)
N(4)−Ni(1)−N(5)	82.52(12)	N(3)−Ni(1)−N(5)	172.95(12)
N(1)−Ni(1)−N(5)	90.79(11)	N(2)−Ni(1)−N(5)	101.85(11)
N(4)−Ni(1)−N(6)	94.99(13)	N(3)−Ni(1)−N(6)	92.79(12)
N(1)−Ni(1)−N(6)	167.04(12)	N(2)−Ni(1)−N(6)	90.28(12)
N(5)−Ni(1)−N(6)	81.04(11)		
Ni(2)−N(8)	2.100(3)	Ni(2)−N(9)	2.121(3)
Ni(2)−N(7)	2.130(3)		
N(8)−Ni(2)−N(9)	82.9(1)	N(8)−Ni(2)−N(9A)	97.2(1)
N(8A)−Ni(2)−N(7)	97.1(1)	N(8)−Ni(2)−N(7)	82.9(1)
N(9)−Ni(2)−N(7)	90.1(1)	N(9A)−Ni(2)−N(7)	89.9(1)

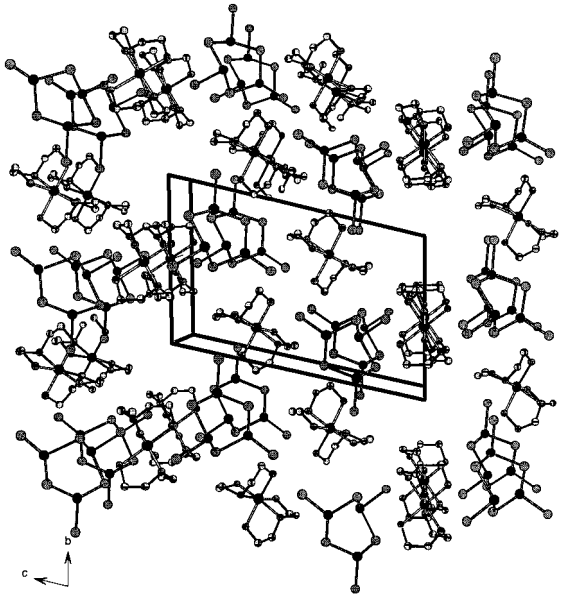

Figure 3. Crystal structure of $[Ni(dien)_2]_3(Sb_3S_6)_2$ viewed along the *a* axis (hydrogen atoms are omitted for clarity)

As mentioned above, the Sb_3S_3 unit usually occurs in a chair- or boat-like conformation, as in $[C_4H_{12}N_2]_{0.5}[CuSb_6S_{10}]$[18] or $[(CH_3NH_2)_{1.0}K_{2.97}][Sb_{12}S_{20}]\cdot 1.34H_2O$.[22] The latter is a rare example of the coexistence of two different conformations in one crystal. Interestingly, the Sb_3S_3 unit in the title compound also has a boat-like conformation. The geometry of this anion was optimised using GAUSSIAN98 indicating that the boat-like conformation is about 2 kcal/mol more stable than the chair-like conformation.

Thermal Investigations

Thermal stability of the complex was investigated using simultaneous differential thermal analysis and thermogravi-

metry (DTA-TG). Heating single crystals of the title compound under helium in a thermobalance lead to decomposition in four steps with a total mass loss of 37.3% with all steps accompanied by endothermic peaks in the DTA curve ($T1_{peak}$ = 246 °C, Δm = 4.1%; $T2_{peak}$ = 260 °C, Δm = 24.4%; $T3_{peak}$ = 277 °C, Δm = 6.0%; and $T4_{peak}$ = 331 °C, Δm = 2.8%) (Figure 4).

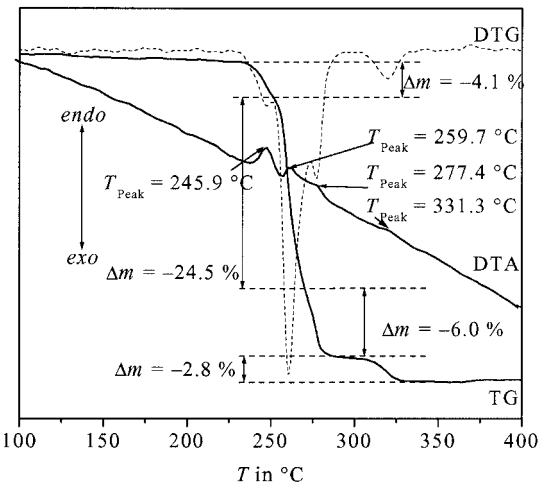

Figure 4. DTA, TG and DTG curves for $[Ni(dien)_2]_3(Sb_3S_6)_2$

Taking only the dien ligands into account, the expected mass loss is 31.4%, which is about 5.9% lower than the experimentally obtained value. This discrepancy may be due, in part, to the emission of H_2S and of solvent molecules (CH_3OH) which are located in the channels of the structure. Elemental analysis and mass spectroscopic investigations are in agreement with this. The elemental analysis gave a C,H and N content of 33.4% (C 16.2, H 4.4, N 12.8%), which is 2% larger than the theoretical content for the dien ligands alone. Mass spectra recorded simultaneously during decomposition showed a very intense signal for H_2S in the last step. Unfortunately, the content of CH_3OH could not be determined using mass spectrometry because of a substantial overlap of the different thermal processes and because of the experimental set-up of our instrument. The grey residue remaining after the thermal decomposition contained NiSbS (Ullmanit) and Sb_2S_3, both of which are frequently found after the thermal decomposition of thioantimonates containing nickel.[4,8,19–21]

Conclusion

The synthesis of thioantimonates was performed in basic solutions under solvothermal conditions. Little is known about the processes occurring in the heterogeneous reaction mixtures and which precursors determine the final structures that are formed under particular conditions. As mentioned above, in the extended structures of thioantimonate-s(III) many different secondary building units may be identified, which are formed by the condensation of the primary SbS_x (x = 3–6) units. After the successful isolation and characterisation of different antimony polysulfides and the $[Sb_4S_8]^{4-}$ anion containing the Sb_4S_4 heteroring, we were able to obtain the smallest known isolated thioantimonate anion $[Sb_3S_6]^{3-}$ containing the Sb_3S_3 ring as the main structural motif. However, the crystallisation of $[Sb_4S_8]^{4-}$ and $[Sb_3S_6]^{3-}$ does not necessarily mean that these species exist under solvothermal conditions. Further studies are necessary for a better understanding of the factors influencing product formation.

Experimental Section

Synthesis

$[Ni(dien)_2]_3(Sb_3S_6)_2$ (1): $[Ni(dien)_2]_3(Sb_3S_6)_2$ was synthesised from Sb (0.1217 g; 1 mmol), S (0.0962 g, 3 mmol), and $Ni(CH_3COO)_2{\cdot}4H_2O$ (0.2487 g; 1 mmol) dissolved in a mixture of dien (1 mL) and methanol (1 mL). The mixture was heated at 140 °C for 4 days in a Teflon^R-lined steel autoclave (volume ca. 20 mL) and was subsequently cooled to room temperature over a 3 h period. The brown crystalline product was filtered off, washed with water and acetone, cleaned in an ultrasonic bath and stored under vacuum. The compound is stable in air, water and acetone. The yield was approximately 30% based on Ni. $[Ni(dien)_2]Cl_2$ and $[Ni(dien)_2]_3(SbS_4)_2$ were identified as by-products.

X-ray Crystallography: The X-ray single-crystal data for **1** were collected at 293 K using a STOE Imaging Plate Diffraction System

Table 3. Crystal data and selected results for the structure refinement of $[Ni(dien)_2]_3(Sb_3S_6)_2$

Empirical formula	$C_{24}H_{78}N_{18}Ni_3Sb_6S_{12}$
Crystal colour	brown
Crystal habit	irregular
Molecular mass [g/mol]	1910.39
Crystal system	triclinic
Space group	$P\bar{1}$
a (Å)	7.1208(5)
b (Å)	12.3254(9)
c (Å)	19.165(2)
α (°)	76.169(8)
β (°)	84.462(9)
γ (°)	85.892(8)
V (Å^3)	1623.6(2)
Z	2
T [K]	293
λ(Mo-K_α) (Å)	0.71073
$d_{calcd.}$ [Mg·cm^{-3}]	1.945
μ(Mo-K_α) [mm^{-1}]	3.73
F(000)	930
2Θ range of data collection (°)	6° ≤ 2Θ ≤ 60°
Index range	$-10 \le h \le 10$
	$-15 \le k \le 17$
	$-27 \le l \le 27$
Reflections collected	19706
Independent reflections	9342
Reflections with $F_o > 4\sigma(F_o)$	8114
$wR2$ for all reflections[a]	0.1014
$R1$ for reflections with $F_o > 4\sigma(F_o)$[b]	0.0354
Goodness of fit	1.028
Largest diff. peak/hole [e·Å^{-3}]	0.99/−1.61

[a] $wR2 = [\Sigma[w(F_o^2 - F_c^2)^2]/\Sigma[w(F_o^2)^2]]^{1/2}$ [b] $R1 = \Sigma||F_o| - |F_c||/\Sigma|F_o|$

(IPDS). The intensities were corrected for Lorentz, polarisation and absorption effects. Structure solution was performed using SHELXS-97.[23] Refinement was done against F^2 by using the software SHELXL-97.[24] The non-hydrogen atoms were refined with anisotropic displacement parameters. The hydrogen atoms were positioned with idealised geometry and refined with isotropic displacement parameters using the riding model. The structure contains additional disordered solvent molecules in the channels for which no appropriate structure model could be found. Therefore, the data were treated with the SQUEEZE option for disordered solvent in PLATON.[25] In the first step, this program calculates the space which can be occupied by disordered solvent molecules starting from the refined structure model. In the next step the sum of electrons in this space is calculated and the measured data file is corrected in a way that these electrons are not considered. This calculation gives a volume of 182.2 Å^3/cell which can be used by disordered solvent. Selected crystal data and details of the structure determination are listed in Table 3.

CCDC-21630 contains the supplementary crystallographic data for this paper. These data can be obtained free of charge at www.ccdc.cam.ac.uk/conts/retrieving.html [or from the Cambridge Crystallographic Data Centre, 12 Union Road, Cambridge CB2 1EZ, UK; Fax: (internat.) +44-1223-336-033; E-mail: deposit@ccdc.cam.ac.uk].

DTA-TG-MS Investigations: DTA-TG-MS measurements were performed using a Netzsch STA-409. The sample (mass: 11.98 mg) was heated in a dynamic He atmosphere (flow rate 75 ml·min^{-1}) in an Al_2O_3 crucible with a heating rate of 4 K/min to 400 °C).

Density Functional Calculations: Spin-restricted DFT calculations using Becke's three parameter hybrid function with the correlation function of Lee, Yang and Parr (B3LYP)[26−28] were performed for the singlet ground state of $[Sb_3S_6]^{3-}$. The LanL2DZ basis set was used for the calculation. This applies Dunning/Huzinaga full double zeta (D95) basis functions[29] to the first row and Los Alamos effective core potentials plus DZ functions on all other atoms.[30,31] Convergence was reached when the relative change in the density matrix between subsequent iterations was less than $1\cdot10^{-8}$. All procedures were used as they are implemented in the GAUSSIAN 98 package.[32]

Acknowledgments

Financial support by the Deutsche Forschungsgemeinschaft and the State Schleswig-Holstein is gratefully acknowledged.

[1] J. Olivier-Fourcade, L. Izghouti, E. Philippot, *Rev. Chim. Miner.* **1981**, *18*, 207−217.
[2] W. S. Sheldrick, H.-J. Häusler, *Z. Anorg. Allgem. Chem.* **1988**, *561*, 149−156.
[3] J. B. Parise, *Science* **1991**, *251*, 293−294.
[4] R. Stähler, W. Bensch, *Z. Anorg. Allg. Chem.* **2002**, *628*, 1657−1662.
[5] H. Rijnberk, C. Näther, M. Schur, I. Jeß, W. Bensch, *Acta Crystallogr., Sect. C* **1998**, *54*, 920−923.
[6] M. Schur, W. Bensch, *Z. Anorg. Allg. Chem.* **1998**, *624*, 310−314.
[7] W. Bensch, M. Schur, *Z. Kristallogr.* **1997**, *212*, 305−307.
[8] W. Bensch, C. Näther, R. Stähler, *Chem. Commun.* **2001**, 477−478.
[9] L. Engelke, W. Bensch, *Acta Crystallogr., Sect. E* **2003**, *59*, 378−380.
[10] G. Cordier, H. Schäfer, *Rev. Chim. Miner.* **1981**, *18*, 218−223.
[11] H. A. Graf, H. Schäfer, *Z. Naturforsch., Teil B* **1972**, *27*, 735−739.
[12] A. V. Powell, S. Boissiere, A. M. Chippindale, *Chem. Mater.* **2000**, *12*, 182−187.
[13] G. Cordier, C. Schwidetzky, H. Schäfer, *J. Solid State Chem.* **1984**, *54*, 84−88.
[14] W. Bensch, M. Schur, *Z. Naturforsch., Teil B* **1997**, *52*, 405−409.
[15] G. Dittmar, H. Schäfer, *Z. Anorg. Allg. Chem.* **1977**, *437*, 183−187.
[16] B. Eisenmann, H. Schäfer, *Z. Naturforsch., Teil B* **1979**, *34*, 383−385.
[17] J. S. Swinnea, A. J. Tenorio, H. Steinfink, *American Mineralogist* **1985**, *70*, 1056−58.
[18] A. V. Powell, R. Paniagua, P. Vaquerio, A. M. Chippindale, *Chem. Mater.* **2002**, *14*, 1220−1224.
[19] R. Stähler, B.-D. Mosel, H. Eckert, W. Bensch, *Angew. Chem.* **2002**, *114*, 4671−4673; *Angew. Chem. Int. Ed.* **2002**, *41*, 4487−4489.
[20] R. Stähler, C. Näther, W. Bensch, *Acta Crystallogr., Sect. C* **2001**, *57*, 26−27.
[21] R. Stähler, W. Bensch, *Eur. J. Inorg. Chem.* **2001**, 3073−3078.
[22] X. Wang, A. J. Jacobson, F. Liebau, *J. Solid State Chem.* **1998**, *140*, 387−395.
[23] G. M. Sheldrick, *SHELXS-97*, University of Göttingen, **1992**.
[24] G. M. Sheldrick, *SHELXL-97*, University of Göttingen, **1997**.
[25] A. L. Spek, *PLATON, A Multipurpose Crystallographic Tool*, Utrecht University, Utrecht, The Netherlands, **2000**.
[26] A. D. Becke, *Phys. Rev. A* **1988**, *38*, 3098.
[27] A. D. Becke, *J. Chem. Phys.* **1993**, *98*, 1372.
[28] A. D. Becke, *J. Chem. Phys.* **1993**, *98*, 5648.
[29] T. H. Dunning, Jr., P. J. Hay in *Modern Theoretical Chemistry* (Ed.: H. F. Schaefer III), Plenum, New York, **1976**.
[30] P. J. Hay, W. R. Wadt, *J. Chem. Phys.* **1985**, *82*, 270 and 299.
[31] W. R. Wadt, P. J. Hay, *J. Chem. Phys.* **1985**, *82*, 284.
[32] M. J. Frisch, G. W. Trucks, H. B. Schlegel, G. E. Scuseria, M. A. Robb, J. R. Cheeseman, V. G. Zakrzewski, J. A. Montgomery, Jr., R. E. Stratmann, J. C. Burant, S. Dapprich, J. M. Millam, A. D. Daniels, K. N. Kudin, M. C. Strain, O. Farkas, J. Tomasi, V. Barone, M. Cossi, R. Cammi, B. Mennucci, C. Pomelli, C. Adamo, S. Clifford, J. Ochterski, G. A. Petersson, P. Y. Ayala, Q. Cui, K. Morokuma, P. Salvador, J. J. Dannenberg, D. K. Malick, A. D. Rabuck, K. Raghavachari, J. B. Foresman, J. Cioslowski, J. V. Ortiz, A. G. Baboul, B. B. Stefanov, G. Liu, A. Liashenko, P. Piskorz, I. Komaromi, R. Gomperts, R. L. Martin, D. J. Fox, T. Keith, M. A. Al-Laham, C. Y. Peng, A. Nanayakkara, M. Challacombe, P. M. W. Gill, B. Johnson, W. Chen, M. W. Wong, J. L. Andres, C. Gonzalez, M. Head-Gordon, E. S. Replogle, J. A. Pople, *GAUSSIAN98* Rev. A.11; Gaussian Inc., Pittsburgh, **2001**.

Received December 4, 2003
Early View Article
Published Online April 7, 2004

4.3 Ergebnisse und Publikationen zur Variation des Chalkogenatoms

4.3.1 Die Verbindung $[C_6H_{21}N_4][Sb_9S_{14}O]$

Zusammenfassung der Veröffentlichung *„[$C_6H_{21}N_4$][$Sb_9S_{14}O$]: The first non centrosymetric open Sb-S framework containing the new [SbS_2O] building unit“*.

Die Darstellung von $[C_6H_{21}N_4][Sb_9S_{14}O]$ erfolgte unter solvothermalen Bedingungen mit einem Eduktgemisch aus Sb_2O_3 (0.5 mmol) und S (3 mmol) und 4 ml 50 %iger tren-Lösung. Das Reaktionsgemisch wurde 7 Tage bei 150 °C erhitzt, als Produkt wurden rote Kristalle (Ausbeute 70 % bezogen auf Antimon) erhalten.

Die Verbindung kristallisiert in der nicht-centrosymmetrischen Raumgruppe $Cmc2_1$ mit vier Formeleinheiten pro Elementarzelle. Das kettenförmige 1-dimensionale $[Sb_9S_{14}O]^{3-}$-Anion und ein dreifach protoniertes tren-Molekül stellen die prinzipiellen Struktureinheiten dar. Das Anion wird aus vier SbS_3-Pyramiden und einer bisher unbekannten SbS_2O-Einheit gebildet. Diese Einheiten sind über gemeinsame Ecken verknüpft und das Anion weist 10-gliedrige Ringe als Strukturmotiv auf. In diesen Ringen befindet sich das tren-Molekül, welches als tetra-dentater „Ligand“ um das Sauerstoffatom angeordnet ist. Der kürzeste Abstand zwischen den Ketten beträgt 3.25 Å, so dass bei Berücksichtigung schwacher Sb-S-Kontakte Schichten in der (001)-Ebene ausgebildet werden (Abb. 4.7, links).

DTA-TG-Experimente ergaben, dass sich die Verbindung $[C_6H_{21}N_4][Sb_9S_{14}O]$ ab einer Temperatur von 220 °C in zwei endothermen Stufen zersetzt wird. Der Gesamtmassenverlust beträgt 11.04 %. In dem grauen Rückstand konnten elementares Sb und Sb_2S_3 mit Röntgenpulverbeugung nachgewiesen werden.

Eine Auswertung der UV/Vis-Spektren nach der Methode von Kubelka-Munk ergibt für $[C_6H_{21}N_4][Sb_9S_{14}O]$ eine Bandlücke von 2.03 eV, so dass die Verbindung als optischer Halbleiter angesehen werden kann (Abb. 4.7, rechts).

Um die Ergebnisse der Einkristallstrukturanalyse zu untermauern, wurden Mössbauerexperimente durchgeführt. Der Vergleich mit den Spektren von SbS_2O (Kermesit) und Sb_2S_3 als Vergleichssubstanzen und eine Anpassung an die aufgenommenen

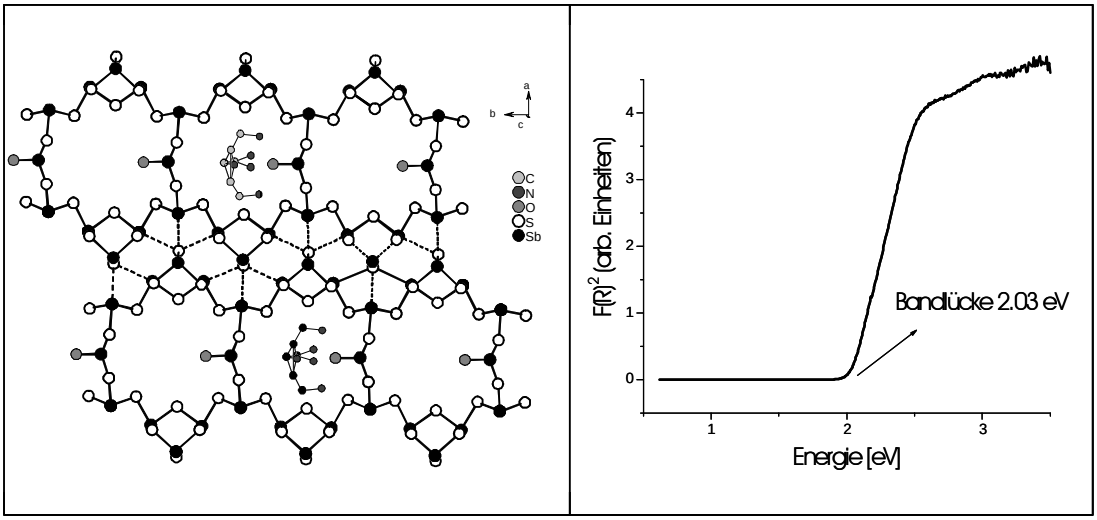

Abbildung 4.7: Kettenstruktur der Verbindung $[C_6H_{21}N_4][Sb_9S_{14}O]$, schwache Sb-S-Bindungen gestrichelt (links), Bestimmung der Bandlücke von $[C_6H_{21}N_4][Sb_9S_{14}O]$ (rechts)

Spektren zeigt eindeutig die Anwesenheit der SbS_2O-Einheit, welche als eigene Spezies im Mössbauerspektrum angefittet werden konnte.

Abschließend sind zwei Punkte hervorzuheben. Erstens ist die in der Struktur enthaltene SbS_2O-Einheit bisher weder in Mineralien noch in synthetisch dargestellten Verbindungen beobachtet worden. Die einzigen bis dato bekannten SbS_xO_y-Einheiten haben die Zusammensetzung $SbSO_2$ und werden zum Beispiel in Kermesit [51] oder in $Pb_{14}Sb_{30}S_{54}O_5$ [52] gefunden.

Zum zweiten wurde die gewünschte Modifizierung der Eigenschaften nicht erreicht. Die physikalischen Eigenschaften wie z.B. die optische Bandlücke und das thermische Zersetzungsverhalten sind mit denen von Thioantimonaten vergleichbar. Eine Ladungsneutralität der Netzwerkstruktur, für die das Vorhandensein von -OH-Gruppen erforderlich wäre, wird nicht beobachtet.

European Journal of Inorganic Chemistry

$[C_6H_{21}N_4][Sb_9S_{14}O]$: The first non centro-symmetric open Sb-S framework containing the new $[SbS_2O]$ building unit

Ragnar Kiebach[1)], Christian Näther[1)], C. Peter Sebastian[2)], Bernd D. Mosel[3)], Rainer Pöttgen[2)] and Wolfgang Bensch[1*)]

1) Institut für Anorganische Chemie der Christian-Albrechts Universität zu Kiel, Olshausenstraße 40, 24098 Kiel, Germany

2) Institut für Anorganische und Analytische Chemie and NRW Graduate School of Chemistry, Westfälische Wilhelms-Universität Münster, Corrensstrasse 30, 48149 Münster, Germany

3) Institut für Physikalische Chemie, Westfälische Wilhelms Universität Münster, Corrensstrasse 30, 48149 Münster, Germany

[*] Prof. Dr. W. Bensch
Institut für Anorganische Chemie
Universität Kiel
Olshausenstraße 40
D-24098 Kiel
Fax: +49-(0)431-880-1520
e-Mail: wbensch@ac.uni-kiel.de

Keywords: Antimony oxysulfides, Hydrothermal Synthesis, Mössbauer spectroscopy, Crystal structure.

Abstract:

$[C_6H_{21}N_4][Sb_9S_{14}O]$ represents the first known thio-oxoantimonate with an organic ion acting as structure director. It contains the hitherto unknown $[SbS_2O]$ unit as a structural motif. The template acts as tetra-dentate ligand around the O atom of the $[SbS_2O]$ group. Depending on the value chosen for the Sb-S bond length the material contains a 1-, 2- or 3-dimensional anion. Crystal structure, thermal investigations, physical properties and results from Mössbauer spectroscopy will be presented.

Introduction:

The variety of microporous polyhedral framework solids has increased severely in the last years.[1] In addition to the well known microporous materials like aluminosilicates and aluminophosphates the group of thioantimonates and antimony oxysulfides blazed a trail to attractive candidates for applications. In the last years remarkable properties like tuneable optical band gaps, superconductivity or photoconductivity were discovered in the group of thioantimonates and/or antimony sulfides.[2-9] Another advantage of this group of compounds compared to aluminosilicates and aluminophosphates is the variety of different primary building units (PBUs), their flexibility to adapt the requirements of the structure directors and the variable dimensionality.[10-18] The combination of properties of oxidic materials with that of sulfides will lead to a new class of materials with designable and interesting properties making them highly attractive for applications like ion-exchanger or catalysts. The so fare unknown $[SbS_2O]$ unit found in $[C_6H_{21}N_4][Sb_9S_{14}O]$(**1**) can be regarded as one "missing link" between oxide and sulfide materials and as a step towards a new class of materials. Here we report the synthesis and characterisation of the new antimony oxysulfide $[C_6H_{21}N_4][Sb_9S_{14}O]$.

Results and discussion:

Crystal Structure:

The compound was prepared under solvothermal conditions using tris(2-aminoethyl)amine (*tren*) as solvent and as structure directing molecule. It crystallises in the non centrosymmetric orthorhombic space group C*mc*2_1 (see experimental section) and consists of infinite $[Sb_9S_{14}O]^{3-}$ chains with protonated amine molecules as counterions. The anion is constructed by interconnection of four unique $[SbS_3]$ and one unique $[SbS_2O]$ group sharing common corners. The $[SbS_2O]$ unit was never observed before in oxysulfide minerals [19-22] or in synthetic antimony oxysulfides. The $[SbS_3]$ and the $[SbS_2O]$ units have typical trigonal pyramidal geometry with Sb-S bond lengths between 2.407(2) and 2.530(2) Å and corresponding S-Sb-S angles between 83.92(8) and 101.05(8) °. The Sb-O bond in the $[SbS_2O]$ of 1.956(10) Å is significantly shorter than the Sb-S bonds. The bond lengths and angles are comparable to those found in other thioantimonates and in antimony

oxysulfides.[2-22] Eight [SbS_3] trigonal pyramids and 2 [SbS_2O] units are joined to form a 10-membered ring in which one tren molecule is located. The diameter of the pore is 7.66 Å × 8.27 Å measured from coordinate to coordinate (Figure 1a). The triply protonated *tren* molecule acts like a tetra-dentate ligand around the oxygen atom of the [SbS_2O] group (Figure 1) reflecting the structure directing effect. The 1-D $[Sb_9S_{14}O]^{3-}$ chain is directed along the *b* axis (Figure 1) and is constructed by condensation of the 10-membered rings mentioned above. The distance between the chains is approximately 3.25 Å and taking the longer Sb-S distances into account layers are formed. The shortest interlayer distance amounts to 3.47 Å. A three dimensional arrangement is achieved by six N-H···S and two N-H···O hydrogen bonds. If the long Sb-S separations up to 3.7 Å are treated as weak interactions the network is 3-dimensional (Figure 1b).

Thermal Investigations:

The thermal stability was investigated using simultaneous differential thermoanalysis (DTA) and thermogravimetry (TG) under an argon atmosphere in the range from 25 to 500°C (Figure 2). The material decomposes in two not well resolved steps with a total mass loss of 11.04% at T_{onset} = 220°C. The decomposition reaction is accompanied by an endothermic event at T_P = 261 °C (T_P = peak temperature). In the grey residue only small amounts of organic components were found (C: 0.254%; H: 0.022%; N: 0.133%; CHN_{sum} = 0.406%). The experimental mass loss of 11.04% is in agreement with that calculated for the removal of the organic cations (Δm_{theo} = 9.67%), the difference of 1.37 % is caused by the emission of H_2S, which was detected in mass spectra. In the X-ray powder pattern of the decomposition products crystalline Sb and Sb_2S_3 could be identified.

Optical properties:

The optical band gap was calculated from UV/Vis data after the method of Kubelka and Munk. An absorption edge is observed at 2.03 eV (600 nm) corresponding to the red colour of $[C_6H_{21}N_4][Sb_9S_{14}O]$ and the material is an optical semi-conductor. In combination with the non-centrosymmetric space group $[C_6H_{21}N_4][Sb_9S_{14}O]$ is a potential candidate for NLO effects.

Mössbauer spectroscopy:

To support the results from single crystal structure refinement ^{121}Sb Mössbauer spectroscopic experiments were performed. As references Sb_2S_3 and Sb_2S_2O (kermesite, contains [SbS_3] and [$SbSO_2$] units) were measured. The ^{121}Sb Mössbauer spectra of Sb_2S_3, Sb_2S_2O (room temperature data) and of $[C_6H_{21}N_4][Sb_9S_{14}O]$ (20 K data) are presented in Figure 3. The fitting parameters are listed in Table 1. The spectrum of Sb_2S_3 shows a single signal at an isomer shift of –14.44(2) mm/s, in good agreement with the literature data.[23] Kermesite, Sb_2S_2O, shows a smaller isomer shift of –12.64(3) mm/s, indicating a smaller *s*-electron density at the antimony nucleus. A small Sb(V)

impurity was included in the fit of the spectrum. Due to the low space group symmetry (triclinic) [24], a small quadrupole splitting occurs for the Sb(III) site (Table 1).

Although the $[C_6H_{21}N_4][Sb_9S_{14}O]$ structure has five crystallographically independent Sb(III) sites, the ^{121}Sb spectrum can be fit with a single signal at an isomer shift of –12.66(3) mm/s. The experimentally observed line width of 4.76(8) mm/s is somewhat enhanced and accounts for the superposition of the five signals. Unfortunately, it was not possible to fit the $[SbS_2O]$ unit as an independent site in the ^{121}Sb Mössbauer spectrum.

Experimental section:

Synthesis:

$[C_6H_{21}N_4][Sb_9S_{14}O]$ was synthesised under hydrothermal conditions using Sb_2O_3 (145 mg, 0.5 mmol) and elemental S (96 mg, 3 mmol in 4ml of a 50% aqueous solution of *tren*. The mixture was heated to 150°C for 7 days in Teflon-lined steel autoclaves (volume ca. 30 ml). The homogeneous product consisting of red crystals was filtered off, washed with distilled water, ethanol and acetone and was dried on air. The yield based on Sb is about 70%. Typical dimensions of the crystals are $0.7 \cdot 0.2 \cdot 0.2$ mm^3. The compound is stable on air for several months.

X-Ray crystallographic study:

X-ray structure analysis and crystallographic data for **1**: The X-ray single-crystal data for **1** were collected using an Imaging Plate Diffraction System (IPDS) from STOE at 293 K. The intensities were corrected for Lorentz, polarisation and absorption effects. Structure solution was performed using SHELXS-97 [25]. Refinement was done against F2 using SHELXL-97.[26]. The non-hydrogen atoms were refined with anisotropic displacement parameters. The hydrogen atoms were positioned with idealised geometry and refined with isotropic displacement parameters using the riding model. Selected crystal data and details of the structure determination are listed in table 1.

Crystallographic data (excluding structure factors) for the structure reported in this paper have been deposited with the Cambridge Crystallographic Data Centre as supplementary Publication no. CCDC-275176. Copies of the data can be obtained free of charge on application to CCDC, 12 Union Road, Cambridge CB21EZ, UK (fax: (+44)1223-336-033; E-mail: deposit@ccdc.cam.ac.uk).

Thermal investigation:

DTA-TG analyses were performed using a Netzsch STA 429 DTA-TG device. The samples were heated in Al_2O_3 crucibles at a rate of 4 K$\cdot$min^{-1} to 600°C under a flow of argon of 100 ml min^{-1}.

Powder diffraction:

X-Ray powder diffraction experiments were performed using a STOE STADI P transmission powder diffractometer with a position sensitive detector and Cu-K_α radiation (λ= 1.540598 Å).

UV/Vis spectroscopy:

UV/Vis spectroscopic investigations were conducted at room temperature using a UV-VIS-NIR two-channel spectrometer Cary 5 from Varian Techtron Pty., Darmstadt. The optical properties of the compounds were investigated by studying the UV/Vis reflectance spectrum of the powdered sample. The absorption data were calculated using the Kubelka-Munk relation for diffuse reflectance data. $BaSO_4$ powder was used as reference material.

Mössbauer spectroscopy:

A $Ba^{121m}SnO_3$ source was used for the Mössbauer spectroscopic experiments. The measurements were carried out in a helium bath cryostat; at 20 K for $[C_6H_{21}N_4][Sb_9S_{14}O]$, and at room temperature for Sb_2S_3 and Sb_2S_2O. The temperature was controlled by a resistance thermometer (±0.5 K accuracy). The Mössbauer source was kept at room temperature. The samples were enclosed in small PVC containers at a thickness corresponding to approximately 10 mg Sb/cm^2.

Acknowledgement:

The state of Schleswig-Holstein and the Deutsche Forschungsgemeinschaft are gratefully acknowledged for financial support.

Captions:

Figure 1a: The $[Sb_9S_{14}O]^{3-}$ chains directed along the *b*-axis. Cations are only shown in the middle. Hydrogen atoms omitted for clarity.

1b: Crystal structure of $[C_6H_{21}N_4][Sb_9S_{14}O]$ with view along the *c*-axis, long Sb-S bonds up to 3.7 Å are considered.

Figure 2: DTA, TG and DTG curves for $[C_6H_{21}N_4][Sb_9S_{14}O]$, given are the mass loss in % and the peak temperature T_p in °C.

Figure 3: Sb^{121} Mössbauer spectra of Sb_2S_3 (top), SbS_2O (middle), $[C_6H_{21}N_4][Sb_9S_{14}O]$ (bottom).

Tables:

Table 1. Crystal data and selected results of the structure refinement for $[C_6H_{21}N_4][Sb_9S_{14}O]$

Empirical formula	$C_6H_{21}N_4OS_{14}Sb_9$
Crystal Colour	red
Crystal Habit	polyhedral
Molecular Mass [g/mol]	1709.86
Crystal System	orthorhombic
Space Group	C*mc*2_1
a [Å]	29.679(2)
b [Å]	9.9798(6)
c [Å]	11.7155(7)
V [Å^3]	3470.1(4)
Z	4
T [K]	293
λ(Mo-K$_\alpha$) [Å]	0.71073
$d_{calcd.}$ [Mg·cm^{-3}]	3.273
μ((Mo-Kα) [mm^{-1}]	7.749
F(000)	3104
Reflections collected	18706
Independent reflections	4217
Reflections with Fo > 4σ(Fo)	3718
wR2 for all reflections[a]	0.0897
R1 for reflections with Fo > 4 σ (Fo)[b]	0.0346
Goodness of fit	1.028
Flack x-parameter	-0.05(4)
Largest diff. peak / hole [e·Å^{-3}]	2.34 /-1.42

[a] $wR2 = [\Sigma[w(F_O^2 - F_c^2)^2] / \Sigma[w(F_o^2)^2]]^{1/2}$ [b] $R1 = \Sigma \; ||Fo| - |Fc|| / \Sigma |Fo|$

Table 2. Selected bond lengths[Å] and angles [°] for $[C_6H_{21}N_4][Sb_9S_{14}O]$]

Sb(1)-S(4)	2.407(2)	Sb(1)-S(1)	2.477(3)
Sb(1)-S(3)	2.493(2)	Sb(2)-S(2)	2.474(2)
Sb(2)-S(1)	2.487(2)	Sb(2)-S(5)	2.492(2)
Sb(3)-S(2)	2.464(2)	Sb(3)-S(3)	2.475(2)
Sb(3)-S(6)	2.530(2)	Sb(4)-S(5)	2.426(3)
Sb(4)-S(6)	2.450(2)	Sb(4)-S(7)	2.488(2)
Sb(5)-O(1)	1.956(10)	Sb(5)-S(7)	2.437(3)
Sb(5)-S(7)	2.437(3)	S(5)-Sb(4)	2.426(3)
N(1)-C(1)	1.499(18)	C(1)-C(2)	1.485(16)
C(2)-N(2)	1.492(14)	N(2)-C(3)	1.50(2)
C(3)-C(4)	1.41(3)	C(4)-N(3)	1.37(3)
S(4)-Sb(1)-S(1)	95.94(8)	S(4)-Sb(1)-S(3)	95.01(7)
S(1)-Sb(1)-S(3)	95.71(8)	S(2)-Sb(2)-S(1)	101.05(8)
S(2)-Sb(2)-S(5)	83.98(8)	S(1)-Sb(2)-S(5)	89.57(9)
S(2)-Sb(3)-S(3)	99.19(8)	S(2)-Sb(3)-S(6)	83.92(8)
S(3)-Sb(3)-S(6)	89.23(8)	S(5)-Sb(4)-S(6)	96.63(9)
S(5)-Sb(4)-S(7)	95.40(10)	S(6)-Sb(4)-S(7)	93.31(8)
O(1)-Sb(5)-S(7)	96.5(3)	O(1)-Sb(5)-S(7)	96.5(3)
S(7)-Sb(5)-S(7)	86.84(12)	Sb(1)-S(1)-Sb(2)	98.86(8)
Sb(3)-S(2)-Sb(2)	105.48(8)	Sb(3)-S(3)-Sb(1)	98.35(8)
Sb(4)-S(5)-Sb(2)	101.96(9)	Sb(4)-S(6)-Sb(3)	100.91(8)
Sb(5)-S(7)-Sb(4)	109.60(11)	C(2)-C(1)-N(1)	111.4(10)
C(1)-C(2)-N(2)	111.3(10)	C(2)-N(2)-C(2)	108.5(12)
C(2)-N(2)-C(3)	112.3(8)	C(2)-N(2)-C(3)	112.3(8)
C(4)-C(3)-N(2)	114.4(16)	N(3)-C(4)-C(3)	130.9(18)

Table 3.

^{121}Sb Mössbauer spectra of Sb_2S_3, Sb_2S_2O (room temperature data) and $[C_6H_{21}N_4][Sb_9S_{14}O]$ (20 K data). δ = isomer shift, ΔE_Q = electric quadrupole interaction parameter, Γ = experimental line width, χ^2 = goodness-of-fit

Compound	δ_1 (mm/s)	ΔE_Q (mm/s)	Γ_1 (mm/s)	δ_2 (mm/s)	Γ_2 (mm/s)	χ^2
Sb_2S_3	-14.44(2)	–	3.92(6)	–	–	1.13(2)
Sb_2S_2O	-12.64(3)	-2.53(9)	4.24(1)	0.63(2)	2.03(5)	1.05(1)
$[C_6H_{21}N_4][Sb_9S_{14}O]$	-12.66(3)	–	4.76(8)	–	–	1.08(1)

References:

[1] A. K. Cheetham, G. Férey, T. Loiseau, *Angew. Chem. Int. Ed.* **1999**, 38, 3268-3292.

[2] M. Schaefer, R. Stähler, R. Kiebach, C. Näther, W. Bensch, *Z. Anorg. Allg. Chem.* **2004**, *630*, 1816-1822.

[3] C.-S. Lee, A. Safa-Sefat, J.E. Greedan, H. Kleinke, *Chem. Mater.* **2003**, *15*, 780-786.

[4] F. Starrost, E.E. Krasovskii, W. Schattke, U. Simon, X. Wang, F. Liebau, *Phys. Rev. Lett*. **1998**, *80*, 3316-3319.

[5] X. Wang, F. Liebau, *Eur. J. Solid State Inorg. Chem.* **1998**, *15*, 27-37.

[6] F. Liebau, *Z. Kristallogr.* **2000**, *215*, 381-383.

[7] U. Simon, V. Gasparian, *Phys. Stat. Sol. B* **2000**, *218*, 151-154.

[8] U. Simon, F. Schüth, S. Schunk, X. Wang, F. Liebau, *Angew. Chem. Int. Ed.* **1997**, *36*, 1121-1124.

[9] F. Starrost, , E.E. Krasovskii, W. Schattke, J. Jockel, U. Simon, R. Adelung, L. Kipp, *Phys. Rev. B* **2000**, *61*, 15697-15706.

[10] R. Stähler, C. Näther, W. Bensch, *J. Solid State Chem.* **2003**, *174*, 264-275.

[11] V. Spetzler, R. Kiebach, C. Näther, W. Bensch, *Z. Anorg. Allg. Chem*. **2004**, *630*, 2398-2404.

[12] R. Kiebach, C. Näther, W. Bensch, *Z. Naturforsch.* **2004**, *59b*, 1314-1319.

[13] R. Kiebach, C. Näther, W. Bensch, R.-D. Hoffmann, R. Pöttgen, *Z. Anorg. Allg. Chem*. **2003**, *629*, 532-538.

[14] P. Vaqueiro, A. M. Chippindale, A. V. Powell, *Inorg. Chem.* **2004**, *43*, 7963-7965.

[15] A.V. Powell, S. Boissiere, A. M. Chippindale, *Chem. Mater.* **2000**, *12*, 182-187.

[16] A.V. Powell, R. Paniagua, P. Vaqueiro, A. M. Chippindale, *Chem. Mater.* **2002**, *12*, 1220-1224.

[17] J.B. Parise, Y. Ko, *Chem. Mater.* **1992**, *4*, 1446-1450.

[18] G. Dittmar, H. Schäfer, *Z. Anorg. Allg. Chem.* **1977**, *437*,183-187.

[19] E.M. Baumgardt, V. Kupcik, *J. Cryst. Growth* **1977**, *37(3)*, 346-348.

[20] V. Kupcik*, Naturwiss.* **1967**, *54(5)*, 114.

[21] A. Meerschaut, P. Palvadeau, Y. Molëo, P. Orlandi, *Eur. J. Mineral.* **2001**, *13*, 779-790.

[22] Y. Molëo, A. Meerschaut, P. Orlandi, P. Palvadeau, *Eur. J. Mineral.* **2000**, *12*, 835-846.

[23] P. E. Lippens, *Solid State Commun.* **2000**, *113*, 399-403.

[24] P. Bonazzi, S. Menchetti, C. Sabelli, *Neues Jahrbuch für Mineralogie, Monatshefte* **1987**, 557-565.

[25] G. M. Sheldrick, SHELXS-97, program for crystal structure determination, University of Göttingen (Germany), 1997.

[26] G. M. Sheldrick, SHELXL-97, program for the refinement of crystal structures, University of Göttingen (Germany), 1997.

Figures:

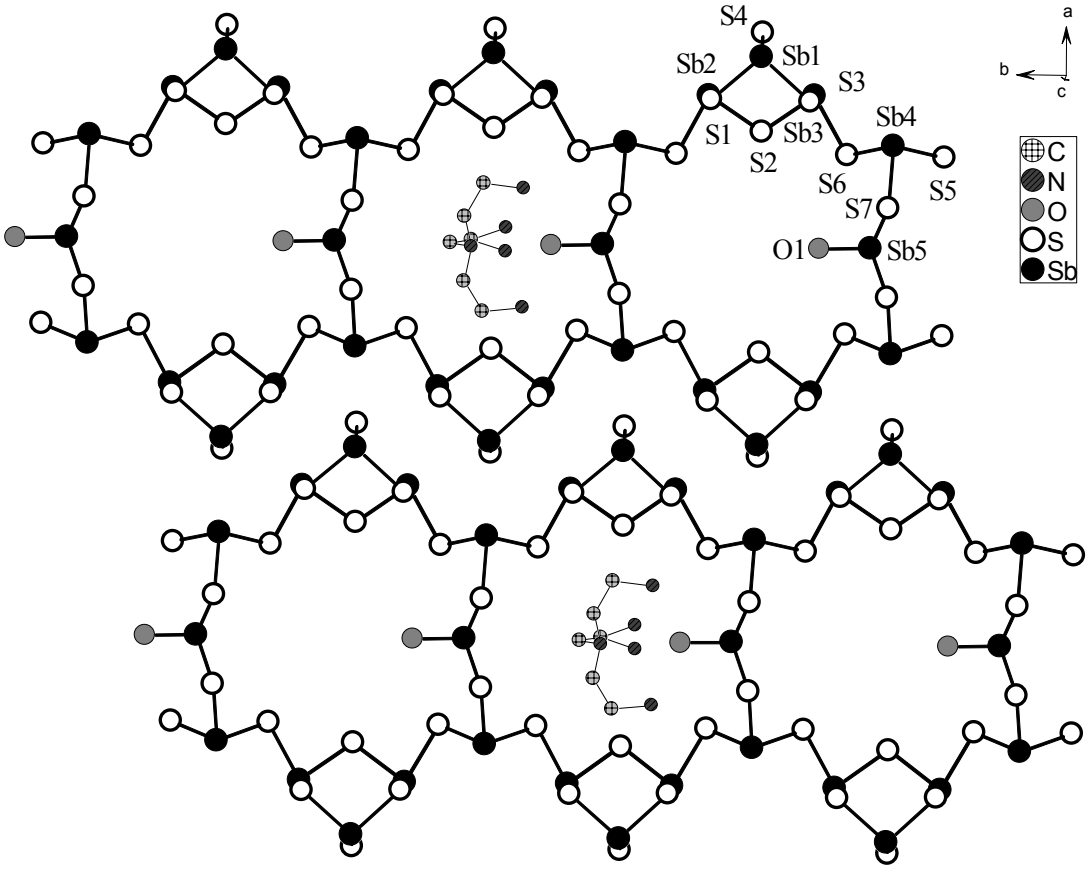

Fig. 1a

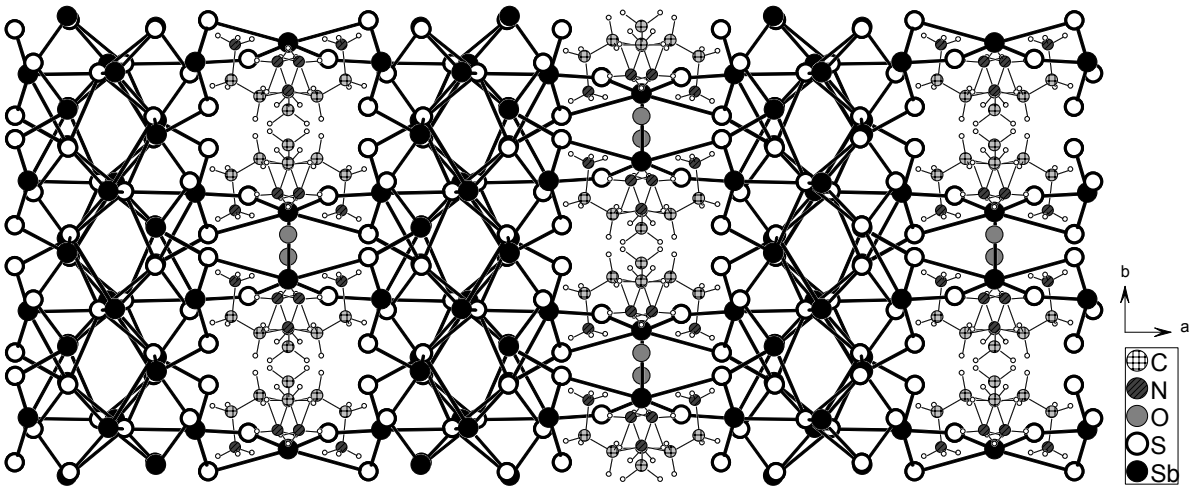

Fig. 1b

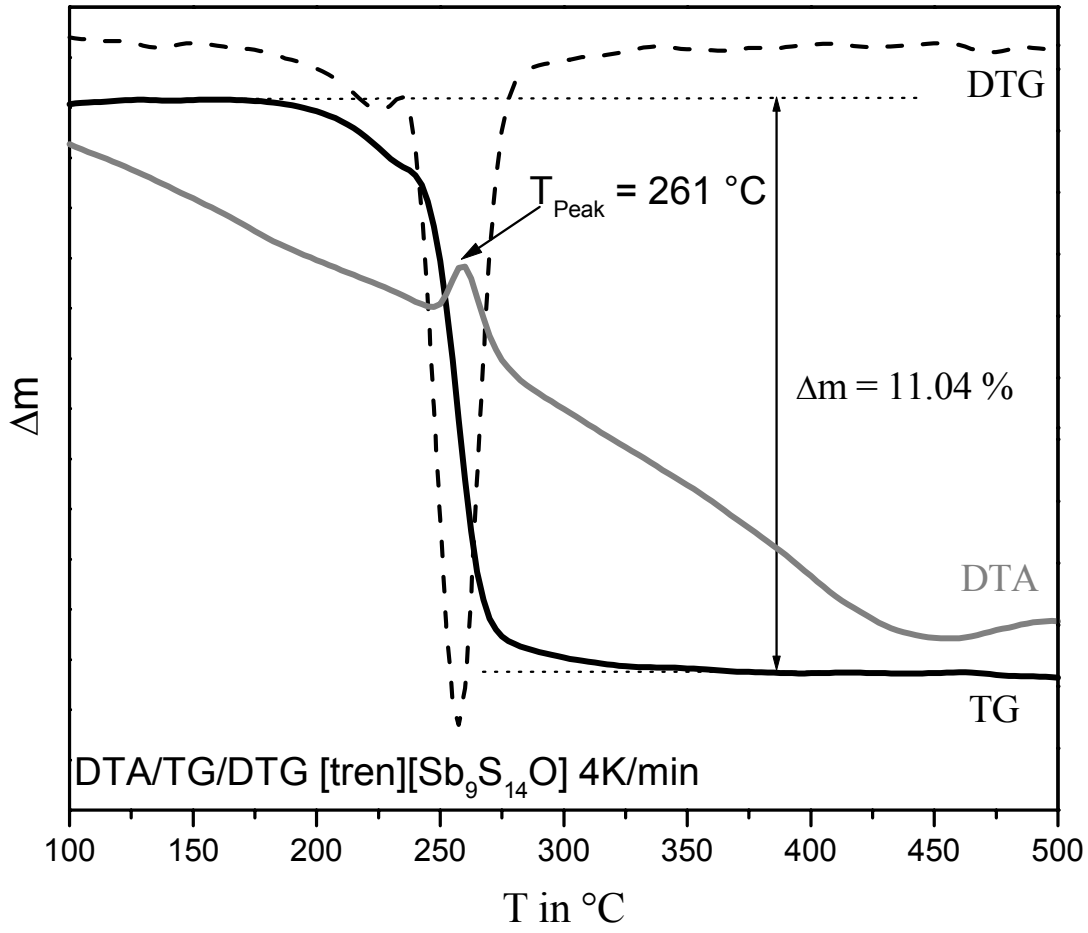
DTG
T Peak = 261 °C
Δm = 11.04 %
DTA
TG
DTA/TG/DTG [tren][Sb9S14O] 4K/min
Δm
100
150
200
250
300
350
400
450
500
T in °C

Fig. 2

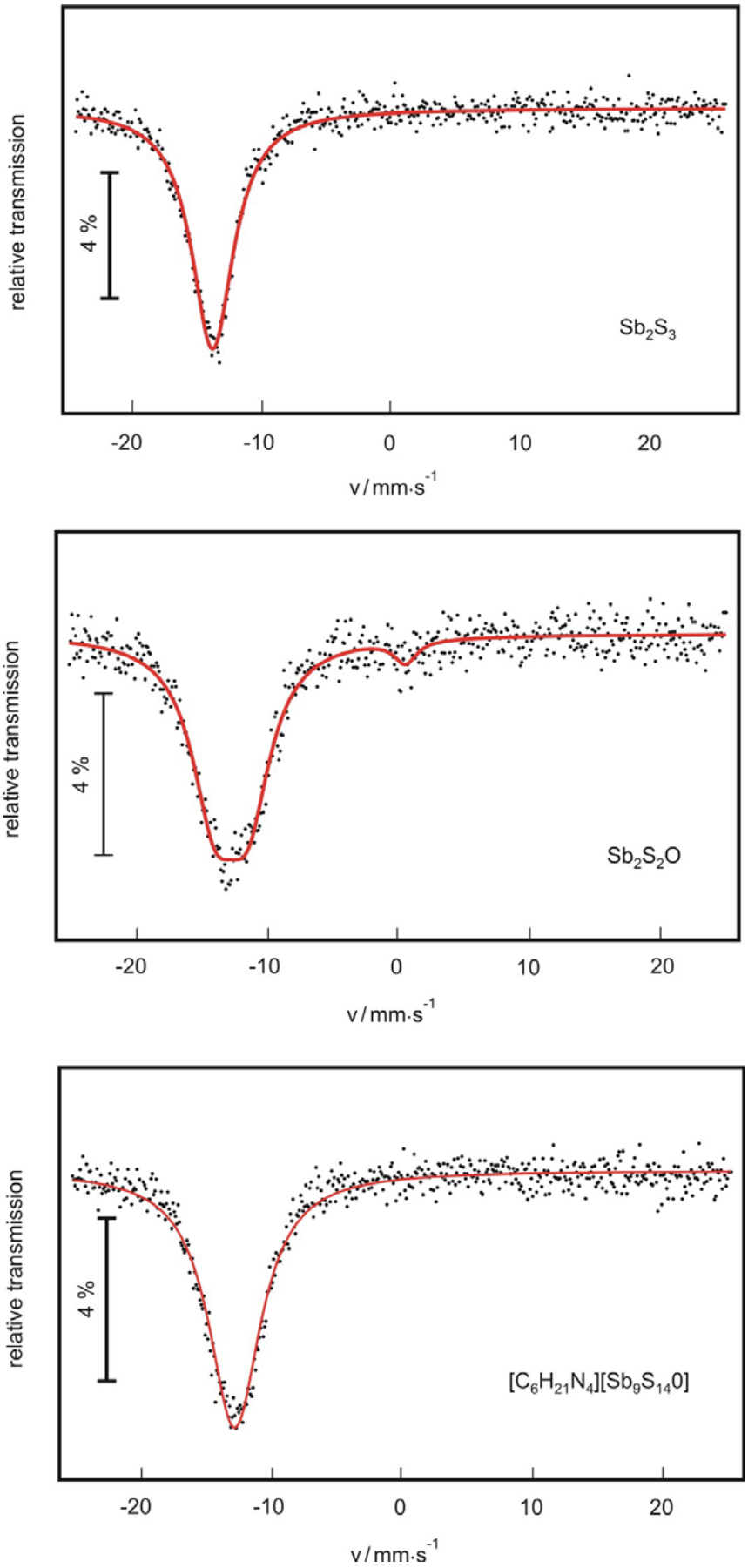
relative transmission
4 %
Sb_2S_3
-20
-10
0
10
20
v / mm·s^{-1}
relative transmission
4 %
Sb_2S_2O
-20
-10
0
10
20
v / mm·s^{-1}
relative transmission
4 %
$[C_6H_{21}N_4][Sb_9S_{14}0]$
-20
-10
0
10
20
v / mm·s^{-1}

Fig. 3

4.3.2 Die Verbindung $[trenH_3]_2[tren]_{0.33}[Sb_6V_{15}O_{42}]\cdot xH_2O$ (3<x<5)

Zusammenfassung des Manuskriptes „*$[trenH_3]_2[tren]_{0.33}[Sb_6V_{15}O_{42}]\cdot xH_2O$ (3<x<5) – The Antimony Analogoue to the Single Molecular Magnet $K_6[As_6V_{15}O_{42}(H_2O)]\cdot 8H_2O$*".

Die Darstellung der Verbindung erfolgte unter solvothermalen Bedingungen bei 150 °C. 5.13 mmol NH_4VO_3 und 2.06 mmol Sb_2O_3 wurden in 4 ml einer 50 %igen tren-Lösung als Edukte vorgelegt und in Stahlautoklaven mit Tefloneinsätzen 7 Tage erhitzt. Das Produkt wurde in Form braun-grüner oktaedrischer Kristalle erhalten (Abb. 4.8, links), die Ausbeute betrug 70 % bezogen auf Antimon.

Die Verbindung $[trenH_3]_2[tren]_{0.33}[Sb_6V_{15}O_{42}]\cdot xH_2O$ (3<x<5) kristallisiert in der trigonalen Raumgruppe $R\bar{3}$ mit 18 Formeleinheiten pro Elementarzelle. Die Struktur besteht aus isolierten $[Sb_6V_{15}O_{42}]^{6-}$-Clustern und drei kristallographisch unterschiedlichen tren-Molekülen als Gegenionen. Die Anionen sind aus 15 VO_5-Pyramiden und 6 SbO_3-Einheiten als primäre Baueinheiten aufgebaut. Jeweils zwei SbO_3-Einheiten sind über eine gemeinsame Ecke zu einer Sb_2O_5-Gruppe verknüpft. Die VO_5-Pyramiden sind über gemeinsame Kanten verbunden und haben gemeinsame Ecken mit Sb_2O_5-Gruppen. Die Sb_2O_5-Gruppen sind dabei so angeordnet, dass der Abstand zwischen ihnen möglichst groß ist. Die Abmessungen des Clusters betragen ca. 10·10 Å. Die Anionen sind in Form von Schichten in der *ab*-Ebene angeordnet, wobei jeweils ein Cluster von sechs weiteren Clustern umgeben ist. Die Stapelung der Schichten entlang der c-Achse kann mit einer *ABAC*-Sequenz beschrieben werden. Zwischen den Anionschichten werden zwei verschiedene alternierende Aminschichten beobachtet. In der ersten Schicht sind die Stickstoffatome der Amine den Sauerstoffatomen der Cluster zugewandt. In der zweiten Schicht wird genau das Gegenteil beobachtet, die Stickstoffatome sind den Clustern abgewandt angeordnet. Unter Berücksichtigung von Sb-O-Kontakten bis 3 Å kommt es zur Bildung eines „$[Sb_{18}V_{45}O_{126}]$-Superclusters" (Abb. 4.8, rechts), der aus drei einzelnen Clustern besteht. Bei der Verknüpfung entsteht im Zentrum des „Superclusters" ein Sb_3O_3-Ring.

Die thermische Zersetzung erfolgt in zwei Stufen mit einem Gesamtmassenverlust von 15.15 %. In der ersten Stufe wird nur das Kristallwasser emittiert, die Emission

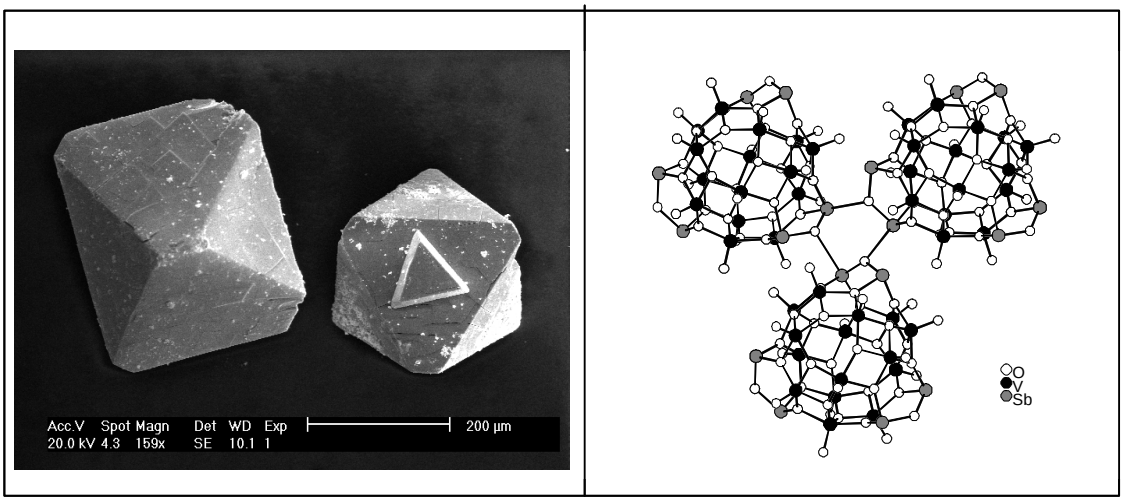

Abbildung 4.8: REM-Aufnahme von Kristallen der Verbindung $[trenH_3]_2[tren]_{0.33}[Sb_6V_{15}O_{42}]\cdot xH_2O$ (3<x<5)(links), $[Sb_{18}V_{45}O_{126}]$-Supercluster in $[trenH_3]_2[tren]_{0.33}[Sb_6V_{15}O_{42}]\cdot xH_2O$ (3<x<5)(rechts)

der tren-Moleklüle erfolgt in der zweiten Stufe. Beide Stufen sind von einem endothermen Signal in der DTA-Kurve begleitet. In dem DTA-Abbauprodukt konnten Sb_2O_3 und V_2O_3 identifiziert werden. Der Wassergehalt variiert von Probe zu Probe, dem entsprechend wird in der TG-Kurve ein variierender Massenabbau in der ersten Stufe beobachtet.

Die intensivste Bande im Ramanspektrum wird bei 961 cm^{-1} beobachtet und kann der V=O-Streckschwingung zugeordnet werden. Weitere V-O-V-Schwingungen werden zwischen 250 cm^{-1} und 360 cm^{-1} beobachtet.

Im UV/Vis-Spektrum werden zwei Absorptionen gefunden. Die erste liegt bei 1.8 eV, die zweite bei 2.11 eV und damit in gutem Einklang mit der braun-grünen Farbe der Verbindung. Am interessantesten ist die strukturelle Ähnlichkeit mit der Verbindung $K_6[As_6V_{15}O_{42}(H_2O)]\cdot 8H_2O$, welche als „Single Molecular Magnet“ intensiv untersucht wurde. In der Verbindung wird ein $[As_6V_{15}O_{42}(H_2O)]^{6-}$-Cluster gefunden, der als As-Analogon zu der Verbindung $[trenH_3]_2[tren]_{0.33}[Sb_6V_{15}O_{42}]\cdot xH_2O$ angesehen werden kann. Magnetmessungen werden zurzeit durchgeführt, das Manuskript befindet sich in der Vorbereitung.

$[trenH_3]_2[tren]_{0.33}[Sb_6V_{15}O_{42}]\cdot xH_2O$ (3<x<5) – The Antimony Analogoue to the Single Molecular Magnet $K_6[As_6V_{15}O_{42}(H_2O)]\cdot 8H_2O$

Ragnar Kiebach, Christian Näther and Wolfgang Bensch [*]

*correspondence address: Prof. Dr. Wolfgang Bensch, Institut für Anorganische Chemie, Christian-Albrechts-Universität Kiel,

Olshausenstr. 40, D-24098 Kiel, Germany

wbensch@ac.uni-kiel.de

RECEIVED DATE (to be automatically inserted after your manuscript is accepted if required according to the journal that you are submitting your paper to)

In the manuscript the solvothermal synthesis, crystal structure, optical, thermal and magnetic properties of $[trenH_3]_2[tren]_{0.33}[Sb_6V_{15}O_{42}]\ xH_2O$ (tren = tris-(2-aminoethyl)-amine) are presented. The title compound represents the first isolated cluster of the $V_{18}O_{42}$ family containing antimony. The anion has a nearly spherical shape and is composed of 15 VO_5 square pyramids and 6 SbO_3 trigonal pyramids. Sb_2O_5 groups are formed by vertex sharing of two SbO_3. The VO_5 pyramids share common edges they have common vertices with the SbO_3 groups. Using the $[V_{18}O_{42}]$ cluster shell as archetype the structure of the $[Sb_6V_{15}O_{42}]^{6-}$ cluster is derived by substituting two VO_5 pyramids by two Sb_2O_5 units leading to the $[Sb^{(III)}_4V^{(IV)}_{16}O_{42}]^{4-}$ moiety. 24 μ_3-O atoms form a cage which can be regarded as a rhombicuboctahedron. The anions are arranged in a layer like fashion in the *ab* plane and they are stacked along the c-axis in an ...ABAC... sequence. Relatively short inter-cluster Sb-O separations are

observed (shortest Sb-O distance: 2.884(8) Å) indicating weak interactions. With these interactions three anions are connected to form a $[Sb_{18}V_{45}O_{126}]$ super cluster. The amine molecules are located in the galleries between successive cluster anions. Two different amine layers are identified in which the tren molecules show different orientations with respect to each other and towards the anions.

Keywords: Antimony; Vanadium oxides; Solvothermal synthesis; Crystal structure; Spectroscopy; Thermal investigation; magnetic properties.

Introduction

There has been much interest in vanadium based oxometallates in the past two decades and their applications due to their potential usage as secondary electrode materials for advanced lithium batteries [1-3] and their interesting properties as inorganic/organic hybrid materials for catalysis and/or sorption [4-7]. One of the most remarkable polyoxovanadate compound is $K_6[As_6V_{15}O_{42}(H_2O)]\cdot 8H_2O$ which was intensively studied due to its molecular nano-magnetic behavior [8-12]. It was reported that $K_6[As_6V_{15}O_{42}(H_2O)]\cdot 8H_2O$ is a single molecular magnet with a low spin system, making the compound of interest for quantum computation [13]. Until now no isolated derivatives of the $V_{18}O_{42}$ family containing Sb were reported, and the only related compounds contain different $[Sb_8V_{14}O_{42}(H_2O)]^{4-}$ clusters which are linked forming one- [14] or two- [15] dimensional networks. Two the best of our knowledge only the crystal structures of antimony vanadates have been reported so far, and investigations including magnetic measurements of such compounds have not been published until now. It can be expected that antimony vanadates with a different composition form a new class of materials with a large potential for several applications. Besides the possible nanoscale magnetic properties of this new group of compounds such clusters also combine two interesting features for catalytic properties. The Keggin-type heteropolycompounds are used as heterogeneous catalysts in oxidation reactions [17] and mixed antimony-vanadium oxides are applied as selective catalysts for the oxidation of o-xylene [18].

The new compound $[trenH_3]_2[tren]_{0.33}[Sb_6V_{15}O_{42}]$ presented in this communication is an example of the rich crystal chemistry of vanadates. This inorganic-organic hybrid compound is the first example containing an isolated $[Sb_6V_{15}O_{42}]^{6-}$ clusters as the main structural feature. In the paper the synthesis, crystal structure, thermal stability, magnetic behavior, Raman and UV/Vis spectra are reported.

Experimental details

Synthesis

The solvothermal synthesis was performed using NH_4VO_3 (Merck, 600 mg, 5 mmol), Sb_2O_3 (Merck, 600 mg, 2 mmol) and 4 ml of a 50 % tren solution as starting agents in a teflon-lined steel autoclave with an inner volume of 30 ml. The autoclave was heated 7 days at 150 °C yielding brown-greenish single crystals (Figure 1) of $[trenH_3]_2[tren]_{0.33}[Sb_6V_{15}O_{42}]$. The crystalline product was filtered off, washed with acetone and water and cleaned in an ultra-sonic bath. The compound is stable on air, in water and acetone. The yield based on Sb is 70 %, no other products were observed in the X-ray powder pattern. Chemical analysis of the product: C: 5.38 %(theo.: 6.69 %), N: 4.04 % (theo 5.20 %), H: 1.78 % (theo 1.92 %).

Structure determination

X-ray intensities were collected on a STOE Imaging Plate Diffraction System (IPDS-1) using monochromatized MoK_α radiation (λ = 0.7107 Å). The intensities were corrected for Lorentz, polarization and absorption effects. Structure solution was performed using SHELXS-97 [19]. Refinement was done against F^2 with SHELXL-97 [20]. Sb, V, O, C and N atoms were refined with anisotropic displacement parameters, except C(21), C(22), N(21), N(22) which are located on special positions. The hydrogen atoms were positioned with idealized geometry and refined with isotropic displacement parameters using a riding model. Disordered water molecules could not be located.

Technical details of data acquisition are listed in Table 1. Atomic coordinates and equivalent displacement parameters are given in Table. 2. The most important distances are collected in Table 3.

X-ray Powder Diffractometry

The X-ray powder patterns were recorded on a STOE Stadi-P diffractometer (Co-K_α radiation, λ = 1.78897 Å) in transmission geometry.

Thermoanalytical Measurements

DTA-TG analyses were performed using a Netzsch STA 429 DTA-TG device. The samples were heated in Al_2O_3 crucibles at a rate of 8 K·min^{-1} to 600°C under a flow of nitrogen of 75 ml min^{-1}.

Raman Spectroscopy

Raman spectra were recorded in the region 100 to 3500 cm^{-1} with a Bruker IFS 66 Fourier Transform Raman spectrometer (wavelength: 541.5 nm).

Solid-State UV/Vis/NIR Spectroscopy

UV/Vis spectroscopic investigations were conducted at room temperature using a UV-VIS-NIR two-channel spectrometer Cary 5 from Varian Techtron Pty., Darmstadt. The optical properties of the compounds were investigated by studying the UV/Vis reflectance spectrum of the powdered sample. The absorption data were calculated using the Kubelka-Munk relation for diffuse reflectance data. $BaSO_4$ powder was used as reference material.

Magnetic measurements

Results and Discussion

Crystal Structure

The new compound $[trenH_3]_2[tren]_{0.33}[Sb_6V_{15}O_{42}]$ crystallizes in the trigonal space group R-3 with 18 formula units per unit cell. All atoms except one N atom are located on general positions. The structure consists of isolated $[Sb^{(III)}_6V^{(IV)}_{15}O_{42}]^{6-}$ clusters and three crystallographically independent tren molecules as charge compensating cations (Figure 2). The anion has a nearly spherical shape and is composed of 15 VO_5 square pyramids and 6 SbO_3 trigonal pyramids. Two SbO_3 groups are connected

via one oxygen atom forming a Sb_2O_5 handle-like moiety (Sb-O = 1.943(7) Å – 1.983(8) Å). As predicted by Müller *et al.* [7] the Sb_2O_5 units avoid a direct contact and are located with the longest possible separation between each other. The VO_5 units share common edges and V_2O_2 as well as V_3O_3 rings are formed. The VO_5 square pyramids have common vertices with the SbO_3 groups. The structure of the $[Sb_6V_{15}O_{42}]^{6-}$ cluster is derived from the $[V_{18}O_{42}]$ cluster shell by substituting two VO_5 pyramids by two Sb_2O_5 units leading to the $[Sb^{(III)}{}_4V^{(IV)}{}_{16}O_{42}]^{4-}$ moiety. The geometry around the square pyramidal VO_5 units is mainly defined by 24 μ_3-O atoms (V-O = 1.918(7) Å - 2.024 (8) Å) forming a cage, which can be regarded as a rhombicuboctahedron comparable with that in Keggin shells, and by 15 terminal oxygen atoms (V-O = 1.600(8) Å - 1.649(8) Å). All values for the V-O bonds and O-V-O angles are comparable with the data found in literature [9,14-16]. For all vanadium atoms bond valance calculations gives average values close to 4.0.

The extensions of the clusters are about 10·10 Å (measured from coordinate to coordinate). The spheres are arranged in a layer like fashion in the *ab* plane (Figure 3) and they are stacked along the c-axis in an .ABAC... sequence (Fig. 4). Within the layers every cluster is surround by 6 neighboured cluster molecules with the shortest inter-cluster Sb-O separation of about 2.884(8) Å. If long Sb-O distances up to 3 Å are considered as weak interactions, three clusters are connected via one Sb_3O_3 ring to form a $[Sb_{18}V_{45}O_{126}]$ super cluster (Fig. 5). The cations occupy the galleries between successive layers (Fig. 4). The ..ABAC.. stacking sequence of the anionic clusters and the resulting long crystallographic c-axis is caused by the special arrangement of the amine ions. Two different kinds of amine layers are found in which the amine molecules show a different orientation with respect to each other and towards the anions. In layer 1 (Fig. 4) the tren molecules are arranged that the four nitrogen atoms are located around the terminal oxygen atoms of the clusters reaching an optimal geometry for N-H···O bonding interactions. Due to the fact that H_2O molecules could not be located during structure refinement their location is not clear. The layer is about two amine molecules thick and for this arrangement the distance between the anionc cluster molecules amounts to 4.713 Å (amine layer 1 in Figure 4). Layer 2 is also two amine molecules thick but the ions show a different orientation compared

to that in layer 1. The N atoms of neighbored tren molecules point to each other and the resulting interlayer distance of 3.463 Å is significantly shorter. But this arrangement also yields short N-H···O separations indicative for strong hydrogen bonding interactions.

Thermal Properties

Heating crystals of $[trenH_3]_2[tren]_{0.33}[Sb_6V_{15}O_{42}]$ under nitrogen a mass loss of 15.15 % is observed. In the dTG curve a two step decomposition mechanism is observed. The first step with a mass loss of 2.71 % is caused by water molecules which were not found during single crystal structure refinement. The emission of H_2O during this step was unambiguously proved with mass spectroscopy experiments. The decomposition experiments were performed several times with different batches of the material and the water content differed from sample to sample. According to the mass loss the amount of H_2O ranges from 3 to 5 per formula unit. The second decomposition step is due to the removal of the tren ligands and is accompanied by one endothermic event at T_{Peak}= 363 °C (Fig. 6). For the complete emission of the tren molecules a mass change of 11.9 % is expected showing a fair agreement with the experimental data. Further heating leads to continuous decomposition and emission of Sb_2O_3 at higher temperatures. The X-ray powder pattern of the decomposition product can be explained with V_2O_3 (Karelianite) and Sb_2O_3. Chemical analyses of the grey residue yields minute amounts of C, N, H (< 0.5 %).

Optical Properties

The Raman spectrum is shown in Figure 7. In the region between 200 and 1000 cm^{-1} three modes belonging to V-O and Sb-O vibrations are observed. The very intense stretching mode of V^{IV}=O is located at 961 cm^{-1}. The resonances at ~ 257 cm^{-1} and 394 cm^{-1} are due to the V-μ_3O-V and the Sb-μ_3O-V stretching modes. The energetic position of the different modes is in good accordance with those reported for other V compounds [10,21-23].

In the UV/Vis spectrum two absorptions are seen (Fig. 8). The first occurs at 1.87 eV (662 nm) and the second one at 2.11 eV (587 nm). The first absorption is caused by an inter-valence transition whereas the second is due to the transition from the valence band to the conduction band.

Magnetic Properties

Die grosse frage….messungen noch nicht gemacht, probe in münster

Acknowledgements: The financial support by the State of Schleswig-Holstein and the Deutsche Forschungsgemeinschaft (DFG) is gratefully acknowledged.

Supporting Information

Crystallographic Data for the structure reported in this paper have been deposited with Cambridge Crystallographic Data Center as supplementary publication number CCDC xxxxx. Copies of the data can be obtained free of charge on application to CCDC, 12 Union Road, Cambridge CB2 1EZ, UK (fax +44-(0)-1223-336-033 or email deposit@ccdc.cam.ac.uk.

References

[1] Whittingham, M.S. J. Electrochem. Soc. 1976, 123, 315.

[2] Walk, C.R.; Gore, J.S. J. Electrochem. Soc. 1975, 122, 68C.

[3] Whittingham, M.S.; Chen, R.; Chirayil, T.; Zavalij, P.Y. Electrochem. Soc. Proc. 1996, 96-95, 76.

[4] Bowes, C.L.; Ozin, G.A. Adv. Mater. 1996, 8, 13.

[5] Belik, A.A.;Azumo, M.; Matsuo, A.; Kindo, K.; Takano, M. Inorg. Chem. 2005, 44, 3762.

[6] Zhang, Y.; Warren, C.J.; Haushalter, R.C. Chem. Mater. 1998, 10, 1059.

[7] Stain, A.; Keller, S.W.; Wallouk, T.E. Science 1993, 259, 1558.

[8] Müller, A.; Döring, J. Z. anorg. allg. Chem., 1991, 595, 251.

[9] Müller, A.; Döring, J. Angew. Chem., Int. Ed. Engl.,1988, 27, 1721.

[10] Zipse, D.; Dalal, N.S.; Vasic, R.; Brooks, J.S.; Kögerle, P. Phys. Rev. B, 2005, 71, 064417.

[11] Chiorescu, I.; Wernsdorfer, W.;. Müller, A.; Bögge, H.; Barbara, B. Phys. Rev. Lett., 2000, 84, 3434.

[12] Barra, A.-L.; Gatteschi, D.; Pardi, L.; Müller, A.; Döring, J. J. Am. Chem. Soc., 1992, 114, 8509.

[13] Leuenbeger, M.N.; Loss, D. Nature, 2001, 410, 789.

[14] Hu, X.-X.; Xu, J.-Q.; Cui, X.-B.; Song, J.-F.; Wang, T.-G. Inorg. Chem. Comm. 2004, 7, 264.

[15] L. Zhang, X. Zhao, J. Xu, T. Wang, J. Chem. Soc., Dalton Trans., 2002, 3275.

[16] R. Kiebach, C. Näther, W. Bensch, Dalton Trans, 2005, in preperation.

[17] Albonetti, S.; Cavani, F.; Trifiro, F.; Gazzano, M.; Aissi, F.C.; Aboukais, A.; Guelton, M. J. Catal. 1994, 146, 491.

[18] Sprengler, J.; Anderle, F.; Bosch, E.; Grasselli, R.K.; Pillep, B.; Behrens, P.; Lapina, O.B.; Shubin, A.A.; Eberle, H.-J.; Knözinger, H. J. Phys. Chem. B 2001, 105, 10772.

[19] Sheldrick, G.M., SHELXS-97, Program for Crystal Structure Determination, University of Göttingen, Germany 1997.

[20] Sheldrick, G.M., SHELXL-97, Program for the Refinement of Crystal Structures, University of Göttingen, Germany 1997.

[21] Lee, S.H.; Cheong, H.M.; Seong, J.M.; Liu, P.; Tracy, C.E.; Mascarenhas, A.; Pitts, J.R., Deb, S.K. J. Appl. Phys. 2002, 92, 1893.

[22] Popovic, Z.V.; Stergiou, V.; Raptis, Y.S.; Konstantionvic, M.J.; Isobe, M.; Ueda, Y.; Moshchalkov, V.V. J. Phys. Condens. Matter, 2002, 14, L583.

[23] Lee, S.H.; Cheong, H.M.; Seong, M.J.; Liu, P.; Tracy, C.E.; Mascarenhas, A.; Pitts, J.R., Deb, S.K. Solid State Ionics 2003, 165, 116.

Tables:

	$[trenH_3]_2[tren]_{0.33}[Sb_6V_{15}O_{42}]$
a / Å	21.5209(9)
c / Å	72.662(4)
V /Å^3	29145(2)
calc. density [g/cm^3]	2.557
Crystal system	trigonal
Space group	R-3
2θ /	5° ≤ 2θ ≤ 55°
hkl range	-25 ≤ h≤ 25
	-25 ≤ k≤ 23
	-86 ≤ l≤ 79
No. coll. Reflections	44476
No. unique reflections	11852
Reflections Fo>4σ(Fo)	8600
Parameters	762
R1 (F0 > 4σ(Fo))	0.0612

wR2 (F0 > 4σ(Fo))	0.1555
R1 (all reflections)	0.0883
wR2 (all reflections)	0.1713
GOF	1.037
ΔF [e/Å^3]	4.97 / -2.31

Table 1: Selected crystallographic data and some refinement results

	x	*y*	*z*	U_{eq}
V(1)	3422(1)	11(1)	4835(1)	8(1)
Sb(1)	5326(1)	7344(1)	994(1)	25(1)
Sb(2)	4382(1)	7878(1)	688(1)	29(1)
Sb(3)	5437(1)	11285(1)	975(1)	27(1)
Sb(4)	7036(1)	12329(1)	714(1)	29(1)
Sb(5)	9263(1)	11192(1)	1038(1)	30(1)
Sb(6)	8806(1)	9672(1)	750(1)	28(1)
V(1)	56911)	10581(1)	531(1)	28(1)
V(2)	6203(1)	8256(1)	560(1)	25(1)
V(3)	7834(1)	9420(1)	1190(1)	24(1)
V(4)	71691)	11645(1)	1169(1)	24(1)
V(5)	49351)	8753(1)	1146(1)	26(1)
V(6)	8505(1)	11112(1)	578(1)	27(1)
V(7)	5676(1)	9267(1)	429(1)	27(1)
V(8)	71261)	8365(1)	883(1)	21(1)
V(9)	7737(1)	10737(1)	1292(1)	23(1)
V(10)	5820(1)	10242(1)	1264(1)	21(1)
V(11)	4699(1)	9537(1)	829(1)	28(1)
V(12)	7518(1)	9551(1)	458(1)	26(1)
V(13)	6310(1)	8821(1)	1283(1)	21(1)
V(14)	7265(1)	11132(1)	444(1)	26(1)

V(15)	83131)	11975(1)	882(1)	25(1)
O(1)	53625)	10866(5)	378(1)	42(2)
O(2)	60565)	7600(4)	418(1)	39(2)
O(3)	82635)	9241(6)	1345(1)	47(2)
O(4)	73165)	12263(5)	1318(1)	43(2)
O(5)	4255(5)	8292(5)	1279(2)	50(2)
O(6)	9219(5)	11572(5)	453(1)	44(2)
O(7)	5238(5)	8963(5)	237(1)	47(2)
O(8)	7298(4)	7722(4)	890(1)	34(2)
O(9)	8137(4)	11047(4)	1492(1)	38(2)
O(10)	5469(4)	10335(5)	1454(1)	37(2)
O(11)	3877(4)	9342(5)	813(2)	46(2)
O(12)	7810(5)	9345(4)	274(1)	40(2)
O(13)	6169(4)	8401(5)	1478(1)	34(2)
O(14)	7498(5)	11596(4)	257(1)	43(2)
O(15)	8963(4)	12799(4)	887(1)	37(2)
O(16)	4525(4)	7196(4)	838(1)	37(2)
O(17)	6147(4)	12137(4)	840(1)	36(2)
O(18)	9442(4)	10506(5)	904(1)	39(2)
O(19)	6318(4)	10298(4)	418(1)	35(2)
O(20)	52874)	10591(4)	779(1)	33(2)
O(21)	6648(4)	11397(4)	591(1)	36(2)
O(22)	5096(4)	9546(4)	584(1)	31(2)
O(23)	6091(4)	7898(4)	814(1)	28(2)
O(24)	6493(4)	9121(4)	423(1)	32(2)
O(25)	7195(4)	8748(4)	636(1)	29(2)
O(26)	5364(4)	8375(4)	583(1)	36(2)
O(27)	6914(4)	8599(4)	1125(1)	25(2)
O(28)	7214(4)	9700(4)	1315(1)	27(2)
O(29)	8348(4)	10459(4)	1148(1)	34(2)

O(30)	8073(4)	9213(4)	941(1)	32(2)
O(31)	6842(4)	10753(4)	1299(1)	28(2)
O(32)	6137(4)	11118(4)	1110(1)	26(2)
O(33)	8009(4)	11541(4)	1124(1)	28(2)
O(34)	7441(4)	12066(4)	920(1)	34(2)
O(35)	5788(4)	9335(4)	1294(1)	28(2)
O(36)	5474(4)	8229(4)	1116(1)	30(2)
O(37)	5058(4)	9690(4)	1083(1)	29(2)
O(38)	4602(4)	8580(4)	885(1)	36(2)
O(39)	8786(4)	11395(4)	839(1)	30(2)
O(40)	8013(4)	11637(4)	630(1)	26(2)
O(41)	7672(4)	10516(4)	430(1)	28(2)
O(42)	8340(4)	10137(4)	627(1)	31(2)
N(1)	3357(6)	10035(5)	1449(1)	36(2)
C(1)	3080(9)	9298(8)	1379(2)	56(4)
C(2)	3340(8)	8881(8)	1482(2)	51(4)
N(2)	2950(6)	8575(7)	1661(2)	46(3)
C(3)	4060(7)	10513(8)	1359(2)	42(3)
C(4)	4530(8)	11160(7)	1475(2)	45(3)
N(3)	4783(6)	10975(5)	1644(1)	39(2)
C(5)	2845(9)	10275(10)	1396(3)	67(5)
C(6)	2241(12)	10035(10)	1530(4)	105(9)
N(4)	2288(12)	10480(8)	1662(2)	98(6)
N(11)	6497(6)	6564(5)	165(1)	37(2)
C(11)	6902(8)	6311(8)	276(2)	47(3)
C(12)	6683(9)	6188(7)	473(2)	51(4)
N(12)	6863(8)	6872(7)	570(2)	54(3)
C(13)	6888(8)	6962(7)	3(2)	44(3)
C(14)	7321(8)	7762(9)	47(2)	60(4)
N(13)	6822(8)	8044(6)	76(2)	60(3)

C(15)	5788(7)	5933(6)	106(2)	43(3)
C(16)	5212(7)	6118(8)	81(3)	57(4)
N(14)	4968(8)	6240(8)	264(3)	97(7)
N(21)	3333	6667	168(4)	79(8)
C(22)	4530(30)	7450(30)	123(7)	190(18)
C(21)	3980(30)	6720(40)	201(10)	260(30)
N(22)	4430(30)	7580(30)-	115(7)	240(20)

Table 2: Atomic coordinates [$\times 10^4$] and equivalent isotropic displacement parameters [$Å^2 \cdot 10^3$] for $[trenH_3]_2[tren]_{0.33}[Sb_6V_{15}O_{42}]$. U_{eq} is calculated as one third of the trace of the orthogonalised U_{ij} tensor.

Selected Bond Length (Å)			
Sb(1)-O(16)	1.951(8)	Sb(1)-O(23)	1.969(8)
Sb(1)-O(36)	1.979(8)	Sb(2)-O(16)	1.971(8)
Sb(2)-O(26)	1.983(8)	Sb(2)-O(38)	1.956(9)
Sb(3)-O(17)	1.964(8)	Sb(3)-O(20)	1.966(8)
Sb(3)-O(32)	1.976(7)	Sb(4)-O(17)	1.969(8)
Sb(4)-O(21)	1.961(8)	Sb(4)-O(34)	1.956(8)
Sb(5)-O(18)	1.959(8)	Sb(5)-O(29)	1.973(8)
Sb(5)-O(39)	1.943(8)	Sb(6)-O(18)	1.975(9)
Sb(6)-O(30)	1.958(8)	Sb(6)-O(42)	1.948(8)
V(1)-O(1)	1.600(8)	V(1)-O(19)	1.921(8)
V(1)-O(20)	2.005(9)	V(1)-O(21)	1.974(8)
V(1)-O(22)	1.972(8)	V(2)-O(2)	1.649(8)
V(2)-O(23)	1.965(8)	V(2)-O(24)	1.918(7)
V(2)-O(25)	1.930(8)	V(2)-O(26)	1.954(8)
V(3)-O(3)	1.619(9)	V(3)-O(27)	1.942(7)
V(3)-O(28)	1.945(7)	V(3)-O(29)	1.961(8)
V(3)-O(30)	1.994(8)	V(4)-O(4)	1.621(8)

V(4)-O(31)	1.929(8)	V(4)-O(32)	1.971(7)
V(4)-O(33)	1.955(7)	V(4)-O(34)	1.976(8)
V(5)-O(5)	1.613(8)	V(5)-O(35)	1.946(8)
V(5)-O(36)	1.993(7)	V(5)-O(37)	1.952(7)
V(5)-O(38)	1.999(9)	V(6)-O(6)	1.627(8)
V(6)-O(39)	1.993(8)	V(6)-O(40)	1.934(7)
V(6)-O(41)	1.927(7)	V(6)-O(42)	1.9778)
V(7)-O(7)	1.630(9)	V(7)-O(19)	1.942(8)
V(7)-O(22)	1.982(8)	V(7)-O(24)	1.934(8)
V(7)-O(26)	2.024(8)	V(8)-O(8)	1.603(8)
V(8)-O(23)	1.996(8)	V(8)-O(25)	1.949(8)
V(8)-O(27)	1.943(7)	V(8)-O(30)	1.986(8)
V(9)-O(9)	1.653(8)	V(9)-O(28)	1.939(8)
V(9)-O(29)	1.994(8)	V(9)-O(31)	1.943(7)
V(9)-O(33)	1.951(8)	V(10)-O(10)	1.630(8)
V(10-O(31)	1.922(7)	V(10)-O(32)	1.998(7)
V(10)-O(35)	1.930(8)	V(10)-O(37)	1.971(8)
V(11)-O(11)	1.605(8)	V(11)-O(20)	2.002(8)
V(11)-O(22)	1.972(9)	V(11)-O(37)	1.967(8)
V(11)-O(38)	2.006(8)	V(12)-O(12)	1.631(9)
V(12)-O(24)	1.935(8)	V(12)-O(25)	1.986(8)
V(12)-O(41)	1.943(7)	V(12)-O(42)	2.001(8)
V(13)-O(13)	1.628(8)	V(13)-O(27)	1.963(7)
V(13)-O(28)	1.936(7)	V(13)-O(35)	1.932(7)
V(13)-O(36)	2.006(8)	V(14)-O(14)	1.612(8)
V(14)-O(19)	1.938(8)	V(14)-O(21)	1.995(9)
V(14)-O(40)	1.960(8)	V(14)-O(41)	1.922(8)
V(15)-O(15)	1.620(8)	V(15)-O(33)	1.947(8)
V(15)-O(34)	2.000(8)	V(15)-O(39)	1.992(8)
V(15)-O(40)	1.959(8)		

Table 3. Selected interatomic distances (Å) for $[trenH_3]_2[tren]_{0.33}[Sb_6V_{15}O_{42}]$. Estimated standard deviations are given in parentheses.

Figure Captions

Figure.1: SEM picture of a single crystals of $[trenH_3]_2[tren]_{0.33}[Sb_6V_{15}O_{42}]$.

Figure 2: $[Sb_6V_{15}O_{42}]^{6-}$ cluster of $[trenH_3]_2[tren]_{0.33}[Sb_6V_{15}O_{42}]$.

Figure 3: Crystal structure of $[trenH_3]_2[tren]_{0.33}[Sb_6V_{15}O_{42}]$ with view along the c axis.

Figure 4: Crystal structure of $[trenH_3]_2[tren]_{0.33}[Sb_6V_{15}O_{42}]$ with view along the c axis. Cations only pictured in top interlayer. Hydrogen atoms omitted for clarity.

Figure 5: $[Sb_{18}V_{45}O_{126}]$ super cluster of $[trenH_3]_2[tren]_{0.33}[Sb_6V_{15}O_{42}]$ considering Sb-O interactions up to 3 Å.

Figure 6: DTA and TG curves for $[trenH_3]_2[tren]_{0.33}[Sb_6V_{15}O_{42}]$; given is the mass loss in % and the peak temperature T_p in °C.

Figure 7: Raman spectrum of $[trenH_3]_2[tren]_{0.33}[Sb_6V_{15}O_{42}]$.

Figure 8: UV/Vis spectrum of $[([trenH_3]_2[tren]_{0.33}[Sb_6V_{15}O_{42}]$.

Figure 9: Temperature dependence of the magnetic susceptibility of $[trenH_3]_2[tren]_{0.33}[Sb_6V_{15}O_{42}]$.

Figures

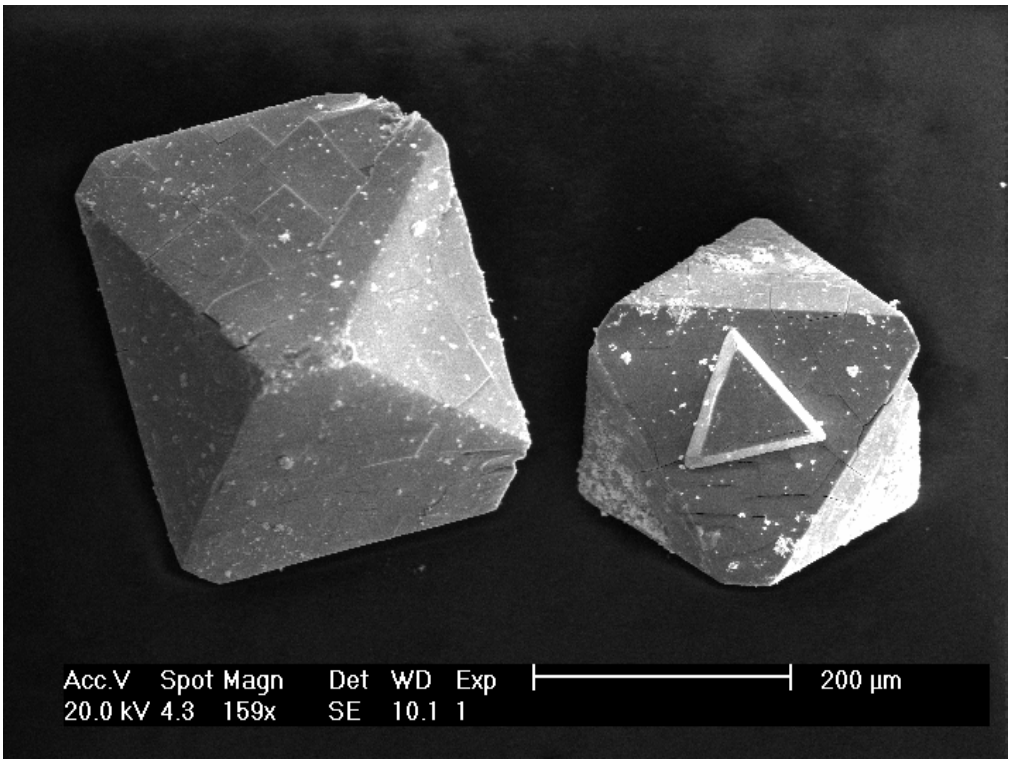

Fig.1

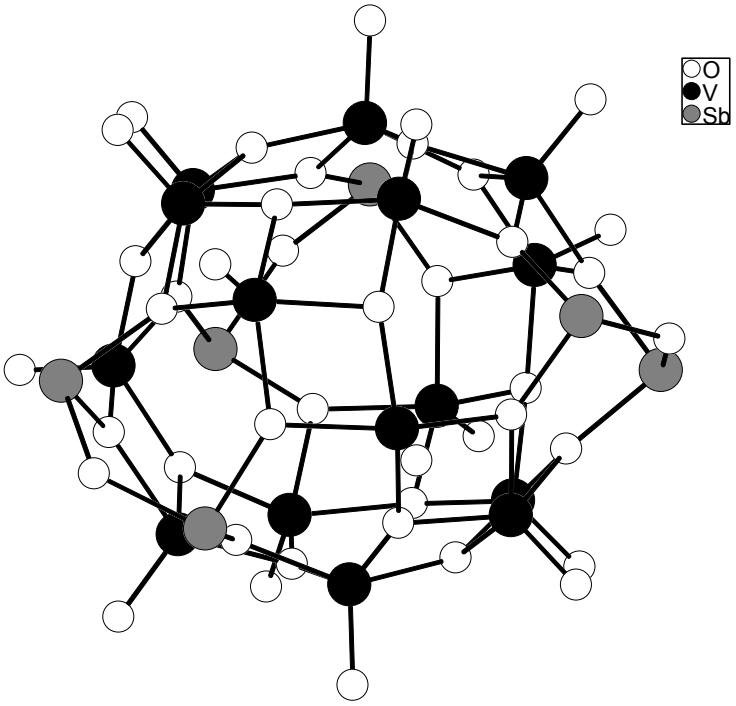

Fig.2

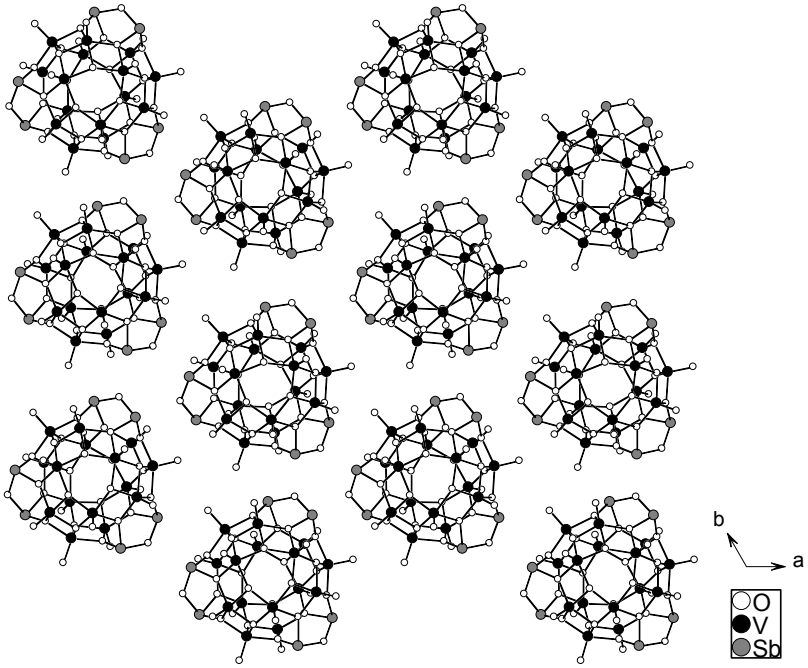

Fig.3

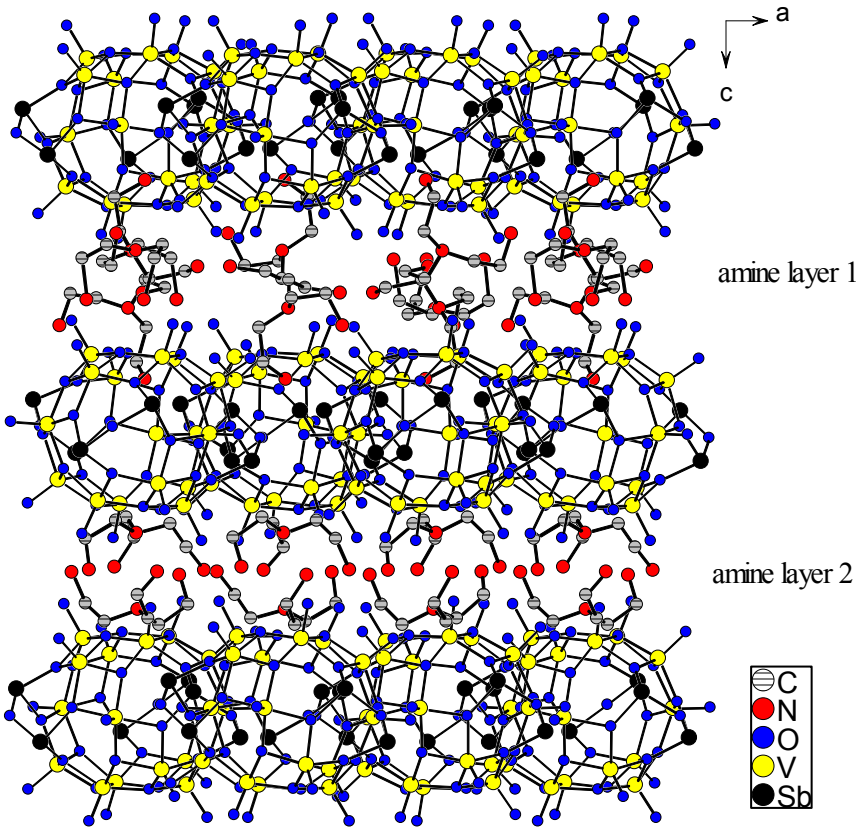

Fig.4

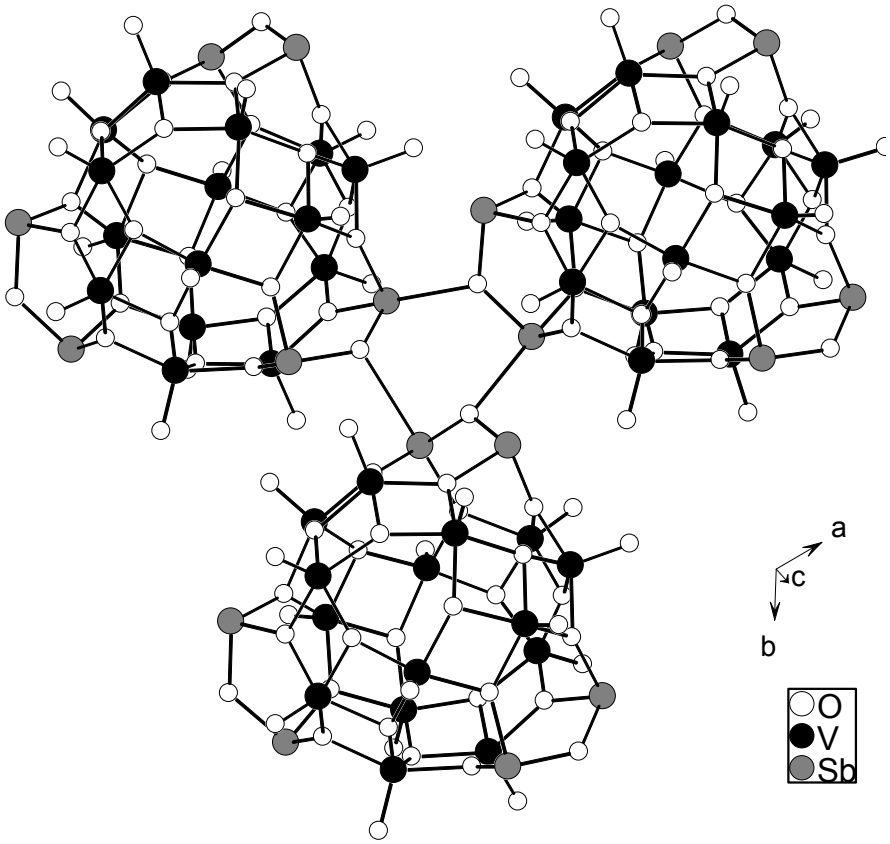
a
c
b
O
V
Sb

Fig.5

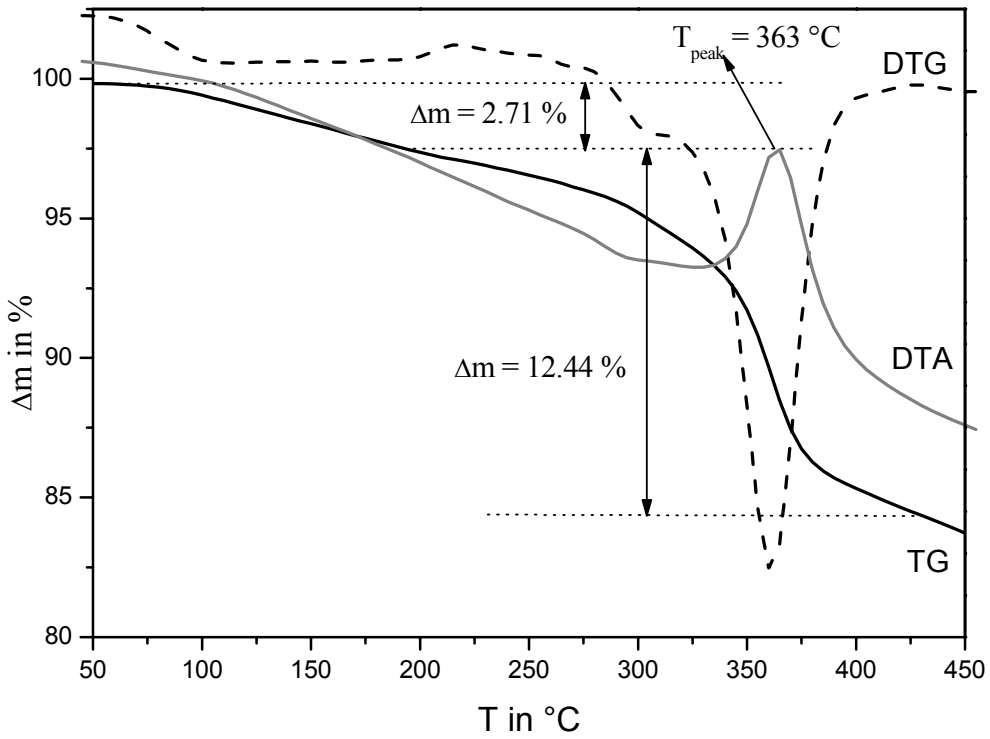
T peak = 363 °C
DTG
Δm = 2.71 %
Δm = 12.44 %
DTA
TG
Δm in %
T in °C
100
95
90
85
80
50
100
150
200
250
300
350
400
450

Fig.6

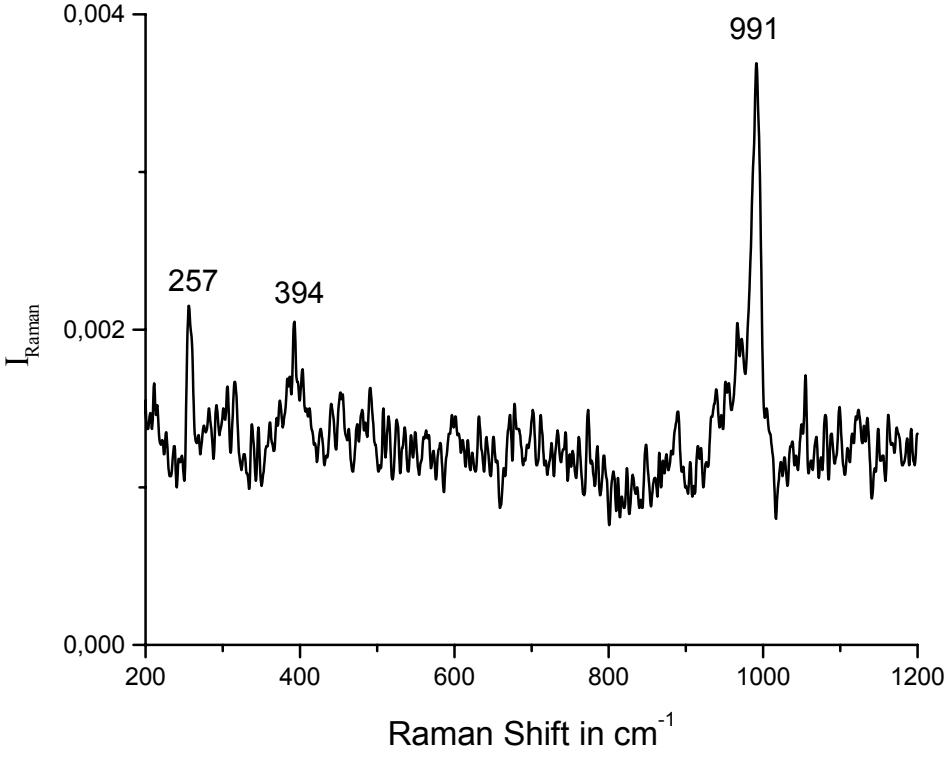
0,004
0,002
0,000
991
257
394
I Raman
200
400
600
800
1000
1200
Raman Shift in cm-1

Fig.7

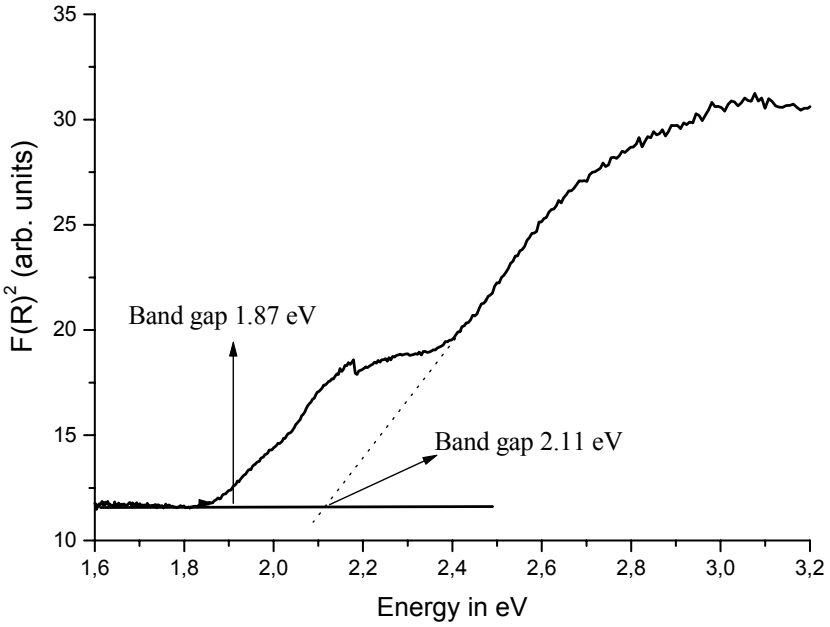
35
30
25
20
15
10
F(R)2 (arb. units)
Band gap 1.87 eV
Band gap 2.11 eV
1,6
1,8
2,0
2,2
2,4
2,6
2,8
3,0
3,2
Energy in eV

Fig.8

4.3.3 Die Verbindungen $[C_6H_{17}N_3]_4[Sb_4V_{16}O_{42}]\cdot 2H_2O$ und $[NH_4]_4[Sb_8V_{14}O_{42}]\cdot 2H_2O$

Zusammenfassung der Veröffentlichung „*$[C_6H_{17}N_3]_4[Sb_4V_{16}O_{42}]\cdot 2H_2O$ and $[NH_4]_4[Sb_8V_{14}O_{42}]\cdot 2H_2O$ – The first isolated Sb derivates of the $[V_{18}O_{42}]$ family*".

Die Darstellung beider Verbindungen erfolgte mit einem Gemisch aus 5.13 mmol NH_4VO_3 und 2.06 mmol Sb_2O_3 bei 150 °C unter solvothermalen Bedingungen. Für die Synthese von $[C_6H_{17}N_3]_4[Sb_4V_{16}O_{42}]\cdot 2H_2O$ (**1**) wurden 4 ml einer 50 %igen 2-Amino-ethyl-piperazin-Lösung eingesetzt. Die Reaktionszeit betrug 7 Tage.

Die Verbindung $[NH_4]_4[Sb_8V_{14}O_{42}]\cdot 2H_2O$ (**2**) wurde in 4 ml einer Mischung aus 15 g N,N,N',N'-Tetrakis-(2-hydroxyethyl)-ethylendiamin and 10 ml H_2O synthetisiert, wobei die Reaktionszeit 14 Tage betrug.

Die Verbindung (**1**) kristallisiert in der triklinen Raumgruppe $P\bar{1}$ mit einer Formeleinheit pro Elementarzelle. Die Struktur besteht aus zwei kristallographisch unabhängigen $[C_6H_{17}N_3]^{2+}$-Kationen und einem isolierten $[Sb_4V_{16}O_{42}]^{8-}$-Cluster als Anion. Zwischen Anionen und Kationen sind zwei Kristallwassermoleküle eingelagert. Das sphärische $[Sb_4V_{16}O_{42}]^{8-}$-Anion ist aus 16 VO_5-Pyramiden und 4 SbO_3-Einheiten aufgebaut (Abb. 4.9, links). Jeweils zwei SbO_3-Einheiten sind über eine gemeinsame Ecke zu einer Sb_2O_5-Gruppe verknüpft. Die VO_5-Pyramiden sind über gemeinsame Kanten zu einem offenen $V_{16}O_{40}$-Käfig verbunden. Eine Vervollständigung des Käfigs zum $[Sb_4V_{16}O_{42}]^{8-}$-Anion erfolgt durch die zwei hantelförmigen Sb_2O_5-Einheiten. Die Anionen sind schichtartig in der (100)-Ebene angeordnet, wobei diese Schichten entlang der *b*-Achse in der Abfolge *AAA* angeordnet sind. Die Kationen und das Kristallwasser befinden sich zwischen den Schichten.

Zwischen den Clustern werden Sb-O-Abstände von 2.85 Å gefunden. Diese liegen deutlich unter der Summe der van-der-Waals-Radien von 3.52 Å. Werden diese schwachen Kontakte berücksichtigt kommt es zur Kondensation der Cluster über $Sb_2V_2O_4$-Ringe und zur Bildung von Ketten entlang der *a*-Achse. Zwischen den Anionen und Kation werden 12 N-H$\cdots$O-Wasserstoffbrückenbindungen gefunden, was auf eine relativ starke Wechselwirkung zwischen den Ionen hindeutet.

Die Verbindung (**2**) kristallisiert in der monklinen Raumgruppe $P2_1/n$ mit vier For-

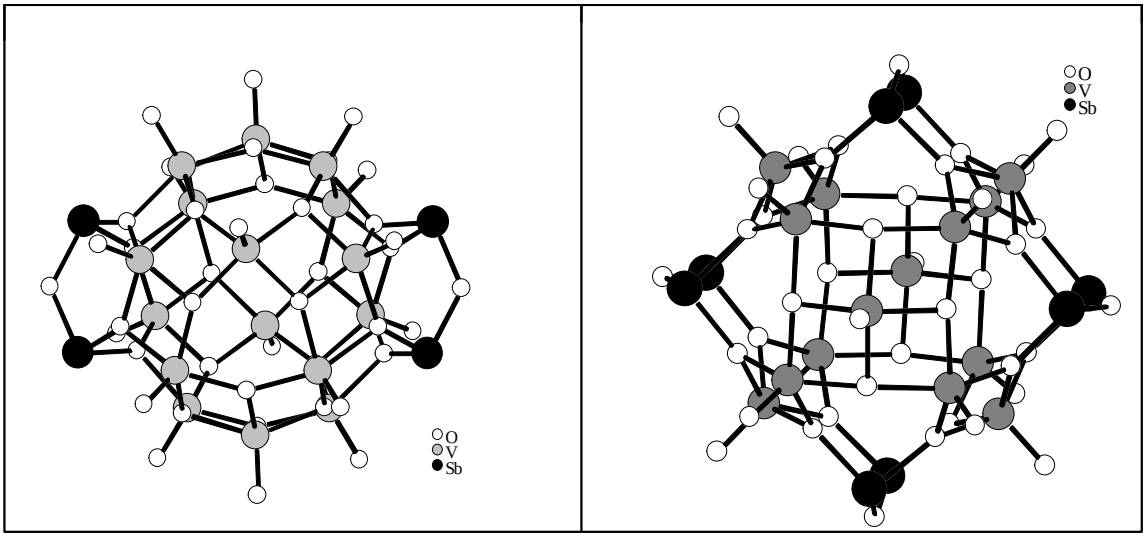

Abbildung 4.9: $[Sb_4V_{16}O_{42}]^{8-}$-Cluster in $[C_6H_{17}N_3]_4[Sb_4V_{16}O_{42}]\cdot 2H_2O$ (links) und $[Sb_8V_{14}O_{42}]^{4-}$-Cluster in $[NH_4]_4[Sb_8V_{14}O_{42}]\cdot 2H_2O$ (rechts)

meleinheiten in der Elementarzelle. Die Struktur wird aus zwei kristallographisch unabhängigen NH^{4+}-Kationen und einem isolierten $[Sb_8V_{14}O_{42}]^{4-}$-Cluster gebildet (Abb. 4.9, rechts). Im Unterschied zu (**1**) werden 14 VO_5-Pyramiden und 8 SbO_3-Einheiten als primäre Baueinheiten beobachtet. Wie in (**1**) sind die VO_5-Einheiten über gemeinsame Kanten verknüpft, die Vervollständigung zum $[Sb_8V_{14}O_{42}]^{4-}$-Anion erfolgt über 4 Sb_2O_5-Gruppen. Die Abfolge der Anionen entlang der *b*-Achse kann mit einer *ABAB*-Stapelfolge beschrieben werden, wobei die Anionen stabförmig entlang [100] angeordnet sind.

Auch in der Verbindung (**2**) werden schwache Intercluster Sb-O-Kontakte unter 3 Å gefunden. Unter Berücksichtigung dieser Bindungen werden die Cluster zu Schichten in der (10-1)-Ebene verknüpft. Die Bindungen zwischen den Sauerstoffatomen der Cluster und der Stickstoffatome der Kationen sind mit $\leq$ 3 Å bemerkenswert kurz und deuten auf starke Wechselwirkungen zwischen Anionen und Kationen hin. Die hohe Ordnung der Stickstoffatome ist Konsequenz dieser Wechselwirkungen.

Die Abmessungen der Anionen in beiden Verbindungen betragen ca. 11·11 Å. Ein weiteres interessantes Strukturmerkmal beider Verbindungen sind koplanare V_8-Ringe

in den Anionen. Berechnungen der Bindungsvalenzsummen ergaben für alle Vanadiumatome einen Wert nahe 4.0, was gut mit Überlegungen zur Ladungsneutralität übereinstimmt.

Als Archetyp kann für die Cluster in beiden Verbindungen die $V_{18}O_{42}$-Strukturfamilie gesehen werden. Ausgehend von einem $V_{18}O_{42}$-Gerüst gelangt man durch formalen Austausch von V=O- gegen Sb_2O_3-Gruppen zu den Verbindungen (**1**) und (**2**). Allgemein lassen sich diese Verbindungen mit der Formel $[(AminH)_mSb_{2x}V_{18-x}O_{42}] \cdot 2H_2O$ beschreiben. Grundgerüst der Cluster ist ein Käfig aus 24 verbrückenden μ_3-O-Atomen.

$[C_6H_{17}N_3]_4[Sb_4V_{16}O_{42}]\cdot 2H_2O$ and $[NH_4]_4[Sb_8V_{14}O_{42}]\cdot 2H_2O$ – The first isolated Sb derivates of the $[V_{18}O_{42}]$ family

Ragnar Kiebach, Christian Näther and Wolfgang Bensch*

Institut für Anorganische Chemie, Christian-Albrechts-Universität Kiel,

Olshausenstr. 40, D-24098 Kiel, Germany

*correspondence address: Prof. Dr. Wolfgang Bensch

Institute for Inorganic Chemistry

University of Kiel

Olshausenstraße 40

D-24098 Kiel

Germany

Abstract:

The solvothermal syntheses and the crystal structures of the two new compounds $[C_6H_{17}N_3]_4[Sb_4V_{16}O_{42}]\cdot 2H_2O$ (**1**) and $[NH_4]_4[Sb_8V_{14}O_{42}]\cdot 2H_2O$ (**2**) are presented. Compound (**1**) crystallises in the triclinic space and (**2**) in the monoclinic space group $P2_1/n$. The structures can be derived from the $[V_{18}O_{42}]$ archetype by replacing two VO_5 square pyramids by two Sb_2O_5 units in (**1**) and four VO_5 square byramids by four Sb_2O_5 moieties in (**2**). In compound (**1**) the clusters are stacked along the *b*-axis in an AAA mode with the cations and water molecules occupying the interstitial space. Between the anions and cations strong N-H···O hydrogen bonds are observed. Neighboured clusters exhibit a relatively short Sb-O separation of 2.852 Å indicating a weak inter-cluster interaction. If this Sb-O contact is considered the clusters are connected via $Sb_2V_2O_4$ rings into infinite chains running along the

a-axis. In compound (**2**) the anions are stacked along the *b*-axis in an ...ABAB... fashion. Within the (100) plane every anion is surrounded by 6 neighboured clusters. Again, relatively short Sb-O contacts (2.831 – 2.976 Å) are found which join the isolated clusters into layers extending in the (10-1) plane. The cations and water molecules are located between these layers. Several short N-O and O-O distances indicate strong hydrogen bonding between cations and anions respectively between the water molecules and the anions.

Keywords: Solvothermal Synthesis, Antimony Vanadates, Organic-Inorganic Hybrid Material.

Introduction:

The discovery of nanoscale magnetic properties of $[Mn_{12}O_{12}(O_2CMe)_{16}(H_2O)_4]$ in 1993 [1] led to an intense research in the field of molecular nano-magnetism and molecules showing this type of magnetism are now called single molecule magnets (SMMs). Until now several SMMs have been discovered including compounds of the $[V_{15}O_{42}]$ family [2], a low-spin system interesting for applications in the field of quantum computation [3]. The typical structure motive in this group of materials are clusters derived from the $[V_{18}O_{42}]$ cluster shells [4-6] in which the VO^{2+} cations are formally replaced by different cationic species, mainly As and Ge oxidic groups [7-10]. The rhombicuboctahedral vanado-arsenate anions $[V_{18-n}As_{2n}O_{42}(X)]^{m-}$ (X = SO_3, SO_4, Cl; *n* = 3,4) are the earliest examples of this type of substitution in which three or four VO_5 square pyramids are replaced by As_2O_5 groups [4,7,8]. The most famous example is the compound $K_6[As_6V_{15}O_{42}(H_2O)]\cdot 8H_2O$ [4,7] which has been studied in detail [11-13], including SMM properties. Until now no isolated derivatives of the $[V_{18}O_{42}]$ family containing Sb are known, the only compounds with Sb are $[Co(en)_2)_2Sb_8V_{14}O_{42}(H_2O)]\cdot 8H_2O$, showing a two dimensional structure, and $[(C_2N_2H_{10})_2\beta\text{-}\{Sb_8V_{14}O_{42}(H_2O)\}](C_2N_2H_8)\cdot 8H_2O$ [14,15], with a one dimensional structure. In the last few

months we successfully synthesised via the solvothermal route different Sb containing $[V_{18}O_{42}]$ derivatives composed of isolated cluster anions with general formula $[(amineH)_mSb_{2x}V_{18-x}O_{42}]\cdot nH_2O$ (x = 2 – 4). Besides the title compounds $[(C_4H_{18}N_4H_3)_2(C_4H_{18}N_4)_{0.33}Sb_6V_{15}O_{42}]$ was also obtained and characterised [16]. This new group of compounds is highly interesting for applications like nanoscale magnetism, and other useful properties can be expected as observed for Keggin type heteropolycompounds which are used as heterogeneous catalysts in oxidation reactions [17] or vanadium-antimonite based materials applied for selective oxidations [18].

Results and discussion:

Crystal structures

*Crystal structure of (**1**):*

Compound (**1**) $[C_6H_{17}N_3]_4[Sb_4V_{16}O_{42}]\cdot 2H_2O$ crystallises in the triclinic space group *P-1* (Table 1) with one formula unit per unit cell. The structure consists of two crystallographically independent double-protonated $[C_6H_{17}N_3]^{2+}$ molecules as cations and isolated $[Sb^{(III)}_4V^{(IV)}_{16}O_{42}]^{8-}$ clusters, which are located on centres of inversion (Figure 1). Between the clusters and the organic structure director two water molecules are found. The spherical anion is constructed by 16 condensed VO_5 square pyramids and 4 SbO_3 trigonal pyramids. Selected bond lengths are presented in Table 2. The SbO_3 groups are connected via one oxygen atom forming a Sb_2O_5 handle-like moiety (Sb-O = 1.934(4) Å – 1.983(4) Å). The Sb_2O_5 units are located at the periphery of the cluster ion preventing direct contact between each other, an arrangement which was predicted by Müller et al. [7]. The VO_5 pyramids share common edges with each other forming an open cage with composition $[V_{16}O_{40}]$. The Sb_2O_5 groups have a common corner with 2 VO_5 pyramids yielding finally the spherical anion. Starting with the $[V_{18}O_{42}]$ cluster shell as archetype the structure of the $[Sb^{(III)}_4V^{(IV)}_{16}O_{42}]^{4-}$ ion is derived by replacing two VO_5 groups by two Sb_2O_5 units beating out the spherical anion.

Due to the interconnection mode of the VO_5 units 24 O atoms act in a μ_3 fashion (V-O: 1.908(5) Å - 2.029(4) Å) forming the cage (Figure 2), and 16 O atoms are terminal (V=O: 1.600(5) - 1.640(4) Å). We note that the cage formed by the O atoms can be regarded as a rhombicuboctahedron reminiscent of that found in the so-called Keggin shells. The shortest V-V separations are between 2.953(2) and 3.061(2) Å (see Table 2) which are about 0.3 – 0.4 Å longer than in elemental V. The extension of the anion measures about 10.8 · 11.2 Å. The clusters are arranged in a layer like fashion within the (100) plane and they are stacked along the *b*-axis in an AAA mode (Figure 3). The cations and water molecules occupy the interstitial space between the cluster ions. 12 N-H···O hydrogen bonds in a range from 1.910 Å to 2.467 Å are found indicating relatively strong interactions between the anion and the cation. A relatively short inter-cluster Sb-O distance of 2.852 Å is observed which is significantly shorter than the sum of the van der Waals radii of O and Sb (3.52 Å) indicating a weak inter-cluster interaction. Considering this Sb-O contact the clusters are connected via $Sb_2V_2O_4$ rings into infinite chains running along the *a*-axis (Figure 4). The distance between the chains is about 5.48 Å, too long for any inter-chain interaction.

Compound (**2**) crystallises in the monoclinic space group $P2_1/n$ with four formula units per unit cell (Table 1) with all atoms residing on general positions. The structure is composed of two crystallographically independent $[NH_4]^+$ cations and isolated $[Sb^{(III)}_8V^{(IV)}_{14}O_{42}]^{4-}$ clusters (Figure 5). In contrast to compound (**1**) the structure of the anion in (**2**) is constructed by 14 VO_5 units and 4 Sb_2O_5 groups (Table 3). The latter are formed by corner-linkage of 8 SbO_3 pyramids (Sb-O = 1.934(5) – 1.996(5) Å). Again, starting with the $[V_{18}O_{42}]$ cluster as the archetype, four VO_5 square pyramids are substituted by four Sb_2O_5 units and in this way the structure can be regarded as an Sb derivative of the $[V_{18}O_{42}]$ structure family. The V-O bonds can be divided in two classes, the 14 terminal V=O bonds (V=O: 1.588(6) - 1.618(4) Å) and the 24 V-μ_3-O bonds (V-O: 1.931(5) - 1.990 (5) Å). The V-V distances cover a range from 2.878(2) Å to 3.085(2) Å (Table 3) which are comparable to that found for compound (**1**). The

extension of the anions measure about 11 · 11 Å. Along the *b*-axis the anions alternate in an ...ABAB... fashion (Figure 6) and along [100] the anions form rods. Alternatively, a layer like arrangement may be identified within the (100) plane with every anion being surrounded by 6 neighboured clusters. The packing is denser than for compound (**1**) which is clearly reflected comparing the densities of (**1**) (D_c = 2.383 g/cm^3) with that of (**2**) (D_c = 3.117 g/cm^3). Again, relatively short Sb-O contacts (2.831 – 2.976 Å) are observed, and considering these distances as weak interactions the isolated clusters are joined into layers extending in the (10-1) plane. The cations and water molecules are arranged between the layers. Interestingly, the three N-O distances between non-terminal O atoms and the two unique nitrogen atoms are shorter than 3 Å (one for N(1), two for N(2); N-O: 2.883-2.991 Å). These distances indicate relatively strong hydrogen bonding interactions explaining the ordered nature of N atoms. Also, for O atoms three relative short O-O contacts are below 3 Å and are found between terminal oxygen atoms and O atoms of H_2O (O-O: 2.772-2.982 Å). The distance between the layers of about 3.4 Å is much shorter than in (**1**).

An interesting structural feature are V_8 rings formed by coplanar V atoms making these compounds interesting candidates for SMM. In compound (**1**) the two rings (ring 1: two V1, two V2, two V3, two V5; ring 2: two V5, two V6, two V7, two V8) are connected via V4 (Figure 7a). In (**2**) two of those rings are (ring 1: two V1, two V3, two V5, two V7; ring 2: two V1, two V2, two V4, two V6) being perpendicular to each other (Figure 7b).

The bond valence sum for all vanadium atoms in both compounds indicates the average oxidation state is close to 4.0.

Experimental section:

Synthesis:

Compound (**1**) was synthesised hydrothermally applying a mixture of 600 mg (2.06 mmol) Sb_2O_3 and 600 mg (5.13 mmol) NH_4VO_3, 2 ml 2-amino-ethyl-piperazine and 2 ml H_2O. The

synthesis was performed in Teflon-lined steel autoclaves which were kept at 150 °C for seven days. After cooling to room temperature the product was washed with water and ethanol. As main product green Sb_2VO_5 (stibivanite) was found. The minor fraction consisted of brownish crystals of (**1**).

For compound (**2**) 600 mg (2.06 mmol) Sb_2O_3 and 600 mg (5.13 mmol) NH_4VO_3 and 4 ml of a mixture of 15 g N,N,N',N'-tetrakis-(2-Hydroxyethyl)-ethylendiamine and 10 ml H_2O was sealed in Teflon-lined steel autoclaves. The reaction mixture was kept at 150 °C for 14 days. The green-brown crystals were washed with water and acetone and dried in vacuum. The yield based on Sb is 40 %. Sb_2O_3 was identified as impurity in the X-ray powder pattern.

Crystal structure determination:

For (**1**) single crystal X-ray intensity data were collected at room temperature on a STOE-1 Imaging Plate Diffraction System with graphite monochromated MoK_α radiation (λ = 0.71073 Å). For (**2**) data collection was performed on a STOE AED II 4 circle diffractometer (graphite monochromated Mo-Kα radiation (λ = 0.71073 Å)) at 293 K. Selected crystal data and details of the structure determination are summarised in Table 1. The intensities were corrected for Lorentz and polarisation effects. Structure solution was performed with SHELXS-97 [19], Refinement was done against F^2 using SHELXL-97 [20]. The non-hydrogen atoms were refined using anisotropic displacement parameters. For compound **1** the C-H and N-H hydrogen atoms were positioned with idealised geometry and were refined using a riding model. The O-H hydrogen atoms were located in difference map and refined with ideal bond lengths using a riding model. In compound **2** the hydrogen atoms cannot be found. Selected bond length and angles are given in Tables 2 and 3. Crystallographic Data for (**1**)(excluding structure factors) have been deposited with Cambridge Crystallographic Data Centre as supplementary publication no. CCDC 286821 (**1**). Copies of the data can be obtained, free of charge, on application to CCDC, 12, Union Road, Cambridge CB2 1 EZ, UK. (fax +44(0)1223-336033 or email: deposit@ccdc.cam.ac.uk). CSD number for (**2**): CSD 415841

(file name NH42V7Sb4O21H2O) contains the supplementary crystallographic data. Email: crysdata@fiz-karlsruhe.de.

References

[1] Sessli, R.; Gatteschi, D.; Caneschi, A.; Novak, M.A. Nature 356 (1993) 141.

[2] Barbara, B.; Chiorescu, I.; Wensdorfer, W.; Bögge, H.; Müller, A. Prog. Theor. Phys. Suppl. 145 (2002), 357.

[3] Leuenberger, M. N.; Loss, D. Nature 410 (2001) 789.

[4] Müller, A.; Döring, J. Z. Anorg. Allg. Chem. 595 (1991) 251.

[5] Johnson, G.K.; Schlemper, E.O. J. Am. Chem. Soc. 100 (1978) 3645.

[6] Müller, A.; Penk, M.; Rohlfing, R.; Krickemeyer, E.; Döring, J. Angew. Chem., Int. Ed. Engl. 29 (1990) 927.

[7] Müller, A.; Döring, J. Angew. Chem., Int. Ed. Engl. 27 (1988) 1721.

[8] Khan, M.; Chen, O.; Zubieta, J. Inorg. Chim. Acta 212 (1993) 251.

[9] Whitfield, T.; Wang, X.; Jacobson, A.J. Inorg. Chem.42 (2003) 3728.

[10] Pitzschke, D.; Näther, C. Bensch, W. Angew. Chem., Int. Ed. Engl., 2005, in press.

[11] Zipse, D.; Dalal, N.S.; Vasic, R.; Brooks, J.S.; Kögerle, P. Phys. Rev. B 71 (2005) 064417.

[12] Chiorescu, I.; Wernsdorfer, W.; Müller, A.; Bögge, H.; Barbara, B. Phys. Rev. Lett. 84 (2000) 3434.

[13] Barra, A.L.; Gatteschi, D.; Pardi, L. Müller, A.; Döring, J. J. Am. Chem. Soc. 114 (1992) 8509.

[14] Zhang, L.; Zhao, X.; Xu, J.; Wang, T. J. Chem. Soc., Dalton Trans. (2002), 3275.

[15] Hu, X.-X.; Xu, J.-Q.; Cui, X.-B.; Song, J.F.; Wang, T.G. Inorg. Chem. Comm. 7 (2004) 264.

[16] Kiebach, R.; Näther, C.; Bensch, W. Inorg. Chem (2005), in preperation.

[17] Albonetti, S.; Cavani, F.; Trifiro, F.; Gazzano, M.; Aissi, F.C.; Aboukais, A.; Guelton, M.J. J. Catal. 146 (1994) 491.

[18] Sprengler, J.; Anderle, F.; Bosch, E.; Grasselli, R.K.; Pillep, B.; Behrens, P.; Lapina, O.P.; Shubin, A.A.; Eberle, H.-J.; Knözinger, H. J. Phys. Chem. B 105 (2001) 10772.

[19] Sheldrick, G.M. SHELXS-97, University of Göttingen (1997).

[20] Sheldrick, G.M. SHELXL-97, University of Göttingen (1997).

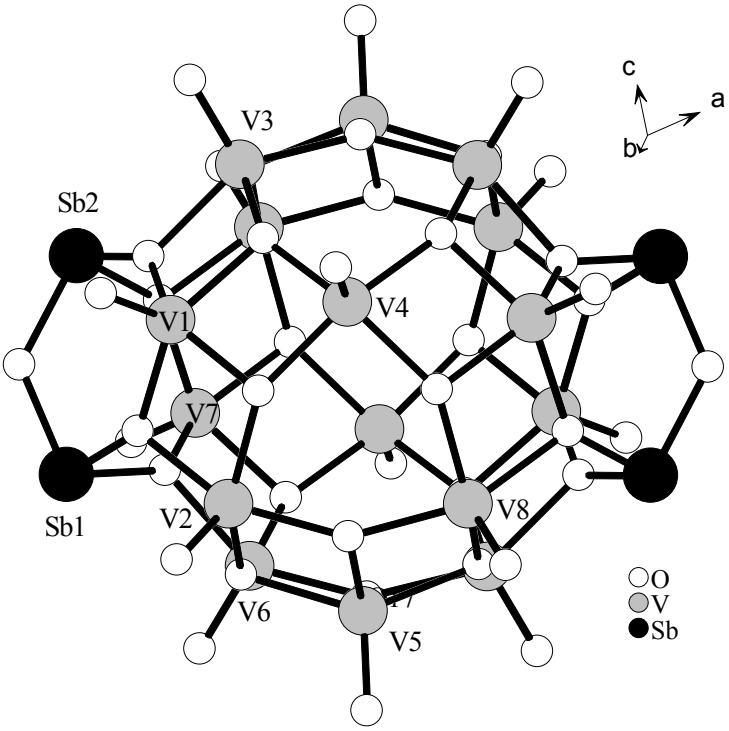

Figure 1: The $[Sb_4V_{16}O_{42}]^{8-}$ cluster of $[C_6H_{17}N_3]_4[Sb_4V_{16}O_{42}]\cdot 2H_2O$ (**1**).

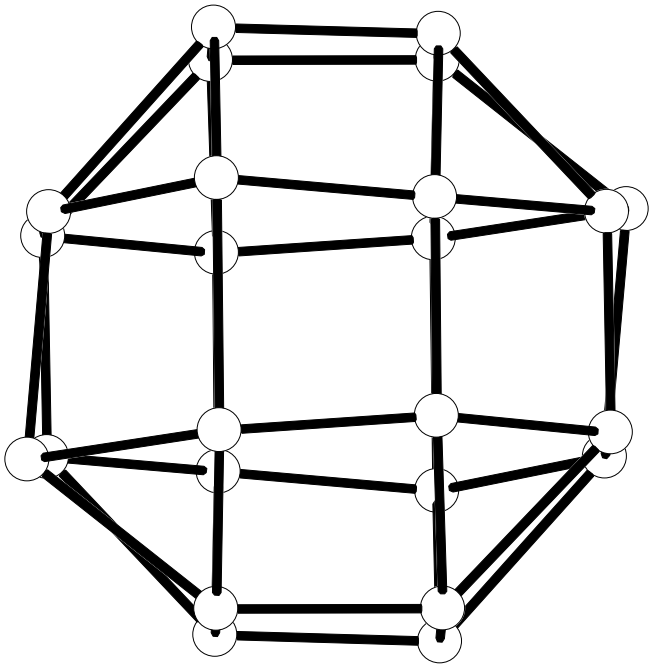

Figure 2: The rhombicuboctahedron spanned by the 24 μ_3-oxygen atoms of the $[Sb_4V_{16}O_{42}]^{8-}$ anion in (**1**).

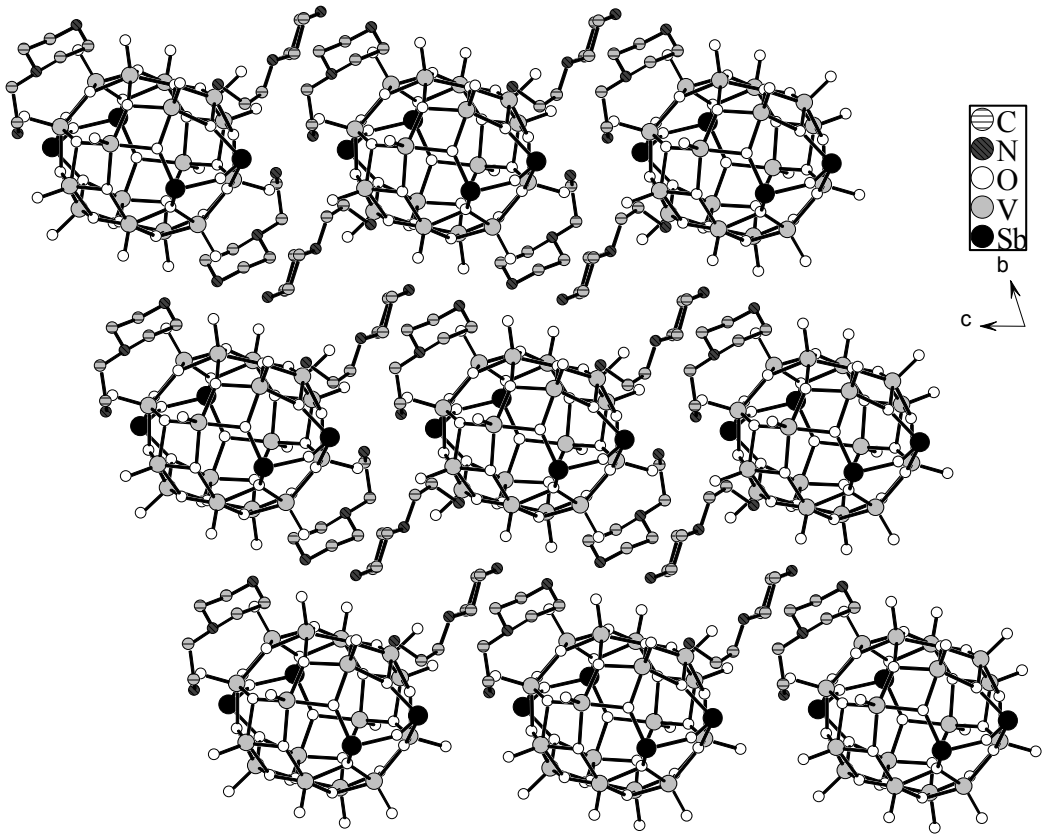

Figure 3: Arrangement of anions and cations in the structure of $[C_6H_{17}N_3]_4[Sb_4V_{16}O_{42}]\cdot 2H_2O$ (**1**) with view along the *a*-axis. Hydrogen atoms omitted for clarity.

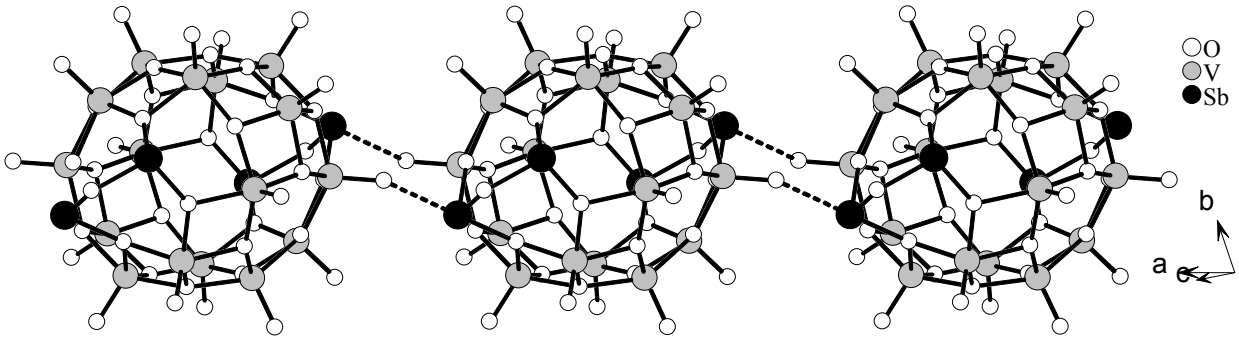

Figure 4: Chains in $[C_6H_{17}N_3]_4[Sb_4V_{16}O_{42}]\cdot 2H_2O$ (**1**) formed by long Sb-O bonds running along the *a*-axis. Long Sb-O bonds are indicated as dashed lines.

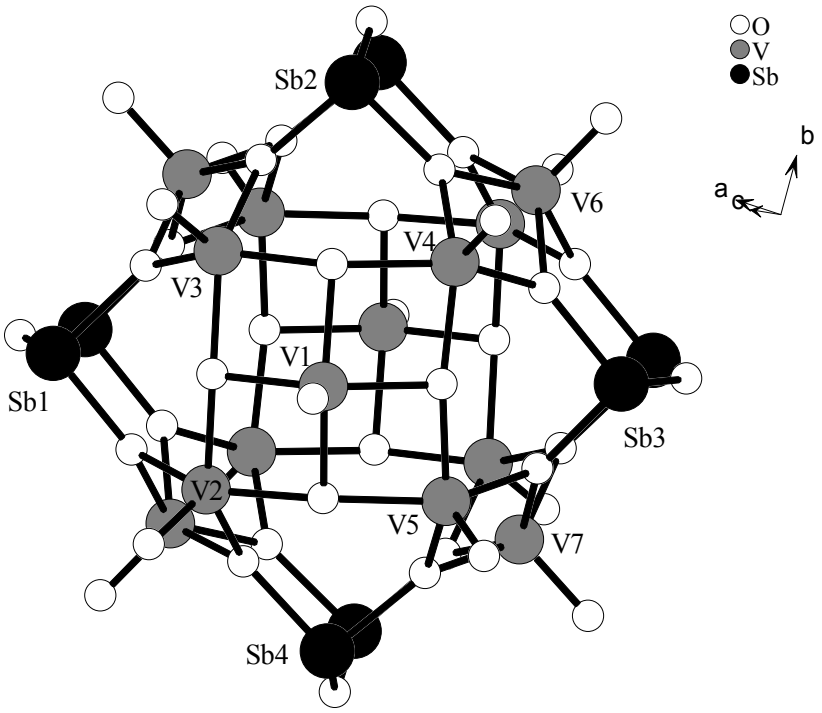

Figure 5: The $[Sb_8V_{14}O_{42}]^{4-}$ cluster in $[NH_4]_4[Sb_8V_{14}O_{42}]\cdot 2H_2O$ (**2**).

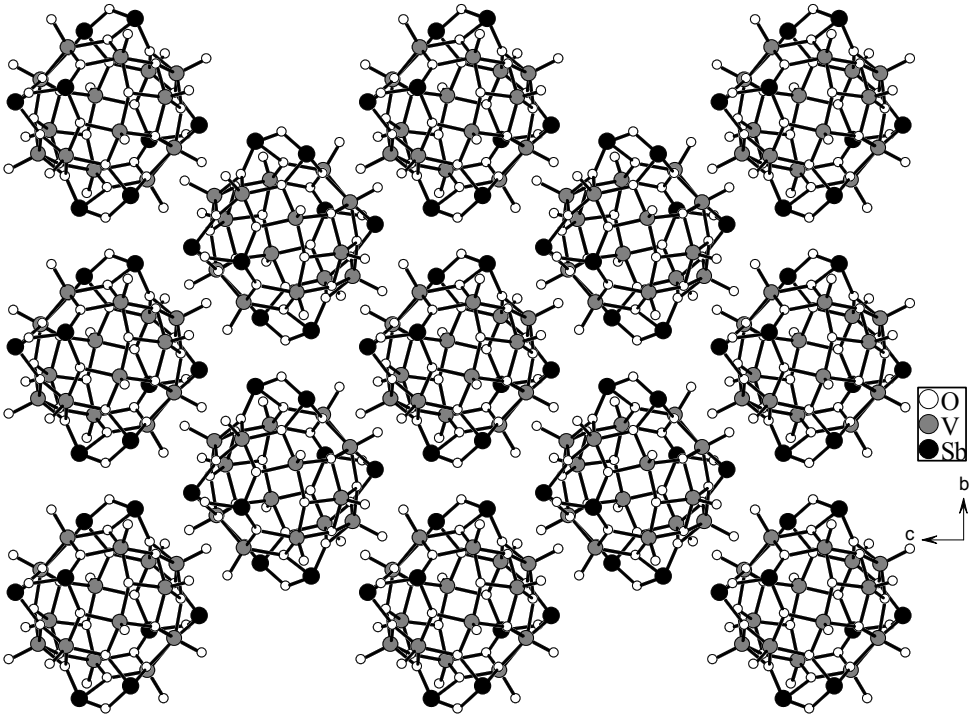

Figure 6: Arrangement of the anions in $[NH_4]_4[Sb_8V_{14}O_{42}]\cdot 2H_2O$ (**2**) with view along the *a*-axis.

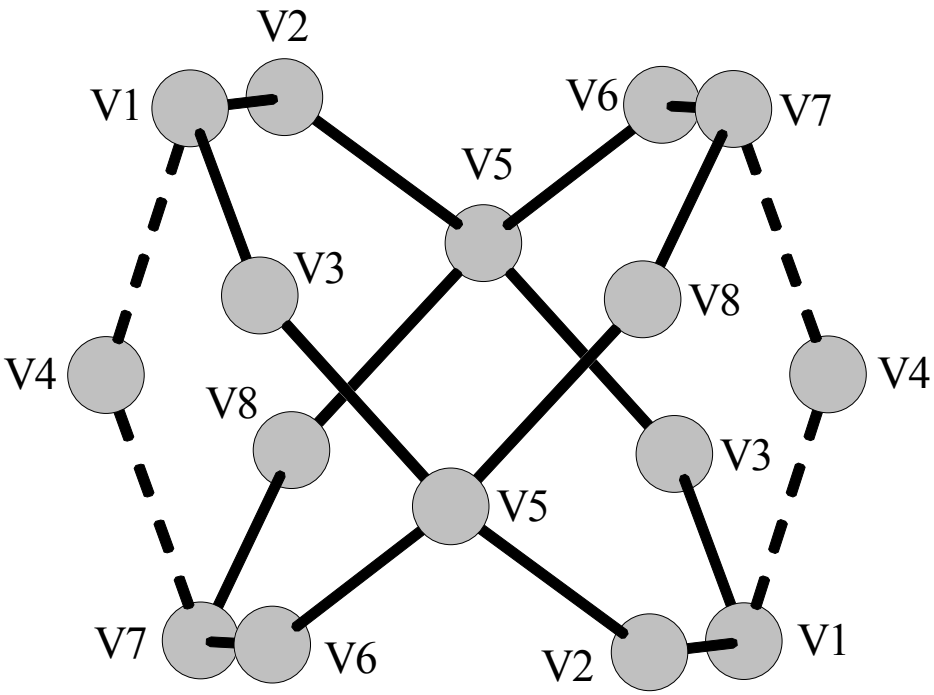

Figure 7a: V_8 rings in $[C_6H_{17}N_3]_4[Sb_4V_{16}O_{42}]\cdot 2H_2O$ (**1**).

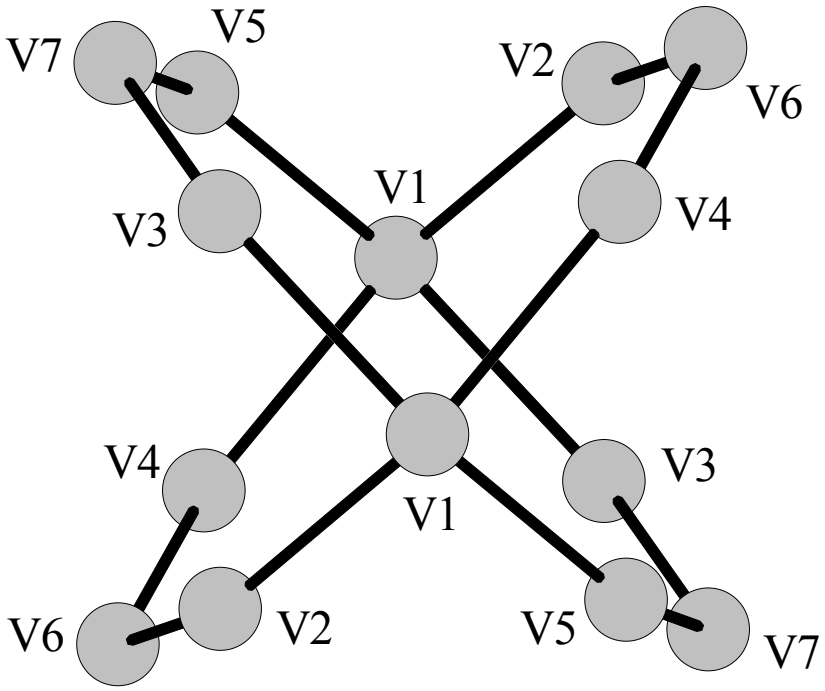

Figure 7b: V_8 rings in $[NH_4]_4[Sb_8V_{14}O_{42}]\cdot 2H_2O$ (**2**).

Table 1

Crystal data and selected refinement results for compounds (**1**) and (**2**).

	(**1**)	(**2**)
Crystal System.	triclinic	monoclinic
a/Å	12.056(2)	12.8396(3)
b/Å	12.583(3)	11.942(2)
c/Å	13.582(3)	17.280(4)
α/°	69.46(3)	90
β/°	66.41(3)	99.77(3)
γ/°	79.53(3)	90
V/Å^3	1766.1(6)	2607.1(9)
Space group	*P*-1	$P2_1/n$
T/K	293	293
Density / g cm^{-3}	2.383	3.117
μ/ mm^{-1}	3.60	7.84
Z	1	4
Reflections collected	15276	13132
unique reflections	8194	6290
Reflections with Fo > 4σ(Fo)	6055	5139
Number of parameters	451	317
R_{int}	0.0467	0.0489
R1 for Fo>4σ(Fo)	0.0460	0.0460
GOOF	0.992	1.089
wR_2 for all reflections	0.1237	0.1398
Δρ[e/Å^3]	-1.61/3.57	-2.374/2.821

Table 2

Selected bond lengths (in Å) for compound (**1**). Estimated standard deviations are given in parentheses.

Sb(1)-O(10)	1.956(4)
Sb(1)-O(15)	1.983(4)
Sb(1)-O(9)	1.967(5)
Sb(2)-O(20)	1.948(4)
Sb(2)-O(21)	1.934(4)
Sb(2)-O(9)	1.950(5)
V(1)-O(1)	1.640(4)
V(1)-O(10)	1.981(4)
V(1)-O(11)	1.919(4)
V(1)-O(12)	1.908(5)
V(1)-O(21)	1.983(4)
V(2)-O(10)	2.018(4)
V(2)-O(12)	1.936(4)
V(2)-O(13)	1.987(4)
V(2)-O(14)	1.936(5)
V(2)-O(2)	1.600(5)
V(3)-O(11)	1.912(4)
V(3)-O(16)	1.615(5)
V(3)-O(17)	1.932(4)
V(3)-O(21)	2.029(4)
V(3)-O(3)	1.984(4)
V(4)-O(11)	1.949(4)
V(4)-O(12)	1.988(4)
V(4)-O(18)	1.957(5)
V(4)-O(19)	1.966(4)
V(4)-O(4)	1.606(4)
V(5)-O(13)	2.006(4)
V(5)-O(14)	1.921(4)
V(5)-O(17)	1.932(4)
V(5)-O(3)	1.948(4)
V(5)-O(5)	1.629(5)
V(6)-O(13)	2.003(4)
V(6)-O(15)	1.992(5)
V(6)-O(17)	1.928(5)
V(6)-O(19)	1.950(4)
V(6)-O(6)	1.614(5)
V(7)-O(15)	1.969(4)
V(7)-O(18)	1.926(4)
V(7)-O(19)	1.929(5)
V(7)-O(20)	1.969(4)
V(7)-O(7)	1.632(4)
V(8)-O(14)	1.941(4)
V(8)-O(18)	1.949(4)
V(8)-O(20)	2.019(4)

V(8)-O(3)	1.965(4)
V(8)-O(8)	1.614(5)
V(2)-V(1)	3.013(2)
V(2)-V(5)	2.988(2)
V(3)-V(1)	3.032(2)
V(3)-V(5)	2.920(2)
V(4)-V(7)	2.953(2)
V(4)-V(1)	2.957(2)
V(5)- V(3)	2.989(2)
V(5)-V(6)	2.989(2)
V(5)-V(8)	2.845(2)
V(6)-V(7)	3.023(2)
V(7)-V(8)	3.061(2)

Table 3

Selected bond lengths (in Å) for compound (**2**). Estimated standard deviations are given in parentheses.

Sb(1)-O(1)	1.965(5)
Sb(1)-O(2)	1.996(5)
Sb(1)-O(7)	1.939(5)
Sb(2)-O(3)	1.969(5)
Sb(2)-O(4)	1.952(6)
Sb(2)-O(5)	1.969(6)
Sb(3)-O(6)	1.984(5)
Sb(3)-O(7)	1.934(5)
Sb(3)-O(8)	1.984(5)
Sb(4)-O(10)	1.969(5)
Sb(4)-O(4)	1.956(6)
Sb(4)-O(9)	1.963(5)
V(1)-O(11)	1.954(6)
V(1)-O(12)	1.970(5)
V(1)-O(13)	1.937(5)
V(1)-O(14)	1.950(5)
V(1)-O(15)	1.609(6)
V(2)-O(1)	1.990(5)
V(2)-O(10)	1.956(5)
V(2)-O(11)	1.933(5)
V(2)-O(14)	1.959(5)
V(2)-O(16)	1.611(6)
V(3)-O(11)	1.957(5)
V(3)-O(12)	1.937(5)
V(3)-O(17)	1.609(6)
V(3)-O(2)	1.969(5)
V(3)-O(3)	1.979(5)
V(4)-O(12)	1.962(5)
V(4)-O(13)	1.938(5)
V(4)-O(18)	1.588(6)
V(4)-O(5)	1.974(6)

V(4)-O(6)	1.971(5)
V(5)-(13)	1.931(5)
V(5)-O(14)	1.952(5)
V(5)-O(20)	1.618(6)
V(5)-O(8)	1.954(5)
V(5)-O(9)	1.981(5)
V(6)-O(1)	1.987(5)
V(6)-O(10)	1.970(5)
V(6)-O(19)	1.601(5)
V(6)-O(5)	1.979(6)
V(6)-O(6)	1.963(5)
V(7)-O(2)	1.967(5)
V(7)-O(21)	1.605(5)
V(7)-O(3)	1.962(5)
V(7)-O(8)	1.948(5)
V(7)-O(9)	1.976(5)
V(1)-V(2)	2.897(2)
V(1)-V(3)	2.934(2)
V(1)-V(4)	2.953(2)
V(1)-V(5)	2.878(2)
V(2)-V(6)	3.084(2)
V(3)-V(7)	3.067(2)
V(4)-V(6)	3.073(2)
V(5)-V(7)	3.085(2)

4.4 Ergebnisse und Publikationen zu chiralen Thioantimonaten

4.4.1 Die Verbindungen $[C_3H_{10}NO]_2[Sb_4S_7]$ (1) und (2)

Zusammenfassung der Veröffentlichung „*[C 3 H 10 NO] 2 [Sb 4 S 7]: Solvothermal syntheses, crystal structures and properties of the first thioantimonates containing aminoalcohols as structure directors* “.

Obwohl beide Verbindungen $[C_3H_{10}NO]_2[Sb_4S_7]$ dieselbe Zusammensetzung aufweisen, unterscheiden sich die Strukturen und die Dimensionalität der beiden $[Sb_4S_7]^{2-}$-Anionen signifikant voneinander.

Beide Verbindungen wurden unter solvothermalen Bedingungen bei unterschiedlichen Temperaturen synthetisiert. 1 mmol Sb und 3 mmol Schwefel wurden in 8 ml 1-Amino-2-propanol sieben Tage in Stahlautoklaven mit Tefloneinsätzen erhitzt. Für $[C_3H_{10}NO]_2[Sb_4S_7]$ (**1**) mit dem 1-dimensionalen $[Sb_4S_7]^{2-}$-Anion betrug die Reaktionstemperatur 140 °C, die Ausbeute in Form roter Kristalle betrug 60 % bezogen auf Antimon. Die Darstellung der Verbindung (**2**) mit dem 2-dimensionalen $[Sb_4S_7]^{2-}$-Anion erfolgte bei 160 °C. Die Ausbeute betrug 80 % bezogen auf Antimon in Form rot-oranger Kristalle.

Verbindung (**1**) kristallisiert in der nicht-centrosymmetrischen, orthorhombischen Raumgruppe *A*bm2 mit vier Formeleinheiten in der Elementarzelle. Das kettenförmige $[Sb_4S_7]^{2-}$-Anion besteht aus ringförmigen Sb_3S_6-Einheiten, welche über trigonale SbS_3-Pyramiden zu Ketten verknüpft sind (Abb. 4.10, links), die parallel zur *b*-Achse verlaufen. Der kürzeste Sb-S-Abstand zwischen den Ketten beträgt 3.43 Å und unter Berücksichtigung dieser langen Sb-S-Bindungen kommt es zur Ausbildung von Schichten in der (100)-Ebene. Der Interschichtabstand beträgt 8.75 Å und es kann angenommen werden, dass die hoch fehlgeordneten Kationen zwischen den anionischen Schichten lokalisiert sind.

Verbindung (**2**) kristallisiert in der triklinen Raumgruppe $P\bar{1}$ mit zwei Formeleinheiten pro Elementarzelle. Als primäre Baueinheiten werden zwei SbS_3- und zwei SbS_4-Einheiten gefunden. Die Verknüpfung dieser Einheiten über gemeinsame Ecken und

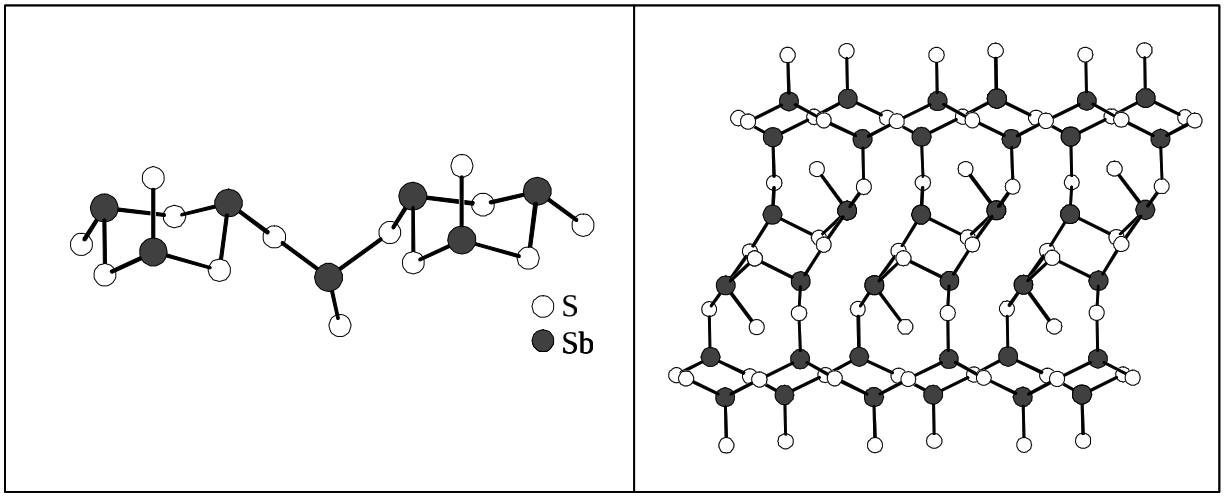

Abbildung 4.10: Kettenförmiges $[Sb_4S_7]^{2-}$-Anion in (**1**) (links) und $[Sb_4S_7]^{2-}$-Schichtanion in (**2**)

Kanten führt zur Bildung der Schichten in der (001)-Ebene (Abb. 4.10, rechts). Dabei werden $Sb_{10}S_{10}$-Ringe als sekundäre Baueinheiten gebildet. Der Interschichtabstand beträgt 7.8 Å. Die Kationen befinden sich zwischen den Schichten. Alle Stickstoffatome sind hierbei auf die Schwefelatome des $[Sb_4S_7]^{2-}$-Anions gerichtet. Alle an N gebundenen Wasserstoffatome sind an N-H$\cdots$S-Wasserstoffbrücken beteiligt.

Bei der Untersuchung der thermischen Stabilität wurde für (**1**) ein dreistufiger Massenabbau ($\Delta m_{(gesamt)} = 24.1$ %) mit endothermen Ereignissen in der DTA-Kurve detektiert. Der thermische Abbau beginnt bereits bei 70 °C und deutet auf eine schwache Einbindung des Amins in die Struktur. Unterstützt wird diese Vermutung durch breite Signale in der DTA-Kurve für die ersten beiden Stufen. Die dritte Stufe beginnt bei 257 °C, das DTA-Signal ist deutlich schärfer. Im grauen DTA-Abbauprodukt konnte im Pulverdiffraktogramm Sb_2S_3 nachgewiesen werden.

Die Verbindung (**2**) zersetzt sich in einer Stufe mit einem Gesamtmassenverlust von 21.1 %. Dieser wird von einem endothermen Signal in der DTA-Kurve begleitet. Das Abbauprodukt ist identisch zu (**1**).

Untersuchungen der Emissionsprodukte für beide Verbindungen mit Massenspektroskopie konnten im Vergleich mit Spektren aus Datenbanken klar zeigen, dass in beiden Verbindungen 1-Amino-2-propanol enthalten ist (Abb. 4.12, rechts).

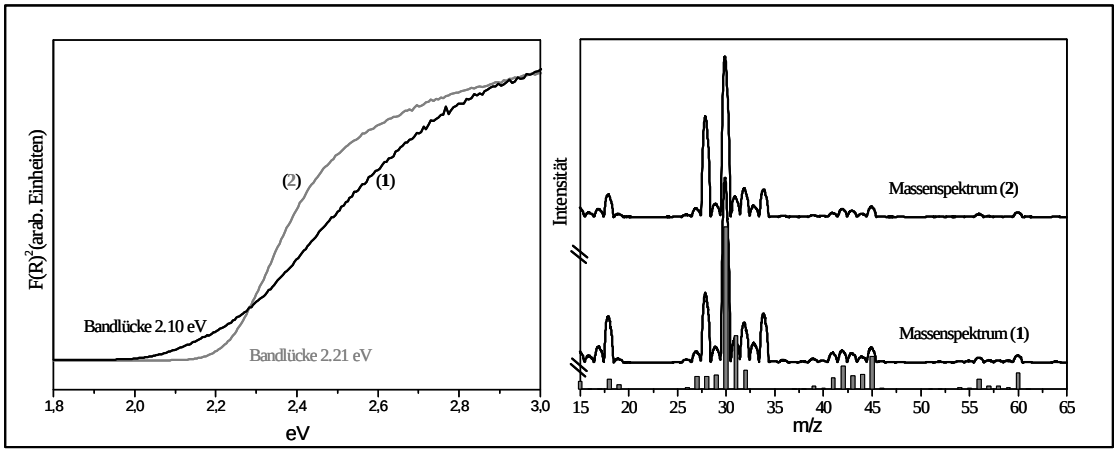

Abbildung 4.11: UV-Vis-Spektren (links) und Massenspektren (rechts)von (**1**) und (**2**)

Die Bestimmung der Bandlücke nach der Methode von Kubelka-Munk ergab einen Wert von 2.10 eV für (**1**) und 2.21 eV für (**2**)(Abb. 4.11, links).

Angemerkt werden muss, dass die Topologie beider Anionen bereits in anderen Thioantimonaten gefunden wurde. Das Verknüpfungsmuster in (**1**) wird in anderen Verbindungen mit einem $[Sb_4S_7]^{2-}$-Anion beobachtet [53][54]. Das 2-dimensionale Sb-S-Netzwerk in (**2**) ist isostrukturell mit einer Reihe von Verbindungen, die 2005 von unserer Arbeitsgruppe veröffentlicht wurde [55]. Interessant an den beiden neuen Verbindungen ist, dass es erstmals gelungen ist, Aminoalkohl als organisches „Templat“ in ein Thioantimonat einzubauen. Dies stellt den ersten Schritt auf dem Weg zu chiralen Thioantimonaten dar. Im Fall von (**1**) und (**2**) wurde ein racemisches Gemisch des Aminoalkohols eingesetzt. Ein weiteres Ziel der synthetischen Arbeiten ist, Übergangsmetallkomplexe mit den Aminoalkoholen in das Sb-S-Netzwerk zu integrieren. Als letzter Schritt soll die Verwendung chiraler Aminoalkohole erfolgen. Die gebildeten Verbindungen kristallisieren dann in chiralen Raumgruppen und wären damit Kandidaten für NLO-Effekte.

$[C_3H_{10}NO]_2[Sb_4S_7]$: Solvothermal syntheses, crystal structures and properties of the first thioantimonates containing aminoalcohols as structure directors

Ragnar Kiebach, Andreas Griebe, Christian Näther and Wolfgang Bensch*

Institut für Anorganische Chemie, Christian-Albrechts-Universität Kiel,

Olshausenstr. 40, D-24098 Kiel, Germany

*correspondence address: Prof. Dr. Wolfgang Bensch,

Institute for Inorganic Chemistry

University of Kiel

Olshausenstraße 40

D-24098 Kiel

Germany

Abstract:

Using solvothermal conditions two new thioantimonates with composition $[C_3H_{10}NO]_2[Sb_4S_7]$ were obtained containing protonated 1-amino-2-propanol as the structure directing molecule. Both compounds have the same composition but the anionic $[Sb_4S_7]^{2-}$ part is significantly different. In (**1**) three trigonal $[SbS_3]$ pyramids are connected via common corners yielding a $[Sb_3S_6]$ ring. These rings are connected by another $[SbS_3]$ unit thus building the one-dimensional $[Sb_4S_7]^{2-}$ chain. In (**2**) a two dimensional $[Sb_4S_7]^{2-}$ anionic network is formed by the interconnection of two trigonal pyramidal $[SbS_3]$ units and two $[SbS_4]$ moieties. A remarkable feature of the structure is a $[Sb_4S_{10}]$ moiety composed of four edge sharing $[SbS_4]$ units. The layered anion contains a $Sb_{10}S_{10}$ ring and the inter-layer distance of about 7.8 Å is caused by the special arrangement of the two crystallographically distinct

protonated 1-amino-2-propanol cations. Both compounds were prepared using the same amount of starting materials but at different reaction temperatures. Hence, the two compounds are another examples for the sensitivity of reaction parameters in solvothermal syntheses. The compounds are optical semiconductors with band gaps of 2.10 eV (**1**) and 2.21 eV (**2**). Thermal decomposition in an inert atmosphere leads to a collapse of the structures and Sb_2S_3 is formed as the reaction product.

Keywords: Solvothermal Synthesis, Thioantimonates, Aminoalcohol, organic-inorganic hybrid material

Introduction:

In the area of microporous materials the class of thioantimonates becomes more and more important and the number of these compounds synthesised via the solvothermal route has grown rapidly in the last few years [1-20]. The remarkable properties like tuneable optical band gaps [21], superconductivity [22], photoconductivity [23] or thermally induced structure transformation [24] discovered during the last few years are as interesting as those reported for oxidic materials like zeolites. Most zeolites are colourless and have a band gap larger than 3.0 eV, whereas in the overwhelming cases sulphides are coloured with optical band gaps covering a large range. Compounds with a zeolite-like structure based on sulphides should show different physical and chemical properties compared with those of oxidic materials. Many efforts were undertaken during the last years to synthesise chiral or at least non-centrosymmetric porous compounds due to their potential as catalysts [25] and as non-linear optical materials. One synthetic strategy is the usage of chiral templates like aminoalcohols with the hope that the chiral information of the template will be transferred to the host structure [26]. Several oxidic compounds containing such templates have been synthesised. But the major problem is that in most cases only the template is chiral and the surrounding

network structure is not. Unfortunately, after removal of the template the compound loses its chiral information and then the remaining network is more or less useless for further applications, and so far only a few chiral porous materials are known [27-29].

In several thioantimonates, transition metal (TMs) ions like Fe, Zn, Mn, or Ni are integrated in the network structure [21,30-34]. The TMs are responsible for the interesting properties mentioned above and in some compounds the organic templates (mostly amines) are coordinated to free sites of the TMs. The coordinative bonds between the transition metal and the N atoms of the ligands are much stronger than the van der Waals and N-H···S hydrogen bonds occurring between uncoordinated templates and the network structure. It should be possible to use then free sites of TMs which are not bound to N atoms of the amines to transfer the chiral information from the ligands to the network. Hence, a challenging synthetic step is to link chiral TMs complexes to the thioantimonate(III) network, hoping that the final compounds are also chiral or at least crystallise in a non-centrosymmetric space group. A first synthetic approach for the solvothermal synthesis of non-centrosymmetric sulphide networks is the application of chiral structure directing molecules, and as pointed out above promising candidates are chiral amines and aminoalcohols. In this report we present the synthesis, crystal structures, thermal and optical properties of two new compounds with the formula $[C_3H_{10}NO]_2[Sb_4S_7]$ using 1-amino-2-propanol as the structure directing molecule. Interestingly, one of the two compounds crystallises in a non-centrosymmetric space group whereas the other is centrosymmetric.

Results and discussion:

Crystal structures

Both compounds have the chemical composition $[C_3H_{10}NO]_2[Sb_4S_7]$ but the structures contain different primary building units (PBUs) and the connection of these units leads to different dimensionalities of the thioantimonate network.

*Crystal structure of (**1**):*

Compound (**1**) crystallises in the non centro-symmetric orthorhombic space group Abm2 with four formula units per unit cell. The atoms Sb(2), S(2) and S(3) are on general positions whereas the other atoms reside on special positions. Crystallographic data are summarised in Table1. Three unique Sb atoms are surrounded by three sulphur atoms each forming $[SbS_3]$ trigonal pyramids as primary building units. The Sb-S bonds lengths range from 2.364(4) Å to 2.509(2) Å and the angles are between 81.5(2)° and 107.5(2)° (Table 2). All geometric parameters are in the range reported for other thioantimonates(III) [1-26,30-34].

Three of the PBUs are connected via common corners yielding a $[Sb_3S_6]$ ring as secondary building unit (SBU), a structure motif often observed in thioantimonates. The rings are connected by another $[SbS_3]$ moiety thus building the one-dimensional $[Sb_4S_7]^{2-}$ chain running along the *b*-axis (Fig. 1). The topology of the anionic chain is very similar with that observed in other compounds with the $[Sb_4S_7]^{2-}$ anion [3,10,13].

It is most likely that the disordered $[C_3H_{10}NO]^+$ cations are located between neighbouring Sb-S chains along the a-axis. The inter-chain separations amount to 8.75 Å along [100] and to 3.43 Å along [001]. When long Sb-S distances between 3.0 and 3.7 Å (Table 3) are considered as weak interactions a two-dimensional layered network extending in the (100) plane is formed (Fig. 2) with the inter-layer distance of 8.75 Å. With the Sb-S long distances the Sb(1) atom is surrounded by five sulfur atoms while Sb(2,3) are sixfold coordinated forming strongly distorted octahedra.

*Crystal structure of (**2**):*

Compound (**2**) crystallizes in the triclinic space group $P\bar{1}$ (Table 1) with the four independent Sb and the seven unique S atoms being located on general positions. The structure consists of a two dimensional $[Sb_4S_7]^{2-}$ anionic network (Fig. 3, top) and of two crystallographically distinct protonated 1-amino-2-propanol cations (Fig. 3, bottom). Note that this compound is isostructural to a group of thioantimonates with general formula $(amine)_2[Sb_4S_7)$ published

recently [2]. Two trigonal pyramidal [SbS_3] units (Sb(3,4)) and two [SbS_4] moieties (Sb(1,2)) are the PBUs forming the $[Sb_4S_7]^{2-}$ anion. The Sb-S distances vary between 2.397(2) and 3.034(2)Å with S-Sb-S angles ranging from 81.7(1) to 166.9(1)° (Table 2). These geometric parameters are observed in many thioantimonates(III) [1-26,30-34]. The [SbS_3] pyramids share common corners to form [Sb_2S_5] chains running along [100]. The two [SbS_4] groups have a common edge yielding a [Sb_2S_6] unit. Adjacent chains are joined via the [Sb_2S_6] groups into a two atoms thick layer (Fig. 4). The layer contains a $Sb_{10}S_{10}$ ring as secondary building unit. Further interconnection to a symmetry related layer proceeds via S(3) atoms thus yielding the final double-layered $[Sb_4S_7]^{2-}$ anion extending in the (001) plane (Fig. 4). A remarkable structural feature is the [Sb_4S_{10}] moiety composed of four edge sharing [SbS_4] units. The large interlayer distance of approximately 7.8 Å is caused by the arrangement of the cations (Fig. 5) which are grouped in pairs with the N atom pointing towards S atoms of the thioantimonate(III) anion. All hydrogen atoms are involved in N-H···S bonding interactions. We note that the arrangement of the organic ions is reminiscent of that found in intercalated clays. The long Sb-S separations (Table 3) are all within the layers enhancing the coordination numbers of Sb(1) and Sb(2) to 5 and of Sb(4) to 4.

Thermal investigations:

Heating compound (1) under dynamic helium atmosphere a decomposition occurs in three steps, clearly observable in the DTG curve, with total mass loss Δ_m = 24.1% (Fig. 6). All events are accompanied by endothermic peaks in the DTA curve (Fig. 6). The thermal decomposition may be separated into two parts with similar mass losses which may correspond to the emission of the two crystallographically unique protonated aminoalcohols. In the first part (Δ_m = 11.1%) the DTA signals are broad and diffuse. Note that in compound (**1**) the organic ions are strongly disordered which may be caused by very weak inter-ionic interactions and/or many energetically equivalent positions for the cations. The decomposition

starts at a relatively low temperature (~70 °C) indicating a weak interaction between the amine and the Sb-S network. In the second part a pronounced one step mass loss of 10.3 % is observed which is accompanied with a sharp endothermic signal in the DTA curve at T_{Peak} = 217. These results indicate a rather complex decomposition mechanism.

Compared to compound (**1**) the decomposition of (**2**) is quite simple. The thermal reaction starts at T = 180 °C and only one step with a total mass loss of 21.1 % is observed (Fig. 7). The decomposition is accompanied by one very broad endothermic peak in the DTA curve at T_{peak} = 232°C. This peak contain an additional shoulder indicating that the reaction is more complex.

For both compounds the experimental mass loss is higher than the theoretical value expected for the emission of the aminoalcohol (17.6 %). The difference of 3.8 % for (**1**) and 3.5 % for (**2**) between the experimental data and the expected theoretical value can be explained by emission of H_2S which was detected by mass spectroscopy. The formation of H_2S during thermal decomposition of organically templated thioantimonates(III) is often observed [2]. The emission of two moles of non-protonated aminoalcohol and one mol H_2S gives a theoretical mass loss of 21.3 % which is in good accordance with the experimental values.

The grey residues remaining after thermal decomposition contained Sb_2S_3, frequently found after thermal decomposition of thioantimonates. CHN analyses were performed and in both cases the sum ΣCHN was smaller than 1% demonstrating that the organic part was nearly completely emitted.

Mass spectroscopy:

Simultaneously recorded mass spectra during the decomposition yield identical results for (**1**) and (**2**) (Fig. 8). The spectra are compared with the mass spectra of 1-amino-2-propanol. All three spectra are almost identical and the different emission can be explained on the basis of the decomposition of the organic molecule as well as the emission of H_2S. The peaks in the experimental spectra located at 34 and 32 m/z correspond to H_2S and S, the latter being a

decomposition product of H_2S. The main result of the MS experiments is the proof for the existence of 1-amino-2-propanol in (**1**) which could not be located in single crystal structure analysis.

UV/Vis spectroscopy:

For both compounds the optical band gap was calculated from UV/Vis data after the method of Kubelka and Munk. The values for (**1**) and (**2**) (Fig. 9) are 2.10 eV (590 nm) and 2.21 eV (560 nm) respectively corresponding to the red (**1**) and orange (**2**) colours of the crystals. Both compounds are optical semi-conductors and in combination with the acentric space group, compound (**1**) is a potential candidate for NLO effects.

Conclusion:

The two new compounds present the first thioantimonates(III) which contain an aminoalcohol as a structure directing molecule. It can be assumed that the number of thioantimonates(III) can be significantly enhanced performing systematic syntheses. In addition, the two compounds are nice examples demonstrating the sensitivity of solvothermal syntheses with respect to the reaction parameters. Increasing the temperature by 20 K leads to the formation of a compound with the same composition but with a different structure. The thioantimonate(III) (2) prepared at the higher temperature (160°C) is layered and shows a slightly larger calculated density than compound (1) which was obtained at 140°C. In the latter compound a one-dimensional thioantimonate(III) anion is found and only weak inter-chain Sb-S interactions are present.

Experimental section:

Synthesis:

The title compounds were prepared in 30 ml Teflon-lined stainless-steel autoclaves. (**1**) was synthesised using a reaction mixture of 121 mg Sb (1 mmol), 96 mg S (3 mmol) and 8 ml 1-amino-2-propanol. The mixture was heated for seven days at 140 °C and then cooled down to

room temperature within 3 h. The red crystals were washed with water, ethanol and acetone (yield 60 % based on Sb). Compound (**2**) was synthesised with the same reaction mixture and only the reaction temperature was increased to 160 °C. The product occurs in form of orange needles (yield 80 % based on Sb) and was cleaned as mentioned above.

Crystal structure determination:

Single crystal X-ray intensity data were collected at room temperature on a STOE-1 Imaging Plate Diffraction System with graphite monochromated MoK_α radiation (λ = 0.71073 Å). Selected crystal data and details of the structure determination are summarized in Table 1. The intensities were corrected for Lorentz and polarization effects. Structure solution was performed with SHELXS-97 [35] and refinement against F^2 using SHELXL-97 [36]. The non-hydrogen atoms were refined using anisotropic displacement parameters. The hydrogen atoms were positioned with idealized positions and refined with isotropic displacement parameters using a riding model. The amine molecules in (**1**) are disordered and no suitable model was found. Therefore the intensity data were corrected using the squeeze option in PLATON [37]. Selected bond length and angles are given in Tables 2 and 3. Crystallographic Data (excluding structure factors) have been deposited with Cambridge Crystallographic Data Centre as supplementary publication no. CCDC 287039 (**1**) and CCDC 287040 (**2**). Copies of the data can be obtained, free of charge, on application to CCDC, 12, Union Road, Cambridge CB2 1 EZ, UK. (fax +44(0)1223-336033 or email: deposit@ccdc.cam.ac.uk).

CHN analyses:

(1, $C_6H_{20}N_2O_2S_7Sb_4$, M = 863.7 g/mol) Calc. %C = 8.34, %H = 2,33 %N = 3.24; found %C = 8.16, %H = 2,21, %N = 3.45; (2, $C_6H_{20}N_2O_2S_7Sb_4$, M = 863.7 g/mol) Calc. %C = 8.34, %H = 2.33 %N = 3.24; found %C = 8.32, %H = 2.18, %N = 3.18.

Thermal investigations:

DTA-TG-MS measurements were conducted simultaneously using a STA-409CD device (Netzsch) with Skimmer coupling, which is equipped with a Balzers QMA 400 Quadrupole

Mass Spectrometer (max. 512 amu). The MS measurements were performed in the analogue and trend scan modes. All measurements were corrected for buoyancy and current effects and were carried out with heating rates of 4 °C/min in Al_2O_3 crucibles under a dynamic helium atmosphere (flow-rate: 75 mL min^{-1}).

UV/Vis spectroscopy:

UV/Vis spectroscopic investigations were conducted at room temperature using a UV-VIS-NIR two-channel spectrometer Cary 5 from Varian Techtron Pty., Darmstadt. The optical properties of the compounds were investigated by studying the UV/Vis reflectance spectrum of the powdered sample. The absorption data were calculated using the Kubelka-Munk relation for diffuse reflectance data. $BaSO_4$ powder was used as reference material.

Acknowledgement: Financial support by the state of Schleswig-Holstein and the Deutsche Forschungsgemeinschaft are acknowledged. Many thanks to Karina Möller for the excellent synthesis optimisation.

References:

[1] Kiebach R., Näther C., Bensch W., Z. Naturforsch. 59b (2004) 1314.

[2] Puls A., Schaefer M., Näther C., Bensch W., Powell A.V., Boissiere S., Chippindale A.M., J. Solid State Chem. 178 (2005) 1171.

[3] Bensch W., Schur M., Z. Naturforsch. 52b (1997) 405.

[4] Spetzler V., Rijnberk H., Näther C., Bensch W., Z. Anorg. Allg. Chem. 630 (2004) 142.

[5] Engelke L., Näther C., Bensch W., Eur. J. Inorg. Chem. (2002) 2936.

[6] Stähler R., Mosel B.-D., Eckert H., Bensch W., Angew. Chem. 114 (2002) 4671; Angew. Chem. Int. Ed. 41 (2002) 4487.

[7] Volk K., Bickert P., Kolmer R., Schäfer H., Z. Naturforsch. 34b (1979) 380.

[8] Cordier G., Schäfer H., Rev. Chim. Miner. 18 (1981) 218.

[9] Cordier G., Schäfer H., Schwidetzky C., Rev. Chim. Miner. 22 (1985) 722.

[10] Dittmar G., Schäfer H., Z. Anorg. Allg. Chem. 437 (1983) 1977.

[11] Stephan H.-O., Kanatzidis M.G., Inorg. Chem. 36 (1997) 6050.

[12] Ko Y., Tan K., Parise J.B, Darovsky A., Chem. Mater. 8 (1996) 493.

[13] Parise J.B., Ko Y., Chem. Mater. 4 (1992) 1446.

[14] Schaefer M., Kurowski D., Pfitzner A., Näther C., Bensch W., Acta. Cryst. E60 (2004) m183.

[15] Pfitzner A., Kurowski D., Z. Kristallogr. 215 (2000) 373.

[16] Vaquiero P., Chippindale A. M., Powell A. V., Inorg. Chem. 43 (2004) 7963.

[17] Powell A.V., Paniagua R., Vaqueiro P., Chippindale A. M., Chem. Mater. 14 (2002) 1220.

[18] Vaqueiro P., Chippindale A. M., Cowley A. R., Powell A.V., Inorg. Chem. 42 (2003) 7846.

[19] Powell A.V., Boissière S., Chippindale A. M., J. Chem. Soc., Dalton Trans. (2000) 4192.

[20] Powell A.V., Boissière S., Chippindale A. M., Chem. Mater. 12 (2000) 182.

[21] Schaefer M., Stähler R., Kiebach R., Bensch W., Z. Anorg. Allg. Chem. 43 (2004) 1816.

[22] Lee C.-S., Safa-Sefat A., Greedan J. E., Kleinke H., Chem. Mater. 15 (2003) 780.

[23] Starrost F., Krasovskii, E. E., Schattke W., Simon U., Wang X., Liebau F., Phys. Rev. Lett. 80 (1998) 3316.

[24] Schaefer M., Näther C., Lehnert N., Bensch W., Inorg. Chem. 43 (2004) 2914.

[25] Li Y., Yu J., Wang Z., Guo M., Xu R., Chem. Mater. (2005) in press.

[26] Davis M. E., Lobo R. F., Chem. Mater. 4 (1992) 756.

[27] Gier T. E., Bu X., Feng P., Stucky G. D., Nature 395 (1998) 154.

[28] Higgins J. B., LaPierre R. B., Schlenker J. L., Rohrmann A. C., Wood J. D., Kerr G. T., Rohrbaugh W. J., Zeolites 8 (1998) 446.

[29] Cheetham A. K., Fjellvåg H., Grier T. E., Kongshaug K. O., Lillerud K. P., Stucky G. D., Stud. Surf. Sci. Catal. 135 (2001) 158.

[30] Kiebach R., Bensch W., Hoffmann R.-D., Pöttgen R., Z. Anorg. Allg. Chem. 629 (2003) 532.

[31] Schaefer M., Näther C., Bensch W., Solid State Sci. 5 (2003) 4525.

[32] Schaefer M., Engelke L., Näther C., Bensch W., Z. Anorg. Allg. Chem. 629 (2003) 1912.

[33] Stähler R., Bensch W., Eur. J. Inorg. Chem. (2001) 3073.

[34] Stähler R., Bensch W., J. Chem. Soc., Dalton Trans. (2001) 2518.

[35] Sheldrick G. M., SHELXS-97, Program for Crystal Structure Solution, University of Göttingen, Germany (1997).

[36] Sheldrick G. M., SHELXL-97, Program for the Refinement of Crystal Structures, University of Göttingen, Germany, 1997.

[37] Spek A. L., PLATON, A Multipurpose Crystallographic Tool, Utrecht University, Utrecht, The Netherlands, 2000.

Table 1

Details of data acquisition and refinement results for compounds (**1**) and (**2**).

	(**1**)	(**2**)
Crystal System.	orthorhombic	triclinic
a /Å	19.6319(17)	7.0100(14)
b /Å	9.9412(7)	11.950(2)
c /Å	11.3727(9)	14.570(3)
α /°	90	113.43(3)
β /°	90	97.86(3)
γ /°	90	92.26(3)
V /Å^3	2219.5(3)	1103.4(4)
Space group	Abm2	P $\bar{1}$
T / K	293	293
Formula	$C_6H_{20}N_2O_2S_7Sb_4$	$C_6H_{20}N_2O_2S_7Sb_4$
M /g·mol	863.7	863.7
Density / g cm-3	2.539	2.599
M / mm^{-1}	5.475	5.508
Z	4	2
Reflections collected	10502	10016
Independent reflections	2667	5157
Reflections with Fo<4σ(Fo)	2298	4460
Number of parameters	59	193
R_{int} /%	5.98	3.62
R1 for Fo>4σ(Fo) / %	3.98	3.25
GOOF	0.965	1.126
*w*R2 for all reflections / %	9.70	9.07
Δρ / e/Å^3	-1.64/1.29	-1.53/1.28
Flack x-parameter	-0.06(5)	-

Table 2
Selected bond length (in Å) and angles (in °) in the compounds (**1**) and (**2**). Estimated standard deviations are given in parentheses.

	(**1**)	(**2**)
Sb1-S1	2.364(4)	2.515(2)
Sb1-S2	2.477(3) (2×)	2.536(2)
Sb1-S3		2.421(2)
Sb1-S3		3.034(2)
Sb2-S2	2.486(2)	
Sb2-S1		2.473(2)
Sb2-S3	2.490(2)	2.781(2)
Sb2-S4	2.480(2)	2.422(2)
Sb2-S5		2.658(2)
Sb3-S3	2.509(2) (2×)	
Sb3-S5	2.391(3)	2.397(2)
Sb3-S6		2.458(2)
Sb3-S7		2.577(2)
Sb4-S2		2.457(2)
Sb4-S6		2.469(2)
Sb4-S7		2.423(2)
S1-Sb1-S2	93.01(2)	84.80(6)
S1-Sb1-S3		90.42(6)
S1-Sb2-S3		87.76(5)
S2-Sb1-S3		97.10(6)
S2-Sb2-S3	92.78(9)	
S2-Sb1-S2	97.32(13)	
S2-Sb2-S4	81.56(8)	
S2-Sb4-S7		94.37(6)
S3-Sb2-S4		87.67(5)
S3-Sb3-S3	95.32(11)	
S3-Sb3-S5	96.37(7)	
S4-Sb2-S5		88.41(6)
S5-Sb3-S7		90.48(6)
S6-Sb3-S7		86.54(6)
S6-Sb4-S7		93.32(6)

Table 3
The long Sb-S separations (< 3.7 Å) in compounds (**1**) and (**2**).

	(**1**)	(**2**)
Sb1-S3		3.034(23)
Sb1-S4	3.086(4)	3.281(71)
Sb1-S5	3.526(6)	
Sb2-S3	3.397(4)	3.638(50)
Sb2-S4		
Sb2-S5	3.181(5)	
Sb2-S5	3.238(2)	
Sb3-S3	3.627(4)	
Sb3-S3		
Sb3-S4		3.083(71)
Sb3-S5	3.429(5)	
Sb4-S4		3.407(53)

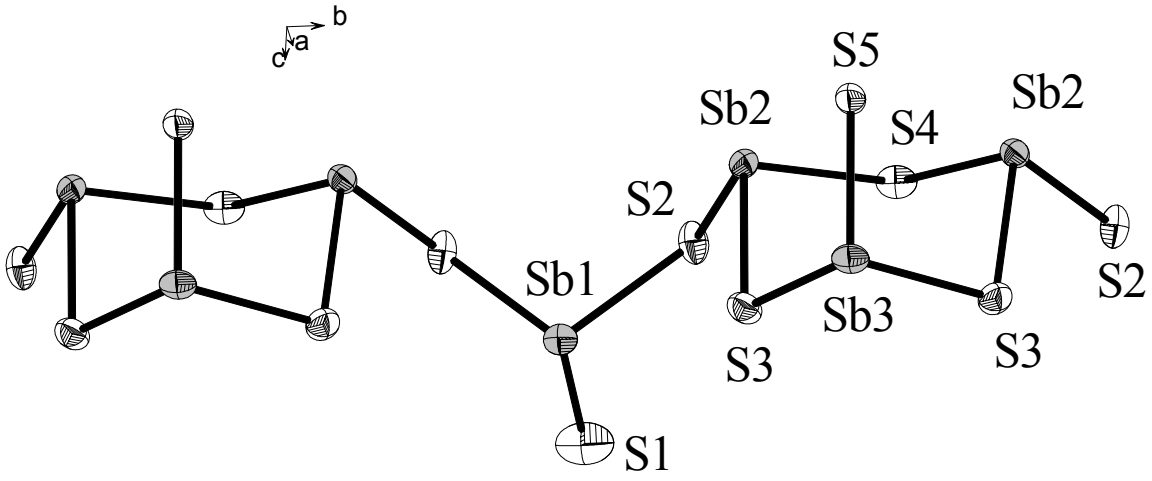

Figure 1: Interconnection of the [SbS_3] trigonal pyramids into the one-dimensional $[Sb_4S_7]^{2-}$ chain running along the *b*-axis in compound (1). Ellipsoids are drawn at the 50% probability level.

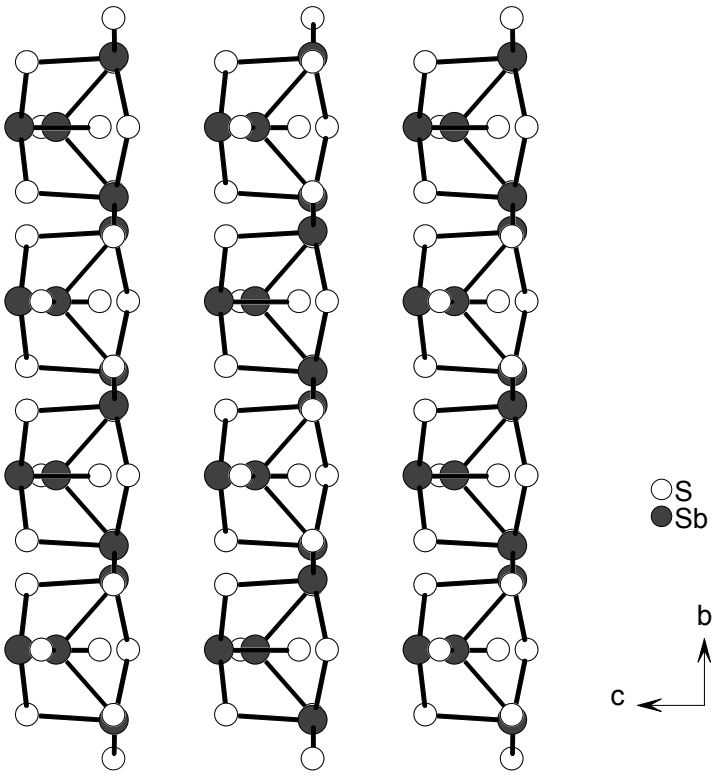

Figure 2: Crystal structure of (**1**) with view along the *a*-axis.

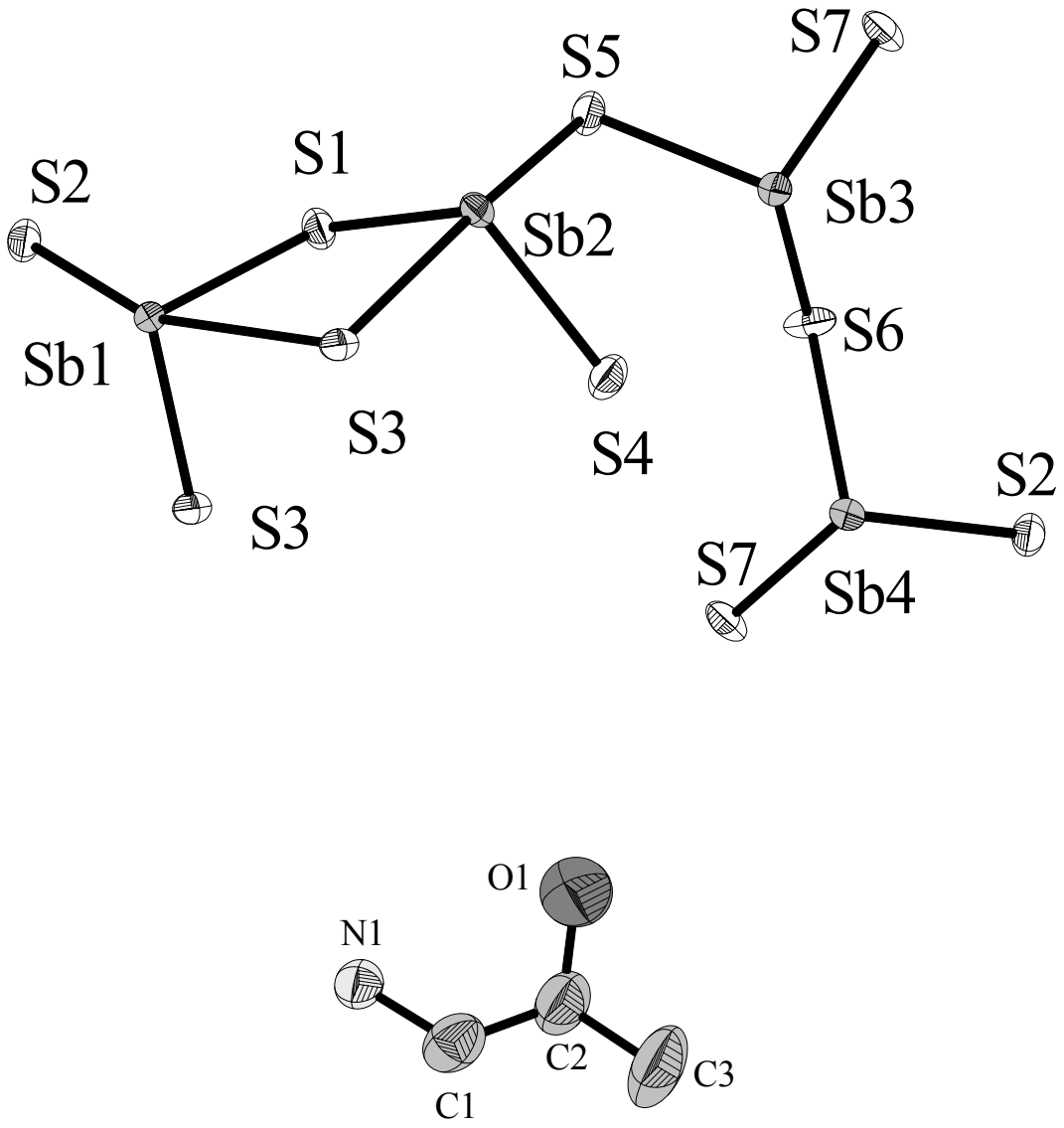

Figure 3: (top) Interconnection of the trigonal [SbS_3] pyramids and the [SbS_4] unit in (**2**). (bottom): $[C_3H_{10}NO]^+$ cation in (**2**). Hydrogen atoms are omitted for clarity. The ellipsoids are drawn at the 50% probability level.

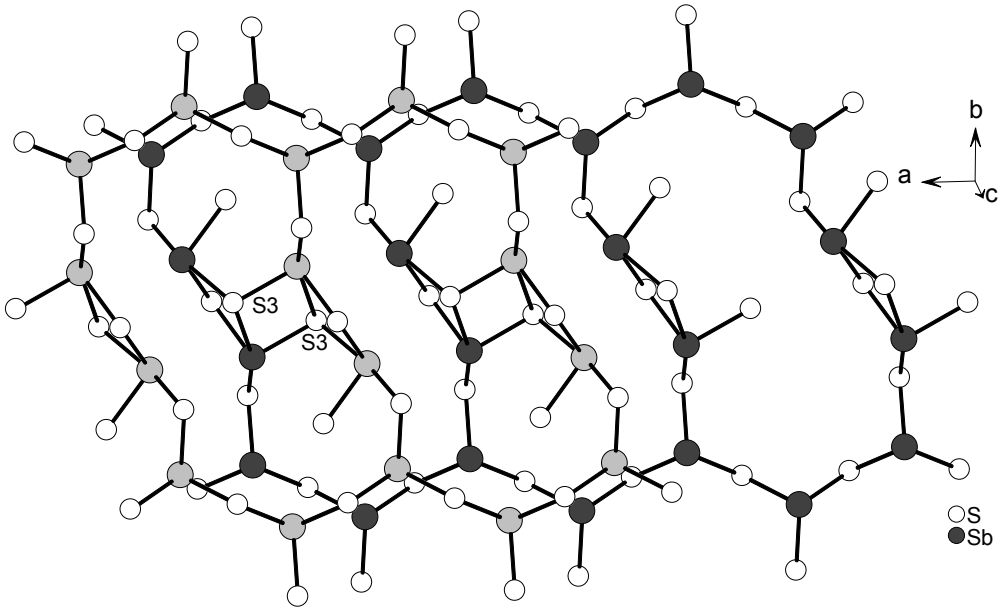

Figure 4: The $[Sb_4S_7]^{2-}$ double layer in compound (**2**). Note that Sb atoms of the two different layers have a different colour.

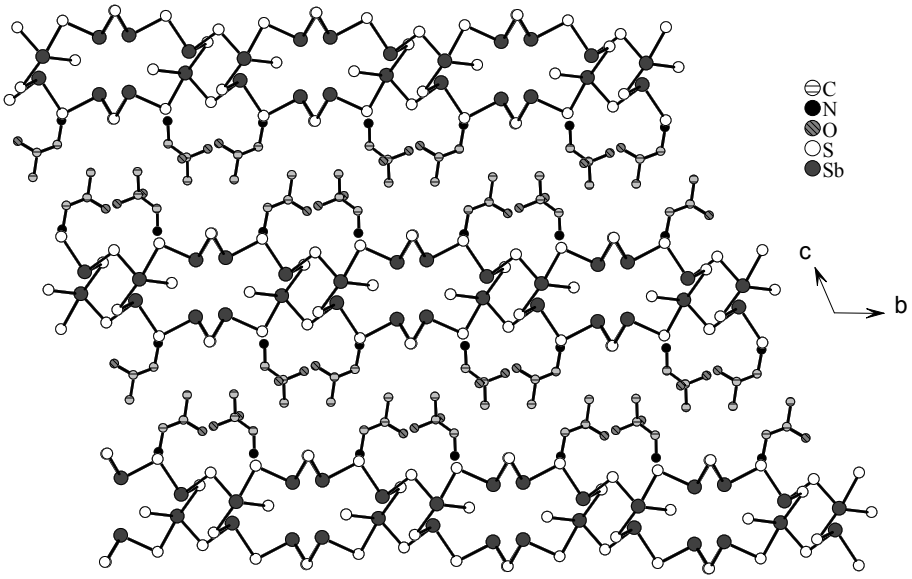

Figure 5: Crystal structure of (**2**) with view along the *a*-axis showing the arrangement of anions and cations.

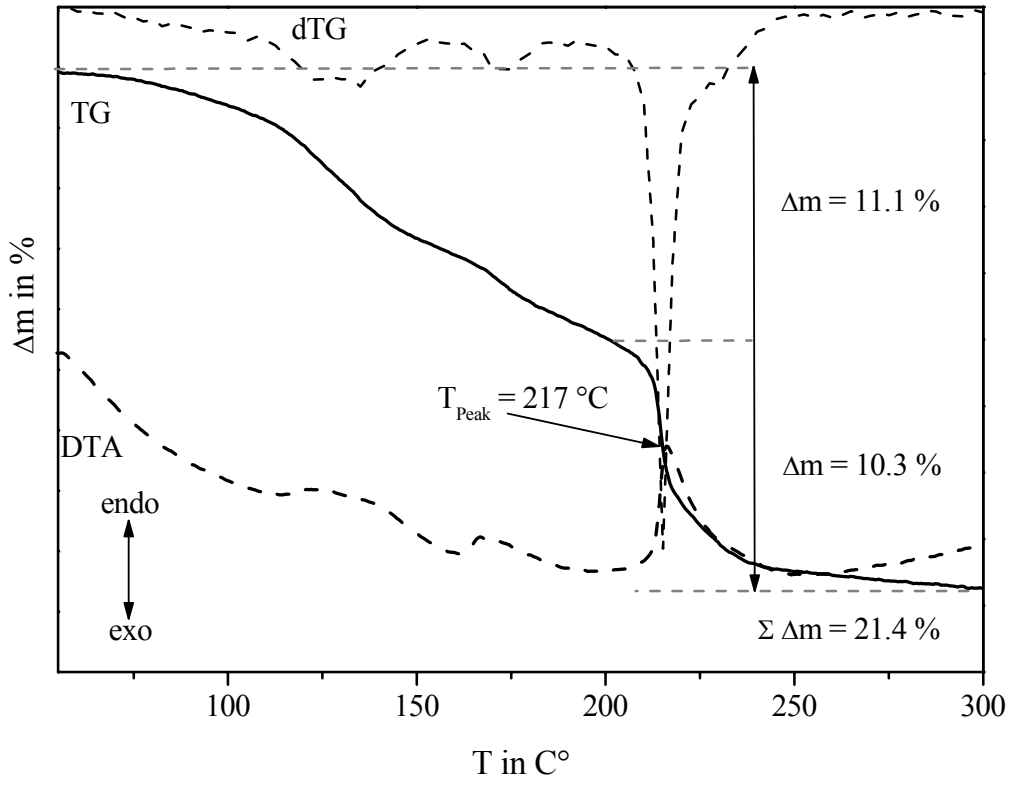

Figure 6: DTA-TG curves for (**1**).

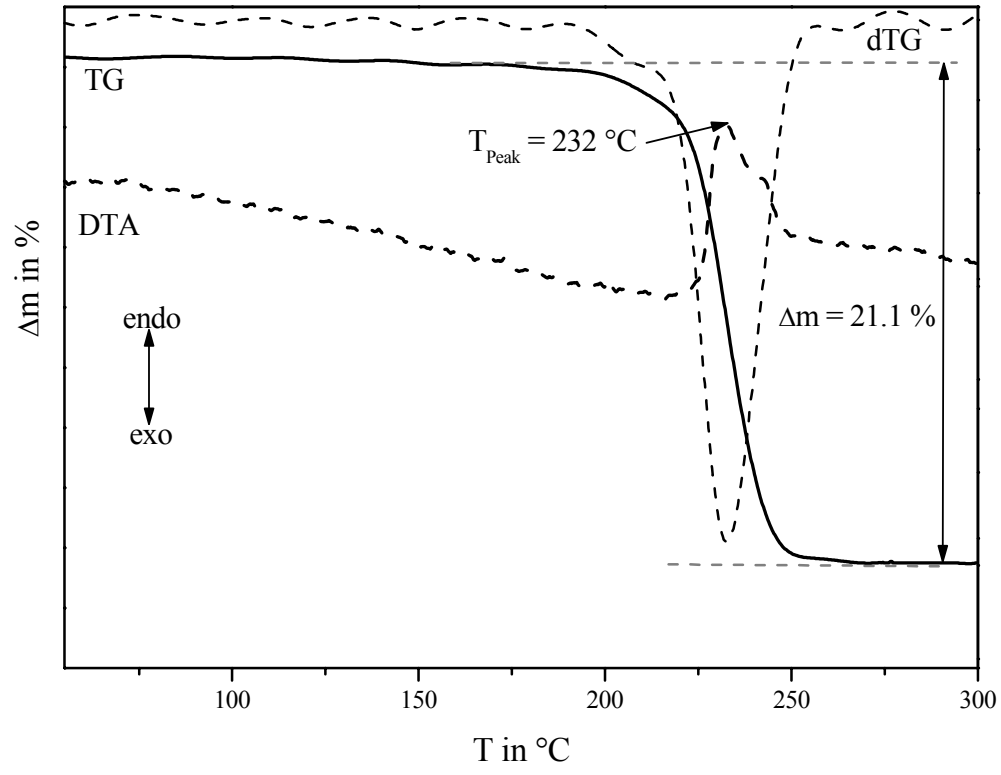

Figure 7: DTA-TG-DTG curves for (**2**).

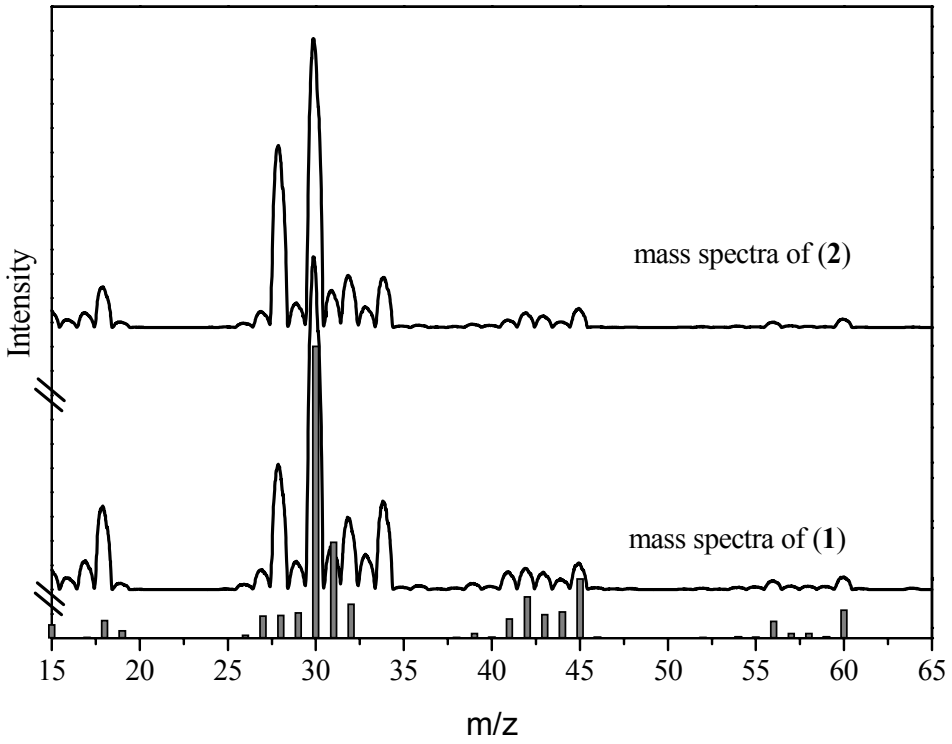

Figure 8: Mass spectra of the thermal decompositions products of (**1**) (bottom), (**2**) (top) and mass spectra for 1-amino-2-propanol taken from database (grey columns).

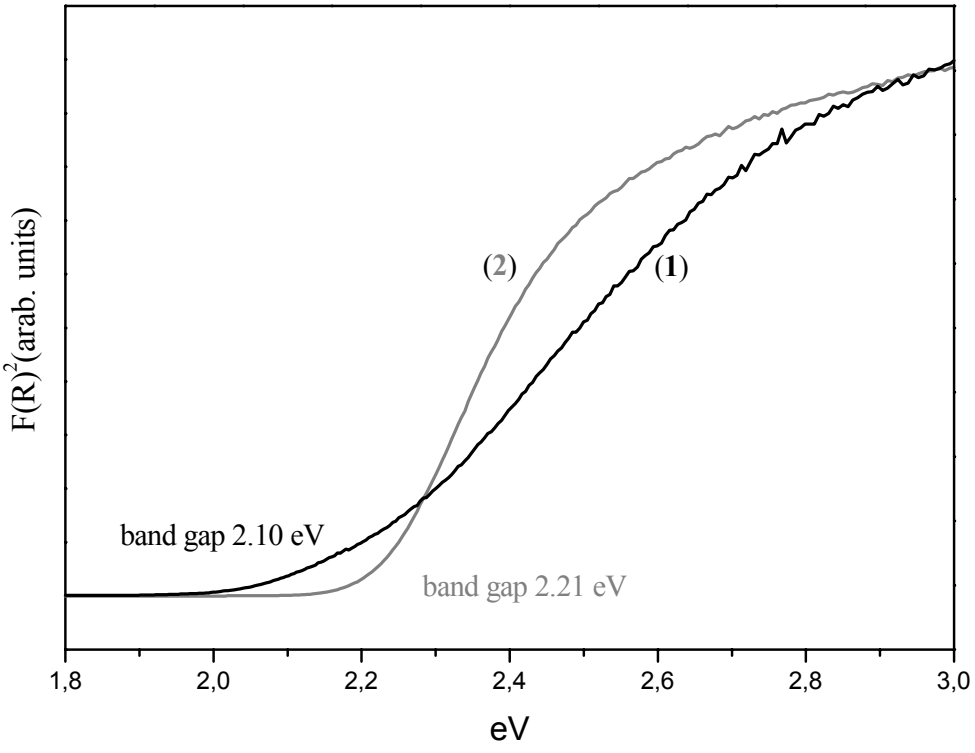

Figure 9: UV/Vis spectra of (**1**) (black line) and (**2**) (grey line).

4.5 Ergebnisse und Publikationen zu in-situ-Untersuchungen mit EDXRD/EXAFS

4.5.1 EDXRD-Untersuchungen zur Bildung von $[C_3H_{12}N_2]_2[Ge_9(OH)_4O_{18}]\cdot$ 2 H_2O

Zusammenfassung der Veröffentlichung „*In-situ Energy Dispersive X-ray Diffraction Studies of the Crystallization of* $(C_3H_{12}N_2)_2Ge_9(OH)_4O_{18}\cdot$ *2* H_2O *under Solvothermal Conditions*“.

Die Kristallisation des Germanates $(C_3H_{12}N_2)_2Ge_9(OH)_4O_{18}\cdot$ 2 H_2O wurde unter solvothermalen Bedingungen in-situ mit Hilfe energiedispersiver Röntgen-Pulverdiffraktometrie (EDXRD) bei 160 °C, 170 °C und 175 °C am Messplatz F3 am HASYLAB untersucht. In dem untersuchten Temperaturbereich konnten während der Bildung von $[C_3H_{12}N_2]_2[Ge_9(OH)_4O_{18}]\cdot$ 2 H_2O keine kristallinen Intermediate oder Precursoren beobachtetet werden. Die Induktionszeit nimmt mit steigender Temperatur signifikant ab. Die Auswertung der Kinetik erfolgte über Sharp-Hancock-Plots und über den Vergleich mit etablierten Modellen für Festkörperreaktionen. Die Kristallisation verläuft in mehreren Schritten, was auf eine Änderung der Kinetik während des Kristallwachstums hindeutet. Die Analyse der Kristallisationskinetik ergibt Reaktionsexponenten, welche gut mit den theoretischen Avrami-Modellen für verschiedene keimbildungskontrollierte Reaktionen übereinstimmen. Die Kristallgrößen und –formen wurden nach verschiedenen Reaktionszeiten mit Rasterelektronenmikroskopie an abgeschreckten Proben untersucht. In Übereinstimmung mit den verschiedenen Modellen sind deutliche Veränderungen der Kristallgrößen und -formen zu beobachten. Bei weiteren Untersuchungen wurden zusätzlich Kristallkeime aus einer bereits abgeschlossenen Reaktion vor Reaktionsbeginn zur Ausgangsmischung zugegeben. Die bei diesen Experimenten erhaltenen Ergebnisse deuten ebenfalls auf eine keimbildungskontrollierte Reaktion mit zwei- oder dreidimensionalem Wachstum der Kristalle über den gesamten Temperaturbereich hin, die Induktionszeit nimmt jedoch durch die Zugabe von Kristallkeimen erheblich ab.

In-situ Energy Dispersive X-ray Diffraction Studies of the Crystallization of $(1,2\text{-DAPH}_2)_2Ge_9(OH)_4O_{18} \cdot 2\ H_2O$ under Solvothermal Conditions

Ragnar Kiebach[a], Michael Schaefer[a], Felix Porsch[b] and Wolfgang Bensch[a,*]

[a] Kiel, Institut für Anorganische Chemie der Universität Kiel
[b] Bonn, Mineralogisch-Petrologisches Institut der Universität Bonn

Received July 1st, 2004.

Dedicated to Professor Oppermann on the Occasion of his 70th Birthday

Abstract. The solvothermal synthesis of the three-dimensional germanate $(1,2\text{-DAPH}_2)_2Ge_9(OH)_4O_{18} \cdot 2\ H_2O$ has been studied with the in-situ energy dispersive X-ray powder diffraction technique (EDXRD). The temperature dependence of the extent of reaction (α) has been investigated at 160 °C, 170 °C and 175 °C. In this temperature region no crystalline precursors or intermediates could be detected. The crystallization proceeds in more than one step suggesting a change of the kinetics during the formation of the crystalline material. The evaluated reaction exponents for the different steps are in good agreement with different Avrami nucleation models. The shape of the crystals was investigated with scanning electron microscopy after quenching the products after different reaction times. In agreement with the different nucleation models significant changes of the crystal sizes and shapes were observed. For the investigation of the effect onto the crystal growth of the compound seed crystals were added to the starting material. Again, the results indicate that over the temperature range the crystallization can be modeled by nucleation-controlled processes with two or three dimensional growth of the crystals.

Keywords: In-situ X-ray diffraction; Kinetics; Solvothermal synthesis; Germanates

In-Situ Untersuchungen der Kristallisation des Germanates $(1,2\text{-DAPH}_2)_2Ge_9(OH)_4O_{18} \cdot 2\ H_2O$ mittels energiedispersiver Röntgen-Pulverdiffraktometrie unter solvothermalen Bedingungen

Inhaltsübersicht. Die Kristallisation des Germanates $(1,2\text{-DAPH}_2)_2Ge_9(OH)_4O_{18} \cdot 2\ H_2O$ wurde unter solvothermalen Bedingungen in-situ mit Hilfe energiedispersiver Röntgen-Pulverdiffraktometrie (EDXRD) bei 160 °C, 170 °C und 175 °C untersucht. In diesem Temperaturbereich traten keine kristallinen Intermediate oder Precursoren auf. Die Kristallisation verläuft in mehreren Schritten, was auf eine Änderung der Kinetik während des Kristallwachstums hindeutet. Die Analyse der Kristallisationskinetik führt zu Reaktionsexponenten, welche gut mit den theoretischen Avrami-Modellen für verschiedene keimbildungskontrollierte Reaktionen übereinstimmen. Die Kristallgrößen und -formen wurden mit Rasterelektronenmikroskopie nach verschiedenen Reaktionszeiten untersucht, nachdem die Proben abgeschreckt wurden. In Übereinstimmung mit den verschiedenen Modellen sind deutliche Veränderungen der Kristallgrößen und -formen zu beobachten. Bei weiteren Untersuchungen wurden zusätzlich Kristallkeime am Beginn der Reaktion zu der Ausgangsmischung gegeben. Die bei diesen Experimenten erhaltenen Ergebnisse deuten ebenfalls auf eine keimbildungskontrollierte Reaktion mit zwei- oder dreidimensionalem Wachstum der Kristalle über den gesamten Temperaturbereich hin.

1 Introduction

During the last few years the solvothermal synthesis experiences a tremendous renaissance as a powerful tool for the preparation of new and exciting solids. Despite the enormous amount of empirical data which are in the meantime acquired syntheses performed under solvothermal conditions are still not well understood, and lengthy 'trial and error' experiments are performed to determine the effect of the reaction conditions onto the product. The number of contributions dealing with in-situ studies of solvothermal reactions is still low. But for a better understanding of the mechanisms occurring during these multicomponent heterogeneous reactions such experiments are essential. Time resolved in-situ energy dispersive X-ray diffraction (EDXRD) is a powerful method to investigate the influence of different parameters, e.g. temperature, pressure, pH value onto the crystallization of a product [1, 2]. Crystalline precursors and/or intermediates could be observed without the necessity to stop the reaction and to work-up the product [2–4]. Another advantage is the short monitoring time which guarantees a good time resolution.

Recently, we published the solvothermal synthesis, crystal structure, and properties of the novel germanate $(1,2\text{-DAPH}_2)_2Ge_9(OH)_4O_{18} \cdot 2\ H_2O$ (1,2-DAP =1,2-diamino-

* Prof. Dr. W. Bensch
Institut für Anorganische Chemie der Universität Kiel
Olshausenstr. 40
D-24098 Kiel
Fax: +49 (0)431/880–1520
e-Mail: wbensch@ac.uni-kiel.de

 DOI: 10.1002/zaac.200400262

propane). In the crystal structure GeO_4 tetrahedra, GeO_5 trigonal bipyramids and GeO_6 octahedra are interconnected to form an anionic $[Ge_9(OH_4)O_{18}]^{4-}$ framework [5]. During our continuing work in the field of in-situ investigations of solvothermal syntheses with energy dispersive X-ray diffraction at beamline F3 at HASYLAB (DESY) we studied the crystal growth of this compound at temperatures between 160 °C and 175 °C. The experimental data are compared with various theoretical models for crystallization kinetics.

2 Experimental

2.1 Synthesis

The title compound was obtained during the in-situ investigations by reacting GeO_2 (Alfa Aesar 99 %, 104.6 mg; 1.0 mmol) in an aqueous solution of 33 % 1,2-DAP (Merck 98 %, 2.0 ml; 7.0 mmol). A special autoclave was used with an internal diameter of 10 mm and an inner volume of 7 ml. The cell design and the technical details were described in [3]. The mixture of the starting material was filled in the autoclave and the delay time between adding and starting of the reaction was about 2 min. The reaction temperatures were then reached after about 1 min. X-ray powder patterns were recorded with acquisition times of 300 s. The spectra were evaluated with EDXPow [6] and the Origin6.0 program package. The reflection profiles were modeled with a Gaussian peak shape. About 0.1 mmol of MoO_3 (Merck 99 %) was added as an internal standard to monitor the intensity fluctuations of the Mo-K_α fluorescence line due to the decreasing power of the primary beam. The intensities of the product reflections were normalized against the peak intensities of the Mo-K_α resonance. To ensure that MoO_3 has no influence onto the reactions we performed experiments without MoO_3. The critical evaluation of all relevant parameters demonstrates that the addition of MoO_3 has no influence onto the different parameters. In the powder diffraction pattern only reflections of the title compound or reflections of MoO_3 together with that of the germanate were observed.

2.2 Synchrotron radiation source

The HASYLAB Beamline F3 receives white synchrotron radiation from a bending magnet with a critical energy of 16 keV and gives a positron beam energy of 4.5 GeV. An energy range from 13.5 to 65 keV can be observed with a maximum at about 20 keV. The diffracted beam is monitored by a nitrogen cooled solid state germanium detector. The detector angle was chosen that all important Bragg reflections can be detected. The d-spacing range is given by $E = 6.199/(d \cdot \sin\theta)$. With a detector angle of approximately 1.90° the observable d-spacing range is 2.9 Å to 13.8 Å. The energy resolution $\Delta d/d$ is about 10^{-2} above 26 keV. The beam was collimated to 0.2 mm giving the best results. More experimental details are found in [3, 4].

3 Results and Discussion

A crucial point of solvothermal syntheses is that changing one parameter of the reaction conditions influences other parameters in a not well understood manner. The product formation often sensitively depends on several experimental variables, i.e. temperature, filling grade, pH value, concentration and kind of the educts etc..

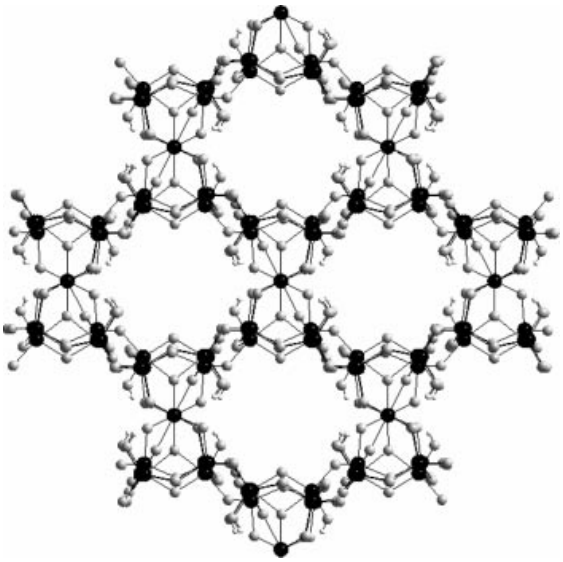

Fig. 1 The $Ge_9(OH)_4O_{18}$ framework of $(1,2\text{-}DAPH_2)_2Ge_9(OH)_4O_{18} \cdot 2\ H_2O$ with view along the [101] direction. Black spheres: Ge; grey spheres: O. The $[1,2\text{-}DAPH_2]^{2+}$ and water molecules are omitted for clarity.

In the present work we investigated the influence of the temperature onto the crystallization of the novel germanate $(1,2\text{-}DAPH_2)_2Ge_9(OH)_4O_{18} \cdot 2\ H_2O$ (Fig. 1). In the energy range chosen several reflections of the final product are observed simultaneously. In Figure 2 a typical spectrum collected at the end of the reaction shows the Bragg reflections of the product and the fluorescence of MoO_3. An escape peak is located at 16 keV and is caused by the Ge detector and another reflection comes from the teflon-liner (37.4 keV). The escape peak is located approximately 10 keV below the energy of the (020) product reflection at 26 keV and occurs only when the crystalline product starts to grow. A sequence of time-resolved spectra is shown in Figure 3. The dissolution of the crystalline GeO_2 powder is seen at 60.4 keV, and within several minutes the solid oxide is dissolved. Note that in the energy region around 60 keV two broad product reflections are located. After an induction time which depends on the reaction temperature (here: 75 min.) the first reflections are observed and the product starts to grow without the occurrence of a crystalline intermediate phase or precursor. We note that all reflections of the material grow simultaneously. The reaction is completed after another 70 min.

The crystallization kinetics were evaluated using the expressions which are well documented in the literature [1, 7−13]. The integrated intensities of the product reflections were normalized against the intensity of the Mo-K_α resonance. To compare the experimental data with the theoretical values of solid-state kinetics the data are expressed as the extent of reaction (α). The value $\alpha(t)$ is the ratio of the normalized intensity at time t to the intensity at time t_∞ and

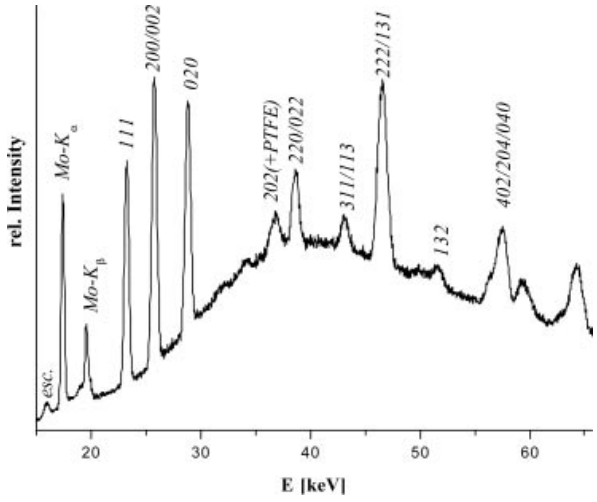

Fig. 2 Powder diffraction pattern recorded at 160 °C. The indices of the most intense lines of the final product and the MoKα-fluorescence are marked. The peak at ~ 16 keV is an electronically ghost peak from the Ge detector.

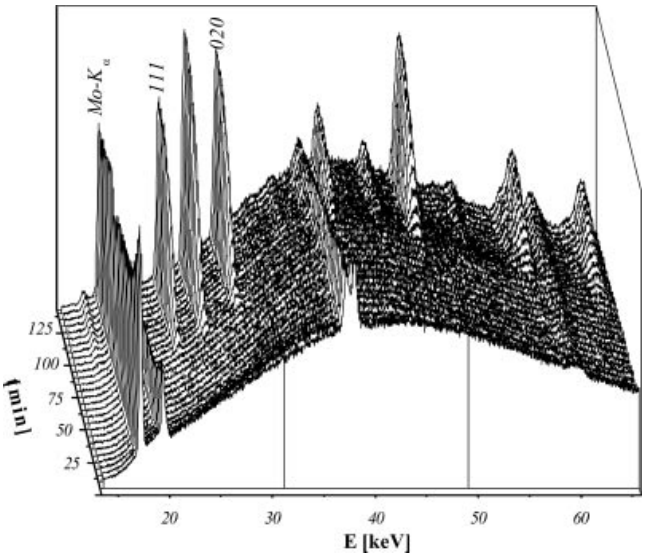

Fig. 3 Time resolved powder diffraction pattern of (1,2-$DAPH_2)_2Ge_9(OH)_4O_{18} \cdot 2\ H_2O$.

is calculated according to $\alpha(t) = I_n(t)/ I_n(t_\infty)$. The comparison of the induction times, t_0, which is the time until the first crystallites are observed in the spectra, decreases from 101 min. at T = 160 °C to about 49 min. at T = 175 °C (compare also Fig. 4). The α(t) vs. time curves show a sigmoidal shape (Fig. 4) which is typical for many solid-state kinetics. With the well known Avrami-Eroféev expression [14−16] which is widely used [1, 9−13] the kinetic parameters *m* (reaction exponent) and *k* (rate constant) were evaluated. Applying the so-called Sharp-Hancock plot (SH plot) the kinetic parameters can also be obtained. The slope of the curve yields the reaction exponent *m* and the intercept with the *y*-axis gives the rate constant *k*. The Avrami

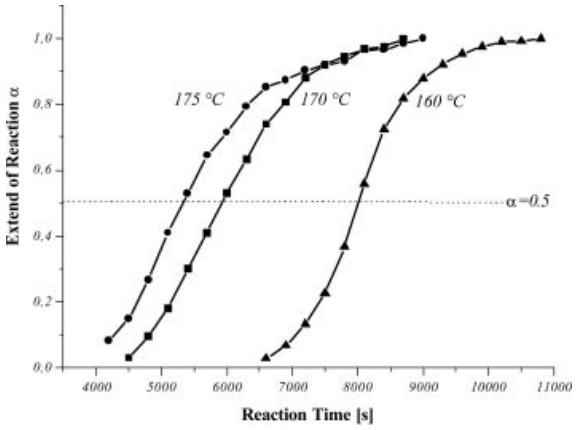

Fig. 4 Extent of reaction a versus time for the (111) reflection at different temperatures.

exponent *m* can be related to the type of nucleation and growth process taking place, including the morphology of the reaction product, i.e. whether the crystals are fibers, needles, plates, sheets, spheres or polygons. In addition, the exponent *m* also includes the type of nucleation, i. e. whether the nuclei all develop at once or there is a continuous nucleation with a constant rate. Hence, the Avrami exponent *m* can be further defined in terms of three aditional constants [17, 18]: $m = (P/S) + Q$. P is a dimensionality constant for the growth of the product with P = 1 for one dimensional growth (fibers, needles), P = 2 for two dimensional growth (plates, sheets), and P = 3 for three dimensional growth (spheres, polygons). S is related to the rate-limiting growth mechanism with S = 1 for interface or phase boundary controlled mechanism and S = 2 for a diffusion controlled growth. Finally, Q is a constant which is determined by the nucleation rate with Q = 1 for a constant nucleation rate, and Q = 0 for nucleation site saturation, i.e. zero nucleation rate. For one mechanism the experimental points in a SH plot are on a straight line over the whole range for α, and if the mechanism changes during the reaction the deviation is immediately seen in such a plot [8]. The evaluation of the kinetic data was performed after subtracting the induction time t_0 from the reaction time *t*.

The Sharp-Hancock plot for data obtained at T = 160 °C is shown in Fig. 5 and it is obvious that the growth of the title compound can be divided into three kinetically different parts. Up to a value of about 0.23 for α the reaction exponent *m* has a value of 2.2, corresponding to two dimensional growth with instantaneous nucleation. In the second part ($0.23 < \alpha < 0.72$) *m* increases to about 3.3 which corresponds to a 2-dimensional growth with continuous nucleation at a constant rate, while in the last part ($\alpha > 0.72$) a decrease of *m* to the first value of about 2.2 is obtained. Different combinations for the above mentioned constants P, S, and Q are possible. For the first region one reasonable choice is S =1 which indicates an interface or phase boundary controlled growth, Q = 0 for an instantaneous nucleation and P = 2.2 for a product morphology between

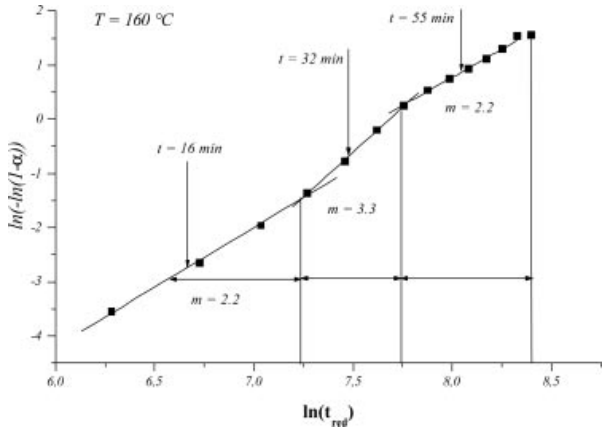

Fig. 5 Sharp-Hancock plot for the data obtained at T = 160 °C. For further details see text.

two (plates) and three dimensional (polygons) crystals. For the second part with m = 3.3 and assuming that S and Q have the same values as before a three dimensional growth is expected. Alternatively, Q = 1 and P = 2.3 indicate a constant rate homogeneous nucleation and a two dimensional grwoth. For the last part a similar mechanism as for the first part may be assumed. Such changes of the crystallization mechanisms should be observable in the shape and size of the crystals. Hence, to compare the crystal shapes at different reaction times quenching experiments were performed. After 16, 32 and 55 min the complete sample was cooled by putting the autoclave into liquid nitrogen. The times were selected according to average times of different parts in the Sharp-Hancock plots (see Fig. 5). The samples were filtered off and washed with water and ethanol. The SEM pictures of the products are shown in Fig.'s 6 a-c (a = 16 min, b = 23 min, c = 55 min). The morphologies seen in the SEM micrographs give further hints what growth processes occur. After 16 min (Fig. 6a) the size of the crystals scatter from less than 1 μm to about 5 μm. Furthermore, the crystals have no regular shape and platelet-like, spherulitic as well as needle-like morphologies are present. The broad size distribution and the not well shaped crystals indicate that a large number of nuclei is formed at once which than start to grow with no preference of a distinct shape. But after 32 min (Fig. 6b), corresponding to the second part in the Sharp-Hancock plot, thin rectangular and pseudo-hexagonal platelets with an average diameter of 3 μm are observed. This observation implies that the growth of the crystals is faster in the lateral direction than in the third dimension. With respect to the two possible explanations of the reaction exponent *m* of 3.3 the second alternative seems to be more plausible. Finally, after 55 min which corresponds to the third part of the crystallization, regular cubes and hexagonal prisms with dimensions of about 5 μm are observed (Fig. 6c). A comparison with the shape and size of the crystals seen after 32 min the crystals are significantly thicker and show larger lateral dimensions.

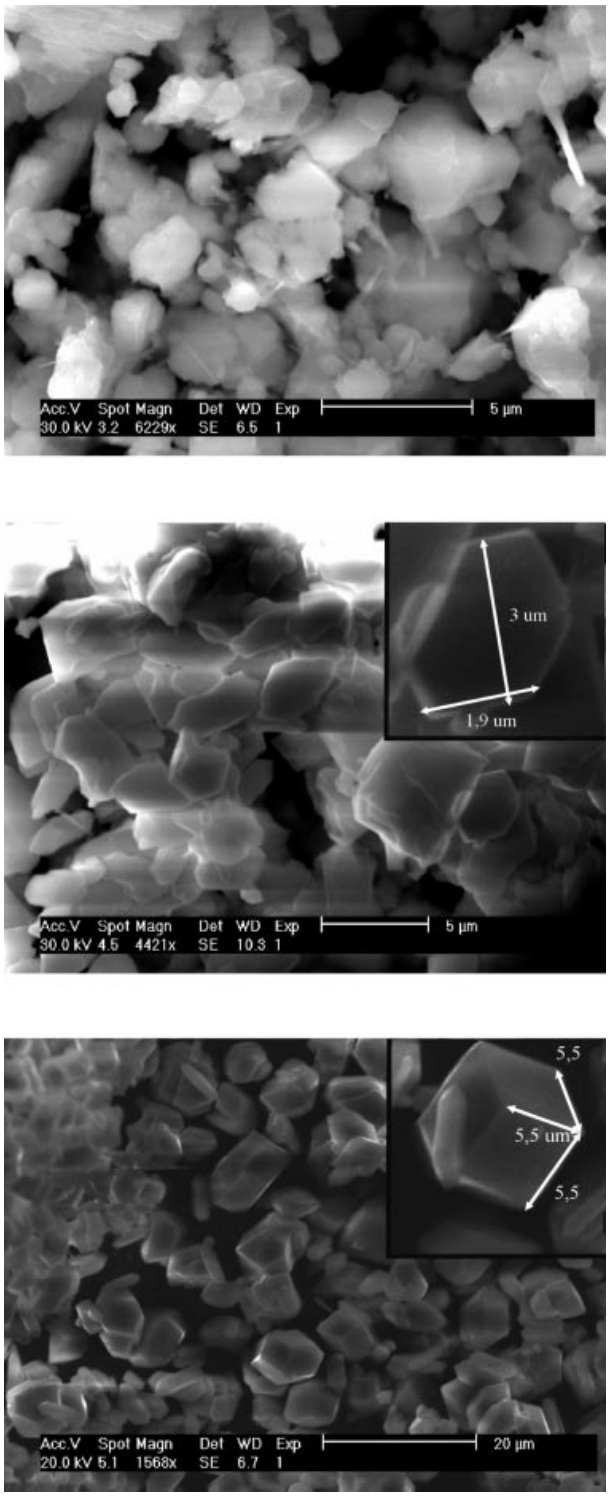

Fig. 6 (top) SEM micrograph of $(1,2\text{-DAPH}_2)_2Ge_9(OH)_4O_{18} \cdot 2\ H_2O$ after 16 min; (middle) SEM micrograph of $(1,2\text{-DAPH}_2)_2Ge_9(OH)_4O_{18} \cdot 2\ H_2O$ after 32 min; (bottom) SEM micrograph of $(1,2\text{-DAPH}_2)_2Ge_9(OH)_4O_{18} \cdot 2\ H_2O$ after 55 min.

Another way to analyze the kinetics is a plot of experimental $t/t_{0.5}$ data vs. α and to compare these data with different theoretical kinetic models (Figure 7, reaction at

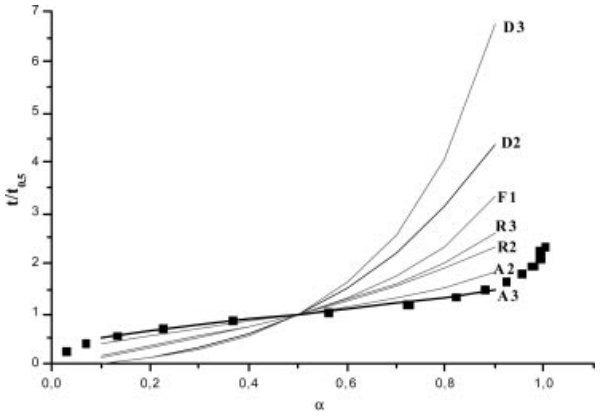

Fig. 7 Comparison of the evolution of experimental $t/t_{0.5}$ data as function of α with different theoretical kinetic models for T = 170 °C. The letters with the numbers are the abbreviations of the different models listed in Table 1.

Table 1 The rate equations for solid-state reactions reported in literature.

Growth Model	Rate Equation f(α) = kt	***m***
Diffusion controlled		
$D_1(\alpha)$	$\alpha^2 = 0.25\ (t/t_{0.5})$	0.62
$D_2(\alpha)$	$(1-\alpha)\ln(1-\alpha) + \alpha = 0.1534\ (t/t_{0.5})$	0.57
$D_3(\alpha)$ [Jander]	$[1-(1-\alpha)^{1/3}]^2 = 0.0425\ (t/t_{0.5})$	0.54
$D_4(\alpha)$ [Ginstling-Brounshtein]	$1-2\alpha/3-(1-\alpha)^{2/3} = 0.0367\ (t/t_{0.5})$	0.57
Phase-boundary controlled		
$R_2(\alpha)$	$1-(1-\alpha)^{1/2} = 0.2929\ (t/t_{0.5})$	1.11
$R_3(\alpha)$	$1-(1-\alpha)^{1/3} = 0.2063\ (t/t_{0.5})$	1.07
First order		
$F1(\alpha)$	$[-\ln(1-\alpha)] = 0.6931\ (t/t_{0.5})$	1.00
Nucleation [Avrami-Erovéef]		
$A2(\alpha)$	$[-\ln(1-\alpha)]^{1/2} = 0.8326\ (t/t_{0.5})$	2.00
$A3(\alpha)$	$[-\ln(1-\alpha)]^{1/3} = 0.885\ (t/t_{0.5})$	3.00

T = 160 °C, Table 1). The comparison of the experimental data with the kinetic expressions that have found application in solid-state kinetics [7, 12, 13] shows that the reaction follows the nucleation-controlled Avrami models A2 and A3 (Table 1). The three different parts are also observable in this figure, in the range of $0.2 < \alpha < 0.8$ the experimental data are in accordance with the kinetic model A3. But above and below this range a deviation towards the model A2 is obtained.

We must note that for all temperatures a change of *m* is observed at a distinct time of the reaction. But for temperatures higher than 160 °C only two different slopes occur in the SH plots suggesting that at these temperatures the first step is too fast for the time resolution of the experiment. For 175 °C the reaction exponent *m* of the first part is slightly larger than 3 and no change is seen in the slope at small α values (Fig. 8). For longer reaction times the value for *m* is about 2.2 (Table 2).

The reactions were also performed with seed crystals because it can be expected that a nucleation controlled reaction is only speed up and the mechanism is not changed (Fig. 9). Indeed, after the crystals were added to the reaction slurry the induction times dramatically decrease whereas the values for *m* are in a similar range as obtained for the reactions without seed crystals (Table 2, Fig. 10).

Table 2 Kinetic parameters obtained by the analysis of the experimental data.

Reaction temperature	t_0 /s	$t_{0.5}$ /s	**Exponent (order) m**
160 °C (with seed crystals; $\alpha < 0.16$)	0	2574	1.6
$(0.16 < \alpha < 0.78)$			3.2
$\alpha > 0.78$)			1.8
160 °C ($\alpha < 0.23$)	6065	1948	2.2
$(0.23 < \alpha < 0.72)$			3.3
$(\alpha > 0.72)$			2.2
170 °C (with seed crystals; $\alpha < 0.29$)	172	2371	2.0
$(0.29 < \alpha < 0.84)$			3.3
$(\alpha > 0.84)$			2.0
170 °C ($\alpha < 0.46$)	3435	2517	3.2
$(\alpha > 0.46)$			2.5
175 °C ($\alpha < 0.64$)	2924	2417	3.3
$(\alpha > 0.64)$			2.2

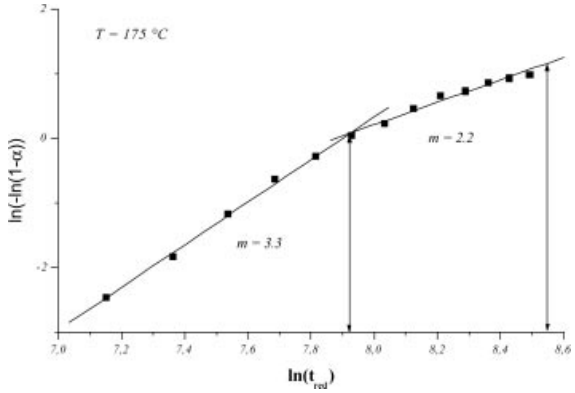

Fig. 8 Sharp-Hancock plot for the data obtained at T = 175 °C. For further details see text.

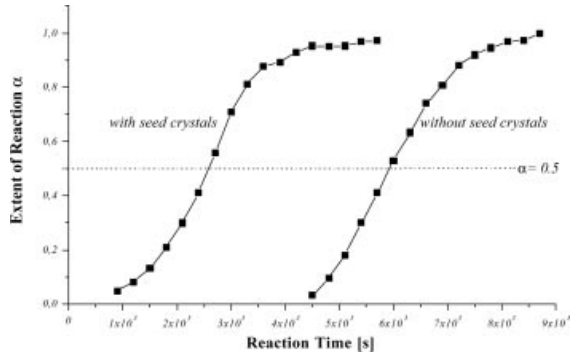

Fig. 9 Comparison of the experimental data at T = 170 °C with and without added seed crystals.

4 Conclusion

Here we presented the in-situ EDXRD studies of the crystallization of the novel germanate $(1,2\text{-DAPH}_2)_2$-

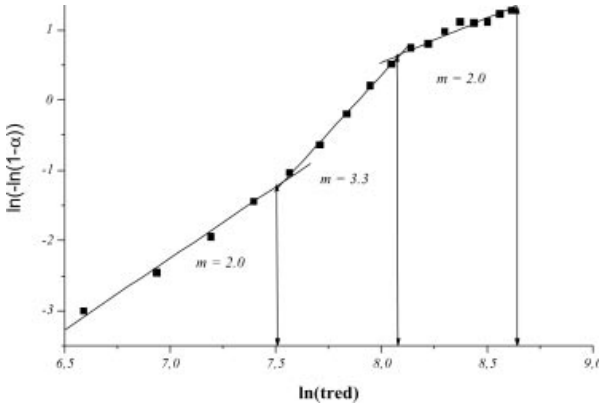

Fig. 10 Sharp-Hancock plot for the data obtained at T = 170 °C with added seed crystals. For further details see text.

$Ge_9(OH)_4O_{18} \cdot 2\ H_2O$ under solvothermal conditions. The experimental data are in good agreement with nucleation-controlled processes. The reactions with seed crystals support these results because only the induction times dramatically decrease but no significant changes are found for the kinetic parameters. Further investigations are under way to study the reaction at even lower temperatures.

Acknowledgements. The work has been supported by the State of Schleswig-Holstein and the Deutsche Forschungsgemeinschaft (DFG). We also thank DESY for measurement time and financial support.

References

[1] R. I. Walton, Th. Loiseau, D. O'Hare, G. Férey, *Chem. Mater.* **1999**, *11*, 3201.
[2] R. J. Francis, S. J. Price, J. S. O. Evans, S. O'Brien, D. O'Hare, *Chem. Mater.* **1996**, *8*, 2102.
[3] L. Engelke, M. Schaefer, M. Schur, W. Bensch, *Chem. Mater.* **2001**, *13*, 1383.
[4] L. Engelke, M. Schaefer, F. Porsch, W. Bensch, *Eur. J. Inorg. Chem.* **2003**, 506.
[5] D. Pitzschke, C. Näther, W. Bensch, *Z. Naturforsch.* **2003**, *58b*, 205.
[6] F. Porsch, EDXPowd, V. 3.15, RTI GmbH, Paderborn, **2002**.
[7] R. J. Francis, J. S. O'Brien, A. M. Fogg, P. Halasyamani, D. O'Hare, Th. Loiseau, G. Férey, *J. Am. Chem. Soc.* **1999**, *121*, 1002.
[8] J. D. Hancock, J. H. Sharp, *J. Am. Ceram. Soc.* **1972**, *55*, 74.
[9] A. P Wilkinson, J. S. Speck, A. K. Cheetham, S. Natarajan, J. M Thomas, *Chem. Mater.* **1994**, *6*, 750.
[10] A. M Fogg, D. O'Hare, *Chem Mater.* **1999**, *11*, 1771.
[11] R. Thompson, *Zeolites*, **1992**, *12*, 680.
[12] J. Sharp, G. Brindley, B. Achar, *J. Am. Ceram. Soc.* **1966**, *49*, 379.
[13] S. Hulbert, *Br. Ceram. Soc.* **1989**, *6*, 11.
[14] M. Avrami, *J. Chem. Phys.* **1939**, *7*, 1103.
[15] M. Avrami, *J. Chem. Phys.* **1940**, *8*, 212.
[16] M. Avrami, *J. Chem. Phys.* **1941**, *9*, 177.
[17] P. W. Brown, J. Pommersheim, G. Frohnsdorff, *Cem. Concr. Res.* **1985**, *15*, 35.
[18] J. J. Thomas, H. M. Jennings, *Chem. Mater.* **1999**, *11*, 1907.

4.5.2 EDXRD/EXAFS-Untersuchungen zur Bildung von $[Co(C_6H_{18}N_4)][Sb_2S_4]$

Zusammenfassung der Veröffentlichung „*A Combined in-situ EDXRD/EXAFS Investigation of the Crystal Growth of [Co($C_6H_{18}N_4$)][Sb_2S_4] under Solvothermal Conditions: Two Different Reaction Pathways Leading to the Same Product*“.

Bei der hier untersuchten Verbindung $[Co(C_6H_{18}N_4)][Sb_2S_4]$ handelt sich um ein 2-dimensionales Thioantimonat, in das Co über eine Bindung an ein S-Atom des Sb-S-Netzwerkes integriert ist (Abb. 4.12, links). Zur Aufklärung des Bildungsmechanismus wurden am HASYLAB komplementäre EDXRD/EXAFS-Messungen durchgeführt.

Die Verbindung $[Co(C_6H_{18}N_4)][Sb_2S_4]$ wird im Temperaturbereich von 105 °C bis 130 °C ohne kristalline Vorläufer oder Zwischenprodukte gebildet (Abb. 4.12, rechts). Die Induktionszeit der Reaktion hängt empfindlich von der Temperatur ab, mit steigender Temperatur wird die Induktionszeit signifikant kürzer und die Bildung des Produktes verläuft schneller. Interessant ist, dass bei Temperaturen oberhalb von 130 °C [Co(tren)][Sb_4S_7] als Hauptprodukt gebildet wird. Am Ende der Reaktion entsteht neben $[Co(C_6H_{18}N_4)][Sb_2S_4]$ zusätzlich $[(tren)_x]Sb_{21}S_{34}$, wobei sich nach ca. 14 h ein Gleichgewicht zwischen den beiden Phasen einstellt. Eine Erklärung für diese Beobachtung könnte sein, dass die notwendige Co^{2+}-Konzentration zur Bildung von $[Co(C_6H_{18}N_4)][Sb_2S_4]$ unterschritten wird, so dass bevorzugt die Co-freie Phase gebildet wird. Da keine kristallinen Intermediate auftreten muss angenommen werden, dass die Umwandlung über einen zeitnahen Amorphisierungs- bzw. Auflösungsschritt verläuft.

Die Auswertung der Kinetik erfolgte über Sharp-Hancock-Plots (SH-Plots) und über den Vergleich mit den Mechanismus-Modellen für Festkörperreaktionen. Bei Reaktionen unterhalb von 115 °C wird ein einheitlicher diffusionskontrollierter Mechanismus beobachtet. Mit steigender Temperatur wird bei längeren Reaktionszeiten ein Wechsel zum Mechanismus erster Ordnung beobachtet, im SH-Plot ist eine Änderung der Steigung zu erkennen. Die Aktivierungsenergie wurde mit einem Arrheniusplot zu 42 kJ/mol bestimmt. Bei Temperaturen unterhalb von 120 °C wird bei einem Drittel der Reaktionen ein anderer Bildungsmechanismus beobachtet. Im zeitaufgelösten Pulverdiffraktogramm ist zuerst nur das Wachstum des (102)-Reflexes zu beobachten, das

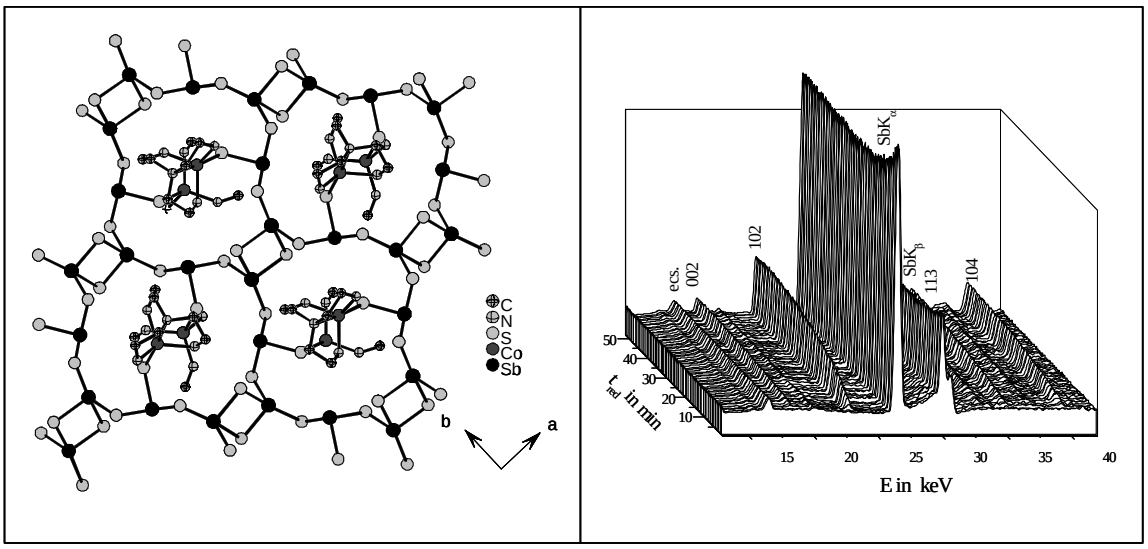

Abbildung 4.12: Kristallstruktur der Verbindung $[Co(C_6H_{18}N_4)][Sb_2S_4]$ (links), zeitaufgelöstes Spektrum bei 120 °C (rechts)

Wachstum der anderen Reflexe setzt später ein. Anzumerken ist, dass die energetische Lage des (102)-Reflexes im Vergleich zu den anderen Spektren leicht verschoben ist. Als mögliche Ursache kommt für den zweiten Bildungsmechanismus der Magnetismus des elementaren Kobalts in Betracht. Elementares Co klebt an der magnetischen Rührpille, und die Auflösung von Co erhält bei niedrigeren Temperaturen eine zufällige Komponente, die sich in Form verschiedener Bildungsmechanismen offenbart. Zur Überprüfung dieser These wurde in weiteren Versuchen $CoCl_2 \cdot 6H_2O$ als Co-Quelle verwendet. In allen Versuchen entsprach der Bildungsmechanismus dem ersten Weg und es ist daher davon auszugehen, dass der Magnetismus von elementarem Co als zusätzlicher Reaktionsparameter berücksichtigt werden muss.

Komplementär wurden EXAFS-Spektren an der Sb-K-Kante aufgenommen. Erstaunlicherweise ändert sich die lokale Nahordnung um das Antimonatom nicht. Diese scheint unabhängig vom pH-Wert, der Temperatur und dem Amin zu sein. Allerdings ändert sich der Kantenhub an der Sb-Kante. Dieser ist direkt proportional zur Sb-Konzentration. Die Änderung der Sb-Konzentration im Reaktionsverlauf kann mit einem sigmoidalen Verlauf beschrieben werden (Abb. 4.13, links). Ein direkter Vergleich mit der Bildung von $[Co(C_6H_{18}N_4)][Sb_2S_4]$ aus EDXRD-Messungen kann nicht

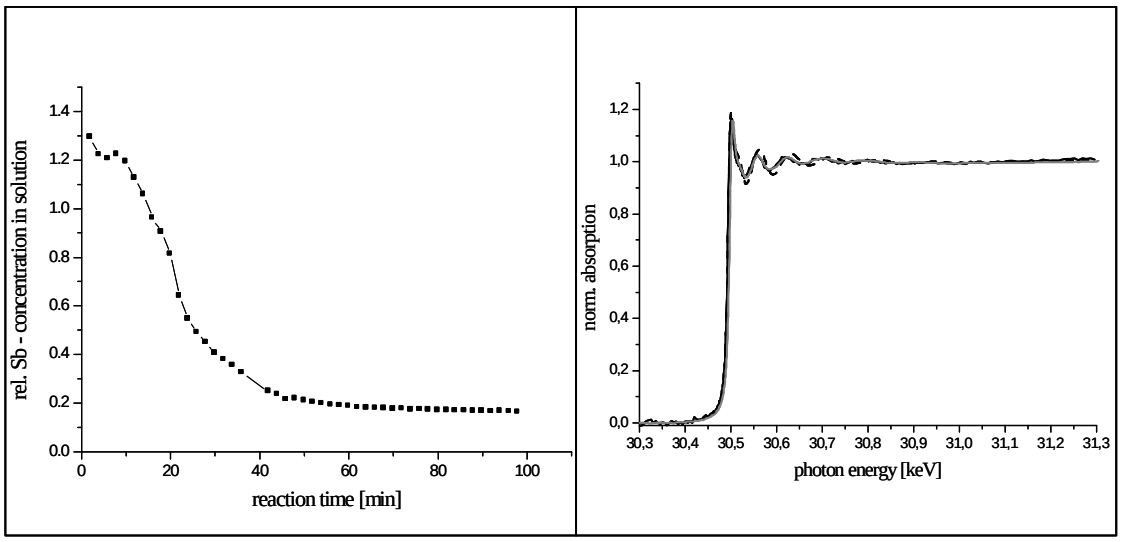

Abbildung 4.13: Verlauf des Sb-Kantenhubs mit der Reaktionszeit (links), EXAFS-Spektren von $[Co(C_6H_{18}N_4)][Sb_2S_4]$ und Vergleichslösungen (rechts)

gezogen werden, da das Rühren zur Aufnahme der EXAFS-Spektren unterbrochen wurde und so eine unterschiedliche Reaktionsführung vorlag.

Bei Simulationen der Spektren erhielt man die besten Ergebnisse für ein Modell, bei dem SbS_3 und SbS_4 als gelöste Antimonspezies koexistieren.

Hervorzuheben ist, dass sich die lokale Nahordnung um das Sb-Atom in Lösung in allen untersuchten Systemen nicht ändert (Abb. 4.13, rechts). Aufgrund der experimentellen EXAFS-Daten ist von monomeren Spezies in Lösung auszugehen. Größere Sb_xS_y-Einheiten überschreiten das Löslichkeitsprodukt und fallen als feste amorphe Verbindungen aus. Versuche EXAFS-Spektren der festen Phase zu erhalten schlugen fehl. Dieser Teil der Reaktion ist nach wie vor als „Black Box“ in der solvothermalen Synthese anzusehen.

Ragnar Kiebach, Nicole Pienack, Marie-Eve Ordolff, Felix Studt and Wolfgang Bensch*

Chem. Mater. **2005**,

A Combined in-situ EDXRD/EXAFS Investigation of the Crystal Growth of $[Co(C_6H_{18}N_4)][Sb_2S_4]$ under Solvothermal Conditions: Two Different Reaction Pathways Leading to the Same Product

The formation of $[Co(C_6H_{18}N_4)][Sb_2S_4]$ under solvothermal conditions was studied with combined in-situ EDXRD/EXAFS experiments. Tow different reaction paths are observed: all product reflections occur simultaneously in the EDXRD or only one reflection is seen indicating that first strong disordered layers are formed which at later stages start to arrange yielding the three-dimensional long range order. The reaction mechanism are evaluated and at the early stages the reactions are controlled by diffusion followed by a more complex behavior. At the end of the formation of $[Co(C_6H_{18}N_4)][Sb_2S_4]$ a second phase is formed which do not contain Co. The in-situ EXAFS experiments demonstrate that independent of the reaction time, the Sb/S ratio and the amine applied only the two species $[SbS_3]$ and $[SbS_4]$ are present in solution.

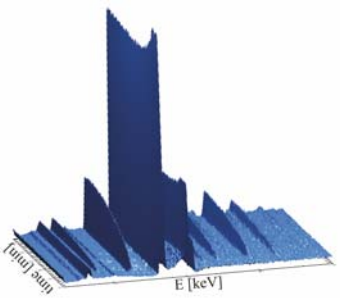

A Combined in-situ EDXRD/EXAFS Investigation of the Crystal Growth of $[Co(C_6H_{18}N_4)][Sb_2S_4]$ under Solvothermal Conditions: Two Different Reaction Pathways Leading to the Same Product

Ragnar Kiebach[†], *Nicole Pienack*[†], *Marie-Eve Ordolff*[†], *Felix Studt*[†], *Wolfgang Bensch**[†]

Institute of Inorganic Chemistry, University of Kiel, Olshausenstraße 40-60, 24098 Kiel, Germany

wbensch@ac.uni-kiel.de

RECEIVED DATE (to be automatically inserted after your manuscript is accepted if required according to the journal that you are submitting your paper to)

- To whom correspondence should be addressed. Tel: +49 431 880-2406, Fax: +49 431 880-1520, email: wbensch@ac.uni-kiel.de

Abstract

The crystal growth and kinetics of the formation of $[Co(C_6H_{18}N_4)][Sb_2S_4]$ were investigated under solvothermal conditions with combined in-situ EDXRD (energy dispersive X-Ray diffraction) and in-situ EXAFS (extended X-ray absorption fine structure*)* at different temperatures. In the overwhelming number of reactions all product reflections occur simultaneously in the EDXRD spectra. A detailed analysis of the extent of reaction α vs. time clearly shows that the mechanism changes during the reaction. Such a change occurs at different temperatures after different reaction times. At the early stages the reactions are controlled by diffusion, and later the reaction exponents *m* suggest a more complex behavior. At the end of the formation of $[Co(C_6H_{18}N_4)][Sb_2S_4]$ a second phase is formed which do not contain Co. The results of the in-situ experiments suggest that $[Co(C_6H_{18}N_4)][Sb_2S_4]$ is not only a meta-stable phase but rather that the second product crystallizes because the Co^{2+} concentration in solution is too low for further formation of $[Co(C_6H_{18}N_4)][Sb_2S_4]$. In the minor cases of the solvothermal reaction a very different growth was observed. At the beginning only one intense reflection occurs in the spectra and after a distinct time all other reflections start to grow simultaneously. This strange behavior indicates that disordered layers are formed at the beginning which start to arrange at later stages yielding the three-dimensional long range order. The in-situ EXAFS experiments performed at the Sb K-edge demonstrate that independent of the reaction time, the Sb/S ratio and the amine applied only the two species SbS_3 and SbS_4 are present in solution.

Keywords

EDXRD, EXAFS, Thioantimonates, In-situ, Kinetic, Solvothermal Synthesis

Introduction

Cobalt containing frameworks are of great interest in catalysis and a lot of research has been done in this field. Important catalysts are cobalt containing acidic zeolites for hydrodesulfurization [1]. Thioantimonates(III) with zeotype structures are also possible candidates for catalytic applications. In the last years a large number of microporous thioantimonates (III) [2-5] have been synthesized. A good example to demonstrate the structural relationship between thioantimonates(III) and zeolites is the 3-dimensional cobalt containing compound $[Co(en)_3][Sb_{12}S_{19}]$ [6] with channels being comparable with those in ZSM-5. The combination of the useful properties of zeolites with manifold properties of thioantimonates(III) like tunable optical band gaps [7], superconductivity [8] or photoconductivity [9] should lead to a new class of compounds with designed physical properties. Recently we published the synthesis and structure of the layered compound $[Co(tren)][Sb_2S_4]$ [10] (tren = tris-(2-aminoethyl)-amine) in which Co^{2+} is part of the thioantimonate(III) network (Figure 1). Such a combination makes the material of interest for further applications and investigations are in progress. Microporous materials are synthesized under solvothermal conditions with organic molecules acting as structure directors. The final crystalline products often show a low density and can be regarded as kinetic controlled products.

Despite the importance of the solvothermal method for the synthesis of new materials like catalysts, ion exchangers and porous materials the reaction mechanisms leading to the crystalline products are not well understood. Compared to the enormous number of experiments performed under solvothermal conditions, experiments for understanding the mechanisms, the kinetics of solvothermal syntheses and exploration of the influence of reaction parameters like temperature, pH-value and volume are quite rare. In the last decade the number of publications [11-16] presenting results of in-situ energy dispersive X-ray diffraction (EDXRD) studies of solvothermal reaction has grown constantly, but the number of reports is still low. EDXRD is a powerful method to investigate the influence of different parameters onto formation of crystalline products. Crystalline precursors and/or intermediates are detected without quenching the reaction and without work-up of the product. But with EDXRD only crystalline phases can be detected, and amorphous phases and very small precursors in the liquid phase cannot be

observed so that this part of a reaction is still a kind of “black box”. Information from amorphous phases or molecules in solution can be acquired with extended X-ray absorption fine structure (EXAFS) experiments because data about the local structure and the local atomic coordination are collected [17-19]. The combination of these two complementary methods yields a much better understanding of the mechanisms occurring during chemical reactions [20-24]. Here we report the EDXRD/EXAFS studies of the system Co/Sb/S/tren, and the kinetic results of the crystal growth of $[Co(tren)][Sb_2S_4]$ are presented.

Experimental Section

The compound $[Co(C_6H_{18}N_4)][Sb_2S_4]$ is obtained by reacting elemental Co (29 mg, 0.5 mmol, Fluka, purum p.a.), Sb (61 mg, 0.5 mmol, Fluka, purum p.a.) and S (48 mg, 1.5 mmol, Fluka, purum p.a.) in 2 ml of an aqueous tren (purum, Fluka) solution (50 %) as solvent. The temperature range for the experiments varied between 105 and 130 °C. Note that above 130 °C only $[Co(tren)Sb_4S_7]$ is formed, below 105 °C no product growth could be observed within five hours, and under static conditions the reaction required several days for completion. The reaction was studied at 105, 110, 115, 120, 125, and 130 °C under isothermal conditions. Additional experiments with $CoCl_2 \cdot 6\ H_2O$ (119 mg, 0.5 mmol, Fluka) were carried out at 120 °C.

Synchrotron radiation source for EDXRD measurements:

HASYLAB Beamline F3 receives white synchrotron radiation from a bending magnet with a critical energy of 16 keV and gives a positron beam energy of 4.5 GeV. An energy range from 13.5 to 65 keV can be observed with a maximum at about 20 keV. The diffracted beam is monitored by a nitrogen cooled solid state germanium detector. The detector angle of approximately 1.90° allowed the detection of Bragg reflections with d-spacing from 2.9 Å to 13.8 Å. The energy resolution $\Delta d/d$ was about 10^{-2} above 26 keV. The beam was collimated to 0.2 mm giving the best results. More experimental details

are found in [12,13]. The in-situ investigations were conducted with autoclaves containing glass liners with an internal diameter of 10 mm and a volume of 10 ml.

Synchrotron radiation source for EXAFS measurements:

The experiments were performed in transmission at the Sb K edge (30491 eV) at beamline X1 (HASYLAB). A Si(311) double crystal was used as monochromator and the measurement time was about 260 sec for each scan. The storage ring operated with injection currents of 140 mA at 4.4 GeV. The stirring of the reaction mixture was interrupted every second spectrum for data acquisition of Sb in solution without influence of the solid phase.

Details of data reduction procedures for energy dispersive X-ray absorption spectra can be found in the literature [25,26]. The data analysis was done with WinXAS 3.0 following recommended procedures [27]. Pre-edge background subtraction and normalization were carried out fitting linear polynomials to the pre-edge and the post-edge region of the spectra, respectively. A smooth atomic background was obtained with a cubic spline refinement procedure. Fitting range in k space, number of splines, and k weighting were optimized to afford a rigid background curve at low k and minimization of low R peaks in the Fourier transformed signal. The radial distribution function FT($\chi(k)$) was obtained by Fourier transforming the k^3 weighted experimental extended fine structure (EXAFS) $\chi(k)$, multiplied by a Bessel window, into R space.

Calculation of theoretical EXAFS spectra and refinement of experimental data were carried out using theoretical back-scattering phases and amplitudes obtained from the ab initio multiple-scattering code FEFF 7 [28]. Parameters obtained with a least-squares fit of the standard EXAFS formula are S_0^2, the passive electron reduction factor, R_j, the inter-atomic distance, the Debye-Waller factor σ_j^2, and the coordination number CN.

EXAFS refinements were carried out in R space to the magnitude and imaginary parts of a Fourier transformed k^3 weighted experimental $\chi(k)$. Further details on the EXAFS refinement procedure employed can be found in [29].

The FT spectra showed only one shell and the fitting must be done with care. The parameters S_0^2, CN, R_j and σ^2 are correlated and some assumptions must be made to get reliable results. The factor S_0^2 depends on the free path lengths which in turn scales with the temperature. The spectra were recorded at 130 °C and a fixed value of 1.05 is reasonable. For Sb containing solutions different values for σ^2 were reported which were used as the upper and lower limit during the refinements, i.e. σ^2 was freely refined within this range. The resulting magnitudes for σ^2 (Table 3) are in excellent agreement with those reported in previous papers. [30,31] The interatomic distance R_j depends on E_0 (zero point of the energy scale) which was fixed to 10 eV in accordance with literature data. Refinement of E_0 with starting values far from 10 always yielded a value very near to 10. The spectra were then refined either with the SbS_3 or the SbS_4 unit with a freely varying CN. In both cases the value for CN was 3.6 giving lower reliability factors than using the same units with fixed coordination numbers. In the next step the spectra were refined with fixed coordination numbers but with a variable ratio of both species. The lowest reliability factor was obtained for a 1:1 mixture of SbS_3 and SbS_4.

Reference measurements were done with a pressed pellet obtained by mixing about 100 mg [Co(tren)][Sb_2S_4] with boron nitride (ratio 1:3). The in-situ experiments were performed in the above mentioned cell under autogenous pressure either under dynamic (with stirring) or static (without stirring) conditions. At the end of the reaction the solid product was used as the reference phase.

For Sb references in the liquid phase 3.04g (25 mmol) Sb and 2.4 g (75 mmol) S were dissolved in 100 ml of a 50 % aqueous diethylenediamine solution and heated under reflux for 2 h. The resulting parent solution (A1) was diluted with 50 vol.% water (A2). This solution was again diluted with 50 vol.% water yielding A3, and this procedure was continued until solution A15 was obtained which contained 0.003 % of solution A1.

Density Functional Theory Calculations:

Spin-restricted DFT calculations using Becke´s three-parameter hybrid functional with the correlation functional of Lee, Yang and Parr (B3LYP) [32-34] were performed for the singlet ground state of SbS_3^{3-}

and SbS_4^{5-}. The LANL2DZ basis set was used for the calculations. It applies Dunning/Huzinaga full double-ζ (D95) basis functions [35] on the first row and Los Alamos effective core potentials plus DZ functions on all other atoms [36,37] All computational procedures were used as they are implemented in the Gaussian 98 package [38].

Results and Discussion

EDXRD

In the spectra several reflections of the product and the Sb resonance are monitored simultaneously (Figure 2). A typical sequence of time resolved spectra is shown in Figure 3. After an induction time, t_{ind}, which strongly depends on the reaction temperature, product peaks starts to grow. Note that the Sb resonance at 26.6 and 31.1 keV as well as an escape peak at 16.5 keV are immediately visible in the spectra. The (102) reflection with the highest intensity corresponds to the layers of the compound. A quantitative analysis of the growth rates shows an identical behavior for different reflections and confirms an isotropic crystallite growth (see also below). In the spectra no hints are seen for the occurrence of crystalline precursors or intermediates. Compared to t_{ind} the half-life time $t_{0.5}$ of crystallization is short and is about 15 % of the time necessary to complete the reaction (Table 1). The first step of the kinetic analysis is the integration of one or several product reflections using a Gaussian function and measuring the corresponding areas. These are then converted to the extent of reaction α using the relation $\alpha(t) = I_n(t)/I_n(t_\infty)$, with $I_n(t)$ being the intensity of the reflection at time t and $I_n(t_\infty)$ is the intensity of this reflection at the end of the reaction ($t = \infty$). In the present analysis the previously integrated intensities at the time t were divided by the intensity of the Sb K_α resonance peak at the same time t to get the normalized intensity relative to the beam intensity, i.e. the data are very accurate due to the correction for fluctuation of primary beam intensity.

The plot of α vs. reaction time t (Figure 4, Table 1) shows a strong temperature dependence of t_{ind}. At 130 °C the value for t_{ind} is 56 min and increases by a factor of 4 at 105 °C (t_{ind} = 204 min). It is

remarkable that the data are reproducible on a very high level despite the long induction period at 105 °C, and according to experimental results the variation of t_{ind} is less then 5 min (< 2.5 %) at 105 °C.

Kinetic analysis

Kinetic analyses are performed by fitting the experimental data to a theoretical expression relating the extent of reaction α vs. time. Several kinetic expressions applied to solid state kinetics are reported, and the general shape of their curves is well documented. A detailed description of the procedure for the evaluation of the data was presented for instance in [12].

The kinetic evaluation was performed after subtraction of t_{ind} from time t and the reduced reaction time (t_{red}) is obtained. The kinetic data for different reaction temperatures are summarized in Table 1. When ln[-ln(1-α)] is plotted vs. ln(t) (the so called Sharp-Hancock plot, abbreviated SH) a straight line is obtained for that part of the reaction which follows the same mechanism [39-41]. A change of the mechanism results in a change of the slope of the curve. From the slope of the linear part of the curve the reaction exponent m can be evaluated (often called the Avrami exponent) and the intercept with the y axis gives the rate constant k [s^{-1}]. The exponent m is then related to the type of nucleation and growth process taking place, including the morphology of the reaction product, i.e. whether the crystals are fibers, needles, plates, sheets, spheres or polygons. The exponent m also includes the type of nucleation, i. e. whether the nuclei all develop at once or continuous nucleation with a constant rate occurs [42,43].

The SH plot for data obtained at T = 115 °C (Fig. 5) clearly shows that the growth can be divided into two different parts. Up to $\alpha \approx 0.77$ the reaction exponent m has a value of 0.59 corresponding to a diffusion controlled growth mechanism (Table 2), and in the second part ($\alpha > 0.77$) m increases to about 1.23. For reactions at T ≤ 110 °C the experimental points are on a straight line nearly over the whole reaction, and only just before the end a slight deviation seems to occur. The nucleation and growth is mainly controlled by diffusion and a first order process may influence the growth at the latest stages of the reaction. It must be kept in mind that the discussion of possible mechanisms based on the exponent m is not always straightforward. The values for m often deviate severely from the theoretical values

listed in Table 2 and there are several reasons for these experimental findings. The simplest assumption is that reactions with different mechanisms proceed parallel and/or successive yielding values different from theoretical ones [44-46]. We note that the values for *m* discussed above deviate from theoretical values, but they are in the range for diffusion controlled mechanisms during the first stage of the reactions with stronger deviations from theoretical values for the later stage. The rate constant *k* and the half-life time exhibit a clear temperature dependence. While the half-life time decreases with increasing temperatures the value for the rate constant increases (Table 2).

More detailed and rigorous analyses were performed comparing all models listed in Table 2 with the experimental data [47-49]. A plot of the experimental $t/t_{0.5}$ data ($t/t_{0.5}$ is the reaction time at $\alpha = 0.5$) vs. α (Fig. 6) allows a direct comparison with the different models under consideration. For T > 110 °C (Fig. 6, T = 115 °C) the experimental data $\alpha < 0.7$ are in accordance with a diffusion control followed by a change towards the first order mechanism F1 for $\alpha > 0.7$. Scaling the time dependent behavior of a reaction to 33 % a better discrimination between the models is possible for higher values of α. Hence, the plot of $t/t_{0.33}$ vs. α (Fig. 7, T = 115 °C) confirms the change of the mechanism at later stages of the reaction. For T ≤ 110 °C the analysis of the data (Fig. 8) suggests that diffusion (D2 and/or D3) is the rate limiting process for the crystal growth, but a definite decision is not possible in agreement with the results from the SH analysis (Fig. 9). The deviations discussed above are also observed in the so called Austin-Rickett plots [50] (Fig. 10).

The activation energy E_A was determined with the Arrhenius equation using the *k* values of the first part of the reactions (Table 2). The plot ln*k* vs. 1/T yields a straight line and $E_A = 42$ kJ/mol is obtained. This result is in comparable with values found in literature [13,15].

At the end of the formation of $[Co(tren)][Sb_2S_4]$, reflections of a second crystalline phase appear in the spectra and several new reflections start to grow simultaneously (Figure 12). This phenomenon is independent from temperature and is observed at the latest stages of every reaction. The second phase was identified as $[tren]_x[Sb_{21}S_{34}]$. Unfortunately, the (102) reflection of $[Co(tren)][Sb_2S_4]$ and the (004/013) peak of the second phase coincide. Hence, the end of crystallization of $[Co(tren)][Sb_2S_4]$ was

evaluated with the (002) reflection and for the second phase $[tren]_x[Sb_{21}S_{34}]$ the overlapping (202/-212) peak was used (Fig. 12). The integrated intensity of the (002) peak of $[Co(tren)][Sb_2S_4]$ passes a maximum which was then defined as the end of the formation of this phase. Exactly at this time the second phase starts to grow and the amount of the first compound starts to decrease (Figure 13).

An in-situ experiment was performed for 14 h after the intensity of reflections of $[Co(tren)][Sb_2S_4]$ just started to decrease to prove whether $[Co(tren)][Sb_2S_4]$ is only a kind of intermediate. During the first 6 h the intensity of (002) of $[Co(tren)][Sb_2S_4]$ drops and an equilibrium between the two phases is reached (Fig. 13). This may be explained on the basis of a partial dissolution/amorphization of $[Co(tren)][Sb_2S_4]$ and the simultaneous crystallization of the new phase. On a microscopic level the following may occur. At the point where the intensities of $[Co(tren)][Sb_2S_4]$ start to decrease the concentration of dissolved Co^{2+} cations is too low for further crystallization, and the transition metal free compound starts to crystallize. The formation of this new phase influences the equilibrium between solid $[Co(tren)][Sb_2S_4]$ and the solution because the concentration of Sb^{3+}/S^{2-} is lowered due to crystallization of $[tren]_x[Sb_{21}S_{34}]$. The strong reduction of the concentration of Sb^{3+}/S^{2-} is accompanied by the partial dissolution of the Co containing compound yielding a new equilibrium for this complex system. To prove that $[Co(tren)][Sb_2S_4]$ is not only dissolved by tren the solid compound was filtered-off after the reaction was complete and 2 ml pure tren was added. No change in the spectra was observed within the next 4 h. The ratio between the two phases was constant demonstrating that the pH-value and the concentration of tren do not alter the equilibrium.

In about 1/3 of the in-situ experiments highly interesting observations for reactions performed at $T \leq 120°C$ were made, i.e. a very different growth behavior of the reaction product was observed (Figure 14). After a temperature dependent induction time only the (102) reflection starts to grow (Figure 14), and after another 28 minutes all other peaks of $[Co(tren)][Sb_2S_4]$ occur and grow simultaneously. The position of the (102) reflection is slightly shifted to smaller energy values at the early stages of reaction (23.27 keV) and reaches 23.05 keV found in the other experiments discussed above (Figure 15). The most possible 'parameter' responsible for this unusual observation is the ferromagnetic behavior of

elemental Co. The slurry is stirred with a magnetic stirrer bar (see Experimental section). When Co sticks at the surface of this bar the dissolution of Co at T ≤ 120°C seems to have a random component. This effect is negligible for T > 120°C due to faster dissolution of Co yielding a concentration of Co^{2+} ions which is large enough for the nucleation and crystallization following the mechanisms presented above. We proofed the hypothesis of this phenomenon and performed in-situ experiments with $CoCl_2 \cdot 6 H_2O$ as Co source. In all these experiments product growth proceeds following the reaction paths discussed in the previous chapter. This experimental finding supports our assumption that the velocity of dissolution of elemental cobalt has a significant influence onto the reaction mechanism.

The SH analysis of the data gives evidences that the crystallization kinetics occurs in three different steps each being characterized by a different reaction exponent *m* (Figure 16). The values for *m* are about 0.4 ($\alpha < 0.33$) and 1.5 ($\alpha > 0.88$) for the first and third stage and deviate from the ideal values listed in Table 2. In the second part of the reaction where all peaks grow simultaneously the value for *m* of 4.0 is unusual large, but may be explained on the basis of constant nucleation[51]. An identical behavior was observed by O'Hare and co-workers [14] during the formation of the tin sulfide TMA-SnS1 and was explained by strongly disordered layers which at later stages of reaction start to arrange yielding the three-dimensional long range order.

EXAFS measurements:

In the last decades many experiments were devoted to identify the soluble species of antimony sulfides in alkaline solutions. Different species were postulated, e.g. SbS_2^-, $Sb_2S_4^{2-}$, $Sb_4S_7^{2-}$ [52], SbS_3^{3-} and SbS_4^{3-} [30,52,53], and $Sb_2S_6^{2-}$ [53]. But until now it is not clear how Sb atoms are coordinated in basic sulfur containing solutions. For a better understanding of the building mechanisms of thioantimonates it is important to identify primary building units existing in reaction solutions using EXAFS experiments.

Reference measurements:

Solutions with different concentrations of Sb/S in diethylentriamine were used as references (see Experimental section). The edge jump scales linearly with the Sb concentration, i.e. lower Sb contents yield smaller jumps. The temperature effect onto the edge jump can be neglected. Interestingly, the

spectra exhibit only different intensities of the peaks but no differences were observed for the shape of the XANES or EXAFS. This result shows that the coordination sphere of Sb is the same for all concentrations.

Measurements during formation of [Co(tren)][Sb_2S_4]

The evolution of the Sb edge height during the reaction at 120 °C is shown in Figure 17. After a short induction time a maximum of the absorption jump Δμx of **1.3** was reached and after 60 minutes the value decreased to 0.2. The change of the edge jump time proceeds not in a linear way but has a sigmoidal shape reminiscent of the curve for the extent of reaction presented in Figure 4. The two curves cannot be compared directly due to the different experimental conditions. The slurry was interrupted to collect the XAFS data (see experimental section), i.e. this interruption increases the reaction time. At the beginning of the reaction elemental Sb is dissolved and the Sb content in solution is very high. Within a few minutes the Sb content decreases dramatically indicating that a solid product is formed which must be amorphous because it is not seen in EDXRD experiments. Hence, it can be assumed that long before crystallization of [Co(tren)][Sb_2S_4] an amorphous precursor is formed. The quality of EXAFS spectra of this amorphous solid was not good enough for an evaluation and the composition of the precursor is not known.

Evaluation of the spectra

During the whole reaction only two different types of spectra were observed. At the beginning the spectra are similar to those recorded for reference A1 (see Experimental section) and at the end the spectra are similar to those obtained with pellets of crystalline [Co(tren)][Sb_2S_4] (Figure 18). This observation suggests that [Co(tren)][Sb_2S_4] is either soluble or that small particles are present in the solution which do not sediment during the time after stirring was stopped. In another experiment the solution was not stirred for 2 h and care was taken that only the solution was investigated with EXAFS. Interestingly, the spectra were identical with those recorded at the beginning of the reaction demonstrating that [Co(tren)][Sb_2S_4] is not dissolved and the spectra obtained at the end of the reaction were caused by small particles of [Co(tren)][Sb_2S_4].

Reactions with other Sb/S/amine slurries were also investigated (0.5 mmol Sb, 1.5 mmol S in 2 mL 50% 2-aminoethylpiperazine at 160 °C; 0.5 mmol Sb, 0.5 mmol Mn, 1.2 mmol S in 2 mL 100% dien at 120 °C) to monitor the influence of the amine onto the formation of the SbS_x species. But for all solutions the spectra were similar, i.e. the environment of Sb in sulfur containing amine solutions is identical. Temperature, volume, pH-value and the kind of the amine have no measurable influence onto the dissolved SbS_x species, which is a quite remarkable and surprising result.

Simulations of EXAFS spectra

The species in solution may be identified comparing simulated EXAFS spectra for different SbS_x species with the experimental data. In the literature [43-45] mainly three different structural species were suggested, i.e. a $Sb_2S_6^{6-}$ ring, the SbS_3^{3-} group and a SbS_4^{3-} unit. The existence of the $Sb_2S_6^{6-}$ ring can be ruled out because the radial distance distribution (Figure 19) shows only one shell around Sb, but a $Sb_2S_6^{6-}$ ring requires a second shell accounting for the Sb-Sb coordination. The two other models were simulated with Gaussian98 (see above) and protonated sulfur atoms had no influence onto the geometry. The structurally optimized clusters were used for FEFF calculations (see experimental section) and the results are summarized in Table 3.

The refinements performed with freely varying coordination numbers (CN) for either SbS_3 or SbS_4 always yield a value for CN near 3.5 suggesting that both species coexist in solution. Therefore, the spectrum was simulated containing a 1:1 mixture of SbS_3 and SbS_4 groups and the resulting FT($\chi(k)$) together with the theoretical XAFS function utilizing phases and amplitudes is shown in Fig.19. The calculated EXAFS function fits perfectly with the experimental $\chi(k)$ for both the phase and the amplitude. This result suggests that only these two groups are present in solution.

Conclusion

The synthesis of compounds under solvothermal conditions is in most cases a black box method, i.e. after a distinct reaction time the reaction vessels are removed from the furnaces and the products are then characterized. The products often consist of mixtures of different compounds and optimization of

the synthesis is time consuming because several reaction parameters have to be varied. In addition crystalline precursors or intermediates may crystallize at short reaction times which will never be "seen" using the conventional synthesis procedure. Such kinetically less stable compounds may have interesting physico-chemical properties. In the present contribution we demonstrated that in-situ EDXRD experiments are powerful to monitor the evolution of the formation of a distinct compound so that phase pure materials can be prepared. But for basic research the reaction mechanisms and kinetics occurring under solvothermal conditions are more interesting. A rigorous analysis of the results recorded as function of different reaction parameters provides information about the kinetics and give hints about the reaction mechanisms. For the present system diffusion is the rate limiting step, and at later stages the reaction exponents indicate more complex kinetics/mechanisms. When the synthesis of the title compound is performed with elemental Co at T ≤ 120 °C a random dissolution of Co influences the reaction path which was immediately detected in the EDXRD spectra. At the beginning only the (102) reflection of the product starts to grow, slightly shifts with reaction time and at later stages of the reaction all other peaks of $[Co(tren)][Sb_2S_4]$ occur and grow simultaneously. These observations are reminiscent of a mechanism where first strong disordered layers are formed which then start to arrange during reaction progress yielding the three-dimensional long range ordered material.

The combination of in-situ EDXRD with in-situ EXAFS experiments provides information about the reaction starting from the very early stages until products starts to crystallize. We have shown that the starting material is dissolved within a short period. According to the EXAFS analysis only two different species are present in the solution. A drastic decrease of dissolved antimony species indicates that a solid product is formed which is not detected in the EDXRD spectra, i.e. the particle sizes are too small and/or the solid is amorphous.

Taking all results into account possible reaction pathways can be postulated which is depicted in Fig. 20. A the beginning of the reaction the starting material is very fast dissolved (see Fig. 20 path 1) and it can be assumed that Co is coordinated by the amine yielding a $[Co(tren)]^{2+}$ complex. According to the EXAFS results monomeric SbS_x units with x = 3 and 4 are formed. Further condensation (see path 2 in

Fig. 20) via common corners and/or edges leads to larger SbS aggregates which are not longer soluble and a solid amorphous phase is formed. For temperatures ≤ 120 °C a preorientation (see path 3 in Fig. 20) of the layers occurs and only the (102) reflection of the product starts to grow in the X-ray powder pattern. In contrast to this observation the normal reaction path does not proceed via this step and all product reflections grow simultaneously which is sketched in Fig. 20 as path 4.

Acknowledgement.

The financial supports of this work by the state of Schleswig-Holstein and the Deutsche Forschungsgemeinschaft (DFG) are acknowledged. We also thank Julia Wienold and Ulrich Ponkratz for help their help at the beamlines X1 and F3 at HASYLAB.

References

[1] Korányi, T.I.; Pham, N.G.; Jentys, A.; Vinek, H. *Stud. Surf. Sci.* Catal. **1997**, *106*, 509.

[2] Stähler, R.; Näther, C.; Bensch, W. *J. Solid State Chem*. **2003**, *174*, 264.

[3] Wang, X.; Liebau, F. *J. Solid State Chem*. **1994**, *111*, 385.

[4] Spetzler, V.; Kiebach, R.; Näther, C.; Bensch, W. *Z. Anorg. Allg. Chem*., **2004**, *630*, 2398.

[5] Kiebach, R.; Näther, C.; Bensch, W. *Z. Naturforsch.* **2004**, *59b*, 1314.

[6] Vaquiero, P.; Chippindale, A.M.; Powell, A.V. *Inorg. Chem.* **2004**, *43*, 7963.

[7] Schaefer, M.; Stähler, R.; Kiebach, W.-R.; Näther, C.; Bensch, W. *Z. Anorg. Allg. Chem.* **2004**, *630*, 1816.

[8] Lee, C.-S.; Safa-Sefat, A.; Greedan, J.E.; Kleinke, H. *Chem. Mater.* **2003**, *15*, 780.

[9] Starrost, F.; Krasovskii, E.E.; Schattke, W.; Simon, U.; Wang, X.; Liebau, F. *Phys. Rev. Lett*. **1998**, *80*, 3316.

[10] Stähler, R.; Bensch, W. *Eur. J. Inorg. Chem.,* **2001**, 3073.

[11] Kiebach, R; Schäfer, M.; Porsch, F.; Bensch, W. *Z. Anorg. Allg. Chem.* **2005**, *631*, 369.

[12] Engelke, L.; Schaefer, M.; Porsch, F.; Bensch, W. *Eur. J. Inorg. Chem.* **2003**, 506.

[13] Engelke, L.; Schaefer, M.; Schur, M.; Bensch, W. *Chem. Mater.* **2001**, *13*, 1383.

[14] Francis, R.J.; Price, J.S.; Evans, J.S.O.; O'Brien, S.; O'Hare, D. *Chem. Mater.* **1996**, *8*,2102.

[15] Bray, H.J; Redfern, S.A.T. *Phys. Chem. Miner.* **1999**, 591.

[16] Christensen, A.N.; Bareges, A.; Nielsen, R.N.; Hazell, R.G.; Norby, P.; Hanson, J.C. *J. Chem. Soc., Dalton Trans.* **2001**, 1611.

[17] Penner-Hahn, J.E. *Coord. Chem. Rev.* **1999**, *190-192*, 1101.

[18] Burattini E.; Dalba, G.; Fornasini, P. *Il Nuovo Cimento* **1986**, *7*, 293.

[19] Červinka, L.; Smotlacha, O.; Bererová, J. ; Tichy, L. *Non.-Cryst. Solids* **1991**, *137-138*, 123.

[20] Sankar, G.; Rey, F.; Thomas, J.M.; Greaves, G.N.; Corma, A.; Dobson, B.R. *J. Chem. Soc. Chem. Commun.* **1994**, 2279.

[21] Thomas, J.M. *Angew. Chem.* **1999**, *111*, 3800.

[22] Rey, F.; Sankar, G.; Thomas, J.M.; Barrett, P.A.; Lewis, D.W.; Catlow, C.R.A.; Clark, S.M.; Greave, G.N. *Chem. Mater.* **1995**, *7*, 1435.

[23] Sankar, G.; Wright, P.A.; Natarajan, S.; Thomas, J.M.; Greves, G.N.; Dent, A.J.; Dobson, B.R.; Ramsdale, C.A.; Jones, R.H. *J. Phys. Chem.* **1993**, *97*, 9550.

[24] Cora, F.; Sankar, G.; Catlow, C.R.A.; Thomas, J.M. *Chem. Commun.* **2002**, 734.

[25] Ressler, T. *J. Phys. IV* **7 1997**, C2 – C269.

[26] Ressler, T., Hagelstein, M., Hatje, U., Metz, W. *J. Phys. Chem. B* **1997**, *101*, 6680.

[27] Koningsberger, D.C.; Prins, R. *X – Ray Absorption Spectroscopy, Chemical Analysis*, 92, Wiley, NewYork, **1988**.

[28] Rehr, J.J.; Booth, C.H.; Bridges, F.; Zabinsky, S.I. *Phys. Rev. Lett.* **1992**, *69*, 3397.

[29] Ressler, T.; Timpe, O.; Neisius, T.; Find, J.; Mestl, G.; Dieterle; M. Schlögl, R. *J. Catal.* **2000**, *191*, 75.

[30] Frederick, J.; Mosselmans, W.; Helz, G. R.; Pattrick, R.A.D.; Charnock, J.M.; Vaughan, D.J. *Appl. Geochem.* **2000**, *15*, 879.

[31] Oelkers, E.H.; Sherman, D.M.; Ragnarsdottir, K.M.; Collins, C. *Chem. Geo.* **1998**, *151*, 21.

[32] Becke, A.D. *Phys. Rev. A* **1988**, *38*, 3098.

[33] Becke, A.D. *J. Chem. Phys.* **1993**, *98*, 1372.

[34] Becke, A.D. *J. Chem. Phys.* **1993**, *98*, 5648.

[35] Dunning, T.H., Jr.; Hay, P.J. In *Modern Theoretical Chemistry*; Schaefer, H. F., III, ed.; Plenum: New York, 1976.

[36] Hay, P.J.; Wadt, W.R. *J. Chem. Phys.* **1985**, *82*, 270.

[37] Wadt, W.R.; Hay, P.J. *J. Chem. Phys.* **1985**, *82*, 284.

[38] Frisch, M.J.; Trucks, G.W.; Schlegel, H.B.; Scuseria, G.E.; Robb, M.A.; Cheeseman, J.R.; Zakrzewski, V.G.; Montgomery, J.A., Jr.; Stratmann, R.E.; Burant, J.C.; Dapprich, S.; Millam, J.M.; Daniels, A.D.; Kudin, K.N.; Strain, M.C.; Farkas, O.; Tomasi, J.; Barone, V.; Cossi, M.; Cammi, R.; Mennucci, B.; Pomelli, C.; Adamo, C.; Clifford, S.; Ochterski, J.; Petersson, G.A.; Ayala, P.Y.; Cui, Q.; Morokuma, K.; Salvador, P.; Dannenberg, J.J.; Malick, D.K.; Rabuck, A.D.; Raghavachari, K.; Foresman, J.B.; Cioslowski, J.; Ortiz, J V.; Baboul, A.G.; Stefanov, B.B.; Liu, G.; Liashenko, A.; Piskorz, P.; Komaromi, I.; Gomperts, R.; Martin, R.L.; Fox, D.J.; Keith, T.; Al-Laham, M.A.; Peng, C. Y.; Nanayakkara, A.; Challacombe, M.; Gill, P.M.W.; Johnson, B.; Chen, W.; Wong, M.W.; Andres, J.L.; Gonzalez, C.: Head-Gordon, M.; Replogle, E.S.; Pople. J.A Gaussian 98 Rev. A.11; Gaussian, Inc.: Pittsburgh, **2001**.

[39] Hancock, J.D.; Sharp, J.H. *J. Am. Ceram. Soc*. **1972**, *55*, 74.

[40] Sharp, J.H.; Brindley, G.W.; Narahari Achar, B.N. *J. Am. Ceram. Soc.* **1966**, 379.

[41] Mohamed, B.M.; Sharp, J.H. *J. Mat. Sci.* **1997**, 1595.

[42] Brown, P.W.; Pommersheim, J.; Frohnsdorff, G. *Cem. Concr. Res.* **1985**, *15*, 35.

[43] Thomas, J.J.; Jennings, H.M. *Chem. Mater.* **1999**, *11*, 1907.

[44] Pradell, T.; Crespo, D.; Clavaguera, N.; Clavaguera-Mora, M.T. *J. Phys. Condens. Matter.* **1998**, *10*, 3833.

[45] Fanfoni, M.; Tomellini, M. *Il Nuovo Cimento* **1998**, *20*, 1171.

[46] Castro, M.; Domínguez-Adame, F.; Sánchez, A.; Podríguez, T. *Appl. Phys. Lett.* **1999**, *75*, 2205.

[47] Avrami, M. *J. Chem. Phys.* **1939**, *7*, 1103.

[48] Avrami, M. *J. Chem. Phys.* **1940**, *8*, 212.

[49] Avrami, M. *J. Chem. Phys.* **1941**, *9*, 177.

[50] Austin, J.B.; Rickett, R.L. *Trans. AIME* **1939**, *135*, 396.

[51] Davies, A.T.; Sankar, G.; Catlow, C.R; Clark, S.M. *J. Phys. Chem. B* **1997**, *101,* 10115.

[52] Wood, S.A. *Geochim. Cosmochim. Acta* **1989**, *53*, 237.

[53] Helz, G.R.; Valerio, M.S.; Capps, N.E. *Environ. Sci. Technol.* **2002**, *36*, 943.

Table 1: Kinetic data obtained by the analysis with Sharp-Hanckock plots

T in °C	Induction time[a)] in min	Reaction time[b)] in min	Half-life time[c)] in min	*m*	$k[s^{-1}]\cdot 10^{-4}$
105 $\alpha<0.71$ $\alpha>0.71$	204	200	18	0.57 0.85	5.20 4.29
110 $\alpha<0.77$ $\alpha>0.77$	113	133	17	0.66 1.29	5.45 4.43
115 $\alpha<0.75$ $\alpha>0.75$	101	62	15	0.59 1.23	6.39 4.64
120 $\alpha<0.68$ $\alpha>0.68$	83	47	9	0.70 1.65	8.74 8.28
125 $\alpha<0.53$ $\alpha>0.53$	66	45	9	0.67 0.98	10.13 11.18
130 $\alpha<0.67$ $\alpha>0.67$	56	38	7	0.55 1.41	10.74 10.81

a) Induction time: time between reaction start and occurrence of first product peaks. b) Reaction time :time between first occurrence of product peaks and end of reaction ($\alpha=1$). c) Half-life time: time between first occurrence of product peaks and $\alpha=0.5$.

Table 2: The rate equations for solid state reactions reported in literature.

Growth Model	Rate Equation $f(\alpha) = kt$	*m*
Diffusion controlled		
$D_1(\alpha)$	$\alpha^2 = 0.25\ (t/t_{0.5})$	0.62
$D_2(\alpha)$	$(1-\alpha)\ln(1-\alpha)+\alpha = 0.1534\ (t/t_{0.5})$	0.57
$D_3(\alpha)$ [Jander]	$[1-(1-\alpha)^{1/3}]^2 = 0.0425\ (t/t_{0.5})$	0.54
$D_4(\alpha)$ [Ginstling-Brounshtein]	$1-2\alpha/3-(1-\alpha)^{2/3} = 0.0367\ (t/t_{0.5})$	0.57
Phase-boundary controlled		
$R_2(\alpha)$	$1-(1-\alpha)^{1/2} = 0.2929\ (t/t_{0.5})$	1.11
$R_3(\alpha)$	$1-(1-\alpha)^{1/3} = 0.2063\ (t/t_{0.5})$	1.07
First order		
$F1(\alpha)$	$[-\ln(1-\alpha)] = 0.6931\ (t/t_{0.5})$	1.00
Nucleation [Avrami-Erovéef]		
$A2(\alpha)$	$[-\ln(1-\alpha)]^{1/2} = 0.8326\ (t/t_{0.5})$	2.00
$A3(\alpha)$	$[-\ln(1-\alpha)]^{1/3} = 0.885\ (t/t_{0.5})$	3.00

Table 3: Results from EXAFS simulations with standard deviations given in parentheses.

	SbS_3	SbS_4	SbS_3	SbS_4
residual	3.51	3.59	1.60	3.58
coordination number	3 (fixed)	4 (fixed)	3.6 (free)	3.5 (free)
σ^2 /Å^2	0.00189(3)	0.00386(4)	0.00308(2)	0.00295(3)

Figure captions

Figure 1: Crystal structure of [Co(tren)][Sb_2S_4] viewed along the *c*-axis.

Figure 2: Energy-dispersive diffraction pattern of [Co(tren)][Sb_2S_4]. The indices of the reflections and the Sb fluorescence are marked.

Figure 3: Time resolved powder pattern recorded at 120 °C. The indices of the most intense lines of the product phase and the **SbK_α** fluorescence line are marked.

Figure 4: Extent of reaction α versus time for the (102) reflection at different reaction times.

Figure 5: Sharp-Hanckock plot for the data at T = 115°C.

Figure 6: Comparison of experimental $t/t_{0.5}$ data as function of α (black squares) with different theoretical models for T = 115 °C. The letters with the numbers are abbreviations of the different models listed in Table 2.

Figure 7: Comparison of experimental $t/t_{0.3}$ data as function of α (black squares) with different theoretical models for T = 115 °C. The letters with the numbers are abbreviations of the different models listed in Table 2.

Figure 8: Comparison of experimental $t/t_{0.5}$ data as function of α (black squares) with different theoretical models for T = 105 °C. The letters with the numbers are abbreviations of the different models listed in table 2. Inset: Sharp-Hanckock plot for the data at T = 105°C.

Figure 9: Sharp-Hanckock plots for all temperatures.

Figure 10: Austin-Rickett plots for all temperatures.

Figure 11: Arrhenius plot of ln k vs. 1/T [K^{-1}] for the first stage of the reaction, determined from Sharp-Hancock plots.

Figure 12: Energy-dispersive diffraction patterns of [Co(tren)][Sb_2S_4] and the second phase. The indices of reflections of the second phase are indicated. Additionally the (102) reflection of [Co(tren)][Sb_2S_4] is marked.

Figure 13: Extent of reaction α versus time for the (002) reflection of [Co(tren)][Sb_2S_4] and the (202/-212) reflections of the second phase $[tren]_x[Sb_{21}S_{34}]$.

Figure 14: Time resolved powder patterns recorded at 120 °C showing the different growth behavior. The indices of the most intense lines of the product phase and the **SbK_α** fluorescence line are marked.

Figure 15: Comparison of the (102) reflection for the two different growth behaviors at 120 °C. Left: unusual growth behavior with peak shift, right with normal growth mechanism.

Figure 16 : Sharp-Hanckock plot for the data at T = 120°C for the product formed by second reaction path.

Figure 17: Evolution of the Sb K edge jump during the reaction.

Figure 18: Changes of EXAFS spectra during the reaction.

Figure 19: Experimental and simulated Fourier transformed $\chi(k)$. Theoretical phases and amplitudes calculated with SbS_3 and SbS_4 units.

Figure 20: Reaction scheme for the formation of [Co(tren)][Sb_2S_4].

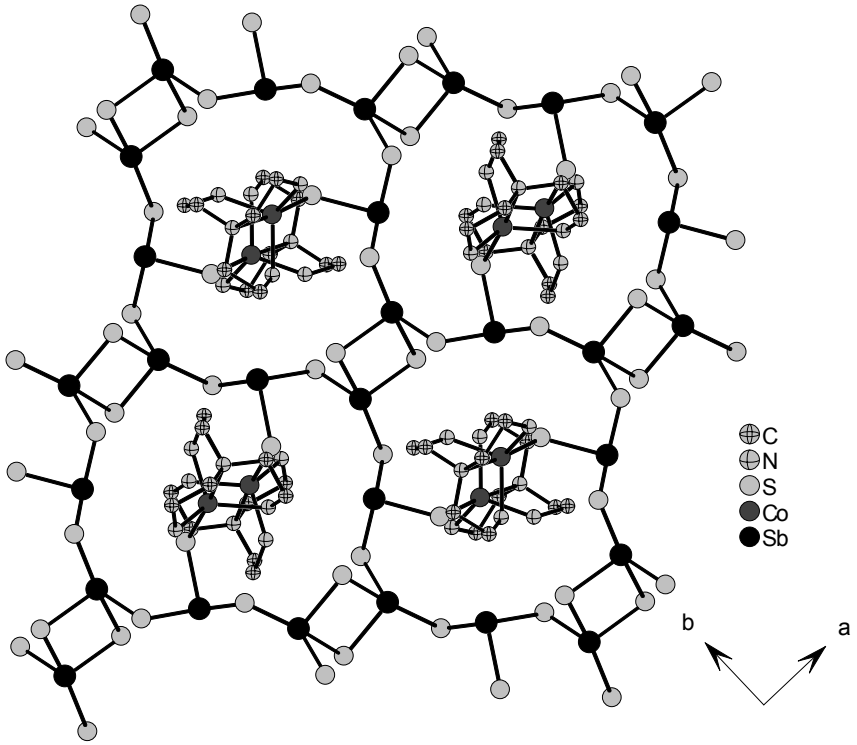
C
N
S
Co
Sb
b
a

Fig.1

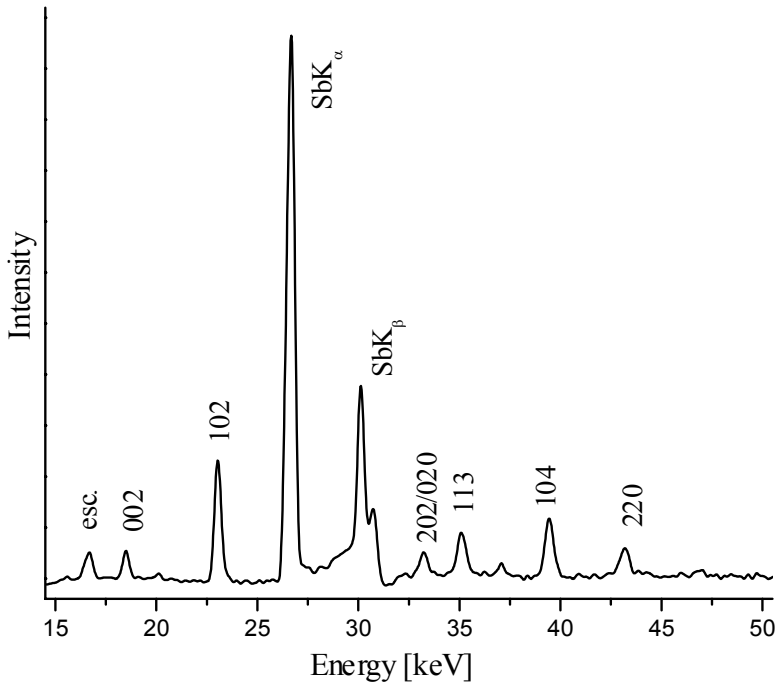
Intensity
esc.
002
102
SbK$_\alpha$
SbK$_\beta$
202/020
113
104
220
15
20
25
30
35
40
45
50
Energy [keV]

Fig.2

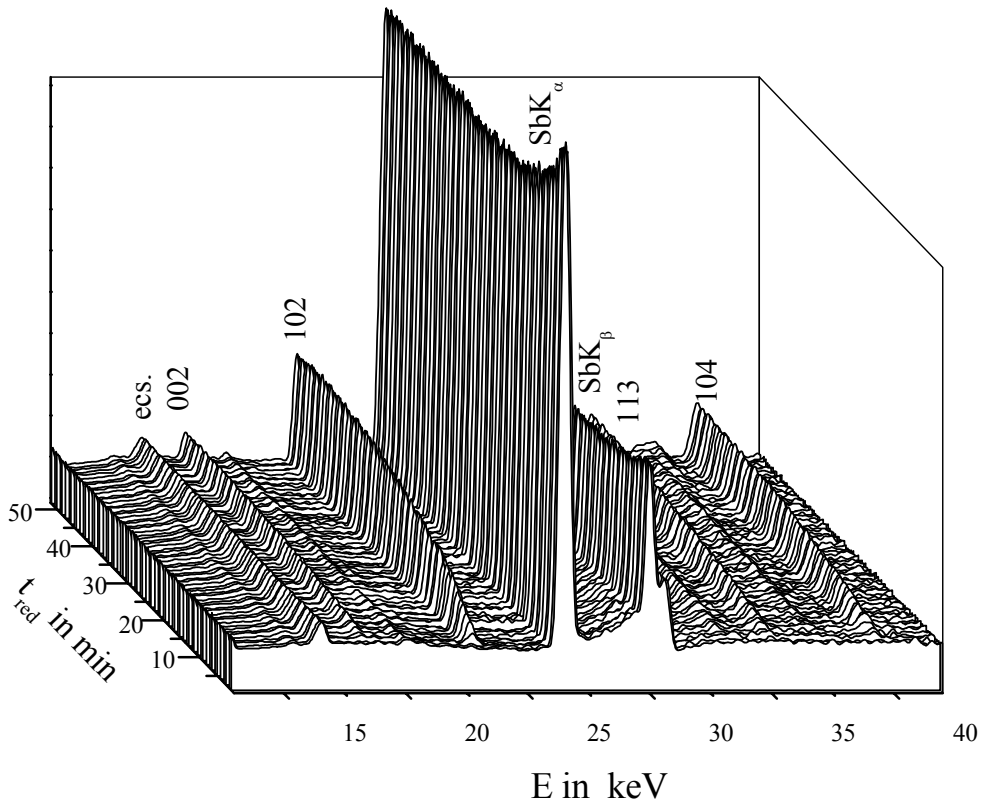
ecs.
002
102
SbK$_\alpha$
SbK$_\beta$
113
104
50
40
30
20
10
t_{red} in min
15
20
25
30
35
40
E in keV

Fig.3

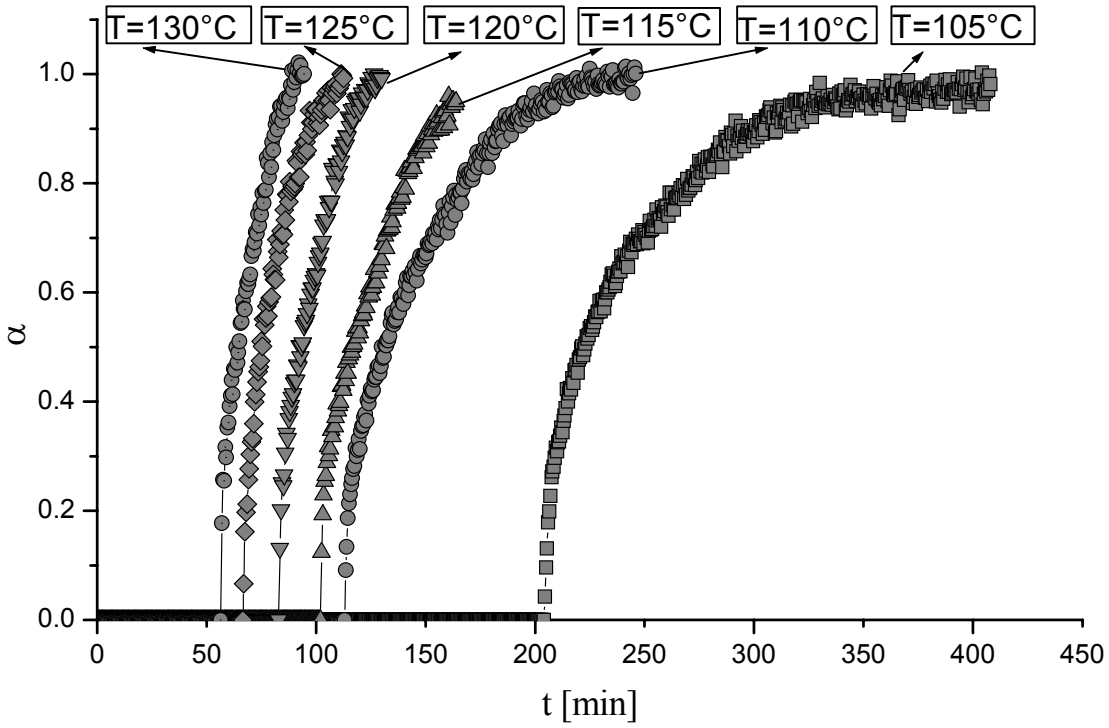
T=130°C
T=125°C
T=120°C
T=115°C
T=110°C
T=105°C
1.0
0.8
0.6
0.4
0.2
0.0
α
0
50
100
150
200
250
300
350
400
450
t [min]

Fig.4

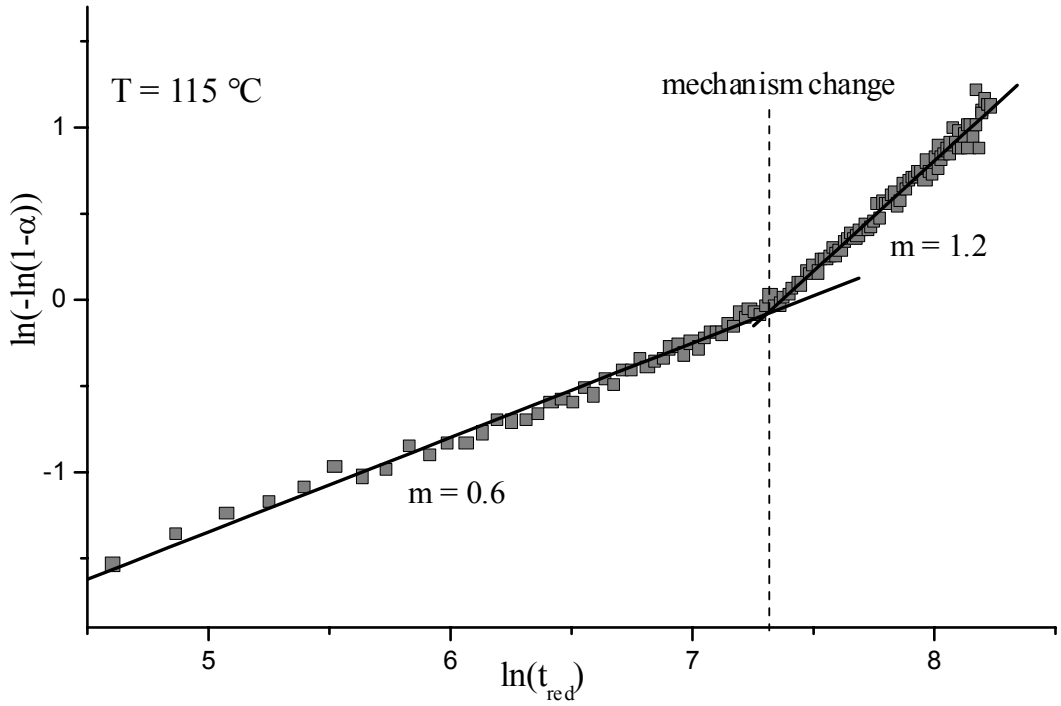
T = 115 °C
mechanism change
m = 1.2
m = 0.6
ln(-ln(1-α))
ln(t_red)
1
0
-1
5
6
7
8

Fig.5

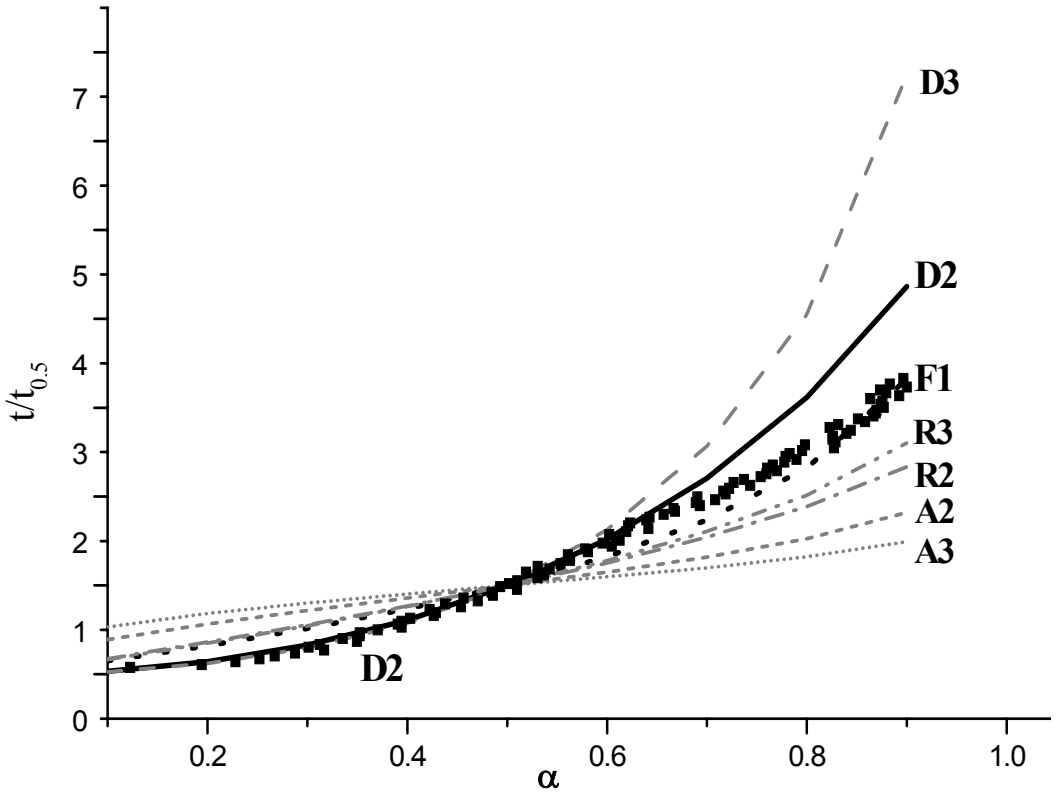
D3
D2
F1
R3
R2
A2
A3
D2
t/t0.5
α
0
1
2
3
4
5
6
7
0.2
0.4
0.6
0.8
1.0

Fig.6

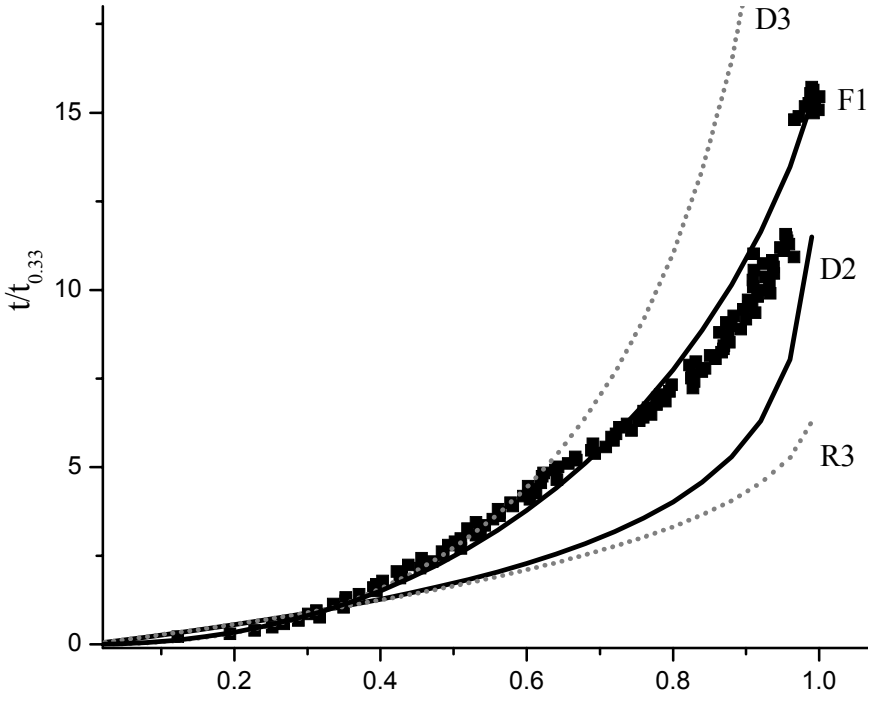
D3
F1
D2
R3
t/t0.33
0
5
10
15
0.2
0.4
0.6
0.8
1.0

Fig:7

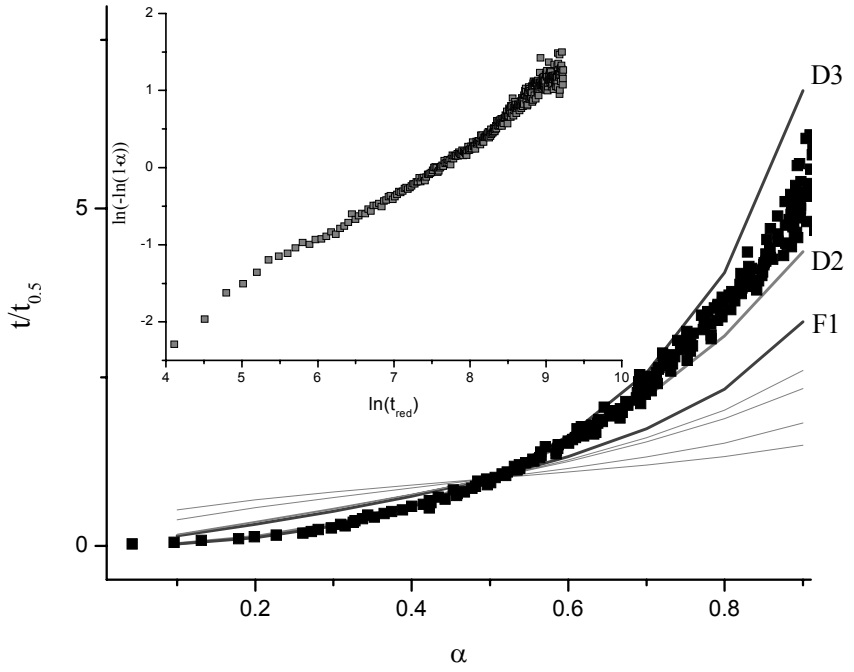
D3
D2
F1
t/t0.5
α
0
5
0.2
0.4
0.6
0.8
ln(-ln(1-α))
ln(tred)
2
1
0
-1
-2
4
5
6
7
8
9
10

Fig.8

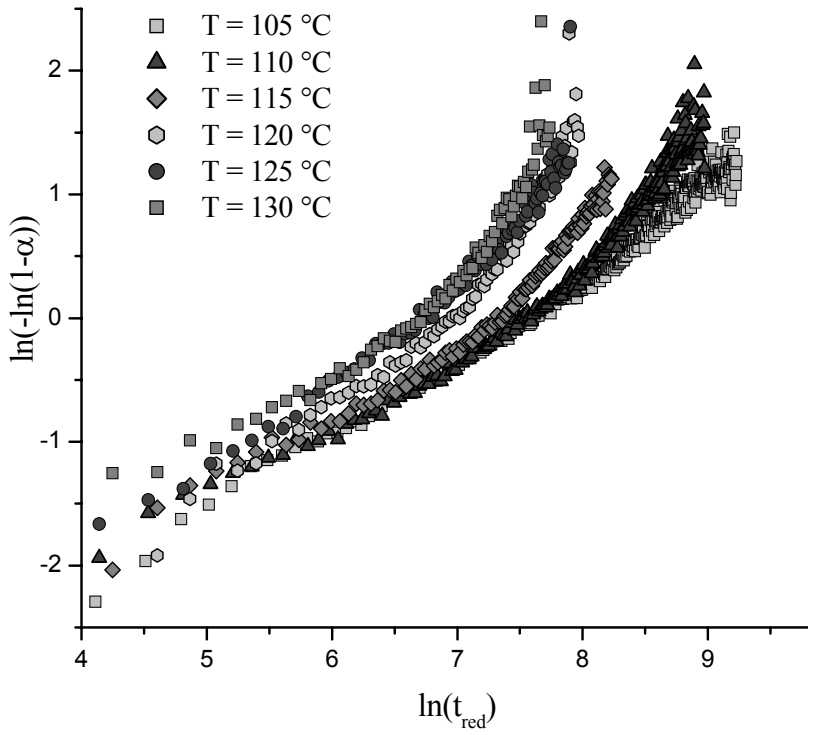
T = 105 °C
T = 110 °C
T = 115 °C
T = 120 °C
T = 125 °C
T = 130 °C
ln(-ln(1-α))
ln(t_red)

Fig.9

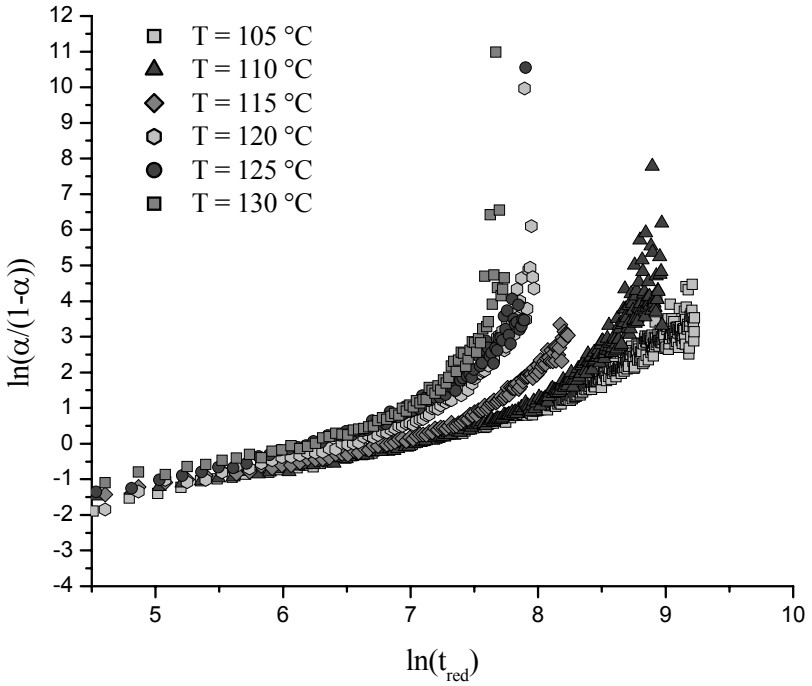
T = 105 °C
T = 110 °C
T = 115 °C
T = 120 °C
T = 125 °C
T = 130 °C
ln(α/(1-α))
ln(t_red)

Fig.10

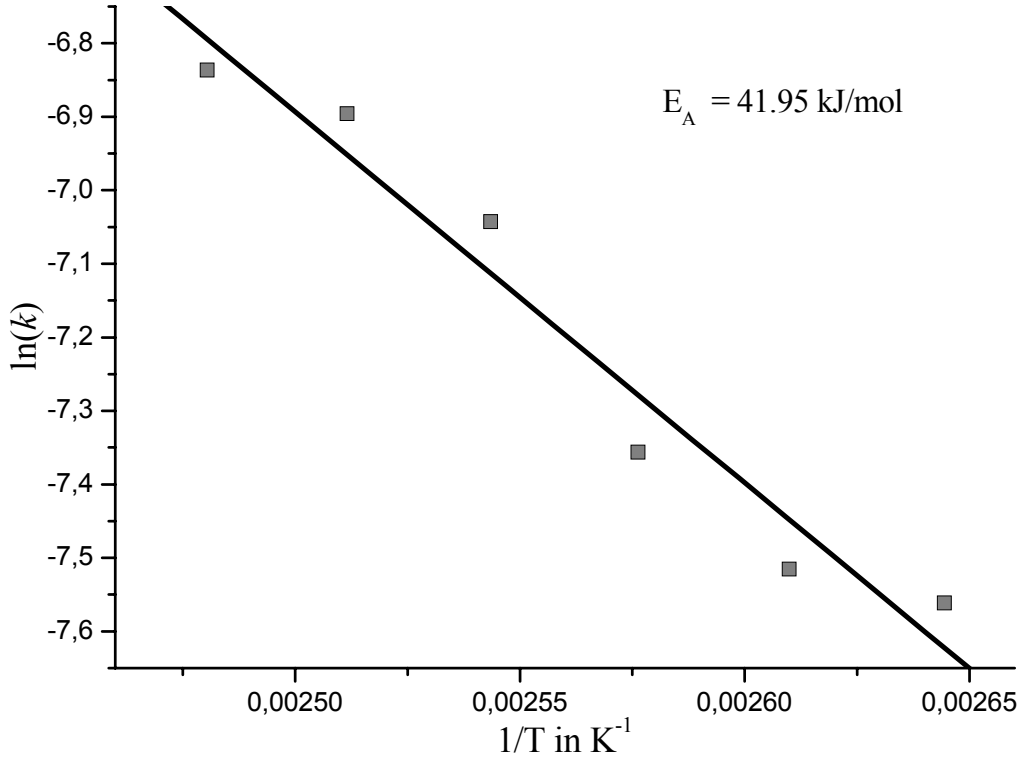
E_A = 41.95 kJ/mol
ln(k)
-6,8
-6,9
-7,0
-7,1
-7,2
-7,3
-7,4
-7,5
-7,6
0,00250
0,00255
0,00260
0,00265
1/T in K^-1

Fig.11

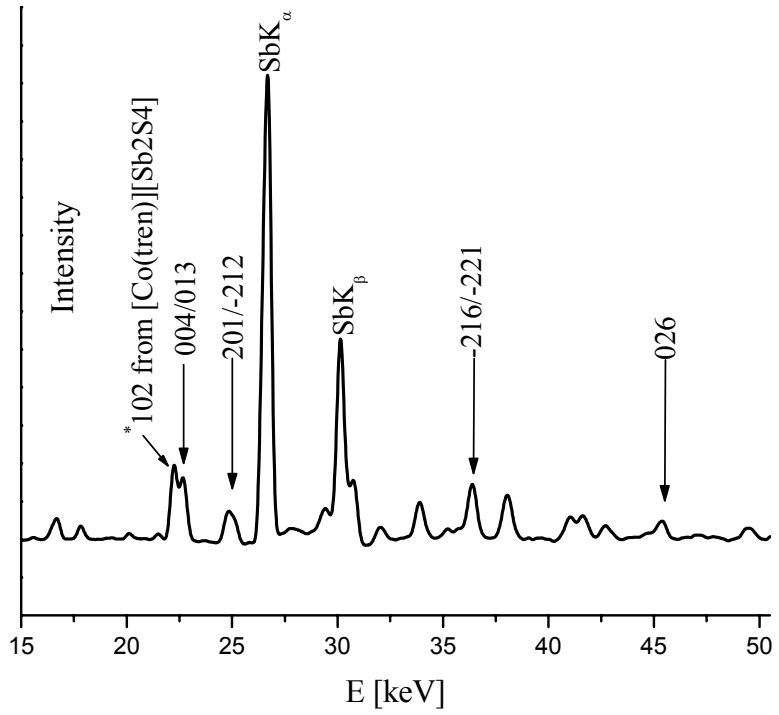
Intensity
*102 from [Co(tren)][Sb2S4]
004/013
201/-212
SbK_α
SbK_β
216/-221
026
15
20
25
30
35
40
45
50
E [keV]

Fig.12

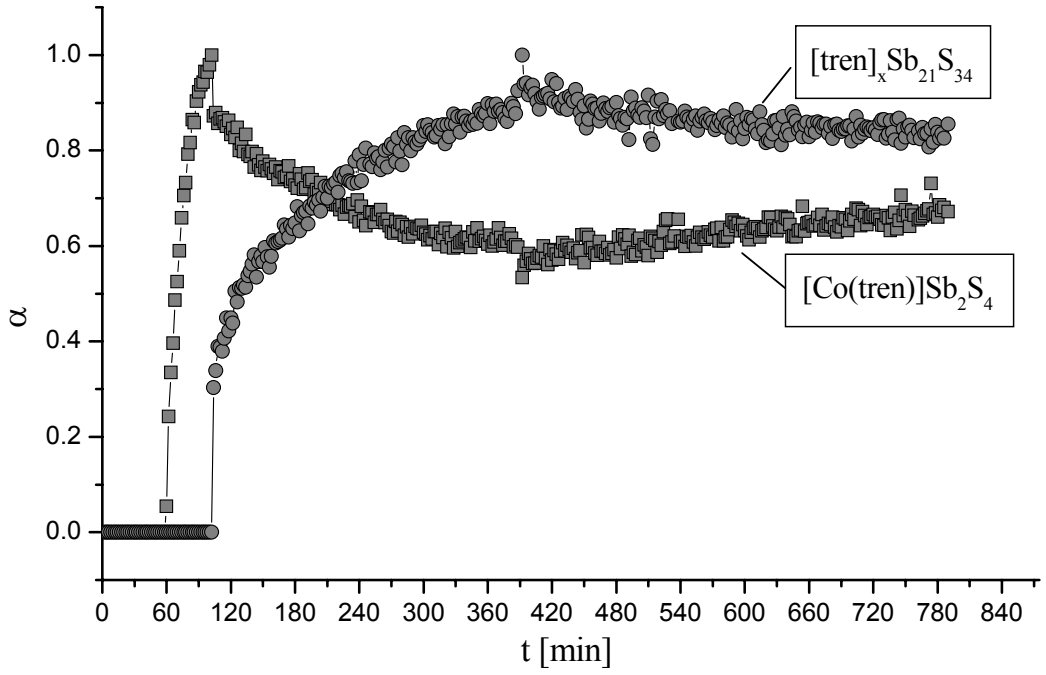
1.0
0.8
0.6
0.4
0.2
0.0
α
0
60
120
180
240
300
360
420
480
540
600
660
720
780
840
t [min]
[tren]$_x$Sb$_{21}$S$_{34}$
[Co(tren)]Sb$_2$S$_4$

Fig.13

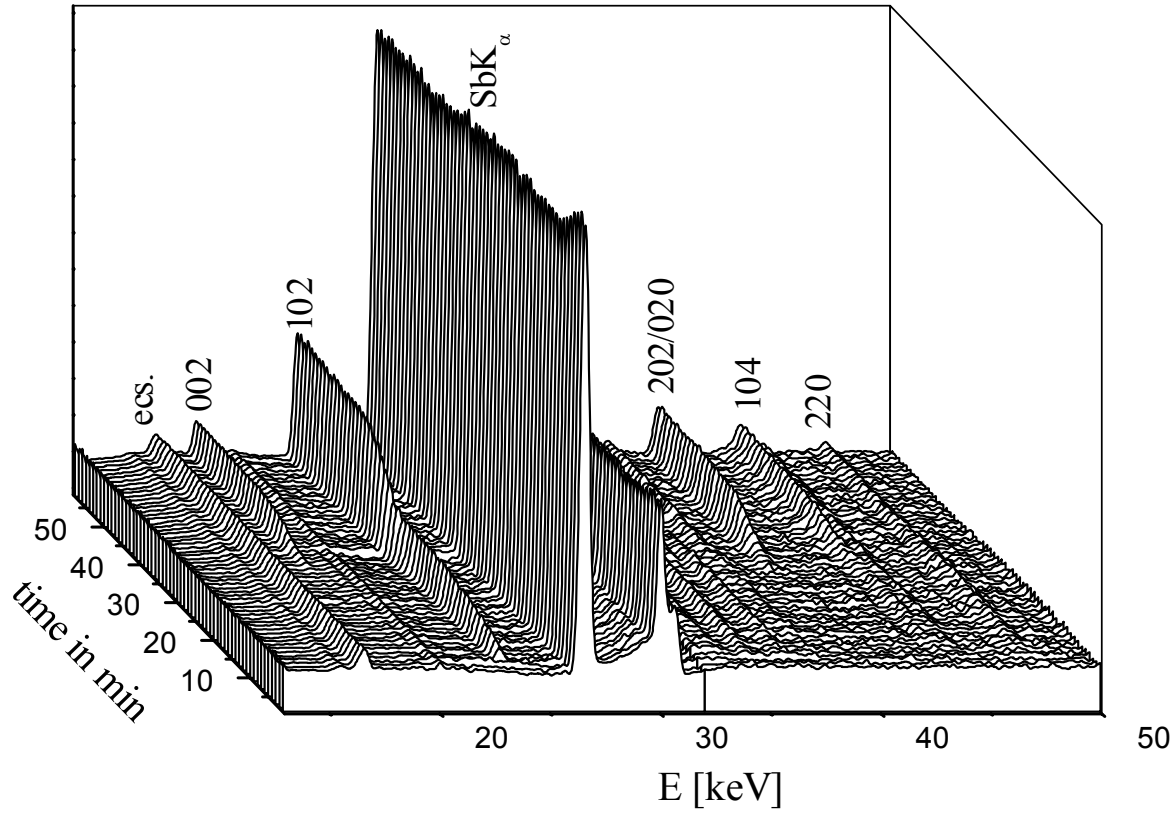
SbK$_\alpha$
ecs.
002
102
202/020
104
220
50
40
30
20
10
time in min
20
30
40
50
E [keV]

Fig.14

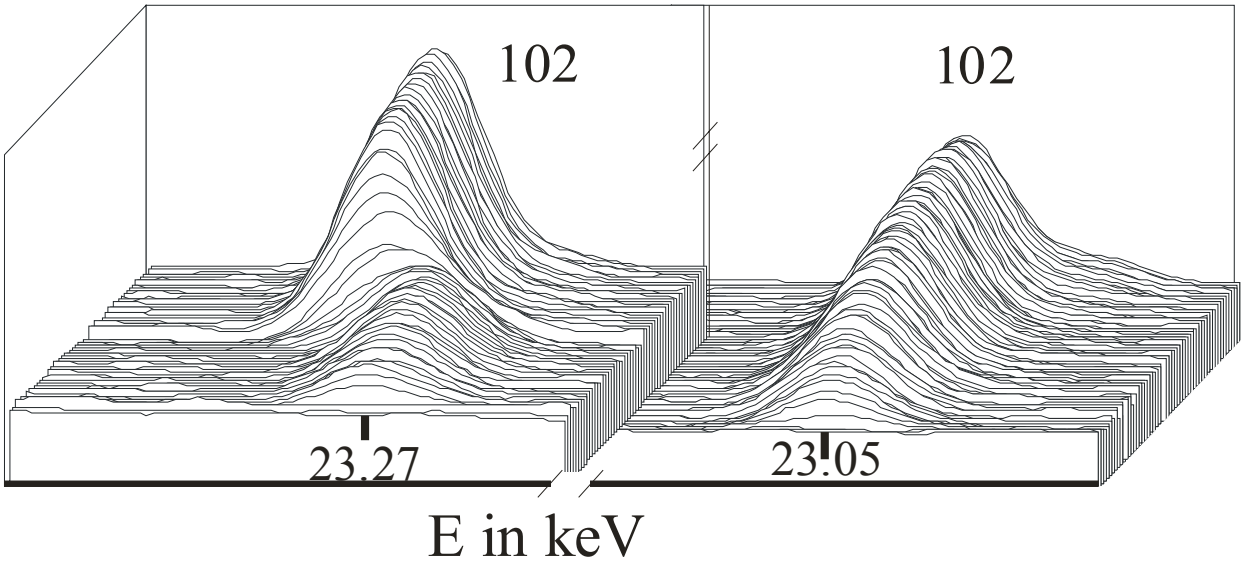
102
102
23.27
23.05
E in keV

Fig.15

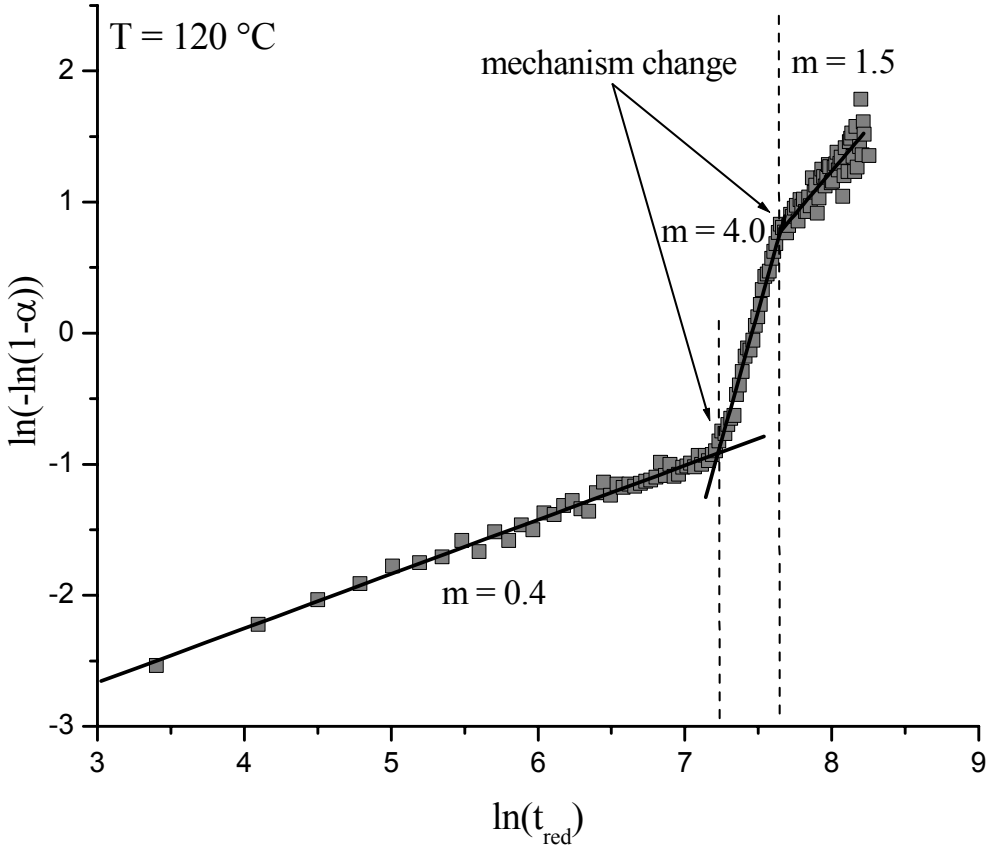
T = 120 °C
mechanism change
m = 1.5
m = 4.0
m = 0.4
ln(-ln(1-α))
ln(t_red)
2
1
0
-1
-2
-3
3
4
5
6
7
8
9

Fig.16

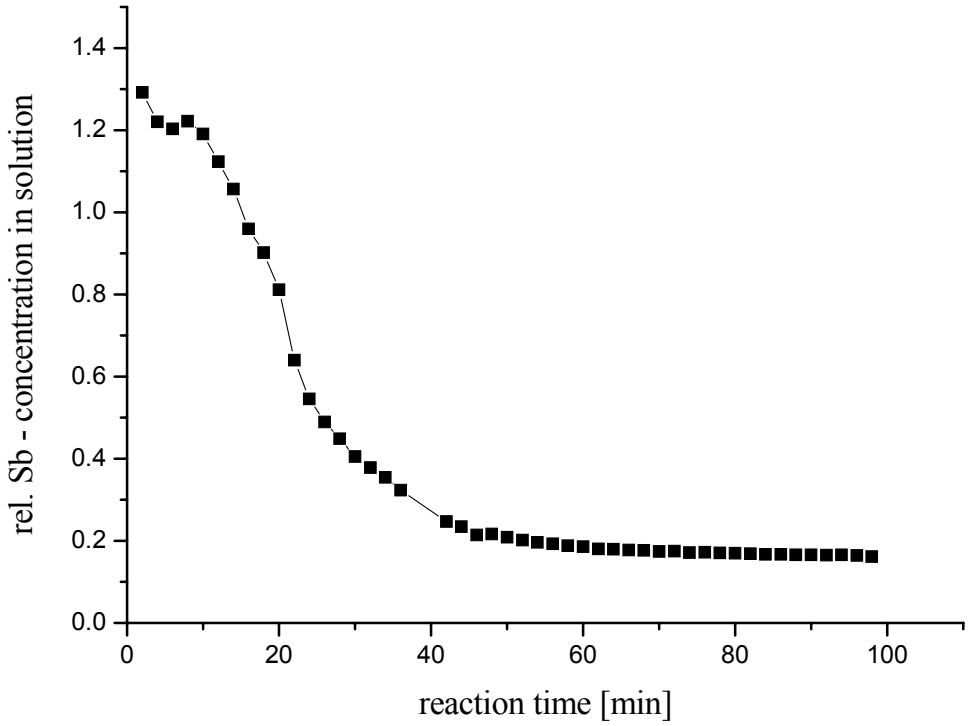
rel. Sb - concentration in solution
reaction time [min]
0.0
0.2
0.4
0.6
0.8
1.0
1.2
1.4
0
20
40
60
80
100

Fig.17

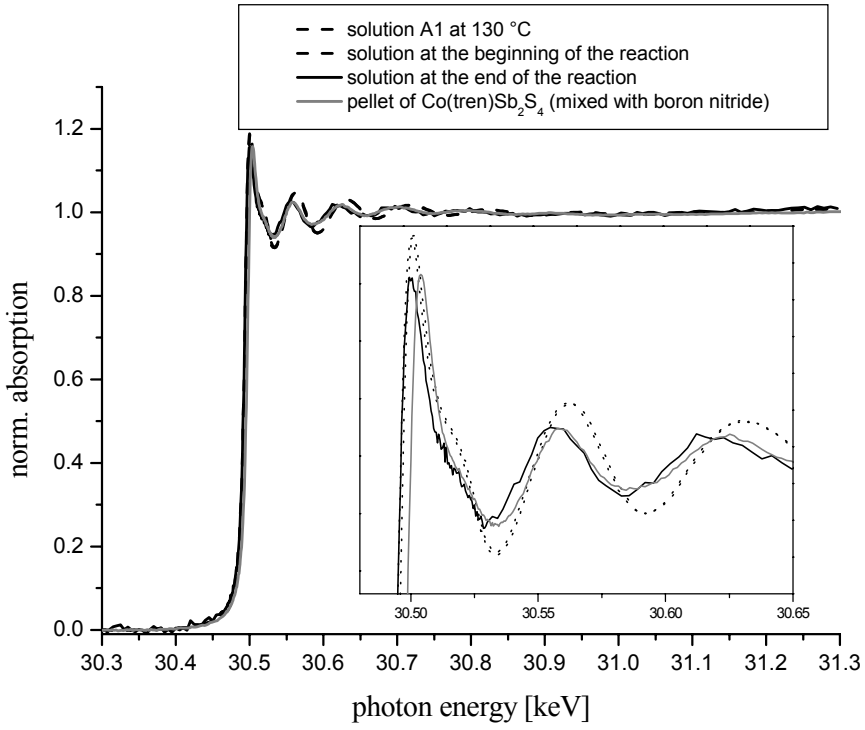
solution A1 at 130 °C
solution at the beginning of the reaction
solution at the end of the reaction
pellet of Co(tren)Sb2S4 (mixed with boron nitride)
norm. absorption
photon energy [keV]
0.0
0.2
0.4
0.6
0.8
1.0
1.2
30.3
30.4
30.5
30.6
30.7
30.8
30.9
31.0
31.1
31.2
31.3
30.50
30.55
30.60
30.65

Fig.18

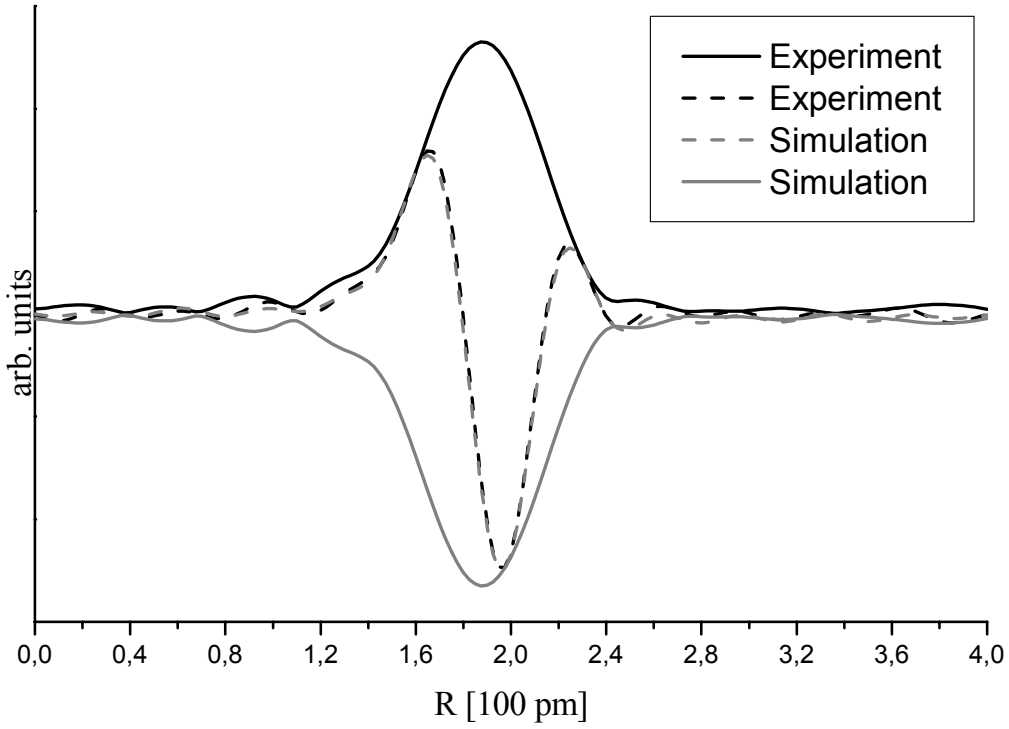
Experiment
Experiment
Simulation
Simulation
arb. units
0,0
0,4
0,8
1,2
1,6
2,0
2,4
2,8
3,2
3,6
4,0
R [100 pm]

Fig.19

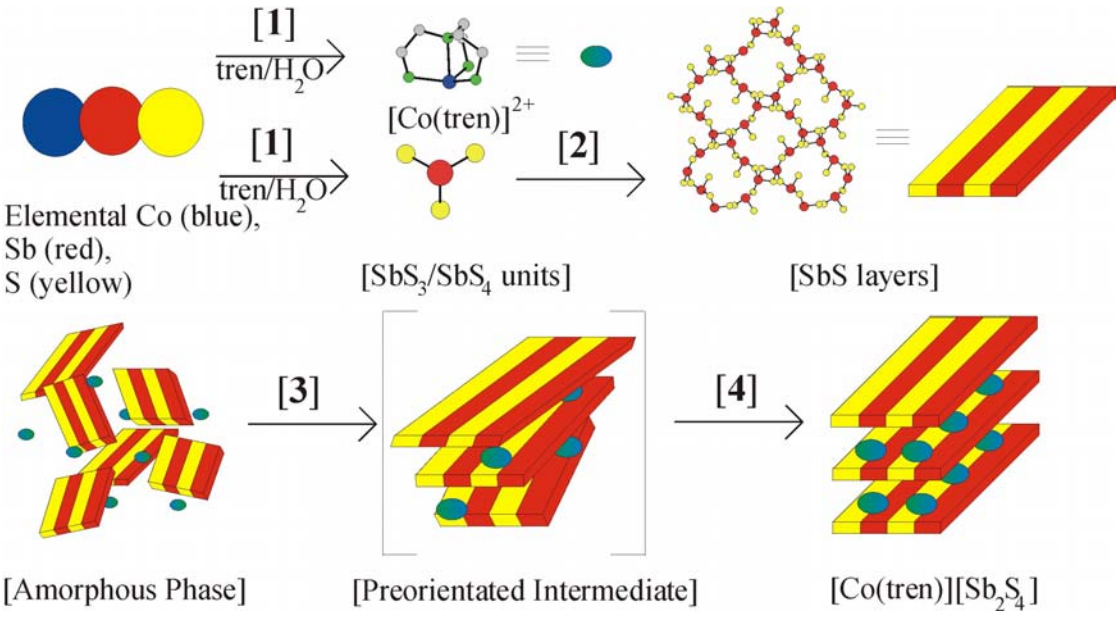
[1]
tren/H2O
[1]
tren/H2O
[Co(tren)]2+
[2]
Elemental Co (blue),
Sb (red),
S (yellow)
[SbS3/SbS4 units]
[SbS layers]
[3]
[4]
[Amorphous Phase]
[Preorientated Intermediate]
[Co(tren)][Sb2S4]

Fig. 20

4.6 Ergebnisse und Publikationen aus internationalen Kooperationen

4.6.1 Die Verbindung $Na_{\frac{2}{3}}Ce_{\frac{1}{2}}TiO_3$

Zusammenfassung der Veröffentlichung „*Solvothermal synthesis and Rietveld structure analysis of two new sodium rare earth titanates* $Na_{\frac{1}{2}}Y_{\frac{1}{2}}TiO3$ *and* $Na_{\frac{2}{3}}Ce_{\frac{1}{2}}TiO_3$“

Von den beiden Verbindungen wird an dieser Stelle nur die Verbindung $Na_{\frac{2}{3}}Ce_{\frac{1}{2}}TiO_3$ diskutiert. Die Darstellung und Charakterisierung erfolgte während eines Forschungsaufenthaltes am Jean Rouxel-Faculte des Sciences de Nantes.

Die Synthese erfolgte unter solvothermalen Bedingungen bei 170 °C. Als Edukte wurden 0.8 mmol $Ce(NO_3)_3{\cdot}6H_2O$, 2 ml (2.4 mmol) 1.2 M $Ti[OCH(CH_3)_2]_4$-Lösung in Ethanol und 5 ml 10 M NaOH-Lösung verwendet. Nach 2 Tagen kristallisierte $Na_{\frac{2}{3}}Ce_{\frac{1}{2}}TiO_3$ in Form eines gelb-grünen Pulvers (Abb. 4.14, links).

Die Strukturverfeinerung wurde mit Röntgenpulverdaten mit der Rietveldmethode durchgeführt. Als Startmodell wurde die Struktur der Verbindung $Na_{0.632}Ce_{0.368}Ti_{0.912}Nb_{0.088}O_3$ verwendet. Die Verbindung kristallisiert in der tetragonalen Raumgruppe $I4/mcm$. Die Na^+/Ce^{4+}-Kationen teilen sich eine kristallographische Lage und sind jeweils von 12 Sauerstoffatomen umgeben (Abb. 4.14, rechts). Das Na:Ce-Verhältnis von 1:2 ergibt sich aus Überlegungen zur Ladungsneutralität. Für die Annahme von Ti^{4+} und Ce^{4+} (Ce^{4+} experimentell durch Magnetmessungen bestätigt) kann einVerhältnis von 1:1 wie in der yttriumhaltigen Verbindung ausgeschlossen werden. Experimentell wurde das Na:Ce-Verhältnis von 2:1 durch EDX-Messungen und durch die Verfeinerung der Besetzungsfaktoren in der Rietveldanalyse bestätigt.

Interessant ist das Auftreten von vierwertigem Cer in der Verbindung. Die bisher synthetisch dargestellten Verbindungen mit vergleichbarer Zusammensetzung enthalten in aller Regel Ce^{3+}. Durch die solvothermale Synthese als Präpärationsmethode könnten sich hier weitere interessante Verbindungen synthetisieren lassen, die durch die klassische Hochtemperatursynthese nicht zugänglich sind.

Die dargestellte Verbindung ist Ausgangsverbindung zur Darstellung von Sulfooxiden. Hier erfolgt eine Umsetzung von $Na_{\frac{2}{3}}Ce_{\frac{1}{2}}TiO_3$ im H_2S-Strom bei Temperaturen

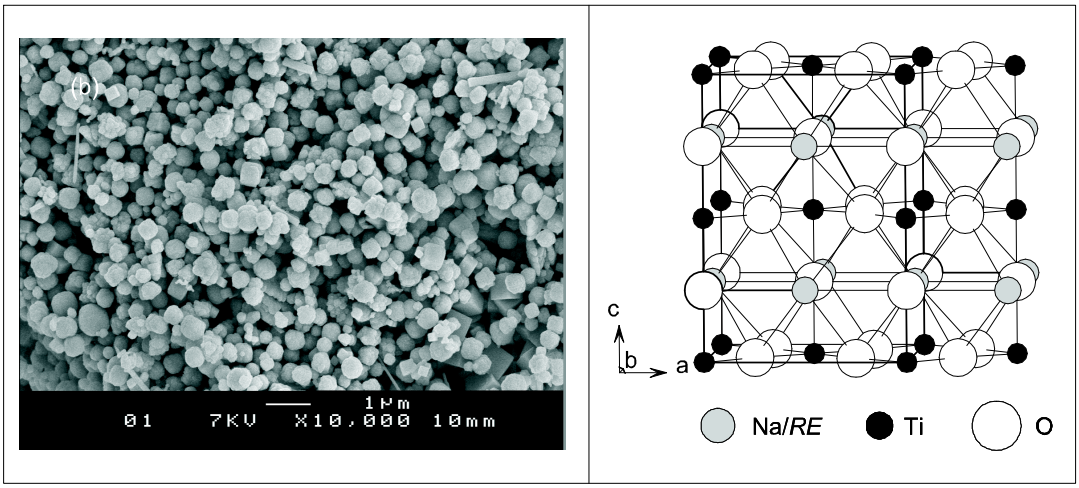

Abbildung 4.14: REM-Aufnahme der Verbindung $Na_{\frac{2}{3}}Ce_{\frac{1}{2}}TiO_3$ (links), Kristallstruktur der Verbindung $Na_{\frac{2}{3}}Ce_{\frac{1}{2}}TiO_3$ (rechts)

um 800 °C.

Die magnetischen Suszeptibilitätsdaten konnten mit einem Curie-Weiss-Gesetz angefittet werden. Der erhaltene Wert für die Curie-Weiss-Konstante von $2.3{\cdot}10^{-3}$ emuKmol^{-1} ist deutlich zu klein für Ce^{3+} (0.81 emuKmol^{-1}), so dass die Anwesenheit von Ce^{3+} in größeren Mengen ausgeschlossen werden kann.

Die optische Bandlücke der Verbindung wurde mit der Methode von Kubelka-Munk zu 2.6 eV bestimmt.

Solvothermal synthesis and Rietveld structure analysis of two new sodium rare earth titanates $Na_{1/2}Y_{1/2}TiO_3$ and $Na_{2/3}Ce_{1/3}TiO_3$

A. Lafond[(1)], I. Sandu[(1)], C. Guillot-Deudon[(1)], R. Kiebach[(2)] , W. Bensch[(2)] and A. Meerschaut[(1)]

[(1)] Institut des Matériaux Jean Rouxel, UMR 6502 CNRS-Université de Nantes, 2, rue de la Houssinière, BP 32229, 44322 Nantes cedex 03, France

[(2)] Institut für Anorganische Chemie, Universität Kiel Olshausenstr. 40, 24098 Kiel, Germany

Corresponding author : Alain.Lafond@cnrs-imn.fr

Abstract

Two new sodium rare-earth titanates $Na_{1/2}Y_{1/2}TiO_3$ and $Na_{2/3}Ce_{1/3}TiO_3$ have been synthesized via a solvothermal route. The structures have been refined by the Rietveld method. The yttrium derivative adopts the same orthorhombic structure (S.G. *Pnma*, a = 5.4172(10) Å; b = 7.6177(12) Å and c = 5.3478(10) Å) as $Na_{1/2}RE_{1/2}TiO_3$ with RE^{3+} (*RE* = La - Lu). On the other hand, both the magnetic susceptibility measurements and the Rietveld structure refinement support the presence of Ce^{4+} ions in the cerium compound with the formula $Na_{2/3}Ce_{1/3}TiO_3$ (S.G. *I4/mcm, no. 140*, a = 5.3997(8) Å; c = 7.630(2) Å). The structure of this compound is closely related to that of the natural Ce-loparite.

Keywords

Rare earth sodium titanate, solvothermal synthesis, Rietveld refinement, cerium, yttrium.

Introduction

In recent years, crystal chemistry investigations of the quaternary rare earth titanium oxychalcogenide compounds have revealed a large variety of new structural types **[1,2]**. Most of these new structures contain structural fragments which can be considered as primary building units **[3]**. In a few cases, these fragments are infinite so that the compounds can be viewed as layered materials. It is well known that such a situation can give interesting physical properties **[4 ,5]**.

Most of the known rare earth titanium oxychalcogenide compounds have been prepared through a high temperature solid state route (typically at 1000°C) starting from a mixture of the corresponding binary oxides and sulfides. Because we are interested in the potential photocatalytic

properties of these materials, we investigated a softer synthetic route which is a two-step process. During the first step, a mixed rare earth titanium oxide is prepared by a solvothermal route. The oxide precursor is then heated under a H_2S/Ar gas flow for a short time (c.a. 2 h) at a moderate temperature (600-800°C). This method is similar to that used by Ishikawa et al. for $Sm_2Ti_2S_2O_5$ **[6]**. Our paper relates to the crystal chemistry description of two new (Na, *RE*)-titanates (*RE* = Y and Ce) which have been prepared during the first step of this synthetic route. These two new compounds belong to the sodium rare earth titanate series **[7-10]**.

Experimental

Solvothermal synthesis

The title compounds have been prepared through the solvothermal reaction described by Ding *et al.* **[11]** starting with the corresponding rare earth nitrate and an alcoholic solution of titanium isopropoxide in a high concentrated sodium hydroxide solution (10 M). Table I shows the details of the synthesis conditions. The starting materials were put into a 30 mL Teflon-lined stainless steel autoclave and then heated at 170°C for 48 h for the cerium derivative and for 72 h for the yttrium derivative respectively. The precipitate was collected and washed with distilled water and acetone. The product was dried under vacuum at room temperature for 2 h. The yttrium derivative is white while the cerium compound is yellow.

X-ray diffraction

The X-ray diffraction analyses have been performed with a Bruker D5000 diffractometer (CuK_α) with the Bragg-Brentano geometry equipped with an energy resolved detector (Moxtek). Table II summarizes the data collection conditions. The cell parameters and the crystal structure refinements were performed by the Rietveld method **[12,13]** using the programs FullProf **[14]** and WinPlotr **[15]**. The background was fitted by a linear interpolation between selected points. The March-Dollase model for preferred orientation was used in all the refinements. The pseudo-Voigt function was applied as the peak-shape model.

Magnetic susceptibility measurements

The magnetic properties of the cerium derivative were studied with a Quantum Design magnetometer. The magnetic moment of the sample (95.07 mg) was measured in the temperature

range 5-300 K under a magnetic field of 0.10 T. The raw data were corrected for both the diamagnetic contribution of the sample holder and the diamagnetic core contribution.

Diffuse reflectance measurements

The UV–visible diffuse reflectance spectrum of the cerium compound was recorded with a Perkin-Elmer Lambda 900 spectrometer with a 0.1 nm resolution. These measurements have been done with the Praying Mantis Diffuse Reflection setup within the 200–800 nm range (6.19-1.55 eV). The absorption K/S data were calculated from the reflectance spectra using the $K/S = (1-R)^2/2R$ Kubelka-Munk function **[16,17]** where $R(\lambda)$, $K(\lambda)$ and $S(\lambda)$ are the reflectance, the absorption coefficient and the scattering coefficient, respectively.

Results and discussion

Chemical analyses with EDX (energy dispersive X-ray spectroscopy) show that both samples contain Na/*RE*/Ti/O. The scanning electron microscopy images (SEM) reveal that the powder samples consist of small cubic grains with a size around 1 μm for the yttrium compound and around 0.25 μm for the cerium derivative (Figure 1).

The magnetic susceptibility of $Na_{2/3}Ce_{1/3}TiO_3$ as a function of the temperature is plotted in Figure 2. At low temperatures a small increase of the susceptibility is observed but this magnetic behavior demonstrates that the compound does not contain Ce^{3+} cations. Indeed, the data were fitted with a modified Curie-Weiss law $(C/(T-\theta) + \chi_o)$. The obtained Curie constant ($2.3.10^{-3}$ emu.K.mol^{-1}) is very small compared to that expected for Ce^{3+} (0.81 emu.K.mol^{-1}) indicating the presence of paramagnetic impurities, but the main phase contains only Ce^{4+} cations. The temperature independent paramagnetism term χ_o is of the same order as that encountered in other Ce(IV) compounds **[18]**.

The optical band gap E_g of $Na_{2/3}Ce_{1/3}TiO_3$ was determined as the intersection point between the energy axis and the line extrapolated from the linear portion of the absorption edge in the K/S versus E(eV) curve (see Figure 3). The value for E_g of 2.6 eV is in agreement with the yellow color of this compound.

Rietveld analyses

The structure of $Na_{1/2}Dy_{1/2}TiO_3$ **[8]** was used as a starting structural model (space group *Pnma*) for the Rietveld refinement of $Na_{1/2}Y_{1/2}TiO_3$. The result demonstrates that the structure of $Na_{1/2}Y_{1/2}TiO_3$ is very similar to that of $Na_{1/2}Dy_{1/2}TiO_3$. This is expected because Y and Dy have the same oxidation state, namely Y^{3+} and Dy^{3+}, and very close cationic radii, 107.5 pm and 108.3 pm respectively for a 9-fold coordination **[19]**. The refined unit cell parameters are: a = 5.4171(10) Å; b = 7.6176(12) Å; c = 5.3477(10) Å. The structural parameters, the agreement factors and the main interatomic distances are gathered in Tables III and IV. Figure 4a shows the observed and calculated X-ray powder patterns.

The sodium cerium titanate ($Na_{1/2}Ce_{1/2}TiO_3$) is known either as a member of the natural mineral family loparite or as a synthetic compound. The latter one was synthesized by high temperature reaction under reductive conditions leading to the formation of Ce^{3+} **[10]**. Both compounds $Na_{1/2}Ce_{1/2}TiO_3$ and $Na_{1/2}Dy_{1/2}TiO_3$ are isostructural; the cell parameters are a = 5.4517(4) Å, b = 7.7058(9) Å and c = 5.4333(6) Å (V = 228.3 $Å^3$) for the former compound. The Rietveld analysis of the cerium compound prepared via the solvothermal route has been performed starting from the structure of $Na_{1/2}Ce_{1/2}TiO_3$. In the first steps of the refinement it appears that the *a* and *c* cell parameters converged to very close values. In addition, we noticed that the refinement of the whole structural model in space group *Pnma* was not possible due to the instability of the atomic position parameters of Na/Ce and O1. Therefore, we decided to refine the structure with the tetragonal structural model of an other natural cerium-loparite $Na_{0.632}Ce_{0.368}Ti_{0.912}Nb_{0.088}O_3$, which crystallizes in space group *I*4/*mcm* **[20]**. The refinement converged within a few cycles leading to quite good agreement factors (R_p = 9.36 %, χ^2 = 1.86 and R_{Bragg} = 5.65 %) without any instability. The magnetic susceptibility behavior excludes the presence of Ce^{3+} in this compound and, assuming the presence of Ti^{4+}, the charge balance cannot be achieved with a 1:1 Na/Ce molar ratio. Thus, the site occupancy factors (s.o.f.) of Na and Ce atoms have been refined. Because these atoms share the same crystallographic site, the individual occupancies have been constrained according to s.o.f.(Na) + s.o.f.(Ce) = 1. The agreement factors decreased (R_p = 9.03 %, χ^2 = 1.80 and R_{Bragg} = 4.50 %) and the obtained s.o.f's are very close to 2/3 and 1/3. In addition, the formerly negative isotropic atomic displacement parameter for Ti (B_{iso} = -1.11(15) $Å^2$) became now positive (B_{iso} = 0.2(2) $Å^2$)

changing the 1:1 ratio to 0.67:/0.33 for Na : Ce. One can definitely conclude that the chemical formulation of our sodium cerium titanate is $Na_{2/3}Ce_{1/3}TiO_3$. The results of the final refinement and the main atomic distances are given in Tables V and VI. The result of the Rietveld refinement is displayed in Figure 4b.

The structures of $Na_{1/2}Y_{1/2}TiO_3$ and $Na_{2/3}Ce_{1/3}TiO_3$ are shown in Figure 5. It is obvious that both structures are closely related. The Na/*RE* atoms are in an irregular twelve-fold oxygen environment with bond distances ranging from 2.30 Å to 3.13 Å (average: 2.71 Å) and from 2.58 Å to 2.82 Å (average: 2.70 Å) for the yttrium and the cerium derivative, respectively. Interestingly, the (Na/Ce)-O bond lengths scatter in a significantly smaller range, i.e. the difference between the longest and shortest bond amounts to 0.24 Å whereas for the Y compound this value is 0.83 Å. In both compounds the average (Na/*RE*)-O distances are larger than the expected for a pure ionic model.

Discussion

This study shows that the structure of $Na_{1/2}Y_{1/2}TiO_3$ prepared through the solvothermal route is isostructural to the $Na_{1/2}RE_{1/2}TiO_3$ family. The cell parameters agree well with the variation of the RE^{3+} radius along the rare earth element series. It appears that the solvothermal route in sodium hydroxide solution is a good way to prepare mono-dispersed micrometer-sized particles of $Na_{1/2}Y_{1/2}TiO_3$. This synthetic approach will probably work with most of the lanthanide elements. It should be noted that in case of La^{3+}, this method leads to sodium-free lanthanum titanate, $La_{2/3}TiO_3$ **[11]**.

The sodium yttrium titanate $Na_{1/2}Y_{1/2}TiO_3$ adopts a structure close to that of sodium free yttrium titanate $YTiO_3$ **[21,22]** with a smaller unit cell volume, $V(Na_{1/2}Y_{1/2}TiO_3) = 220.67$ Å^3 and $V(YTiO_3) = 230.95$ Å^3. The shrinkage of the unit cell when Y is replaced by $(Na_{0.5}Y_{0.5})$ is consistent with the lowering of the Ti-O bond distances from 2.02-2.08 Å in $YTiO_3$ to 1.91-1.95 Å in $Na_{1/2}Y_{1/2}TiO_3$, and the increase of the calculated bond valence sum of Ti from 3.05 in $YTiO_3$ to 4.28 in $Na_{1/2}Y_{1/2}TiO_3$. The charge balances in the two titanate compounds are achieved with Ti^{3+} in $YTiO_3$ and Ti^{4+} in $Na_{1/2}Y_{1/2}TiO_3$.

Applying the solvothermal method, a new sodium cerium titanate has been prepared. The Rietveld refinement results suggest that the chemical composition of this compound is

$Na_{2/3}Ce_{1/3}TiO_3$ for which the charge balance has to be formulated as $(Na^+)_{2/3}(Ce^{4+})_{1/3}(Ti^{4+})(O^{2-})_3$. The proposed oxidation state of Ce agrees perfectly with the results of the magnetic measurement. The presence of Ce^{4+} in this compound is also supported by the shrinkage of the unit cell volume compared to that of $Na_{1/2}Ce_{1/2}TiO_3$, from 228.3 $Å^3$ to 222.5 $Å^3$ in good agreement with the evolution of cationic radii for Ce^{3+} of 134 pm and for Ce^{4+} of 114 pm for a 12-fold coordination. The strong oxidizing conditions during the solvothermal synthesis process is probably responsible of the high oxidation state of cerium in $Na_{2/3}Ce_{1/3}TiO_3$. It is worth noting that in the natural parent compound $Na_{0.632}Ce_{0.368}Ti_{0.912}Nb_{0.088}O_3$, the charge balance is achieved if one considers that a part (50%) of the cerium is Ce^{4+}.

Conclusion

Two new sodium rare earth titanates have been prepared through a solvothermal method. The structures of these compounds are related to the perovskite structure with small distortions due to the distribution of two cations, namely Na and *RE*, on the same atomic site. The chemical composition of $Na_{2/3}Ce_{1/3}TiO_3$, is different from those of the other sodium rare earth titanates, with general composition $Na_{1/2}RE_{1/2}TiO_3$, because cerium adopts the +IV oxidation state beside the +III common oxidation state for the rare earth elements. On the other hand, the compound $Na_{2/3}Ce_{1/3}TiO_3$ is isostructural to the natural Ce-loparite whith a tetragonal symmetry.

Acknowledgement

Authors would like to thank Alain Barreau for his technical assistance for the SEM images.

References

1 M. Goga, R. Seshadri, V. Ksenofontov, P. Gütlich and W. Tremel, *Chem. Commun.*, 979-980 (1999).

2 S. J. Clarke, S. G. Denis, O. J. Rutt, T. L. Hill, M. A. Hayward, G. Hyett and Z. A. Gal, *Chem. Mater.*, **15**(26), 5065-5072 (2003).

3 V. Meignen, L. Cario, A. Lafond, Y. Moëlo, C. Guillot-Deudon and A. Meerschaut, *J. Solid State Chem.*, **177**, 2810-2817 (2004).

4 S. Okada, M. Matoba, S. Fukumoto, S. Soyano, Y. Kamihara, T. Takeuchi, H. Yoshida, K. Ohoyoma and Y. Yamaguchi, *J. Appl. Phys.*, **91**(10), 8861-8863 (2002).

5 A. Ishikawa, T. Takata, J. N. Kondo, M. Hara, H. Kobayashi and K. Domen, *J. Am. Chem. Soc.*, **124**, 13547-13553 (2002).

6 A. Ishikawa, Y. Yamada, T. Takata, J. N. Kondo, M. Hara, H. Kobayashi and K. Domen, *Chem. Mater.*, **15**, 4442-4446 (2003).

7 S. Pai-Hsuan, T. Nakamura, Y. Shan, Y. Inaguma and M. Itoh, *Ferroelectrics*, **200**(1-4), 93-107 (1997).

8 Y. J. Shan, T. Nakamura, Y. Inaguma and M. Itoh, *Solid State Ionics*, **108**, 123-128 (1998).

9 W. F. Zhang, Z. Yin, M. S. Zhang and J. L. Fang, *J. Mater. Sci. Let.*, **18**, 813-815 (1999).

10 A. R. Chakhmouradian, R. H. Mitchell, A. V. Pankov and N. V. Chukanov, *Miner. Mag.*, **63**(4), 519-534 (1999).

11 Z. Ding, M. Zhang and J. Han, *Mater. Phys. Mech.*, **4**, 107-110 (2001).

12 H. M. Rietveld, *Acta Crist.*, **22**, 151 (1967).

13 H. M. Rietveld, *J. Appl. Cryst.*, **2**, 65 (1969).

14 J. Rodríguez-Carvajal, FullProf, http://www-llb.cea.fr/fullweb/fp2k/fp2k.htm, (2001)

15 T. Roisnel and J. Rodriguez-Carvajal, **378-381**(EPDIC 7, Part 1), 118-123 (2001).

16 P. Kubelka and F. Munck, *Z. Tech. Phys.*, **12**, 593-601 (1931).

17 P. Kubelka, *J. Opt. Soc. Am.*, **38**, 448-457 (1948).

18 Y. Prots, R. Niewa, W. Schnelle and R. Kniep, *Z. Anorg. Allg. Chem.*, **628**, 1590-1596 (2002).

19 R. D. Shannon, *Acta Cryst.*, **A32**, 751-767 (1976).

20 R. H. Mitchell, P. C. Burns and A. R. Chakhmouradian, *Can. Miner.*, **38**, 145-152 (2000).

21 J. R. Hester, K. Tomimoto, H. Noma, F. P. Okamura and J. Akimitsu, *Acta Cryst.*, **B53**, 739-744 (1997).

22 D. A. MacLean, H. N. Ng and J. E. Greedan, *J. Solid State Chem.*, **30**, 35-44 (1979).

23 J.-F. Bérar and P. Lelann, *J. Appl. Cryst.*, **24**, 1-5 (1991).

Tables

Table I: Composition of the starting mixture for solvothermal syntheses of $Na_{1/2}Y_{1/2}TiO_3$ and $Na_{2/3}Ce_{1/3}TiO_3$.

	$Na_{1/2}Y_{1/2}TiO_3$	$Na_{2/3}Ce_{1/3}TiO_3$
$Y(NO_3)_3,6H_2O$ or $Ce(NO_3)_3,6H_2O$	1.2 mmol	0.8 mmol
titanium isopropoxide ($Ti[OCH(CH_3)_2]_4$) Solution in absolute ethanol (1.2 M)	2.4 mmol (2 mL)	2.4 mmol (2 mL)
NaOH solution (10M)	5 mL	5 mL

Table II: Conditions of the powder X-ray diffraction analysis of $Na_{1/2}Y_{1/2}TiO_3$ and $Na_{2/3}Ce_{1/3}TiO_3$ ($\lambda(CuK\alpha)$=1.540598/1.54439 Å, T = 293 K)

	$Na_{1/2}Y_{1/2}TiO_3$	$Na_{2/3}Ce_{1/3}TiO_3$
2θ range	10-112°	5-100°
2θ step	0.03°	0.02°
Time per step	18 s	10 s

Table III: Atomic positions and isotropic displacement parameters for synthetic $Na_{1/2}Y_{1/2}TiO_3$ (S.G. *Pnma, no. 62*, a = 5.4171(10) Å; b = 7.6176(12) Å; c = 5.3477(10) Å).

Atom	Position	*x*	*y*	*z*	B_{iso} (Å^2)
Ti	*4b*	0	0	0	0.2(15)
Na/Y[(1)]	*4c*	0.472(10)	1/4	-0.005(2)	1.48(15)
O1	*4c*	0.510(5)	1/4	0.424(7)	1.6(3)[(2)]
O2	*8d*	0.280(4)	-0.037(3)	0.224(4)	1.6(3)[(2)]

(1) Both site occupancy factors of Na and Y have been fixed to 0.5.

(2) Atomic displacement parameters of O1 and O2 have been constrained to be equal.

Final agreement factors: R_p = 6.7 %, R_{wp} = 9.1 %, R_B = 3.8 %, χ^2 = 3.2

Table IV: Selected bond distances for $Na_{1/2}Y_{1/2}TiO_3$

Atom1	Atom2	multiplicity	distance (Å)
Ti	O2	2	1.92(2)
	O1	2	1.948(6)
	O2	2	1.95(2)
Na/Y	O1	1	2.30(4)
	O2	2	2.41(2)
	O1	1	2.54(3)
	O2	2	2.57(2)
	O2	2	2.71(2)
	O1	1	2.94(3)
	O1	1	3.06(4)
	O2	2	3.13(2)

Table V: Atomic positions and isotropic displacement parameters for $Na_{2/3}Ce_{1/3}TiO_3$ (S.G. *I4/mcm, no. 140*, a = 5.3997(8) Å; c = 7.630(2) Å).

Atom	Position	*x*	*y*	*z*	*s.o.f.*	B_{iso} (Å^2)
Ti	*4b*	0	0	0	1	0.2(2)
Na/Ce	*4c*	0	1/2	1/4	0.666(1)/0.334(1)	1.11(15)
O1	*4c*	0	0	1/4	1	4.0(3)[(1)]
O2	*8d*	0.272(3)	0.0772(3)	0	1	4.0(3)[(1)]

[(1)] Atomic displacement parameters of O1 and O2 have been constrained to be equal.

Final agreement factors: R_p = 9.0 %, R_{wp} = 14.5 %, R_B = 4.5 %, χ^2 = 1.8

Table VI: Selected bond distances for $Na_{2/3}Ce_{1/3}TiO_3$

Atom1	Atom2	multiplicity	distance (Å)
Ti	O1	2	1.90760(6)
	O2	4	1.92(2)
Na/Ce	O2	2	2.583(11)
	O1	4	2..69983(6)
	O2	4	2.820(11)

In all tables estimated standard deviations are taken into account applying local correlation according Berar and Lelann **[23]**.

Figures captions

Figure 1: Scanning electron microscopy images (SEM) of $Na_{1/2}Y_{1/2}TiO_3$ (a) and $Na_{2/3}Ce_{1/3}TiO_3$ (b).

Figure 2: Magnetic susceptibility of $Na_{2/3}Ce_{1/3}TiO_3$ versus T. The solid line corresponds to the fit of the data according to the modified Curie-Weiss law ($C/(T-\theta) + \chi_o$). The applied field was 0.1 T. The increase of the susceptibility at low temperature is due to the contribution of a small quantity of a paramagnetic impurity.

Figure 3: UV-vis diffuse reflectance spectrum for $Na_{2/3}Ce_{1/3}TiO_3$.

Figure 4: X-ray powder diffraction pattern of $Na_{1/2}Y_{1/2}TiO_3$ (a) and $Na_{2/3}Ce_{1/3}TiO_3$ (b). Rietveld profile and difference pattern. The refinement of $Na_{1/2}Y_{1/2}TiO_3$ also included a secondary phase Y_2O_3, present in about 4 wt.% (S.G. $Ia\bar{3}$; a = 10.598(3) Å). In the case of the Ce derivative, two impurities have been taken into account : CeO_2 (2.7 wt %, S.G. *Fm*-3*m* a = 5.4091(6) Å) and $Na_2Ti_6O_{13}$ (3.5 wt%, S.G. *C*2/*m* a = 15.107(8) Å, b = 3.7415(14) Å, c = 9.169(4) Å and β = 99.00(5)°). The contribution of the second impurity is within the background for $2\theta > 35°$ and the corresponding Bragg peaks have been removed.

Figure 5: Representation of structures of $Na_{1/2}Y_{1/2}TiO_3$ (a), S.G. *Pnma* and $Na_{2/3}Ce_{1/3}TiO_3$ (b), S.G. *I*4*/mcm*. The unit cells are represented by a bold line.

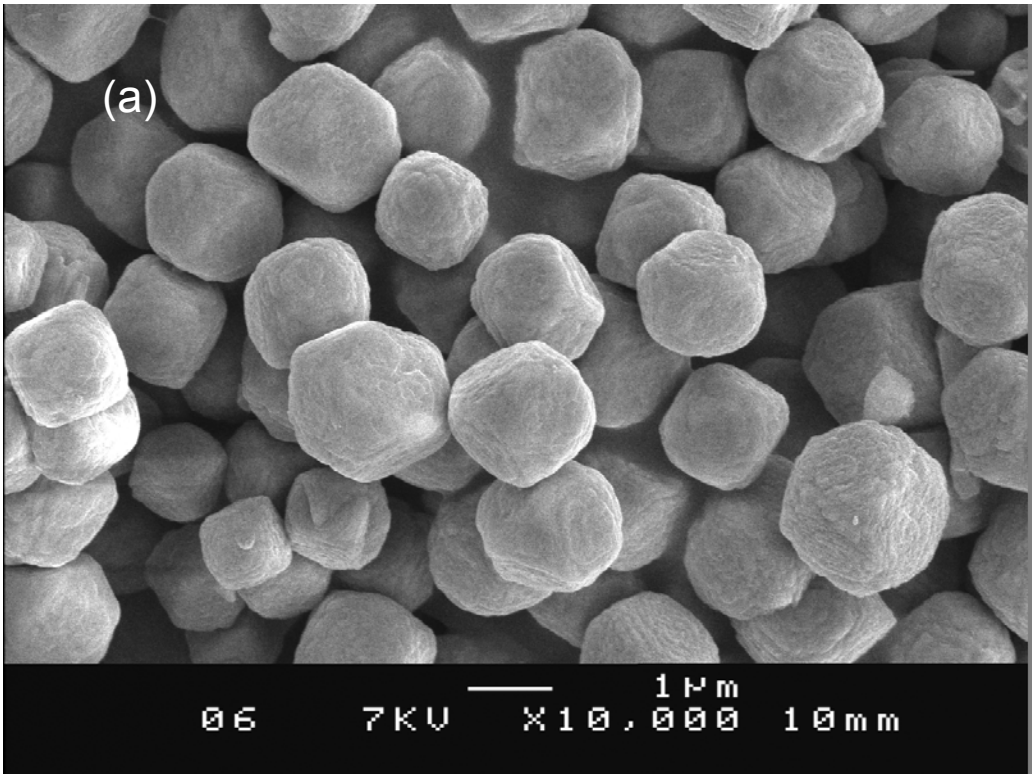

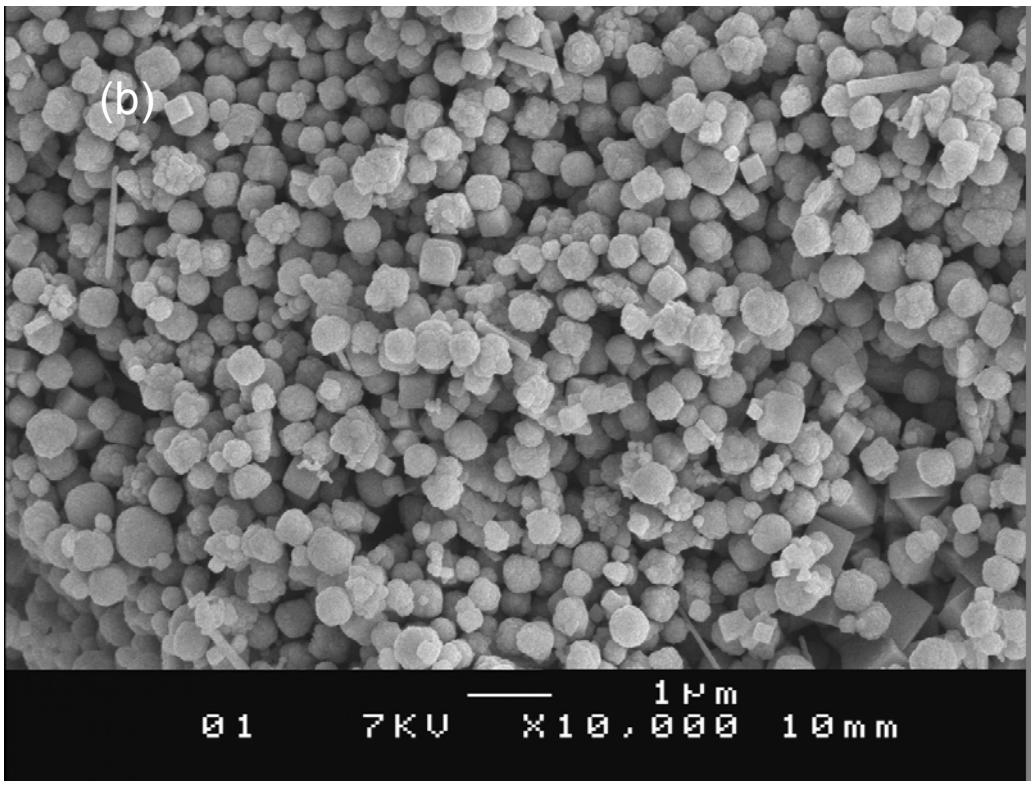

Lafond et al. Figures 1a & 1b

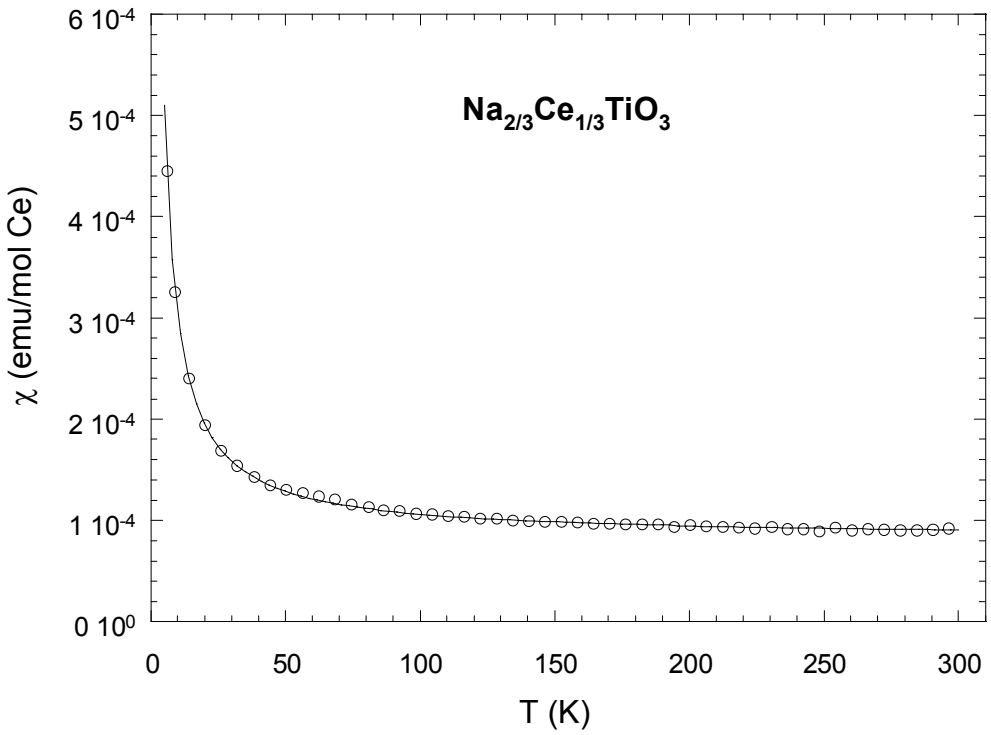

Lafond et al. Figure 2

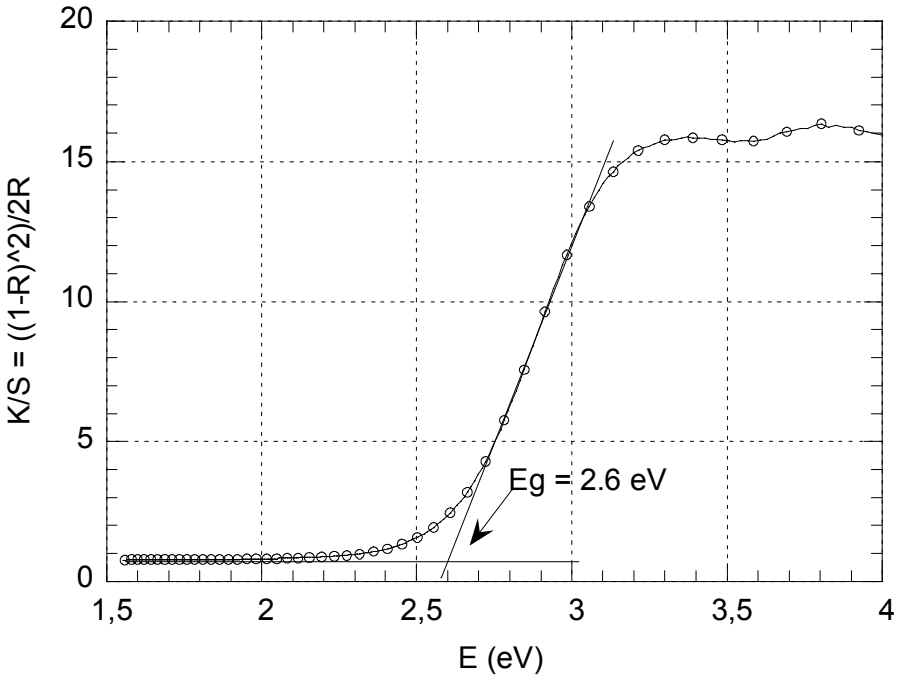

Lafond et al. Figure 3

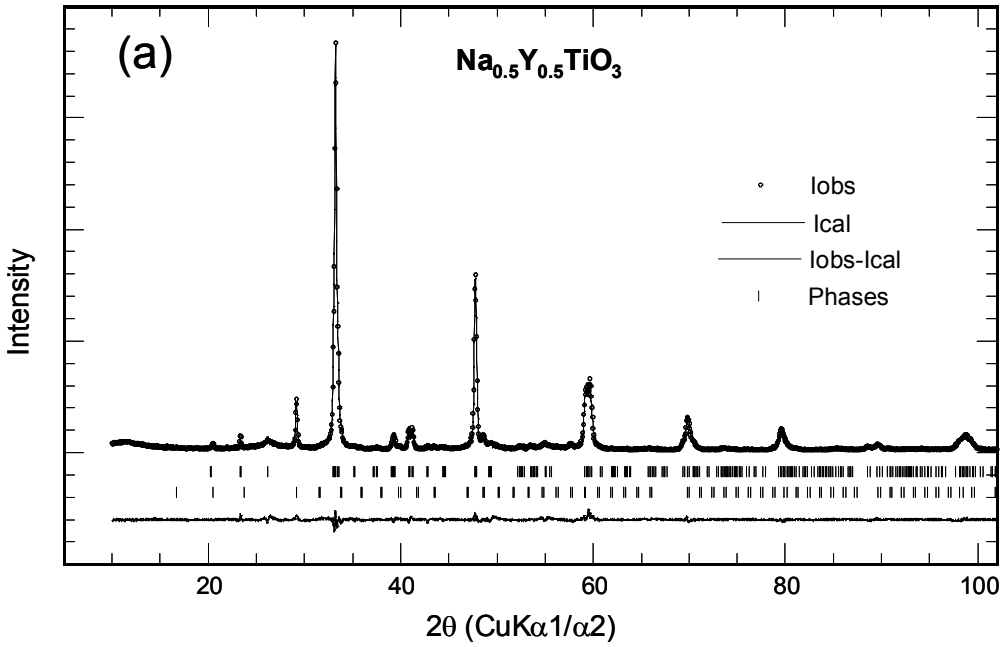

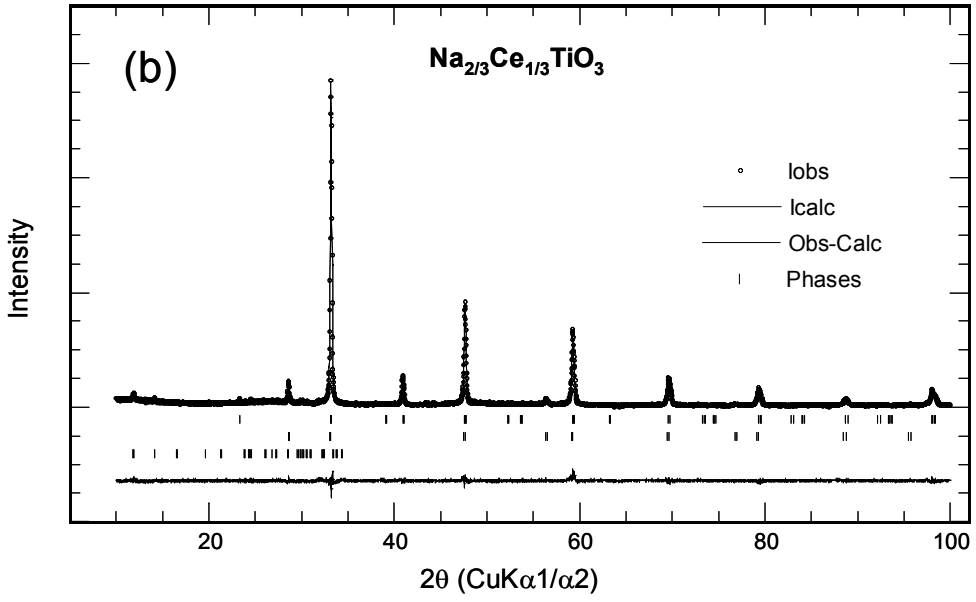

Lafond et al. Figures 4a & 4b

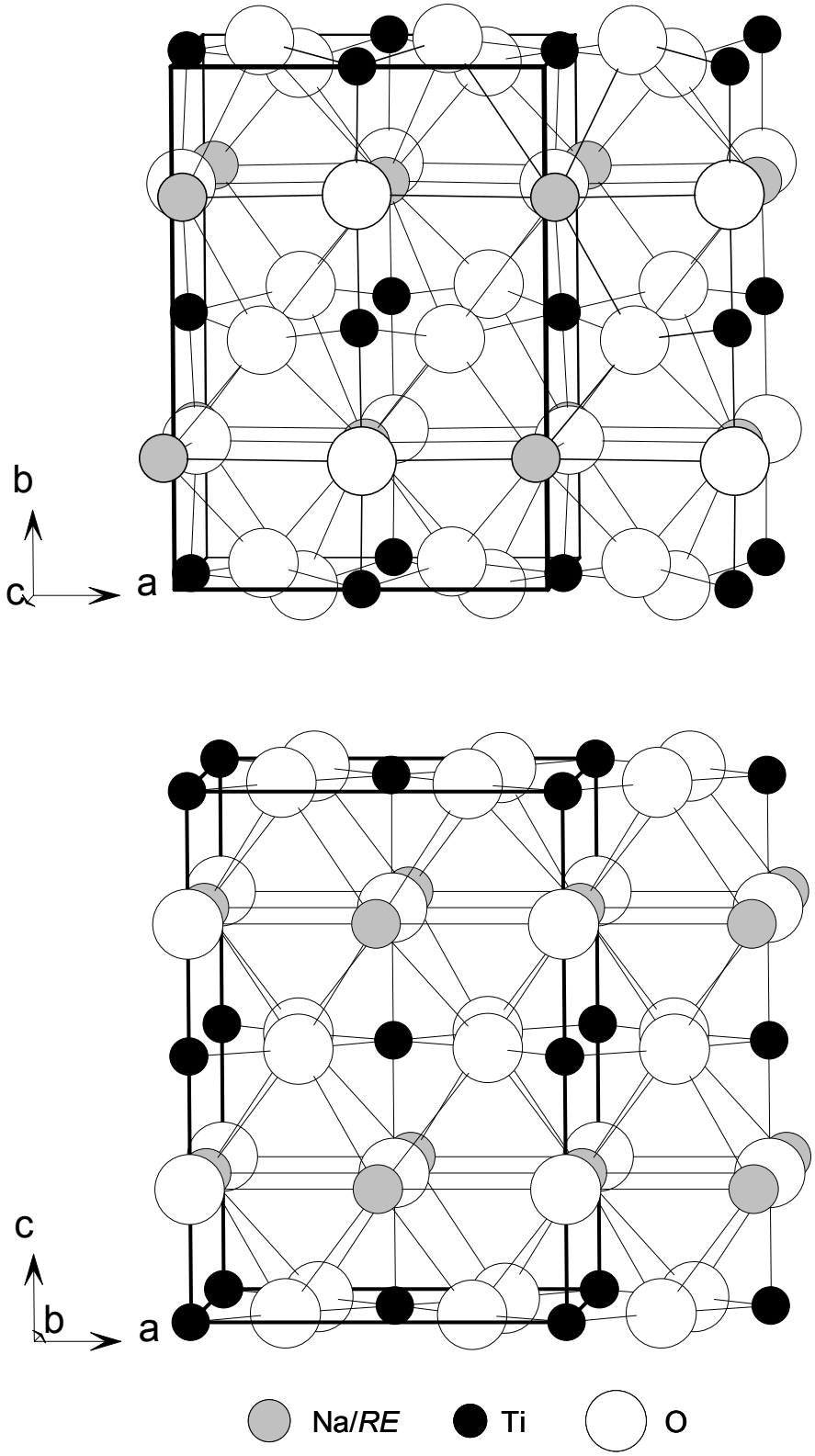

Lafond et al. Figures 5a & 5b

4.6.2 EDXRD-Untersuchungen zur Bildung von MO_3-Nanopartikeln

Zusammenfassung der Veröffentlichung „*Untersuchungen der solvothermalen Bildung von MoO_3-Fasern mit Hilfe komplementärer in-situ EXAFS/EDXRD-Techniken*“

Hier werden nur die Ergebnisse der EDXRD-Untersuchung diskutiert, welche in dieser Kooperation von unserer Arbeitsgruppe erhalten wurden.

Die Reaktion wurde in der in Kapitel 3.1.1 vorgestellten in-situ-Zelle durchgeführt. Ein typischer Reaktionsansatz bestand aus 1.27 mmol $MoO_3{\cdot}2H_2O$ in einer Lösung von 0.4 ml Eisessig und 1.1 ml Wasser. Die Reaktionstemperatur variierte zwischen 80 und 120 °C

Zu Beginn der Reaktion sind neben den Mo-Fluoreszenzen die charakteristischen Reflexe von $MoO_3{\cdot}2H_2O$ zu beobachten. Nach einer temperaturabhängigen Induktionszeit (im mittel ca. 8 min) setzt die Produktbildung ein. Kristalline Zwischenphasen oder Intermediate wurden nicht beobachtet (Abb 4.15, links). Nach 8 weiteren Minuten ist die Reaktion abgeschlossen. Die Kristallisationskurve (Abb 4.15, rechts) (α(t) gegen t) hat einen sigmoidalen Verlauf, der für die Kinetik vieler Festkörperreaktionen charakteristisch ist.

Aufgrund der ungewöhnlich schnellen Reaktion war eine quantitative Auswertung nicht möglich.

Hydrothermalsynthesen

DOI: 10.1002/ange.200500514

Untersuchung der solvothermalen Bildung von MoO_3-Fasern mithilfe komplementärer In-situ-EXAFS/EDXRD-Techniken**

*Alexej Michailovski, Jan-Dierk Grunwaldt, Alfons Baiker, Ragnar Kiebach, Wolfgang Bensch und Greta R. Patzke**

Für die Entwicklung von Nanomaterialien sind effiziente und flexible Verfahren zur Synthese von Nanoteilchen eine unabdingbare Voraussetzung.[1–5] Unter den vielfältigen anorganischen Nanomaterialien zeichnen sich Übergangsmetalloxide durch eine besonders große Bandbreite wichtiger Eigenschaften und Anwendungen aus.[6,7] Funktionalisierung und Ausrichtung solcher nanoskaligen Oxide werden durch die Verwendung von Teilchen mit anisotroper Morphologie enorm erleichtert.[8] Unter den Übergangsmetalloxiden nimmt MoO_3 eine besondere Stellung ein, da es für zahlreiche technische Prozesse, z. B. in der Katalyse[9–11] und der Sensortechnologie,[12–13] geeignet ist. Wir haben daher vor kurzem eine einfach anzuwendende und handhabbare Solvothermalsynthese für MoO_3-Fasern mit einem hohen Aspektverhältnis entwickelt.[14–15]

Solvothermalreaktionen sind vielseitige Syntheseverfahren, die den jeweiligen präparativen Anforderungen angepasst werden können.[16] Dies wird insbesondere zur Steuerung der Partikelgröße bei der Synthese anorganischer Nanomaterialien genutzt.[17–18] Schwierig bleibt allerdings die Kontrolle der vielfältigen Parameter, die zur Entwicklung einer rationalen und planbaren Festkörpersynthese mithilfe von Solvothermalprozessen nötig sind. Kommt im Falle von Nanomaterialien noch die Steuerung der Morphologie hinzu, so wird dieses Unterfangen noch wesentlich schwieriger. Da der Einfluss der Reaktionsparameter für Solvothermalreaktionen bislang noch nicht systematisch untersucht worden ist, geht einer erfolgreichen Solvothermalsynthese von Nanoteilchen oft noch ein beträchtliches Maß an „Versuch und Irrtum“ voraus. Daher ist es unerlässlich, die Mechanismen von Solvothermalreaktionen aufzuklären, will man sie optimieren und für technische Zwecke nutzen.

Meist benötigen Solvothermalreaktionen dickwandige Reaktionsgefäße, sodass ihre direkte Beobachtung nur durch aufwändige In-situ-Techniken unter Verwendung von Synchrotronstrahlung hoher Intensität möglich ist.[19–22] Im Allgemeinen ist die Entwicklung geeigneter in-situ-spektroskopischer Methoden für Reaktionen unter erhöhtem Druck eine schwierige Aufgabe für Chemiker und Materialwissenschaftler.[23] Zwar können kinetische Informationen von orientierendem Charakter auch durch das Abschrecken von Solvothermalreaktionen mithilfe gängiger Labortechniken gewonnen werden – diese Methode ist aber nur zulässig, wenn die isolierten Materialien dabei keine irreversiblen Veränderungen erfahren und das Vorliegen von Artefakten ausgeschlossen werden kann. Der Schwerpunkt der bislang an Solvothermalreaktionen durchgeführten In-situ-Studien liegt auf den Gebieten der Zeolithe,[24–26] Open-Framework-Materialien,[27–28] Silicatmineralien[29–30] und sulfidischen Systeme.[22,31] Entsprechende Untersuchungen an Übergangsmetalloxiden erfolgten bevorzugt an ternären Verbindungen von hohem technischem Interesse, darunter Bismutmolybdate[32] und $BaTiO_3$.[33] Die Zahl binärer Oxidsysteme wie ZrO_2,[34] die mit In-situ-Techniken charakterisiert worden sind, ist hingegen bedeutend kleiner. Demzufolge ist nur wenig darüber bekannt, auf welchen Wegen sie durch Solvothermalsynthese in Nanomaterialien überführt werden.

Hier stellen wir die erste übergreifende In-situ-Untersuchung zum Wachstum von MoO_3-Fasern vor, bei der EDXRD (energiedispersive Röntgendiffraktometrie) und XANES/EXAFS (X-ray absorption near-edge structure/extended X-ray absorption fine structure) als komplementäre Methoden eingesetzt wurden. Während XRD-Analysen die Fernordnung in einer Verbindung erfassen, gibt die XANES/EXAFS-Spektroskopie einen Einblick in die unmittelbare Koordinationssphäre des betrachteten Atoms.[35–37] Solche Informationen sind entscheidend für das Verständnis der solvothermalen Bildung von Nanoteilchen, da amorphe Festkörper und kleine Teilchen (typischerweise unter 50 Å) nicht durch Braggsche Beugung erfasst werden können. Das Aufstellen einer Hypothese über den Bildungsmechanismus erfordert darüber hinaus die simultane Untersuchung der Vorgänge und der auftretenden Molybdänspezies in der flüssigen wie in der festen Phase. Dies wurde mithilfe einer speziell konstruierten EXAFS-Zelle realisiert (siehe Hintergrundinformationen).[38] Mit dieser Zelle können sowohl kristalline als auch amorphe Zwischenprodukte in beiden Phasen der Reaktionsmischung beobachtet werden, was eine umfassende Charakterisierung der solvothermalen Prozesse ermöglicht. Die

[*] Dipl-Chem. A. Michailovski, Dr. G. R. Patzke
Laboratorium für Anorganische Chemie
ETH Hönggerberg, 8093 Zürich (Schweiz)
Fax: (+41) 1-633-4692
E-mail: patzke@inorg.chem.ethz.ch
Dr. J.-D. Grunwaldt, Prof. Dr. A. Baiker
Institute for Chemical and Bioengineering
ETH Hönggerberg, 8093 Zürich (Schweiz)
Dipl.-Chem. R. Kiebach, Prof. Dr. W. Bensch
Institut für Anorganische Chemie
Universität Kiel, 24098 Kiel (Deutschland)

[**] Wir danken Prof. Dr. R. Nesper (ETH Zürich) für die Unterstützung dieser Arbeit. Für die Gewährung von Messzeit an den Beamlines X1 und F3 für In-situ-EXAFS bzw. EDXRD-Experimente danken wir dem HASYLAB (DESY, Hamburg). Wir danken den Messplatzbetreuern, Julia Wienold und M. Hermann, sowie Matteo Caravati und Michael Ramin (ICAB, ETH Zürich) für ihre Hilfe bei den EXAFS-Messungen. Diese Arbeit wurde von der ETH Zürich, dem Schweizerischen Nationalfonds (MaNEP – Materials with Novel Electronic Properties) und dem Nationalen Forschungsprogramm „Supramolecular Functional Materials“ finanziert. EXAFS = extended X-ray absorption fine structure, EDXRD = energiedispersive Röntgendiffraktometrie.

Hintergrundinformationen zu diesem Beitrag sind im WWW unter http://www.angewandte.de zu finden oder können beim Autor angefordert werden.

  DOI: 10.1002/ange.200500514

Analyse aller kristallinen Komponenten erfolgt dann durch ergänzende EDXRD-Messungen.

Die Solvothermalsynthese von MoO_3-Fasern gestaltet sich relativ einfach: Gelbe Molybdänsäure, $MoO_3{\cdot}2H_2O$, wird nach wenigen Stunden im Autoklaven im Temperaturbereich von 180–220 °C quantitativ in das anisotrope Produkt überführt.[14] Die Reaktion kann in Wasser oder Essigsäure durchgeführt werden, und das Aspektverhältnis der entstehenden Fasern ist mit Längen über 10 μm und Durchmessern zwischen 100 und 150 nm durchweg hoch. Die Reaktionsparameter können relativ flexibel gewählt werden, das Vorliegen von $MoO_3{\cdot}2H_2O$ ist dagegen eine notwendige Voraussetzung für das Gelingen der Reaktion.[14] Die ähnlichen, schichtartigen Strukturen von MoO_3 und $MoO_3{\cdot}2H_2O$ sind durch eine topotaktische Dehydrierung miteinander verknüpft, die über die Zwischenstufe β-$MoO_3{\cdot}H_2O$ verläuft.[39] Erste Untersuchungen zur Bildung von faserförmigem MoO_3 in verschiedenen Medien deuteten jedoch auf einen abweichenden Reaktionsweg unter Solvothermalbedingungen hin.[14]

Orientierende Ex-situ-Experimente unter Abschrecken der Reaktion von $MoO_3{\cdot}2H_2O$ zu faserförmigem MoO_3 zeigten, dass die Faserbildung im Temperaturbereich zwischen 80 und 180 °C einsetzt (siehe *Experimentelles*). Die Reaktion kann mit dem Auge verfolgt werden, da sie mit einer Farbänderung von der gelben Molybdänsäure hin zu einem blaugrauen Produkt einhergeht. Dies rührt von einer geringfügigen partiellen Reduktion von MoO_3 her, deren Anteil weit unter der Nachweisgrenze der üblichen analytischen Methoden liegt. Bei einer Reaktionstemperatur von 80 °C blieb die gelbe Farbe des Ausgangsmaterials unverändert, während nach 12 min Reaktionszeit bei 100 °C ein scharfer Farbumschlag eintrat. Mit steigender Reaktionstemperatur nahm dieses Zeitintervall auf 6 min (120 °C) und schließlich auf 2 min (180 °C) ab.

Diese Beobachtungen sind im Einklang mit den entsprechenden Rasterelektronenmikroskopie(REM)-Aufnahmen und Pulverdiffraktogrammen (Abbildung 1, I): Bei 80 °C weist $MoO_3{\cdot}2H_2O$ (JCPDS 39–363; $P2_1/n$, $a = 10.618(5)$, $b = 13.825(7)$, $c = 10.482(5)$ Å, $\beta = 91.61(4)°$) noch keine signifikanten strukturellen (Abbildung 1, Ia, unten) oder morphologischen (Abbildung 1, Ia, oben) Veränderungen auf. Bei 100 °C ist hingegen die Dehydrierung zu MoO_3 bereits abgeschlossen (Abbildung 1, Ib, unten), und die Bildung des faserförmigen Produkts beginnt (Abbildung 1, Ib, oben). Höhere Reaktionstemperaturen im Bereich zwischen 100 und

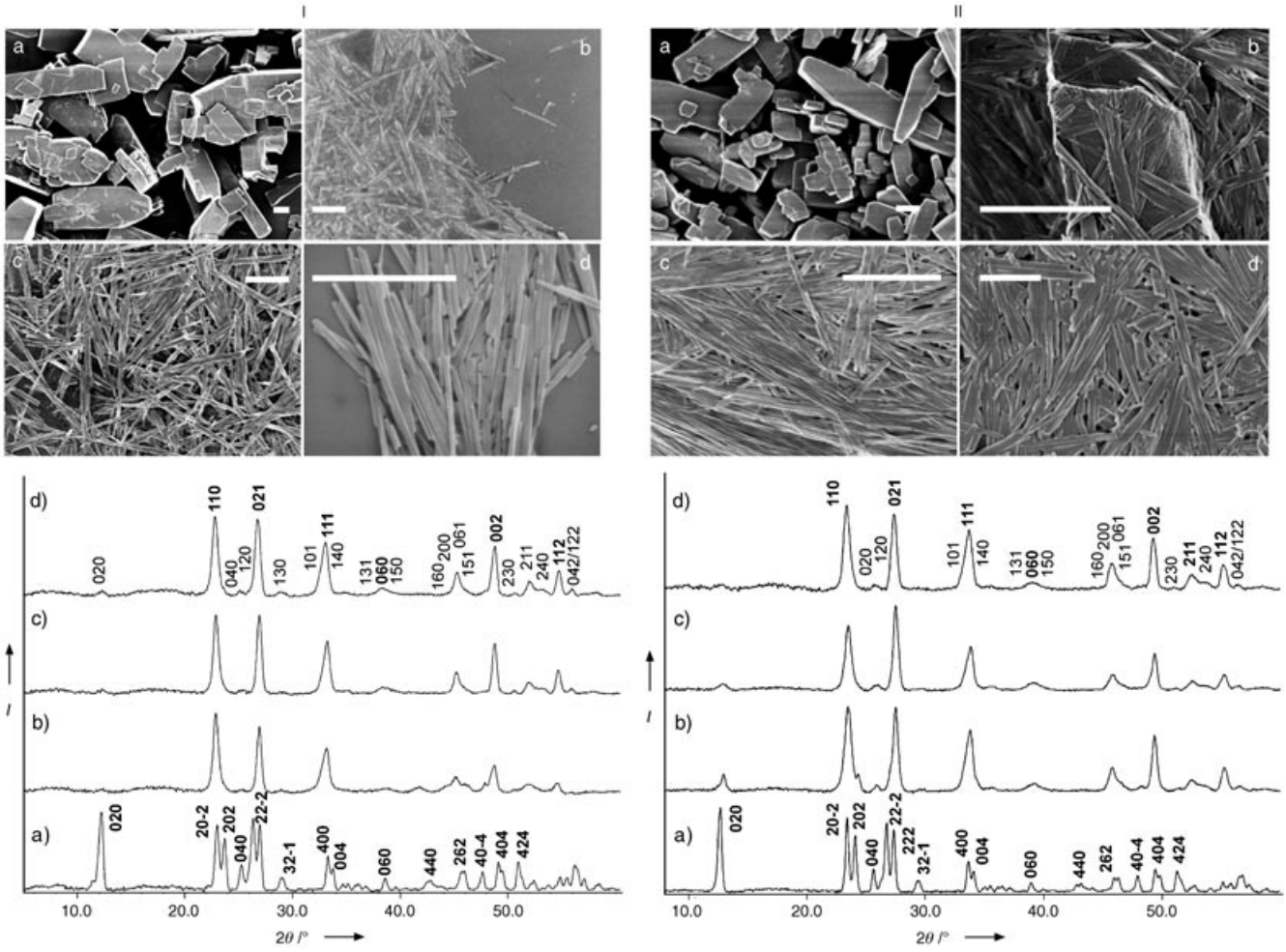

Abbildung 1. REM-Aufnahmen (I/II, oben, Maßstab = 1 μm) und Pulverdiffraktogramme (I/II, unten) der isolierten Produkte nach Abschrecken der Reaktion von $MoO_3{\cdot}2H_2O$ in I) Essigsäure oder II) Wasser bei 80 °C (a), 100 °C (b), 120 °C (c) und 180 °C (Essigsäure) bzw. 150 °C (H_2O) (d).

180 °C tragen zu einer Verbesserung der faserförmigen Morphologie (Abbildung 1, Ic,d, oben) und der Kristallinität bei (vergleiche die (061)-, (002)- und (112)-Reflexe in Abbildung 1, Ic,d, unten). Eine analoge Serie von Ex-situ-Abschreckexperimenten in Wasser bestätigte die Zeitskala der Reaktion, da die quantitative Bildung von MoO_3-Fasern bei 150 °C nach 3–4 min beendet war (Abbildung 1, IId, oben/unten). Die Werte der relativen Intensitäten im Pulverdiffraktogramm der abgeflachten, faserartigen Produkte weichen von den Literaturdaten ab (vergleiche JCPDS 35-609; *Pbnm*, $a = 3.963$, $b = 13.856$, $c = 3.697$ Å). Vermutlich tragen sowohl Stapelfehler in der Wachstumsrichtung[40] entlang [001] als auch eine Vorzugsorientierung der MoO_3-Fasern auf dem Flachbett-Probenträger zu dieser Abweichung bei.

Untersuchungen mit der Transmissionselektronenmikroskopie (TEM) an Proben, die nach 20-minütiger Behandlung abgeschreckt wurden, zeigen das Vorliegen von Stapelfehlern an, die wiederum zur Deutung der Reflexverbreiterungen in den Pulverdiffraktogrammen herangezogen werden können (Abbildung 1). Wie aus Abbildung 2 ersichtlich, sind klar

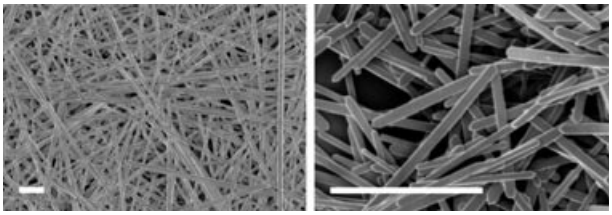

Abbildung 2. Repräsentative REM-Aufnahmen von MoO_3-Nanofasern (Maßstab = 2 μm) nach abgeschlossener Reaktion.

separierte Fasern mit gut ausgeprägten Kanten und Enden durch längere Reaktionszeiten bei der Solvothermalsynthese erhältlich (16–24 h bei 180 °C). Schon bei einer Reaktionstemperatur von 100 °C ist nur noch ein sehr geringer Rest mikrokristalliner gelber Molybdänsäure in den Produkten zu finden [siehe Pulverdiffraktogramme (Abbildung 1, II, unten) und REM-Aufnahmen (Abbildung 1, IIb, oben)].

Die Temperaturabhängigkeit der Bildung von MoO_3-Fasern wurde mithilfe von In-situ-Röntgenabsorptionsspektroskopie untersucht. Dabei ermöglicht die neu konstruierte Autoklavenmesszelle sowohl die Beobachtung der flüssigen Phase als auch der Fest-flüssig-Grenzfläche (siehe Hintergrundinformationen). Im vorliegenden Fall ist die Untersuchung der flüssigen Phase unverzichtbar, um zwischen einer topotaktischen Dehydrierung und einem alternativen Auflösungs-Kristallisations-Mechanismus unterscheiden zu können. Dazu wurden XANES-Spektren an der an der Molybdän-K-Kante bei der Umsetzung von $MoO_3 \cdot 2H_2O$ in Wasser im unteren Teil der Zelle (vorwiegend feste Phase, Abbildung 3a,b) sowie im mittleren Teil der Zelle (flüssige Phase, Abbildung 3c) im Temperaturintervall zwischen 25 und 150 °C aufgenommen. Nach Beginn der Reaktion blieb die flüssige Phase bis 50 °C frei von Molybdänverbindungen (Abbildung 3c), und die feste Phase zeigte das für $MoO_3 \cdot 2H_2O$ typische XANES-Spektrum. Erste Änderungen traten bei 90 °C auf, und schließlich setzte die Reaktion bei 99 °C ein (Abbildung 3a,b). Aus den XANES- und den

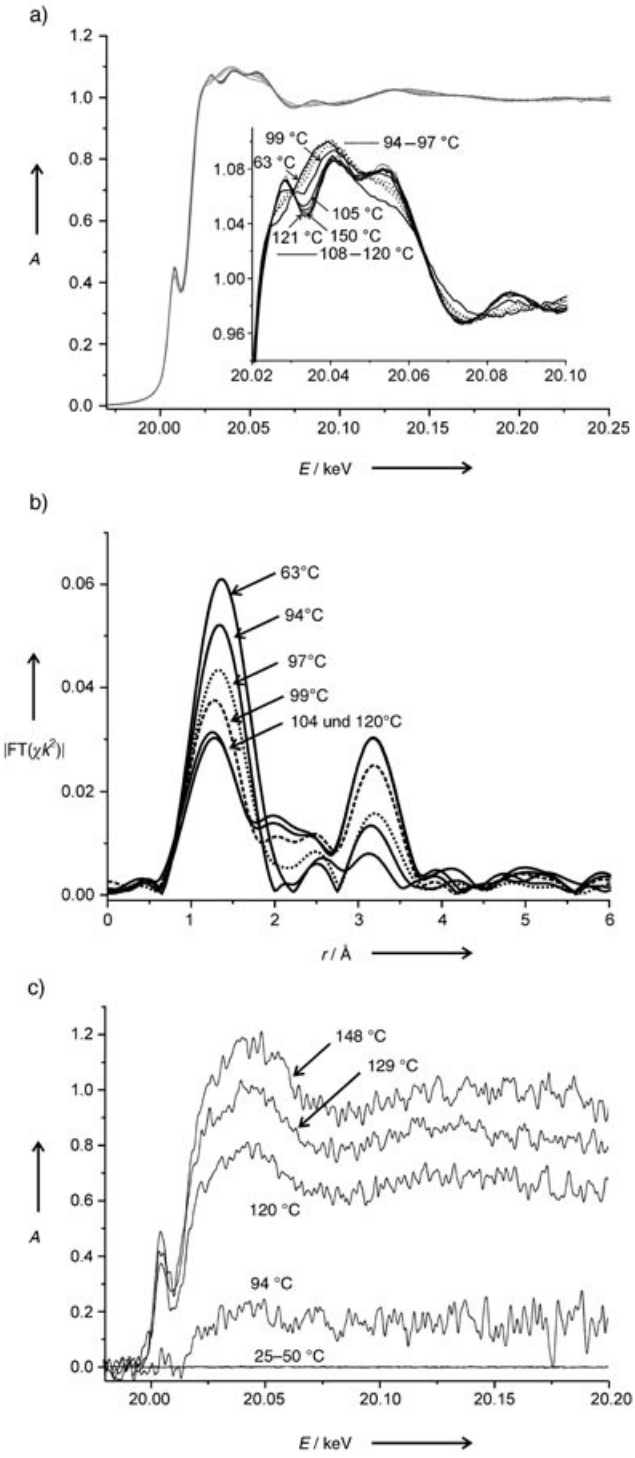

Abbildung 3. a) Verlauf der Röntgenabsorptionsspektren an der Molybdän-K-Kante während der Hydrothermalsynthese von $MoO_3 \cdot 2H_2O$ zu MoO_3-Fasern (feste Phase), b) Fourier-transformierte EXAFS-Spektren, c) Entsprechende XANES-Spektren an der Molybdän-K-Kante der flüssigen Phase während der Reaktion. Als Referenz für die Intensität des Absorptionsverlaufs fungiert das bei 150 °C aufgenommene Spektrum.

Fourier-transformierten EXAFS-Spektren (Abbildung 3a,b) ist ersichtlich, dass die kontinuierliche Umwandlung von $MoO_3 \cdot 2H_2O$ in MoO_3-Fasern bei 99 °C einsetzt. Hinweise auf das Auftreten von Zwischenprodukten konnten nicht gefun-

den werden (siehe Referenzspektren in den Hintergrundinformationen). Gleichzeitig steigt die Konzentration wasserlöslicher Spezies ab ca. 95 °C signifikant an und nimmt kontinuierlich bis 150 °C zu. In diesem Temperaturbereich setzt die Trennung in einzelne MoO_3-Fasern ein (siehe Abbildung 1, I/II, oben). Sobald die ersten löslichen Molybdänspezies auftreten, beginnt die Reaktion. Die Reaktionsgeschwindigkeit steigt mit der Temperatur, was zu der beobachteten Erhöhung der Konzentration von Mo-Spezies in Lösung führt. Die Reaktion ist diffusionskontrolliert, da die Reaktionsgeschwindigkeit bei Verwendung einer Glaswolle-Deckschicht (siehe *Experimentelles*) abnimmt. Insgesamt sind alle diese Beobachtungen deutlich besser im Einklang mit einer Reaktion in Lösung als mit einer topotaktischen Umwandlung.

Die Zeitabhängigkeit der Bildung von MoO_3-Fasern aus $MoO_3{\cdot}2H_2O$ wurde mit In-situ-EDXRD-Experimenten untersucht. Abbildung 4a zeigt eine typische zeitabhängige Entwicklung der Diffraktogramme für die Reaktion bei

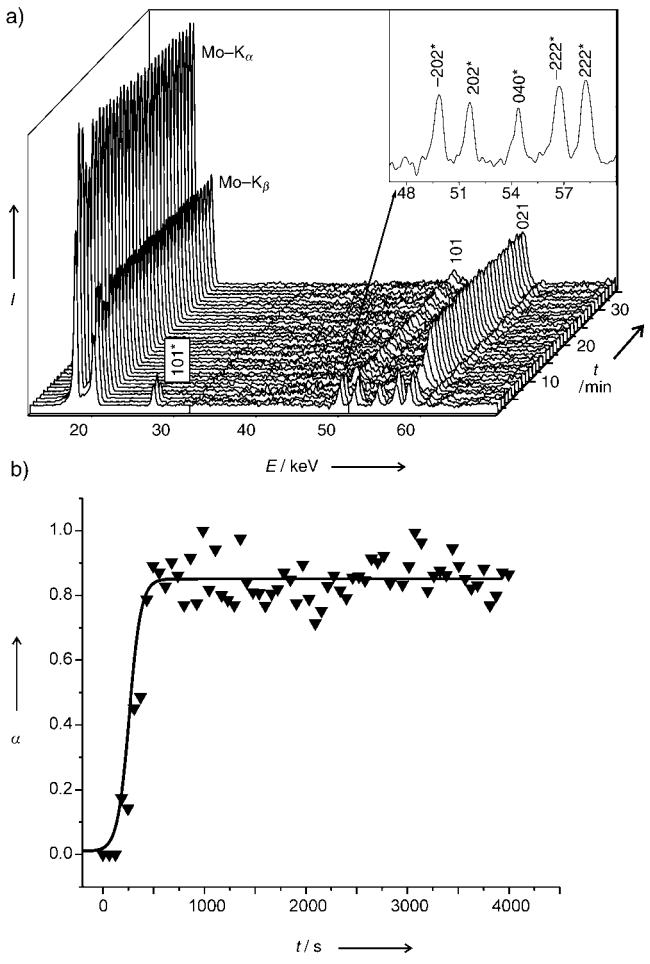

Abbildung 4. a) Zeitaufgelöste Pulverdiffraktogramme bei 120 °C nach Abzug des Untergrunds. Die Indices des Ausgangsmaterials (markiert mit *), das Produkt sowie die Mo-Fluoreszenzen sind gekennzeichnet (der Einschub zeigt eine Vergrößerung des ersten Spektrums). b) Zeitabhängiger Reaktionsgrad α, bestimmt mittels des (021)-Reflexes bei 120 °C. Die Kristallisationskurve kann mit einem sigmoidalen Verlauf angepasst werden.

120 °C in Essigsäure. Zu Beginn der Reaktion treten die Mo-Signale und die charakteristischen Reflexe von $MoO_3{\cdot}2H_2O$ (Einschub in Abbildung 4a) auf. Nach einer temperaturabhängigen Induktionszeit (hier: 8 min) werden keine Reflexe des Startmaterials mehr beobachtet. Danach setzt die Produktbildung unter gleichzeitigem Anstieg der Intensität aller Reflexe ein, ohne dass ein kristallines Zwischenprodukt beobachtet wird. Nach weiteren 7–8 min ist die Reaktion beendet. Die Kristallisationskurve ($\alpha(t)$ gegen t) hat einen sigmoidalen Verlauf (Abbildung 4b), der für die Kinetik vieler Festkörperreaktionen charakteristisch ist. Die Geschwindigkeit der vorliegenden Reaktion ist verglichen mit der anderer Festkörperreaktionen relativ hoch, weshalb eine weitere quantitative Auswertung der kinetischen Daten nicht möglich war.

Die Ergebnisse zeigen, dass die solvothermale Bildung von MoO_3-Fasern ein schneller Prozess ist, der nach wenigen Minuten Reaktionsdauer bei Temperaturen deutlich unter 180 °C beendet ist. Darüber hinaus ergibt sich ein einheitliches Bild des Reaktionsverlaufs, das mit einem Auflösungs-Kristallisations-Mechanismus ohne das Auftreten kristalliner Zwischenprodukte im Einklang ist. Die hohe Anisotropie des faserförmigen MoO_3 ist daher wahrscheinlich auf die höhere Wachstumsgeschwindigkeit des orthorhombischen α-MoO_3 in [001]-Richtung zurückzuführen (*Pbnm*, $a = 3.9630$, $b = 13.856$, $c = 3.6966$ Å).[41–42]

Die hier vorgestellte Strategie ist ein vielseitiger Weg zum besseren Verständnis von Solvothermalreaktionen. Nach Abgrenzen der Reaktionsparameter durch orientierende Ex-situ-Abschreckexperimente können in der neu entwickelten Autoklavenzelle die temperaturabhängigen Fest-flüssig-Gleichgewichte durch In-situ-EXAFS-Spektroskopie verfolgt werden. Kinetische In-situ-EDXRD-Untersuchungen liefern die entscheidenden komplementären Strukturinformationen. Auf diese Weise können die Rolle des Startmaterials und der Mechanismus einer Solvothermalreaktion aus unterschiedlichen Blickwinkeln betrachtet werden. Die so gewonnenen Einsichten sind wichtig für die Optimierung von Synthesen in technischem Maßstab. Der vorgestellte Ansatz ist ein Schritt auf dem Weg zu einem rationalen Konzept für die Solvothermalsynthese von Nanomaterialien – und darüber hinaus zum generellen Verständnis von Synthesen, die über lösliche und/oder amorphe Zwischenprodukte verlaufen.

Experimentelles

Für die Abschreckexperimente wurden 180 mg (1 mmol) $MoO_3{\cdot}2H_2O$, 0.5 mL Eisessig und 1.5 mL Wasser in einer Glasampulle (Innenvolumen: 23 mL) unter Atmosphärendruck abgeschmolzen. Die Ampullen wurden 20 min auf 80, 100, 120 oder 180 °C geheizt und anschließend bei −8 °C in einer Eis/NaCl-Kältemischung abgeschreckt. Die Produkte wurden durch mehrfaches Zentrifugieren in Wasser, Ethanol und Aceton abgetrennt und durch Elektronenmikroskopie (REM, LEO-1530-(FEG)-Mikroskop mit einer Beschleunigungsspannung von 1 kV) sowie mittels Pulverdiffraktometrie (STOE-STADI-P2-Diffraktometer, Flachbett-Probenträger, $Cu_{K\alpha}$-Strahlung) charakterisiert.

Die In-situ-EXAFS- und XANES-Experimente wurden an der Beamline X1 am HASYLAB (DESY, Hamburg) durchgeführt. 50 mg $MoO_3{\cdot}2H_2O$ wurden zwischen Glaswollestopfen eingebettet, um die

feste Phase zu fixieren, und anschließend zusammen mit 3 mL Wasser in eine neu konstruierte spektroskopische Zelle gegeben (siehe Hintergrundinformationen). Die EXAFS-Scans an der Molybdän-K-Kante wurden unter stationären Bedingungen (feste und flüssige Phase) zwischen 19850 und 21200 eV aufgenommen und mit einer Mo-Referenzfolie kalibriert. Die Veränderung der Reaktionsbedingungen wurde mit schnelleren Scans im QEXAFS-Modus zwischen 19950 und 20450 eV (110 s/Spektrum) verfolgt. Die Probe wurde bis 150 °C in Schritten von 1.5 K min^{-1} von Raumtemperatur auf 50, 94, 120 und 150 °C geheizt. Die Rohdaten wurden mit der entsprechenden Referenzfolie energiekalibriert und nach Abzug des Untergrunds normalisiert (Software: WINXAS 3.0[43]). Die Fourier-Transformation der EXAFS-Daten für die dynamische Änderung wurde auf die k^3-gewichteten Funktionen im Intervall $k = 3.5$–9.3 $Å^{-1}$ angewendet.

Im Zuge der In-situ-EDXRD-Experimente (HASYLAB-Beamline F3, Hamburg) wurden MoO_3-Nanofasern durch die Umsetzung von 230.0 mg (1.27 mmol) $MoO_3 \cdot 2H_2O$ in einer Lösung von 0.4 mL Eisessig und 1.1 mL Wasser erhalten. Die Reaktion wurde unter autogenem Druck und isothermen Bedingungen in verschraubbaren Glasröhrchen als Autoklaveneinsätzen durchgeführt (siehe Hintergrundinformationen).[22,31] Das Reaktionsgefäß wurde in den Autoklaven überführt, und die Reaktion wurde mit einer zeitlichen Verzögerung von ca. 1 min gestartet. Nach ca. 30 s wurde die Reaktionstemperatur erreicht, und Pulverdiffraktogramme wurden mit einer Aufnahmezeit von 120 s angefertigt. Die Diffraktogramme wurden mithilfe des Programms EDXPow ausgewertet.[44] Die Reflexprofile wurden mit einer Gaußkurve angenähert, und die Reflexintensitäten des Produkts wurden anhand der entsprechenden Intensitäten für die $Mo_{K\alpha}$-Fluoreszenz standardisiert.

Eingegangen am 10. Februar 2005,
veränderte Fassung am 17. Mai 2005
Online veröffentlicht am ■■. ■■ ■■■■

Stichwörter: EXAFS-Spektroskopie · Hydrothermalsynthesen · In-situ-Spektroskopie · Molybdänoxid · Nanomaterialien

[1] *Encyclopaedia of Nanoscience and Nanotechnology* (Hrsg.: H. S. Nalwa), American Scientific Publishers, Stevenson Ranch, CA, **2004**.
[2] *Nanoparticles* (Hrsg.: G. Schmid), Wiley-VCH, Weinheim, **2004**.
[3] *The Chemistry of Nanostructured Materials* (Hrsg.: P. Yang), World Scientific Publishers, Singapore, **2003**.
[4] R. Tenne, *Angew. Chem.* **2003**, *115*, 5280; *Angew. Chem. Int. Ed.* **2003**, *42*, 5124.
[5] C. N. R. Rao, A. K. Cheetham, *J. Mater. Chem.* **2001**, *11*, 2887.
[6] C. N. R. Rao, B. Raveau, *Transition Metal Oxides*, VCH Publishers, New York, **1995**.
[7] C. N. R. Rao, F. L. Deepak, G. Gundiah, A. Govindaraj, *Prog. Solid State Chem.* **2003**, *31*, 5.
[8] G. R. Patzke, F. Krumeich, R. Nesper, *Angew. Chem.* **2002**, *114*, 2554; *Angew. Chem. Int. Ed.* **2002**, *41*, 2446.
[9] J. Haber, E. Lalik, *Catal. Today* **1997**, *33*, 119.
[10] J. B. Wagner, S. B. Abd Hamid, D. Othman, O. Timpe, S. Knobl, D. Niemeyer, D. S. Su, R. Schlögl, *J. Catal.* **2004**, *225*, 87.
[11] A. Baiker, P. Dollenmeier, A. Reller, *J. Catal.* **1987**, *103*, 394.
[12] A. K. Prasad, P. I. Gouma, *J. Mater. Sci.* **2003**, *38*, 4347.
[13] S. S. Sunu, E. Prabhu, V. Jayaraman, K. J. Guanasekar, T. K. Seshariji, T. Guanasekaran, *Sens. Actuators B* **2004**, *101*, 161.
[14] G. R. Patzke, A. Michailovski, F. Krumeich, R. Nesper, J.-D. Grunwaldt, A. Baiker, *Chem. Mater.* **2004**, *16*, 1126.
[15] A. Michailovski, F. Krumeich, G. R. Patzke, *Helv. Chim. Acta* **2004**, *87*, 1029.
[16] K. Byrappa, M. Yoshimura, *Handbook of Hydrothermal Technology*, Noyes, Park Ridge, NJ, **2001**.
[17] R. I. Walton, *Chem. Soc. Rev.* **2002**, *31*, 230.
[18] G. Demazeau, *J. Mater. Chem.* **1999**, *9*, 15.
[19] R. I. Walton, D. O'Hare, *Chem. Commun.* **2000**, 2283.
[20] A. K. Cheetham, C. F. Mellot, *Chem. Mater.* **1997**, *9*, 229.
[21] R. I. Walton, A. Norquist, R. I. Smith, D. O'Hare, *Faraday Discuss.* **2002**, *122*, 331.
[22] L. Engelke, M. Schaefer, M. Schur, W. Bensch, *Chem. Mater.* **2001**, *13*, 1383.
[23] J.-D. Grunwaldt, R. Wandeler, A. Baiker, *Catal. Rev. Sci. Eng.* **2003**, *45*, 1.
[24] R. I. Walton, T. Loiseau, D. O'Hare, G. Férey, *Chem. Mater.* **1999**, *11*, 3201.
[25] R. E. Morris, S. J. Weigel, P. Norby, J. C. Hanson, A. K. Cheetham, *J. Synchrotron Radiat.* **1996**, *3*, 301.
[26] D. Hooper, P. Barnes, J. K. Cockcroft, A. C. Jupe, S. D. M. Jacques, S. P. Bailey, F. Lupo, M. Vickers, M. Hanfland, *Phys. Chem. Chem. Phys.* **2003**, *5*, 4946.
[27] R. J. Francis, S. O'Brien, A. M. Fogg, P. Shiv Halasyamani, D. O'Hare, T. Loiseau, G. Férey, *J. Am. Chem. Soc.* **1999**, *121*, 1002.
[28] P. Norby, J. C. Hanson, *Catal. Today* **1998**, *39*, 301.
[29] S. Shaw, S. M. Clark, C. M. B. Henderson, *Chem. Geol.* **2000**, *167*, 129.
[30] S. Shaw, M. B. Henderson, S. M. Clark, *Am. Mineral.* **2002**, *87*, 533.
[31] L. Engelke, M. Schaefer, F. Porsch, W. Bensch, *Eur. J. Inorg. Chem.* **2003**, 506.
[32] A. M. Beale, G. Sankar, *Chem. Mater.* **2003**, *15*, 146.
[33] R. I. Walton, F. Millange, R. I. Smith, T. C. Hansen, D. O'Hare, *J. Am. Chem. Soc.* **2001**, *123*, 12547.
[34] F. Lupo, J. K. Cockcroft, P. Barnes, P. Stukas, M. Vickers, C. Norman, H. Bradshaw, *Phys. Chem. Chem. Phys.* **2004**, *6*, 1837.
[35] B. S. Clausen, H. Topsøe, R. Frahm, *Adv. Catal.* **1998**, *42*, 315.
[36] J.-D. Grunwaldt, B. S. Clausen, *Top. Catal.* **2002**, *18*, 37.
[37] G. Sankar, J. M. Thomas, *Top. Catal.* **1999**, *8*, 1.
[38] J.-D. Grunwaldt, M. Ramin, M. Rohr, A. Michailovski, G. R. Patzke, A. Baiker, *Rev. Sci. Instrum.* **2005**, *76*, 054104 .
[39] J. R. Günter, *J. Solid State Chem.* **1972**, *5*, 354.
[40] D. B. Williams, C. B. Carter, *Transmission Electron Microscopy*, Plenum, New York, **1996**.
[41] J. Li, P. Wei, W. Ruigang, J. Chen, *Key Eng. Mater.* **2002**, *224–226*, 367.
[42] G. Andersson, A. Magneli, *Acta Chem. Scand.* **1950**, *4*, 793.
[43] T. Ressler, *J. Synchrotron Radiat.* **1998**, *5*, 118.
[44] F. Porsch, *EDXPow*, V. 3.15, RTI GmbH, Paderborn **2002**.

Zuschriften

Hydrothermalsynthesen

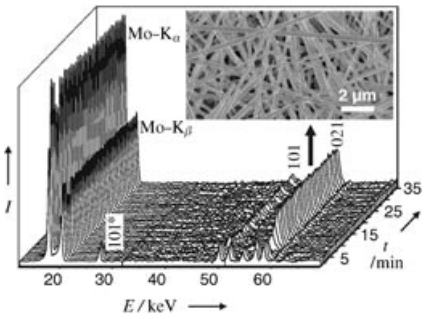

In Minutenschnelle: Die hydrothermale Bildung von faserförmigem MoO_3 wurde mit komplementären In-situ-Methoden verfolgt. Die In-situ-EDXRD-Untersuchungen zeigen, dass die quantitative Bildung innerhalb weniger Minuten beendet ist (Bild: zeitaufgelöste Pulverdiffraktogramme bei 120 °C). Eine speziell konstruierte In-situ-EXAFS-Zelle macht es möglich, die feste und die flüssige Phase gleichzeitig zu untersuchen. Diese Strategie liefert wichtige Informationen zum Wachstumsmechanismus der MoO_3-Fasern.

4.6.3 EDXRD-Untersuchungen zur Bildung von Alkaliwolframaten

Aus dem folgenden Manuskript werden an dieser Stelle nur die EDXRD-Untersuchungen zur Bildung von $WO_3 \cdot 0.33H_2O$ diskutiert, die in einer Kooperation mit der Arbeitsgruppe Patzke (ETH Zürich) durchgeführt wurden.

Zum Zeitpunkt der Abgabe dieser Doktorarbeit befand sich die Veröffentlichung im Stadium der Vorbereitung, eine Einreichung ist für Januar 2006 geplant.

Untersucht wurde die solvothermale Synthese von Alkaliwolframaten mit der allgemeinen Formel $M_xWO_{3-x} \cdot 0.33H_2O$ (M = Alkalimetall). Besonders interessant ist, welche Rolle die Alkalikationen auf verschiedene Produkteigenschaften wie z.B. die Morphologie ausüben. Am HASYLAB am Messplatz F3 wurde die Kinetik zur Bildung von $M_xWO_{3-x} \cdot 0.33H_2O$ unter solvothermalen Bedingungen mit in-situ-EDXRD untersucht. Zusätzlich wurde der Einfluss von verschiedenen Alkaliionen auf den Reaktionsverlauf verfolgt.

Ein typischer Reaktionsansatz bestand aus 248 mg (0.08 mmol) $(NH_4)_8H_2W_{12}O_{41}$ und 1.5 ml 25 %ige Essigsäure. Die Reaktionstemperatur betrug 200 °C. Variiert wurde die Zugabe des Alkaliions. Jeweils 1 mmol des entsprechenden Alkalichlorids (Li, Na, K, Rb, Cs) wurden den entsprechenden Reaktionsansätzen zugesetzt.

Die Produktbildung setzt ca. nach 20 Minuten ein, kristalline Intermediate werden nicht beobachtet (Abb. 4.16, links). Einen Einfluss der Alkaliionen auf den Reaktionsmechanismus konnte nicht festgestellt werden, der Verlauf der SH-Plots ist identisch. Der Vergleich mit theoretischen Modellen deutet auf einen nukleationskontrollierten Mechanismus hin.

Deutliche Unterschiede sind hingegen bei der Induktionszeit und der totalen Reaktionszeit zu beobachten (Abb. 4.6, rechts). Allgemein lässt sich sagen, dass die Anwesenheit von Alkaliionen die Reaktionsdauer verkürzt. Bei der Induktionszeit hingegen kommt es zu unterschiedlichen Effekten: Die Anwesenheit von Na oder K verzögert den Reaktionsstart, während die Präsenz von Li, Rb oder Cs eine verkürzte Induktionszeit bewirkt.

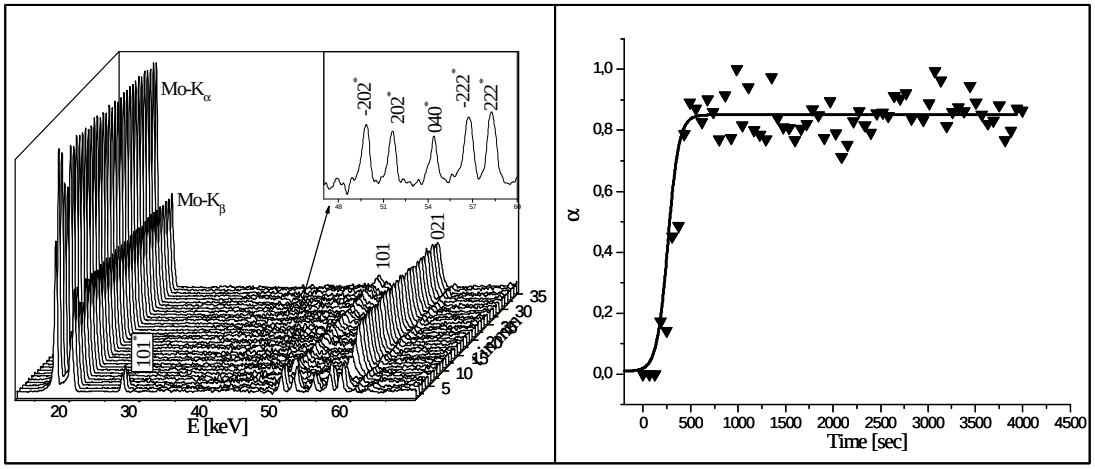

Abbildung 4.15: Zeitaufgelöstes Pulverdiffraktogramm bei 90 °C; Einschub zeigt vergrößert die indizierten Eduktreflexe (links), Reaktionsverlauf (rechts)

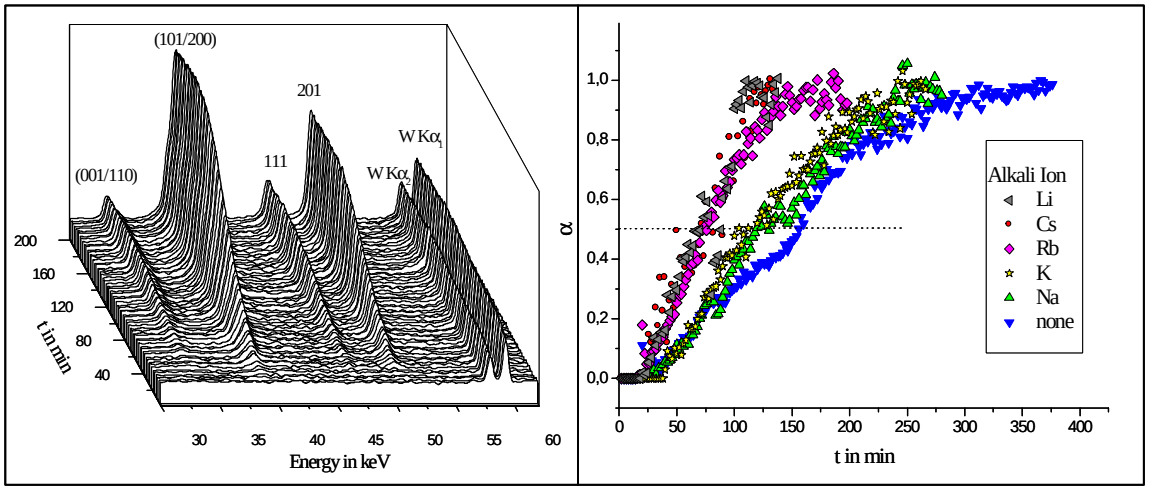

Abbildung 4.16: Zeitaufgelöstes Pulverdiffraktogramm bei 200 °C in der Gegenwart von Rb (links), Einfluss der Alkalikationen auf den Reaktionsverlauf (rechts)

1. Introduction

Tungsten bronzes (M_xWO_3) and tungsten oxides ($M_xWO_{3+x/2}$) have attracted considerable interest due to their interesting chemical, electrochemical and electronic properties.[1] Hence, they are promising materials for applications as active electrodes, e.g. in electrochromic devices, in large scale static displays[2] and in catalysis.[3] The open structures of tungsten bronzes and oxides readily incorporate cations, such as hydrogen or lithium, so that the modification of the host tungstate framework opens up new options for synthesizing tailor-made materials.[4]

Three main types of $M_xWO_3/M_xWO_{3+x/2}$ (M = H, NH_4, Li – Cs) tungsten oxide frameworks have been described: the cubic form, the hexagonal tungstates (HTB) and the pyrochlore (P) type. The majority of the $M_xWO_{3+x/2}$ tungsten oxides adopts either the HTB or in the P form. Both structure types contain tunnels: in the HTB phase, the one-dimensional tunnels run along the c-axis, whereas they intersect in a three-dimensional fashion in the P type.[1, 5] Consequently, the two phases exhibit different intercalation behavior and reactivity: the P type preferably hosts the larger cations (Rb, Cs)[6, 7], readily intercalates lithium cations and exhibits an active redox chemistry.[8] A 2D-variation of the P-type has been reported for $xMO \cdot WO_3$ (M = Tl, Ba, Pb) systems.[9] The HTB $M_xWO_{3+x/2}$ tungsten oxides are less prone to ion exchange processes, but more suitable for lithium intercalation. Their redox chemistry ($M_xWO_3 \leftrightarrow M_xWO_{3+x/2}$) involves the diffusion of oxygen atoms in and out of the hexagonal channel systems so that they must move around the incorporated alkali cations.[10] The latter can either be located in the hexagonal cavity or in the preceding window site of the hexagonal tunnel. Depending on the size and on the amount of the incorporated cations, two different structural models have been proposed. Sodium cations are too small to stabilize the HTB framework at higher temperatures, and they are situated in the hexagonal channel windows of HTB-$Na_xWO_{3+x/2} \cdot nH_2O$ where they are "sandwiched" by H_2O molecules (or hydroxyl ions).[10, 11] Larger cations (M = K – Cs) can only be incorporated into the hexagonal tunnels of HTB-$xM_2O \cdot WO_3$ on two suitable sets of positions so that the maximum extent of cation incorporation should be limited to $x \leq 2/9$. However, higher contents are often analytically determined, and they are explained in terms of a tungsten vacancy model ($M_xW_{1-y/6}O_3$, with $y = 6x/(6+x)$).[9, 12, 13]

HTB- and P alkali tungsten oxides have preferably been accessed through soft chemistry routes (Table 1), but considerably less is known about their transformation upon the nanoscale.[14, 15, 16, 17, 18] In order to address a specific structure type, a careful adjustment of the cation size, the synthetic parameters (especially the pH value) and the precursor material is required (Table 1). The resulting structure type strongly depends upon the tungstate species present in solution. Their kinetic study is demanding, because the reaction equilibria involved cover an extremely wide range of reaction rates. Therefore, the preparation of nanoscale HTB/P-tungsten oxides is a challenging task, and in the following, we present a convenient hydrothermal pathway to access anisotropic and nanostructured hexagonal tungstates.

Starting from our previous work on the synthesis of nanoscale ammonium pyrochlore tungstates from ammonium metatungstate (AMT: $(NH_4)_6[H_2W_{12}O_{40}]\cdot 2H_2O$),[19] we have systematically studied the hydrothermal formation of nanoscale alkali tungsten oxides in MCl/AMT-systems (M = Li – Cs) with respect to morphochemistry and kinetics. To the best of our knowledge, a comprehensive morphological study of the alkali tungsten oxides has never been undertaken. As little is known about alkali tungstate formation upon microwave irradiation,[20] selected MCl/AMT-systems were investigated under microwave-hydrothermal conditions.[21] Furthermore, we evaluate the kinetics of nanoscale alkali tungstate formation using both in situ-EXAFS and EDXRD.[22]

2. Experimental

Standard hydrothermal conditions. The following standard hydrothermal procedure was applied for the preparation of alkali/ammonium tungstates from ammonium metatungstate (AMT: $(NH_4)_6[H_2W_{12}O_{40}]\cdot 2H_2O$): 248 mg AMT (1 mmol W), 2 mL 25 Vol.% acetic acid (HAc) and 2 mmol MCl (M = Li – Cs) were added to a Teflon-lined stainless-steel autoclave with a capacity of 23 ml. The autoclave was then sealed, heated for 2 d at 180 °C, and subsequently cooled to r.t. The resulting precipitate was collected by filtration, washed with distilled H_2O, EtOH, and Et_2O or acetone and dried in air.

Microwave-hydrothermal experiments. The microwave-hydrothermal (M-H) experiments were performed using a MARS5 (CEM Corp., Matthews, NC) microwave digestion system. The microwave system operates at a frequency of 2.45 GHz with a

maximum power of 1200W. The experiments were carried out in double-walled digestion vessels having an inner non-reactive Teflon PFA liner and an outer Ultem polyetherimide shell of high mechanical strength. Temperature and pressure probes allow the reaction to be controlled by monitoring the temperature and pressure within a control vessel. The maximum operating temperature and pressure for the system are 240°C and 350 psi, respectively. In a typical procedure, 248 mg AMT (1 mmol W, 5 mL 25 Vol.% acetic acid (HAc) and 1 mmol or 5 mmol MCl (M = Li – Cs)) were treated for 4 hours at 180 °C using the above microwave digestion system.

Analytical methods. X-ray powder diffraction analyses were conducted on a STOE STADI-P2 diffractometer in transmission mode (flat sample holders, Ge monochromated $CuK_{\alpha 1}$ radiation) equipped with a position-sensitive detector (resolution ca. 0.01° in 2θ). For scanning electron microscopy (SEM), performed on a LEO 1530 (FEG) microscope with 1 keV electrons, samples were dispersed in ethanol and subsequently deposited on a silicon wafer. A CamScan CS-44 electron microscope with an EDAX-Phoenix energy-dispersive X-ray spectrometer (EDXS) was employed for approximate elemental analyses. The scanning transmission electron microscopy (STEM) image was recorded on a Philips Tecnai 30F microscope, operated at 300 kV (field emission cathode). In the STEM mode, the electron beam was placed on a selected spot, and an elemental analysis by energy-dispersive X-ray spectroscopy (EDS, EDAX detector) was performed there. FTIR spectra were recorded on a Perkin-Elmer Spectrum 2000 FTIR spectrometer in the range from 500 to 4000 cm^{-1}. C, H, and N analysis was carried out by means of combustion test methods on a LECO CHN-900. Alkali contents were determined by laser ablation inductively coupled plasma mass spectroscopy (LA-ICP-MS). Laser ablation sampling was performed using an ArF 193 nm excimer laser (GeoLas Q, MicroLas, Göttingen, Germany) which was coupled to an ICP-MS instrument (Elan 6100 DRC+ Perkin Elmer, SCIEX, Concord, Ontario, Canada).

In situ EXAFS experiments. The *in situ* X-ray absorption spectroscopy experiments were performed at ANKA-XAS using an EXAFS cell that allows monitoring both the bottom and the middle of the autoclave cell up to 200 bar and 200 °C.[23] The cell was equipped with a PEEK-inlet and the penetration length was about 5 mm through the solution. A Si(111) double crystal monochromator was used and higher harmonics were

effectively removed by detuning of the crystals to 70% of the maximum intensity. Three ionization chambers before and after the in situ cell and a reference foil for energy calibration were used for the incident and outcoming X-ray intensities. The beam size was cut to 5 x 1 mm and the in situ batch reactor cell aligned using the x,z,θ-table. The EXAFS scans around the W L_3-edge were recorded between 10.05 and 11.8 keV under stationary conditions (liquid solution and solid material) and calibrated using the W reference foil. Faster spectra during the change of the reaction conditions were recorded around the W L_3-edge. The raw data were background corrected, normalized and Fourier transformed using the WINXAS 3.0 software.[24] The experiment was performed in the following way: The spectroscopic cell was filled with 3 ml of a solution of AMT in 25 Vol.% HAc (0.05 M in W), closed and heated to 200 °C stepwise. Then the hydrothermal reaction was performed over a time period of 4 h at 200 °C, cooled down and the material was analysed by EXAFS, XRD and SEM. A second experiment was analogously performed, adding CsCl (0.1 mol/l).

In situ EDXRD experiments. The in situ energy dispersive X-ray diffraction experiments were performed at HASYLAB Beamline F3 that received white synchrotron radiation from a bending magnet with a critical energy of 16 keV (DORIS ring with positron beam energy of 4.5 GeV). An energy range from 13.5 to 65 keV can be observed with a maximum at about 20 keV. The diffracted beam is monitored by a nitrogen cooled solid state germanium detector. The detector angle was chosen so that all important Bragg reflections can be detected. The d-spacing range is given by $E = 6.199/(d \cdot \sin\theta)$. With a detector angle of approximately 1.90° the observable d-spacing range is 2.9 Å to 13.8 Å. The energy resolution $\Delta d/d$ is about 10^{-2} above 26 keV. The beam was collimated to 0.2 mm giving the best results. A more detailed experimental description can be found in the literature.[25, 26] For the in-situ investigations autoclaves with glass liners with an internal diameter of 10 mm and a volume of 10 ml were used. They were filled with 1.5 ml of a solution of AMT in 25 Vol.% HAc (0.67 M in W) and 1.5 mmol MCl (M = Li – Cs), closed and heated to 200 °C.

3. Experimental Results

3.1. Hydrothermal Synthesis

As outlined in the introduction, the alkali tungsten oxide type emerging from a given hydrothermal reaction is a function of the cation radius and of the synthetic conditions. In the MCl/AMT/HAc (M = Li – Cs) systems, the ammonium cations of the AMT precursor may be incorporated into the newly formed hexagonal tunnels in addition to the alkali cations. Extensive optimization experiments aiming for phase pure nanoparticles exhibiting uniform morphologies with large aspect ratios (if applicable) were conducted starting from a setpoint of hydrothermal reference parameters (cf. Experimental). For hydrothermal experiments conducted in acetic acid solutions, the initial and final pH values are in the range of 2 – 3. When H_2O is used instead of acetic acid, the initial pH is between 5 and 6. Room-temperature precipitation experiments in the CsCl/AMT/HAc- and CsCl/AMT/H_2O systems led to the formation of the Keggin cluster compound $Cs_6[H_2W_{12}O_{40}]\cdot 2H_2O$. We will discuss its crystal structure elsewhere which is one of the rare examples of a homonuclear alkali Keggin compound.[27] Its presence indicates that the Keggin cluster anion, $[H_2W_{12}O_{40}]^{6-}$, is the predominant species in solution. Figure 1 illustrates the influence of the reaction parameters upon the morphology of the emerging nanoscale tungstates: the particle shape can be most conveniently addressed by adjusting the concentration of the precursor material. Furthermore, variations in pH and reaction time affect the particle morphology. Therefore, the kinetics of the transformation of AMT into HTB tungsten oxides has been investigated with the help of ex situ and in situ experiments (section 3.4. – 3.5.).

3.1.1. Role of the alkali cations: structural and analytical chemistry

Table 2 provides a summary of the hydrothermal parameter study in the MCl/AMT-systems: the smallest cation, Li^+, supports the formation of orthorhombic (O) lithium tungstates only under special conditions (cf. 3.1.2.), and the HTB phase generally prevails in the MCl/AMT (M = Li – K)-systems. Note that the crystallinity of the products considerably decreases in the presence of potassium cations, as has been observed in previous studies. Among the MCl/AMT (M = Rb, Cs) systems, the reaction conditions must be optimized to obtain phase pure HTB- or P alkali tungstates. As expected, the latter tungstates are preferably formed in the presence of the larger Cs^+

cation. The larger the cation, the more pronounced its stabilizing influence upon the tungstate channel system: a competitive experiment involving the simultaneous reaction of AMT with equimolar amounts of the entire MCl series (M = Li – Cs) led to the exclusive incorporation of Cs^+ into HTB-$Cs_{0.27}W_{0.957}O_3 \cdot nH_2O$.

The fraction of ammonium cations incorporated into the HTB alkali tungstates depends on the size of the alkali cation. According to elemental analyses, the Li- and Na-HTB systems readily incorporate ammonium cations, whereas the potassium compounds take up only a minimal fraction of NH_4^+. The Rb- and Cs-HTB phases are practically ammonium-free. The water content of the samples follows the same trend and decreases from the Li- to the Cs-HTB tungsten oxides. The results are in line with the IR spectra of the HTB alkali tungstates (Figure 2 a): the intensity of the NH_4^+ bending vibration around 1400 cm^{-1} decreases from the Li- to the Cs-HTB tungstate and so does the OH bending vibration around 1600 cm^{-1}. The narrow OH bending vibrations for Li- and Na-HTB indicate the presence of structural water molecules. LA-ICP-MS techniques (cf. Experimental) were employed for the determination of M:W (M = Li – Cs) ratios, and the ranges for the individual cations are displayed in Figure 2 b. Li^+ and Na^+ can be substituted by NH_4^+ over a wide compositional range, and most of the alkali tungstates exceed the limiting M:W ratios of 0.17:1 (M = Na) or 0.22 : 1 (M = K – Cs), respectively, for the incorporation of cations into the hexagonal tunnels (cf. representative compositions: Table 2). Therefore, they are described in terms of the above-mentioned tungsten vacancy model.

3.1.2. Role of the alkali cations: morphology

The alkali cations do not only exert a structure-directing effect, but they also lead to characteristic nanoscale morphologies of the alkali tungstates (Table 2). Reference hydrothermal experiments in the AMT/HAc-system afford HTB-$(NH_4)_{0.26}W_{0.958}O_3 \cdot nH_2O$ nanorods (cf. Figure 9 a), whereas the smaller cations (M = Li – K, NH_4) lead to the formation of fibrous HTB tungstates with microscale lengths and diameters around 100 nm. Maximum aspect ratios are obtained in the presence of sodium cations. The larger cations (M = Rb, Cs) yield nanoscale hexagonal phases consisting of small, stacked nanorods that tend to arrange into hierarchical patterns (Table 2).

In Table 3, the change in morphology induced by selected parameter variations is compared to the results obtained under standard conditions (cf. Experimental). Selected hydrothermal parameters were optimized to improve the morphological uniformity and the aspect ratio of the emerging hexagonal tungstate particles. As summed up in Figure 1, low initial AMT concentrations and the replacement of acetic acid by H_2O exerted the most significant influence on the tungstate morphology.

LiCl/AMT: Figure 3 illustrates how the aspect ratio of Li-HTB nanorods obtained under standard conditions (a) can be enhanced in the presence of low tungstate concentrations (b). Further dilution of the precursor material (c) leads to the formation of orthorhombic lithium tungstate with a flower-like growth pattern that is characteristic of orthorhombic tungstates (cf. the morphology of orthorhombic ammonium tungstates, Figure 8 a). The small nanorods emerging from the surface of the μm-sized "flower leaves" might exhibit a hexagonal structure, because the broadened reflections in the XRD patterns of nanoscale O- and HTB-tungstates differ only with respect to an additional reflection at 2θ = 18° in the orthorhombic phase.[28] The precipitation of orthorhombic (1.03-1.32)$Li_2O{\cdot}WO_3{\cdot}$(0.74-0.99) H_2O from tungstate solutions (Table 1) has been reported, but no further morphological information has been given.

NaCl/AMT: Under standard hydrothermal conditions, the morphology of Li- and Na-HTB tungstate nanorods is almost identical (Figures 3 a, 4 a). However, low tungstate concentration affords Na-HTB tungstate rods in the NaCl/AMT/H_2O system with microscale lengths and diameters around 100 nm (Figure 4 b). Their aspect ratio can be maximized when the tungstate concentration is decreased to 0.007 M (Figure 4 c – d).

KCl/AMT: Although the KCl/AMT/H_2O system provides well-developed nanorods with aspect ratios similar to those obtained from NaCl solutions (cf. Figures 4 and 5), the XRD patterns of the products reveal that they are almost amorphous and the yields are considerably lower than in the sodium-based systems. Tungsten concentrations lower than 0.07 M did not afford an increase in aspect ratio or crystallinity.

RbCl/AMT systems: The presence of the larger rubidium cations induces a significant morphological change: Rb-HTB tungstates are obtained as cylindrical stacks consisting of small nanorods (Figure 6, Table 2). They tend to agglomerate under standard conditions (Figure 6 a). Their intergrowth can be reduced by applying a low initial

tungstate concentration (c(W) = 0.007 M) in H_2O (Figure 6 c). Unlike in the Na- and K-based systems, the aspect ratio of the hierarchically grown nanorods remains unchanged upon precursor dilution.

Cs/AMT systems: The morphology of Cs-HTB tungstates is similar to their Rb-analogues, except for a strong tendency of the individual cylinders towards the formation of hierarchically structured microspheres (Figure 6 c). Under standard hydrothermal conditions, they are formed together with pyrochlore caesium tungstates that exhibit a characteristic microscale cubic morphology (Figure 6 d). Up to now, only few synthetic approaches towards phase pure Cs-HTB tungstates are known (cf. Table 1). In this study, we present a new hydrothermal pathway to phase-pure nanostructured hexagonal cesium tungstates. They can be obtained from the CsCl/AMT/HAc system with initial tungsten concentrations around 0.007 M (Figure 6 f).

The formation of phase pure Cs-HTB from low AMT concentrations agrees well with previous studies on the reaction of ammonium paratungstate (ATP: $(NH_4)_{10}W_{12}O_{41}\cdot 5H_2O$) under reflux conditions in acetic acid/ethylene glycol/ethanol media. The formation of HTB- and P phases depends on the solubility of the ATP precursor: when the precursor material is dissolved completely before the reaction is started, the HTB-ammonium tungstate is formed, whereas an immediate reaction without previous dissolution of ATP leads to the formation of the P-ammonium tungstate. Consequently, the partial dissolution of ATP leads to a mixture of both phases.

Alkaline earth cations: Although a new 2D pyrochlore type has been proposed for Tl-, Ba- and Pb-tungstates, screening experiments in the $BaCl_2$/AMT/HAc system only brought forward a Ba-HTB phase with no distinct morphological features. Previous experiments in the presence of Sr^{2+} failed to afford Sr-based tungstates. Nevertheless, hydrothermal reactions with low tungstate concentrations (c(W) = 0.07 M) in the $SrCl_2$/AMT/HAc system have now brought forward the first Sr-HTB tungstate (Figure 7). The new compound forms microspheres with diameters of 3 – 6 μm that are hierarchically sub-structured into rods with an average diameter of 100 nm (Figure 7, left, bottom). The presence of strontium in the individual rods has been verified in terms of EDX spot analyses (Figure 7, right). Elemental analyses indicate the presence of ammonium cations in addition to Sr^{2+}.

3.2. Microwave-Hydrothermal Experiments

In order to investigate the influence of microwave-hydrothermal conditions on the phase and on the morphology of the emerging tungstates, we have conducted experiments in the AMT/HAc reference system and in the MCl/AMT/HAc (M = Li, Rb - Cs) systems at low and high M : W ratios (1 : 2 and 5 : 1). The emerging phases and their morphological features are summed up in Table 4.

AMT/HAc reference system: Whereas the conventional-hydrothermal synthesis led to the formation of HTB-$(NH_4)_{0.26}W_{0.958}O_3 \cdot nH_2O$ nanorods from AMT (Figure 8 a, Table 2), microwave-hydrothermal treatments afforded an orthorhombic tungsten oxide, O-$(NH_4)_{0.03}W_{0.995}O_3 \cdot 0.47\ H_2O$ (Figure 8 b), with an XRD pattern that is closely related to orthorhombic $WO_3 \cdot 0.33H_2O$. O-$(NH_4)_{0.03}W_{0.995}O_3 \cdot 0.47\ H_2O$ was formed quantitatively as characteristic microflower-like aggregates (diameters around 4 μm) consisting of hierarchically arranged nanosheets with a thickness of 100 nm and below. Previous conventional-hydrothermal syntheses of $WO_3 \cdot 0.33H_2O$ had demonstrated that a rather narrow temperature window (< 120 °C) must be maintained for its formation. Furthermore, previous work has shown that the emerging morphology is very sensitive towards the preparative conditions: the hydrothermal reaction of pre-treated tungstic acid gel under N_2/O_2 atmosphere yielded micrometer-sized needle aggregates of $WO_3 \cdot 0.33H_2O$, whilst the hydrothermal treatment of ripened $WO_3 \cdot 2H_2O$ provided microscale octagonal platelets of $WO_3 \cdot 0.33H_2O$. Therefore, the microwave-hydrothermal approach is a novel and efficient pathway to obtain nanostructured orthorhombic tungstates in gram quantities.

LiCl/AMT systems: Microwave-hydrothermal treatment at low Li : W ratios did neither affect the phase nor the morphology of the emerging Li-HTB tungstates (Figure 9 b) with respect to conventional-hydrothermal reference experiments (Figure 5 a). The lithium content of the products has been determined as $Li_{0.10}W_{0.98}O_3 \cdot yH_2O$, and it is in the range of the (Li:W)-ratios obtained from conventional hydrothermal experiments. When a M:W ratio of 5 : 1 was applied, however, the orthorhombic phase was formed. It exhibits the same hierarchically structured microflower morphology that has been observed in the AMT/HAc system (Figure 8 b), whereas a conventional-hydrothermal reference

experiment in the presence of excess LiCl at the given tungsten concentration afforded Li-HTB nanorods. The morphology of the orthorhombic lithium tungsten oxide grown under microwave-hydrothermal conditions differs considerably from the particle shape of orthorhombic lithium tungstates obtained under conventional-hydrothermal conditions (Figure 3 c – d). Despite the high Li:W-ratio in the starting material, the lithium content of the flower-like orthorhombic tungstate was determined as $Li_{0.02}W_{0.997}O_3 \cdot nH_2O$, thereby pointing to a limited lithium uptake of the orthorhombic phase.

CsCl/AMT systems: Whilst the RbCl/AMT/HAc systems showed little response towards microwave-hydrothermal treatments, they drastically altered the course of the reaction in the CsCl/AMT/HAc system at low Cs : W ratios (Table 4, Figure 10 a). Instead of the expected Cs-HTB- or Cs-P tungstates, microcrystals of a hitherto unidentified cesium tungstate were the main product resulting from the microwave-hydrothermal reaction. The XRD pattern of the product resembles $7Li_2WO_4 \cdot 4H_2O$,[29] and hierarchically structured cesium tungstate microspheres are formed as a side product. Their fraction falls below the detection limit of the XRD method. However, Cs-HTB tungstate with a similar substructured spherical morphology were obtained from microwave-hydrothermal treatments in the presence of excess CsCl (Figure 10 b, Table 4). Therefore, microwave-hydrothermal syntheses are an elegant option to cut short the optimization work that is required to set up a soft chemistry route to nanostructured, phase-pure Cs-HTB tungstate.[12]

In summary, microwave-hydrothermal techniques are a straightforward and effective method to expand the product spectrum of nanostructured alkali/ammonium tungstates.

3.3. Conventional-Hydrothermal Synthesis: Influence of the Reaction Time

In order to gain a deeper understanding of the role of the reaction time and of the course of the reaction, selected MCl/AMT systems were subjected to hour-scale reaction times (standard reaction time = 2 d, cf. Experimental) or to 18 d-hydrothermal treatments. The resulting phases and morphologies are summed up and compared to reference experiments (standard conditions: 2 d) in Table 5.

Short-time experiments: The quantitative conversion of AMT into M-HTB tungstates in the presence of the smaller cations (M = Li - Na) is finished after 2 – 4 h of hydrothermal

treatment. However, the morphology of the products still exhibits a considerable degree of agglomeration (Table 5, Figure 11 a) so that longer reaction times are required to obtain separate rod-shaped particles.

Long-time experiments: Generally, the typical morphology of the nanostructured alkali tungstates remains unchanged after 18 d of hydrothermal treatment (Table 5). No particle ripening or further agglomeration is observed. Figure 12 illustrates this trend for orthorhombic lithium tungsten oxides (cf. Figure 3 c – d) and for Cs-HTB tungstates (cf. Figure 7 d – f). Elongated reaction times enhance the crystallinity of most products. As a result, the potassium tungstate fibers are no longer amorphous (cf. above), but they display two sharp, prominent reflections around $2\theta = 23°$ and 47°. These are typical (00l) or (h00) reflections for several tungsten oxide hydrates, so that the structure of the potassium tungstate nanorods emerging after 18 d of hydrothermal treatment may contain a layered motif. Note that a hypothetical lamellar compound represented as $K^+[K_5W_{18}O_{57}]^-$ would be formed if every seventh layer of a $K_{1/3}WO_{3+1/6}$ tungstate were vacant and potassium cations were inserted instead.

3.4. Time-dependent conversion of AMT into nanoscale tungstates: in situ EXAFS and ex situ quenching experiments

Next, the timescale of tungstate formation was estimated more precisely with the help of ex situ quenching experiments performed in the AMT/HAc- and CsCl/AMT/HAc systems. In addition, the time-dependent formation of nanoscale tungstates was studied with in situ EXAFS experiments performed in an EXAFS cell that is similar to an autoclave with PEEK inlay (cf. Experimental).[30, 31, 22, 23] Due to the similar local environment of tungsten both in the AMT precursor and in the HTB-tungstates, EXAFS spectra were required to uncover the structural transformations. All products emerging from in situ EXAFS experiments were subsequently characterized in terms of XRD patterns and SEM images (cf. Figures 13 and 15).

3.4.1. Timescale of hexagonal tungstate formation in the AMT/HAc system

The ex situ experiments in the AMT/HAc system starting from low tungsten concentrations (0.05 M) reveal that the conversion of AMT into the rod-shaped

hexagonal tungstate phase is in progress between 1 and 2 h of reaction time (Figure 13). After 1 h, the surface of the starting material exhibits the first onset of nanostructuring (Figure 13 a (top)), but the small amount of material formed was not sufficient for XRD analysis. The formation of nanorods sets in around 2 h (Figure 13 b (top)), and the XRD pattern indicates that AMT has been converted into the hexagonal tungstate phase in the presence of amorphous residual material. Prolonged hydrothermal treatments (2 d) are required to finalize the growth process of the nanorods and to improve the crystallinity of the final product (Figure 13 d).

In situ EXAFS investigation of the AMT/HAc system with a tungsten concentration of 0.05 M in the starting material revealed that during stepwise heating to 200 °C, no changes at all – neither in the XANES nor in the EXAFS region – were detected, indicating that the symmetry around the W absorber atom did not change and no solid materials were formed. At 200 °C, only after more than 2 hours a change both in the XANES and in the EXAFS spectrum was observed, indicating the onset of the reaction (Figure 14). After 4 h, phase pure HTB-tungstate nanorods were formed (Figure 13 c). These observations agree well with the ex situ experiments, but may be slowed down due to the lower concentration of AMT in the solution. Note the significant difference to the previously reported XANES/EXAFS data on the formation of MoO_3 nanorods: in this hydrothermal system, the structural changes occurred more rapidly. Since the local environment of tungsten changes only slightly, more detailed EXAFS spectra were required here.

3.4.2. Reaction timescale in the CsCl/AMT/HAc system

The ex situ kinetic experiments in the CsCl/AMT/HAc system demonstrate that the reaction timescale is not significantly altered when the tungsten concentration in the system is kept at 0.05 M and CsCl is added (1 M). Like in the AMT/HAc system, very little amounts of product exhibiting surface nanostructuring precipitate after 1 h (Figure 15 a, top), and the XRD pattern recorded after 2 h of reaction time indicates the presence of phase pure Cs-HTB tungstate and amorphous residues. After 2 d of reaction time, the starting material has been quantitatively converted into hierarchically structured

microspheres (Figure 15 c). As outlined above, their crystallinity and morphology is further improved by 18 d-treatments (Figure 15 d).

The addition of CsCl had no effect on the respective in situ EXAFS experiments as well: at 200 °C, no products were observed before an induction time of 2 h so that the AMT/HAc and the CsCl/AMT/HAc systems display similar kinetics. Figure 15 b shows that phase-pure Cs-HTB tungstate has been formed after a reaction time of 4 h in the in situ EXAFS cell (bottom) and that the characteristic stacked nanorods are beginning to emerge (top). In both systems investigated, only small changes occur during cooling from 200 °C to room temperature. Their reaction kinetics proceed on an hour scale, and they differ considerably from the previously studied hydrothermal synthesis of MoO_3 nanorods.[22, 23]

3.5. Time-dependent conversion of AMT into nanoscale tungstates: in situ EDXRD investigations

Ex situ experiments conducted at higher tungsten concentrations (0.67 M) in the AMT/HAc system indicated that the conversion of the starting material into nanoscale tungstates begins after approx. 19 min. This observation points to a quicker onset than has been observed for lower tungsten contents in the starting material (cf. 3.4.). Generally, the product formation under solvothermal conditions depends on several experimental parameters, e. g. pH-value, temperature, volume, pressure and/or kind of educt source.[25, 26, 32] In the previous section it was clearly demonstrated that the presence of the alkali cation significantly influences the morphology of the reaction product. Therefore, the influence of these ions onto the kinetics and the mechanisms of crystal growth are studied with in situ EDXRD experiments starting from tungsten concentrations of 0.67 M at a reaction temperature of 200 °C. In the energy range chosen several reflections of the product and the W resonances are monitored simultaneously (Figure 16). A typical sequence of time resolved spectra is shown in Figure 16. After an induction time t_{ind} that depends on the kind of the alkali ion, the product peaks of the hexagonal tungstate phase start to grow. Note that the W resonances at 57.98 and 59.31 keV are immediately visible in the spectra. The product peak with the highest intensity is the (200) reflection. A quantitative analysis of the growth rates shows identical behaviour

for different reflections and confirms an isotropic crystallite growth. No hints are seen in the spectra for the occurrence of crystalline precursors or intermediates.

The integrated intensities of the product reflections were normalized against the intensity of the most intense W K_α resonance. The plots of the extent of reaction α (ratio of the normalized intensity at the reaction time $\boldsymbol{t}$ by the intensity at the time $\boldsymbol{t_\infty}$) against the reaction time $\boldsymbol{t}$ (Figure 17) demonstrate that $t_{\boldsymbol{ind}}$ and $\boldsymbol{t_{0.5}}$ depend on the kind of the alkali ion. In general, the presence of alkali ions leads to a decrease of the reaction time, i.e. the chemical reaction is faster with M^+ ions. Interestingly, the presence of Na^+ and K^+ ions first delays the beginning of the reaction (t_{ind} increases) but the overall reaction time is shorter than without these ions. In contrast, the presence of Li^+, Rb^+ or Cs^+ reduces both t_{ind} and the half-life time significantly (Table 6).

The morphology of the products formed in the course of in situ EDXRD experiments was investigated in terms of SEM images recorded after the reaction. As has been observed for the ex situ experiments mentioned above and for the in situ EXAFS studies (cf. Figures 13 and 15), all products show the onset of nanostructuring, but longer reaction times are required to fully develop the characteristic particle morphologies depending on the cation (Figures 3 – 6).

Kinetic analysis. Kinetic studies are useful because quantitative information such as half-life and rate constants can be evaluated. In addition, information about the reaction mechanism is acquired. Kinetic analyses are performed by fitting the experimental data to a theoretical expression relating the extent of reaction α vs. time. Several kinetic expressions applied to solid state kinetics have been reported, and the general shape of their curves is well documented. A detailed description of evaluation of data has been provided in the literature. The kinetic evaluation was performed after subtracting the induction time t_0 from time t. The kinetic data for different reactions are summarised in Table 6. When $\ln[-\ln(1-\alpha)]$ versus $\ln(t)$ is plotted (the so called Sharp-Hancock plot, abbreviated SH) a straight line is obtained for that part of the reaction which follows the same mechanism.[33] A change in the mechanism during the reaction leads to a change in the slope of the curve. From the slope of the linear part of the curve the reaction exponent m can be evaluated. The Avrami exponent m is the related to the type of nucleation and growth process taking place, including the morphology of the reaction product, i.e.

whether the crystals are fibres, needles, plates, sheets, spheres or polygons. The exponent *m* also includes the type of nucleation, i.e. whether the nuclei all develop at once or there is a continuous nucleation with a constant rate.[34, 35] While the induction times and half-life times depend on the presence of the alkali ion, no influence onto the reaction mechanism is observed. A typical SH-plot is shown in Figure 18. The experimental points are on a straight line over the whole reaction indicating that there is no change of the reaction mechanism. The reaction exponent *m* has a value of ~ 1.5 (Table 6) which is in the region of values for phase boundary control and nucleation controlled growth mechanism (Table 7, mechanism A2, m = 2).

For more detailed and rigorous analyses all models listed in Table 7 were compared with the experimental data.[36] For a decision what model is most appropriate the experimental $t/t_{0.5}$ data ($t/t_{0.5}$ is the reaction time at $\alpha = 0.5$) are plotted vs. α. The result is shown in Figure 19 and the procedure allows a direct comparison with the different models under consideration. For all reactions the experimental data fit with a nucleation control (model A2, Table 7) confirming the results from the above discussed SH-plots.

4. Discussion

The structure and morphology of nanoscale tungstates generated from hydrothermal processes depends on the synthetic conditions and on the cations incorporated into the parent tungstate framework. In the MCl/ammonium metatungstate (M = Li – Cs) hydrothermal systems, the Li-, Na- and K-based compounds adopt the hexagonal tungsten bronze (HTB) structure, whereas the presence of Rb^+ and Cs^+ gives rise to both HTB and pyrochlore tungstates. The phase preferences[8] of the individual cations are accompanied by specific morphological profiles: the HTB phases containing lithium, sodium or potassium exhibit an anisotropic, rod-shaped morphology. Among them, the hexagonal sodium tungstates display maximum values of the aspect ratio. Contrary to the fibrous materials obtained with the smaller alkali cations, the rubidium- and cesium-based HTB particles exhibit a hierarchical growth pattern of small nanorods that are stacked into cylindrical arrangements.

The preparative options provided by the alkali chloride-additives can be applied upon the quick and efficient microwave-hydrothermal production of nanoscale alkali tungstates,

e.g. to cut out the optimisation work required to generate phase pure nanoscale Cs-HTB tungstates. This method furthermore provides access to flower-like nanostructured orthorhombic tungstates when applied in the absence of alkali cations. Interestingly, the orthorhombic phase can as well be formed with an excess of LiCl in the reaction medium, while lower Li:W ratios lead to the microwave-hydrothermal formation of Li-containing HTB nanorods. However, the orthorhombic tungstates take up only negligible amounts of lithium cations so that their formation might be due to a surface effect of Li^+, thereby rendering it an "additive" in the true sense of the word.

Ex situ- and long time-experiments in the MCl/ammonium metatungstate (AMT; M = Li – Cs) hydrothermal systems point out that the kinetics of nanoscale tungstate growth are generally slower than those observed for the hydrothermal formation of MoO_3 fibers. This was verified by a combined in situ EXAFS/EDXRD study: firstly, the conversion of ammonium tungstate into ammonium- and cesium-containing HTB nanorods, respectively, was studied for low AMT concentrations. Under the given conditions, the onset of product formation was observed after approx. 2 h. Furthermore, additional ex situ experiments indicated that the kinetics of HTB nanorod formation might be concentration-dependent. As in situ EDXRD methods are better suited for the study of tungstate growth at higher tungsten concentrations, they were subsequently employed to investigate the influence of the alkali cations on the kinetics of the reaction. For a complete monitoring of the structural changes occurring during the transformation of the AMT precursor into hexagonal tungstates, both in situ XANES and EXAFS methods are required. Whereas the induction times (10 – 30 min.) vary with the alkali cation, all of them accelerate the conversion of AMT into nanoscale tungstates. Nevertheless, the alkali-based hydrothermal processes still take more than an hour to completion, and at least 2 d of further treatment are required to obtain a fully developed anisotropic morphology. Note that the tendency towards nanofiber formation is most pronounced with Na^+ and K^+ that exhibit the longest induction times. In spite of their different induction times, the alkali cations generally support a nucleation controlled growth mechanism. The nucleation control might account for the longer onset times observed for lower AMT concentrations in the in situ EXAFS experiments: all in all, both in situ approaches demonstrate that the hour-scale kinetics of ammonium tungstate formation is

slow in comparison with the hydrothermal preparation of MoO_3 rods that is quantitatively finished after 15 min. However, the morphology of the MoO_3 rods cannot be controlled with the help of alkali cations to a comparable extent.[37]

Conclusion. The present study outlines how the one-step hydrothermal formation of nanoscale tungstates can be accessed by alkali halides to generate alkali HTB tungstates with various morphologies. A systematic hydrothermal field study has been conducted to track down the optimal parameter windows for the different product types. Their formation process has been explored with a combination of in situ EXAFS and EDXRD methods so that key mechanistic and kinetic information is now available to fine-tune the synthetic protocol for further applications. The presence of alkali cations speeds up the hydrothermal process. Although they all support a nucleation control mechanism for the formation of nanoscale hexagonal tungstates, their individual reaction kinetics differ from each other. Further studies are now required to investigate whether the kinetic behaviour of the alkali cations is linked to their different morphological profiles in the hydrothermal synthesis of nanostructured tungstates. In this way, the combination of hydrothermal parameter screenings with complementary in situ techniques is a step towards the true "design" of tungsten oxide-based nanomaterials.

Acknowledgements. We thank Prof. Dr. R. Nesper (Laboratory of Inorganic Chemistry, ETH Zürich) for his steady interest and for the continuous support of this work. This work was supported by the ETH Zurich, by the Swiss National Science Foundation (MaNEP – Materials with Novel Electronic Properties), and by the National Research Program "Supramolecular Functional Materials".We gratefully acknowledge HASYLAB (DESY, Hamburg) for providing beamtime at beamline X1 and F3 for in situ EXAFS and XRD experiments, respectively. We thank Dr. F. Gao for carrying out microwave syntheses. We thank Prof. Dr. D. Günther and Ms. Kathrin Hametner (Laboratory of Inorganic Chemistry, ETH Zürich) for LA-ICP-MS analyses.

Compound	Type	Synthesis	Precursor	Lit.
$(1.03\text{-}1.32)Li_2O{\cdot}WO_3{\cdot}(0.74\text{-}0.99)\ H_2O$	O	solution	M_2WO_4, HCl or HNO_3, 100 °C	[16]
$Li_{0.20}WO_{3.10}{\cdot}0.5\ H_2O$	HTB	hydrothermal	M_2WO_4, HCl, 155 °C	[8]
$Li_{(0.10\text{-}0.42)}WO_{(3.05\text{-}3.21)}{\cdot}0.56\text{-}0.88\ H_2O$	HTB	solution	Li_2WO_4, HCl, 125 - 200 °C	[4]
$(0.08\text{-}0.14)Na_2O{\cdot}WO_3{\cdot}(0.67\text{-}0.85)H_2O$	HTB	solution	M_2WO_4, HCl or HNO_3, 100 °C	[16]
$Na_{0.26}WO_{3.13}{\cdot}0.5H_2O$	HTB	hydrothermal	M_2WO_4, HCl, 155 °C	[8]
$Na_{0.55}WO_{3.275}$	P	hydrothermal	M_2WO_4, HCl, 155 °C	[8]
$0.33\ KO_{0.5}{\cdot}WO_3$	HTB	solution	M-IPA and MCl, RT	[9]
$(0.07\text{-}0.11)K_2O{\cdot}WO_3{\cdot}(0.49\text{-}0.67)H_2O$	HTB	solution	M_2WO_4, HCl or HNO_3, 100 °C	[16]
$K_xW_{1-y/6}O_3$	HTB	heating	K-IPA, air, 500 °C	[13]
$0.23\ RbO_{0.5}{\cdot}WO_3$	HTB	solution	M-IPA and MCl, RT	[9]
$Rb_xWO_{3+x/2}$	P	hydrothermal	M_2WO_4, HCl, 155 °C	[8]
$Rb_{1.1}W_{1.65}O_{5.5}$	P	solid state	h-WO_3, Rb_2CO_3, 300 °C	[7]
$Cs_xW_{1-y/6}O_3$ (x = 0.3)	HTB	solution	Cs-poor IPA and CsCl, RT	[12]
$Cs_xW_{1-y/6}O_3$	P	solution	Cs-rich IPA and CsCl	[12]
$0.45\ CsO_{0.5}{\cdot}WO_3$	P	solution	M-IPA and MCl, RT	[9]
$(Cs_2O)_xW_2O_6$ $(0.3<x<0.5)$	P	solution	$Na_2WO_4{\cdot}2H_2O$, HCl, Cs_2CO_3, 90 °C	[15]
$Cs_xWO_{3+x/2}$	P	hydrothermal	M_2WO_4, HCl, 155 °C	[8]
Cs_xWO_{3+y}	P	ball-milling	WO_3, Cs_2CO_3	[17]
$Cs_{1.1}W_{1.65}O_{5.5}$	P	solid state	h-WO_3, Cs_2CO_3, 300 °C	[7]
$(0.04\text{-}0.073)\{(NH_4)_2O)\}{\cdot}WO_3{\cdot}(0.38\text{-}0.82)H_2O$	HTB	solution	M_2WO_4, HCl or HNO_3, 100 °C	[16]
$(NH_4)_{0.20}WO_{3.10}$	HTB	hydrothermal	M_2WO_4, HCl, 155 °C	[8]
$Ba_xW_{1-y/3}O_3$	2D-P	solution	M-IPA and MCl_2, RT	[9]
$Tl_xW_{1-y/6}O_3$	2D-P	solution	M-IPA and MCl_2, RT	[9]
$Pb_xW_{1-y/3}O_3$	2D-P	solution	M-IPA and MCl_2, RT	[9]

Table 1. Synthesis of HTB-/P-alkali tungstates(VI) with soft chemistry methods

Cation	Phase	Typical Morphology	Representative Composition (HTB)
Li^+	HTB/O	HTB: rods (diam.: 20 – 30 nm, length: 200 – 400 nm) O: μm-sized flower-like aggregates with dendritic nanorods	$(NH_4)_{0.15}Li_{0.14}W_{0.953}O_3 \cdot 0.85\ H_2O$
Na^+	HTB	Rods: μm-scale lengths (max. 12 μm), diam. ca. 100 nm	$(NH_4)_{0.12}Na_{0.20}W_{0.949}O_3 \cdot 0.61\ H_2O$
K^+	HTB	Rods: μm-scale lengths (max. 3 μm), diam. ca. 100 nm	$(NH_4)_{0.02}K_{0.33}W_{0.944}O_3 \cdot 0.45\ H_2O$
Rb^+	HTB / P	HTB: stacked rods (ca. 200 × 800 nm), hierarchical patterns P: cubic microcrystals	$Rb_{0.31}W_{0.951}O_3 \cdot nH_2O$
Cs^+			$Cs_{0.33}W_{0.948}O_3 \cdot 0.22\ H_2O$
NH_4^+ (AMT-ref.)	HTB	Rods: diam. 7 – 15 nm, length: 80 – 250 nm	$(NH_4)_{0.26}W_{0.958}O_3 \cdot nH_2O$

Table 2. Synthetic profiles of the alkali cations in the hydrothermal formation of alkali tungstates(VI)

Parameter	Uniformity / a.r. unchanged	Uniformity / a.r. improved	Uniformity / a.r. deteriorated
MCl :AMT = 0.25 : 1	Li, Na	---	K, Rb, Cs
MCl :AMT = 4 : 1	K, Cs (P)	Rb	Li, Na
MCl/AMT/H_2O	Na, Rb (P), Cs (P)	Li	K
c(W) = 0.07 M	---	**Li**, Na, K, Cs (P)	Rb
c(W) = 0.07 M, H_2O	---	Na, **K**, Rb (P)	Li, Cs (P)
c(W) = 0.007 M	---	Li (orth.), Na, K, **Cs**	Rb
c(W) = 0.007 M, H_2O	---	**Na, Rb**	Cs (P)

Table 3. Effects of hydrothermal parameter variations on the morphology of nanostructured alkali tungstates(VI) (bold: optimum results).

Cation	(M:W)	Phase	Morphology
AMT only	**Reference**	O	microflowers (av. 6 μm) made of sheets (< 100 nm thick)
LiCl	**1 : 2**	HTB	nanorods, diam.: ca. 40 nm, length: ca. 500 nm
LiCl	**5 : 1**	O	microflowers (max. 6 μm) made of sheets (50 nm thick)
RbCl	**1 : 2**	HTB	microspheres (2-4 μm) made of rods (ca. 200 × 30 nm)
RbCl	**5 : 1**	HTB	agglomerated nanorods (ca. 100 × 50 nm)
CsCl	**1 : 2**	unknown	microrystals; microspheres (2-4 μm) of rods (diam.: 50 nm)
CsCl	**5 : 1**	HTB	microspheres (1-3 μm) made of rods (diam.: 15 - 50 nm)

Table 4. Microwave-hydrothermal synthesis of alkali tungstates for comparison with conventional-hydrothermal reactions.

MCl / Parameter	c(W)	t / h	Phase	Morphology	Change compared to 2 d
LiCl / 220 °C	0.07	2	HTB	nanorods, diam.: 20-30 nm, length: 200 – 400 nm	NO
NaCl	0.07	4	HTB	microspheres consisting of rods (length ca. 1 µm, diam. ca. 100 nm)	--
NaCl / 220 °C	0.07	2	HTB	rods: length ca. 2 µm, diam. 100 . 200 nm, intergrown	--
		t / d			
LiCl	0.07	18	HTB	nanorods, diam.: 20-30 nm, length: 200 – 400 nm	NO
LiCl	0.007	18	O	microflowers with dendritic nanorods	NO
NaCl	0.07	18	HTB	rods: length ca. 3 µm, diam. ca. 100 nm	NO
NaCl / H_2O	0.007	18	HTB + amorph.	rods: lengths ca. 12 µm, diam. ca. 100 nm + microplatelets (side product)	NO
KCl / H_2O	0.007	18	layered cpd.	rods: lengths up to 2 µm, diam. < 100 nm	NO
RbCl / H_2O	0.07	18	P, little HTB	HTB: few hierarchical rods, ca. 100 × 200 nm	NO
CsCl	0.007	18	HTB	Hierarchical microspheres made of stacked rods (ca. 200 × 800 nm)	+
CsCl / (Cs:W) = 4	0.5	18	HTB + P	HTB: stacked rods (ca. 200 × 800 nm), slightly improved	+

Table 5. Hydrothermal parameters and emerging phases and morphologies of short-time (top) and long-time (bottom) experiments in the MCl/AMT systems (M = Li – Cs) (+ = morphology improved with respect to 2 d reaction time, -- = morphology deterioration with respect to 2 d reaction time).

Alkali Ion	t_{ind} in min	$t_{0.5}$ in min	Reaction time in min	Reaction time in min	*m*	Growth Model
none	14	134	292	292	1,44	A2/A3
Cs	9	70,7	143	143	1,61	A2/A3
Na	21	103	225	225	1,47	A2
Rb	11	67,2	151	151	1,68	A2
K	33	77	223	223	1,31	A2/R3
Li	12	68	130	130	1,51	A2

Table 6. Kinetic data for all in situ EDXRD experiments.

Growth Model	Rate Equation $f(\alpha) = kt$	*m*
Diffusion controlled		
$D_1(\alpha)$	$\alpha^2 = 0.25\ (t/t_{0.5})$	0.62
$D_2(\alpha)$	$(1-\alpha)\ln(1-\alpha) + \alpha = 0.1534\ (t/t_{0.5})$	0.57
$D_3(\alpha)$ [Jander]	$[1-(1-\alpha)^{1/3}]^2 = 0.0425\ (t/t_{0.5})$	0.54
$D_4(\alpha)$ [Ginstling-Brounshtein]	$1-2\alpha/3-(1-\alpha)^{2/3} = 0.0367\ (t/t_{0.5})$	0.57
Phase-boundary controlled		
$R_2(\alpha)$	$1-(1-\alpha)^{1/2} = 0.2929\ (t/t_{0.5})$	1.11
$R_3(\alpha)$	$1-(1-\alpha)^{1/3} = 0.2063\ (t/t_{0.5})$	1.07
First order		
$F1(\alpha)$	$[-\ln(1-\alpha)] = 0.6931\ (t/t_{0.5})$	1.00
Nucleation [Avrami-Erovéef]		
$A2(\alpha)$	$[-\ln(1-\alpha)]^{1/2} = 0.8326\ (t/t_{0.5})$	2.00
$A3(\alpha)$	$[-\ln(1-\alpha)]^{1/3} = 0.885\ (t/t_{0.5})$	3.00

Table 7. The rate equations for solid state reactions reported in literature.

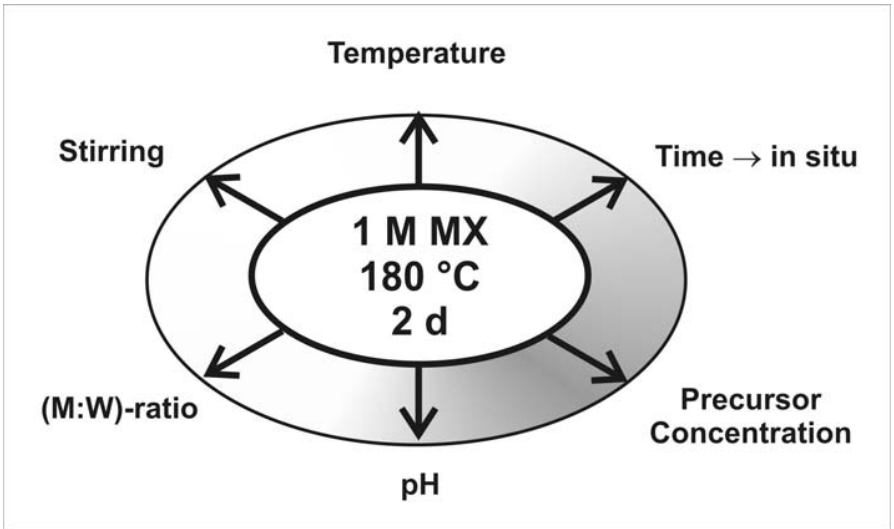

Figure 1. Influence of the reaction parameters in the hydrothermal formation of nanostructured alkali tungstates(VI).

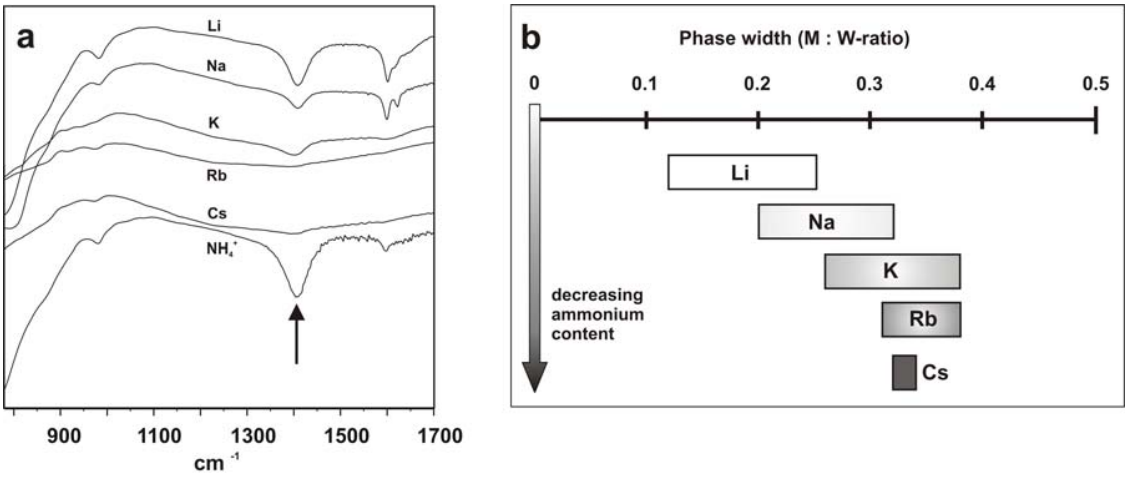

Figure 2. (a) Representative IR spectra of HTB-alkali tungstates(VI) (the arrow indicates the characteristic NH_4^+ bending vibration around 1400 cm^{-1}), (b) M:W-ratio (M = Li – Cs) in HTB-alkali tungstates(VI) as determined from LA-ICP-MS techniques (b)

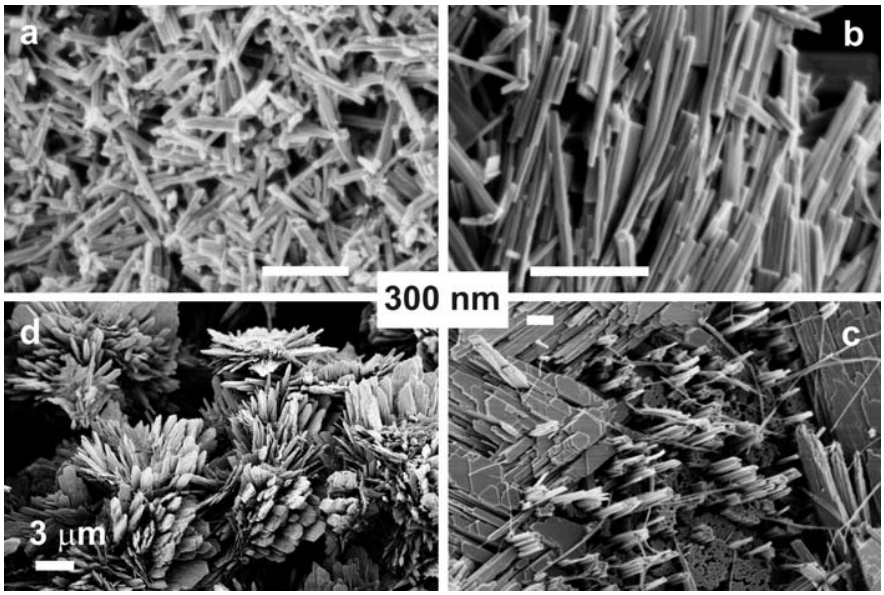

Figure 3. Representative SEM images of lithium tungstates synthesized (a) under standard conditions, (b) upon AMT dilution (c(W) = 0.07 M), (c, d) from highly diluted AMT solution (c(W) = 0.007 M)

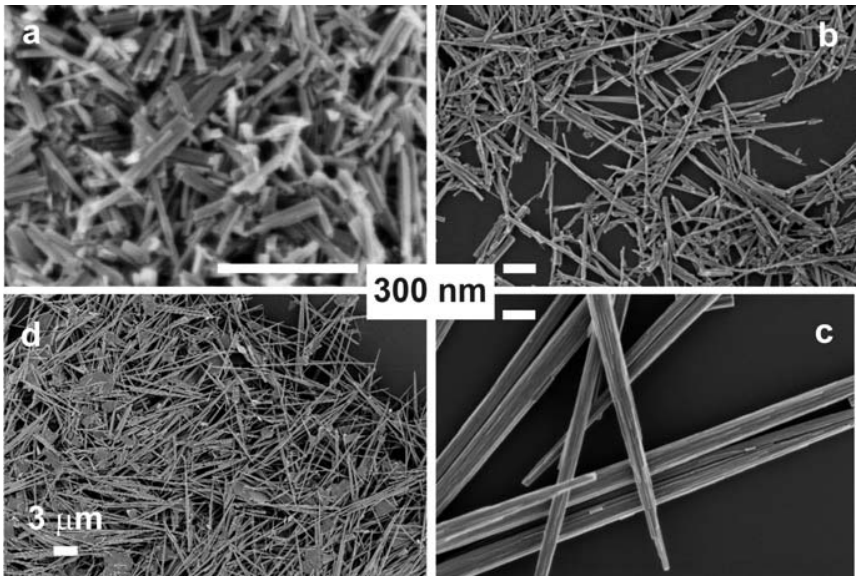

Figure 4. Representative SEM images of Na-HTB-tungstate rods synthesized (a) under standard conditions, (b) upon AMT dilution (c(W) = 0.07 M in H_2O), (c) from highly diluted AMT solutions (c(W) = 0.007 M in H_2O)

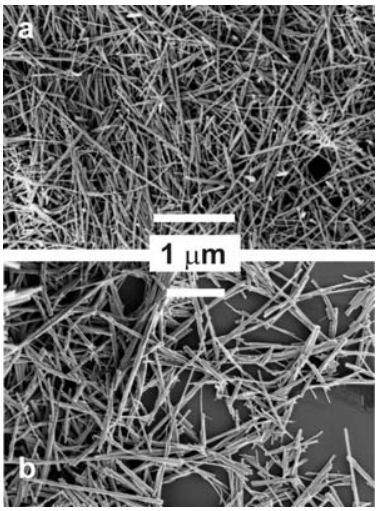

Figure 5. Representative SEM images of K-HTB tungstate rods synthesized in the KCl/AMT H_2O system (a) with standard precursor concentration, (b) upon AMT dilution (c(W) = 0.07 M in H_2O)

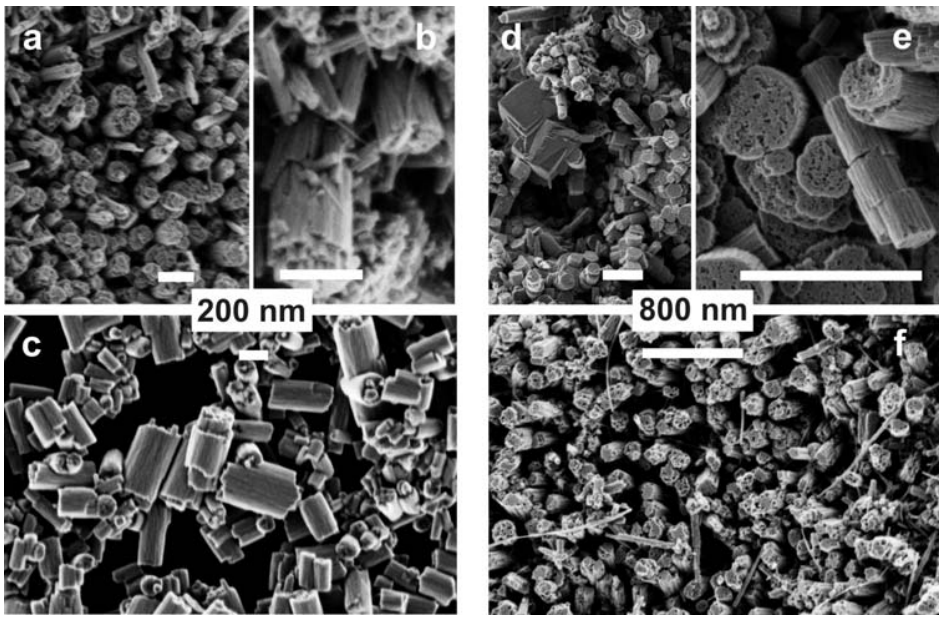

Figure 6. Representative SEM images of nanostructured Rb-(a - c) and Cs(d – f)-HTB tungstate rods: (a, b, d, e; *d: note the cubic cesium pyrochlore microcrystals*) synthesized under standard conditions, (c) grown from diluted RbCl/AMT/H_2O solutions (c(W) = 0.007 M in H_2O), (f) prepared from diluted CsCl/AMT/HAc systems (c(W) = 0.007 M)

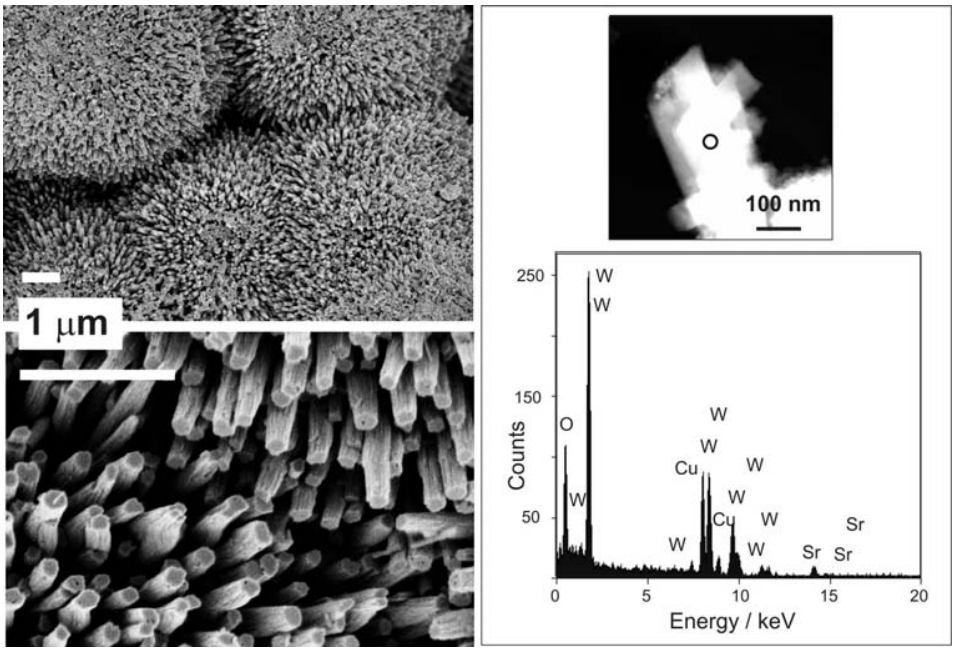

Figure 7. Representative SEM images (left) and representative EDX spot analysis of nanostructured Sr-HTB tungstates

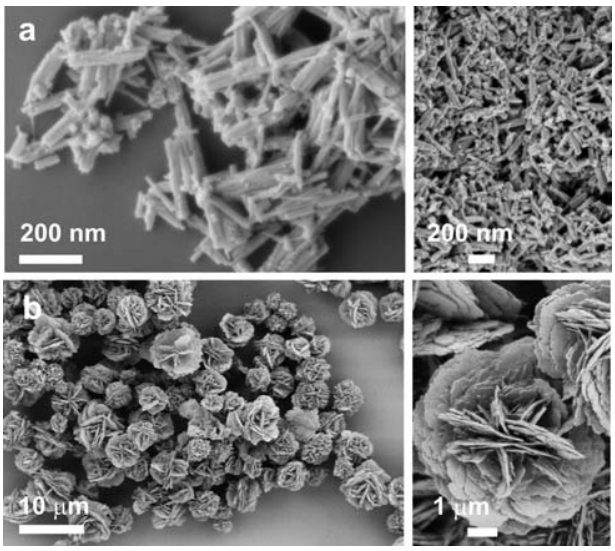

Figure 8. Representative SEM images of (a) NH_4-HTB nanorods formed under standard hydrothermal conditions in the AMT/HAc system, (b) orthorhombic ammonium tungstates(VI) synthesized from microwave-hydrothermal synthesis (AMT/HAc)

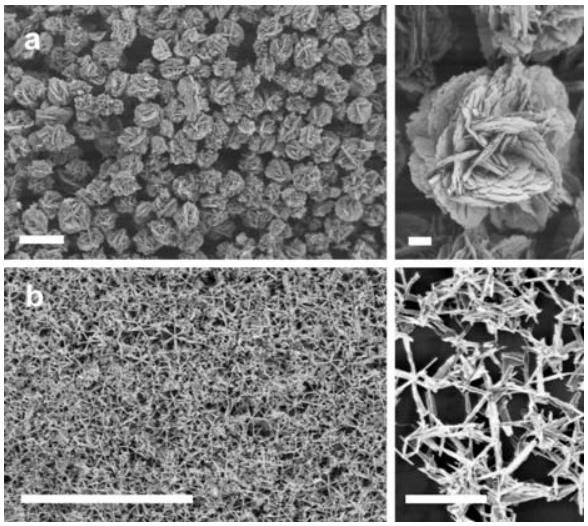

Figure 9. Representative SEM images (scale bar = 1 μm) of lithium tungstates synthesized from microwave-hydrothermal treatment (a) under standard conditions, (b) with a (M:W)-ratio of 5:1

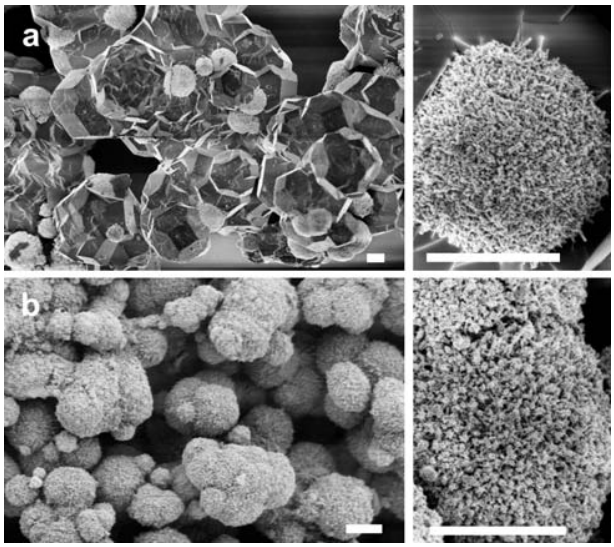

Figure 10. Representative SEM images (scale bar = 1 μm) of cesium tungstates synthesized from microwave-hydrothermal treatment (a) under standard conditions, (b) with a (M:W)-ratio of 5:1

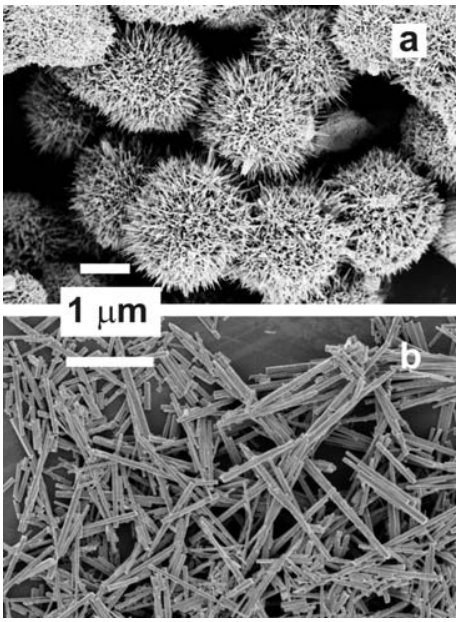

Figure 11. Representative SEM images of Na-HTB tungstate rods (c(W) = 0.07 M): (a) after 4 h of hydrothermal treatment, (b) after 18 d of hydrothermal treatment

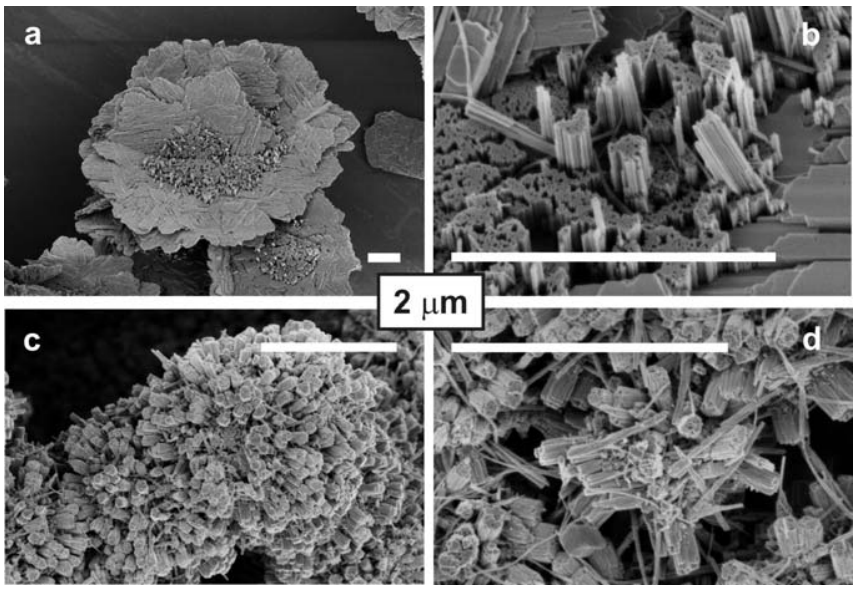

Figure 12. Representative SEM images of nanostructured tungstates after 18d of hydrothermal treatment (c(W) = 0.007 M): (a, b) Li-O tungstates, (c, d) Cs-HTB tungstates

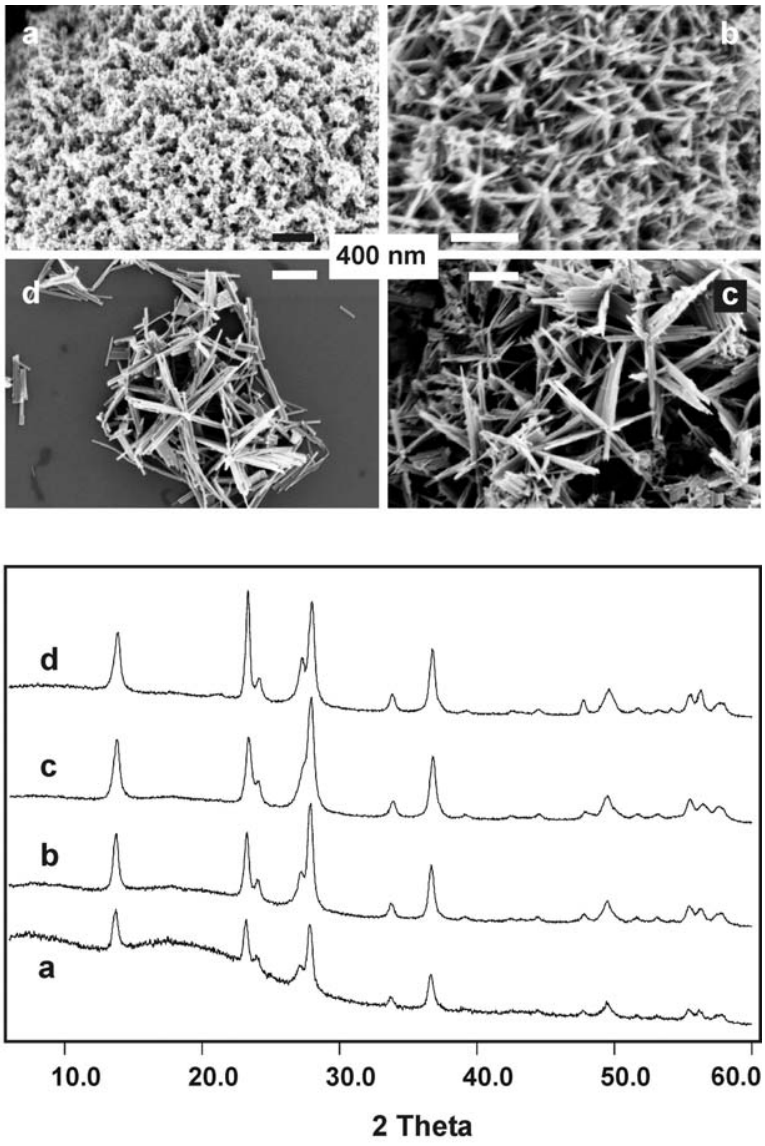

Figure 13. SEM images (top) and XRD patterns (bottom) monitoring the timescale of NH_4-HTB tungstate formation; top: (a) 1 h (ex situ), (b) 2 h (ex situ), (c) 4 h (in situ EXAFS) (d) 2 d (standard hydrothermal conditions), bottom: (a) 2 h (ex situ), (b) 3 h (ex situ), (c) 4 h (in situ EXAFS), (d) 2 d (standard hydrothermal conditions).

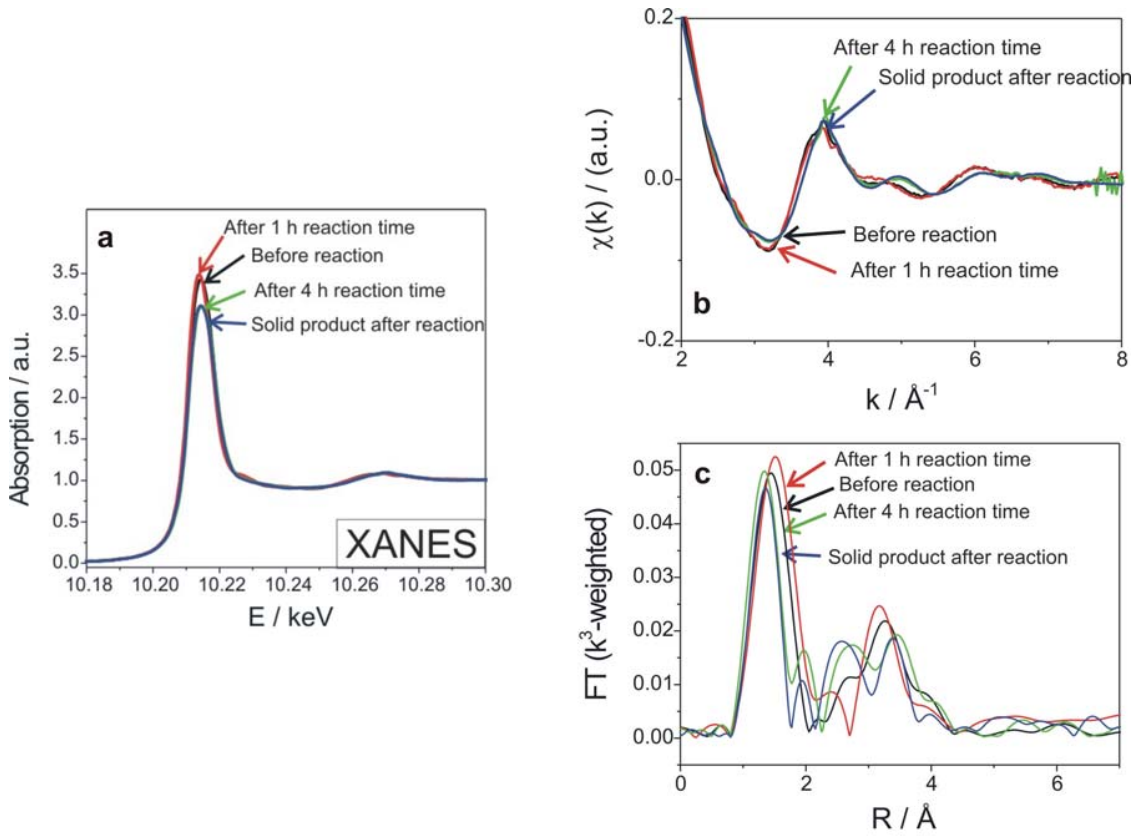

Figure 14. (a) XANES and (b) EXAFS data at the W L_3-edge taken during the hydrothermal synthesis of nanoscale ammonium tungstate from AMT; (c) shows the corresponding Fourier transformed EXAFS-data (k^3-weighted $\chi(k)$-function).

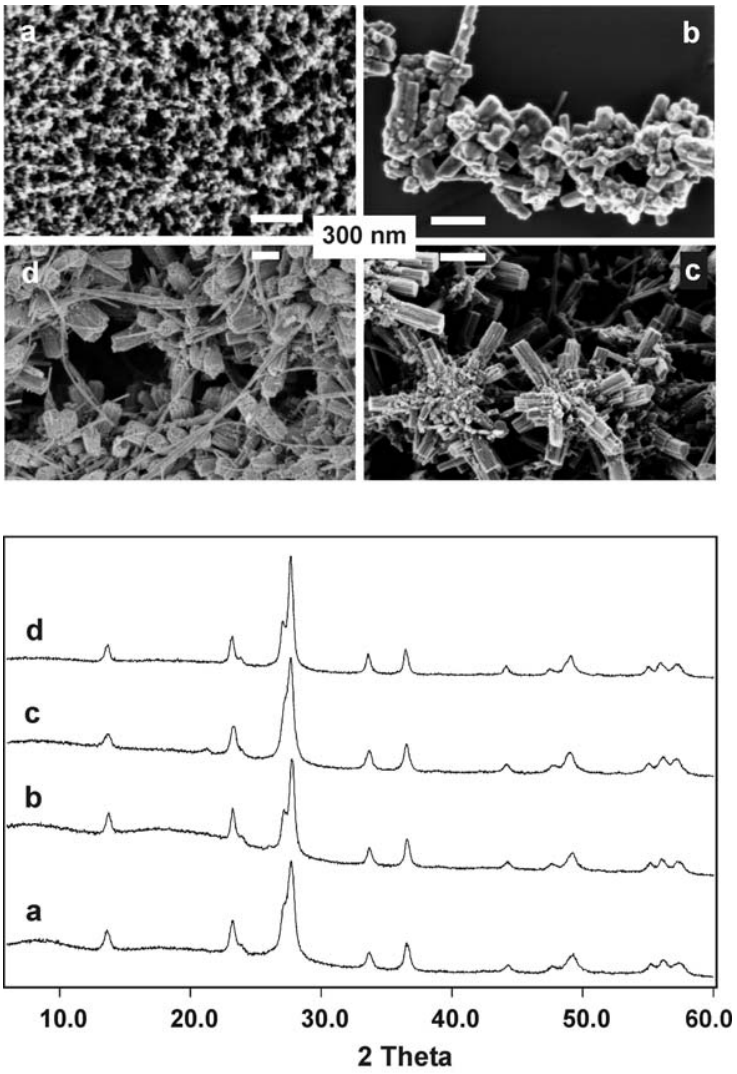

Figure 15. SEM images (top) and XRD patterns (bottom) monitoring the timescale of Cs-HTB tungstate formation; top: (a) 1 h (ex situ), (b) 4 h (in situ EXAFS), (c) 2 d (standard hydrothermal reaction), (d) 18 d (long-time experiment); bottom: (a) 2 h (ex situ), (b) 4 h (in situ EXAFS), (c) 2 d (standard hydrothermal reaction), (d) 18 d (long-time experiment).

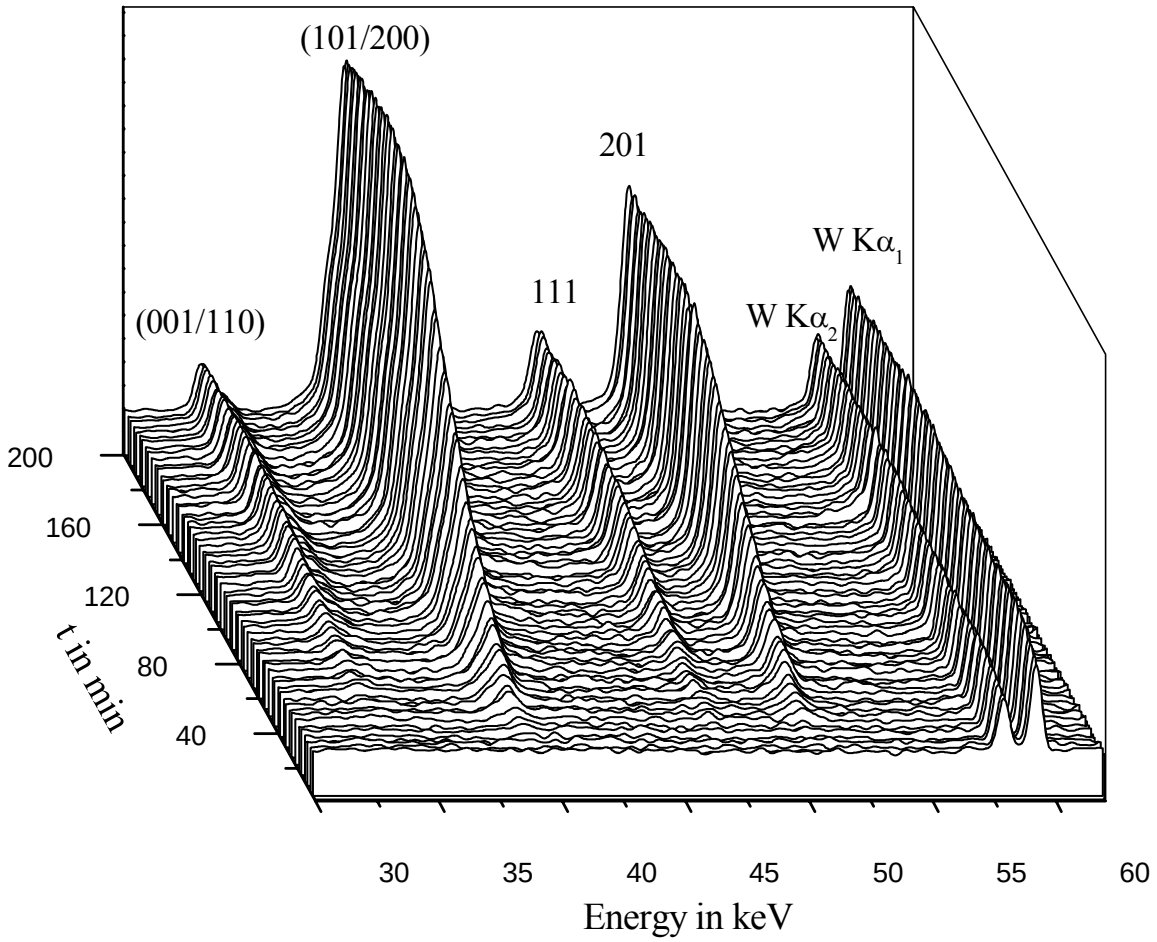

Figure 16. Time resolved powder pattern recorded at 200 °C and the presence of Rb. The indices of the most intense lines of the product phase and the W fluorescence lines are marked.

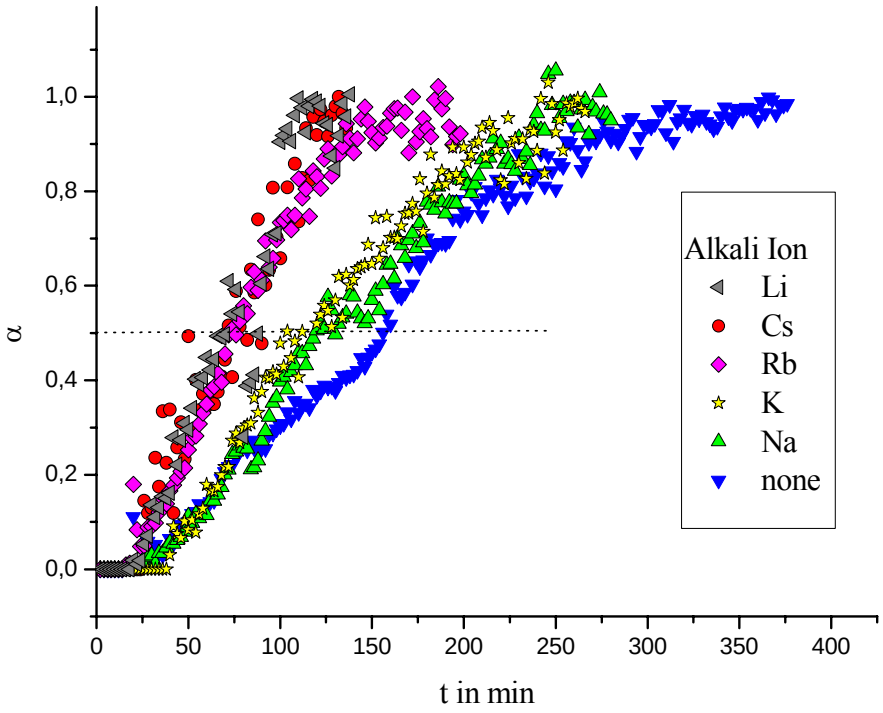

Figure 17. Extent of reaction α versus time for the (101/200) reflections for different alkali ions.

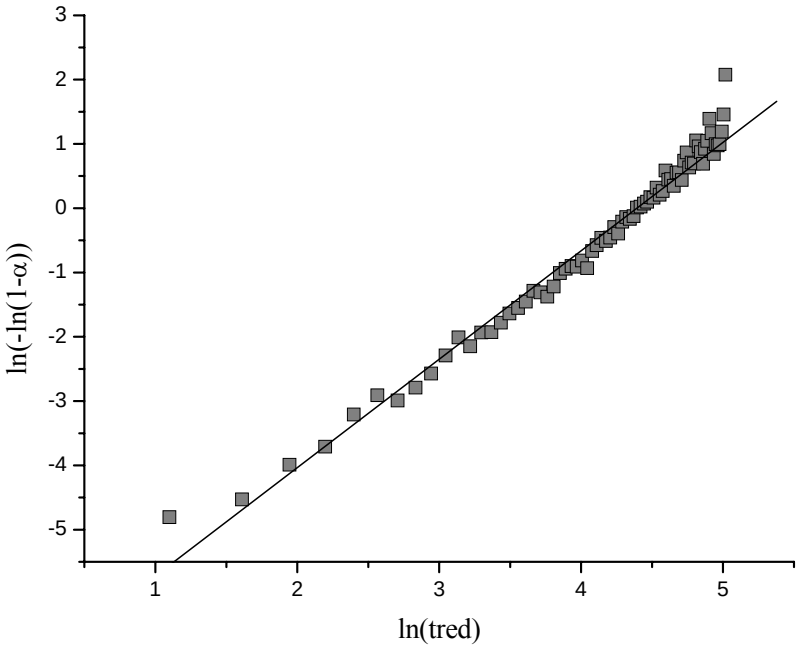

Figure 18. Sharp-Hanckock plot.

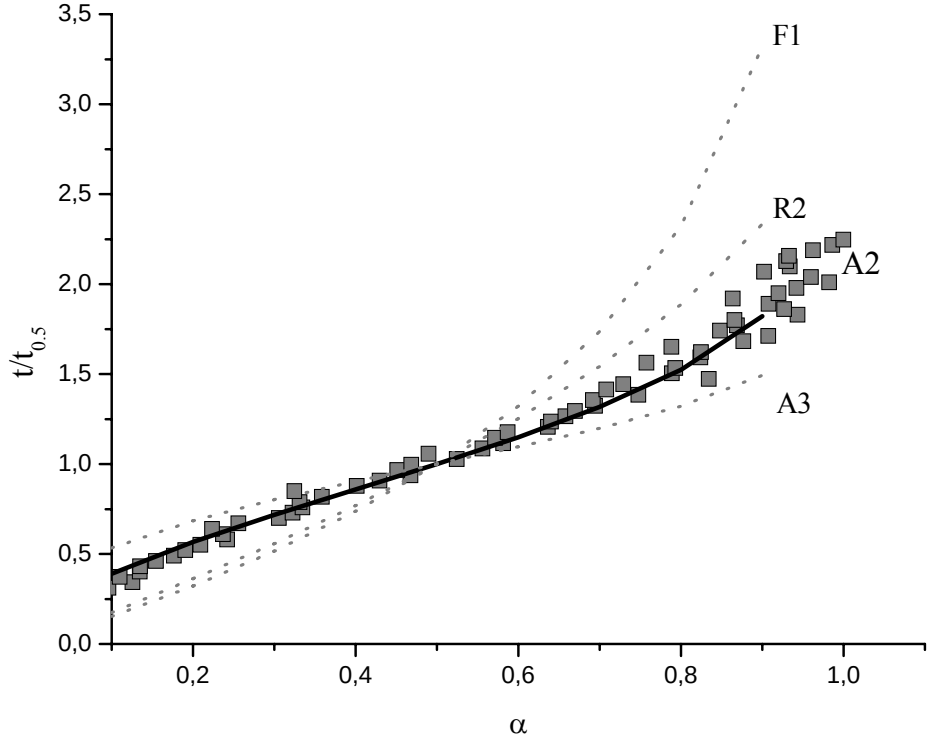

Figure 19. Comparison of the evolution of experimental $t/t_{0.5}$ data as a function of α (gray squares) with different theoretical models. The letters with the numbers are abbreviations of the different models listed in Table 7.

References

[1] Guo, J.-D.; Reis, K. P; Whittingham, M. S, *Solid State Ionics* **1992**, *53-56*, 305.

[2] Whittingham, M. S. in: *Solid State Devices*, eds. B. V. R. Chowdari and S. Radhakrishnan (World Scientific, Singapore, 1988).

[3] Francke, L.; Durand, E.; Demourgues, A.; Vimont, A.; Daturi, M.; Tressaud, A., *J. Mater. Chem.* **2003**, *13*, 2330.

[4] Yu, A.; Kumagai, N.; Liu, Z.; Lee, J. Y., *J. Solid State Electrochem.* **1998**, *2*, 394.

[5] Guo, J.-D.; Whittingham, M. S., *Int. J. Modern Phys. B*, **1993**, 4145.

[6] Chévrier, G.; Tuoboul, M.; Driouiche, A.; Figlarz, M., *J. Mater. Chem.* **1992**, *2(6)*, 639.

[7] Driouiche, A.; Abraham, F.; Touboul, M.; Figlarz, M.; *Mat. Res. Bull.* **1991**, *26*, 901.

[8] Reis, K. P.; Ramanan, A.; Whittingham, M. S., *J. Solid State Chem.* **1992**, *96*, 31.

[9] Kudo, T.; Oi, J.; Kishimoto, A.; Hiratani, M., *Mat. Res. Bull.* **1991**, *26*, 779.

[10] Reis, K. P.; Prince, E.; Whittingham, M. S., *Chem. Mater.* **1992**, *4*, 307.

[11] Reis, K. P.; Ramanan, A.; Whittingham, M. S., *Chem. Mater.* **1990**, *2*, 219.

[12] Oi, J.; Kishimoto, A.; Kudo, T., *J. Solid State Chem.* **1993**, *103*, 176.

[13] Tsuyumoto, I.; Kishimoto, A.; Kudo, T., *Solid State Ionics* **1993**, *59*, 211.

[14] Huo, L.; Zhao, H.; Mauvy, F.; Fourcade, S.; Labrugere, C.; Pouchard, M.; Grenier, J.-C., *Solid State Sci.* **2004**, *6*, 679.

[15] Coucou, A.; Figlarz, M., *Solid State Ionics* **1988**, *28 – 30*, 1762.

[16] Kumagai, N.; Matsuura, Y.; Umetzu, Y.; Tanno, K., *Solid State Ionics* **1992**, *53 – 56*, 324.

[17] Laruelle, S.; Figlarz, M., *J. Solid State Chem.* **1994**, *111*, 172.

[18] Reis, K. P.; Ramanan, A.; Whittingham, M. S., *J. Solid State Chem.* **1991**, *91*, 394.

[19] Michailovski, A.; Krumeich, F.; Patzke, G. R., *Mat. Res. Bull.* **2004**, *39*, 887.

[20] Pfeifer, J.; Badaljan, E.; Tekula-Buxbaum, P.; Kovács, T.; Geszti, O.; Tóth, A. L.; Lunk, H.-J., *J. Crystal Growth* **1996**, *169*, 727.

[21] Komarneni, S., *Current Sci.* **2003**, *85*, 1730.

[22] Michailovski, A.; Grunwaldt, J.-D.; Baiker, A.; Kiebach, R.; Bensch, W.; Patzke, G. R., *Angew Chem. Int. Ed.* **2005**, *44*, 5643.

[23] Grunwaldt, J.-D.; Ramin, M.; Rohr, M.; Michailovski, A.; Patzke, G. R.; Baiker, A., *Rev. Sci. Instr.* **2005**, *76*, 054104.

[24] Ressler, T., *J. Synchrotron Radiat.* **1998**, *5*, 118.

[25] Engelke, L.; Schaefer, M.; Porsch, F.; Bensch, W., *Eur. J. Inorg. Chem.* **2003**, *3*, 506.

[26] Engelke, L.; Schaefer, M.; Schur, M.; Bensch, W., *Chem. Mater.* **2001**, *13*, 1383.

[27] Michailovski, A.; Patzke, G. R., *in preparation.*

[28] Gerand, B.; Nowogrocki, G.; Figlarz, M., *J. Solid State Chem.* **1981**, *38*, 312.

[29] Hullen, A., *Ber. Bunsenges. Phys. Chem.* **1966**, *70*, 598.

[30] Ramin, M.; Grunwaldt, J.-D.; Baiker, A., *J. Catal.* **2005**, *234*, 256.

[31] Rohr, M.; Grunwaldt, J.-D.; Baiker, A., *J. Catal.* **2005**, *229*, 149.

[32] Kiebach, R; Schäfer, M.; Porsch, F.; Bensch, W., *Z. Anorg. Allg. Chem.* **2005**, *631*, 369; Francis, R.J.; Price, J.S.; Evans, J.S.O.; O'Brien, S.; O'Hare, D., *Chem. Mater.* **1996**, *8*, 2102; Bray, H.J; Redfern, S.A.T., *Phys. Chem. Minerals*, **1999**, 591; Christensen, A.N.; Bareges, A.; Nielsen, R. N.; Hazell, R.G.; Norby, P.; Hanson, J.C., *J. Chem. Soc., Dalton Trans*, **2001**, 1611.

[33] Hancock, J.D.; Sharp; J.H., *J. Am. Ceram. Soc.*, **1972**, *55*, 74; Sharp, J.H.; Brindley, G.W.; Narahari Achar, B.N., *J. Am. Ceram. Soc.*, **1966**, 379; Mohamed, B.M.; Sharp, J.H., *J. Mat. Sci.*, **1997**, 1595.

[34] Brown, P.W.; Pommersheim, J.; Frohnsdorff, G. *Cem. Concr. Res.* **1985**, *15*, 35.

[35] Thomas, J.J.; Jennings, H.M., *Chem. Mater.* **1999**, *11*, 1907.

[36] Avrami, M., *J. Chem. Phys.* **1939**, *7*, 1103; Avrami, M., *J. Chem. Phys.* **1940**, *8*, 212; Avrami, M., *J. Chem. Phys.* **1941**, *9*, 177.

[37] Michailovski, A., Krumeich, F., Patzke, G. R., *Helv. Chim. Acta* **2004**, *87*, 1029.

4.7 Sonstige Ergebnisse

4.7.1 Die Verbindung $[(V^{(IV)}(C_4H_{13}N_3))_3V_2^{(V)}O_{11}]$

Zusammenfassung der Arbeit *„[(V(IV)(C4H13N3))3V2(V)O11] – An inorganic-organic hybrid compound containing the chiral mixed-valent vanadium(IV/V) oxide cluster as main structural building unit“*.

Zeitgleich zur Fertigstellung der Arbeit wurden Strukturdaten und Ergebnisse der magnetischen Eigenschaften der Verbindung $[(V^{(IV)}(C_4H_{13}N_3))_3V_2^{(V)}O_{11}]$ von einer anderen Arbeitsgruppe publiziert [56]. Von einer Veröffentlichung wurde daher abgesehen.

Zur Darstellung von $[(V^{(IV)}(C_4H_{13}N_3))_3V_2^{(V)}O_{11}]$ wurde NH_4VO_3 (5 mmol) in einem Gemisch aus 3 ml Wasser und 1 ml dien für 7 Tage bei 150 °C unter solvothermalen Bedingungen erhitzt. Das Reaktionsprodukt fiel in Form von grün-braunen Kristallen mit einer Ausbeute von 80 % bezogen auf Vanadium an.

$[(V^{(IV)}(C_4H_{13}N_3))_3V_2^{(V)}O_{11}]$ kristallisiert in der chiralen, hexagonalen Raumgruppe $P6_3$ mit sechs Formeleinheiten pro Elementarzelle. Der V_5O_{11}-Kern besteht aus zwei $V^{(V)}O_4$-Tetraedern und drei $V^{(VI)}O_3$-Gruppen. Durch Verknüpfung über gemeinsame Ecken ensteht die V_5O_{11}-Einheit mit einer zu Adamantan ähnlichen Struktur. Die Koordinationssphäre der $V^{(VI)}O_3$-Gruppen wird durch jeweils einen dien-Liganden vervollständigt. Jeweils sechs dieser Cluster ordnen sich in Form eines Sechsecks an, so dass ein Wabenmuster als Packungsbild entsteht (Abb. 4.17, links). Der Durchmesser einer Wabe beträgt ca. 10 Å (gemessen von Koordinate zu Koordinate unter Vernachlässigung der dien-Liganden).

Die thermische Zersetzung von $[(V^{(IV)}(C_4H_{13}N_3))_3V_2^{(V)}O_{11}]$ beginnt bei einer Temperatur von 309 °C und erfolgt in einer Stufe (Gesamtmassenverlust von 42.1 %), welche von einem endothermen Ereignis in der DTA-Kurve begleitet wird. Der beobachtete Gesamtmassenverlust stimmt gut mit dem theoretischen Verlust von 42.01 % der dien-Liganden überein. Als Abbauprodukt konnte im Pulverdiffraktogramm V_2O_3 identifiziert werden.

Im Ramanspektrum konnten die Moden verschiedenen V-O- und V-N-Schwingungen

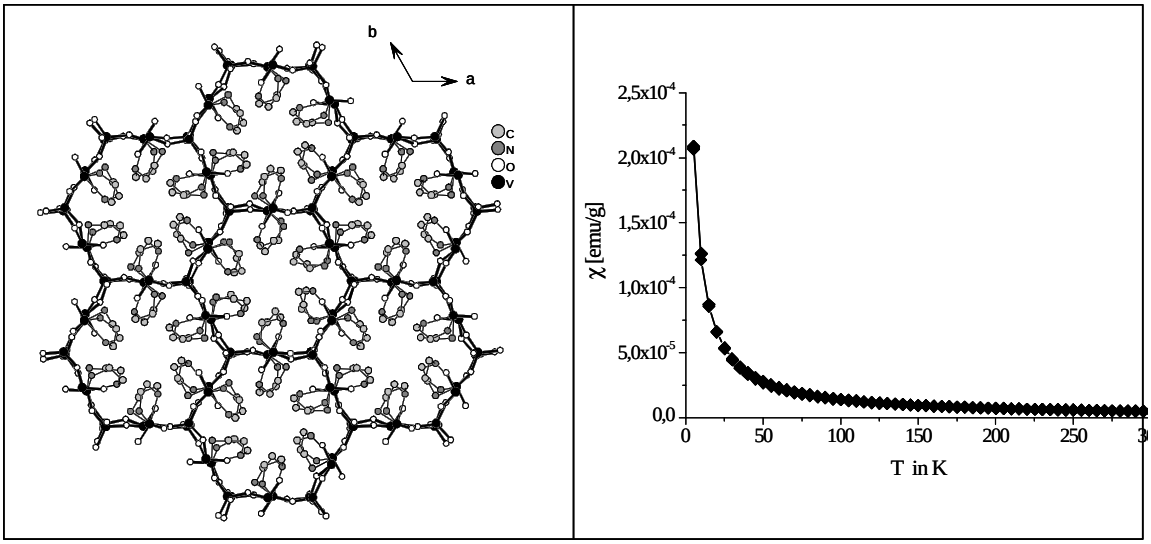

Abbildung 4.17: Wabenstrutur in $[(V^{(IV)}(C_4H_{13}N_3))_3V_2^{(V)}O_{11}]$ (links), Ergebnis der magnetischeSuszeptibilität von $[(V^{(IV)}(C_4H_{13}N_3))_3V_2^{(V)}O_{11}]$ (rechts)

zugeordnet werden. Die intensivste Mode bei 1007 cm^{-1} entspricht der $V^{(V)}$=O-Schwingung.

Die optische Bandlücke konnte aus UV/Vis-Spektren zu 3.06 eV bestimmt werden. Zusätzlich werden in niedrigeren Energiebereichen zwischen 2.1 bis 2.7 eV intervalence-charge-transfer-Übergänge beobachtet.

Das magnetische Verhalten kann über den gesamten Temperaturbereich mit einem Curie-Weiss-Gesetz beschrieben werden. Verantwortlich für das paramagnetische Verhalten sind die $V^{(IV)}$-Atome (Abb. 4.17, rechts).

$[(V^{(IV)}(C_4H_{13}N_3))_3V^{(V)}_2O_{11}]$ – An inorganic-organic hybrid compound containing the chiral mixed-valent vanadium(IV/V) oxide cluster as main structural building unit

Ragnar Kiebach, Christian Näther and Wolfgang Bensch [*]

*correspondence address: Prof. Dr. Wolfgang Bensch, Institut für Anorganische Chemie, Christian-Albrechts-Universität Kiel,

Olshausenstr. 40, D-24098 Kiel, Germany

wbensch@ac.uni-kiel.de

RECEIVED DATE (to be automatically inserted after your manuscript is accepted if required according to the journal that you are submitting your paper to)

In this work we will present the solvothermal synthesis, crystal structure, optical, thermal and magnetic properties of the first chiral mixed-valent vanadyl-vanadate-cluster with an organic template, $[(V^{(IV)}(C_4H_{13}N_3))_3V^{(V)}_2O_{11}]$ (dien = diethylendiamine).

Vanadium; Vanadiumoxides; Solvothermal synthesis; Crystal structure; Spectroscopy; Thermal investigation; magnetic properties.

Introduction

There has been much interest in vanadium based oxometallates in the past two decades and their applications due to their potential usage as secondary electrode materials for advanced lithium batteries [1-3] and their interesting properties as inorganic/organic hybrid materials built by polyoxometal building blocks for electromagnetism, catalysis and/or sorption [4-7]. The great interest especially for vanadium oxides arises from the fact that V can adopt different oxidation states which can result in interesting properties, e.g. the insertion/removal of lithium ions especially in layered structures of these compounds. The structures of such frameworks are composed of different VO_x (x = 4, 5, 6) coordination polyhedra [8-11]. Most interest is centered on V^{III}, V^{IV}, and V^{V} containing compounds [12-14] with the V atoms being in square pyramidal and/or distorted octahedral coordination polyhedra. The two polyhedra are similar and in the VO_6 octahedron an O is at the corner opposite to the vanadyl group. The similarity of the VO_5 and VO_6 polyhedra makes it possible to change the oxidation state of V without significant distortion of the framework [15]. It was shown by Chirayil *et al.* [16] that under hydrothermal conditions it is possible to control the framework type simply by changing the pH-value. Most framework structures with amines as organic templates are composed of 1-D infinite anionic chains [17,18] or 2-D anionic layered structures [19-21]. Including transition metals like Zn also 3-D compounds are formed [22-24]. It should be also noted that compounds containing clusters like $V_{10}O_{28}$ or V_8O_{14} were reported [25,26].

The new compound $[(V^{(IV)}(C_4H_{13}N_3))_3V^{(V)}_2O_{11}]$ presented in this communication is another example of the rich crystal chemistry of vanadates. This inorganic-organic hybrid compound is the first example containing a V_5O_{11} cluster as the main structural feature. The mixed-valent state, chirality and the thermal stability up to relatively high temperatures makes it an interesting candidate for applications. In the paper the synthesis, structure, magnetic properties, Raman spectra and UV/Vis spectra are reported.

Experimental details

Synthesis

The solvothermal synthesis was performed using NH_4VO_3 (Merck, 600 mg, 5 mmol) and 4 ml of a 25% dien solution as starting agents in a teflon lined steel autoclave with an inner volume of 30 ml. The autoclave was heated 7 days at 120 °C yielding brown-greenish single crystals (Figure 1) of $[(V^{(IV)}(C_4H_{13}N_3))_3V^{(V)}_2O_{11}]$. The crystalline product was filtered off, washed with acetone and water and cleaned in an ultra sonic bath. The compound is stable on air, water and acetone. The yield based on V is 80 %, no other products were observed. Chemical analyses of the product :C: 18.5 %(theo.: 19.4 %), N: 16.1 % (theo 17.1 %), H: 5.7 % (theo 5.7 %).

Structure determination

X-ray intensities were collected on a STOE Imaging Plate Diffraction System (IPDS) using monochromatized MoK_α radiation (λ = 0.7107 Å). The intensities were corrected for Lorentz, polarization and absorption effects. Structure solution was performed using SHELXS-97 [26]. Refinement was done against F^2 with SHELXL-97 [27]. V, O, C and N atoms were refined with anisotropic displacement parameters. The hydrogen atoms were positioned with idealized geometry and refined with isotropic displacement parameters using a riding model. The crystal was racemically twinned and therefore, a twin refinement was undertaken (BASF parameter = 0.2953(1)

Technical details of data acquisition are listed in Table 1. Atomic coordinates and equivalent displacement parameters are given in Table. 2. The most important distances and angels are collected in Table 3.

X-ray Powder Diffractometry

The X-ray powder patterns were recorded on a STOE Stadi-P diffractometer (Co-K_α radiation, λ = 1.78897 Å) in transmission geometry.

Thermoanalytical Measurements

DTA-TG analyses were performed using a Netzsch STA 429 DTA-TG device. The samples were heated in Al_2O_3 crucibles at a rate of 4 $K \cdot min^{-1}$ to 600°C under a flow of argon of 100 ml min^{-1}.

Raman Spectroscopy

Raman spectra were recorded in the region 100 to 3500 cm^{-1} with a Bruker IFS 66 Fourier Transform Raman spectrometer (wavelength: 541.5 nm).

Solid-State UV/Vis/NIR Spectroscopy

UV/Vis spectroscopic investigations were conducted at room temperature using a UV-VIS-NIR two-channel spectrometer Cary 5 from Varian Techtron Pty., Darmstadt. The optical properties of the compounds were investigated by studying the UV/Vis reflectance spectrum of the powdered sample. The absorption data were calculated using the Kubelka-Munk relation for diffuse reflectance data. $BaSO_4$ powder was used as reference material.

Magnetic measurements

Magnetic susceptibility was measured on a MPMS SQUID device (Quantum Design) in the temperature range from 5 to 300 K with an external field of 1 T kOe. The raw data were corrected for core diamagnetism.

Results and Discussion

Crystal Structure

The title compound crystallizes in the chiral hexagonal space group $P6_3$ with six formula units per unit cell and all atoms being located on general positions. The $[V_5O_{11}]$ core of the neutral hybrid compound contains two $V^{(V)}O_4$ tetrahedra and three $V^{(IV)}O_3$ groups (Figure 2). In both polyhedra the V atoms have short bonds to an oxygen atom in apical position which is typical for the V=O double-bond in a vanadyl group. Each of the two VO_4 tetrahedra and the VO_3 polyhedra are connected via common corners forming a distorted adamantane-like V_5O_{11} cluster (Figure 2). The V-O distances vary from 1.621(2) to 1.964(2) Å with the V=O distances being significantly shorter (1.621(2) to 1.674(3) Å) compared to the other V-O bond lengths (Table 3). The O-V-O angles in the VO_3 groups range from 88.4 (1) to 113.4(1)° and those of the VO_4 tetrahedra (107.7(2) to 113.4(1)°) indicate a moderate distortion from

ideal tehrahedral geometry (Table 3). Both the distances and angles are in accordance with the values known from literature [9,12-14,17-25]. The coordination sphere of the $V^{IV}O_3$ units is completed by N atoms of dien molecules acting as tri-dentate ligands leading to an octahedral environment for the V^{IV} atoms (Figure 2 and 3). In the present structure the amine N atoms have bonds to the V atoms which is surprising because in most vanadates the protonated amine molecules are located between the anions and the interaction between cations and anions is due to hydrogen bonding. As expected the V-N distances (2.145(2) – 2.345(2) Å) are longer than the V-O bonds. The N-V-N angles varying from 74.84(8) to 95.00(2) are in accordance with those reported in literature [28-30] (Table 3). The three-dimensional arrangement is achieved by hydrogen bonds between the amine hydrogen atoms and the vanadyl O atoms. The N-H···O distances range from 2.026(2) to 2.654(2) Å, the N-H-O angels vary between 134.781) and 164.5(1)°.

In the crystal structure six $[(V^{(IV)}(C_4H_{13}N_3))_3V^{(V)}{}_2O_{11}]$ molecules form a hexagon-like arrangement which resembles the a honeycomb pattern. Always three molecules are on the same height and the other three being generated by the 6_3 screw axis on a different level. Neglecting the dien molecules a "backbone" is build by the VO_x units forming channels along the c axis. The diameter of the channels is about 10.9 Å measured from coordinate to coordinate. Six dien molecules point toward the center of the channels with the shortest intermolecular distance of about 4 Å.

Thermal Properties

The thermal stability was investigated using simultaneous differential thermal analysis and thermogravimetry experiments. Heating selected crystals of $[(V^{(IV)}(C_4H_{13}N_3))_3V^{(V)}{}_2O_{11}]$ under argon a mass loss of 42.1 % is observed at T_{onset} = 309 °C which is accompanied by one endothermic event at T_{Peak}= 327 °C (Figure 4). It has to be mentioned that the decomposition starts at a remarkable high temperature. For the removal of the dien ligands a mass change of 42.01 % is expected showing the good agreement to the experimental data. The X-ray powder pattern of the decomposition product shows broad modulations and weak reflections which can be explained with V_2O_3. Chemical analyses of the gray residue yields minute amounts of C, N, H (< 0.5 %).

Optical Properties

The Raman spectrum is shown in Figure 5. In region between 700 and 1000 cm^{-1} several modes belonging to V-O and V-N are observed. The very intense stretching mode of V^{IV}=O is located at 923 cm^{-1}. For the V^{V}=O group a peak at 1007 cm^{-1} is observed. The resonances at ~ 740 cm^{-1} is due to the V-O-V stretching modes. The modes at 877 cm^{-1} and 840 cm^{-1} can be assigned to V-N modes, but a clear assignment cannot be made. The different modes are in good accordance with those reported for other V compounds [15,31-33].

In the UV/Vis spectrum two absorptions are seen (Fig. 6). The first may be explained by an inter-valence charge transfer transition between V^{IV} and V^{V} and the second is due the optical absorption edge. The optical band gap was calculated after the method of Kubelka and Munk and yields 3.06 eV.

Magnetic Properties

Formal valence considerations suggest that three V atoms occur as V^{IV} (d^1) and two V atoms are present as V^{V} (d^0). The magnetic susceptibility and the inverse susceptibility vs. temperature are plotted in Figure 7. As expected for the presence of V^{IV} centers a paramagnetic behavior is observed over the whole temperature range. The susceptibility curve was fitted with a Curie-Weiss law yielding μ_{exp} = 1.69 μ_B per V atom which is typical for V^{IV} with a $3d^{(1)}$ spin configuration. The Curie constant θ = -1.94 K is a clear indication that no intermolecular magnetic exchange interactions are present.

Acknowledgements: The financial support by the State of Schleswig-Holstein and the Deutsche Forschungsgemeinschaft (DFG) is gratefully acknowledged.

Supporting Information

Crystallographic Data for the structure reported in this paper have been deposited with Cambridge Crystallographic Data Center as supplementary publication number CCDC 263975. Copies of the data can be obtained free of charge on application to CCDC, 12 Union Road, Cambridge CB2 1EZ, UK (fax

+44-(0)-1223-336-033 or email deposit@ccdc.cam.ac.uk.SUPPORTING INFORMATION PARAGRAPH (Word Style “TE_Supporting_Information”).

References

[1] Whittingham, M.S. *J. Electrochem. Soc.* **1976**, *123*, 315.

[2] Walk, C.R.; Gore, J.S. *J. Electrochem. Soc.* **1975**, *122*, 68C.

[3] Whittingham, M.S.; Chen, R.; Chirayil, T.; Zavalij, P.Y. *Electrochem. Soc. Proc.* **1996**, *96-95*, 76.

[4] Bowes, C.L.; Ozin, G.A. *Adv. Mater.* **1996**, *8*, 13.

[5] Belik, A.A.;Azumo, M.; Matsuo, A.; Kindo, K.; Takano, M. *Inorg. Chem.* **2005**, *44*, 3762.

[6] Zhang, Y.; Warren, C.J.; Haushalter, R.C. *Chem. Mater.* **1998**, *10*, 1059.

[7] Stain, A.; Keller, S.W.; Wallouk, T.E. *Science* **1993**, *259*, 1558.

[8] Galy, J.; Carpy, A. *Acta Cryst.B* **1975**, *31*, 1794.

[9] Riou, D.; Ferey, G.; *J. Solid State Chem.* **1995**, *120*, 137.

[10] Walterson, K.; Forslund, B. *Acta Cryst. B.* **1977**, *33*, 784.

[11] Walterson, K.; Forslund, B. *Acta Cryst. B.* **1977**, *33*, 789.

[12] Zhang, Y.; Clearfield, A.; Haushalter, R.C. *Chem. Mater.* **1995**, *7*, 1221.

[13] Harrison, W.T.A.; Hsu, K.; Jacobson, A.J. *Chem. Mater.* **1995**, *7*, 2004.

[14] Haushalter, R.C.; Wang, Z.; Meyer, L.M.; Dhingra, S.S.; Thompson, M.E.; Zubieta, J. *Chem. Mater* **1994**, *6*, 1463.

[15] Lee, S.H.; Cheong, H.M.; Seong, J.M.; Liu, P.; Tracy, C.E.; Mascarenhas, A.; Pitts, J.R., Deb, S.K. *J. Appl. Phys.* **2002**, *92*, 1893.

[16] Chirayil, T.G.; Boylan, E.A.; Mamak, M.; Zavalij, P.Y.; Whittingham, M.S. *Chem. Comm.* **1997**, 33.

[17] Bensch, W.; Hug, P.; Reller, A.; Oswald, H.R. *Mater. Res. Bull.* **1987** *22*, 577.

[18] Tyrselova, J.; Kuchta, L.; Pavelicik, F. *Acta Crystallogr. C* **1995**, *51*, 1752.

[19] Chirayil, T.; Zavalij, P.Y.; Whittingham, M.S. *J. Mater. Chem.* **1997**, 2193.

[20] Riou, D.; Ferey, G. *Inorg. Chem.* **1995**, *34*, 6520.

[21] Zhang, Y.; Haushalter, R.C.; Clearfield, A. *Inorg. Chem.* **1996**, *35*, 4950.

[22] Pecquenard, B.; Zavalij, P.Y.; Whittigham, M.S. *J. Mater. Chem.* **1998**, 1255.

[23] Zhang, Y.; Haushalter, R.C.; Clearfield, A. *Chem. Comm.* **1996**, 1055.

[24] Janauer, G.G.; Dobley, A.D.; Zavalij, P.Y.; Whittingham, M.S. *Chem. Mater.* **1997**, *9*, 647.

[25] Hegetschweiler, K.; Morgenstern, B.; Zubieta, J.; Hagrman, P.J.; Lima, N.; Sessoli, R.; Totti, F. *Angew. Chem.* **2004**, *116*, 3518.

[26] Sheldrick, G.M., SHELXS-97, Program for Crystal Structure Determination, University of Göttingen, Germany **1997**.

[27] Sheldrick, G.M., SHELXL-97, Program for the Refinement of Crystal Structures, University of Göttingen, Germany **1997**.

[28] Khan, M.I.; Haushalter, R.C.; O'Connor, C.J.; Tao, C.; Zubieta, J. *Chem. Mater.* **1995**, *7*, 2807.

[29] Meyer, L.M.; Haushalter, R.C.; Zubieta; J. *J. Solid State Chem.* **1996**, *125*, 200.

[30] Daniels, L.M.; Murillo, C.A.; Rodrigues, K.G. *Inorg. Chim. Acta.* **1995**, *229*, 27.

[31] Popovic, Z.V.; Stergiou, V.; Raptis, Y.S.; Konstantionvic, M.J.; Isobe, M.; Ueda, Y.; Moshchalkov, V.V. *J. Phys. Condens. Matter*, **2002**, *14*, L583.

[32] Lee, S.H.; Cheong, H.M.; Seong, M.J.; Liu, P.; Tracy, C.E.; Mascarenhas, A.; Pitts, J.R., Deb, S.K. *Solid State Ionics* **2003**, *165*, 116.

[33] Zipse, D.; Dalal, N.S.; Vasic, R.; Brooks, J.S.; Kögerler, P. *Phys. Rev. B* **2005**, *71(6)*, 064417.

Tables:

	$[(V^{(IV)}(C_4H_{13}N_3))_3V^{(V)}{}_2O_{11}]$
a / Å	18.8920(9)
c / Å	13.0938(6)
V /Å^3	4047.2(3)
calc. density [g/cm^3]	1.822
Crystal system	hexagonal
Space group	$P6_3$
2θ /	$4.98° \leq 2\theta \leq 55.2°$
hkl range	$-24 \leq h \leq 24$
	$-24 \leq k \leq 24$
	$-17 \leq l \leq 71$
No. coll. Reflections	38943
No. unique reflections	6468
Reflections $F_o > 4\sigma(F_o)$	5819
Parameters	336
R1 ($F_0 > 4\sigma(F_o)$)	0.0255
wR2 ($F_0 > 4\sigma(F_o)$)	0.0616
R1 (all reflections)	0.0311
wR2 (all reflections)	0.0641
GOF	1.043
δF [e/Å^3]	0.34 / - 0.45

Table 1: Selected crystallographic data and some refinement results

	X	Y	Z	U_{eq}
V(1)	3422(1)	11(1)	4835(1)	8(1)
V(2)	3290(1)	18(1)	7735(1)	8(1)
V(3)	3400(1)	1587(1)	6389(1)	10(1)
V(4)	4877(1)	-46(1)	6305(1)	10(1)
V(5)	1764(1)	-1516(1)	6138(1)	11(1)
O(1)	3378(1)	197(2)	3599(2)	23(1)
O(2)	3329(1)	-135(1)	8988(2)	19(1)
O(3)	2568(1)	1625(1)	6244(2)	25(1)
O(4)	5766(1)	772(1)	6395(2)	24(1)
O(5)	1694(1)	-2405(1)	6262(2)	25(1)
O(6)	3268(1)	687(1)	5543(2)	19(1)
O(7)	4368(1)	103(1)	5083(2)	15(1)
O(8)	2645(1)	-966(1)	5132(2)	20(1)
O(9)	3191(1)	887(1)	7589(2)	17(1)
O(10)	4193(1)	199(1)	7173(2)	20(1)
O(11)	2481(1)	-855(1)	7233(2)	21(1)
C(1)	4617(2)	2625(2)	8005(2)	25(1)
C(2)	5225(2)	2594(2)	7274(2)	23(1)
C(3)	5149(2)	2146(2)	5489(2)	20(1)
C(4)	4875(2)	2678(2)	4943(3)	25(1)
C(5)	4501(2)	-1488(2)	7788(3)	27(1)
C(6)	3677(2)	-1746(2)	7298(2)	22(1)
C(7)	3973(2)	-1893(2)	5513(2)	28(1)
C(8)	4615(2)	-1343(2)	4751(2)	27(1)
C(9)	806(2)	-1085(2)	7603(2)	27(1)
C(10)	912(2)	-486(2)	6767(2)	29(1)
C(11)	1242(2)	-426(2)	4938(2)	24(1)
C(12)	626(2)	-1287(2)	4614(3)	29(1)
N(1)	3967(1)	2627(1)	7397(2)	20(1)
N(2)	4776(1)	1941(1)	6513(2)	15(1)
N(3)	3978(1)	2288(1)	5001(2)	24(1)
N(4)	5028(1)	-597(2)	7691(2)	21(1)
N(5)	3815(1)	-1410(1)	6258(2)	16(1)
N(6)	5298(1)	-679(2)	5342(2)	18(1)
N(7)	741(1)	-1824(1)	7140(2)	18(1)
N(8)	1496(1)	-447(1)	5994(2)	14(1)
N(9)	965(1)	-1830(1)	4824(2)	23(1)

Table 2: Atomic coordinates [$\times 10^4$] and equivalent isotropic displacement parameters [$Å^2 \cdot 10^3$] for $[(V^{(IV)}(C_4H_{13}N_3))_3V^{(V)}{}_2O_{11}]$. U_{eq} is calculated as one third of the trace of the orthogonalised U_{ij} tensor.

			Selected Bond Length (Å)
V(1)-O(1)	1.667(3)	V(3)-N(3)	2.192(2)
V(1)-O(6)	1.717(2)	V(4)-O(4)	1.622(2)

V(1)-O(7)	1.739(2)	V(4)-O(7)	1.958(2)
V(1)-O(8)	1.732(2)	V(4)-O(10)	1.943(2)
V(2)-O(2)	1.674(3)	V(4)-N(4)	2.181(2)
V(2)-O(9)	1.751(2)	V(4)-N(5)	2.345(2)
V(2)-O(10)	1.728(2)	V(4)-N(6)	2.145(2)
V(2)-O(11)	1.722(2)	V(5)-O(5)	1.625(2)
V(3)-O(3)	1.621(2)	V(5)-O(8)	1.964(2)
V(3)-O(6)	1.937(2)	V(5)-O(11)	1.939(2)
V(3)-O(9)	1.963(2)	V(5)-N(7)	2.162(2)
V(3)-N(1)	2.156(2)	V(5)-N(8)	2.322(2)
V(3)-N(2)	2.343(2)	V(5)-N(9)	2.168(2)
		Selected Angles (deg)	
O(1)-V(1)-O(6)	108.8(2)	O(4)-V(4)-O(10)	103.0(2)
O(1)-V(1)-O(8)	109.7(2)	O(10)-V(4)-O(7)	90.6(2)
O(1)-V(1)-O(7)	108.5(2)	O(4)-V(4)-N(4)	94.3(2)
O(6)-V(1)-O(7)	111.9(2)	O(4)-V(4)-N(5)	163.6(2)
O(6)-V(1)-O(8)	107.72)	O(4)-V(4)-N(6)	94.5(2)
O(8)-V(1)-O(7)	110.3(2)	O(7)-V(4)-N(4)	160.0(2)
O(2)-V(2)-O(9)	107.7(2)	O(7)-V(4)-N(5)	85.7(2)
O(2)-V(2)-O(10)	109.1(2)	O(7)-V(4)-N(6)	86.9(2)
O(2)-V(2)-O(11)	107.6(2)	O(10)-V(4)-N(6)	162.3(2)
O(10)-V(2)-O(9)	109.0(2)	O(10)-V(4)-N(5)	88.4(2)
O(11)-V(2)-O(9)	113.4(2)	O(10)-V(4)-N(4)	83.6(2)
O(11)-V(2)-O(10)	110.0(2)	N(4)-V(4)-N(5)	75.0(2)
O(3)-V(3)-O(6)	105.7(2)	N(6)-V(4)-N(4)	92.9(2)
O(3)-V(3)-O(9)	104.5(2)	N(6)-V(4)-N(5)	74.0(2)
O(6)-V(3)-O(9)	88.4(2)	O(5)-V(5)-O(8)	102.9(2)
O(3)-V(3)-N(1)	94.7(2)	O(5)-V(5)-O(11)	105.2(2)
O(3)-V(3)-N(2)	163.3(2)	O(11)-V(5)-O(8)	91.2(2)
O(3)-V(3)-N(3)	94.4(2)	O(5)-V(5)-N(7)	93.6(2)
O(6)-V(3)-N(1)	159.7(2)	O(5)-V(5)-N(8)	165.1(2)
O(6)-V(3)-N(2)	85.9(2)	O(5)-V(5)-N(9)	96.4(2)
O(6)-V(3)-N(3)	82.1(2)	O(8)-V(5)-N(7)	163.1(2)
O(9)-V(3)-N(1)	88.0(2)	O(8)-V(5)-N(8)	88.9(2)
O(9)-V(3)-N(2)	87.6(2)	O(8)-V(5)-N(9)	84.4(2)
O(9)-V(3)-N(3)	160.6(2)	O(11)-V(5)-N(7)	88.1(2)
N(1)-V(3)-N(2)	73.9(2)	O(11)-V(5)-N(8)	83.4(2)
N(1)-V(3)-N(3)	95.0(2)	O(11)-V(5)-N(9)	158.4(2)
N(3)-V(3)-N(2)	74.8(2)	N(7)-V(5)-N(8)	74.3(2)
O(4)-V(4)-O(7)	105.7(2)	N(7)-V(5)-N(9)	90.1(2)

Table 3. Selected interatomic distances (Å) and angles (°) for $[(V^{(IV)}(C_4H_{13}N_3))_3V^{(V)}{}_2O_{11}]$. Estimated standard deviations are given in parentheses.

Figure Captions

Figure.1: SEM picture of a single crystal of $[(V^{(IV)}(C_4H_{13}N_3))_3V^{(V)}{}_2O_{11}]$.

Figure 2:V_5O_{11} cluster of $[(V^{(IV)}(C_4H_{13}N_3))_3V^{(V)}{}_2O_{11}]$. C and H atoms are omitted for clarity.

Figure 3: Crystal structure of $[(V^{(IV)}(C_4H_{13}N_3))_3V^{(V)}{}_2O_{11}]$ with view along the a axis.

Figure 4: DTA and TG curves for $[(V^{(IV)}(C_4H_{13}N_3))_3V^{(V)}{}_2O_{11}]$, given is the mass loss in % and the peak temperature T_p in °C.

Figure 5: Raman spectra of $[(V^{(IV)}(C_4H_{13}N_3))_3V^{(V)}{}_2O_{11}]$.

Figure 6: UV/Vis spectra of $[(V^{(IV)}(C_4H_{13}N_3))_3V^{(V)}{}_2O_{11}]$.

Figure 7: Temperature dependence of the magnetic susceptibility of $[(V^{(IV)}(C_4H_{13}N_3))_3V^{(V)}{}_2O_{11}]$.

Figures

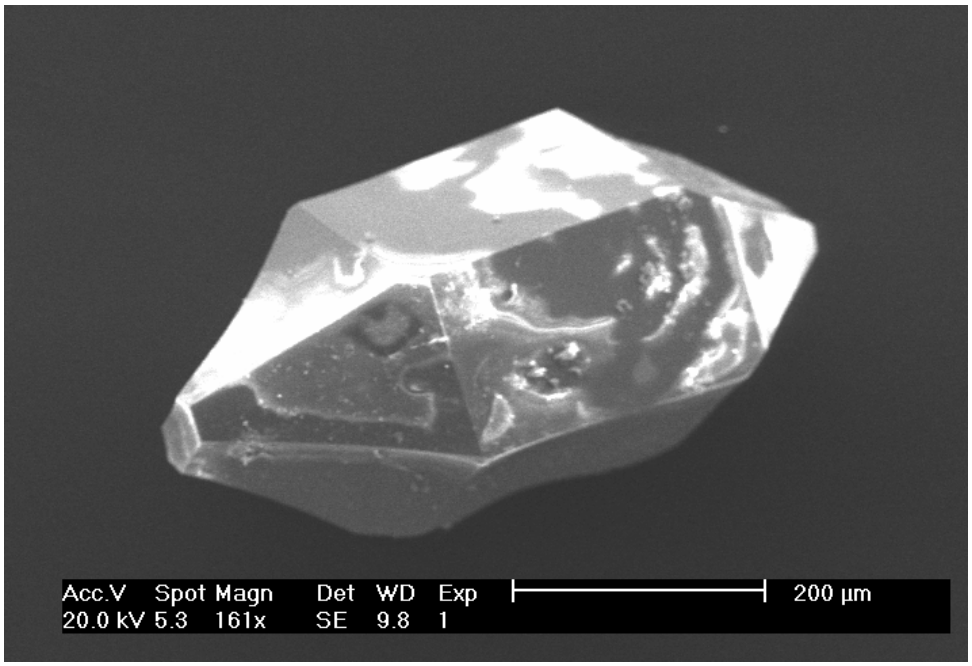

Fig.1

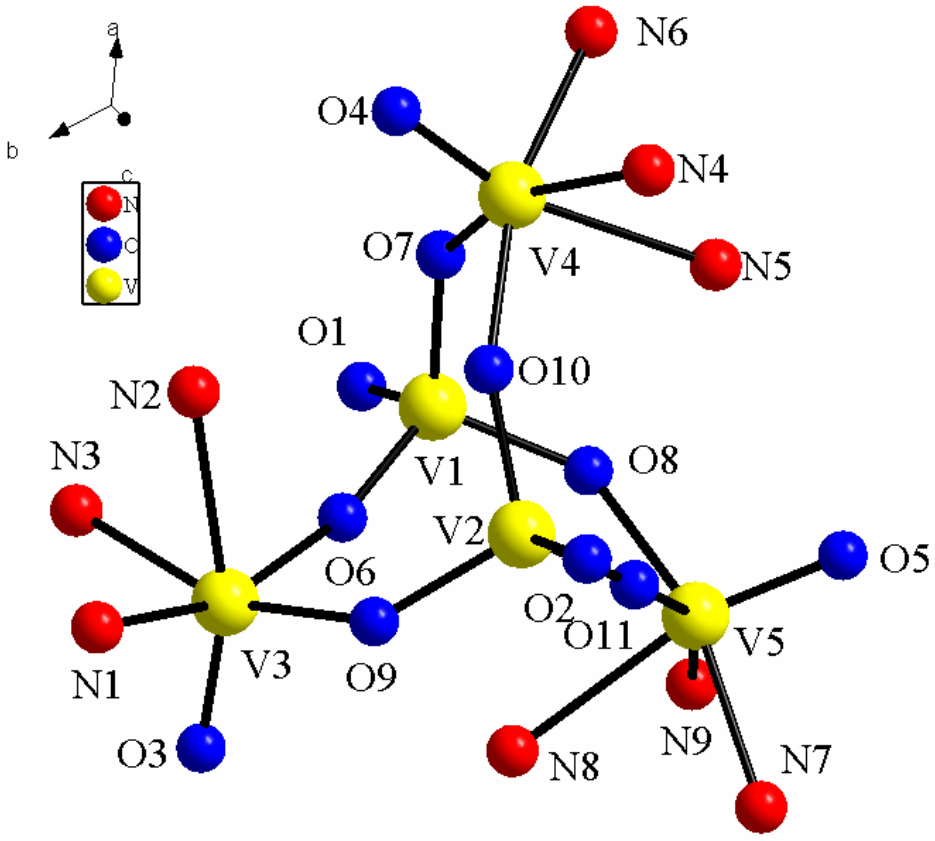

Fig.2

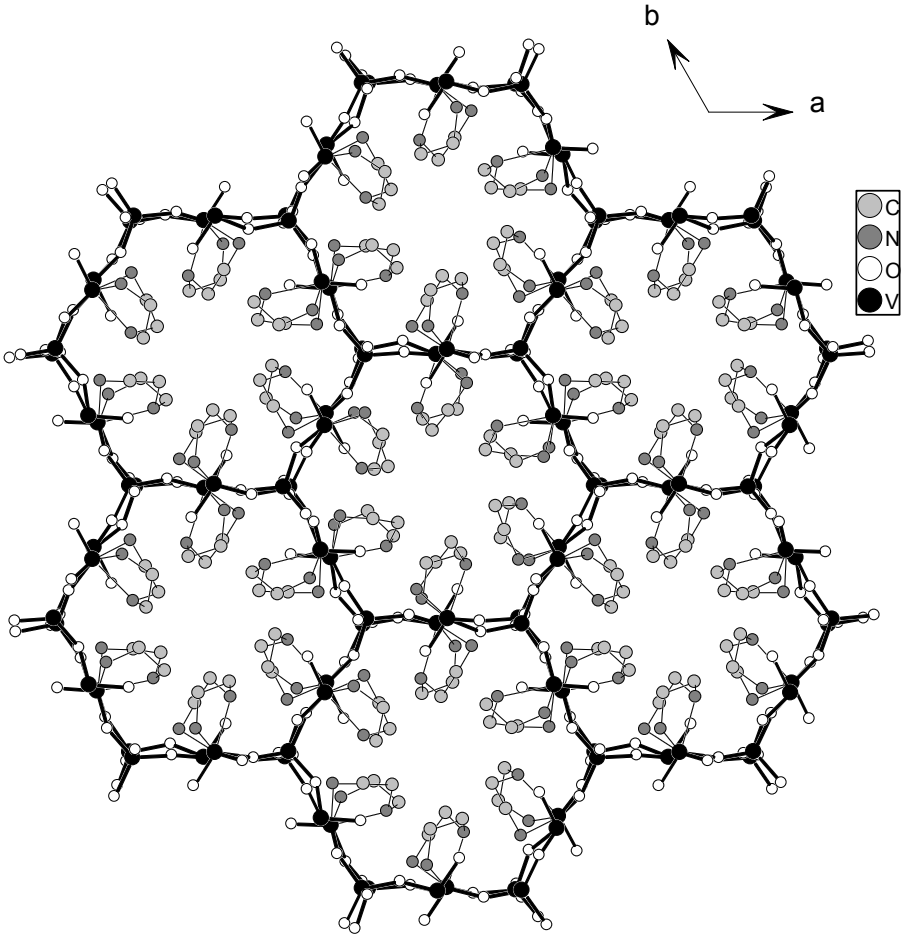

Fig.3

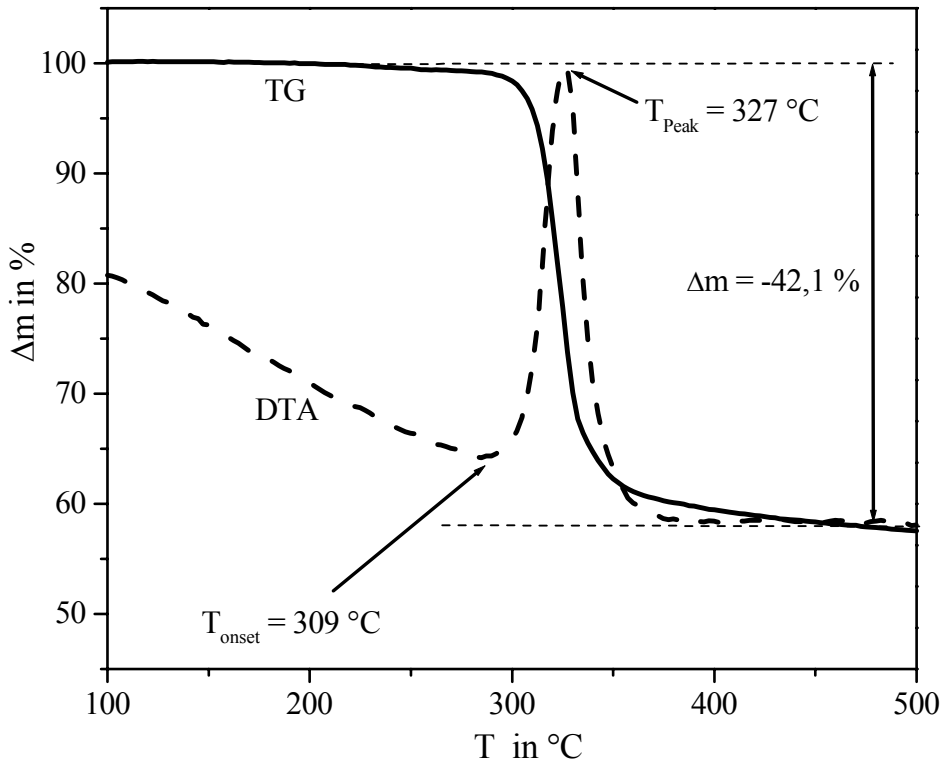
100
90
80
70
60
50
Δm in %
TG
DTA
T_Peak = 327 °C
Δm = -42,1 %
T_onset = 309 °C
100
200
300
400
500
T in °C

Fig.4

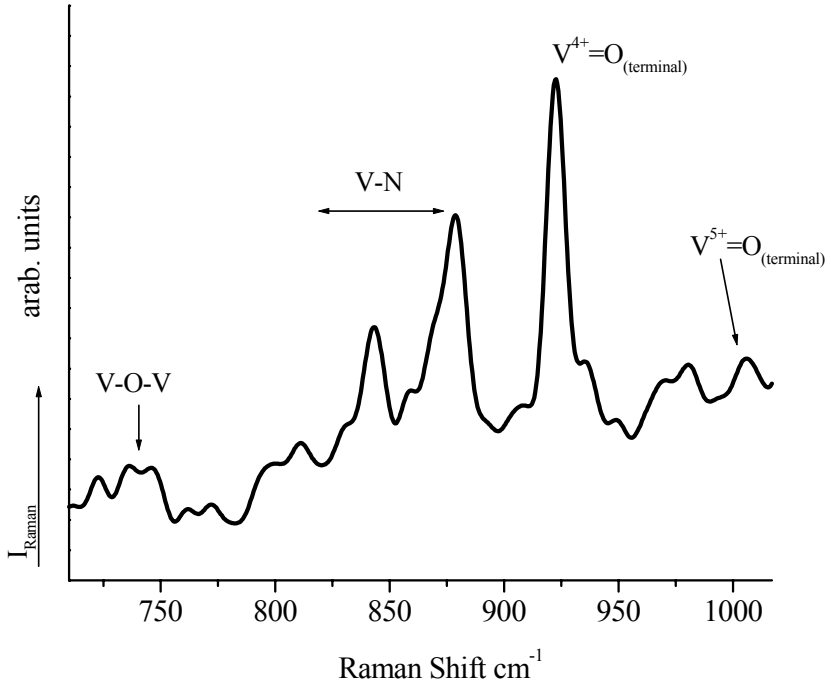
V4+=O(terminal)
V-N
V5+=O(terminal)
arab. units
V-O-V
I_Raman
750
800
850
900
950
1000
Raman Shift cm-1

Fig.5

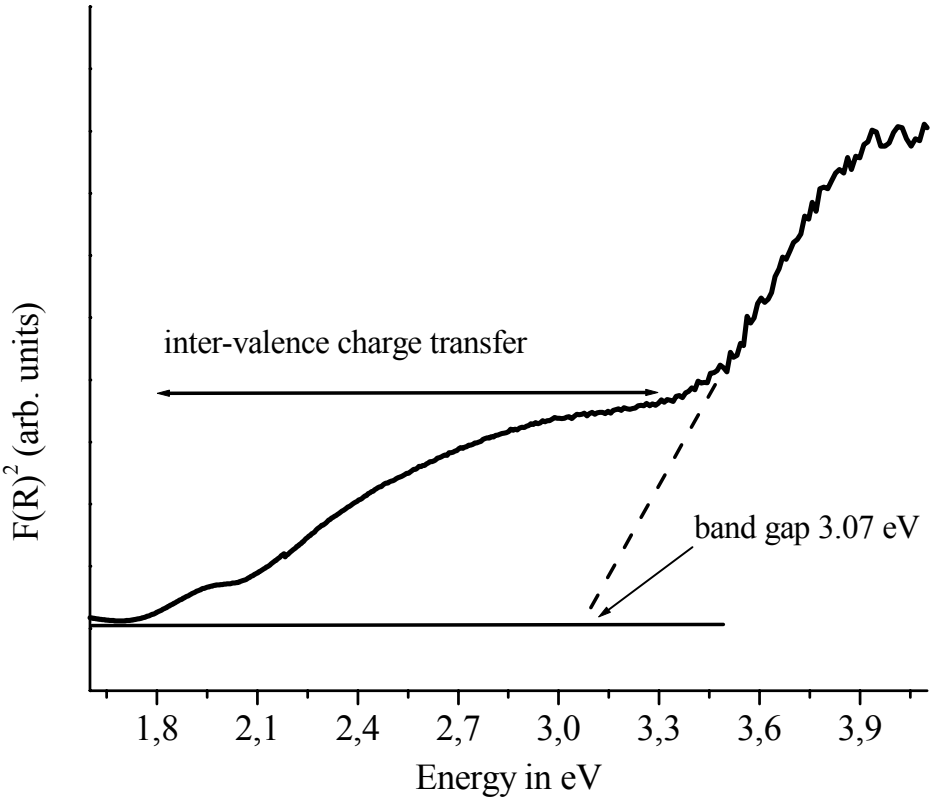
inter-valence charge transfer
band gap 3.07 eV
F(R)^2 (arb. units)
1,8
2,1
2,4
2,7
3,0
3,3
3,6
3,9
Energy in eV

Fig.6

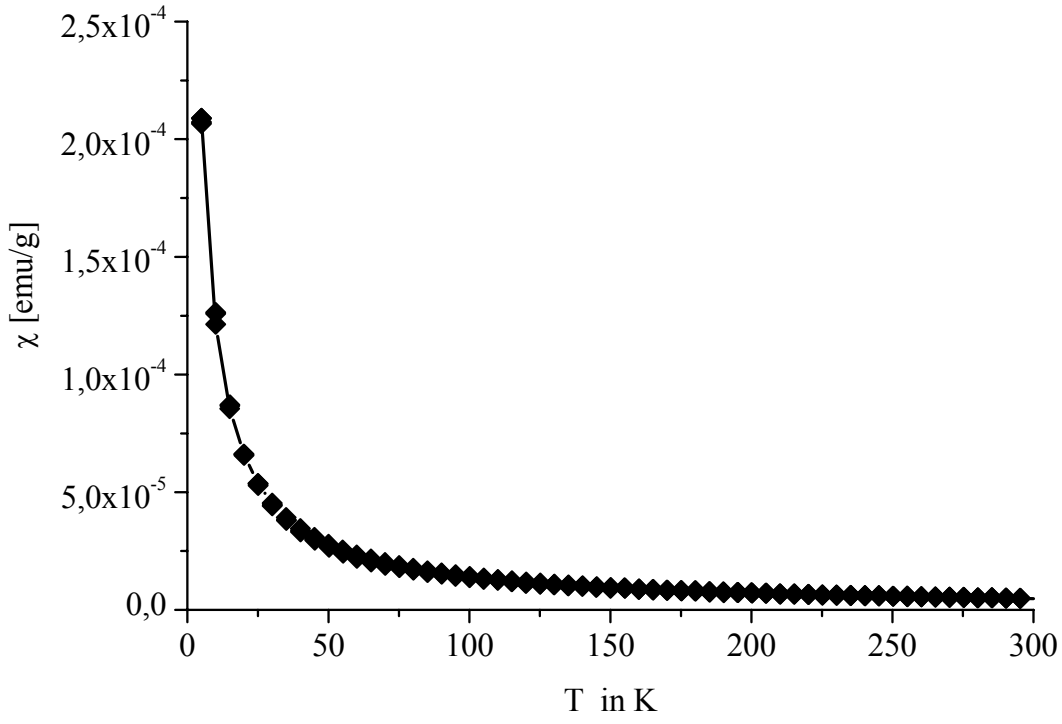
2,5x10^{-4}
2,0x10^{-4}
1,5x10^{-4}
1,0x10^{-4}
5,0x10^{-5}
0,0
χ [emu/g]
0
50
100
150
200
250
300
T in K

Fig.7

5 Ausblick

Ziel der Doktorarbeit waren die Synthese und Charakterisierung chemisch modifizierter Thioantimonatnetzwerke. Die Versuche zur Modifizierung erwiesen sich als erfolgreich und führten zur Darstellung neuer Verbindungen. Zusätzlich gelang die Synthese dreier bisher unbekannter übergangsmetallfreier Thioantimonate. Diese drei Verbindungen entstanden bei Versuchen eisenhaltige Thioantimonatnetzwerke zu synthetisieren. Allerdings wurde das als Edukt zugegebene Eisen nicht in die Verbindungen $[C_6H_{17}N_3][Sb_{10}S_{16}]$, $[C_7H_{13}N_2]_3[Sb_9S_{15}]$ und $[C_6H_9N_2][Sb_8S_{13}]\cdot 2.5H_2O$ integriert. Die Gegenwart von $Fe^{2+/3+}$ erwies sich nur bei der Synthese von $[C_6H_{17}N_3][Sb_{10}S_{16}]$ als notwendig, die anderen beiden Verbindungen lassen sich mit höheren Ausbeuten ohne die Präsenz von Eisenionen darstellen. Obwohl bereits mehr als 50 übergangsmetallfreie Thioantimonate dargestellt wurden, ist die Synthese neuer Verbindungen noch lange nicht erschöpft. Es ist anzunehmen, dass die Variationen der Synthesebedingungen und die Wahl der strukturdirigierenden Moleküle auch in Zukunft zu einer Vielzahl neuer Verbindungen führen werden.

Während die Integration von Eisen bei den oben erwähnten Verbindungen nicht gelang, konnte das Konzept bei den Verbindungen $[Fe(C_6H_{18}N_4)][FeSbS_4]$, $[Fe(C_6H_{13}N_3)_2][Fe_2Sb_4S_{10}]$ und $[Fe(C_6H_{18}N_4)][Sb_4S_7]$ Fe-Kationen zu integrieren erfolgreich umgesetzt werden. Bei allen Synthesen wurde mit Eisen(III)-Edukten gearbeitet. Bei der Syntheseoptimierung zur Darstellung der Verbindung $[Fe(C_6H_{18}N_4)][Sb_4S_7]$ haben sich Eisen(II)edukte als geeigneter für die Ausbeute erwiesen. Dies könnte ein Ansatzpunkt für zukünftige Synthesen sein, besonders wenn in der Zielverbindung zweiwertiges Eisen vorliegt. Durch Variation des „Templats“ und durch Einsatz von Fe-Edukten in verschiedenen Oxidationsstufen ist die Darstellung neuer eisenhaltiger Thioantimonate mit interessanten Eigenschaften zu erwarten.

Dass die Wahl des Lösungsmittels ebenfalls eine entscheidende Rolle spielt, konnte mit der Darstellung von $[Ni(C_4H_{13}N_3)_2]_3[(Sb_3S_6)_2]$ nachgewiesen werden. Die Verwendung von Methanol statt Wasser war der entscheidende Schritt für die Darstellung dieser neuen Verbindung. Bei zukünftigen Synthesen sollte die Variation der Lösungsmittel ebenfalls als Parameter bedacht werden, wobei völlig neue Synthesebedingungen durch ionische Flüssigkeiten geschaffen werden könnten.

Die Modifizierung von Thioantimonaten durch partielle Substitution des Schwefels durch Sauerstoff erwies sich als weniger erfolgreich, und nur die Verbindung $[C_6H_{20}N_4][Sb_9S_{14}O]$ konnte dargestellt werden. Die Eigenschaften dieser Verbindung sind mit denen reiner Thioantimonate vergleichbar. Eine Möglichkeit für zukünftige Experimente wären Synthesen oberhalb von 250 °C. Die EXAFS-Untersuchungen von Sherman et al. [31] deuten auf eine Substitution von Schwefel durch Sauerstoff in der Koordinationssphäre des Antimonatoms in Lösung hin. Synthesen unter diesen Bedingungen erfordern allerdings andere Reaktionsgefäße und die Überprüfung, ob unter diesen extremen Bedingungen Amine geeignete Lösungsmittel sind.

Bei dem Verzicht auf Schwefel als Edukt und Präsenz von V^{5+}-Quellen gelang die Synthese von drei bisher unbekannten Verbindungen $[trenH_3]_2[tren]_{0.33}[Sb_6V_{15}O_{42}]\cdot xH_2O$ $(3<x<5)$, $[C_6H_{17}N_3]_4[Sb_4V_{16}O_{42}]\cdot 2H_2O$ und $[NH_4]_4[Sb_8V_{14}O_{42}]\cdot 2H_2O$. Die magnetischen Eigenschaften dieser Verbindungen könnten von besonderem Interesse sein. Die Arsenderivate dieses Verbindungstyps haben Eigenschaften von „Single Molecular Magnets“. Aufgrund experimenteller Probleme konnten die magnetischen Eigenschaften der Sb-Derivate noch nicht untersucht werden. Die Variation des Strukturdirektors wird mit großer Wahrscheinlichkeit zu neuen Verbindungen führen. Die Erfahrung hat gezeigt, dass die durchschnittliche Anzahl an Versuchen zur Darstellung von Einkristallen wesentlich geringer ist als beispielsweise bei der Darstellung von Thioantimonaten. Die ersten Versuche, bei denen andere Eduktquellen eingesetzt wurden, erwiesen sich ebenfalls als erfolgreich. Wird bei der Synthese von $[NH_4]_4[Sb_8V_{14}O_{42}]\cdot 2H_2O$ statt NH_4VO_3 KVO_3 verwendet, so erhält man Kristalle die Sb, V und K enthalten. Verbindungen mit dieser Elementkombination sind interessant, da sie ein Sb-Derivat zu der in der Einleitung erwähnten Verbindung $K_6[As_6V_{15}O_{42}(H_2O)]\cdot 8H_2O$ darstellen könnten. Allerdings war die Qualität der Kristalle für Einkristalluntersuchungen bisher nicht ausreichend.

Für die Synthese von Thioantimonaten mit chiralen „Templaten“ bzw. mit chiralen Netzwerkstrukturen konnten in dieser Doktorarbeit erste wichtige Vorarbeiten erfolgreich abgeschlossenen werden. So gelang die Synthese von zwei Verbindungen mit der Summenformel $[C_3H_{10}NO]_2[Sb_4S_7]$. Beide enthalten einen Aminoalkohol als organisches „Templat“, welcher in Form eines racemischen Gemisches eingesetzt wurde. Ebenfalls erfolgreich waren orientierende Versuche Mn als Übergangsmetall in die Netzwerkstruktur zu integrieren, die Kristalle waren qualitativ zu schlecht für eine Einkristallstrukturanalyse. Bei weiterführenden Experimenten sollte der Schwerpunkt auf der Integration von Übergangsmetallen liegen. Dabei sollten Übergangsmetalle verwendetet werden, welche in Thioantimonaten eine Verschiebung der optischen Bandlücke zu höheren Energien (ca. 3 eV) verursachen. An solchen Verbindungen lassen sich Untersuchungen des NLO-Effektes in der Praxis leichter durchführen als an tief gefärbten Materialien. Wenn dieser Schritt erfolgreich abgeschlossen ist, kann statt eines racemischen Gemisches der chirale Aminoalkohol eingesetzt werden.

Im Laufe der Doktorarbeit konnten vier Projekte zur Untersuchung der Bildungsmechanismen mit Hilfe von in-situ-EDXRD abgeschlossen werden. Das erste befasste sich mit der Kristallisation des Germanates $(C_3H_{12}N_2)_2Ge_9(OH)_4O_{18}\cdot 2H_2O$ und dem Einfluss der Verwendung von Kristallisationskeimen auf den Reaktionsverlauf. Unterstützt wurden die Ergebnisse der in-situ-Untersuchungen durch SEM-Aufnahmen der Produkte zu unterschiedlichen Reaktionszeiten. Bei der zweiten untersuchten Verbindung handelt es sich um $[Co(tren)][Sb_2S_4]$. Interessanterweise wurden unterschiedliche Reaktionswege, abhängig von Temperatur und Eduktquelle, beobachtet. Die in Lösung vorhandenen Antimonspezies wurden mit in-situ-EXAFS charakterisiert. Zwei Projekte wurden in Kooperation mit der Arbeitsgruppe von Greta Patzke von der ETH-Zürich durchgeführt. Im ersten Projekt wurde die Bildung von nanokristallinem MoO_3 mit in-situ-EDXRD untersucht. Das zweite Projekt beschäftigte sich mit Synthese nanokristalliner Wolframoxide und dem Einfluss von Alkaliionen auf die Morphologie und die Reaktionsmechanismen.

Die Verschiedenheit der einzelnen Projekte demonstriert die vielseitigen Anwendungsmöglichkeiten von in-situ-EDXRD-Untersuchungen. Besonders bei der solvothermalen Synthese erlaubt diese Methode Einblicke in die zeitaufgelöste Bildung der Reaktionsprodukte. Solche Erkenntnisse können unter Laborbedingungen nicht erhalten

werden. Besonders interessant ist die Kombination von in-situ-EDXRD/EXAFS, da die komplementären Methoden Einblicke in kristalline wie auch in amorphe oder in Lösung befindliche Produkte bzw. Zwischenprodukte erlauben. Während die kristallinen Spezies und in Lösung befindliche Spezies der untersuchten Reaktionen zumindest teilweise charakterisiert sind, herrscht über amorphe Zwischenprodukte Unklarheit. Einen Einblick könnten EXAFS-Untersuchungen ausgefrorener, nach unterschiedlichen Reaktionszeiten abgeschreckter Proben geben.

Während eines Gastaufenthaltes am Institut des Materiaux Jean Rouxel-Faculte des Sciences de Nantes konnte die Verbindung $Na_{\frac{2}{3}}Ce_{\frac{1}{2}}TiO_3$ unter solvothermalen Bedingungen dargestellt werden. Da keine Einkristalle vorhanden waren, wurde die Struktur aus Pulverdaten verfeinert. Als Strukturmodell dienten die kristallographischen Daten der Verbindung $Na_{0.632}Ce_{0.368}Ti_{0.912}Nb_{0.088}O_3$. Die Synthese von $Na_{\frac{2}{3}}Ce_{\frac{1}{2}}TiO_3$ verdeutlicht die breiten Anwendungsmöglichkeiten der solvothermalen Methode. Sie erlaubt die Darstellung von Verbindungen, die bisher nur durch Hochtemperatursynthesen zugänglich waren.

6 Literaturverzeichnis

[1] W. Bensch R. Stähler. *Acta Crystallogr.*, C58:m537, 2002.

[2] A. Powell P. Vaquiero, A.M. Chippindale. *Inorg. Chem.*, 43:7963, 2004.

[3] A. Powell P. Vaqueiro, A.M. Chippindale. *Polyhedron*, 22:2839, 2003.

[4] W. Bensch M. Schaefer, C. Näther. *Monatsh. Chem.*, 135:461, 2004.

[5] M. Wachold W.S. Sheldrick. *Angew. Chem.*, 109:214, 1997.

[6] A. Puls. *Doktorarbeit, Universität Kiel*, 2006.

[7] R. Stähler. *Doktorarbeit, Universität Kiel*, 2002.

[8] L. Engelke. *Doktorarbeit, Universität Kiel*, 2002.

[9] M. Schaefer. *Doktorarbeit, Universität Kiel*, 2003.

[10] R. Kiebach W. Bensch M. Schaefer, R. Stähler. *Z. Anorg. Allg. Chem.*, 43:1816, 2004.

[11] N. Lehnert W. Bensch M. Schaefer, C. Näther. *Inorg. Chem.*, 43:2914, 2004.

[12] J.E. Greedan H. Kleinke C.-S. Lee, A. Safa-Sefat. *Chem. Mater.*, 15:780, 2003.

[13] W. Bensch R. Stähler. *Z. Anorg. Allg. Chem.*, 628:1657, 2002.

[14] F. Liebau X. Wang. *Eur. J. Solid State Inorg. Chem.*, 15:27, 1998.

[15] S. Schunk X. Wang F. Liebau U. Simon, F. Schüth. *Angew. Chem. Int. Ed.*, 36:1117, 1998.

[16] W. Schattke J. Jockel U. Simon R. Adelung L. Kipp F. Starrost, E.E. Krasovskii. *Phys. Rev. B*, 61:115697, 2000.

[17] J. Döring A. Müller. *Z. Anorg. Allg. Chem.*, 595:251, 1991.

[18] F. Trifiro M. Gazzano F.C. Aissi A. Aboukais M.J. Guelton S. Albonetti, F. Cavani. *J. Catal.*, 146:491, 1994.

[19] E. Bosch R.K. Grasselli B. Pillep P. Behrens O.B. Lapina A.A. Shubin H.-J. Eberle H. Knözinger J. Sprengler, F. Anderle. *J. Phys. Chem. B*, 105:10772, 2001.

[20] J. Döring A. Müller. *Angew. Chem.Int. Ed. Engl.*, 27:1721, 1988.

[21] R. Vasic J.S. Brooks P. Kögerle D. Zipse, N.S. Dalal. *Phys. Rev. B*, 71:064417, 2005.

[22] G.S. Lisetskaya A.K. Babko. *Russ. J. Inorg. Chem.*, 1:95, 1956.

[23] S. Gosh K.P. Dubey. *Z. Anorg. Allg. Chem.*, 319:204, 1962.

[24] G. Tunell R.H. Arntson, F.W. Dickson. *Science*, 153:1673, 1966.

[25] N.N. Kolpakova. *Geochem. Intl.*, 19:46, 1982.

[26] O.P. Demin V.S. Shestiko. *Russ. J. Inorg. Chem.*, 16:1679, 1971.

[27] S. Wood. *Geochim. Cosmoschim. Acta*, 53:237, 1989.

[28] J.A. Tosell. *Geochim. Cosmoschim. Acta*, 58:5093, 1994.

[29] G.R. Helz R.A.D. Pattrick J.M. Charnock D.J.Vaughan J. Frederick, W. Mosselmans. *Appl. Geochem.*, 15:879, 2000.

[30] E.H. Oelkers D.M. Sherman, K.V. Ragnarsdottir. *Chem. Geo.*, 167:161, 2000.

[31] J.M. Charnock R.A.D. Pattrick D.J. Vaughan C.D. Garner G.R. Helz, J.A. Tosell. *Geochim. Cosmochim. Acta*, 59:4591, 1995.

[32] www.hasylab.desy.de/Faciltity/Exp.Stations.

[33] R.A. Young. *The Rietveld Method, Oxford University Press, New York*, 1993.

[34] A. Rabenau. *Angew. Chem.*, 97:1017, 1985.

[35] M. Schaefer. *Diplomarbeit, Universität Kiel*, 2000.

[36] G.M. Sheldrick. *SHELXS97, Program for the Solution of Crystal Structures, Universität Göttingen*, 1997.

[37] G.M. Sheldrick. *SHELXL97, Program for the Refinement of Crystal Structures, Universität Göttingen*, 1997.

[38] A.L. Spek. *PLATON, A Multipurpose Crystallographic Tool, Utrecht University, Utrecht, The Netherlands*, 2000.

[39] Stoe & Cie. *X-Red, V. 1.11, Stoe & Cie GmbH, Darmstadt, Germany*, 1998.

[40] Stoe& Cie. *X-shape, V. 1.03, Stoe & Cie GmbH, Darmstadt, Germany*, 1998.

[41] Stoe &Cie. *WinXPOW, V. 1.04, Stoe & Cie GmbH, Darmstadt, Germany*, 1999.

[42] Netzsch. *Netzsch-TA Windows Software, V. 4.1.2, Selb. Germany*, 2001.

[43] K. Brandenburg. *DIAMOND, Release 2.1. e, Crystal Impact GbR, Bonn, Germany*, 1999.

[44] T. Ressler. *WinXAS 3.1*, 2004.

[45] J.J. Rehr S.D. Conradson A.L. Ankudinov, B. Ravel. *Phys. Rev. B*, 58:7565, 1998.

[46] J.J. Rehr J. Sims H. Hung A.L. Ankudinov, C.E. Bouldin. *Phys. Rev. B*, 65:104107, 2002.

[47] J. Rodriguez-Carvajal. *FULLPROF, Lab. Leon Brillouin*, 2005.

[48] F. Porsch. *EDXPowd, V. 3.15, RTI GmbH, Paderborn*, 2002.

[49] W. Bensch R. Stähler, C. Näther. *Acta Cryst.*, C57:26, 2001.

[50] R. Stähler W. Bensch, C. Näther. *Chem. Commun.*, page 477, 2001.

[51] V. Kupcik E.M. Baumgardt. *J. Cryst. Growth*, 37(3):346, 1977.

[52] P. Orlandi P. Palvadeau Y. Moleo, A. Meerschaut. *Eur. J. Mineral.*, 12:835, 2000.

[53] M. Schur W. Bensch. *Z. Naturforsch.*, 52b:405, 1997.

[54] Y. Ko J.B. Parise. *Chem. Mater.*, 4:1446, 1992.

[55] C. Näther W. Bensch A.V. Powell S. Boissiere A.M.Chippindale A. Puls, M. Schaefer. *J. Solid State Chem.*, 178:1171, 2005.

[56] A.-Q. Wu B. Liu L.-Z. Cai J.-S. Huang M.L. Fu, G.-C. Guo. *Eur. J. Inorg. Chem.*, page 3104, 2005.

7 Messprotokolle

7.1 Messprotokoll für die Verbindung $[C_6H_{17}N_3][Sb_{10}S_{16}]$

Table 1. Crystal data and structure refinement for $[C_6H_{17}N_3][Sb_{10}S_{16}]$.

Identification code	$[C_6H_{17}N_3][Sb_{10}S_{16}]$ (RK245)
Empirical formula	$C_6H_{17}N_3S_{16}Sb_{10}$
Formula weight	1861.69
Temperature	293(2) K
Wavelength	0.71073 Å
Crystal system	Monoclinic
Space group	$P2_1/c$
Unit cell dimensions	a = 11.530(2) Å
	b = 25.042(5) Å β= 111.25(3)°.
	c = 13.709(3) Å
Volume	3689.1(13) $Å^3$
Z	4
Density (calculated)	3.352 Mg/m^3
Absorption coefficient	8.116 mm^{-1}
F(000)	3360
Crystal size	0.1·0.13·0.5 mm^3
Theta range for data collection	1.63 to 27.01°.
Index ranges	0<=h<=14, -32<=k<=13, -17<=l<=16
Reflections collected	13220
Independent reflections	8071 [R(int) = 0.0305]
Completeness to theta = 27.01°	99.8 %
Refinement method	Full-matrix least-squares on F^2
Data / restraints / parameters	8071 / 0 / 316
Goodness-of-fit on F^2	1.102
Final R indices [I>2sigma(I)]	R1 = 0.0310, wR2 = 0.0788
R indices (all data)	R1 = 0.0389, wR2 = 0.0814
Largest diff. peak and hole	2.350 and -1.426 e.$Å^{-3}$

Table 2. Atomic coordinates (x 10^4) and equivalent isotropic displacement parameters (Å^{2}x 10^3)for $[C_6H_{17}N_3][Sb_{10}S_{16}]$. U(eq) is defined as one third of the trace of the orthogonalized U_{ij} tensor.

	x	y	z	U(eq)
Sb(1)	8311(1)	10366(1)	4808(1)	20(1)
Sb(2)	8002(1)	8853(1)	4272(1)	28(1)
Sb(3)	9844(1)	9125(1)	7204(1)	24(1)
Sb(4)	13144(1)	9692(1)	8107(1)	22(1)
Sb(5)	16434(1)	10123(1)	9230(1)	22(1)
Sb(6)	15408(1)	10161(1)	6421(1)	25(1)
Sb(7)	18722(1)	10637(1)	7423(1)	24(1)
Sb(8)	20349(1)	10795(1)	10316(1)	21(1)
Sb(9)	21942(1)	11238(1)	8458(1)	24(1)
Sb(10)	21241(1)	12687(1)	8721(1)	29(1)
S(1)	6428(1)	10717(1)	3353(1)	24(1)
S(2)	9043(1)	9904(1)	3595(1)	22(1)
S(3)	7291(2)	9525(1)	5227(1)	27(1)
S(4)	10079(1)	8708(1)	5631(1)	24(1)
S(5)	11969(2)	8883(1)	8343(1)	27(1)
S(6)	15207(1)	9324(1)	9402(1)	26(1)
S(7)	17085(1)	9692(1)	7877(1)	24(1)
S(8)	14723(1)	10609(1)	7709(1)	25(1)
S(9)	16677(2)	10944(1)	6189(1)	32(1)
S(10)	18325(1)	11014(1)	8934(1)	25(1)
S(11)	19859(2)	11428(1)	7137(1)	30(1)
S(12)	21539(2)	11566(1)	9979(1)	27(1)
S(13)	21048(1)	10212(1)	9255(1)	23(1)
S(14)	22665(2)	12141(1)	8188(2)	35(1)
S(15)	22991(2)	13126(1)	10059(2)	76(1)
S(16)	20982(2)	13294(1)	7257(2)	47(1)
N(1)	6143(8)	12338(4)	3136(8)	75(3)
N(2)	7629(10)	12917(4)	4924(7)	74(3)
N(3)	4038(9)	11614(4)	2330(10)	105(5)
C(1)	5893(9)	12895(4)	3261(8)	54(2)
C(2)	6245(10)	13030(5)	4388(8)	71(3)
C(3)	7945(14)	12363(5)	4799(14)	133(8)
C(4)	7478(11)	12243(5)	3602(12)	113(6)
C(5)	5678(11)	12171(6)	2054(11)	101(5)
C(6)	4276(10)	12038(5)	1715(10)	86(4)

Sb(1)-S(2)	2.4158(15)	Sb(1)-S(1)	2.5156(17)
Sb(1)-S(3)	2.5749(17)	Sb(2)-S(3)	2.4498(17)
Sb(2)-S(4)	2.4703(18)	Sb(2)-S(15)#1	2.494(2)
Sb(3)-S(5)	2.4564(18)	Sb(3)-S(4)	2.4974(15)
Sb(3)-S(16)#1	2.5089(19)	Sb(4)-S(1)#2	2.4528(15)
Sb(4)-S(5)	2.5227(17)	Sb(4)-S(6)	2.5687(18)
Sb(4)-S(2)#2	2.9261(18)	Sb(5)-S(7)	2.4847(15)
Sb(5)-S(6)	2.5103(17)	Sb(5)-S(8)	2.5954(17)
Sb(6)-S(8)	2.4516(16)	Sb(6)-S(7)	2.5111(17)
Sb(6)-S(9)	2.5333(19)	Sb(7)-S(10)	2.4652(15)
Sb(7)-S(9)	2.4749(19)	Sb(7)-S(11)	2.4842(18)
Sb(8)-S(13)	2.3956(15)	Sb(8)-S(10)	2.4765(18)
Sb(8)-S(12)	2.5064(17)	Sb(9)-S(12)	2.4377(16)
Sb(9)-S(11)	2.474(2)	Sb(9)-S(14)	2.4846(18)
Sb(10)-S(15)	2.442(3)	Sb(10)-S(14)	2.4448(17)
Sb(10)-S(16)	2.4475(18)	S(1)-Sb(4)#2	2.4528(15)
S(2)-Sb(4)#2	2.9261(18)	S(15)-Sb(2)#3	2.494(2)
S(16)-Sb(3)#3	2.5089(19)	N(1)-C(5)	1.445(14)
N(1)-C(1)	1.447(12)	N(1)-C(4)	1.456(14)
N(2)-C(3)	1.462(16)	N(2)-C(2)	1.522(15)
N(3)-C(6)	1.443(18)	C(3)-C(4)	1.56(2)
C(1)-C(2)	1.486(14)	C(5)-C(6)	1.548(16)
S(2)-Sb(1)-S(1)	92.17(5)	S(2)-Sb(1)-S(3)	93.63(5)
S(1)-Sb(1)-S(3)	97.45(5)	S(3)-Sb(2)-S(4)	96.80(5)
S(3)-Sb(2)-S(15)#1	91.01(10)	S(4)-Sb(2)-S(15)#1	93.67(7)
S(5)-Sb(3)-S(4)	92.89(6)	S(5)-Sb(3)-S(16)#1	90.35(7)
S(4)-Sb(3)-S(16)#1	94.54(6)	S(1)#2-Sb(4)-S(5)	92.60(6)
S(1)#2-Sb(4)-S(6)	90.23(5)	S(5)-Sb(4)-S(6)	91.69(5)
S(1)#2-Sb(4)-S(2)#2	82.18(5)	S(5)-Sb(4)-S(2)#2	91.86(5)
S(6)-Sb(4)-S(2)#2	171.76(5)	S(7)-Sb(5)-S(6)	93.26(6)
S(7)-Sb(5)-S(8)	87.23(5)	S(6)-Sb(5)-S(8)	99.12(5)
S(8)-Sb(6)-S(7)	89.87(5)	S(8)-Sb(6)-S(9)	95.08(6)
S(7)-Sb(6)-S(9)	98.53(6)	S(10)-Sb(7)-S(9)	91.93(6)
S(10)-Sb(7)-S(11)	95.54(6)	S(9)-Sb(7)-S(11)	94.06(6)
S(13)-Sb(8)-S(10)	95.83(5)	S(13)-Sb(8)-S(12)	91.76(5)
S(10)-Sb(8)-S(12)	96.62(6)	S(12)-Sb(9)-S(11)	97.24(6)
S(12)-Sb(9)-S(14)	89.94(6)	S(11)-Sb(9)-S(14)	90.26(6)
S(15)-Sb(10)-S(14)	90.86(8)	S(15)-Sb(10)-S(16)	99.13(11)
S(14)-Sb(10)-S(16)	89.85(6)	Sb(4)#2-S(1)-Sb(1)	97.47(6)
Sb(1)-S(2)-Sb(4)#2	88.18(5)	Sb(2)-S(3)-Sb(1)	100.08(6)
Sb(2)-S(4)-Sb(3)	102.20(6)	Sb(3)-S(5)-Sb(4)	100.30(6)
Sb(5)-S(6)-Sb(4)	93.54(5)	Sb(5)-S(7)-Sb(6)	92.07(5)
Sb(6)-S(8)-Sb(5)	90.82(5)	Sb(7)-S(9)-Sb(6)	97.14(6)
Sb(7)-S(10)-Sb(8)	98.47(6)	Sb(9)-S(11)-Sb(7)	99.10(6)

Table 3. Bond lengths [Å] and angles [°] for $[C_6H_{17}N_3][Sb_{10}S_{16}]$.

Sb(9)-S(12)-Sb(8)	100.60(6)	Sb(10)-S(14)-Sb(9)	99.60(6)
Sb(10)-S(15)-Sb(2)#3	103.89(9)	Sb(10)-S(16)-Sb(3)#3	102.67(6)
C(5)-N(1)-C(1)	112.7(10)	C(5)-N(1)-C(4)	110.1(10)
C(1)-N(1)-C(4)	109.3(8)	C(3)-N(2)-C(2)	112.4(10)
N(1)-C(1)-C(2)	110.5(10)	C(1)-C(2)-N(2)	107.7(8)
N(2)-C(3)-C(4)	107.5(11)	N(1)-C(4)-C(3)	109.7(12)
N(1)-C(5)-C(6)	109.2(11)	N(3)-C(6)-C(5)	112.4(11)

Symmetry transformations used to generate equivalent atoms:
#1 -x+3,y-1/2,-z+3/2 #2 -x+2,-y+2,-z+1 #3 -x+3,y+1/2,-z+3/2

Table 4. Anisotropic displacement parameters ($Å^2 x\ 10^3$) for $[C_6H_{17}N_3][Sb_{10}S_{16}]$. The anisotropic displacement factor exponent takes the form: $-2\pi^2[\ h^2\ a^{*2}U_{11} + ... + 2\ h\ k\ a^*\ b^*\ U_{12}\ ]$.

	U_{11}	U_{22}	U_{33}	U_{23}	U_{13}	U_{12}
Sb(1)	21(1)	25(1)	14(1)	0(1)	4(1)	2(1)
Sb(2)	32(1)	27(1)	20(1)	-1(1)	1(1)	0(1)
Sb(3)	25(1)	27(1)	20(1)	-3(1)	8(1)	-2(1)
Sb(4)	23(1)	28(1)	16(1)	-1(1)	6(1)	0(1)
Sb(5)	22(1)	29(1)	14(1)	0(1)	4(1)	1(1)
Sb(6)	20(1)	40(1)	14(1)	1(1)	4(1)	3(1)
Sb(7)	22(1)	31(1)	17(1)	-2(1)	7(1)	-1(1)
Sb(8)	25(1)	22(1)	15(1)	-1(1)	6(1)	1(1)
Sb(9)	27(1)	22(1)	25(1)	0(1)	12(1)	0(1)
Sb(10)	36(1)	24(1)	31(1)	4(1)	18(1)	4(1)
S(1)	23(1)	30(1)	17(1)	-1(1)	4(1)	7(1)
S(2)	21(1)	25(1)	18(1)	-1(1)	7(1)	3(1)
S(3)	26(1)	31(1)	24(1)	4(1)	11(1)	3(1)
S(4)	25(1)	26(1)	19(1)	-1(1)	7(1)	1(1)
S(5)	27(1)	28(1)	24(1)	6(1)	5(1)	0(1)
S(6)	23(1)	30(1)	22(1)	6(1)	4(1)	2(1)
S(7)	21(1)	32(1)	17(1)	0(1)	5(1)	5(1)
S(8)	22(1)	32(1)	19(1)	2(1)	6(1)	4(1)
S(9)	25(1)	44(1)	25(1)	11(1)	6(1)	2(1)
S(10)	23(1)	32(1)	21(1)	-2(1)	8(1)	4(1)
S(11)	33(1)	34(1)	22(1)	5(1)	8(1)	-3(1)
S(12)	36(1)	25(1)	20(1)	-3(1)	11(1)	-7(1)
S(13)	27(1)	21(1)	22(1)	-2(1)	10(1)	1(1)
S(14)	41(1)	23(1)	53(1)	0(1)	33(1)	-2(1)
S(15)	54(1)	60(2)	76(2)	-36(1)	-21(1)	33(1)
S(16)	75(1)	39(1)	43(1)	20(1)	42(1)	32(1)
N(1)	47(5)	55(5)	99(7)	-31(5)	-4(4)	2(4)
N(2)	93(7)	63(6)	49(4)	-11(4)	4(4)	-10(5)

N(3)	55(6)	43(5)	167(12)	-7(6)	-20(6)	3(5)
C(1)	43(5)	40(5)	78(6)	-13(4)	20(4)	1(4)
C(2)	68(7)	78(8)	70(7)	-23(6)	30(6)	-8(6)
C(3)	90(10)	56(8)	171(16)	-12(9)	-51(10)	24(7)
C(4)	62(7)	71(8)	152(13)	-66(9)	-26(7)	35(6)
C(5)	56(7)	121(12)	103(9)	-70(9)	0(6)	18(7)
C(6)	49(6)	82(9)	94(9)	-42(7)	-11(6)	9(6)

Table 5. Hydrogen coordinates (x 10^4) and isotropic displacement parameters ($Å^2$x 10^3) for $[C_6H_{17}N_3][Sb_{10}S_{16}]$.

	x	y	z	U(eq)
H(2A)	8060	13134	4656	89
H(2B)	7859	12991	5611	89
H(3A)	3222	11555	2118	157
H(3B)	4323	11708	3002	157
H(3C)	4421	11318	2250	157
H(1A)	5015	12968	2896	65
H(1B)	6362	13117	2955	65
H(2C)	5770	12815	4698	85
H(2D)	6074	13403	4467	85
H(3D)	7547	12125	5140	159
H(3E)	8838	12311	5111	159
H(4A)	7909	12471	3272	135
H(4B)	7656	11875	3489	135
H(5A)	6130	11858	1972	122
H(5B)	5799	12453	1617	122
H(6A)	3830	12356	1784	103
H(6B)	3960	11935	984	103

Table. 6 Hydrogen bonds with H..A < r(A) + 2.000 Angstroms and <DHA > 110 deg.

D-H	*d(D-H)*	*d(H..A)*	*<DHA*	*d(D..A)*	*A*
N2-H2A	0.900	2.418	150.56	3.232	S10 [x-1, -y+5/2, z-1/2]
N2-H2B	0.900	2.621	133.09	3.302	S5 [-x+2, y+1/2, -z+3/2]
N3-H3A	0.890	2.684	151.97	3.495	S16 [x-2, -y+5/2, z-1/2]
N3-H3A	0.890	2.871	125.15	3.461	S12 [x-2, y, z-1]
N3-H3C	0.890	2.715	138.96	3.436	S1
N3-H3C	0.890	2.933	140.35	3.663	S6 [-x+2, -y+2, -z+1]

7.2 Messprotokoll für die Verbindung $[C_7H_{13}N_2]_3[Sb_9S_{15}]$

Table 1. Crystal data and structure refinement for $[C_7H_{13}N_2]_3[Sb_9S_{15}]$.

Identification code	$[C_7H_{13}N_2]_3[Sb_9S_{15}]$ (RK522)
Empirical formula	$C_{21}H_{39}N_6S_{15}Sb_9$
Formula weight	1952.32 g/mol
Temperature	293(2) K
Wavelength	0.71073 Å
Crystal system	Monoclinic
Space group	$P2_1/c$
Unit cell dimensions	a = 10.2634(6) Å
	b = 23.6843(12) Å β= 102.430(7)°
	c = 20.4655(11) Å
Volume	4858.2(5) $Å^3$
Z	4
Density (calculated)	2.560 Mg/m^3
Absorption coefficient	5.485 mm^{-1}
F(000)	3464
Crystal size	0.5 x 0.2 x 0.2 mm^3
Theta range for data collection	2.21 to 26.92°.
Index ranges	-13<=h<=13, -30<=k<=30, -26<=l<=24
Reflections collected	41616
Independent reflections	10341 [R(int) = 0.0310]
Completeness to theta = 26.92°	98.3 %
Refinement method	Full-matrix least-squares on F^2
Data / restraints / parameters	10341 / 2 / 461
Goodness-of-fit on F^2	1.028
Final R indices [I>2sigma(I)]	R1 = 0.0341, wR2 = 0.0784
R indices (all data)	R1 = 0.0553, wR2 = 0.0880
Largest diff. peak and hole	0.847 and -1.284 e.$Å^{-3}$

Table 2. Atomic coordinates (x 10^4) and equivalent isotropic displacement parameters ($Å^2$x 10^3) for $[C_7H_{13}N_2]_3[Sb_9S_{15}]$. U(eq) is defined as one third of the trace of the orthogonalized U_{ij} tensor.

	x	y	z	U(eq)
Sb(1)	4239(1)	3860(1)	5651(1)	26(1)
Sb(2)	4574(1)	4556(1)	7363(1)	32(1)
Sb(3)	4326(1)	2897(1)	7347(1)	23(1)
Sb(4)	4323(1)	2128(1)	5686(1)	26(1)
Sb(5)	4659(1)	458(1)	5721(1)	23(1)
Sb(6)	4278(1)	1122(1)	3997(1)	25(1)
Sb(7)	4286(1)	2859(1)	3994(1)	25(1)
Sb(8)	4509(1)	4556(1)	4023(1)	27(1)
Sb(9)	4194(1)	3873(1)	2344(1)	25(1)
S(1)	2881(2)	4087(1)	6493(1)	36(1)
S(2)	3158(1)	4632(1)	8183(1)	32(1)
S(3)	5881(1)	3733(1)	7794(1)	36(1)
S(4)	5755(1)	2286(1)	8173(1)	30(1)
S(5)	5752(1)	2749(1)	6501(1)	27(1)
S(6)	2787(1)	3114(1)	5175(1)	30(1)
S(7)	5927(1)	1285(1)	6168(1)	29(1)
S(8)	2935(1)	913(1)	4849(1)	29(1)
S(9)	2824(1)	1864(1)	3510(1)	29(1)
S(10)	5745(1)	2267(1)	4833(1)	30(1)
S(11)	5843(1)	3738(1)	4422(1)	32(1)
S(12)	3153(1)	4635(1)	4869(1)	31(1)
S(13)	2762(1)	4109(1)	3149(1)	31(1)
S(14)	2783(1)	3123(1)	1856(1)	32(1)
S(15)	3216(1)	4647(1)	1521(1)	29(1)
N(1)	-1133(4)	1009(2)	4980(3)	44(1)
C(1)	-1586(9)	1223(3)	4292(5)	71(2)
C(7)	-1680(7)	491(4)	5212(3)	60(2)
C(2)	-520(20)	1634(10)	4096(12)	78(6)
C(3)	287(14)	1867(6)	4677(8)	41(3)
N(2)	418(18)	1701(8)	5316(10)	76(4)
C(4)	-282(12)	1257(5)	5521(7)	25(3)
C(5)	-159(12)	949(6)	6184(6)	40(2)
C(6)	-846(14)	374(6)	5820(7)	49(3)
C(2')	-514(15)	192(7)	5863(8)	56(4)
C(3')	-266(12)	666(6)	6381(7)	50(3)
C(4')	-197(15)	1306(7)	5300(9)	55(4)
N(2')	142(11)	1182(5)	6101(6)	18(2)
C(5')	0(20)	1822(9)	4944(13)	72(5)
C(6')	-798(15)	1790(7)	4371(8)	48(3)
N(3)	373(16)	1329(7)	5840(9)	9(3)
C(14)	9753(7)	3568(3)	6856(4)	53(2)

N(11)	8805(8)	3899(4)	6487(4)	24(2)
C(11)	8237(18)	4395(8)	6750(10)	33(5)
N(12)	10334(9)	3695(4)	7423(5)	36(2)
C(12)	9200(20)	4516(9)	7428(11)	59(5)
C(13)	9660(16)	4065(7)	7773(9)	54(4)
C(15)	10315(14)	3102(6)	6323(8)	50(3)
C(16)	9370(30)	3308(12)	5636(14)	111(8)
C(17)	8332(12)	3686(6)	5810(7)	42(3)
N(11')	8740(11)	3647(6)	6421(6)	23(2)
C(11')	8306(19)	3386(9)	5842(10)	73(5)
N(12')	10425(19)	2943(8)	6718(10)	91(5)
C(12')	8837(17)	3060(7)	5775(8)	58(4)
C(13')	9373(19)	2676(8)	6212(10)	76(5)
C(15')	9780(30)	4077(14)	7514(16)	118(10)
C(16')	8880(30)	4463(15)	7284(18)	109(12)
C(17')	7990(20)	4220(9)	6525(12)	76(5)
N(12A)	10560(30)	3298(11)	7029(14)	24(5)
C(11A)	8020(50)	4320(20)	6830(20)	6(10)
N(21)	1147(11)	5982(5)	6553(6)	51(3)
C(21)	1557(17)	5415(7)	6386(9)	52(4)
C(22)	555(14)	5187(6)	5801(7)	52(3)
C(23)	273(14)	5644(6)	5258(7)	52(3)
N(22)	-149(11)	6193(5)	5550(7)	47(3)
C(24)	339(11)	6331(6)	6211(7)	31(2)
C(25)	-90(17)	6858(8)	6508(9)	46(3)
C(26)	794(19)	6745(8)	7216(10)	72(4)
C(27)	1640(20)	6221(9)	7213(11)	74(5)
N(21')	329(14)	6545(8)	6433(8)	54(3)
C(21')	-440(50)	7000(20)	6370(30)	71(12)
C(22')	690(20)	7324(9)	7140(11)	88(6)
C(23')	1260(30)	7004(12)	7567(15)	106(7)
N(22')	81(19)	6143(8)	5919(12)	78(5)
C(24')	1238(13)	6350(6)	6931(7)	49(3)
C(25')	1670(20)	6586(10)	7456(11)	95(6)
C(26')	1936(19)	5771(8)	6840(10)	77(5)
C(27')	1040(40)	5593(13)	6117(16)	55(10)
C(28')	81(19)	6143(8)	5919(12)	78(5)
N(21A)	1238(13)	6350(6)	6931(7)	49(3)
C(22A)	1120(70)	5440(30)	6480(30)	71(16)
C(23A)	420(40)	5716(15)	5855(19)	39(7)
N(22A)	1670(20)	6586(10)	7456(11)	95(6)
C(24A)	329(14)	6545(8)	6433(8)	54(3)
C(27A)	-430(30)	7074(11)	6646(15)	36(5)

Table 3. Bond lengths [Å] and angles [°] for $[C_7H_{13}N_2]_3[Sb_9S_{15}]$.

Sb(1)-S(6)	2.3810(13)	Sb(1)-S(1)	2.4966(14)
Sb(1)-S(12)	2.5304(13)	Sb(2)-S(3)	2.4231(15)
Sb(2)-S(2)	2.4509(14)	Sb(2)-S(1)	2.4695(14)
Sb(3)-S(4)	2.4562(13)	Sb(3)-S(5)	2.5215(13)
Sb(3)-S(3)	2.5835(13)	Sb(4)-S(5)	2.4578(12)
Sb(4)-S(10)	2.5253(13)	Sb(4)-S(7)	2.6410(13)
Sb(4)-S(6)	2.8848(13)	Sb(5)-S(7)	2.4189(12)
Sb(5)-S(15)#1	2.4452(13)	Sb(5)-S(8)	2.4737(13)
Sb(6)-S(9)	2.3793(12)	Sb(6)-S(8)	2.4940(13)
Sb(6)-S(2)#2	2.5418(13)	Sb(7)-S(10)	2.4595(13)
Sb(7)-S(4)#2	2.5111(13)	Sb(7)-S(11)	2.6553(13)
Sb(7)-S(9)	2.8547(13)	Sb(8)-S(11)	2.4115(14)
Sb(8)-S(12)	2.4511(13)	Sb(8)-S(13)	2.4795(13)
Sb(9)-S(14)	2.3724(13)	Sb(9)-S(13)	2.4968(13)
Sb(9)-S(15)	2.5444(12)	S(2)-Sb(6)#1	2.5418(13)
S(4)-Sb(7)#1	2.5111(13)	S(15)-Sb(5)#2	2.4452(13)
N(1)-C(4')	1.254(16)	N(1)-C(4)	1.384(14)
N(1)-C(7)	1.471(9)	N(1)-C(1)	1.475(10)
C(1)-C(6')	1.559(17)	C(1)-C(2)	1.58(2)
C(7)-C(6)	1.378(16)	C(7)-C(2')	1.738(18)
C(2)-C(3)	1.41(3)	C(3)-N(2)	1.34(3)
N(2)-C(4)	1.39(2)	N(2)-N(3)	1.40(3)
C(4)-C(5)	1.522(19)	C(5)-N(3)	1.33(2)
C(5)-C(6)	1.637(19)	C(2')-C(3')	1.53(2)
C(3')-N(2')	1.448(17)	C(4')-N(3)	1.13(2)
C(4')-C(5')	1.46(3)	C(4')-N(2')	1.63(2)
C(5')-C(6')	1.28(3)	C(14)-N(12)	1.224(12)
C(14)-N(11')	1.229(13)	C(14)-N(11)	1.346(11)
C(14)-N(12')	1.683(19)	C(14)-C(15)	1.735(16)
C(14)-C(15')	1.80(3)	N(11)-C(17)	1.455(15)
N(11)-C(11)	1.47(2)	N(11)-C(11A)	1.54(4)
C(11)-C(12)	1.55(3)	N(12)-C(13)	1.40(2)
C(12)-C(13)	1.31(3)	C(12)-C(11A)	1.60(5)
C(15)-N(12A)	1.49(3)	C(15)-C(16)	1.60(3)
C(16)-C(17)	1.49(3)	N(11')-C(11')	1.33(2)
N(11')-C(17')	1.60(2)	N(12')-C(13')	1.47(3)
C(12')-C(13')	1.31(2)	C(15')-C(16')	1.32(4)
C(16')-C(11A)	1.18(6)	C(16')-C(17')	1.72(4)
N(21)-C(24)	1.271(16)	N(21)-C(27)	1.45(2)
N(21)-C(21)	1.47(2)	C(21)-C(22)	1.50(2)
C(22)-C(23)	1.53(2)	C(23)-N(22)	1.532(17)
N(22)-C(24)	1.376(19)	C(24)-C(25)	1.49(2)
C(25)-C(26)	1.56(3)	C(26)-C(27)	1.52(3)
N(21')-C(24')	1.31(2)	N(21')-C(21')	1.33(5)

N(21')-N(22')	1.40(2)	N(21')-C(27A)	1.59(3)
C(21')-C(22')	1.90(5)	C(22')-C(23')	1.21(3)
C(22')-C(27A)	1.48(3)	C(23')-C(25')	1.11(3)
N(22')-C(27')	1.632(19)	C(24')-C(25')	1.21(3)
C(24')-C(26')	1.58(2)	C(26')-C(22A)	1.26(6)
C(26')-C(27')	1.618(19)	C(22A)-C(23A)	1.47(8)
S(6)-Sb(1)-S(1)	92.80(5)	S(6)-Sb(1)-S(12)	97.33(5)
S(1)-Sb(1)-S(12)	92.59(5)	S(3)-Sb(2)-S(2)	99.95(5)
S(3)-Sb(2)-S(1)	98.52(5)	S(2)-Sb(2)-S(1)	95.59(5)
S(4)-Sb(3)-S(5)	92.41(4)	S(4)-Sb(3)-S(3)	88.62(5)
S(5)-Sb(3)-S(3)	86.80(4)	S(5)-Sb(4)-S(10)	92.45(4)
S(5)-Sb(4)-S(7)	88.07(4)	S(10)-Sb(4)-S(7)	87.15(4)
S(5)-Sb(4)-S(6)	87.80(4)	S(10)-Sb(4)-S(6)	89.80(4)
S(7)-Sb(4)-S(6)	174.76(4)	S(7)-Sb(5)-S(15)#1	100.52(4)
S(7)-Sb(5)-S(8)	99.40(4)	S(15)#1-Sb(5)-S(8)	94.88(4)
S(9)-Sb(6)-S(8)	92.76(4)	S(9)-Sb(6)-S(2)#2	95.16(5)
S(8)-Sb(6)-S(2)#2	94.50(4)	S(10)-Sb(7)-S(4)#2	91.49(4)
S(10)-Sb(7)-S(11)	89.10(5)	S(4)#2-Sb(7)-S(11)	85.57(4)
S(10)-Sb(7)-S(9)	88.07(4)	S(4)#2-Sb(7)-S(9)	90.08(4)
S(11)-Sb(7)-S(9)	174.75(4)	S(11)-Sb(8)-S(12)	100.91(5)
S(11)-Sb(8)-S(13)	99.88(4)	S(12)-Sb(8)-S(13)	96.29(5)
S(14)-Sb(9)-S(13)	93.07(5)	S(14)-Sb(9)-S(15)	98.20(4)
S(13)-Sb(9)-S(15)	94.07(4)	Sb(2)-S(1)-Sb(1)	100.62(5)
Sb(2)-S(2)-Sb(6)#1	98.40(5)	Sb(2)-S(3)-Sb(3)	103.71(5)
Sb(3)-S(4)-Sb(7)#1	100.68(5)	Sb(4)-S(5)-Sb(3)	101.52(4)
Sb(1)-S(6)-Sb(4)	101.94(4)	Sb(5)-S(7)-Sb(4)	103.30(4)
Sb(5)-S(8)-Sb(6)	100.01(5)	Sb(6)-S(9)-Sb(7)	103.23(4)
Sb(7)-S(10)-Sb(4)	101.60(5)	Sb(8)-S(11)-Sb(7)	105.09(5)
Sb(8)-S(12)-Sb(1)	98.71(5)	Sb(8)-S(13)-Sb(9)	97.75(5)
Sb(5)#2-S(15)-Sb(9)	99.27(4)		

Symmetry transformations used to generate equivalent atoms:
#1 x,-y+1/2,z+1/2 #2 x,-y+1/2,z-1/2

Table 4. Anisotropic displacement parameters ($Å^2 x\ 10^3$) for $[C_7H_{13}N_2]_3[Sb_9S_{15}]$. The anisotropic displacement factor exponent takes the form: $-2\pi^2[\ h^2\ a^{*2}U_{12} + ...\ + 2\ h\ k\ a^*\ b^*\ U_{11}\ ]$.

	U_{11}	U_{22}	U_{33}	U_{23}	U_{13}	U_{12}
Sb(1)	36(1)	24(1)	16(1)	-1(1)	3(1)	-1(1)
Sb(2)	58(1)	23(1)	18(1)	-1(1)	15(1)	-9(1)
Sb(3)	33(1)	19(1)	17(1)	0(1)	6(1)	2(1)
Sb(4)	36(1)	26(1)	17(1)	-3(1)	6(1)	-4(1)
Sb(5)	35(1)	20(1)	15(1)	-1(1)	6(1)	2(1)
Sb(6)	31(1)	25(1)	18(1)	0(1)	4(1)	3(1)
Sb(7)	35(1)	24(1)	16(1)	0(1)	5(1)	2(1)
Sb(8)	43(1)	23(1)	17(1)	0(1)	10(1)	-5(1)
Sb(9)	33(1)	25(1)	16(1)	0(1)	5(1)	0(1)
S(1)	54(1)	35(1)	21(1)	-6(1)	13(1)	-5(1)
S(2)	46(1)	30(1)	20(1)	2(1)	9(1)	8(1)
S(3)	36(1)	32(1)	40(1)	-12(1)	10(1)	-6(1)
S(4)	38(1)	35(1)	19(1)	6(1)	10(1)	10(1)
S(5)	36(1)	29(1)	18(1)	-4(1)	9(1)	-6(1)
S(6)	35(1)	24(1)	29(1)	-6(1)	1(1)	2(1)
S(7)	33(1)	25(1)	27(1)	1(1)	-1(1)	-2(1)
S(8)	34(1)	34(1)	18(1)	3(1)	5(1)	2(1)
S(9)	32(1)	24(1)	30(1)	5(1)	3(1)	-1(1)
S(10)	37(1)	36(1)	17(1)	4(1)	7(1)	8(1)
S(11)	35(1)	29(1)	31(1)	-7(1)	2(1)	-1(1)
S(12)	46(1)	29(1)	21(1)	4(1)	12(1)	9(1)
S(13)	33(1)	39(1)	21(1)	-3(1)	7(1)	1(1)
S(14)	37(1)	24(1)	33(1)	-4(1)	0(1)	2(1)
S(15)	41(1)	27(1)	22(1)	3(1)	10(1)	6(1)
N(1)	22(2)	47(3)	61(3)	-18(2)	1(2)	-12(2)
C(1)	75(5)	60(5)	71(5)	2(4)	-1(4)	-13(4)
C(7)	48(4)	93(5)	45(4)	-22(4)	22(3)	-46(4)
C(14)	44(3)	66(4)	47(4)	8(3)	2(3)	2(3)

7.3 Messprotokoll für die Verbindung $[C_6H_9N_2][Sb_8S_{13}]\cdot 2.5H_2O$

Table 1. Crystal data and structure refinement for $[C_6H_9N_2][Sb_8S_{13}]\cdot 2.5H_2O$.

Identification code	$[C_6H_9N_2][Sb_8S_{13}]\cdot 2.5H_2O$ (RK682)
Empirical formula	$C_6H_9N_2O_{2.50}S_{13}Sb_8$
Formula weight	1540.03 g/mol
Temperature	293(2) K
Wavelength	0.71073 Å
Crystal system	Monoclinic
Space group	$P2_1/m$
Unit cell dimensions	a = 7.2080(5) Å
	b = 25.7407(15) Å β= 96.960(8)°
	c = 15.9366(12) Å
Volume	2935.1(3) $Å^3$
Z	4
Density (calculated)	3.396 Mg/m^3
Absorption coefficient	8.182 mm^{-1}
F(000)	2684
Crystal size	0.3 x 0.6 x 0.1 mm^3
Theta range for data collection	2.58 to 26.93°.
Index ranges	-8<=h<=8, -32<=k<=32, -20<=l<=20
Reflections collected	23170
Independent reflections	6145 [R(int) = 0.0401]
Completeness to theta = 26.93°	94.4 %
Refinement method	Full-matrix least-squares on F^2
Data / restraints / parameters	6145 / 0 / 254
Goodness-of-fit on F^2	0.997
Final R indices [I>2sigma(I)]	R1 = 0.0299, wR2 = 0.0712
R indices (all data)	R1 = 0.0415, wR2 = 0.0750
Largest diff. peak and hole	1.619 and -1.119 $e.Å^{-3}$

Table 2. Atomic coordinates (x 10^4) and equivalent isotropic displacement parameters ($Å^2$x 10^3) for $[C_6H_9N_2][Sb_8S_{13}]\cdot 2.5H_2O$. U(eq) is defined as one third of the trace of the orthogonalized U_{ij} tensor.

	x	y	z	U(eq)
Sb(1)	7039(1)	5153(1)	1274(1)	18(1)
Sb(2)	7836(1)	4442(1)	3481(1)	17(1)
Sb(3)	2942(1)	4621(1)	4124(1)	17(1)
Sb(4)	4948(1)	3245(1)	3995(1)	17(1)
Sb(5)	3747(1)	3991(1)	6421(1)	16(1)
Sb(6)	-1265(1)	4087(1)	7038(1)	18(1)
Sb(7)	-330(1)	3368(1)	5105(1)	16(1)
Sb(8)	-2168(1)	4635(1)	9106(1)	18(1)
S(1)	8953(2)	5608(1)	306(1)	18(1)
S(2)	6400(3)	4329(1)	327(1)	23(1)
S(3)	9561(2)	4726(1)	2164(1)	20(1)
S(7)	5805(2)	4312(1)	4915(1)	16(1)
S(5)	2054(2)	3726(1)	3526(1)	17(1)
S(6)	6771(2)	3572(1)	2870(1)	19(1)
S(4)	4984(2)	4876(1)	2877(1)	17(1)
S(8)	3861(4)	2500	3059(2)	26(1)
S(9)	1189(2)	4463(1)	5638(1)	16(1)
S(10)	1927(2)	3867(1)	7689(1)	18(1)
S(11)	-1921(3)	3223(1)	6399(1)	22(1)
S(12)	2808(2)	3134(1)	5745(1)	18(1)
S(13)	-1079(4)	2500	4462(1)	20(1)
S(14)	-2766(3)	3812(1)	8306(1)	26(1)
O(1)	-709(17)	2500	2397(7)	63(3)
O(2)	3006(12)	3872(3)	1529(4)	63(2)
O(3)	-628(15)	3348(4)	1139(7)	96(3)
C(1)	1890(50)	2500	-850(20)	134(10)
C(1')	4170(50)	2500	-1006(19)	122(9)
C(2)	4070(40)	2966(9)	-605(15)	63(6)
C(2')	2610(60)	2971(14)	-480(20)	104(11)
N(1)	4520(40)	2942(9)	214(15)	75(6)
N(1')	3440(50)	2986(11)	353(18)	97(8)
C(3)	4420(30)	2500	670(13)	80(5)
C(4)	310(60)	2500	-1690(20)	163(13)
C(4')	3900(50)	2500	-2040(20)	138(11)
N(2)	1709(19)	2500	-2425(8)	54(3)
N(2')	5510(50)	2500	-2268(19)	158(10)

Table 3. Bond lengths [Å] and angles [°] for $[C_6H_9N_2][Sb_8S_{13}]\cdot 2.5H_2O$.

Sb(1)-S(3)	2.4293(17)	Sb(1)-S(1)	2.4841(16)
Sb(1)-S(2)	2.6117(16)	Sb(2)-S(4)	2.4329(16)
Sb(2)-S(6)	2.5238(16)	Sb(2)-S(3)	2.6681(16)
Sb(2)-S(7)	2.8781(16)	Sb(3)-S(7)	2.4190(16)
Sb(3)-S(5)	2.5447(15)	Sb(3)-S(4)	2.6941(16)
Sb(3)-S(9)	2.8838(16)	Sb(4)-S(5)	2.4629(17)
Sb(4)-S(6)	2.4937(16)		
Sb(4)-S(8)	2.4972(16)	Sb(5)-S(9)	2.4244(16)
Sb(5)-S(12)	2.5100(15)	Sb(5)-S(10)	2.5584(16)
Sb(6)-S(11)	2.4680(16)	Sb(6)-S(10)	2.4724(18)
Sb(6)-S(14)	2.5075(17)	Sb(7)-S(12)	2.4413(17)
Sb(7)-S(13)	2.4888(10)	Sb(7)-S(11)	2.5068(17)
Sb(8)-S(2)#1	2.4407(16)	Sb(8)-S(1)#2	2.4719(17)
Sb(8)-S(14)	2.4833(17)	S(1)-Sb(8)#2	2.4719(17)
S(2)-Sb(8)#3	2.4407(16)	S(8)-Sb(4)#4	2.4972(16)
S(13)-Sb(7)#4	2.4888(10)	C(1)-C(2')	1.42(4)
C(1)-C(2')#4	1.42(4)	C(1)-C(4)	1.65(5)
C(1)-C(1')	1.69(4)	C(1)-C(2)#4	1.98(4)
C(1')-C(2)	1.37(3)	C(1')-C(2)#4	1.37(3)
C(1')-C(4')	1.63(4)	C(1')-C(2')#4	1.91(5)
C(1')-C(2')	1.91(5)	C(2)-N(1)	1.31(3)
C(2)-N(1')	1.65(4)	C(2')-N(1')	1.39(4)
C(2')-N(1)	1.66(5)	N(1)-C(3)	1.36(2)
N(1')-C(3)	1.49(3)	C(3)-N(1)#4	1.36(2)
C(3)-N(1')#4	1.49(3)	C(4)-N(2)	1.64(4)
C(4')-N(2')	1.26(4)	C(4')-N(2)	1.62(4)
S(3)-Sb(1)-S(1)	98.25(6)	S(3)-Sb(1)-S(2)	92.13(6)
S(1)-Sb(1)-S(2)	95.54(5)	S(4)-Sb(2)-S(6)	92.96(6)
S(4)-Sb(2)-S(3)	90.85(5)	S(6)-Sb(2)-S(3)	95.06(5)
S(4)-Sb(2)-S(7)	83.18(5)	S(6)-Sb(2)-S(7)	92.47(5)
S(3)-Sb(2)-S(7)	170.62(5)	S(7)-Sb(3)-S(5)	93.24(5)
S(7)-Sb(3)-S(4)	87.49(5)	S(5)-Sb(3)-S(4)	94.52(5)
S(7)-Sb(3)-S(9)	87.16(5)	S(5)-Sb(3)-S(9)	94.00(5)
S(4)-Sb(3)-S(9)	170.18(5)		
S(5)-Sb(4)-S(6)	96.49(5)	S(5)-Sb(4)-S(8)	90.69(7)
S(6)-Sb(4)-S(8)	89.08(7)	S(9)-Sb(5)-S(12)	94.09(5)
S(9)-Sb(5)-S(10)	92.22(5)	S(12)-Sb(5)-S(10)	95.25(5)
S(11)-Sb(6)-S(10)	95.06(6)	S(11)-Sb(6)-S(14)	89.87(6)
S(10)-Sb(6)-S(14)	93.89(6)	S(12)-Sb(7)-S(13)	95.45(6)
S(12)-Sb(7)-S(11)	96.44(6)	S(13)-Sb(7)-S(11)	96.14(7)
S(2)#1-Sb(8)-S(1)#2	94.83(6)	S(2)#1-Sb(8)-S(14)	94.02(6)
S(1)#2-Sb(8)-S(14)	94.36(6)	Sb(8)#2-S(1)-Sb(1)	102.20(5)
Sb(8)#3-S(2)-Sb(1)	97.83(6)	Sb(1)-S(3)-Sb(2)	101.32(6)
Sb(3)-S(7)-Sb(2)	91.85(5)	Sb(4)-S(5)-Sb(3)	100.17(6)

Sb(4)-S(6)-Sb(2)	100.58(5)	Sb(2)-S(4)-Sb(3)	96.16(5)
Sb(4)-S(8)-Sb(4)#4	100.36(9)	Sb(5)-S(9)-Sb(3)	96.81(5)
Sb(6)-S(10)-Sb(5)	100.38(5)	Sb(6)-S(11)-Sb(7)	96.98(6)
Sb(7)-S(12)-Sb(5)	98.68(5)	Sb(7)-S(13)-Sb(7)#4	127.63(9)
Sb(8)-S(14)-Sb(6)	96.19(6)		

Symmetry transformations used to generate equivalent atoms:
#1 x-1,y,z+1 #2 -x+1,-y+1,-z+1 #3 x+1,y,z-1
#4 x,-y+1/2,z

Table 4. Anisotropic displacement parameters ($Å^2 x\ 10^3$) for $[C_6H_9N_2][Sb_8S_{13}]\cdot 2.5H_2O$. The anisotropic displacement factor exponent takes the form: $-2\pi^2[\ h^2\ a^{*2}U_{11} + ... + 2\ h\ k\ a^*\ b^*\ U_{12}\ ]$.

	U_{11}	U_{22}	U_{33}	U_{23}	U_{13}	U_{12}
Sb(1)	16(1)	24(1)	15(1)	4(1)	4(1)	1(1)
Sb(2)	16(1)	16(1)	20(1)	2(1)	1(1)	0(1)
Sb(3)	17(1)	14(1)	21(1)	3(1)	1(1)	2(1)
Sb(4)	19(1)	12(1)	18(1)	1(1)	2(1)	2(1)
Sb(5)	17(1)	15(1)	16(1)	-1(1)	0(1)	0(1)
Sb(6)	21(1)	19(1)	16(1)	-2(1)	3(1)	2(1)
Sb(7)	20(1)	15(1)	14(1)	-1(1)	0(1)	1(1)
Sb(8)	18(1)	23(1)	13(1)	1(1)	3(1)	0(1)
S(1)	19(1)	20(1)	15(1)	4(1)	3(1)	-1(1)
S(2)	29(1)	23(1)	18(1)	-2(1)	10(1)	-9(1)
S(3)	19(1)	27(1)	15(1)	5(1)	5(1)	6(1)
S(7)	17(1)	16(1)	15(1)	2(1)	3(1)	2(1)
S(5)	18(1)	15(1)	19(1)	0(1)	1(1)	2(1)
S(6)	22(1)	14(1)	22(1)	-2(1)	7(1)	-1(1)
S(4)	18(1)	16(1)	16(1)	4(1)	3(1)	2(1)
S(8)	37(2)	11(1)	27(1)	0	-8(1)	0
S(9)	18(1)	14(1)	17(1)	-1(1)	2(1)	1(1)
S(10)	21(1)	19(1)	15(1)	-2(1)	3(1)	1(1)
S(11)	24(1)	22(1)	21(1)	-5(1)	6(1)	-4(1)
S(12)	20(1)	12(1)	20(1)	-2(1)	1(1)	1(1)
S(13)	30(1)	13(1)	15(1)	0	-6(1)	0
S(14)	31(1)	30(1)	18(1)	-7(1)	8(1)	-11(1)
O(1)	61(8)	66(7)	62(7)	0	12(5)	0
O(2)	71(6)	75(5)	43(4)	13(4)	6(3)	6(4)
O(3)	89(8)	83(6)	116(8)	42(6)	15(6)	6(5)

7.4 Messprotokoll für die Verbindung $[Fe(C_6H_{18}N_4)][FeSbS_4]$

Table 1. Crystal data and structure refinement for $[Fe(C_6H_{18}N_4)][FeSbS_4]$.

Identification code	$[Fe(C_6H_{18}N_4)][FeSbS_4]$ (RK150)	
Empirical formula	$C_6H_{18}Fe_2N_4S_4Sb$	
Formula weight	507.93 g/mol	
Temperature	293(2) K	
Wavelength	0.71073 Å	
Crystal system	Triclinic	
Space group	P-1	
Unit cell dimensions	a = 8.3370(8) Å	α= 107.354(11)°
	b = 9.6277(9) Å	β= 99.145(11)°
	c = 10.7138(10) Å	γ = 100.944(11)°
Volume	784.27(13) $Å^3$	
Z	2	
Density (calculated)	2.151 Mg/m^3	
Absorption coefficient	4.051 mm^{-1}	
F(000)	498	
Crystal size	0.2 x 0.3 x 0.1 mm^3	
Theta range for data collection	2.50 to 27.95°.	
Index ranges	-10<=h<=10, -12<=k<=12, -14<=l<=14	
Reflections collected	7533	
Independent reflections	3464 [R(int) = 0.0501]	
Completeness to theta = 27.95°	91.9 %	
Refinement method	Full-matrix least-squares on F^2	
Data / restraints / parameters	3464 / 0 / 164	
Goodness-of-fit on F^2	1.040	
Final R indices [I>2sigma(I)]	R1 = 0.0364, wR2 = 0.0907	
R indices (all data)	R1 = 0.0421, wR2 = 0.0938	
Extinction coefficient	0.0162(17)	
Largest diff. peak and hole	1.361 and -2.143 $e.Å^{-3}$	

Table 2. Atomic coordinates (x 10^4) and equivalent isotropic displacement parameters ($Å^2$x 10^3) for [Fe($C_6H_{18}N_4$)][$FeSbS_4$]. U(eq) is defined as one third of the trace of the orthogonalized U_{ij} tensor.

	x	y	z	U(eq)
Sb(1)	3852(1)	3953(1)	2894(1)	23(1)
Fe(1)	2567(1)	6660(1)	1410(1)	31(1)
Fe(2)	1704(1)	5362(1)	5381(1)	25(1)
S(1)	2532(1)	4036(1)	756(1)	28(1)
S(2)	3580(1)	6349(1)	4320(1)	28(1)
S(3)	6727(1)	4891(2)	2778(1)	37(1)
S(4)	-4(1)	3177(1)	4047(1)	34(1)
N(3)	1666(5)	7040(4)	-409(3)	36(1)
N(1)	5239(4)	7511(4)	1792(4)	38(1)
N(4)	2859(5)	9218(4)	2159(4)	38(1)
C(4)	1974(7)	9492(6)	3263(5)	52(1)
C(3)	329(7)	8398(6)	2918(6)	55(1)
C(2)	4649(7)	9969(6)	2609(8)	75(2)
C(1A)	5674(12)	9066(11)	2880(9)	40(2)
C(1B)	5820(20)	9053(19)	2220(20)	64(5)
N(2)	453(4)	6857(4)	2306(4)	38(1)
C(5)	2179(8)	8630(6)	-291(5)	54(1)
C(6)	2016(9)	9612(6)	1047(6)	63(2)

Table 3. Bond lengths [Å] and angles [°] for $[Fe(C_6H_{18}N_4)][FeSbS_4]$.

Sb(1)-S(1)	2.4096(10)	Sb(1)-S(2)	2.4313(9)
Sb(1)-S(3)	2.4322(10)	Fe(1)-N(3)	2.135(4)
Fe(1)-N(1)	2.149(3)	Fe(1)-N(2)	2.149(3)
Fe(1)-N(4)	2.302(4)	Fe(1)-S(1)	2.4044(12)
Fe(2)-S(4)#1	2.2095(11)	Fe(2)-S(4)	2.2178(12)
Fe(2)-S(3)#2	2.2916(12)	Fe(2)-S(2)	2.2986(10)
Fe(2)-Fe(2)#1	2.7197(10)	S(3)-Fe(2)#2	2.2916(12)
S(4)-Fe(2)#1	2.2095(11)	N(3)-C(5)	1.470(6)
N(1)-C(1B)	1.378(17)	N(1)-C(1A)	1.533(10)
N(4)-C(2)	1.461(6)	N(4)-C(6)	1.470(8)
N(4)-C(4)	1.476(6)	C(4)-C(3)	1.478(8)
C(3)-N(2)	1.464(6)	C(2)-C(1A)	1.388(14)
C(2)-C(1B)	1.462(18)	C(5)-C(6)	1.506(7)
S(1)-Sb(1)-S(2)	98.40(4)	S(1)-Sb(1)-S(3)	96.45(4)
S(2)-Sb(1)-S(3)	95.57(4)	N(3)-Fe(1)-N(1)	103.10(15)
N(3)-Fe(1)-N(2)	99.47(14)	N(1)-Fe(1)-N(2)	142.52(14)
N(3)-Fe(1)-N(4)	78.21(14)	N(1)-Fe(1)-N(4)	78.19(14)
N(2)-Fe(1)-N(4)	77.62(14)	N(3)-Fe(1)-S(1)	105.60(10)
N(1)-Fe(1)-S(1)	96.88(11)	N(2)-Fe(1)-S(1)	105.41(11)
N(4)-Fe(1)-S(1)	174.45(10)	S(4)#1-Fe(2)-S(4)	104.20(4)
S(4)#1-Fe(2)-S(3)#2	111.65(4)	S(4)-Fe(2)-S(3)#2	111.15(5)
S(4)#1-Fe(2)-S(2)	111.29(5)	S(4)-Fe(2)-S(2)	112.26(4)
S(3)#2-Fe(2)-S(2)	106.41(4)	S(4)#1-Fe(2)-Fe(2)#1	52.24(3)
S(4)-Fe(2)-Fe(2)#1	51.96(3)	S(3)#2-Fe(2)-Fe(2)#1	126.44(4)
S(2)-Fe(2)-Fe(2)#1	127.15(4)	Fe(1)-S(1)-Sb(1)	99.29(4)
Fe(2)-S(2)-Sb(1)	96.34(4)	Fe(2)#2-S(3)-Sb(1)	103.38(4)
Fe(2)#1-S(4)-Fe(2)	75.80(4)	C(5)-N(3)-Fe(1)	112.6(3)
C(1B)-N(1)-C(1A)	28.4(9)	C(1B)-N(1)-Fe(1)	115.8(7)
C(1A)-N(1)-Fe(1)	106.2(4)	C(2)-N(4)-C(6)	112.5(5)
C(2)-N(4)-C(4)	112.6(4)	C(6)-N(4)-C(4)	110.3(4)
C(2)-N(4)-Fe(1)	108.4(3)	C(6)-N(4)-Fe(1)	107.9(3)
C(4)-N(4)-Fe(1)	104.8(3)	N(4)-C(4)-C(3)	112.5(4)
N(2)-C(3)-C(4)	111.4(4)	C(1A)-C(2)-N(4)	114.6(6)
C(1A)-C(2)-C(1B)	29.5(8)	N(4)-C(2)-C(1B)	117.1(8)
C(2)-C(1A)-N(1)	113.2(7)	N(1)-C(1B)-C(2)	118.4(11)
C(3)-N(2)-Fe(1)	115.0(3)	N(3)-C(5)-C(6)	109.8(4)
N(4)-C(6)-C(5)	111.5(5)		

Symmetry transformations used to generate equivalent atoms:
#1 -x,-y+1,-z+1 #2 -x+1,-y+1,-z+1

Table 4. Anisotropic displacement parameters ($Å^2 x\ 10^3$) for $[Fe(C_6H_{18}N_4)][FeSbS_4]$. The anisotropic displacement factor exponent takes the form: $-2\pi^2[\ h^2\ a^{*2}U_{11} + ...\ + 2\ h\ k\ a^*\ b^*\ U_{12}\ ]$.

	U_{11}	U_{22}	U_{33}	U_{23}	U_{13}	U_{12}
Sb(1)	21(1)	24(1)	26(1)	9(1)	4(1)	8(1)
Fe(1)	20(1)	25(1)	44(1)	7(1)	7(1)	6(1)
Fe(2)	16(1)	36(1)	28(1)	12(1)	7(1)	10(1)
S(1)	28(1)	29(1)	23(1)	5(1)	-2(1)	8(1)
S(2)	25(1)	28(1)	32(1)	9(1)	11(1)	8(1)
S(3)	21(1)	68(1)	36(1)	29(1)	13(1)	20(1)
S(4)	23(1)	35(1)	42(1)	7(1)	9(1)	12(1)
N(3)	35(2)	35(2)	32(2)	6(1)	9(1)	5(2)
N(1)	25(2)	39(2)	54(2)	21(2)	13(2)	9(2)
N(4)	33(2)	30(2)	42(2)	2(1)	7(1)	6(1)
C(4)	61(3)	45(2)	42(2)	-3(2)	11(2)	25(2)
C(3)	50(3)	61(3)	69(3)	24(3)	33(3)	31(3)
C(2)	38(3)	39(3)	111(5)	-17(3)	12(3)	-3(2)
C(1A)	22(4)	39(4)	44(5)	8(4)	-1(3)	-9(3)
C(1B)	27(6)	45(8)	120(17)	31(12)	16(10)	8(6)
N(2)	29(2)	52(2)	42(2)	24(2)	13(1)	14(2)
C(5)	71(4)	44(3)	45(3)	17(2)	13(2)	3(3)
C(6)	92(5)	36(2)	57(3)	15(2)	13(3)	14(3)

Table 5. Hydrogen coordinates (x 10^4) and isotropic displacement parameters (Å^{2}x 10^3) for [Fe($C_6H_{18}N_4$)][$FeSbS_4$].

	x	y	z	U(eq)
H(3A)	2058	6486	-1072	43
H(3B)	538	6731	-636	43
H(1A)	5775	6897	2080	45
H(1B)	5541	7585	1040	45
H(4A)	1807	10499	3480	62
H(4B)	2668	9436	4055	62
H(3C)	-88	8479	3725	66
H(3D)	-467	8635	2298	66
H(2A)	4993	10345	1922	90
H(2B)	4820	10829	3415	90
H(1A1)	5580	8941	3733	48
H(1A2)	6831	9569	2967	48
H(1B1)	6251	9315	1512	76
H(1B2)	6760	9346	2988	76
H(2C)	-492	6342	1671	45
H(2D)	508	6419	2940	45
H(5A)	1476	8808	-1011	65
H(5B)	3333	8876	-370	65
H(6A)	2506	10656	1173	75
H(6B)	837	9500	1054	75

Table. 6 Hydrogen bonds with H..A < r(A) + 2.000 Angstroms and <DHA > 110 deg.

D-H	d(D-H)	d(H..A)	<DHA	d(D..A)	A
N2-H1N2	0.900	2.676	148.07	3.472	S1 [-x+2, -y+1, -z+1]
N3-H3A	0.900	2.404	176.48	3.302	S3 [-x+1, -y+1, -z]
N3-H3B	0.900	2.497	168.04	3.382	S1 [-x, -y+1, -z]
N1-H1A_a	0.900	2.484	169.39	3.373	S3
N1-H1B_a	0.900	2.977	133.55	3.656	S1 [-x+1, -y+1, -z]
N2-H2C	0.900	2.752	148.32	3.550	S1 [-x, -y+1, -z]
N2-H2D	0.900	2.769	120.61	3.319	S2

7.5 Messprotokoll für die Verbindung $[Fe(C_4H_{13}N_3)_2][Fe_2Sb_4S_{10}]$

Table 1. Crystal data and structure refinement for $[Fe(C_4H_{13}N_3)_2][Fe_2Sb_4S_{10}]$.

Identification code	$[Fe(C_4H_{13}N_3)_2][Fe_2Sb_4S_{10}]$ (Rk119)	
Empirical formula	$C_8H_{26}Fe_3N_6S_{10}Sb_4$	
Formula weight	1181.50 g/mol	
Temperature	293(2) K	
Wavelength	0.71073 Å	
Crystal system	Triclinic	
Space group	P-1	
Unit cell dimensions	a = 7.7104(18) Å	α= 76.182(15)°
	b = 9.863(2) Å	β= 83.644(12)°
	c = 10.524(3) Å	γ= 68.229(14)°
Volume	721.5(3) $Å^3$	
Z	1	
Density (calculated)	2.719 Mg/m^3	
Absorption coefficient	5.890 mm^{-1}	
F(000)	558	
Crystal size	0.1 x 0.15 x 0.3 mm^3	
Theta range for data collection	1.99 to 30.03°.	
Index ranges	0<=h<=10, -12<=k<=13, -14<=l<=14	
Reflections collected	4504	
Independent reflections	4213 [R(int) = 0.0760]	
Completeness to theta = 30.03°	99.9 %	
Refinement method	Full-matrix least-squares on F^2	
Data / restraints / parameters	4213 / 0 / 143	
Goodness-of-fit on F^2	1.093	
Final R indices [I>2sigma(I)]	R1 = 0.0255, wR2 = 0.0676	
R indices (all data)	R1 = 0.0324, wR2 = 0.0699	
Extinction coefficient	0.0043(4)	
Largest diff. peak and hole	2.002 and -1.394 $e.Å^{-3}$	

Table 2. Atomic coordinates (x 10^4) and equivalent isotropic displacement parameters ($Å^2$x 10^3) for $[Fe(C_4H_{13}N_3)_2][Fe_2Sb_4S_{10}]$. U(eq) is defined as one third of the trace of the orthogonalized U_{ij} tensor.

	x	y	z	U(eq)
Sb(1)	8254(1)	8848(1)	9757(1)	18(1)
Sb(2)	4498(1)	7009(1)	10135(1)	19(1)
S(1)	8104(1)	11374(1)	8665(1)	21(1)
S(2)	10438(1)	7950(1)	8000(1)	25(1)
S(3)	5392(1)	9028(1)	8717(1)	20(1)
S(4)	6589(1)	6200(1)	11954(1)	25(1)
S(5)	8452(1)	4931(1)	8942(1)	23(1)
Fe(1)	9008(1)	4522(1)	11055(1)	19(1)
Fe(2)	5000	10000	5000	26(1)
N(1)	7454(5)	9152(5)	3611(3)	38(1)
C(1)	8962(5)	7962(5)	4393(4)	39(1)
C(2)	8178(5)	6868(5)	5254(4)	34(1)
N(2)	6526(4)	7640(3)	6004(3)	24(1)
N(3)	3345(6)	8791(5)	4449(4)	46(1)
C(3)	5141(6)	6893(5)	6281(4)	32(1)
C(4)	4061(6)	7184(5)	5068(4)	36(1)

Table 3. Bond lengths [Å] and angles [°] for $[Fe(C_4H_{13}N_3)_2][Fe_2Sb_4S_{10}]$.

Sb(1)-S(1)	2.4474(10)	Sb(1)-S(2)	2.4546(10)
Sb(1)-S(3)	2.5004(10)	Sb(2)-S(4)#1	2.4291(11)
Sb(2)-S(4)	2.4291(11)	Sb(2)-S(3)	2.4570(10)
Sb(2)-S(1)#2	2.4886(10)	S(1)-Sb(2)#2	2.4886(10)
S(5)-Fe(1)#3	2.2163(10)	S(5)-Fe(1)	2.2234(11)
Fe(1)-S(4)#1	2.2758(10)	Fe(1)-S(2)#3	2.2974(11)
Fe(1)-Fe(1)#3	2.7342(10)	Fe(2)-N(2)	2.234(3)
Fe(2)-N(3)	2.239(4)	Fe(2)-N(1)	2.283(4)
N(1)-C(1)	1.465(5)	C(1)-C(2)	1.499(6)
C(2)-N(2)	1.473(4)	N(2)-C(3)	1.476(5)
N(3)-C(4)	1.476(6)	C(3)-C(4)	1.513(6)
S(1)-Sb(1)-S(2)	87.43(3)	S(1)-Sb(1)-S(3)	94.64(3)
S(2)-Sb(1)-S(3)	95.72(4)	S(4)-Sb(2)-S(3)	102.30(3)
S(4)-Sb(2)-S(1)#2	92.39(3)	S(3)-Sb(2)-S(1)#2	96.60(3)
Sb(1)-S(1)-Sb(2)#2	103.16(3)	Fe(1)#3-S(2)-Sb(1)	93.47(4)
Sb(2)-S(3)-Sb(1)	103.37(3)	Fe(1)-S(4)-Sb(2)	96.48(4)
Fe(1)#3-S(5)-Fe(1)	76.03(3)	S(5)#3-Fe(1)-S(5)	103.97(3)
S(5)#3-Fe(1)-S(4)#1	108.49(4)	S(5)-Fe(1)-S(4)	107.86(4)
S(5)#3-Fe(1)-S(2)#3	110.90(4)	S(5)-Fe(1)-S(2)#3	109.31(4)
S(4)-Fe(1)-S(2)#3	115.62(4)	N(2)#4-Fe(2)-N(3)#4	77.99(13)
N(2)-Fe(2)-N(3)#4	102.01(13)	N(2)#4-Fe(2)-N(3)	102.01(13)

N(2)-Fe(2)-N(3)	77.99(13)	N(2)#4-Fe(2)-N(1)#4	75.67(12)
N(2)-Fe(2)-N(1)#4	104.33(12)	N(3)#4-Fe(2)-N(1)#4	94.42(17)
N(3)-Fe(2)-N(1)#4	85.58(17)	N(2)#4-Fe(2)-N(1)	104.33(12)
N(2)-Fe(2)-N(1)	75.67(12)	N(3)#4-Fe(2)-N(1)	85.58(17)
N(3)-Fe(2)-N(1)	94.42(17)	C(1)-N(1)-Fe(2)	107.8(2)
N(1)-C(1)-C(2)	108.7(3)	N(2)-C(2)-C(1)	110.8(3)
C(2)-N(2)-C(3)	113.2(3)	C(2)-N(2)-Fe(2)	113.2(2)
C(3)-N(2)-Fe(2)	106.4(2)	C(4)-N(3)-Fe(2)	111.7(2)
N(2)-C(3)-C(4)	110.7(3)	N(3)-C(4)-C(3)	111.2(3)

Symmetry transformations used to generate equivalent atoms:
#1 x,y,z #2 -x+1,-y+2,-z+2 #3 -x+2,-y+1,-z+2 #4 -x+1,-y+2,-z+1

Table 4. Anisotropic displacement parameters ($Å^2 x\ 10^3$) for $[Fe(C_4H_{13}N_3)_2][Fe_2Sb_4S_{10}]$. The anisotropic displacement factor exponent takes the form: $-2\pi^2[\ h^2\ a^{*2}U_{11} + ... + 2\ h\ k\ a^*\ b^*\ U_{12}\ ]$.

	U_{11}	U_{22}	U_{33}	U_{23}	U_{13}	U_{12}
Sb(1)	16(1)	16(1)	22(1)	-3(1)	2(1)	-5(1)
Sb(2)	17(1)	15(1)	26(1)	-6(1)	3(1)	-6(1)
S(1)	17(1)	16(1)	29(1)	-5(1)	7(1)	-5(1)
S(2)	24(1)	16(1)	29(1)	-3(1)	10(1)	-5(1)
S(3)	18(1)	20(1)	20(1)	-3(1)	0(1)	-7(1)
S(4)	22(1)	23(1)	23(1)	-6(1)	3(1)	0(1)
S(5)	21(1)	24(1)	24(1)	-4(1)	0(1)	-9(1)
Fe(1)	16(1)	15(1)	22(1)	-3(1)	3(1)	-4(1)
Fe(2)	20(1)	25(1)	30(1)	-2(1)	-1(1)	-7(1)
N(1)	30(2)	48(2)	27(2)	4(2)	2(1)	-10(2)
C(1)	23(2)	44(2)	35(2)	3(2)	3(1)	-4(2)
C(2)	28(2)	33(2)	30(2)	-6(2)	7(1)	-1(1)
N(2)	23(1)	26(1)	20(1)	-4(1)	4(1)	-7(1)
N(3)	46(2)	45(2)	48(2)	4(2)	-21(2)	-23(2)
C(3)	36(2)	32(2)	27(2)	-3(1)	6(1)	-16(2)
C(4)	38(2)	39(2)	38(2)	-12(2)	1(2)	-20(2)

Table 5. Hydrogen coordinates (x 10^4) and isotropic displacement parameters (Å^{2}x 10^3) for $[Fe(C_4H_{13}N_3)_2][Fe_2Sb_4S_{10}]$.

	x	y	z	U(eq)
H(1A)	7106	8797	3009	46
H(1B)	7843	9902	3193	46
H(1C)	9493	8383	4925	47
H(1D)	9943	7462	3822	47
H(2A)	7832	6336	4720	41
H(2B)	9123	6143	5854	41
H(2)	6919	7653	6783	29
H(3A)	2142	9198	4697	55
H(3B)	3393	8900	3573	55
H(3C)	4282	7262	6972	38
H(3D)	5776	5826	6580	38
H(4A)	4868	6628	4448	43
H(4B)	3023	6834	5302	43

Table. 6 Hydrogen bonds with H..A < r(A) + 2.000 Angstroms and <DHA > 110 deg.

D-H	*d(D-H)*	*d(H..A)*	*<DHA*	*d(D..A)*	*A*
N3-H3B	0.900	2.845	147.33	3.635	S1 [-x+1, -y+2, -z+1]
N1-H1B	0.900	2.876	172.38	3.770	S2 [-x+2, -y+2, -z+1]
N1-H1A	0.900	2.732	113.21	3.195	S3 [-x+1, -y+2, -z+1]
N2-H2	0.910	2.640	135.38	3.349	S3
N2-H2	0.910	3.015	124.51	3.610	S5

7.6 Messprotokoll für die Verbindung $[Fe(C_6H_{18}N_4)][Sb_4S_7]$

Table 1. Crystal data and structure refinement for $[Fe(C_6H_{18}N_4)][Sb_4S_7]$.

Identification code	$[Fe(C_6H_{18}N_4)][Sb_4S_7]$ (RK156)
Empirical formula	$C_6H_{18}FeN_4S_7Sb_4$
Formula weight	913.51 g/mol
Temperature	293(2) K
Wavelength	0.71073 Å
Crystal system	Monoclinic
Space group	$P2_1/c$
Unit cell dimensions	a = 8.0030(16) Å
	b = 10.562(2) Å β= 90.81(3)°
	c = 25.955(5) Å
Volume	2193.7(8) $Å^3$
Z	4
Density (calculated)	2.766 Mg/m^3
Absorption coefficient	6.173 mm^{-1}
F(000)	1696
Crystal size	0.1 x 0.08 x 0.06 mm^3
Theta range for data collection	2.49 to 28.10°.
Index ranges	-10<=h<=10, -13<=k<=13, -34<=l<=34
Reflections collected	20987
Independent reflections	5329 [R(int) = 0.0460]
Completeness to theta = 28.10°	99.6 %
Refinement method	Full-matrix least-squares on F^2
Data / restraints / parameters	5329 / 0 / 200
Goodness-of-fit on F^2	1.031
Final R indices [I>2sigma(I)]	R1 = 0.0364, wR2 = 0.0930
R indices (all data)	R1 = 0.0404, wR2 = 0.0960
Extinction coefficient	0.00319(18)
Largest diff. peak and hole	1.386 and -1.540 $e.Å^{-3}$

Table 2. Atomic coordinates (x 10^4) and equivalent isotropic displacement parameters ($Å^2$x 10^3) for $[Fe(C_6H_{18}N_4)][Sb_4S_7]$. U(eq) is defined as one third of the trace of the orthogonalized U_{ij} tensor.

	x	y	z	U(eq)
Sb(1)	7255(1)	7312(1)	5972(1)	21(1)
Sb(2)	5512(1)	6614(1)	7308(1)	27(1)
Sb(3)	1148(1)	7933(1)	6841(1)	22(1)
Sb(4)	4435(1)	9941(1)	7456(1)	26(1)
Fe	7388(1)	3862(1)	5545(1)	24(1)
S(1)	7283(2)	5977(1)	5222(1)	27(1)
S(2)	7636(1)	5717(1)	6634(1)	25(1)
S(3)	10180(2)	8003(2)	5932(1)	36(1)
S(4)	3423(1)	6453(1)	6608(1)	28(1)
S(5)	6824(1)	8680(1)	7142(1)	30(1)
S(6)	3271(2)	8119(1)	7851(1)	32(1)
S(7)	2618(2)	9907(1)	6680(1)	32(1)
N(1)	7554(5)	1745(4)	5761(2)	26(1)
N(2)	9944(5)	3723(4)	5788(2)	31(1)
N(3)	6783(6)	2964(4)	4831(2)	31(1)
N(4)	5199(5)	3616(4)	5991(2)	33(1)
C(1)	7564(6)	1015(5)	5277(2)	31(1)
C(2)	6372(7)	1610(5)	4887(2)	35(1)
C(3)	9140(6)	1597(5)	6057(2)	34(1)
C(4)	10512(6)	2387(5)	5824(2)	33(1)
C(5)	6095(7)	1435(5)	6077(2)	36(1)
C(6)	5498(7)	2586(6)	6369(2)	41(1)

Table 3. Bond lengths [Å] and angles [°] for $[Fe(C_6H_{18}N_4)][Sb_4S_7]$.

Sb(1)-S(1)	2.4030(12)	Sb(1)-S(2)	2.4218(11)
Sb(1)-S(3)	2.4564(13)	Sb(2)-S(4)#1	2.4571(14)
Sb(2)-S(4)	2.4571(14)	Sb(2)-S(5)#1	2.4618(14)
Sb(2)-S(5)	2.4618(14)	Sb(2)-S(2)	2.6326(13)
Sb(2)-S(6)#1	2.7929(14)	Sb(2)-S(6)	2.7929(14)
Sb(3)-S(7)	2.4331(12)	Sb(3)-S(3)#2	2.4758(14)
Sb(3)-S(4)	2.4811(12)	Sb(3)-S(4)#1	2.4811(12)
Sb(4)-S(6)#1	2.3767(14)	Sb(4)-S(6)	2.3767(14)
Sb(4)-S(7)	2.4686(14)	Sb(4)-S(5)	2.4776(13)
Sb(4)-S(5)#1	2.4776(13)	Fe-N(4)	2.129(4)
Fe-N(3)	2.132(4)	Fe-N(2)	2.137(4)
Fe-N(1)	2.308(4)	Fe-S(1)	2.3870(13)
S(3)-Sb(3)#3	2.4758(14)		
N(1)-C(5)	1.473(6)	N(1)-C(1)	1.475(6)
N(1)-C(3)	1.483(6)	N(2)-C(4)	1.486(7)

N(3)-C(2)	1.475(7)	N(4)-C(6)	1.482(7)
C(1)-C(2)	1.518(7)	C(3)-C(4)	1.512(7)
C(5)-C(6)	1.515(8)		
S(1)-Sb(1)-S(2)	99.44(4)	S(1)-Sb(1)-S(3)	96.90(5)
S(2)-Sb(1)-S(3)	97.25(5)	S(4)#1-Sb(2)-S(4)	0.00(4)
S(4)#1-Sb(2)-S(5)#1	102.69(4)	S(4)-Sb(2)-S(5)#1	102.69(4)
S(4)#1-Sb(2)-S(5)	102.69(4)	S(4)-Sb(2)-S(5)	102.69(4)
S(4)#1-Sb(2)-S(2)	85.58(4)	S(4)-Sb(2)-S(2)	85.58(4)
S(5)#1-Sb(2)-S(2)	85.51(4)	S(5)-Sb(2)-S(2)	85.51(4)
S(4)#1-Sb(2)-S(6)#1	88.73(4)	S(4)-Sb(2)-S(6)#1	88.73(4)
S(5)#1-Sb(2)-S(6)#1	82.10(4)	S(5)-Sb(2)-S(6)#1	82.10(4)
S(2)-Sb(2)-S(6)#1	164.90(4)	S(4)#1-Sb(2)-S(6)	88.73(4)
S(4)-Sb(2)-S(6)	88.73(4)	S(5)#1-Sb(2)-S(6)	82.10(4)
S(5)-Sb(2)-S(6)	82.10(4)	S(2)-Sb(2)-S(6)	164.90(4)
S(7)-Sb(3)-S(3)#2	87.47(5)	S(7)-Sb(3)-S(4)	98.04(5)
S(3)#2-Sb(3)-S(4)	90.37(5)	S(7)-Sb(3)-S(4)#1	98.04(5)
S(3)#2-Sb(3)-S(4)#1	90.37(5)	S(6)#1-Sb(4)-S(7)	96.33(4)
S(6)-Sb(4)-S(7)	96.33(4)	S(6)#1-Sb(4)-S(5)	90.90(5)
S(6)-Sb(4)-S(5)	90.90(5)	S(7)-Sb(4)-S(5)	99.89(5)
S(6)#1-Sb(4)-S(5)#1	90.90(5)	S(6)-Sb(4)-S(5)#1	90.90(5)
S(7)-Sb(4)-S(5)#1	99.89(5)	N(4)-Fe-N(3)	103.92(18)
N(4)-Fe-N(2)	128.52(18)	N(3)-Fe-N(2)	115.50(17)
N(4)-Fe-N(1)	78.18(16)	N(3)-Fe-N(1)	78.01(15)
N(2)-Fe-N(1)	79.08(15)	N(4)-Fe-S(1)	106.25(12)
N(3)-Fe-S(1)	95.99(12)	N(2)-Fe-S(1)	101.31(12)
N(1)-Fe-S(1)	173.38(11)	Fe-S(1)-Sb(1)	105.40(5)
Sb(1)-S(2)-Sb(2)	98.34(4)	Sb(1)-S(3)-Sb(3)#3	103.67(5)
Sb(2)-S(4)-Sb(3)	105.64(5)	Sb(2)-S(5)-Sb(4)	94.92(4)
Sb(4)-S(6)-Sb(2)	89.12(4)	Sb(3)-S(7)-Sb(4)	98.77(4)
C(5)-N(1)-C(1)	111.8(4)	C(5)-N(1)-C(3)	111.5(4)
C(1)-N(1)-C(3)	111.8(4)	C(5)-N(1)-Fe	107.9(3)
C(1)-N(1)-Fe	107.5(3)	C(3)-N(1)-Fe	105.9(3)
C(4)-N(2)-Fe	112.0(3)	C(2)-N(3)-Fe	113.1(3)
C(6)-N(4)-Fe	108.8(3)	N(1)-C(1)-C(2)	109.9(4)
N(3)-C(2)-C(1)	109.2(4)	N(1)-C(3)-C(4)	110.8(4)
N(2)-C(4)-C(3)	109.1(4)	N(1)-C(5)-C(6)	111.0(4)
N(4)-C(6)-C(5)	107.8(4)		

Symmetry transformations used to generate equivalent atoms:
#1 x,y,z #2 x-1,y,z #3 x+1,y,z

Table 4. Anisotropic displacement parameters ($Å^2 x\ 10^3$) for $[Fe(C_6H_{18}N_4)][Sb_4S_7]$. The anisotropic displacement factor exponent takes the form: $-2\pi^2[\ h^2\ a^{*2}U_{11} + ...\ + 2\ h\ k\ a^*\ b^*\ U_{12}\ ]$.

	U_{11}	U_{22}	U_{33}	U_{23}	U_{13}	U_{12}
Sb(1)	18(1)	20(1)	23(1)	-1(1)	-4(1)	2(1)
Sb(2)	27(1)	29(1)	24(1)	5(1)	0(1)	7(1)
Sb(3)	17(1)	22(1)	29(1)	2(1)	1(1)	-1(1)
Sb(4)	25(1)	25(1)	29(1)	-7(1)	-3(1)	2(1)
Fe	23(1)	23(1)	26(1)	3(1)	0(1)	-1(1)
S(1)	38(1)	23(1)	20(1)	1(1)	-2(1)	-1(1)
S(2)	24(1)	27(1)	24(1)	2(1)	-1(1)	8(1)
S(3)	24(1)	54(1)	30(1)	3(1)	-3(1)	-12(1)
S(4)	23(1)	27(1)	35(1)	-6(1)	-2(1)	4(1)
S(5)	22(1)	34(1)	34(1)	-7(1)	2(1)	-1(1)
S(6)	35(1)	36(1)	25(1)	2(1)	9(1)	6(1)
S(7)	32(1)	23(1)	41(1)	11(1)	-16(1)	-8(1)
N(1)	26(2)	27(2)	26(2)	5(2)	0(1)	-1(2)
N(2)	25(2)	33(2)	36(2)	-2(2)	3(2)	-3(2)
N(3)	35(2)	30(2)	29(2)	-2(2)	-10(2)	6(2)
N(4)	26(2)	28(2)	44(2)	-8(2)	8(2)	2(2)
C(1)	34(2)	26(2)	33(2)	2(2)	-3(2)	4(2)
C(2)	37(3)	31(2)	36(3)	-2(2)	-11(2)	-1(2)
C(3)	34(2)	38(3)	29(2)	15(2)	-4(2)	2(2)
C(4)	24(2)	41(3)	35(2)	5(2)	-3(2)	6(2)
C(5)	37(3)	28(2)	43(3)	11(2)	5(2)	-7(2)
C(6)	40(3)	40(3)	43(3)	2(2)	18(2)	-9(2)

Table 5. Hydrogen coordinates (x 10^4) and isotropic displacement parameters ($Å^2$x 10^3) for $[Fe(C_6H_{18}N_4)][Sb_4S_7]$.

	x	y	z	U(eq)
H(1N2)	10587	4140	5562	38
H(2N2)	10071	4098	6097	38
H(1N3)	5905	3365	4684	38
H(2N3)	7655	3042	4618	38
H(1N4)	4957	4340	6157	39
H(2N4)	4326	3417	5784	39
H(1A)	7228	148	5344	37
H(1B)	8685	1001	5140	37
H(2A)	6469	1186	4557	42
H(2B)	5230	1519	5002	42
H(3A)	9469	713	6058	41
H(3B)	8973	1856	6411	41
H(4A)	11514	2336	6038	40
H(4B)	10774	2069	5484	40
H(5A)	6393	770	6319	43
H(5B)	5198	1123	5856	43
H(6A)	4475	2391	6549	49
H(6B)	6337	2845	6622	49

Table. 6 Hydrogen bonds with H..A < r(A) + 2.000 Angstroms and <DHA > 110 deg.

D-H	d(D-H)	d(H..A)	<DHA	d(D..A)	A
N2-H1N2	0.900	2.676	148.07	3.472	S1 [-x+2, -y+1, -z+1]
N2-H2N2	0.900	2.955	127.47	3.574	S2
N3-H1N3	0.900	2.657	146.09	3.441	S1 [-x+1, -y+1, -z+1]
N3-H2N3	0.900	2.516	148.57	3.317	S3 [-x+2, -y+1, -z+1]
N4-H1N4	0.900	2.813	166.54	3.694	S4
N4-H1N4	0.900	2.860	118.29	3.381	S2
N4-H2N4	0.900	2.966	143.04	3.725	S1 [-x+1, -y+1, -z+1]

7.7 Messprotokoll für die Verbindung $[Ni(C_4H_{13}N_3)_2]_3(Sb_3S_6)_2$

Table 1. Crystal data and structure refinement for $[Ni(C_4H_{13}N_3)_2]_3(Sb_3S_6)_2$.

Identification code	$[Ni(C_4H_{13}N_3)_2]_3(Sb_3S_6)_2$ (RK067)	
Empirical formula	$C_{24}H_{78}N_{18}Ni_3S_{12}Sb_6$	
Formula weight	1910.39	
Temperature	293(2) K	
Wavelength	0.71073 Å	
Crystal system	Triclinic	
Space group	P-1	
Unit cell dimensions	a = 7.1208(5) Å	α= 76.169(8)°
	b = 12.3254(9) Å	β= 84.462(9)°
	c = 19.1645(14) Å	γ= 85.892(8)°
Volume	1623.6(2) $Å^3$	
Z	2	
Density (calculated)	1.954 Mg/m^3	
Absorption coefficient	3.726 mm^{-1}	
F(000)	930	
Crystal size	0.2 x 0.2 x 0.15 mm^3	
Theta range for data collection	2.88 to 30.43°.	
Index ranges	-10<=h<=10, -15<=k<=17, -27<=l<=27	
Reflections collected	19706	
Independent reflections	9342 [R(int) = 0.0350]	
Completeness to theta = 30.43°	95.0 %	
Refinement method	Full-matrix least-squares on F^2	
Data / restraints / parameters	9342 / 0 / 287	
Goodness-of-fit on F^2	1.028	
Final R indices [I>2sigma(I)]	R1 = 0.0354, wR2 = 0.0971	
R indices (all data)	R1 = 0.0409, wR2 = 0.1014	
Extinction coefficient	0.0060(4)	
Largest diff. peak and hole	0.986 and -1.608 $e.Å^{-3}$	

Remarks:
The structure contains disordered solvent molecules. Therefore, the intensity data were corrected using the Squeeze option in Platon.

Table 2. Atomic coordinates (x 10^4) and equivalent isotropic displacement parameters ($Å^2$x 10^3) for $[Ni(C_4H_{13}N_3)_2]_3(Sb_3S_6)_2$. U(eq) is defined as one third of the trace of the orthogonalized U_{ij} tensor.

	x	y	z	U(eq)
Sb(1)	14207(1)	6684(1)	7513(1)	28(1)
Sb(2)	9839(1)	8704(1)	7525(1)	28(1)
Sb(3)	9700(1)	6699(1)	6445(1)	27(1)
S(1)	12722(1)	8095(1)	8156(1)	35(1)
S(2)	11118(1)	8521(1)	6317(1)	33(1)
S(3)	11400(1)	5630(1)	7477(1)	35(1)
S(4)	15286(1)	5376(1)	8504(1)	37(1)
S(5)	9898(2)	10627(1)	7423(1)	39(1)
S(6)	11185(1)	6118(1)	5454(1)	37(1)
Ni(1)	5466(1)	7585(1)	3603(1)	25(1)
N(1)	5174(5)	5895(2)	4162(2)	35(1)
C(1)	3844(7)	5363(3)	3825(3)	46(1)
C(2)	2310(6)	6230(3)	3530(2)	42(1)
N(2)	3182(4)	7225(2)	3070(2)	31(1)
C(3)	3864(8)	7069(4)	2347(2)	53(1)
C(4)	5776(9)	7507(5)	2096(2)	61(1)
N(3)	7027(5)	7231(3)	2680(2)	42(1)
C(5)	7350(5)	8414(3)	4669(2)	38(1)
C(6)	5403(6)	8106(3)	5023(2)	38(1)
N(4)	7875(4)	7769(3)	4120(2)	38(1)
N(5)	4021(4)	8143(2)	4491(2)	28(1)
C(7)	3099(5)	9253(3)	4220(2)	35(1)
C(8)	4348(5)	9973(3)	3628(2)	35(1)
N(6)	5088(5)	9330(2)	3100(2)	33(1)
Ni(2)	10000	5000	10000	21(1)
N(7)	12433(4)	5903(2)	10012(2)	29(1)
C(9)	11877(5)	6894(3)	10305(2)	35(1)
C(10)	10216(6)	6629(3)	10870(2)	36(1)
N(8)	8713(4)	6099(2)	10609(1)	26(1)
C(11)	7376(5)	6854(3)	10160(2)	36(1)
C(12)	8142(6)	7218(3)	9378(2)	35(1)
N(9)	9080(4)	6268(2)	9125(1)	30(1)

Table 3. Bond lengths [Å] and angles [°] for $[Ni(C_4H_{13}N_3)_2]_3(Sb_3S_6)_2$.

Sb(1)-S(4)	2.3310(9)	Sb(1)-S(3)	2.4756(10)
Sb(1)-S(1)	2.4838(9)	Sb(2)-S(5)	2.3333(9)
Sb(2)-S(2)	2.4617(9)	Sb(2)-S(1)	2.4623(9)
Sb(3)-S(6)	2.3216(9)	Sb(3)-S(3)	2.4702(9)
Sb(3)-S(2)	2.4774(9)	Ni(1)-N(4)	2.114(3)
Ni(1)-N(3)	2.114(3)	Ni(1)-N(1)	2.117(3)
Ni(1)-N(2)	2.127(3)	Ni(1)-N(5)	2.134(3)
Ni(1)-N(6)	2.145(3)	N(1)-C(1)	1.467(6)
C(1)-C(2)	1.522(6)	C(2)-N(2)	1.467(5)
N(2)-C(3)	1.477(5)	C(3)-C(4)	1.494(8)
C(4)-N(3)	1.459(7)	C(5)-N(4)	1.471(5)
C(5)-C(6)	1.516(6)	C(6)-N(5)	1.474(5)
N(5)-C(7)	1.473(4)	C(7)-C(8)	1.517(5)
C(8)-N(6)	1.467(5)	Ni(2)-N(8)#1	2.100(3)
Ni(2)-N(8)	2.100(3)	Ni(2)-N(9)	2.121(3)
Ni(2)-N(9)#1	2.121(3)	Ni(2)-N(7)	2.130(3)
Ni(2)-N(7)#1	2.130(3)	(7)-C(9)	1.477(4)
C(9)-C(10)	1.523(5)	C(10)-N(8)	1.477(5)
N(8)-C(11)	1.470(4)	C(11)-C(12)	1.518(5)
C(12)-N(9)	1.466(4)		
S(4)-Sb(1)-S(3)	93.47(3)	S(4)-Sb(1)-S(1)	98.40(3)
S(3)-Sb(1)-S(1)	99.56(3)	S(5)-Sb(2)-S(2)	102.22(3)
S(5)-Sb(2)-S(1)	99.00(3)	S(2)-Sb(2)-S(1)	98.00(3)
S(6)-Sb(3)-S(3)	104.70(3)	S(6)-Sb(3)-S(2)	101.46(3)
S(3)-Sb(3)-S(2)	97.68(3)	N(4)-Ni(1)-N(3)	94.70(14)
N(4)-Ni(1)-N(1)	93.88(13)	N(3)-Ni(1)-N(1)	95.88(13)
N(4)-Ni(1)-N(2)	173.65(12)	N(3)-Ni(1)-N(2)	81.48(13)
N(1)-Ni(1)-N(2)	81.52(12)	N(4)-Ni(1)-N(5)	82.52(12)
N(3)-Ni(1)-N(5)	172.95(12)	N(1)-Ni(1)-N(5)	90.79(11)
N(2)-Ni(1)-N(5)	101.85(11)	N(4)-Ni(1)-N(6)	94.99(13)
N(3)-Ni(1)-N(6)	92.79(12)	N(1)-Ni(1)-N(6)	167.04(12)
N(2)-Ni(1)-N(6)	90.28(12)	N(5)-Ni(1)-N(6)	81.04(11)
C(1)-N(1)-Ni(1)	110.5(2)	N(1)-C(1)-C(2)	108.8(3)
N(2)-C(2)-C(1)	109.6(3)	C(2)-N(2)-C(3)	112.6(3)
C(2)-N(2)-Ni(1)	107.6(2)	C(3)-N(2)-Ni(1)	110.1(3)
N(2)-C(3)-C(4)	113.0(4)	N(3)-C(4)-C(3)	111.0(4)
C(4)-N(3)-Ni(1)	107.0(3)	N(4)-C(5)-C(6)	109.1(3)
N(5)-C(6)-C(5)	112.4(3)	C(5)-N(4)-Ni(1)	109.9(2)
C(7)-N(5)-C(6)	114.9(3)	C(7)-N(5)-Ni(1)	108.8(2)
C(6)-N(5)-Ni(1)	107.6(2)	N(5)-C(7)-C(8)	111.3(3)
N(6)-C(8)-C(7)	109.7(3)	C(8)-N(6)-Ni(1)	111.2(2)
N(8)#1-Ni(2)-N(9)	97.22(10)	N(8)-Ni(2)-N(9)	82.78(10)
N(8)#1-Ni(2)-N(7)	97.08(11)	N(8)-Ni(2)-N(7)	82.92(11)
N(9)-Ni(2)-N(7)	90.14(11)	N(9)#1-Ni(2)-N(7)	89.86(11)

C(9)-N(7)-Ni(2)	109.6(2)	N(7)-C(9)-C(10)	109.4(3)
N(8)-C(10)-C(9)	111.8(3)	C(11)-N(8)-C(10)	116.6(3)
C(11)-N(8)-Ni(2)	107.5(2)	C(10)-N(8)-Ni(2)	108.19(19)
N(8)-C(11)-C(12)	112.7(3)	N(9)-C(12)-C(11)	110.7(3)
C(12)-N(9)-Ni(2)	111.0(2)		

Symmetry transformations used to generate equivalent atoms:
#1 -x+2,-y+1,-z+2

Table 4. Anisotropic displacement parameters ($Å^2$x 10^3) for $[Ni(C_4H_{13}N_3)_2]_3(Sb_3S_6)_2$. The anisotropic displacement factor exponent takes the form: $-2\pi^2[h^2 a^{*2}U_{11} + ... + 2 h k a^* b^* U_{12}]$

	U_{11}	U_{22}	U_{33}	U_{23}	U_{13}	U_{12}
Sb(1)	27(1)	28(1)	26(1)	-6(1)	0(1)	4(1)
Sb(2)	31(1)	24(1)	27(1)	-3(1)	1(1)	3(1)
Sb(3)	22(1)	30(1)	28(1)	-8(1)	-3(1)	0(1)
S(1)	43(1)	30(1)	36(1)	-12(1)	-11(1)	8(1)
S(2)	44(1)	27(1)	27(1)	-5(1)	0(1)	-2(1)
S(3)	46(1)	29(1)	30(1)	-2(1)	-10(1)	-6(1)
S(4)	38(1)	35(1)	40(1)	-7(1)	-16(1)	9(1)
S(5)	49(1)	25(1)	43(1)	-8(1)	-6(1)	11(1)
S(6)	45(1)	35(1)	31(1)	-12(1)	1(1)	1(1)
Ni(1)	27(1)	21(1)	26(1)	-8(1)	-1(1)	3(1)
N(1)	39(2)	23(1)	39(2)	-3(1)	-3(1)	5(1)
C(1)	58(3)	22(1)	57(2)	-8(1)	-10(2)	2(2)
C(2)	40(2)	35(2)	53(2)	-14(2)	-6(2)	-6(2)
N(2)	36(1)	26(1)	33(1)	-12(1)	-4(1)	5(1)
C(3)	64(3)	63(3)	38(2)	-26(2)	-5(2)	0(2)
C(4)	81(4)	72(3)	34(2)	-22(2)	7(2)	-6(3)
N(3)	43(2)	41(2)	43(2)	-19(1)	9(1)	3(1)
C(5)	35(2)	44(2)	39(2)	-13(1)	-14(1)	2(2)
C(6)	44(2)	42(2)	30(2)	-11(1)	-5(1)	2(2)
N(4)	27(1)	48(2)	38(2)	-9(1)	-3(1)	2(1)
N(5)	28(1)	26(1)	32(1)	-10(1)	2(1)	0(1)
C(7)	34(2)	31(2)	42(2)	-17(1)	-2(1)	8(1)
C(8)	39(2)	21(1)	48(2)	-12(1)	-13(2)	4(1)
N(6)	39(2)	25(1)	35(1)	-6(1)	-1(1)	1(1)
Ni(2)	21(1)	20(1)	21(1)	-5(1)	-2(1)	-1(1)
N(7)	24(1)	33(1)	29(1)	-8(1)	-1(1)	-3(1)
C(9)	32(2)	31(1)	46(2)	-13(1)	-5(1)	-7(1)
C(10)	40(2)	37(2)	35(2)	-18(1)	-3(1)	-1(1)
N(8)	27(1)	26(1)	26(1)	-6(1)	2(1)	-1(1)
C(11)	29(2)	34(2)	44(2)	-11(1)	0(1)	6(1)

C(12)	43(2)	26(1)	34(2)	-3(1)	-7(1)	5(1)
N(9)	32(1)	28(1)	27(1)	-5(1)	-2(1)	1(1)

Table 5. Hydrogen coordinates (x 10^4) and isotropic displacement parameters (Å^{2}x 10^3) for $[Ni(C_4H_{13}N_3)_2]_3(Sb_3S_6)_2$.

	x	y	z	U(eq)
H(1N1)	6308	5522	4158	41
H(2N1)	4754	5864	4624	41
H(1A)	3283	4746	4178	55
H(1B)	4504	5071	3437	55
H(2A)	1513	5918	3253	50
H(2B)	1527	6436	3926	50
H(1N2)	2314	7811	3021	37
H(3A)	2973	7446	2005	63
H(3B)	3908	6277	2355	63
H(4A)	6317	7188	1701	74
H(4B)	5659	8313	1919	74
H(1N3)	8052	7645	2564	50
H(2N3)	7410	6503	2765	50
H(5A)	7346	9209	4447	46
H(5B)	8264	8249	5029	46
H(6A)	5486	7358	5332	46
H(6B)	4965	8618	5324	46
H(1N4)	8372	7091	4329	46
H(2N4)	8754	8125	3792	46
H(1N1)	3111	7657	4697	34
H(7A)	2820	9624	4614	42
H(7B)	1914	9164	4034	42
H(8A)	3624	10632	3392	42
H(8B)	5387	10216	3835	42
H(1N6)	6203	9592	2889	40
H(2N6)	4281	9419	2755	40
H(1N7)	13274	5460	10286	34
H(2N7)	12982	6120	9561	34
H(9A)	11524	7520	9919	42
H(9B)	12934	7101	10521	42
H(10A)	10656	6130	11302	43
H(10B)	9701	7314	10995	43
H(1N8)	8042	5688	11000	32
H(11A)	7083	7512	10353	43

H(11B)	6211	6480	10185	43
H(12A)	7114	7531	9082	42
H(12B)	9036	7795	9329	42
H(1N9)	10079	6504	8814	35
H(2N9)	8272	5986	8889	35

7.8 Messprotokoll für die Verbindung $[C_6H_{21}N_4][Sb_9S_{14}O]$

Table 1. Crystal data and structure refinement for $[C_6H_{21}N_4][Sb_9S_{14}O]$.

Identification code	$[C_6H_{21}N_4][Sb_9S_{14}O]$ (RK359)
Empirical formula	$C_6H_{21}N_4OS_{14}Sb_9$
Formula weight	1709.86
Temperature	293(2) K
Wavelength	0.71073 Å
Crystal system	Orthorhombic
Space group	$Cmc2_1$
Unit cell dimensions	a = 29.679(2) Å
	b = 9.9798(6) Å
	c = 11.7155(7) Å
Volume	3470.1(4) $Å^3$
Z	4
Density (calculated)	3.273 Mg/m^3
Absorption coefficient	7.749 mm^{-1}
F(000)	3104
Crystal size	0.1 x 0.1 x 0.1 mm^3
Theta range for data collection	2.75 to 27.97°.
Index ranges	-38<=h<=38, -13<=k<=13, -15<=l<=15
Reflections collected	18706
Independent reflections	4217 [R(int) = 0.0495]
Completeness to theta = 27.97°	99.2 %
Refinement method	Full-matrix least-squares on F^2
Data / restraints / parameters	4217 / 1 / 167
Goodness-of-fit on F^2	1.028
Final R indices [I>2sigma(I)]	R1 = 0.0346, wR2 = 0.0857
R indices (all data)	R1 = 0.0423, wR2 = 0.0897
Absolute structure parameter	-0.05(4)
Extinction coefficient	0.00030(4)
Largest diff. peak and hole	2.338 and -1.420 $e.Å^{-3}$

Table 2. Atomic coordinates (x 10^4) and equivalent isotropic displacement parameters ($Å^2$x 10^3) for $[C_6H_{21}N_4][Sb_9S_{14}O]$. U(eq) is defined as one third of the trace of the orthogonalized U_{ij} tensor.

	x	y	z	U(eq)
Sb(1)	2549(1)	2670(1)	10636(1)	27(1)
Sb(2)	3135(1)	4698(1)	8363(1)	25(1)
Sb(3)	3124(1)	760(1)	8287(1)	25(1)
Sb(4)	3685(1)	-2250(1)	9755(1)	25(1)
Sb(5)	5000	-1424(1)	9303(1)	33(1)
S(1)	3095(1)	4538(3)	10479(2)	30(1)
S(2)	3606(1)	2722(2)	7906(2)	27(1)
S(3)	3115(1)	847(2)	10398(2)	29(1)
S(4)	2323(1)	2694(2)	8663(2)	27(1)
S(5)	3874(1)	5869(2)	8534(2)	33(1)
S(6)	3866(1)	-487(2)	8374(2)	31(1)
S(7)	4436(1)	-2119(3)	10693(2)	39(1)
O(1)	5000	476(10)	9711(10)	41(2)
N(1)	4246(3)	8497(11)	5732(10)	50(2)
C(1)	4191(4)	7004(14)	5717(11)	50(3)
C(2)	4592(4)	6320(13)	6199(11)	46(3)
N(2)	5000	6563(13)	5485(11)	36(3)
C(3)	5000	5737(18)	4412(18)	53(4)
C(4)	5000	6490(30)	3393(19)	128(15)
N(3)	5150(8)	7770(20)	3171(19)	64(7)

Table 3. Bond lengths [Å] and angles [°] for $[C_6H_{21}N_4][Sb_9S_{14}O]$.

Sb(1)-S(4)	2.407(2)	Sb(1)-S(1)	2.477(3)
Sb(1)-S(3)	2.493(2)	Sb(2)-S(2)	2.474(2)
Sb(2)-S(1)	2.487(2)	Sb(2)-S(5)	2.492(2)
Sb(3)-S(2)	2.464(2)	Sb(3)-S(3)	2.475(2)
Sb(3)-S(6)	2.530(2)	Sb(4)-S(5)#1	2.426(3)
Sb(4)-S(6)	2.450(2)	Sb(4)-S(7)	2.488(2)
Sb(5)-O(1)	1.956(10)	Sb(5)-S(7)#2	2.437(3)
Sb(5)-S(7)	2.437(3)	S(5)-Sb(4)#3	2.426(3)
N(1)-C(1)	1.499(18)	C(1)-C(2)	1.485(16)
C(2)-N(2)	1.492(14)	N(2)-C(3)	1.50(2)
C(3)-C(4)	1.41(3)	C(4)-N(3)	1.37(3)
S(4)-Sb(1)-S(1)	95.94(8)	S(4)-Sb(1)-S(3)	95.01(7)
S(1)-Sb(1)-S(3)	95.71(8)	S(2)-Sb(2)-S(1)	101.05(8)
S(2)-Sb(2)-S(5)	83.98(8)	S(1)-Sb(2)-S(5)	89.57(9)
S(2)-Sb(3)-S(3)	99.19(8)	S(2)-Sb(3)-S(6)	83.92(8)
S(3)-Sb(3)-S(6)	89.23(8)	S(5)#1-Sb(4)-S(6)	96.63(9)
S(5)#1-Sb(4)-S(7)	95.40(10)	S(6)-Sb(4)-S(7)	93.31(8)
O(1)-Sb(5)-S(7)#2	96.5(3)	O(1)-Sb(5)-S(7)	96.5(3)
S(7)#2-Sb(5)-S(7)	86.84(12)	Sb(1)-S(1)-Sb(2)	98.86(8)
Sb(3)-S(2)-Sb(2)	105.48(8)	Sb(3)-S(3)-Sb(1)	98.35(8)
Sb(4)#3-S(5)-Sb(2)	101.96(9)	Sb(4)-S(6)-Sb(3)	100.91(8)
Sb(5)-S(7)-Sb(4)	109.60(11)	C(2)-C(1)-N(1)	111.4(10)
C(1)-C(2)-N(2)	111.3(10)	C(2)#2-N(2)-C(2)	108.5(12)
C(2)#2-N(2)-C(3)	112.3(8)	C(2)-N(2)-C(3)	112.3(8)
C(4)-C(3)-N(2)	114.4(16)	N(3)-C(4)-N(3)#2	38(2)
N(3)-C(4)-C(3)	130.9(18)	N(3)#2-C(4)-C(3)	130.9(18)

Symmetry transformations used to generate equivalent atoms:
#1 x,y-1,z #2 -x+1,y,z #3 x,y+1,z

Table 4. Anisotropic displacement parameters ($Å^2$x 10^3) for $[C_6H_{21}N_4][Sb_9S_{14}O]$. The anisotropic displacement factor exponent takes the form: $-2\pi^2[h^2 a^{*2}U_{11} + ... + 2 h k a^* b^* U_{12}]$

	U_{11}	U_{22}	U_{33}	U_{23}	U_{22}	U_{12}
Sb(1)	25(1)	36(1)	21(1)	-1(1)	5(1)	1(1)
Sb(2)	25(1)	23(1)	26(1)	-1(1)	1(1)	2(1)
Sb(3)	25(1)	24(1)	24(1)	-1(1)	-2(1)	1(1)
Sb(4)	21(1)	26(1)	29(1)	2(1)	1(1)	-1(1)
Sb(5)	33(1)	37(1)	30(1)	-3(1)	0	0
S(1)	32(1)	34(1)	25(1)	-5(1)	0(1)	0(1)
S(2)	26(1)	25(1)	31(1)	0(1)	5(1)	1(1)
S(3)	28(1)	33(1)	25(1)	4(1)	0(1)	2(1)
S(4)	27(1)	30(1)	25(1)	-1(1)	-2(1)	0(1)
S(5)	26(1)	25(1)	49(1)	-2(1)	8(1)	-2(1)
S(6)	30(1)	27(1)	37(1)	6(1)	4(1)	2(1)
S(7)	26(1)	54(2)	37(1)	10(1)	-4(1)	-4(1)
O(1)	42(5)	22(5)	60(7)	-7(5)	0	0
N(1)	46(5)	49(6)	56(6)	6(5)	8(5)	8(5)
C(1)	34(5)	67(8)	47(6)	9(6)	3(5)	-1(5)
C(2)	34(5)	45(7)	60(7)	9(6)	-5(5)	-5(5)
N(2)	34(6)	31(7)	44(7)	4(5)	0	0
C(3)	40(8)	47(10)	71(12)	-12(9)	0	0
C(4)	280(50)	74(18)	30(10)	-16(11)	0	0
N(3)	69(16)	79(16)	44(11)	-23(11)	3(9)	-10(11)

7.9 Messprotokoll für die Verbindung $[C_6H_{17}N_3]_4[Sb_4V_{16}O_{42}]\cdot 2H_2O$

Table 1.

Crystal data and structure refinement for $C_6H_{17}N_3]_4[Sb_4V_{16}O_{42}]\cdot 2H_2O$.

Identification code	$[C_6H_{17}N_3]_4[Sb_4V_{16}O_{42}]\cdot 2H_2O$ (RK539)	
Empirical formula	$C_{24}H_{62}N_{12}O_{44}Sb_4V_{16}$	
Formula weight	2524.87 g/mol	
Temperature	293(2) K	
Wavelength	0.71073 Å	
Crystal system	Triclinic	
Space group	P-1	
Unit cell dimensions	a = 12.056(2) Å	α= 69.46(3)°.
	b = 12.583(3) Å	β= 66.41(3)°.
	c = 13.582(3) Å	γ = 79.53(3)°.
Volume	1766.1(6) $Å^3$	
Z	1	
Density (calculated)	2.383 Mg/m^3	
Absorption coefficient	3.605 mm^{-1}	
F(000)	1224	
Crystal size	0.4 x 0.2 x 0.2 mm^3	
Theta range for data collection	2.47 to 28.06°	
Index ranges	-15<=h<=15, -16<=k<=16, 17<=l<=17	
Reflections collected	15276	
Independent reflections	8194 [R(int) = 0.0467]	
Completeness to theta = 28.06°	95.7 %	
Refinement method	Full-matrix least-squares on F^2	
Data / restraints / parameters	8194 / 0 / 451	
Goodness-of-fit on F^2	0.994	
Final R indices [I>2sigma(I)]	R1 = 0.0461, wR2 = 0.1128	
R indices (all data)	R1 = 0.0707, wR2 = 0.1239	
Largest diff. peak and hole	3.567 and -1.621 e.$Å^{-3}$	

Table 2. Atomic coordinates (x 10^4) and equivalent isotropic displacement parameters (Å^{2}x 10^3) for $[C_6H_{17}N_3]_4[Sb_4V_{16}O_{42}]\cdot 2H_2O$. U(eq) is defined as one third of the trace of the orthogonalized U_{ij} tensor.

	x	y	z	U(eq)
Sb(1)	736(1)	6273(1)	590(1)	17(1)
Sb(2)	8734(1)	4826(1)	-3167(1)	18(1)
V(2)	2614(1)	4667(1)	-1130(1)	13(1)
V(4)	4350(1)	2199(1)	267(1)	13(1)
V(3)	3385(1)	2978(1)	2895(1)	14(1)
V(1)	2032(1)	3346(1)	1331(1)	13(1)
V(5)	4545(1)	6191(1)	-2963(1)	14(1)
V(6)	3354(1)	7562(1)	-1373(1)	14(1)
V(7)	6983(1)	2453(1)	-960(1)	12(1)
V(8)	5899(1)	4077(1)	-2663(1)	12(1)
O(1)	930(4)	2474(4)	1877(4)	21(1)
O(2)	1677(4)	4479(4)	-1612(4)	26(1)
O(3)	3778(4)	4309(3)	3138(4)	16(1)
O(4)	4016(5)	939(4)	481(4)	24(1)
O(5)	4415(5)	6632(4)	-4193(4)	27(1)
O(6)	2651(5)	8695(4)	-1907(4)	28(1)
O(7)	7733(4)	1306(4)	-1228(4)	22(1)
O(8)	6180(4)	3721(4)	-3775(4)	23(1)
O(9)	293(4)	5876(4)	2232(4)	23(1)
O(10)	1562(4)	4827(3)	404(4)	18(1)
O(11)	3404(4)	2530(4)	1681(4)	18(1)
O(12)	3062(4)	3277(4)	-140(4)	17(1)
O(13)	2941(4)	6309(3)	-1739(4)	14(1)
O(14)	4209(4)	4608(4)	-2270(4)	18(1)
O(15)	2286(4)	6917(4)	234(4)	20(1)
O(16)	2713(5)	2039(4)	4079(4)	27(1)
O(17)	5108(4)	2648(3)	2514(4)	17(1)
O(18)	5510(4)	2805(4)	-1270(4)	17(1)
O(19)	5844(4)	2020(4)	577(4)	17(1)
O(20)	7452(4)	3748(3)	-2355(4)	18(1)
O(21)	7961(4)	5996(4)	-2459(4)	19(1)
C(1)	2543(8)	3934(7)	-4077(7)	37(2)
C(2)	2689(9)	2661(7)	-3873(7)	39(2)
C(3)	4030(9)	1286(8)	-3054(8)	45(2)
C(4)	4433(9)	917(9)	-2063(9)	51(2)
C(5)	1988(8)	1570(8)	-1900(7)	41(2)
C(6)	2288(9)	1164(8)	-844(8)	43(2)
C(7)	1685(7)	-3189(6)	6128(7)	30(2)
C(8)	866(7)	-2775(6)	5433(6)	26(1)
C(9)	194(7)	-1382(6)	4078(6)	30(2)
C(10)	199(8)	-164(7)	3357(7)	36(2)

C(11)	2237(7)	-1365(6)	3911(6)	29(2)
C(12)	2267(8)	-102(7)	3212(8)	40(2)
N(1)	3689(6)	4321(5)	-4170(5)	30(1)
N(2)	3010(7)	2093(5)	-2876(6)	34(2)
N(3)	3408(7)	400(5)	-1015(6)	39(2)
N(4)	1551(5)	-2496(5)	6841(5)	27(1)
N(5)	1001(5)	-1605(4)	4716(5)	21(1)
N(6)	1467(7)	146(5)	2567(5)	38(2)
O(22)	2723(10)	-315(8)	5689(8)	86(3)

Table 3. Bond lengths [Å] and angles [°] for $[C_6H_{17}N_3]_4[Sb_4V_{16}O_{42}]\cdot 2H_2O$.

Sb(1)-O(10)	1.957(4)	Sb(1)-O(9)	1.967(5)
Sb(1)-O(15)	1.983(4)	Sb(2)-O(21)	1.934(4)
Sb(2)-O(20)	1.948(4)	Sb(2)-O(9)#1	1.949(5)
V(2)-O(2)	1.600(5)	V(2)-O(12)	1.936(4)
V(2)-O(14)	1.936(5)	V(2)-O(13)	1.986(4)
V(2)-O(10)	2.018(4)	V(2)-V(5)	2.988(2)
V(2)-V(1)	3.0125(18)	V(4)-O(4)	1.606(4)
V(4)-O(11)	1.949(4)	V(4)-O(18)	1.957(5)
V(4)-O(19)	1.965(4)	V(4)-O(12)	1.988(4)
V(4)-V(7)	2.9528(18)	V(4)-V(1)	2.9568(18)
V(3)-O(16)	1.615(5)	V(3)-O(11)	1.912(4)
V(3)-O(17)	1.932(4)	V(3)-O(3)	1.984(4)
V(3)-O(21)#1	2.029(4)	V(1)-O(1)	1.640(4)
V(1)-O(12)	1.908(5)	V(1)-O(11)	1.919(4)
V(1)-O(10)	1.981(4)	V(1)-O(21)#1	1.984(4)
V(5)-O(5)	1.629(5)	V(5)-O(14)	1.920(4)
V(5)-O(17)#1	1.931(4)	V(5)-O(3)#1	1.948(4)
V(5)-O(13)	2.006(4)	V(6)-O(6)	1.613(5)
V(6)-O(17)#1	1.928(5)	V(6)-O(19)#1	1.950(4)
V(6)-O(15)	1.992(5)	V(6)-O(13)	2.003(4)
V(7)-O(7)	1.631(4)	V(7)-O(18)	1.926(4)
V(7)-O(19)	1.928(5)	V(7)-O(15)#1	1.969(4)
V(7)-O(20)	1.969(4)	V(8)-O(8)	1.614(5)
V(8)-O(14)	1.941(4)	V(8)-O(18)	1.949(4)
V(8)-O(3)#1	1.965(4)	V(8)-O(20)	2.019(4)
O(3)-V(5)#1	1.948(4)	O(3)-V(8)#1	1.965(4)
O(9)-Sb(2)#1	1.949(5)	O(15)-V(7)#1	1.969(4)
O(17)-V(6)#1	1.928(5)	O(17)-V(5)#1	1.931(4)
O(19)-V(6)#1	1.950(4)	O(21)-V(1)#1	1.984(4)
O(21)-V(3)#1	2.029(4)	C(1)-N(1)	1.491(10)
C(1)-C(2)	1.516(12)	C(2)-N(2)	1.461(10)
C(3)-N(2)	1.443(12)	C(3)-C(4)	1.504(13)
C(4)-N(3)	1.487(13)	C(5)-N(2)	1.443(12)
C(5)-C(6)	1.511(12)	C(6)-N(3)	1.494(12)

C(7)-N(4)	1.464(9)	C(7)-C(8)	1.533(10)
C(8)-N(5)	1.447(8)	C(9)-N(5)	1.476(8)
C(9)-C(10)	1.501(11)	C(10)-N(6)	1.500(12)
C(11)-N(5)	1.461(9)	C(11)-C(12)	1.537(11)
C(12)-N(6)	1.473(12)		
O(10)-Sb(1)-O(9)	98.02(19)	O(10)-Sb(1)-O(15)	91.61(19)
O(9)-Sb(1)-O(15)	93.53(19)	O(21)-Sb(2)-O(20)	98.8(2)
O(21)-Sb(2)-O(9)#1	95.68(18)	O(20)-Sb(2)-O(9)#1	97.07(19)
O(2)-V(2)-O(12)	112.8(2)	O(2)-V(2)-O(14)	106.3(2)
O(12)-V(2)-O(14)	88.69(19)	O(2)-V(2)-O(13)	107.8(2)
O(12)-V(2)-O(13)	139.44(18)	O(14)-V(2)-O(13)	80.70(18)
O(2)-V(2)-O(10)	104.3(2)	O(12)-V(2)-O(10)	78.66(18)
O(14)-V(2)-O(10)	149.47(19)	O(13)-V(2)-O(10)	90.99(18)
O(4)-V(4)-O(11)	105.1(2)	O(4)-V(4)-O(18)	110.5(2)
O(11)-V(4)-O(18)	144.46(19)	O(4)-V(4)-O(19)	105.9(2)
O(11)-V(4)-O(19)	90.85(18)	O(18)-V(4)-O(19)	79.97(19)
O(4)-V(4)-O(12)	107.9(2)	O(11)-V(4)-O(12)	78.60(18)
O(18)-V(4)-O(12)	90.09(19)	O(19)-V(4)-O(12)	146.13(19)
O(16)-V(3)-O(11)	109.1(2)	O(16)-V(3)-O(17)	107.2(2)
O(11)-V(3)-O(17)	91.73(19)	O(16)-V(3)-O(3)	111.5(2)
O(11)-V(3)-O(3)	139.01(19)	O(17)-V(3)-O(3)	81.93(18)
O(16)-V(3)-O(21)#1	105.6(2)	O(11)-V(3)-O(21)#1	77.81(18)
O(17)-V(3)-O(21)#1	147.1(2)	O(3)-V(3)-O(21)#1	85.90(17)
O(1)-V(1)-O(12)	110.3(2)	O(1)-V(1)-O(11)	108.8(2)
O(12)-V(1)-O(11)	81.31(19)	O(1)-V(1)-O(10)	109.6(2)
O(12)-V(1)-O(10)	80.24(18)	O(11)-V(1)-O(10)	141.2(2)
O(1)-V(1)-O(21)#1	111.1(2)	O(12)-V(1)-O(21)#1	137.9(2)
O(11)-V(1)-O(21)#1	78.77(18)	O(10)-V(1)-O(21)#1	92.78(18)
O(5)-V(5)-O(14)	109.3(2)	O(5)-V(5)-O(17)#1	115.0(2)
O(14)-V(5)-O(17)#1	135.55(19)	O(5)-V(5)-O(3)#1	109.5(2)
O(14)-V(5)-O(3)#1	85.69(18)	O(17)#1-V(5)-O(3)#1	82.88(18)
O(5)-V(5)-O(13)	110.9(2)	O(14)-V(5)-O(13)	80.59(18)
O(17)#1-V(5)-O(13)	80.93(18)	O(3)#1-V(5)-O(13)	139.59(18)
O(6)-V(6)-O(17)#1	109.2(2)	O(6)-V(6)-O(19)#1	107.1(2)
O(17)#1-V(6)-O(19)#1	91.15(19)	O(6)-V(6)-O(15)	106.7(2)
O(17)#1-V(6)-O(15)	144.1(2)	O(19)#1-V(6)-O(15)	78.03(18)
O(6)-V(6)-O(13)	105.9(2)	O(17)#1-V(6)-O(13)	81.08(18)
O(19)#1-V(6)-O(13)	146.86(18)	O(15)-V(6)-O(13)	89.53(18)
O(7)-V(7)-O(18)	114.2(2)	O(7)-V(7)-O(19)	108.1(2)
O(18)-V(7)-O(19)	81.66(19)	O(7)-V(7)-O(15)#1	111.5(2)
O(18)-V(7)-O(15)#1	133.84(19)	O(19)-V(7)-O(15)#1	79.12(18)
O(7)-V(7)-O(20)	109.0(2)	O(18)-V(7)-O(20)	78.57(18)
O(19)-V(7)-O(20)	142.49(19)	O(15)#1-V(7)-O(20)	92.13(19)
O(8)-V(8)-O(14)	103.4(2)	O(8)-V(8)-O(18)	113.8(2)
O(14)-V(8)-O(18)	91.01(19)	O(8)-V(8)-O(3)#1	108.5(2)
O(14)-V(8)-O(3)#1	84.69(18)	O(18)-V(8)-O(3)#1	137.30(18)

O(8)-V(8)-O(20)	106.2(2)	O(14)-V(8)-O(20)	150.41(19)
O(18)-V(8)-O(20)	76.84(18)	O(3)#1-V(8)-O(20)	86.34(17)
N(1)-C(1)-C(2)	108.0(7)	N(2)-C(2)-C(1)	110.1(6)
N(2)-C(3)-C(4)	109.5(8)	N(3)-C(4)-C(3)	109.2(8)
N(2)-C(5)-C(6)	110.9(8)	N(3)-C(6)-C(5)	109.5(7)
N(4)-C(7)-C(8)	113.8(6)	N(5)-C(8)-C(7)	114.9(6)
N(5)-C(9)-C(10)	111.7(6)	N(6)-C(10)-C(9)	110.0(6)
N(5)-C(11)-C(12)	108.5(6)	N(6)-C(12)-C(11)	110.1(7)
C(3)-N(2)-C(5)	110.6(7)	C(3)-N(2)-C(2)	113.8(7)
C(5)-N(2)-C(2)	112.1(7)	C(4)-N(3)-C(6)	112.8(7)
C(8)-N(5)-C(11)	113.4(5)	C(8)-N(5)-C(9)	107.0(5)
C(11)-N(5)-C(9)	108.5(6)	C(12)-N(6)-C(10)	109.9(6)

Symmetry transformations used to generate equivalent atoms:
#1 -x+1,-y+1,-z

Table 4. Anisotropic displacement parameters ($Å^2 x\ 10^3$) for $[C_6H_{17}N_3]_4[Sb_4V_{16}O_{42}]\cdot 2H_2O$. The anisotropic displacement factor exponent takes the form: $-2\pi^2[\ h^2\ a^{*2}U_{11} + ...\ + 2\ h\ k\ a^*\ b^*\ U_{12}\ ]$.

	U_{11}	U_{22}	U_{33}	U_{23}	U_{13}	U_{12}
Sb(1)	15(1)	17(1)	19(1)	-7(1)	-5(1)	-1(1)
Sb(2)	18(1)	20(1)	15(1)	-8(1)	0(1)	-5(1)
V(2)	12(1)	12(1)	12(1)	-4(1)	-2(1)	-2(1)
V(4)	13(1)	13(1)	11(1)	-4(1)	-1(1)	-3(1)
V(3)	14(1)	16(1)	11(1)	-5(1)	-1(1)	-5(1)
V(1)	12(1)	13(1)	12(1)	-5(1)	-1(1)	-5(1)
V(5)	14(1)	17(1)	11(1)	-5(1)	-3(1)	-3(1)
V(6)	15(1)	14(1)	14(1)	-7(1)	-4(1)	-2(1)
V(7)	14(1)	10(1)	12(1)	-6(1)	-2(1)	-1(1)
V(8)	13(1)	13(1)	11(1)	-5(1)	-2(1)	-2(1)
O(1)	18(2)	14(2)	29(3)	-5(2)	-5(2)	-6(2)
O(2)	24(2)	32(3)	26(3)	-5(2)	-13(2)	-8(2)
O(3)	16(2)	16(2)	18(2)	-7(2)	-5(2)	-4(2)
O(4)	32(3)	18(2)	25(2)	-9(2)	-6(2)	-11(2)
O(5)	29(3)	36(3)	19(2)	-8(2)	-12(2)	-3(2)
O(6)	32(3)	23(2)	29(3)	-7(2)	-16(2)	4(2)
O(7)	26(2)	17(2)	22(2)	-9(2)	-6(2)	4(2)
O(8)	27(2)	25(2)	15(2)	-8(2)	-5(2)	1(2)
O(9)	12(2)	31(2)	22(2)	-13(2)	0(2)	-1(2)
O(10)	25(2)	12(2)	12(2)	-5(2)	0(2)	0(2)
O(11)	15(2)	24(2)	14(2)	-10(2)	-2(2)	2(2)
O(12)	16(2)	19(2)	14(2)	-5(2)	-3(2)	0(2)
O(13)	16(2)	12(2)	15(2)	-6(2)	-3(2)	-3(2)
O(14)	14(2)	16(2)	20(2)	-8(2)	-1(2)	0(2)
O(15)	18(2)	30(2)	11(2)	-10(2)	4(2)	-13(2)

O(16)	26(3)	33(3)	14(2)	-2(2)	1(2)	-13(2)
O(17)	17(2)	16(2)	18(2)	-7(2)	-5(2)	-3(2)
O(18)	17(2)	18(2)	14(2)	-4(2)	-2(2)	-6(2)
O(19)	17(2)	22(2)	15(2)	-8(2)	-4(2)	-7(2)
O(20)	18(2)	15(2)	19(2)	1(2)	-7(2)	-7(2)
O(21)	21(2)	19(2)	24(2)	-13(2)	-13(2)	3(2)
C(1)	32(4)	45(5)	29(4)	-11(3)	-11(4)	4(3)
C(2)	58(6)	35(4)	30(4)	-3(3)	-23(4)	-13(4)
C(3)	47(5)	41(5)	38(5)	-6(4)	-11(5)	-2(4)
C(4)	42(5)	60(6)	47(6)	-8(5)	-20(5)	-5(4)
C(5)	40(5)	49(5)	33(5)	-17(4)	-6(4)	-7(4)
C(6)	56(6)	42(5)	32(5)	-15(4)	-15(4)	1(4)
C(7)	33(4)	27(4)	28(4)	-8(3)	-14(3)	6(3)
C(8)	34(4)	22(3)	21(3)	-2(3)	-10(3)	-8(3)
C(9)	30(4)	35(4)	25(4)	-7(3)	-15(3)	4(3)
C(10)	38(4)	38(4)	23(4)	-9(3)	-10(4)	10(3)
C(11)	27(4)	28(3)	24(4)	-5(3)	-2(3)	-5(3)
C(12)	38(5)	32(4)	34(5)	-5(3)	4(4)	-13(3)
N(1)	38(4)	26(3)	24(3)	-7(2)	-8(3)	-6(3)
N(2)	50(4)	30(3)	27(3)	-5(3)	-19(3)	-5(3)
N(3)	68(5)	20(3)	33(4)	-7(3)	-22(4)	-4(3)
N(4)	19(3)	37(3)	17(3)	-3(2)	-7(3)	4(2)
N(5)	22(3)	17(2)	18(3)	-3(2)	-5(2)	0(2)
N(6)	69(5)	12(3)	21(3)	-2(2)	-9(3)	2(3)
O(22)	112(8)	73(6)	90(7)	-1(5)	-57(6)	-47(5)

Table 5. Hydrogen coordinates (x 10^4) and isotropic displacement parameters ($Å^2$x 10^3) for $[C_6H_{17}N_3]_4[Sb_4V_{16}O_{42}]\cdot 2H_2O$.

	x	y	z	U(eq)
H(1A)	2385	4316	-4767	44
H(1B)	1868	4111	-3455	44
H(2A)	1937	2379	-3763	47
H(2B)	3318	2495	-4527	47
H(3A)	4692	1632	-3740	54
H(3B)	3803	631	-3137	54
H(4A)	5113	368	-2175	61
H(4B)	4692	1567	-1997	61
H(5A)	1763	931	-2012	49
H(5B)	1302	2115	-1811	49
H(6A)	2415	1811	-676	52
H(6B)	1618	756	-210	52
H(7A)	1502	-3965	6604	36
H(7B)	2522	-3194	5617	36
H(8A)	1034	-3257	4963	31
H(8B)	29	-2865	5947	31
H(9A)	-625	-1564	4604	36
H(9B)	455	-1870	3602	36
H(10A)	-312	-53	2926	43
H(10B)	-126	325	3834	43
H(11A)	2488	-1835	3418	35
H(11B)	2789	-1533	4312	35
H(12A)	2003	364	3710	49
H(12B)	3089	81	2696	49
H(1C)	3625	5069	-4294	45
H(1D)	4303	4155	-4741	45
H(1E)	3823	3972	-3531	45
H(3C)	3632	230	-418	47
H(3D)	3240	-253	-1048	47
H(4C)	2045	-2780	7223	40
H(4D)	789	-2499	7323	40
H(4E)	1739	-1786	6409	40
H(6C)	1738	-254	2073	45
H(6D)	1473	889	2173	45
H(1)	3214	-855	5750	129
H(2)	2973	289	5208	129

7.10 **Messprotokoll für die Verbindung $[C_6H_{21}N_3]_2[C_6H_{18}N_3]_{0.33}[Sb_6V_{15}O_{42}]$**

Table 1. Crystal data and structure refinement for $[C_6H_{21}N_3]_2[C_6H_{18}N_3]_{0.33}[Sb_6V_{15}O_{42}]$.

Identification code	$[C_6H_{21}N_4]_2[C_6H_{18}N_4]_{0.33}[Sb_6V_{15}O_{42}]$ (RK312)
Empirical formula	$C_{14}H_{48}N_{9.33}O_{42}Sb_6V_{15}$
Formula weight	2512.4
Temperature	293(2) K
Wavelength	0.71073 Å
Crystal system	Rhomboedric
Space group	R-3
Unit cell dimensions	a = 21.5209(9) Å
	b = 21.5209(9) Å
	c = 72.662(4) Å
Volume	29145(2) $Å^3$
Z	18
Density (calculated)	2.557 Mg/m^3
Absorption coefficient	4.598 mm^{-1}
F(000)	20958
Crystal size	0.4 x 0.35 x 0.3 mm^3
Theta range for data collection	2.25 to 25.35°
Index ranges	-25<=h<=25, -25<=k<=23, -86<=l<=79
Reflections collected	44476
Independent reflections	11852 [R(int) = 0.0618]
Completeness to theta = 25.35°	99.6 %
Refinement method	Full-matrix least-squares on F^2
Data / restraints / parameters	11852 / 0 / 762
Goodness-of-fit on F^2	1.037
Final R indices [I>2sigma(I)]	R1 = 0.0612, wR2 = 0.1555
R indices (all data)	R1 = 0.0883, wR2 = 0.1713
Largest diff. peak and hole	4.970 and -2.315 e.$Å^{-3}$

Table 2. Atomic coordinates (x 10^4) and equivalent isotropic displacement parameters ($Å^2$x 10^3) for $[C_6H_{21}N_3]_2[C_6H_{18}N_3]_{0.33}[Sb_6V_{15}O_{42}]$. U(eq) is defined as one third of the trace of the orthogonalized U_{ij} tensor.

	x	y	z	U(eq)
Sb(1)	5326(1)	7344(1)	994(1)	25(1)
Sb(2)	4382(1)	7878(1)	688(1)	29(1)
Sb(3)	5437(1)	11285(1)	975(1)	27(1)
Sb(4)	7036(1)	12329(1)	714(1)	29(1)
Sb(5)	9263(1)	11192(1)	1038(1)	30(1)
Sb(6)	8806(1)	9672(1)	750(1)	28(1)
V(1)	5691(1)	10581(1)	531(1)	28(1)
V(2)	6203(1)	8256(1)	560(1)	25(1)
V(3)	7834(1)	9420(1)	1190(1)	24(1)
V(4)	7169(1)	11645(1)	1169(1)	24(1)
V(5)	4935(1)	8753(1)	1146(1)	26(1)
V(6)	8505(1)	11112(1)	578(1)	27(1)
V(7)	5676(1)	9267(1)	429(1)	27(1)
V(8)	7126(1)	8365(1)	883(1)	21(1)
V(9)	7737(1)	10737(1)	1292(1)	23(1)
V(10)	5820(1)	10242(1)	1264(1)	21(1)
V(11)	4699(1)	9537(1)	829(1)	28(1)
V(12)	7518(1)	9551(1)	458(1)	26(1)
V(13)	6310(1)	8821(1)	1283(1)	21(1)
V(14)	7265(1)	11132(1)	444(1)	26(1)
V(15)	8313(1)	11975(1)	882(1)	25(1)
O(1)	5362(5)	10866(5)	378(1)	42(2)
O(2)	6056(5)	7600(4)	418(1)	39(2)
O(3)	8263(5)	9241(6)	1345(1)	47(2)
O(4)	7316(5)	12263(5)	1318(1)	43(2)
O(5)	4255(5)	8292(5)	1279(2)	50(2)
O(6)	9219(5)	11572(5)	453(1)	44(2)
O(7)	5238(5)	8963(5)	237(1)	47(2)
O(8)	7298(4)	7722(4)	890(1)	34(2)
O(9)	8137(4)	11047(4)	1492(1)	38(2)
O(10)	5469(4)	10335(5)	1454(1)	37(2)
O(11)	3877(4)	9342(5)	813(2)	46(2)
O(12)	7810(5)	9345(4)	274(1)	40(2)
O(13)	6169(4)	8401(5)	1478(1)	34(2)
O(14)	7498(5)	11596(4)	257(1)	43(2)
O(15)	8963(4)	12799(4)	887(1)	37(2)
O(16)	4525(4)	7196(4)	838(1)	37(2)
O(17)	6147(4)	12137(4)	840(1)	36(2)
O(18)	9442(4)	10506(5)	904(1)	39(2)
O(19)	6318(4)	10298(4)	418(1)	35(2)
O(20)	5287(4)	10591(4)	779(1)	33(2)

O(21)	6648(4)	11397(4)	591(1)	36(2)
O(22)	5096(4)	9546(4)	584(1)	31(2)
O(23)	6091(4)	7898(4)	814(1)	28(2)
O(24)	6493(4)	9121(4)	423(1)	32(2)
O(25)	7195(4)	8748(4)	636(1)	29(2)
O(26)	5364(4)	8375(4)	583(1)	36(2)
O(27)	6914(4)	8599(4)	1125(1)	25(2)
O(28)	7214(4)	9700(4)	1315(1)	27(2)
O(29)	8348(4)	10459(4)	1148(1)	34(2)
O(30)	8073(4)	9213(4)	941(1)	32(2)
O(31)	6842(4)	10753(4)	1299(1)	28(2)
O(32)	6137(4)	11118(4)	1110(1)	26(2)
O(33)	8009(4)	11541(4)	1124(1)	28(2)
O(34)	7441(4)	12066(4)	920(1)	34(2)
O(35)	5788(4)	9335(4)	1294(1)	28(2)
O(36)	5474(4)	8229(4)	1116(1)	30(2)
O(37)	5058(4)	9690(4)	1083(1)	29(2)
O(38)	4602(4)	8580(4)	885(1)	36(2)
O(39)	8786(4)	11395(4)	839(1)	30(2)
O(40)	8013(4)	11637(4)	630(1)	26(2)
O(41)	7672(4)	10516(4)	430(1)	28(2)
O(42)	8340(4)	10137(4)	627(1)	31(2)
N(1)	3357(6)	10035(5)	1449(1)	36(2)
C(1)	3080(9)	9298(8)	1379(2)	56(4)
C(2)	3340(8)	8881(8)	1482(2)	51(4)
N(2)	2950(6)	8575(7)	1661(2)	46(3)
C(3)	4060(7)	10513(8)	1359(2)	42(3)
C(4)	4530(8)	11160(7)	1475(2)	45(3)
N(3)	4783(6)	10975(5)	1644(1)	39(2)
C(5)	2845(9)	10275(10)	1396(3)	67(5)
C(6)	2241(12)	10035(10)	1530(4)	105(9)
N(4)	2288(12)	10480(8)	1662(2)	98(6)
N(11)	6497(6)	6564(5)	165(1)	37(2)
C(11)	6902(8)	6311(8)	276(2)	47(3)
C(12)	6683(9)	6188(7)	473(2)	51(4)
N(12)	6863(8)	6872(7)	570(2)	54(3)
C(13)	6888(8)	6962(7)	3(2)	44(3)
C(14)	7321(8)	7762(9)	47(2)	60(4)
N(13)	6822(8)	8044(6)	76(2)	60(3)
C(15)	5788(7)	5933(6)	106(2)	43(3)
C(16)	5212(7)	6118(8)	81(3)	57(4)
N(14)	4968(8)	6240(8)	264(3)	97(7)
N(21)	3333	6667	168(4)	79(8)
C(22)	4530(30)	7450(30)	123(7)	190(18)
C(21)	3980(30)	6720(40)	201(10)	260(30)
N(22)	4430(30)	7580(30)	-115(7)	240(20)

Table 3. Bond lengths [Å] and angles [°] for $[C_6H_{21}N_3]_2[C_6H_{18}N_3]_{0.33}[Sb_6V_{15}O_{42}]$.

Sb(1)-O(16)	1.951(8)	Sb(1)-O(23)	1.969(8)
Sb(1)-O(36)	1.979(8)	Sb(2)-O(38)	1.956(9)
Sb(2)-O(16)	1.971(8)	Sb(2)-O(26)	1.983(8)
Sb(3)-O(17)	1.964(8)	Sb(3)-O(20)	1.966(8)
Sb(3)-O(32)	1.976(7)	Sb(4)-O(34)	1.956(8)
Sb(4)-O(21)	1.961(8)	Sb(4)-O(17)	1.969(8)
Sb(5)-O(39)	1.943(8)	Sb(5)-O(18)	1.959(8)
Sb(5)-O(29)	1.973(8)	Sb(6)-O(42)	1.948(8)
Sb(6)-O(30)	1.958(8)	Sb(6)-O(18)	1.975(9)
V(1)-O(1)	1.600(8)	V(1)-O(19)	1.921(8)
V(1)-O(22)	1.972(8)	V(1)-O(21)	1.974(8)
V(1)-O(20)	2.005(9)	V(2)-O(2)	1.649(8)
V(2)-O(24)	1.918(7)	V(2)-O(25)	1.930(8)
V(2)-O(26)	1.954(8)	V(2)-O(23)	1.965(8)
V(3)-O(3)	1.619(9)	V(3)-O(27)	1.942(7)
V(3)-O(28)	1.945(7)	V(3)-O(29)	1.961(8)
V(3)-O(30)	1.994(8)	V(4)-O(4)	1.621(8)
V(4)-O(31)	1.929(8)	V(4)-O(33)	1.955(7)
V(4)-O(32)	1.971(7)	V(4)-O(34)	1.976(8)
V(5)-O(5)	1.613(8)	V(5)-O(35)	1.946(8)
V(5)-O(37)	1.952(7)	V(5)-O(36)	1.993(7)
V(5)-O(38)	1.999(9)	V(6)-O(6)	1.627(8)
V(6)-O(41)	1.927(7)	V(6)-O(40)	1.934(7)
V(6)-O(42)	1.977(8)	V(6)-O(39)	1.993(8)
V(7)-O(7)	1.630(9)	V(7)-O(24)	1.934(8)
V(7)-O(19)	1.942(8)	V(7)-O(22)	1.982(8)
V(7)-O(26)	2.024(8)	V(8)-O(8)	1.603(8)
V(8)-O(27)	1.943(7)	V(8)-O(25)	1.949(8)
V(8)-O(30)	1.986(8)	V(8)-O(23)	1.996(8)
V(9)-O(9)	1.653(8)	(9)-O(28)	1.939(8)
V(9)-O(31)	1.943(7)	V(9)-O(33)	1.951(8)
V(9)-O(29)	1.994(8)	V(10)-O(10)	1.630(8)
V(10)-O(31)	1.922(7)		
V(10)-O(35)	1.930(8)	V(10)-O(37)	1.971(8)
V(10)-O(32)	1.998(7)	V(11)-O(11)	1.605(8)
V(11)-O(37)	1.967(8)	V(11)-O(22)	1.972(9)
V(11)-O(20)	2.002(8)	V(11)-O(38)	2.006(8)
V(12)-O(12)	1.631(9)	V(12)-O(24)	1.935(8)
V(12)-O(41)	1.943(7)	V(12)-O(25)	1.986(8)
V(12)-O(42)	2.001(8)	V(13)-O(13)	1.628(8)
V(13)-O(35)	1.932(7)	V(13)-O(28)	1.936(7)
V(13)-O(27)	1.963(7)	V(13)-O(36)	2.006(8)
V(14)-O(14)	1.612(8)	V(14)-O(41)	1.922(8)
V(14)-O(19)	1.938(8)	V(14)-O(40)	1.960(8)
V(14)-O(21)	1.995(9)	V(15)-O(15)	1.620(8)

V(15)-O(33)	1.947(8)	V(15)-O(40)	1.959(8)
V(15)-O(39)	1.992(8)	V(15)-O(34)	2.000(8)
N(1)-C(1)	1.476(17)	N(1)-C(5)	1.482(18)
N(1)-C(3)	1.486(16)	C(1)-C(2)	1.48(2)
C(2)-N(2)	1.51(2)	C(3)-C(4)	1.51(2)
C(4)-N(3)	1.474(17)	C(5)-C(6)	1.49(2)
C(6)-N(4)	1.32(3)	N(11)-C(13)	1.451(17)
N(11)-C(11)	1.476(17)	N(11)-C(15)	1.511(17)
C(11)-C(12)	1.49(2)	C(12)-N(12)	1.495(17)
C(13)-C(14)	1.53(2)	C(14)-N(13)	1.49(2)
C(15)-C(16)	1.49(2)	C(16)-N(14)	1.50(2)
N(21)-C(21)#1	1.37(6)	N(21)-C(21)	1.37(6)
C(22)-C(21)	1.54(7)	C(22)-N(22)	1.78(6)
O(16)-Sb(1)-O(23)	96.7(3)	O(16)-Sb(1)-O(36)	97.0(3)
O(23)-Sb(1)-O(36)	91.9(3)		
O(38)-Sb(2)-O(16)	96.0(3)	O(38)-Sb(2)-O(26)	94.7(4)
O(16)-Sb(2)-O(26)	95.3(3)	O(17)-Sb(3)-O(20)	96.0(3)
O(17)-Sb(3)-O(32)	96.4(3)	O(20)-Sb(3)-O(32)	94.2(3)
O(34)-Sb(4)-O(21)	94.4(3)	O(34)-Sb(4)-O(17)	96.3(3)
O(21)-Sb(4)-O(17)	97.2(3)	O(39)-Sb(5)-O(18)	97.2(4)
O(39)-Sb(5)-O(29)	93.0(3)	O(18)-Sb(5)-O(29)	95.3(3)
O(42)-Sb(6)-O(30)	95.3(3)	O(42)-Sb(6)-O(18)	95.4(3)
O(30)-Sb(6)-O(18)	94.1(3)	O(1)-V(1)-O(19)	109.7(4)
O(1)-V(1)-O(22)	113.9(4)	O(19)-V(1)-O(22)	83.5(3)
O(1)-V(1)-O(21)	106.0(4)	O(19)-V(1)-O(21)	77.9(3)
O(22)-V(1)-O(21)	139.7(3)	O(1)-V(1)-O(20)	110.2(4)
O(19)-V(1)-O(20)	140.0(3)	O(22)-V(1)-O(20)	78.4(3)
O(21)-V(1)-O(20)	93.4(3)	O(2)-V(2)-O(24)	109.7(4)
O(2)-V(2)-O(25)	109.5(4)	O(24)-V(2)-O(25)	83.2(3)
O(2)-V(2)-O(26)	111.9(4)	O(24)-V(2)-O(26)	78.0(3)
O(25)-V(2)-O(26)	138.2(3)	O(2)-V(2)-O(23)	108.5(4)
O(24)-V(2)-O(23)	141.6(3)	O(25)-V(2)-O(23)	80.3(3)
O(26)-V(2)-O(23)	91.8(3)	V(8)-V(2)-V(7)	130.69(7)
O(3)-V(3)-O(27)	113.4(4)	O(3)-V(3)-O(28)	108.0(4)
O(27)-V(3)-O(28)	81.4(3)	O(3)-V(3)-O(29)	108.5(5)
O(27)-V(3)-O(29)	137.4(3)	O(28)-V(3)-O(29)	78.6(3)
O(3)-V(3)-O(30)	109.7(4)	O(27)-V(3)-O(30)	80.5(3)
O(28)-V(3)-O(30)	142.1(3)	O(29)-V(3)-O(30)	92.9(3)
O(4)-V(4)-O(31)	108.2(4)	O(4)-V(4)-O(33)	113.1(4)
O(31)-V(4)-O(33)	82.3(3)	O(4)-V(4)-O(32)	108.5(4)
O(31)-V(4)-O(32)	77.8(3)	O(33)-V(4)-O(32)	137.6(3)
O(4)-V(4)-O(34)	110.2(4)	O(31)-V(4)-O(34)	141.4(3)
O(33)-V(4)-O(34)	79.8(3)	O(32)-V(4)-O(34)	93.2(3)
O(5)-V(5)-O(35)	109.9(5)	O(5)-V(5)-O(37)	112.8(4)
O(35)-V(5)-O(37)	82.4(3)	O(5)-V(5)-O(36)	108.8(4)
O(35)-V(5)-O(36)	78.2(3)	O(37)-V(5)-O(36)	138.0(3)

O(5)-V(5)-O(38)	108.8(5)	O(35)-V(5)-O(38)	141.1(3)
O(37)-V(5)-O(38)	79.7(3)	O(36)-V(5)-O(38)	92.7(3)
O(6)-V(6)-O(41)	112.0(4)	O(6)-V(6)-O(40)	112.3(4)
O(41)-V(6)-O(40)	84.1(3)	O(6)-V(6)-O(42)	111.2(4)
O(41)-V(6)-O(42)	77.4(3)	O(40)-V(6)-O(42)	136.5(3)
O(6)-V(6)-O(39)	107.2(4)	O(41)-V(6)-O(39)	140.7(3)
O(40)-V(6)-O(39)	79.0(3)	O(42)-V(6)-O(39)	91.1(3)
O(7)-V(7)-O(24)	107.9(5)	O(7)-V(7)-O(19)	111.1(4)
O(24)-V(7)-O(19)	90.0(3)	O(7)-V(7)-O(22)	106.4(4)
O(24)-V(7)-O(22)	145.3(3)	O(19)-V(7)-O(22)	82.7(3)
O(7)-V(7)-O(26)	104.1(4)	O(24)-V(7)-O(26)	75.9(3)
O(19)-V(7)-O(26)	144.7(4)	O(22)-V(7)-O(26)	90.8(3)
O(8)-V(8)-O(27)	112.4(4)	O(8)-V(8)-O(25)	113.1(4)
O(27)-V(8)-O(25)	134.5(3)	O(8)-V(8)-O(30)	102.2(4)
O(27)-V(8)-O(30)	80.6(3)	O(25)-V(8)-O(30)	88.8(3)
O(8)-V(8)-O(23)	104.7(4)	O(27)-V(8)-O(23)	90.7(3)
O(25)-V(8)-O(23)	79.1(3)	O(30)-V(8)-O(23)	153.0(3)
O(9)-V(9)-O(28)	105.8(4)	O(9)-V(9)-O(31)	106.9(4)
O(28)-V(9)-O(31)	90.5(3)	O(9)-V(9)-O(33)	109.0(4)
O(28)-V(9)-O(33)	145.1(3)	O(31)-V(9)-O(33)	82.0(3)
O(9)-V(9)-O(29)	107.2(4)	O(28)-V(9)-O(29)	78.0(3)
O(31)-V(9)-O(29)	145.8(3)	O(33)-V(9)-O(29)	89.3(3)
O(10)-V(10)-O(31)	106.7(4)	O(10)-V(10)-O(35)	104.4(4)
O(31)-V(10)-O(35)	90.9(3)	O(10)-V(10)-O(37)	109.9(4)
O(31)-V(10)-O(37)	143.3(3)	O(35)-V(10)-O(37)	82.3(3)
O(10)-V(10)-O(32)	108.5(4)	O(31)-V(10)-O(32)	77.3(3)
O(35)-V(10)-O(32)	147.0(3)	O(37)-V(10)-O(32)	89.0(3)
O(11)-V(11)-O(37)	113.6(5)	O(11)-V(11)-O(22)	110.8(5)
O(37)-V(11)-O(22)	135.6(3)	O(11)-V(11)-O(20)	105.9(4)
O(37)-V(11)-O(20)	90.4(3)	O(22)-V(11)-O(20)	78.5(3)
O(11)-V(11)-O(38)	102.1(4)	O(37)-V(11)-O(38)	79.2(3)
O(22)-V(11)-O(38)	90.8(3)	O(20)-V(11)-O(38)	152.0(3)
O(12)-V(12)-O(24)	105.5(4)	O(12)-V(12)-O(41)	108.8(4)
O(24)-V(12)-O(41)	92.4(3)	O(12)-V(12)-O(25)	108.3(4)
O(24)-V(12)-O(25)	81.3(3)	O(41)-V(12)-O(25)	142.7(3)
O(12)-V(12)-O(42)	109.7(4)	O(24)-V(12)-O(42)	144.8(3)
O(41)-V(12)-O(42)	76.4(3)	O(25)-V(12)-O(42)	87.8(3)
O(13)-V(13)-O(35)	106.3(4)	O(13)-V(13)-O(28)	104.6(4)
O(35)-V(13)-O(28)	91.3(3)	O(13)-V(13)-O(27)	109.7(4)
O(35)-V(13)-O(27)	143.9(3)	O(28)-V(13)-O(27)	81.1(3)
O(13)-V(13)-O(36)	108.3(4)	O(35)-V(13)-O(36)	78.2(3)
O(28)-V(13)-O(36)	147.1(3)	O(27)-V(13)-O(36)	89.2(3)
O(14)-V(14)-O(41)	106.0(4)	O(14)-V(14)-O(19)	110.4(4)
O(41)-V(14)-O(19)	89.3(3)	O(14)-V(14)-O(40)	108.8(4)
O(41)-V(14)-O(40)	83.6(3)	O(19)-V(14)-O(40)	140.7(3)
O(14)-V(14)-O(21)	108.5(4)	O(41)-V(14)-O(21)	145.5(3)
O(19)-V(14)-O(21)	77.0(3)	O(40)-V(14)-O(21)	87.3(3)

O(15)-V(15)-O(33)	113.9(4)	O(15)-V(15)-O(40)	111.7(4)
O(33)-V(15)-O(40)	134.4(3)	O(15)-V(15)-O(39)	104.8(4)
O(33)-V(15)-O(39)	89.7(3)	O(40)-V(15)-O(39)	78.4(3)
O(15)-V(15)-O(34)	103.3(4)	O(33)-V(15)-O(34)	79.3(3)
O(40)-V(15)-O(34)	90.9(3)	O(39)-V(15)-O(34)	151.9(3)
C(1)-N(1)-C(5)	108.3(12)	C(1)-N(1)-C(3)	108.6(11)
C(5)-N(1)-C(3)	108.8(10)	C(2)-C(1)-N(1)	114.2(11)
C(1)-C(2)-N(2)	113.7(12)	N(1)-C(3)-C(4)	112.0(10)
N(3)-C(4)-C(3)	112.5(10)	N(1)-C(5)-C(6)	112.4(16)
N(4)-C(6)-C(5)	118.9(18)	C(13)-N(11)-C(11)	112.9(11)
C(13)-N(11)-C(15)	109.1(10)	C(11)-N(11)-C(15)	110.0(10)
N(11)-C(11)-C(12)	113.6(12)	C(11)-C(12)-N(12)	111.8(11)
N(11)-C(13)-C(14)	110.2(11)	N(13)-C(14)-C(13)	109.4(12)
C(16)-C(15)-N(11)	113.3(10)	C(15)-C(16)-N(14)	110.5(15)
C(21)#1-N(21)-C(21)#2	117.0(19)	C(21)-C(22)-N(22)	115(4)
N(21)-C(21)-C(22)	104(5)		

Symmetry transformations used to generate equivalent atoms:
#1 -y+1,x-y+1,z #2 -x+y,-x+1,z

Table 4. Anisotropic displacement parameters ($Å^2 x\ 10^3$) for $[C_6H_{21}N_3]_2[C_6H_{18}N_3]_{0.33}[Sb_6V_{15}O_{42}]$. The anisotropicdisplacement factor exponent takes the form: $-2\pi^2[\ h^2\ a^{*2}U_{11} + ...\ + 2\ h\ k\ a^*\ b^*\ U_{12}\ ]$.

	U_{11}	U_{22}	U_{33}	U_{23}	U_{13}	U_{12}
Sb(1)	25(1)	22(1)	26(1)	5(1)	0(1)	9(1)
Sb(2)	25(1)	26(1)	32(1)	0(1)	-9(1)	8(1)
Sb(3)	29(1)	30(1)	26(1)	1(1)	-3(1)	17(1)
Sb(4)	38(1)	22(1)	25(1)	2(1)	0(1)	13(1)
Sb(5)	21(1)	31(1)	35(1)	-6(1)	0(1)	11(1)
Sb(6)	29(1)	31(1)	29(1)	0(1)	8(1)	18(1)
V(1)	33(1)	27(1)	23(1)	0(1)	-10(1)	14(1)
V(2)	33(1)	21(1)	17(1)	-2(1)	-1(1)	12(1)
V(3)	24(1)	31(1)	20(1)	-5(1)	-3(1)	15(1)
V(4)	23(1)	26(1)	22(1)	-6(1)	-2(1)	12(1)
V(5)	21(1)	29(1)	28(1)	8(1)	3(1)	13(1)
V(6)	29(1)	25(1)	25(1)	2(1)	8(1)	11(1)
V(7)	32(1)	24(1)	20(1)	0(1)	-7(1)	11(1)
V(8)	25(1)	21(1)	18(1)	-2(1)	2(1)	12(1)
V(9)	22(1)	30(1)	18(1)	-7(1)	-4(1)	14(1)
V(10)	23(1)	30(1)	16(1)	2(1)	2(1)	16(1)
V(11)	22(1)	24(1)	36(1)	3(1)	-8(1)	10(1)
V(12)	34(1)	25(1)	17(1)	0(1)	4(1)	15(1)
V(13)	24(1)	28(1)	12(1)	3(1)	2(1)	15(1)
V(14)	34(1)	22(1)	18(1)	1(1)	-2(1)	12(1)
V(15)	23(1)	23(1)	26(1)	-2(1)	3(1)	9(1)
O(1)	45(5)	44(5)	36(5)	3(4)	-9(4)	22(4)
O(2)	52(5)	36(4)	30(5)	-9(3)	0(4)	23(4)
O(3)	46(5)	74(6)	39(5)	4(4)	-4(4)	42(5)
O(4)	47(5)	37(4)	44(6)	-21(4)	-9(4)	20(4)
O(5)	37(5)	45(5)	63(7)	18(5)	29(4)	18(4)
O(6)	36(4)	47(5)	45(6)	9(4)	23(4)	17(4)
O(7)	52(5)	41(5)	36(5)	5(4)	-15(4)	13(4)
O(8)	44(5)	33(4)	31(5)	-5(3)	-4(3)	24(4)
O(9)	39(4)	40(5)	34(5)	-12(4)	-11(4)	18(4)
O(10)	39(4)	54(5)	33(5)	3(4)	8(4)	34(4)
O(11)	25(4)	37(5)	75(7)	4(4)	-8(4)	14(4)
O(12)	45(5)	37(4)	32(5)	-1(4)	8(4)	17(4)
O(13)	44(4)	47(5)	20(4)	10(3)	4(3)	27(4)
O(14)	59(6)	29(4)	31(5)	6(3)	-6(4)	14(4)
O(15)	32(4)	30(4)	43(5)	0(3)	6(4)	12(3)
O(16)	35(4)	22(4)	45(5)	4(3)	-10(4)	7(3)
O(17)	42(4)	27(4)	42(5)	5(3)	3(4)	19(4)
O(18)	28(4)	45(5)	50(6)	-6(4)	6(4)	22(4)
O(19)	41(4)	32(4)	29(5)	-3(3)	0(3)	16(4)
O(20)	43(4)	25(4)	29(4)	-2(3)	-7(3)	16(3)

O(21)	40(4)	29(4)	39(5)	-7(3)	-10(4)	17(4)
O(22)	28(4)	26(4)	37(5)	2(3)	-4(3)	11(3)
O(23)	33(4)	26(4)	22(4)	-2(3)	-2(3)	13(3)
O(24)	37(4)	26(4)	30(4)	6(3)	-1(3)	15(3)
O(25)	33(4)	29(4)	23(4)	3(3)	5(3)	14(3)
O(26)	34(4)	31(4)	43(5)	12(4)	2(4)	15(3)
O(27)	27(4)	25(3)	21(4)	0(3)	-1(3)	12(3)
O(28)	28(4)	33(4)	20(4)	-7(3)	-3(3)	15(3)
O(29)	30(4)	30(4)	40(5)	-8(3)	4(3)	15(3)
O(30)	30(4)	32(4)	27(4)	-3(3)	5(3)	10(3)
O(31)	26(4)	37(4)	23(4)	-3(3)	0(3)	17(3)
O(32)	26(4)	27(4)	26(4)	0(3)	-7(3)	13(3)
O(33)	24(4)	24(4)	30(4)	0(3)	2(3)	7(3)
O(34)	36(4)	42(4)	27(4)	3(3)	3(3)	23(4)
O(35)	26(4)	35(4)	26(4)	0(3)	-1(3)	18(3)
O(36)	24(4)	38(4)	29(4)	-7(3)	-3(3)	17(3)
O(37)	21(3)	25(4)	38(5)	3(3)	-1(3)	11(3)
O(38)	38(4)	28(4)	37(5)	4(3)	-8(4)	13(3)
O(39)	30(4)	39(4)	23(4)	-5(3)	-2(3)	19(3)
O(40)	30(4)	25(3)	27(4)	-1(3)	-2(3)	16(3)
O(41)	36(4)	24(4)	19(4)	-5(3)	-10(3)	11(3)
O(42)	37(4)	28(4)	29(4)	-1(3)	-3(3)	17(3)
N(1)	53(6)	39(5)	22(5)	0(4)	-2(4)	27(5)
C(1)	57(9)	60(9)	56(10)	-19(7)	-29(7)	33(7)
C(2)	53(8)	56(8)	56(9)	-23(7)	-11(7)	36(7)
N(2)	43(6)	63(7)	30(6)	-14(5)	-10(5)	25(6)
C(3)	47(7)	57(8)	27(7)	6(6)	6(5)	30(6)
C(4)	65(9)	37(7)	38(8)	19(5)	18(6)	31(6)
N(3)	46(6)	37(5)	27(6)	1(4)	4(4)	16(5)
C(5)	51(9)	81(11)	80(12)	45(10)	31(8)	42(8)
C(6)	73(13)	44(9)	180(30)	-8(13)	50(15)	17(9)
N(4)	160(18)	58(9)	50(10)	17(7)	43(10)	36(10)
N(11)	59(6)	43(6)	17(5)	0(4)	-1(4)	33(5)
C(11)	62(8)	58(8)	34(8)	-12(6)	-7(6)	39(7)
C(12)	73(10)	27(6)	41(8)	-1(5)	-19(7)	16(6)
N(12)	80(9)	47(7)	42(7)	-9(5)	-11(6)	36(6)
C(13)	53(8)	43(7)	33(7)	1(5)	8(6)	22(6)
C(14)	49(8)	68(10)	50(10)	4(8)	6(7)	20(8)
N(13)	87(10)	39(6)	44(8)	-1(5)	6(7)	23(6)
C(15)	55(8)	31(6)	35(7)	-1(5)	3(6)	15(6)
C(16)	35(7)	44(8)	80(12)	-9(7)	-3(7)	12(6)
N(14)	47(8)	64(9)	132(16)	-49(10)	29(9)	-7(7)

Table 5. Hydrogen coordinates (x 10^4) and isotropic displacement parameters (Å^{2}x 10^3) for $[C_6H_{21}N_3]_2[C_6H_{18}N_3]_{0.33}[Sb_6V_{15}O_{42}]$.

	x	y	z	U(eq)
H(1A)	2560	9046	1385	67
H(1B)	3217	9323	1251	67
H(2A)	3847	9187	1507	61
H(2B)	3288	8490	1404	61
H(3A)	3978	10669	1241	50
H(3B)	4305	10245	1337	50
H(4A)	4941	11496	1403	54
H(4B)	4263	11396	1509	54
H(5A)	2651	10087	1275	80
H(5B)	3099	10794	1389	80
H(6A)	1809	9905	1460	126
H(6B)	2174	9600	1589	126
H(11A)	7409	6663	269	57
H(11B)	6834	5867	224	57
H(12A)	6924	5967	535	61
H(12B)	6170	5859	481	61
H(13A)	6553	6882	-96	52
H(13B)	7208	6795	-38	52
H(14A)	7607	7838	157	72
H(14B)	7643	8015	-54	72
H(15A)	5855	5746	-9	52
H(15B)	5635	5557	198	52
H(16A)	4808	5731	17	68
H(16B)	5391	6548	7	68
H(22A)	5010	7525	143	228
H(22B)	4499	7822	193	228
H(21A)	4015	6336	139	314
H(21B)	4055	6691	332	314

7.11 **Messprotokoll für die** Verbindung $[NH_4]_4[Sb_8V_{14}O_{42}]\cdot 2H_2O$

Table 1. Crystal data and structure refinement for $[NH_4]_4[Sb_8V_{14}O_{42}]\cdot 2H_2O$

Identification code	$[NH_4]_4[Sb_8V_{14}O_{42}]\cdot 2H_2O$ (RK680)
Empirical formula	$H_{20}N_4O_{44}Sb_8V_{14}$
Formula weight	2467.34 g/mol g/mol
Temperature	293(2) K
Wavelength	0.71073 Å
Crystal system	Monoclinic
Space group	$P2_1/n$
Unit cell dimensions	a = 12.839(3) Å
	b = 11.924(2) Å β= 99.77(3)°.
	c = 17.280(4)
Volume	2607.1(9) $Å^3$
Z	4
Density (calculated)	3.117 Mg/m^3
Absorption coefficient	6.541 mm^{-1}
F(000)	2220
Crystal size	0.2 x 0.2 x 0.15 mm^3
Theta range for data collection	1.83 to 28.02°.
Index ranges	0<=h<=16, -15<=k<=15, -22<=l<=22
Reflections collected	12809
Independent reflections	6290 [R(int) = 0.0489]
Completeness to theta = 28.02°	99.8 %
Refinement method	Full-matrix least-squares on F^2
Data / restraints / parameters	6290 / 0 / 317
Goodness-of-fit on F^2	1.089
Final R indices [I>2sigma(I)]	R1 = 0.0450, wR2 = 0.1322
R indices (all data)	R1 = 0.0591, wR2 = 0.1398
Extinction coefficient	0.00063(11)
Largest diff. peak and hole	2.821 and -2.374 $e.Å^{-3}$

Table 2. Atomic coordinates (x 10^4) and equivalent isotropic displacement parameters ($Å^2$x 10^3) for $[NH_4]_4[Sb_8V_{14}O_{42}]\cdot 2H_2O$. U(eq) is defined as one third of the trace of the orthogonalized U_{ij} tensor.

	x	y	z	U(eq)
Sb(1)	8569(1)	3942(1)	1191(1)	20(1)
Sb(2)	6745(1)	8345(1)	-658(1)	22(1)
Sb(3)	3058(1)	5473(1)	-2608(1)	19(1)
Sb(4)	4864(1)	1136(1)	-793(1)	21(1)
V(1)	6780(1)	4324(1)	-1646(1)	20(1)
V(2)	7036(1)	2696(1)	-383(1)	19(1)
V(3)	7819(1)	5731(1)	-348(1)	18(1)
V(4)	5499(1)	6390(1)	-1898(1)	17(1)
V(5)	4694(1)	3363(1)	-1966(1)	17(1)
V(6)	3885(1)	7704(1)	-1130(1)	17(1)
V(7)	2716(1)	3274(1)	-1173(1)	16(1)
O(1)	7339(4)	3015(4)	763(3)	22(1)
O(2)	7887(4)	5372(4)	772(3)	22(1)
O(3)	7193(4)	7082(4)	55(3)	22(1)
O(4)	6072(4)	9260(5)	53(3)	26(1)
O(5)	5427(4)	7570(5)	-1108(3)	27(1)
O(6)	3978(4)	6446(4)	-1848(3)	21(1)
O(7)	1764(4)	5848(5)	-2234(3)	24(1)
O(8)	3377(4)	4154(4)	-1907(3)	21(1)
O(9)	4051(4)	2464(4)	-1206(3)	22(1)
O(10)	5837(4)	1995(4)	-8(3)	22(1)
O(11)	7614(4)	4137(4)	-598(3)	23(1)
O(12)	6894(4)	5920(4)	-1348(3)	20(1)
O(13)	5358(4)	4791(4)	-2088(3)	22(1)
O(14)	6078(4)	2963(4)	-1376(3)	22(1)
O(15)	7472(5)	4054(6)	-2317(4)	36(1)
O(16)	7858(5)	1761(6)	-580(4)	39(2)
O(17)	8989(5)	6060(6)	-485(4)	34(1)
O(18)	5729(5)	6988(6)	-2673(3)	33(1)
O(19)	3519(5)	8839(5)	-1592(3)	29(1)
O(20)	4619(5)	2746(5)	-2807(3)	31(1)
O(21)	1753(4)	2553(5)	-1638(3)	28(1)
O(22)	5204(12)	7990(20)	-4169(8)	181(11)
N(1)	-240(8)	4528(7)	-2375(7)	51(2)
N(2)	8260(8)	6454(9)	-2459(6)	57(3)

Table 3. Bond lengths [Å] and angles [°] for $[NH_4]_4[Sb_8V_{14}O_{42}]\cdot 2H_2O$

Sb(1)-O(7)#1	1.939(5)	Sb(1)-O(1)	1.965(5)
Sb(1)-O(2)	1.996(5)	Sb(2)-O(4)	1.952(6)
Sb(2)-O(5)	1.969(6)	Sb(2)-O(3)	1.969(5)
Sb(3)-O(7)	1.934(5)	Sb(3)-O(8)	1.984(5)
Sb(3)-O(6)	1.984(5)	Sb(4)-O(4)#1	1.956(6)
Sb(4)-O(9)	1.963(5)	Sb(4)-O(10)	1.969(5)
V(1)-O(15)	1.609(6)	V(1)-O(13)	1.937(5)
V(1)-O(14)	1.950(5)	V(1)-O(11)	1.954(6)
V(1)-O(12)	1.970(5)	V(2)-O(16)	1.611(6)
V(2)-O(11)	1.933(5)	V(2)-O(10)	1.956(5)
V(2)-O(14)	1.959(5)	V(2)-O(1)	1.990(5)
V(3)-O(17)	1.609(6)	V(3)-O(12)	1.937(5)
V(3)-O(11)	1.957(5)	V(3)-O(2)	1.969(5)
V(3)-O(3)	1.979(5)	V(4)-O(18)	1.588(6)
V(4)-O(13)	1.938(5)	V(4)-O(12)	1.962(5)
V(4)-O(6)	1.971(5)	V(4)-O(5)	1.974(6)
V(5)-O(20)	1.618(6)	V(5)-O(13)	1.931(5)
V(5)-O(14)	1.952(5)	V(5)-O(8)	1.954(5)
V(5)-O(9)	1.981(5)	V(6)-O(19)	1.601(5)
V(6)-O(6)	1.963(5)	V(6)-O(10)#1	1.970(5)
V(6)-O(5)	1.979(6)	V(6)-O(1)#1	1.987(5)
V(7)-O(21)	1.605(5)	V(7)-O(8)	1.948(5)
V(7)-O(3)#1	1.962(5)	V(7)-O(2)#1	1.967(5)
V(7)-O(9)	1.976(5)		
O(7)#1-Sb(1)-O(1)	97.6(2)	O(7)#1-Sb(1)-O(2)	94.3(2)
O(1)-Sb(1)-O(2)	94.0(2)	O(4)-Sb(2)-O(5)	93.9(2)
O(4)-Sb(2)-O(3)	98.4(2)	O(5)-Sb(2)-O(3)	91.6(2)
O(7)-Sb(3)-O(8)	94.6(2)	O(7)-Sb(3)-O(6)	95.3(2)
O(8)-Sb(3)-O(6)	91.3(2)	O(4)#1-Sb(4)-O(9)	94.9(2)
O(4)#1-Sb(4)-O(10)	93.6(2)	O(9)-Sb(4)-O(10)	93.8(2)
O(15)-V(1)-O(13)	111.9(3)	O(15)-V(1)-O(14)	109.9(3)
O(13)-V(1)-O(14)	83.7(2)	O(15)-V(1)-O(11)	111.2(3)
O(13)-V(1)-O(11)	136.9(2)	O(14)-V(1)-O(11)	83.5(2)
O(15)-V(1)-O(12)	110.8(3)	O(13)-V(1)-O(12)	81.3(2)
O(14)-V(1)-O(12)	139.3(2)	O(11)-V(1)-O(12)	82.1(2)
O(16)-V(2)-O(11)	106.7(3)	O(16)-V(2)-O(10)	110.8(3)
O(11)-V(2)-O(10)	142.5(2)	O(16)-V(2)-O(14)	105.3(3)
O(11)-V(2)-O(14)	83.8(2)	O(10)-V(2)-O(14)	87.0(2)
O(16)-V(2)-O(1)	108.5(3)	O(11)-V(2)-O(1)	90.3(2)
O(10)-V(2)-O(1)	77.5(2)	O(14)-V(2)-O(1)	145.9(2)
O(17)-V(3)-O(12)	106.7(3)	O(17)-V(3)-O(11)	107.3(3)
O(12)-V(3)-O(11)	82.9(2)	O(17)-V(3)-O(2)	108.1(3)
O(12)-V(3)-O(2)	145.1(2)	O(11)-V(3)-O(2)	89.3(2)
O(17)-V(3)-O(3)	107.4(3)	O(12)-V(3)-O(3)	89.7(2)

O(11)-V(3)-O(3)	145.2(2)	O(2)-V(3)-O(3)	77.5(2)
O(18)-V(4)-O(13)	108.9(3)	O(18)-V(4)-O(12)	104.6(3)
O(13)-V(4)-O(12)	81.5(2)	O(18)-V(4)-O(6)	110.5(3)
O(13)-V(4)-O(6)	88.6(2)	O(12)-V(4)-O(6)	144.9(2)
O(18)-V(4)-O(5)	107.5(3)	O(13)-V(4)-O(5)	143.5(2)
O(12)-V(4)-O(5)	90.8(2)	O(6)-V(4)-O(5)	77.4(2)
O(20)-V(5)-O(13)	105.2(3)	O(20)-V(5)-O(14)	105.6(3)
O(13)-V(5)-O(14)	83.8(2)	O(20)-V(5)-O(8)	110.2(3)
O(13)-V(5)-O(8)	89.0(2)	O(14)-V(5)-O(8)	144.1(2)
O(20)-V(5)-O(9)	112.4(3)	O(13)-V(5)-O(9)	142.2(2)
O(14)-V(5)-O(9)	88.1(2)	O(8)-V(5)-O(9)	76.4(2)
O(20)-V(5)-V(1)	105.4(2)	O(13)-V(5)-V(1)	41.99(16)
O(14)-V(5)-V(1)	42.45(16)	O(8)-V(5)-V(1)	125.67(17)
O(9)-V(5)-V(1)	124.54(17)	O(19)-V(6)-O(6)	112.0(3)
O(19)-V(6)-O(10)#1	109.3(3)	O(6)-V(6)-O(10)#1	138.6(2)
O(19)-V(6)-O(5)	106.6(3)	O(6)-V(6)-O(5)	77.5(2)
O(10)#1-V(6)-O(5)	89.1(2)	O(19)-V(6)-O(1)#1	110.0(3)
O(6)-V(6)-O(1)#1	90.4(2)	O(10)#1-V(6)-O(1)#1	77.3(2)
O(5)-V(6)-O(1)#1	143.3(2)	O(21)-V(7)-O(8)	110.2(3)
O(21)-V(7)-O(3)#1	106.8(3)	O(8)-V(7)-O(3)#1	142.9(2)
O(21)-V(7)-O(2)#1	107.5(3)	O(8)-V(7)-O(2)#1	91.6(2)
O(3)#1-V(7)-O(2)#1	77.9(2)	O(21)-V(7)-O(9)	108.8(3)
O(8)-V(7)-O(9)	76.6(2)	O(3)#1-V(7)-O(9)	90.9(2)
O(2)#1-V(7)-O(9)	143.7(2)		

Symmetry transformations used to generate equivalent atoms:
#1 -x+1,-y+1,-z

Table 4 Anisotropic displacement parameters ($Å^2 x\ 10^3$) for $[NH_4]_4[Sb_8V_{14}O_{42}]\cdot 2H_2O$.. The anisotropic displacement factor exponent takes the form: $-2\pi^2[\ h^2\ a^{*2}U_{11} + ...\ + 2\ h\ k\ a^*\ b^*\ U_{12}\ ]$.

	U_{11}	U_{22}	U_{33}	U_{23}	U_{13}	U_{12}
Sb(1)	17(1)	20(1)	25(1)	1(1)	5(1)	2(1)
Sb(2)	25(1)	19(1)	23(1)	3(1)	7(1)	-5(1)
Sb(3)	23(1)	17(1)	17(1)	2(1)	3(1)	0(1)
Sb(4)	29(1)	14(1)	21(1)	-1(1)	6(1)	1(1)
V(1)	23(1)	20(1)	21(1)	-2(1)	11(1)	-1(1)
V(2)	20(1)	16(1)	21(1)	-1(1)	6(1)	2(1)
V(3)	17(1)	18(1)	19(1)	1(1)	5(1)	-1(1)
V(4)	19(1)	16(1)	16(1)	2(1)	5(1)	-2(1)
V(5)	21(1)	14(1)	17(1)	-1(1)	6(1)	-1(1)
V(6)	20(1)	13(1)	18(1)	2(1)	4(1)	1(1)
V(7)	17(1)	14(1)	17(1)	-1(1)	3(1)	-3(1)
O(1)	23(2)	23(3)	20(2)	0(2)	5(2)	-5(2)
O(2)	34(3)	18(2)	15(2)	-1(2)	3(2)	6(2)
O(3)	33(3)	18(2)	17(2)	5(2)	6(2)	5(2)
O(4)	30(3)	17(2)	34(3)	0(2)	10(2)	-4(2)
O(5)	24(3)	25(3)	32(3)	-9(2)	7(2)	-1(2)
O(6)	21(2)	18(2)	23(2)	-3(2)	2(2)	0(2)
O(7)	25(3)	25(3)	21(2)	1(2)	2(2)	4(2)
O(8)	20(2)	18(2)	26(3)	6(2)	8(2)	0(2)
O(9)	22(2)	18(2)	28(3)	5(2)	9(2)	1(2)
O(10)	28(3)	18(2)	20(2)	1(2)	4(2)	-5(2)
O(11)	25(3)	17(2)	26(3)	0(2)	6(2)	-2(2)
O(12)	21(2)	19(2)	18(2)	1(2)	1(2)	-3(2)
O(13)	22(2)	18(2)	25(2)	0(2)	3(2)	-3(2)
O(14)	23(2)	17(2)	25(3)	2(2)	8(2)	0(2)
O(15)	36(3)	39(4)	39(3)	-7(3)	21(3)	-3(3)
O(16)	36(3)	30(3)	54(4)	-1(3)	13(3)	14(3)
O(17)	25(3)	40(4)	40(3)	-2(3)	11(2)	-10(3)
O(18)	34(3)	36(3)	29(3)	12(3)	8(2)	0(3)
O(19)	38(3)	20(3)	27(3)	5(2)	1(2)	2(2)
O(20)	39(3)	30(3)	26(3)	-11(2)	11(2)	-13(3)
O(21)	23(3)	30(3)	27(3)	-4(2)	-4(2)	-9(2)
O(22)	118(11)	350(30)	90(9)	120(14)	67(9)	123(15)
N(1)	44(5)	34(4)	81(7)	-13(5)	30(5)	-2(4)
N(2)	58(6)	49(5)	73(7)	22(5)	42(5)	-1(5)

7.12 Messprotokoll für die Verbindung $[C_3H_{10}NO]_2[Sb_4S_7]$

Table 1. Crystal data and structure refinement for $[C_3H_{10}NO]_2[Sb_4S_7]$.

Identification code	[1-Amino-2-propanol]$_2$[Sb_4S_7] (RK98)
Empirical formula	$C_6H_{20}N_2O_2S_7Sb_4$
Formula weight	863.66
Temperature	293(2) K
Wavelength	0.71073 Å
Crystal system	Orthorhombic
Space group	Abm2
Unit cell dimensions	a = 19.6319(17) Å
	b = 9.9412(7) Å
	c = 11.3727(9) Å
Volume	2219.5(3) Å^3
Z	4
Density (calculated)	2.539 Mg/m^3
Absorption coefficient	5.475 mm^{-1}
F(000)	1548
Crystal size	0.12 x 0.11 x 0.10 mm^3
Theta range for data collection	2.91 to 27.93°.
Index ranges	-25<=h<=25, -11<=k<=11, -14<=l<=14
Reflections collected	10502
Independent reflections	2667 [R(int) = 0.0598]
Completeness to theta = 27.93°	94.7 %
Refinement method	Full-matrix least-squares on F^2
Data / restraints / parameters	2667 / 1 / 59
Goodness-of-fit on F^2	0.965
Final R indices [I>2sigma(I)]	R1 = 0.0398, wR2 = 0.0952
R indices (all data)	R1 = 0.0457, wR2 = 0.0970
Absolute structure parameter	-0.06(5)
Extinction coefficient	0.00192(15)
Largest diff. peak and hole	1.285 and -1.638 e.Å^{-3}

Remarks.
The non-hydrogen atoms were refined using anisotropic displacement parameters.
The amine molecules are disordered and no suitable structure model was found. Therefore, the intensity data were corrected using the Squeeze option in Platon.

Table 2. Atomic coordinates (x 10^4) and equivalent isotropic displacement parameters (Å^{2}x 10^3) for $[C_3H_{10}NO]_2[Sb_4S_7]$. U(eq) is defined as one third of the trace of the orthogonalized U_{ij} tensor.

	x	y	z	U(eq)
Sb(1)	6988(1)	7500	3904(1)	25(1)
Sb(2)	5935(1)	4512(1)	2458(1)	20(1)
Sb(3)	5040(1)	2500	4826(1)	24(1)
S(1)	8174(2)	7500	4266(4)	52(1)
S(2)	7068(1)	5629(2)	2472(2)	29(1)
S(3)	5895(1)	4364(3)	4643(2)	26(1)
S(4)	6653(2)	2500	2101(2)	23(1)
S(5)	4693(2)	2500	2810(3)	26(1)

Table 3. Bond lengths [Å] and angles [°] for for $[C_3H_{10}NO]_2[Sb_4S_7]$.

Sb(1)-S(1)	2.364(4)	Sb(1)-S(2)	2.477(3)
Sb(1)-S(2)#1	2.477(3)	Sb(2)-S(4)	2.4801(18)
Sb(2)-S(2)	2.486(2)	Sb(2)-S(3)	2.490(2)
Sb(3)-S(5)	2.391(3)	Sb(3)-S(3)	2.509(2)
Sb(3)-S(3)#2	2.509(2)	S(4)-Sb(2)#2	2.4801(18)
S(1)-Sb(1)-S(2)	93.01(9)	S(1)-Sb(1)-S(2)#1	93.01(9)
S(2)-Sb(1)-S(2)#1	97.32(13)	S(4)-Sb(2)-S(2)	81.56(8)
S(4)-Sb(2)-S(3)	97.70(9)	S(2)-Sb(2)-S(3)	92.78(9)
S(5)-Sb(3)-S(3)	96.37(7)	S(5)-Sb(3)-S(3)#2	96.37(7)
S(3)-Sb(3)-S(3)#2	95.23(11)	Sb(1)-S(2)-Sb(2)	106.45(8)
Sb(2)-S(3)-Sb(3)	98.48(8)	Sb(2)#2-S(4)-Sb(2)	107.48(11)

Symmetry transformations used to generate equivalent atoms:
#1 x,-y+3/2,z #2 x,-y+1/2,z

Table 4. Anisotropic displacement parameters (Å^{2}x 10^3)for for $[C_3H_{10}NO]_2[Sb_4S_7]$. The anisotropic displacement factor exponent takes the form: $-2\pi^2[h^2a^{*2}U_{11} + ... + 2 h k a^* b^* U_{12}]$

	U_{11}	U_{22}	U_{33}	U_{23}	U_{13}	U_{12}
Sb(1)	28(1)	26(1)	21(1)	0	-1(1)	0
Sb(2)	26(1)	17(1)	18(1)	1(1)	0(1)	0(1)
Sb(3)	26(1)	31(1)	13(1)	0	3(1)	0
S(1)	39(2)	80(4)	38(2)	0	-7(2)	0
S(2)	28(1)	19(1)	39(1)	-3(1)	5(1)	-3(1)
S(3)	34(1)	23(1)	19(1)	-3(1)	1(1)	-2(1)
S(4)	24(1)	21(2)	23(1)	0	6(1)	0
S(5)	36(2)	21(2)	19(1)	0	-3(1)	0

7.13 Messprotokoll für die Verbindung $[C_3H_{10}NO]_2[Sb_4S_7]$

Table 1. Crystal data and structure refinement for $[C_3H_{10}NO]_2[Sb_4S_7]$.

Identification code	[1-amino-2-propanol]$_2$[Sb_4S_7] (RK133)	
Empirical formula	$C_6H_{20}N_2O_2S_7Sb_4$	
Formula weight	863.66 g/mol	
Temperature	293(2) K	
Wavelength	0.71073 Å	
Crystal system	Triclinic	
Space group	P-1	
Unit cell dimensions	a = 7.0100(14) Å	α= 113.43(3)°.
	b = 11.950(2) Å	β= 97.86(3)°.
	c = 14.570(3) Å	γ= 92.26(3)°.
Volume	1103.4(4) Å^3	
Z	2	
Density (calculated)	2.599 Mg/m^3	
Absorption coefficient	5.508 mm^{-1}	
F(000)	804	
Crystal size	1.2 x 0.7 x 1.1 mm^3	
Theta range for data collection	2.87 to 28.00°.	
Index ranges	-9<=h<=9, -15<=k<=15, -19<=l<=19	
Reflections collected	10016	
Independent reflections	5157 [R(int) = 0.0362]	
Completeness to theta = 28.00°	96.7 %	
Refinement method	Full-matrix least-squares on F^2	
Data / restraints / parameters	5157 / 0 / 193	
Goodness-of-fit on F^2	1.126	
Final R indices [I>2sigma(I)]	R1 = 0.0325, wR2 = 0.0882	
R indices (all data)	R1 = 0.0397, wR2 = 0.0907	
Largest diff. peak and hole	1.275 and -1.529 e.Å^{-3}	

Table 2. Atomic coordinates (x 10^4) and equivalent isotropic displacement parameters (Å^{2}x 10^3) for $[C_3H_{10}NO]_2[Sb_4S_7]$. U(eq) is defined as one third of the trace of the orthogonalized U_{ij} tensor.

	x	y	z	U(eq)
Sb(1)	8782(1)	959(1)	4362(1)	17(1)
Sb(2)	14399(1)	1623(1)	5338(1)	19(1)
Sb(3)	16144(1)	4856(1)	6232(1)	18(1)
Sb(4)	21371(1)	6393(1)	6349(1)	18(1)
S(1)	6561(2)	-980(1)	3359(1)	22(1)
S(2)	8074(2)	1362(1)	2772(1)	23(1)
S(3)	11571(2)	-155(1)	3933(1)	20(1)
S(4)	12364(3)	3150(1)	5181(1)	29(1)
S(5)	16512(2)	3385(1)	6964(1)	27(1)
S(6)	14267(2)	6228(2)	7444(1)	26(1)
S(7)	19187(2)	6183(2)	7438(1)	24(1)
N(1)	3007(10)	1169(6)	2455(5)	39(2)
O(1)	2751(19)	-1466(9)	1503(7)	95(3)
C(1)	2482(16)	429(10)	1369(7)	56(2)
C(2)	3294(18)	-766(10)	1002(7)	60(3)
C(3)	2730(20)	-1491(13)	-121(8)	88(4)
N(2)	-1316(11)	-3556(7)	2480(5)	47(2)
O(2)	320(30)	-3645(16)	793(14)	75(4)
C(4)	-2280(20)	-4014(14)	1461(12)	64(4)
C(5)	-1530(30)	-3382(16)	864(13)	71(4)
C(6)	-2700(30)	-3848(19)	-188(15)	88(5)
O(2')	-2910(80)	-5060(40)	400(40)	108(14)
C(4')	-1030(60)	-3440(40)	1570(30)	57(9)
C(5')	-2820(60)	-3490(40)	860(30)	53(9)
C(6')	-2560(70)	-3110(50)	20(40)	67(11)
O(2A)	-1490(50)	-2140(30)	1260(20)	70(8)

Table 3. Bond lengths [Å] and angles [°] for $[C_3H_{10}NO]_2[Sb_4S_7]$.

Sb(1)-S(3)	2.4211(16)	Sb(1)-S(1)	2.5152(18)
Sb(1)-S(2)	2.5360(16)	Sb(2)-S(4)	2.4223(17)
Sb(2)-S(1)#1	2.4726(16)	Sb(2)-S(5)	2.658(2)
Sb(2)-S(3)	2.781(2)	Sb(3)-S(5)	2.3969(16)
Sb(3)-S(6)	2.4575(18)	Sb(3)-S(7)	2.5773(19)
Sb(4)-S(7)	2.4232(17)	Sb(4)-S(2)#2	2.4570(17)
Sb(4)-S(6)#3	2.4694(17)	S(1)-Sb(2)#1	2.4726(16)
S(2)-Sb(4)#2	2.4570(17)	S(6)-Sb(4)#4	2.4694(17)
N(1)-C(1)	1.457(11)	O(1)-C(2)	1.383(14)
C(1)-C(2)	1.480(14)	C(2)-C(3)	1.501(14)
N(2)-C(4)	1.418(16)	N(2)-C(4')	1.43(4)
O(2)-C(5)	1.35(2)	C(4)-C(5)	1.49(2)
C(5)-C(6)	1.51(2)	O(2')-C(5')	1.71(6)
C(4')-C(5')	1.49(6)	C(5')-C(6')	1.50(6)
S(3)-Sb(1)-S(1)	90.42(6)	S(3)-Sb(1)-S(2)	97.10(6)
S(1)-Sb(1)-S(2)	84.80(6)	S(4)-Sb(2)-S(1)#1	109.23(6)
S(4)-Sb(2)-S(5)	88.41(6)	S(1)#1-Sb(2)-S(5)	81.70(6)
S(4)-Sb(2)-S(3)	87.67(5)	S(1)#1-Sb(2)-S(3)	87.76(5)
S(5)-Sb(2)-S(3)	166.86(5)	S(5)-Sb(3)-S(6)	97.61(6)
S(5)-Sb(3)-S(7)	90.48(6)	S(6)-Sb(3)-S(7)	86.54(6)
S(7)-Sb(4)-S(2)#2	94.37(6)	S(7)-Sb(4)-S(6)#3	93.32(6)
S(2)#2-Sb(4)-S(6)#3	89.54(6)	Sb(2)#1-S(1)-Sb(1)	104.14(6)
Sb(4)#2-S(2)-Sb(1)	95.68(6)	Sb(1)-S(3)-Sb(2)	98.05(6)
Sb(3)-S(5)-Sb(2)	92.25(6)	Sb(3)-S(6)-Sb(4)#4	103.60(6)
Sb(4)-S(7)-Sb(3)	105.61(6)	N(1)-C(1)-C(2)	114.9(8)
O(1)-C(2)-C(1)	111.1(10)	O(1)-C(2)-C(3)	109.2(11)
C(1)-C(2)-C(3)	113.0(9)	C(4)-N(2)-C(4')	43.3(18)
N(2)-C(4)-C(5)	113.3(13)	O(2)-C(5)-C(4)	107.0(15)
O(2)-C(5)-C(6)	109.0(16)	C(4)-C(5)-C(6)	110.7(15)
N(2)-C(4')-C(5')	116(4)	C(4')-C(5')-C(6')	117(4)
C(4')-C(5')-O(2')	88(3)	C(6')-C(5')-O(2')	108(4)

Symmetry transformations used to generate equivalent atoms:
#1 -x+2,-y,-z+1 #2 -x+3,-y+1,-z+1 #3 x+1,y,z
#4 x-1,y,z

Table 4. Anisotropic displacement parameters ($Å^2 x\ 10^3$) for $[C_3H_{10}NO]_2[Sb_4S_7]$. The anisotropic displacement factor exponent takes the form: $-2\pi^2[\ h^2\ a^{*2}U_{11} + ...\ + 2\ h\ k\ a^*\ b^*\ U_{12}\ ]$.

	U_{11}	U_{22}	U_{33}	U_{23}	U_{13}	U_{12}
Sb(1)	13(1)	16(1)	24(1)	11(1)	3(1)	2(1)
Sb(2)	15(1)	18(1)	27(1)	10(1)	7(1)	1(1)
Sb(3)	16(1)	19(1)	24(1)	12(1)	4(1)	3(1)
Sb(4)	13(1)	19(1)	21(1)	9(1)	2(1)	1(1)
S(1)	21(1)	19(1)	25(1)	11(1)	-1(1)	-4(1)
S(2)	25(1)	18(1)	28(1)	13(1)	-1(1)	-1(1)
S(3)	15(1)	20(1)	25(1)	9(1)	2(1)	4(1)
S(4)	30(1)	21(1)	34(1)	15(1)	-8(1)	1(1)
S(5)	27(1)	19(1)	35(1)	16(1)	-11(1)	-5(1)
S(6)	17(1)	29(1)	27(1)	8(1)	1(1)	10(1)
S(7)	16(1)	30(1)	26(1)	13(1)	1(1)	-7(1)
N(1)	41(4)	37(3)	38(3)	13(3)	12(3)	-2(3)
O(1)	134(10)	79(6)	72(6)	32(5)	10(6)	8(6)
C(1)	55(6)	72(6)	43(5)	25(5)	6(4)	16(5)
C(2)	72(7)	63(6)	39(5)	13(4)	7(5)	13(5)
C(3)	109(11)	95(9)	38(5)	4(6)	7(6)	33(8)
N(2)	48(4)	70(5)	44(4)	37(4)	22(3)	33(4)

Table 5. Hydrogen coordinates (x 10^4) and isotropic displacement parameters (Å^{2}x 10^3) for $[C_3H_{10}NO]_2[Sb_4S_7]$.

	x	y	z	U(eq)
H(1N1)	2490	1877	2613	59
H(2N1)	4290	1315	2621	59
H(3N1)	2563	767	2795	59
H(1O1)	2052	-1093	1906	143
H(1A)	2912	896	1009	67
H(1B)	1081	282	1200	67
H(2)	4708	-603	1154	73
H(3A)	3266	-2263	-314	132
H(3B)	3216	-1041	-473	132
H(3C)	1343	-1633	-294	132
H(2A)	-1817	-3967	2798	71
H(2B)	-1463	-2764	2792	71
H(2C)	-62	-3651	2488	71
H(2D)	-2042	-4256	2323	71
H(2E)	-1910	-2929	2851	71
H(2F)	-175	-3559	2832	71
H(1O2)	864	-3183	596	112
H(4A)	-3650	-3921	1459	77
H(4B)	-2146	-4883	1133	77
H(5A)	-1560	-2494	1213	85
H(6A)	-2194	-3427	-558	132
H(6B)	-4024	-3702	-143	132
H(6C)	-2615	-4712	-533	132
H(2')	-3415	-5297	775	163
H(4C)	-271	-4083	1208	69
H(4D)	-264	-2661	1756	69
H(5B)	-3904	-3155	1205	64
H(6D)	-3798	-3184	-386	100
H(6E)	-1726	-3631	-397	100
H(6F)	-1995	-2276	298	100

7.14 Messprotokoll für die Verbindung $[C_4H_{13}N_3]_3[V_5O_{11}]$

Table 1. Crystal data and structure refinement for $[C_4H_{13}N_3]_3[V_5O_{11}]$.

Identification code	$[C_4H_{13}N_3]_3[V_5O_{11}]$ (RK711)
Empirical formula	$C_{12}H_{39}N_9O_{11}V_5$
Formula weight	740.22 g/mol
Temperature	293(2) K
Wavelength	0.71073 Å
Crystal system	Hexagonal
Space group	$P6_3$
Unit cell dimensions	a = 18.8920(9) Å
	c = 13.0938(6) Å
Volume	4047.2(3) $Å^3$
Z	6
Density (calculated)	1.822 Mg/m^3
Absorption coefficient	1.734 mm^{-1}
F(000)	2262
Crystal size	0.4 x 0.3 x 0.25 mm^3
Theta range for data collection	2.49 to 27.96°.
Index ranges	-24<=h<=24, -24<=k<=24, -17<=l<=17
Reflections collected	38927
Independent reflections	6468 [R(int) = 0.0339]
Completeness to theta = 27.96°	99.4 %
Refinement method	Full-matrix least-squares on F^2
Data / restraints / parameters	6468 / 1 / 336
Goodness-of-fit on F^2	1.043
Final R indices [I>2sigma(I)]	R1 = 0.0255, wR2 = 0.0616
R indices (all data)	R1 = 0.0311, wR2 = 0.0641
Absolute structure parameter	0.00(5)
Extinction coefficient	0.0021(2)
Largest diff. peak and hole	0.343 and -0.455 $e.Å^{-3}$

Table 2. Atomic coordinates (x 10^4) and equivalent isotropic displacement parameters ($Å^2$x 10^3) for $[C_4H_{13}N_3]_3[V_5O_{11}]$ U(eq) is defined as one third of the trace of the orthogonalized U_{ij} tensor.

	x	y	z	U(eq)
V(1)	3422(1)	11(1)	4835(1)	8(1)
V(2)	3290(1)	18(1)	7735(1)	8(1)
V(3)	3400(1)	1587(1)	6389(1)	10(1)
V(4)	4877(1)	-46(1)	6305(1)	10(1)
V(5)	1764(1)	-1516(1)	6138(1)	11(1)
O(1)	3378(1)	197(2)	3599(2)	23(1)
O(2)	3329(1)	-135(1)	8988(2)	19(1)
O(3)	2568(1)	1625(1)	6244(2)	25(1)
O(4)	5766(1)	772(1)	6395(2)	24(1)
O(5)	1694(1)	-2405(1)	6262(2)	25(1)
O(6)	3268(1)	687(1)	5543(2)	19(1)
O(7)	4368(1)	103(1)	5083(2)	15(1)
O(8)	2645(1)	-966(1)	5132(2)	20(1)
O(9)	3191(1)	887(1)	7589(2)	17(1)
O(10)	4193(1)	199(1)	7173(2)	20(1)
O(11)	2481(1)	-855(1)	7233(2)	21(1)
C(1)	4617(2)	2625(2)	8005(2)	25(1)
C(2)	5225(2)	2594(2)	7274(2)	23(1)
C(3)	5149(2)	2146(2)	5489(2)	20(1)
C(4)	4875(2)	2678(2)	4943(3)	25(1)
C(5)	4501(2)	-1488(2)	7788(3)	27(1)
C(6)	3677(2)	-1746(2)	7298(2)	22(1)
C(7)	3973(2)	-1893(2)	5513(2)	28(1)
C(8)	4615(2)	-1343(2)	4751(2)	27(1)
C(9)	806(2)	-1085(2)	7603(2)	27(1)
C(10)	912(2)	-486(2)	6767(2)	29(1)
C(11)	1242(2)	-426(2)	4938(2)	24(1)
C(12)	626(2)	-1287(2)	4614(3)	29(1)
N(1)	3967(1)	2627(1)	7397(2)	20(1)
N(2)	4776(1)	1941(1)	6513(2)	15(1)
N(3)	3978(1)	2288(1)	5001(2)	24(1)
N(4)	5028(1)	-597(2)	7691(2)	21(1)
N(5)	3815(1)	-1410(1)	6258(2)	16(1)
N(6)	5298(1)	-679(2)	5342(2)	18(1)
N(7)	741(1)	-1824(1)	7140(2)	18(1)
N(8)	1496(1)	-447(1)	5994(2)	14(1)
N(9)	965(1)	-1830(1)	4824(2)	23(1)

Table 3. Bond lengths [Å] and angles [°] for $[C_4H_{13}N_3]_3[V_5O_{11}]$.

V(1)-O(1)	1.667(3)	V(1)-O(6)	1.7171(19)
V(1)-O(8)	1.7319(19)	V(1)-O(7)	1.7385(18)
V(2)-O(2)	1.674(3)	V(2)-O(11)	1.7222(19)
V(2)-O(10)	1.728(2)	V(2)-O(9)	1.7514(18)
V(3)-O(3)	1.6208(19)	V(3)-O(6)	1.9365(19)
V(3)-O(9)	1.963(2)	V(3)-N(1)	2.156(2)
V(3)-N(3)	2.192(2)	V(3)-N(2)	2.343(2)
V(4)-O(4)	1.622(2)	V(4)-O(10)	1.943(2)
V(4)-O(7)	1.958(2)	V(4)-N(6)	2.145(2)
V(4)-N(4)	2.181(2)	V(4)-N(5)	2.345(2)
V(5)-O(5)	1.625(2)	V(5)-O(11)	1.9385(19)
V(5)-O(8)	1.964(2)	V(5)-N(7)	2.162(2)
V(5)-N(9)	2.168(2)	V(5)-N(8)	2.322(2)
C(1)-N(1)	1.466(4)	C(1)-C(2)	1.518(4)
C(2)-N(2)	1.480(3)	C(3)-N(2)	1.472(3)
C(3)-C(4)	1.520(4)	C(4)-N(3)	1.473(4)
C(5)-N(4)	1.471(4)	C(5)-C(6)	1.520(4)
C(6)-N(5)	1.470(3)	C(7)-N(5)	1.464(4)
C(7)-C(8)	1.513(4)	C(8)-N(6)	1.490(4)
C(9)-N(7)	1.469(4)	C(9)-C(10)	1.513(4)
C(10)-N(8)	1.472(3)	C(11)-N(8)	1.470(3)
C(11)-C(12)	1.513(4)	C(12)-N(9)	1.480(4)
O(1)-V(1)-O(6)	108.79(11)	O(1)-V(1)-O(8)	109.74(11)
O(6)-V(1)-O(8)	107.68(9)	O(1)-V(1)-O(7)	108.48(10)
O(6)-V(1)-O(7)	111.89(9)	O(8)-V(1)-O(7)	110.25(9)
O(2)-V(2)-O(11)	107.64(10)	O(2)-V(2)-O(10)	109.07(10)
O(11)-V(2)-O(10)	109.99(10)	O(2)-V(2)-O(9)	107.63(11)
O(11)-V(2)-O(9)	113.36(9)	O(10)-V(2)-O(9)	109.04(9)
O(3)-V(3)-O(6)	105.63(11)	O(3)-V(3)-O(9)	104.51(12)
O(6)-V(3)-O(9)	88.43(9)	O(3)-V(3)-N(1)	94.65(11)
O(6)-V(3)-N(1)	159.65(9)	O(9)-V(3)-N(1)	87.98(9)
O(3)-V(3)-N(3)	94.42(12)	O(6)-V(3)-N(3)	82.12(9)
O(9)-V(3)-N(3)	160.56(8)	N(1)-V(3)-N(3)	94.98(10)
O(3)-V(3)-N(2)	163.24(10)	O(6)-V(3)-N(2)	85.92(8)
O(9)-V(3)-N(2)	87.62(8)	N(1)-V(3)-N(2)	73.93(8)
N(3)-V(3)-N(2)	74.84(8)	O(4)-V(4)-O(10)	103.03(11)
O(4)-V(4)-O(7)	105.69(11)	O(10)-V(4)-O(7)	90.63(9)
O(4)-V(4)-N(6)	94.47(11)	O(10)-V(4)-N(6)	162.33(9)
O(7)-V(4)-N(6)	86.87(9)	O(4)-V(4)-N(4)	94.26(12)
O(10)-V(4)-N(4)	83.57(10)	O(7)-V(4)-N(4)	160.01(8)
N(6)-V(4)-N(4)	92.86(10)	O(4)-V(4)-N(5)	163.56(10)
O(10)-V(4)-N(5)	88.36(8)O(7)-V(4)-N(5)		85.71(8)
N(6)-V(4)-N(5)	74.02(9)	N(4)-V(4)-N(5)	75.04(9)

O(5)-V(5)-O(11)	105.18(12)	O(5)-V(5)-O(8)	102.89(12)
O(11)-V(5)-O(8)	91.19(8)	O(5)-V(5)-N(7)	93.58(11)
O(11)-V(5)-N(7)	88.14(9)	O(8)-V(5)-N(7)	163.09(8)
O(5)-V(5)-N(9)	96.41(12)	O(11)-V(5)-N(9)	158.41(9)
O(8)-V(5)-N(9)	84.39(9)	N(7)-V(5)-N(9)	90.05(9)
O(5)-V(5)-N(8)	165.08(9)	O(11)-V(5)-N(8)	83.41(8)
O(8)-V(5)-N(8)	88.88(8)	N(7)-V(5)-N(8)	74.25(8)
N(9)-V(5)-N(8)	75.40(8)	V(1)-O(6)-V(3)	164.99(12)
V(1)-O(7)-V(4)	133.82(11)	V(1)-O(8)-V(5)	139.15(11)
V(2)-O(9)-V(3)	129.65(12)	V(2)-O(10)-V(4)	155.61(13)
V(2)-O(11)-V(5)	154.00(13)	N(1)-C(1)-C(2)	108.0(2)
N(2)-C(2)-C(1)	109.2(2)	N(2)-C(3)-C(4)	109.1(2)
N(3)-C(4)-C(3)	109.3(2)	N(4)-C(5)-C(6)	109.3(2)
N(5)-C(6)-C(5)	108.7(2)	N(5)-C(7)-C(8)	110.8(2)
N(6)-C(8)-C(7)	107.2(2)	N(7)-C(9)-C(10)	109.2(2)
N(8)-C(10)-C(9)	110.6(2)	N(8)-C(11)-C(12)	108.7(2)
N(9)-C(12)-C(11)	109.0(2)	C(1)-N(1)-V(3)	111.43(17)
C(3)-N(2)-C(2)	113.3(2)	C(3)-N(2)-V(3)	109.13(16)
C(2)-N(2)-V(3)	112.09(16)	C(4)-N(3)-V(3)	116.49(19)
C(5)-N(4)-V(4)	116.23(19)	C(7)-N(5)-C(6)	113.3(2)
C(7)-N(5)-V(4)	111.91(17)	C(6)-N(5)-V(4)	108.64(16)
C(8)-N(6)-V(4)	111.58(17)	C(9)-N(7)-V(5)	110.83(16)
C(11)-N(8)-C(10)	113.7(2)	C(11)-N(8)-V(5)	108.40(15)
C(10)-N(8)-V(5)	112.58(16)	C(12)-N(9)-V(5)	116.20(18)

Table 4. Anisotropic displacement parameters ($Å^2$x 10^3) for $[C_4H_{13}N_3]_3[V_5O_{11}]$. The anisotropic displacement factor exponent takes the form: $-2\pi^2[h^2 a^{*2}U_{11} + ... + 2 h k a^* b^* U_{12}]$.

	U_{11}	U_{22}	U_{33}	U_{23}	U_{13}	U_{12}
V(1)	8(1)	9(1)	8(1)	-1(1)	0(1)	5(1)
V(2)	9(1)	8(1)	8(1)	-1(1)	-1(1)	4(1)
V(3)	11(1)	8(1)	14(1)	-1(1)	1(1)	6(1)
V(4)	6(1)	10(1)	13(1)	1(1)	0(1)	4(1)
V(5)	9(1)	6(1)	15(1)	-2(1)	-2(1)	2(1)
O(1)	25(1)	32(1)	14(1)	1(1)	-3(1)	18(1)
O(2)	22(1)	17(1)	12(1)	2(1)	-2(1)	6(1)
O(3)	21(1)	30(1)	34(1)	-3(1)	-1(1)	20(1)
O(4)	14(1)	20(1)	28(1)	-1(1)	-4(1)	1(1)
O(5)	27(1)	12(1)	35(1)	-2(1)	-5(1)	9(1)
O(6)	18(1)	15(1)	24(1)	-7(1)	0(1)	8(1)
O(7)	14(1)	17(1)	15(1)	2(1)	-1(1)	8(1)
O(8)	15(1)	13(1)	30(1)	-2(1)	7(1)	5(1)
O(9)	23(1)	14(1)	18(1)	6(1)	10(1)	12(1)
O(10)	20(1)	22(1)	23(1)	3(1)	7(1)	14(1)
O(11)	19(1)	15(1)	25(1)	-7(1)	-12(1)	6(1)
C(1)	21(1)	28(2)	21(1)	-9(1)	0(1)	9(1)
C(2)	16(1)	24(1)	23(1)	-6(1)	-5(1)	4(1)
C(3)	18(1)	21(1)	23(1)	3(1)	8(1)	11(1)
C(4)	27(1)	24(1)	22(1)	9(1)	9(1)	11(1)
C(5)	30(2)	29(2)	25(1)	12(1)	3(1)	18(1)
C(6)	21(1)	19(1)	26(1)	12(1)	8(1)	9(1)
C(7)	33(2)	16(1)	29(1)	-5(1)	-2(1)	8(1)
C(8)	40(2)	27(1)	20(1)	-6(1)	-2(1)	23(1)
C(9)	32(2)	33(2)	16(1)	-1(1)	12(1)	17(1)
C(10)	38(2)	32(1)	30(1)	5(1)	12(1)	27(1)
C(11)	26(1)	30(1)	20(1)	11(1)	0(1)	17(1)
C(12)	23(1)	39(2)	24(2)	2(1)	-12(1)	14(1)
N(1)	21(1)	12(1)	26(1)	-5(1)	4(1)	8(1)
N(2)	14(1)	14(1)	18(1)	3(1)	4(1)	6(1)
N(3)	30(1)	25(1)	21(1)	8(1)	4(1)	17(1)
N(4)	21(1)	27(1)	15(1)	1(1)	-4(1)	12(1)
N(5)	11(1)	15(1)	22(1)	3(1)	0(1)	7(1)
N(6)	20(1)	22(1)	19(1)	3(1)	4(1)	15(1)
N(7)	15(1)	19(1)	15(1)	7(1)	2(1)	5(1)
N(8)	10(1)	12(1)	15(1)	3(1)	2(1)	4(1)
N(9)	22(1)	22(1)	17(1)	-7(1)	-8(1)	7(1)

Table 5. Hydrogen coordinates (x 10^4) and isotropic displacement parameters ($Å^2$x 10^3) for $[C_4H_{13}N_3]_3[V_5O_{11}]$.

	x	y	z	U(eq)
H(1A)	4390	2154	8454	30
H(1B)	4887	3115	8420	30
H(2A)	5537	3116	6931	28
H(2B)	5603	2485	7650	28
H(3A)	4981	1649	5102	24
H(3B)	5739	2436	5548	24
H(4A)	5125	3214	5260	30
H(4B)	5046	2748	4234	30
H(5A)	4426	-1641	8503	32
H(5B)	4755	-1762	7453	32
H(6A)	3351	-2338	7274	26
H(6B)	3384	-1543	7697	26
H(7A)	3470	-2259	5156	33
H(7B)	4157	-2223	5866	33
H(8A)	4810	-1650	4365	32
H(8B)	4388	-1114	4277	32
H(9A)	1271	-838	8063	32
H(9B)	317	-1226	7994	32
H(10A)	389	-656	6447	35
H(10B)	1109	52	7061	35
H(11A)	1713	-204	4488	29
H(11B)	1000	-80	4896	29
H(12A)	120	-1476	4989	35
H(12B)	509	-1298	3891	35
H(1N1)	4177	3089	7026	24
H(2N2)	3586	2619	7818	24
H(2)	4789	1490	6730	18
H(1N3)	3764	1951	4461	28
H(2N3)	3843	2680	4938	28
H(4C)	5552	-478	7725	25
H(4D)	4936	-360	8231	25
H(5)	3353	-1411	6059	19
H(1N6)	5676	-321	4905	22
H(2N6)	5537	-894	5728	22
H(1N7)	272	-2088	6782	21
H(2N7)	726	-2161	7635	21
H(8)	1976	25	6101	16
H(1N9)	1244	-1833	4268	27
H(2N9)	545	-2341	4910	27

8 Publikationsliste

8.1 Publikationen

R. Kiebach, W. Bensch, R.-D. Hoffmann, R. Pöttgen, S*olvothermal Syntheses and Characterisation of the New Iron Thioantimonates(III) [Fe($C_6H_{18}N_4$)]FeSbS_4 and [Fe($C_4H_{13}N_3$)2]$Fe_2Sb_4S_{10}$ containing Fe(II) and Fe(III) and the protein-analogous [2Fe(III)-2S]$^{2+}$-Cluster, Z. Anorg. Allg. Chem.*, 629, 532-538, **2003**.

M. Schaefer, R. Stähler, W.-R. Kiebach, C. Näther, W. Bensch, *Four new Thioantimonates(III) with the general formula [TM(tren)]Sb_4S_7 (TM = Mn, Fe, Co, Zn) synthesised under solvothermal conditions, Z. Anorg. Allg. Chem.*, 630, 1816-1822, **2004.**

R. Kiebach, F. Studt, C. Näther, W. Bensch, *[Ni($C_4H_{13}N_3$)$_2$]$_3$(Sb_3S_6)$_2$: the first structure containing isolated heterocyclic [Sb_3S_6]$^{3-}$ anions, Eur. J. Inorg. Chem.*, 2553-2556, **2004.**

V. Spetzler, R. Kiebach, C. Näther, W. Bensch, *Two novel Thioantimonates(III) with the Same Stoichiometric Sb:S Ratio but Different Crystal Structures: Solvothermal Synthesis, Crystal Structures, Thermal Stability and Spectroscopy of ($C_6N_3H_{17}$)Sb_6S_{10} and ($C_7N_2H_{13}$)$_3Sb_9S_{15}$, Z. Anorg. Allg. Chem.*, 630, 2398-2404, **2004.**

R. Kiebach, C. Näther, W. Bensch, *Solvothermal Synthesis of [$C_6H_{17}N_3$]$Sb_{10}S_{16}$: A New Thioantimonate(III) with an in-situ Formed Organic Amine Cation, Z. Naturforsch.*, 59b, 1314 - 1319, **2004.**

R. Kiebach, M. Schaefer, F. Porsch, W. Bensch, *In-situ Energy Dispersive X-ray Diffraction Studies of the Crystallization of (1,2-DAPH2)$_2$Ge$_9$(OH)$_4$O$_{18}$ · 2 H$_2$O under Solvothermal Conditions, Z. Anorg. Allg. Chem.*, 631, 369-374, **2005.**

Michailovski, J.-D. Grunwaldt, A. Baiker, R.Kiebach, W. Bensch, G. R. Patzke, *Solvothermal formation of MoO_3 fibers studied by complementary in situ-EXAFS/EDXRD techniques, Angew. Chemie*, 117, 5787-5792, **2005.**

A. Puls, C. Näther, R. Kiebach, W.Bensch, *The structure directing effectof organic cations onto the crystal structures of layered thioantimonates(III): Solvothermal synthesis and crystal structures of five new compounds containing the $[Sb_8S_{13}]^{2-}$−anion, J. Solid State Science,* **2005***,* submitted.

R. Kiebach, R. Warratz, W. Bensch, *$[Fe^{(II)}(C_6H_{14}N_2)_2][Sb_3S_5]_2$ – From Microporous Thioantimonates Networks to Pillared Systems*, *J. Am. Chem. Soc.*, **2006**, in preparation.

R. Kiebach, C. Näther, C.P. Sebastian, B.D. Mosel, R. Pöttgen, W. Bensch, *$[C_6H_{21}N_4][Sb_9S_{14}O]$: The first non centro-symetric open Sb-S framework containing the new $[SbS_2O]$ building unit, J. Eur. Inorg. Chem.*, **2005**, submitted.

R. Kiebach, C. Näther, W. Bensch, *$[trenH_3]_2[tren]_{0.33}[Sb_6V_{15}O_{42}]\cdot xH_2O$ (3<x<5) – The Antimony Analogoue to the Single Molecular Magnet $K_6[As_6V_{15}O_{42}(H_2O)]\cdot 8H_2O$, Inorg. Chem.*, **2006**, in preparation.

R. Kiebach, C. Näther, W. Bensch, *$[C_6H_{17}N_3]_4[Sb_4V_{16}O_{42}]\cdot 2H_2O$ and $[NH_4]_4[Sb_8V_{14}O_{42}]\cdot 2H_2O$ – The first isolated Sb derivates of the $[V_{18}O_{42}]$ family*, *Solid State Science*, **2005**, submitted.

R. Kiebach, A. Griebe, C. Näther, W. Bensch, *$[C_3H_{10}NO]_2[Sb_4S_7]$: Solvothermal syntheses, crystal structures and properties of the first thioantimonates containing aminoalcohols as structure directors*, *Solid State Scienes*, **2005**, accepted.

R. Kiebach, Nicole P., M.-E. Ordolff, F. Studt, W. Bensch, *A Combined in-situ EDXRD/EXAFS Investigation of the Crystal Growth of [Co($C_6H_{18}N_4$)][Sb_2S_4] under Solvothermal Conditions: Two Different Reaction Pathways Leading to the Same Product, Chem. Mater.*, **2005**, accepted.

A. Lafond, I. Sandu, C. Guillot-Deudon, R. Kiebach , W. Bensch, A. Meerschaut, *Solvothermal synthesis and Rietveld structure analysis of two new sodium rare earth titanates* $Na_{\frac{1}{2}}Y_{\frac{1}{2}}TiO3$ *and* $Na_{\frac{2}{3}}Ce_{\frac{1}{2}}TiO_3$, *J. Solid State Science*, **2005**, submitted.

Michailovski, J.-D. Grunwaldt, A. Baiker, R.Kiebach, W. Bensch, G. R. Patzke, *Solvothermal formation of* WO_3 *studied by complementary in situ-EXAFS/EDXRD techniques*, *Chem. Mater.*, **2006**, in preparation.

M. Behrens, R. Kiebach, W. Bensch, *Synthesis and Properties of Thin Films of* Cr_3Se_4 *crystallising from Cr/Se-Multilayers, Inorg. Chem.*, **2005**, submitted.

M. Behrens, O. Riemenschneider, R. Kiebach, W. Bensch, *Lithium Intercalation into Monoclinic* Cr_4TiSe_8*: Synthesis, Structural Phase Transition and Properties of* $Li_xCr_4TiSe_8$ *(x = 0. 1 – 2.8), Chem. Europ. J.*, **2005**, submitted.

8.2 Tagungsbeiträge

Solvothermal Synthesis of $Mn_2Sb(III)_2S_5[C_4H_9(NH_2)_2]$: Time Resolved Crystallisation Studies using EDXRD, R. Kiebach, L. Engelke, M. Schaefer, R. Stähler, W. Bensch, User Meeting at DESY, Hamburg **2001**.

[Fe(II)(tren)]Fe(III)SbS_4]: Ein neues Thioantmonat mit gemischvaletem Eisen und proteinanalogen [2Fe(III)2S]$^{2+}$-Clustern, R. Kiebach, C. Näther, W. Bensch, GDCh Festkörper-Tagung, **2002**, Dresden. Z. Anorg. Allg. Chem. 2002, 628, 2176.

$[Ni(C_4H_{13}N_4)_2]_3(Sb_3S_6)_2$: Das erste Thioantimonat(III) mit isoliertem cyclischem $[Sb_3S_6]^{3-}$-Anion, R. Kiebach, F. Studt, C. Näther, W. Bensch, 11. Jahrestagung der

Deutschen Gesellschaft für Kristallographie, **2003**, Berlin. Z. Kristallogr. Suppl. 20, 138, 2003.

$[Fe(C_6H_{18}N_4)]FeSbS_4$: Solvothermale Synthese und Charakterisierung eines Thioantmonats(III) mit gemischvalentem Eisen und Protein-analogen $[2Fe(III)\text{-}2S]^{2+}$-Clustern, R. Kiebach, W. Bensch, Doktorandenseminar Rothenberge, 13.-15.11.**2002**.

An in-situ-EDXRD study of the conversion of $[Ni(dien)_2]_2Sb_4S_9$ containing mixed-valent Sb(III,V) to $[Ni(dien)_2]Sb_4S_7 \cdot H2O$ composed of Sb(III), M. Schaefer, R. Kiebach, R. Stähler, W. Bensch, User Meeting at DESY, Hamburg **2003**.

Solvothermal Synthesis and Structure of the new Thioantimonate $[C_6H_{17}N_3]Sb_{10}S_{16}$, R. Kiebach, W. Bensch, 9th ECSSC **2003**, Stuttgart, Sep. 3.-6. P064.

$[C_7H_{13}N_2]_3[Sb_9S_{15}]$: Synthese, Kristallstruktur und Charakterisierung eines neuen Thioantimonats, R. Kiebach, C. Näther, S. Wriedt, W. Bensch, 12. Jahrestagung der Deutschen Gesellschaft für Kristallographie, **2004**, Jena, Z. Kristallogr. Suppl. 21, 167, 2004.

In-situ Energy-Dispersive X-ray Diffraction Studies of the Crystallisation of $(1,2\text{-}DAPH_2)_2Ge_9(OH)_4O_{18} \cdot 2\,H_2O$ Under Solvothermal Conditions, R. Kiebach, M. Schaefer, F. Porsch, W. Bensch, DESY, Annual Report **2004.**

$[Fe(II)(C_6H_{14}N_2)_2][Sb(III)_6S_{10}]$: Ein Thioantimonat mit über $Fe(II)(C_6H_{14}N_2)_2^{2+}$-Kationen verknüpften Sb-S-Schichten, R. Kiebach, W. Bensch, 12. Vortragstagung FG Festkörperchemie und Materialforschung Marburg, 13.-15. September **2004.**

$[C_6H_{21}N_4][Sb_9S_{14}O]$: Das erste Oxosulfid von Antimon mit einem organischen Templat, R. Kiebach, W. Bensch, 7. Norddeutsches Doktorandenkolloquium, Hamburg, **2004**.

Combined In-situ Energy-Dispersive X-ray Diffraction and In-situ EXAFS Studies of the Crystallisation of $[Co(tren)][Sb_2S_4]$ Under Solvothermal Conditions, R. Kiebach, M. E. Ordolff, N. Pienack, W. Bensch, DESY, Annual Report **2004**.

$[C_6H_{21}N_4][Sb_9S_{14}O]$: Ein neues Antimon-Oxisulfid mit einem organischen Templat, R. Kiebach, W. Bensch, 13. Jahrestagung der DGK, Köln **2005**.

Kombinierte in-situ EDXRD/EXAFS Untersuchungen zum Kristallwachstum von $[Co(tren)]Sb_2S_4$ unter solvothermalen Bedingungen, R. Kiebach, W. Bensch, 7. Norddeutsches Doktorandenkolloquium, Warnemünde, **2005**.

Eidesstattliche Erklärung

Hiermit versichere ich an Eides statt, dass ich die vorliegende Arbeit selbständig – abgesehen von der Beratung durch meinen wissenschaftlichen Lehrer – und nur unter Verwendung der angegebenen Hilfsmittel angefertigt habe. Die Dissertation wird ausschließlich an dieser Stelle zur Promotion vorgelegt.

Kiel, Dezember 2005